Aeroelastic instabilities of an airfoil in transitional flow regimes

Diogo Sabino

THÈSE

En vue de l'obtention du

DOCTORAT DE L'UNIVERSITÉ DE TOULOUSE

Délivré par : *l'Université Toulouse 3 Paul Sabatier (UT3 Paul Sabatier)*

Présentée et soutenue le *07/06/2022* **par :**

Diogo Ferreira Sabino

Aeroelastic instabilities of an airfoil in transitional flow regimes

---

JURY

Ardeshir Hanifi	Docent, KTH Royal Institute of Technology	Rapporteur
Jean-Christophe Robinet	Professeur, Arts et Métiers ParisTech	Rapporteur
Stefania Cherubini	Professeure associée, Politecnico di Bari	Examinatrice
Paolo Luchini	Professeur émérite, Université de Salerne	Examinateur
Guilhem Michon	Professeur, ISAE-SUPAERO	Examinateur
François Charru	Professeur, UT3 Paul Sabatier	Examinateur
Vincent Mons	Ingénieur Chercheur, ONERA	Invité
Rémi Bourguet	Chercheur CNRS, IMFT	Invité
Olivier Marquet	Maître de Recherche, ONERA	Co-directeur de Thèse
David Fabre	Maître de Conférences, UT3 Paul Sabatier	Directeur de Thèse

---

École doctorale et spécialité :
MEGEP : Dynamique des fluides
Unité de Recherche :
Institut de Mécanique des Fluides de Toulouse (UMR 5502)
Directeur(s) de Thèse :
David Fabre et *Olivier Marquet*
Rapporteurs :
Ardeshir Hanifi et *Jean-Christophe Robinet*

Acknowledgements

I wish to express my gratitude to my supervisors, Olivier Marquet and David Fabre, for their dedication and willingness to help and guide me throughout the course of this research. In particular, I would like to thank them for their invaluable insights into the different problems studied in this thesis.

I would like to express my appreciation to all the members of the jury for the critical reading of this manuscript and examination of the results presented in it.

My appreciation is extended to the different colleagues that I met during this process at ONERA, as well as to all my friends in Portugal.

Finally, a special thanks goes to my family, whose support was truly inestimable.

Diogo Ferreira Sabino

Abstract

This thesis investigates aeroelastic instability phenomena arising in coupled fluid–structure interactions, considering the flow around a rigid airfoil mounted on a torsion spring. The focus is on the *laminar separation flutter* phenomenon, namely a self-sustained pitch oscillation detected experimentally on a NACA0012 airfoil in the transitional Reynolds number regime ($Re \in [10^4 - 10^5]$) at low incidences, characterised by the separation of an initially laminar boundary layer followed by its transition and subsequent reattachment. The main objective of this thesis is to explain this phenomenon in terms of instability concepts. For this, a combination of numerical approaches involving two- and three-dimensional Navier–Stokes simulations—the latter referred to as Direct Numerical Simulations (DNS)—along with linear stability analyses (LSA) around a mean flow or a periodic flow (Floquet analysis) is employed. A second objective is to numerically explore the different nonlinear regimes appearing in the low-to-moderate Reynolds number regime. The first part of this thesis is devoted to the characterisation of the fluid flow around the airfoil considering fixed incidences. Two-dimensional time-marching simulations are first employed, showing the emergence of high frequency vortex shedding oscillations for $Re \approx 8\,000$. A hydrodynamic stability analysis (Floquet) is then employed to characterise the transition to a three-dimensional flow and DNS is eventually used to characterise both instantaneous and averaged flow quantities at $Re = 50\,000$. An analysis of the mean forces exerted on a fixed-incidence wing allows to detect a negative aerodynamic stiffness (torque-to-incidence ratio) in the range $|\alpha| \lesssim 2^\circ$, indicating a static instability. The second part of this thesis is devoted to the characterisation of the primary instability of the coupled fluid–structure system using LSA around the mean and periodic flow fields. Considering the symmetrical equilibrium position $\alpha = 0^\circ$, the analyses show the presence of an unstable static mode, in accordance with the existence of a negative aerodynamic stiffness. In the third part of this thesis, the emergence of self-sustained flutter oscillations is investigated via two-dimensional aeroelastic simulations. The investigation shows that the system first transitions towards a pitch oscillation around the nonsymmetrical equilibrium position ($\alpha \neq 0^\circ$), with coexistence of chaotic and quasi-periodic solutions for the same structural parameters, and subsequently transitions towards a pitch oscillation around the symmetrical position ($\alpha = 0^\circ$) as the Reynolds number increases. In the last part of this thesis, an attempt is made to explain the destabilisation of the nonsymmetrical equilibrium positions leading to a quasi-periodic behaviour using LSA around the mean and periodic flow fields at fixed incidences. Even if these analyses are unable to predict an unstable eigenmode, we conclude that the inclusion of the Reynolds stress term in the mean flow perturbation dynamics has an important effect.

Keywords — Aeroelastic instabilities, transitional Reynolds number, laminar separation flutter, linear stability, Floquet analysis.

Résumé

Cette thèse porte sur l'étude de l'instabilité aéroélastique provenant de l'interaction fluide–structure, dans le cas d'une aile rigide montée sur un ressort en torsion. L'étude est centrée sur le phénomène de flottement dû à un décollement laminaire, et plus précisément sur les oscillations (en torsion) auto-entretenues détectées expérimentalement pour un profil NACA0012 à faible incidence, dans la gamme de nombre de Reynolds dits transitionnels ($Re \in [10^4 - 10^5]$), caractérisé par un décollement de la couche limite initialement laminaire, suivi d'une transition et d'un rattachement. L'objectif principal de cette thèse est d'expliquer ce phénomène en se basant sur des concepts d'instabilité. Pour ce faire, différentes approches numériques ont été conduites: des simulations numériques bidimensionnelles et des simulations numériques tridimensionnelles (DNS). Ces approches ont en suite servi de base à des analyses de stabilité linéaire (LSA) autour d'un champ moyen ou d'un champ périodique (analyse de Floquet). Le deuxième objectif vise à explorer les différents régimes non linéaires qui apparaissent dans cette gamme de Reynolds. La première partie de cette thèse est consacrée à la caractérisation de l'écoulement autour de l'aile pour des angles d'incidence fixes. Des simulations temporelles bidimensionnelles montrent l'apparition d'oscillations à haute fréquence associées à la separation tourbillonnaire en aval du profil à partir de $Re \approx 8\,000$. Une analyse de stabilité hydrodynamique (Floquet) est réalisée pour caractériser la transition vers un écoulement tridimensionnel. Des simulations tridimensionnelles sont ensuite réalisées pour $Re = 50\,000$ afin de caractériser l'écoulement instantané et moyenné. L'analyse des forces moyennes exercées sur l'aile à incidence fixe permettent de détecter une rigidité aérodynamique négative (rapport moment-incidence) pour la gamme $|\alpha| \lesssim 2°$, indiquant une instabilité aéroélastique statique. La deuxième partie de cette thèse concerne la caractérisation de l'instabilité primaire fluide–structure en utilisant une analyse LSA autour des champs moyen et périodique. En considérant la position d'équilibre symétrique $\alpha = 0°$, l'analyses montrent la présence d'un mode statique instable, en accord avec l'existence d'une rigidité aérodynamique négative. Dans une troisième partie, l'émergence de l'oscillation de flottement est étudiée via des simulations aéroélastiques bidimensionnelles. Cette investigation montre que l'apparition des oscillations se fait dans un premier temps autour d'une position d'équilibre non nulle ($\alpha \neq 0°$), où des solutions chaotiques et quasi-périodiques coexistent pour les mêmes paramètres structuraux, et évolue vers un régime où les oscillations se font autour de $\alpha = 0°$. La dernière partie de cette thèse essaie d'expliquer la déstabilisation des positions d'équilibre non nulles conduisant à un comportement quasi-périodique à l'aide d'analyses LSA autour des champs moyens et périodiques à incidence fixe. Même si ces analyses sont incapables de prédire un mode propre instable, nous concluons que l'inclusion du terme des contraintes de Reynolds dans la dynamique de perturbation de l'écoulement moyen a un effet important.

Mots-Clés — Instabilités aéroélastiques, nombres de Reynolds transitionnelles, flottement dû à un décollement laminaire, stabilité linéaire, analyse de Floquet.

Contents

Acknowledgements i
Abstract iii
Résumé v
Contents vii
List of figures xi
List of tables xix
Nomenclature xxiii

Introduction **1**

1 Problem description and numerical tools **17**
1.1 Incompressible flow model 17
1.1.1 Inertial and non-inertial reference frames 17
1.1.2 Inertial frame formulation 18
1.1.3 Space derivatives on the non-inertial frame 20
1.1.4 Time derivative on the non-inertial frame 20
1.1.5 Non-inertial frame formulation 21
1.2 Torsion rigid-body model 22
1.3 Fluid–structure formalism 25
1.3.1 Triple decomposition of the state variables 26
1.3.2 Response of the structure to a harmonic forcing 28
1.3.3 Quasi-steady equilibrium positions of the fluid–structure system 30
1.4 Linear stability analyses based on fast time scale dynamics 31
1.4.1 Equations governing a periodic flow 31
1.4.2 Linearised equations 32
1.4.3 Floquet FSI linear stability analysis 34
1.4.4 Mean flow FSI linear stability analysis: classical formulation 35
1.5 Linear stability analysis based on slow time scale dynamics 38
1.5.1 Equations governing the slow time scale dynamics 38
1.5.2 Mean flow FSI linear stability analysis: Reynolds stress formulation 40
1.6 Quasi-steady fluid approximation 42
1.7 Numerical discretisation 45
1.7.1 Boundary conditions on the numerical domain 45
1.7.2 Weak formulation 46

1.7.3 Mesh generation . . . 48
1.7.4 MPI implementation and domain decomposition . . . 50
1.7.5 Space discretisation: Finite Element Method . . . 50
1.7.6 Numerical stabilisations: Streamline Upwind/Petrov–Galerkin (SUPG) and grad-div . . . 53
1.7.7 Time discretisation of the three-dimensional Navier–Stokes equations . . . 55
1.7.8 Time discretisation of the two-dimensional FSI equations . . . 58
1.7.9 Modular approach for fluid–structure Jacobian inversion . . . 60
1.7.10 Time discretisation of the linearised two-dimensional FSI equations . . . 60
1.8 Preliminary results: numerical validation . . . 62
1.8.1 Mesh convergence . . . 62
1.8.2 Influence of the lateral boundary condition on the three-dimensional computations . . . 64
1.8.3 Influence of the SUPG and grad-div stabilisations . . . 64
1.8.4 Influence of the three-dimensional time discretisation parameters . . . 67

2 Flow around a fixed NACA0012 profile wing 71
2.1 Two-dimensional flow description . . . 71
2.1.1 Emergence of a vortex shedding at $\alpha = 0°$ . . . 71
2.1.2 Flow field description for $\alpha \geq 0°$ . . . 75
2.1.3 Characterisation of the base and mean aerodynamic efforts for $\alpha \geq 0°$ . . . 77
2.1.4 Characterisation of the aerodynamic stiffness at $\alpha = 0°$ . . . 81
2.1.5 Emergence of three-dimensional structures: hydrodynamic Floquet analysis . . . 84
2.2 Three-dimensional flow description: Direct Numerical Simulations . . . 88
2.2.1 Instantaneous flow description at $Re = 50\,000$ and $\alpha = 0°$ . . . 89
2.2.2 Spectral flow description at $Re = 50\,000$ and $\alpha = 0°$ . . . 94
2.2.3 Instantaneous and spectral flow descriptions at $Re = 50\,000$ and $\alpha > 0°$ . . . 97
2.2.4 Comparison between two- and three-dimensional results for $Re = 50\,000$ . . . 102
2.3 Decomposition of the pressure component on the mean aerodynamic moment . . . 104
2.3.1 Mathematical formulation . . . 104
2.3.2 Results for $\alpha = 0.5°$ and $\alpha = 1°$ . . . 106
2.3.3 Results for $\alpha = 1.5°$ and $\alpha = 2°$ . . . 110

3 Methods for mean flow FSI linear stability analyses 115
3.1 Introduction . . . 115
3.2 Methods for mean flow analyses in fluid–structure problems . . . 116
3.2.1 Method for computing the full eigenvalue spectrum . . . 117
3.2.2 Definition of the fluid and solid transfer functions . . . 119
3.2.3 Newton method for a reduced-size nonlinear eigenproblem . . . 121
3.2.4 Quasi-steady approximation method . . . 122
3.2.5 Rational function approximation of the fluid transfer function . . . 123
3.3 Application of the various methods for $Re = 50\,000$ and $\alpha = 0°$ . . . 125
3.3.1 Full eigenvalue spectrum: purely-hydrodynamic mean flow analysis . . . 126
3.3.2 Full eigenvalue spectrum: mean flow FSI analysis . . . 127
3.3.3 Newton method for a reduced-size nonlinear eigenproblem . . . 129

3.3.4 Description of the fluid and solid transfer functions . . . 131
3.3.5 Quasi-steady approximation results . . . 135
3.3.6 Results for the rational function approximation of the fluid transfer function . . . 136

4 Primary aeroelastic instability **141**
4.1 Introduction . . . 141
4.2 Mean flow analysis of the primary instability at $Re = 50\,000$ and $\alpha = 0°$ . . . 142
4.2.1 Description of the divergence and flutter eigenmodes . . . 143
4.2.2 Effect of the structural parameters . . . 145
4.2.3 Effect of the Reynolds number and airfoil geometry . . . 147
4.2.4 Comparison between analyses around a mean flow from 2D and 3D simulations . . . 149
4.2.5 Comparison between classical and Reynolds stress formulations of the mean flow stability analyses 149
4.3 Floquet analysis of the primary instability at $Re = 20\,000$ and $\alpha = 0°$ . . . 150
4.3.1 Description of the divergence and flutter Floquet eigenmodes . . . 151
4.3.2 Harmonic content of the divergence Floquet eigenmode over a period . . . 153
4.3.3 Comparison with the mean flow eigenvalues/eigenmodes . . . 154
4.3.4 Comparison with the nonlinear simulations . . . 155

5 Nonlinear FSI temporal simulations **157**
5.1 Introduction . . . 157
5.2 Quasi-steady equilibrium positions for mean flow solutions from 2D simulations at $Re = 20\,000$ . . . 158
5.3 Different FSI nonlinear regimes for $Re = 20\,000$ . . . 160
5.3.1 Regime R_1: weak oscillations around $\overline{\alpha} = 0°$ . . . 161
5.3.2 Regime R_2: weak oscillations around $\overline{\alpha} \neq 0°$ . . . 163
5.3.3 Regime R_3: strong oscillations around $\overline{\alpha} \neq 0°$ . . . 166
5.3.4 Regime R_4: intermittent switching strong oscillations . . . 171
5.3.5 Regime R_5: quasi-periodic oscillations . . . 174
5.4 Bifurcation diagram of the nonlinear dynamics for $Re = 20\,000$ as function of the structural stiffness . . . 176
5.5 Reynolds number effect on the FSI nonlinear dynamics for fixed structural parameters . . . 179
5.5.1 Quasi-steady equilibrium positions for mean flow solutions from 2D simulations at $Re = 50\,000$ . . . 179
5.5.2 Regime R_6: laminar separation flutter . . . 180

6 Secondary aeroelastic instability **185**
6.1 Linear stability analyses around mean and periodic flow solutions at $Re = 20\,000$ . . . 185
6.1.1 Classical formulation of the mean flow linear stability analyses . . . 187
6.1.2 Reynolds stress formulation of the mean flow linear stability analyses . . . 190
6.1.3 Floquet linear stability analyses . . . 193
6.2 Mean flow linear stability analyses at $Re = 50\,000$ . . . 195
6.3 Quasi-steady equilibrium positions for mean flow solutions from 3D simulations . . . 196
6.3.1 Classical formulation of the mean flow linear stability analyses . . . 196

Conclusions and perspectives **199**

A Notes on the fluid model derivation and the airfoil geometry generation **205**
A.1 Additional notes on the fluid model derivation . . . 205
A.2 Airfoil geometry generation . . . 207
A.3 Relation between the convection term of the mean flow Navier–Stokes momentum equation and the quantity Q . . . 208
A.4 Linearisation of the SUPG and grad-div stabilisations . . . 209

B Notes on several numerical aspects **211**
B.1 Numerical inversion of a matrix . . . 211
B.1.1 Direct approach for matrix inversion . . . 211
B.1.2 Iterative approach for matrix inversion . . . 212
B.1.3 Preconditioning strategies . . . 213
B.2 Numerical method for solving the Floquet eigenproblem . . . 213

C Stability analysis of a NACA0012 airfoil at low incidences **215**
C.1 Base flow linear stability analysis: onset of the vortex shedding . . . 215
C.2 Hydrodynamic Floquet stability analysis: onset of three-dimensional instabilities . . . 217

D Notes on the approximation of the fluid transfer function via a Taylor expansion **219**
D.0.1 Taylor expansion of the fluid transfer function around origin . . . 219
D.0.2 Taylor expansion of the fluid transfer function around complex value . . . 220

E Mean flow fluid–structure analysis based on RANS aerodynamic model **221**
E.1 Problem description . . . 221
E.1.1 Reynolds-averaged Navier–Stokes equations . . . 221
E.1.2 Spalart–Allmaras closure model . . . 223
E.1.3 Turbulence transition model . . . 226
E.2 Numerical aspects and preliminary results . . . 227
E.2.1 Meshes for two-dimensional RANS computations . . . 227
E.2.2 Mesh convergence . . . 227
E.2.3 Newton method . . . 228
E.2.4 Spalart–Allmaras model validation . . . 230
E.2.5 Influence of the SUPG stabilisation and h_K definition . . . 232
E.3 RANS mean flow description for $Re = 50\,000$ and $\alpha = 0°$ . . . 232
E.3.1 Mean flow for SA model with $\tilde{\nu}^\infty = 0$ . . . 232
E.3.2 Mean flow for SA-BC model . . . 234
E.4 RANS mean flow FSI linear stability analysis for $Re = 50\,000$ and $\alpha = 0°$ . . . 235
E.5 RANS mean flow description for $Re = 50\,000$ and $\alpha > 0°$ . . . 237

Bibliography **241**

List of figures

1 Illustrations of the failed attempted flight of Professor Samuel Langley at the beginning of the 20^{th} century and of the in-flight aeroelastic tests performed with the SB-9 glider in 1970 . . . 1
2 Schematic representation of the divergence and flutter instabilities of a NACA0012 airfoil with a pitch degree of freedom . . . 2
3 Critical reduced velocity for the SDOF pitching flutter versus the moment of inertia for various Mach numbers 5
4 Schematic illustration of a two-dimensional laminar boundary layer separation and of a laminar separation bubble . . . 6
5 Time- and spanwise-averaged distributions of the friction and pressure coefficients associated to DNS simulations at $Re = 50\,000$ and $\alpha = 5^\circ$ . . . 7
6 Representation of different types of laminar separation bubbles: a short bubble, a long bubble and a trailing-edge bubble . . . 8
7 Evolution of the drag and lift coefficients with the angle of attack . . . 9
8 Laminar separation flutter illustrations: ILES instantaneous solutions and time history of the angular displacement for different structural stiffness values . . . 11
9 Aeroelastic eigenvalues of a mean flow LSA for different Reynolds numbers at $\alpha = 0^\circ$ . . . 13

1.1 Schematic illustration of the transformation between the inertial and non-inertial frames . . . 18
1.2 Schematic illustration of the damped spring-mounted NACA0012 airfoil . . . 22
1.3 Illustration of the triple decomposition of a state variable . . . 26
1.4 Illustration of a slow and fast time scale signals on the time and frequency domains, along with their product 28
1.5 Evolution of the magnitude of the transfer function H_θ^{dim} with the forced frequency . . . 30
1.6 Schematic illustration of the 2D and 3D computational domains . . . 46
1.7 Two-dimensional triangular mesh around the NACA0012 airfoil . . . 48
1.8 Three-dimensional mesh visualisation around the NACA0012 profile wing . . . 49
1.9 Illustration of the two- and three-dimensional standard element cells and degrees of freedom of the finite element spaces . . . 51
1.10 Effect of the lateral boundary condition of the 3D computations on the upper surface friction coefficient distribution of the time- and spanwise-averaged flow . . . 64
1.11 Spatial structure of the τ_{SUPG} and τ_{GD} numerical stabilisations . . . 65
1.12 Effect of the grad-div stabilisation of the three-dimensional simulations on the discrete mass conservation 66
1.13 Effect of the SUPG stabilisation on mean flow FSI linear stability analysis . . . 66

2.1 Two-dimensional instantaneous flow solutions at $\alpha = 0^\circ$ for $Re = 7\,000$, $Re = 8\,000$ and $Re = 20\,000$ . . . 72

2.2 Evolution of the vortex shedding frequency present on two-dimensional unsteady simulations at $\alpha = 0°$ and evolution of the abscissa of the boundary layer separation point on the airfoil surface at $\alpha = 0°$ with the Reynolds number for two-dimensional base and mean flows . . . 73
2.3 Time history of the aerodynamic moment coefficient for $Re = 20\,000$ at $\alpha = 0°$ and $\alpha = 3.64°$ . . . 74
2.4 Two-dimensional base and mean flow solutions at $Re = 20\,000$ for $\alpha = 0°$ and $\alpha = 3.64°$ . . . 75
2.5 Two-dimensional mean flow solution at $Re = 20\,000$ and $\alpha = 3.64°$: close-up on the recirculation zone of the upper surface . . . 75
2.6 Distributions of the friction and pressure coefficients of two-dimensional mean flow solutions along the airfoil at $Re = 20\,000$ for $\alpha = 0°$ and $\alpha = 3.64°$ . . . 76
2.7 Variation of the distributions of the friction and pressure coefficients of two-dimensional mean flow solutions along the airfoil at $Re = 20\,000$ with the angle of attack . . . 77
2.8 Aerodynamic moment and lift coefficients evolution with the angle of attack for two-dimensional base and mean flow solutions at $Re = 20\,000$ . . . 78
2.9 Aerodynamic moment coefficient evolution with the angle of attack for two-dimensional mean flow solutions at different Reynolds numbers and evolution of the vortex shedding frequency with the angle of attack for two-dimensional unsteady simulations at different Reynolds numbers . . . 79
2.10 Time history of the aerodynamic moment coefficient for $Re = 50\,000$ at different angles of attack . . . 80
2.11 Two-dimensional mean flow solutions at $Re = 50\,000$ for $\alpha = 1.8°$ and $\alpha = 1.9°$ . . . 81
2.12 Evolution of aerodynamic moment and lift stability derivatives, m_z^α and C_L^α, for $\alpha = 0°$ with the Reynolds number for two-dimensional base and mean flow solutions . . . 82
2.13 Evolution of the aerodynamic centre location, X_{AC}, with the Reynolds number for two-dimensional base and mean flow solutions at $\alpha = 0°$ . . . 83
2.14 Floquet analysis around periodic flow solution at $Re = 30\,000$ and $\alpha = 0°$ . . . 86
2.15 Absolute value of the Floquet multiplier as a function of the spanwise wavenumber for different Reynolds numbers at $\alpha = 0°$ . . . 87
2.16 Instantaneous spanwise velocity of two synchronous eigenmodes for $\beta = 50$ at $Re = 50\,000$ and $\alpha = 0°$ . . . 87
2.17 Neutral curve in the parameter space $Re - \beta$ for the first and second synchronous Floquet eigenmodes at $\alpha = 0°$ . . . 88
2.18 Three-dimensional visualisation of a DNS snapshot at $Re = 50\,000$ and $\alpha = 0°$ . . . 89
2.19 Time history of the streamwise and cross-stream velocities, U and V, for the DNS simulation at $Re = 50\,000$ and $\alpha = 0°$ . . . 90
2.20 Time history of the lift and drag coefficients for the DNS simulation at $Re = 50\,000$ and $\alpha = 0°$ . . . 91
2.21 Zoom on the time history of the drag coefficient for the DNS simulation at $Re = 50\,000$ and $\alpha = 0°$, along with two different time- and spanwise-averaged flow solutions . . . 91
2.22 Three-dimensional visualisations of DNS snapshots at $Re = 50\,000$ and $\alpha = 0°$: close-up near trailing edge . 93
2.23 Time history of the cross-stream vorticity along an axis oriented in the z-direction, for the DNS simulation at $Re = 50\,000$ and $\alpha = 0°$ . . . 93
2.24 Spectral density estimation of the streamwise velocity on a point and of the lift coefficient for the DNS simulation at $Re = 50\,000$ and $\alpha = 0°$ . . . 94
2.25 Three-dimensional visualisation of the time-averaged flow solution for the DNS simulation at $Re = 50\,000$ and $\alpha = 0°$ . . . 95
2.26 Three-dimensional visualisation of the time-averaged and first harmonic flow solution for the DNS simulation at $Re = 50\,000$ and $\alpha = 0°$ . . . 95

2.27 Time- and spanwise-averaged flow solution at $Re = 50\,000$ and $\alpha = 0°$ . . . 96
2.28 Spanwise-averaged Reynolds stress components at $Re = 50\,000$ and $\alpha = 0°$ . . . 96
2.29 Three-dimensional visualisations of DNS snapshots at $Re = 50\,000$ and $\alpha > 0°$ . . . 97
2.30 Three-dimensional visualisations of a zoom near the trailing edge of the wing of DNS snapshots at $Re = 50\,000$ and $\alpha > 0°$ . . . 98
2.31 Time history and spectral density estimation of the streamwise velocity on a point for the DNS simulations at $Re = 50\,000$ for $\alpha = 0.5°$ and $\alpha = 2°$ . . . 98
2.32 Time- and spanwise-averaged flow solutions at $Re = 50\,000$ and $\alpha > 0°$ . . . 99
2.33 Distributions of the friction and pressure coefficients of time- and spanwise-averaged flow solutions along the airfoil at $Re = 50\,000$ and $\alpha > 0°$ . . . 100
2.34 Lift and quarter-chord aerodynamic moment coefficients evolution with the angle of attack for the time- and spanwise-averaged flow solutions at $Re = 50\,000$ . . . 101
2.35 Aerodynamic moment coefficient and corresponding pressure and friction components evolution with the angle of attack for the time- and spanwise-averaged flow solutions at $Re = 50\,000$ . . . 101
2.36 Comparison between the two- and three-dimensional mean flow solutions at $Re = 50\,000$ as function of the angle of attack . . . 103
2.37 Spatial distribution of the quantity $-\nabla p \nabla \phi_M$, associated to the time- and spanwise-averaged flow solutions at $Re = 50\,000$ for $\alpha = 0.5°$ and $\alpha = 1°$ . . . 107
2.38 Evolution of the y integral along the x direction of the quantity $-\nabla p \nabla \phi_M$, associated to the time- and spanwise-averaged flow solutions at $Re = 50\,000$ for $\alpha = 0.5°$ and $\alpha = 1°$ . . . 107
2.39 Spatial distribution of the convective and Reynolds stress terms, associated to the time- and spanwise-averaged flow solutions at $Re = 50\,000$ for $\alpha = 0.5°$ and $\alpha = 1°$ . . . 108
2.40 Evolution of the three volume integrated terms of the pressure component of the aerodynamic moment coefficient with the angle of attack, associated to the time- and spanwise-averaged flow solutions at $Re = 50\,000$ 108
2.41 Spatial distribution of the quantities $2\phi_M Q_p$ and $2\phi_M Q_n$, associated to the time- and spanwise-averaged flow solutions at $Re = 50\,000$ for $\alpha = 0.5°$ and $\alpha = 1°$ . . . 109
2.42 Evolution of the y integral along the x direction of the quantities $2\phi_M Q_p$ and $2\phi_M Q_n$, associated to the time- and spanwise-averaged flow solutions at $Re = 50\,000$ for $\alpha = 0.5°$ and $\alpha = 1°$ . . . 109
2.43 Evolution of volume integrated contributions from $2\phi_M Q_p$ and $2\phi_M Q_n$ with the angle of attack at $Re = 50\,000$ 110
2.44 Spatial distribution of the quantity $-\nabla p \nabla \phi_M$, associated to the time- and spanwise-averaged flow solutions at $Re = 50\,000$ for $\alpha = 1.5°$ and $\alpha = 2°$ . . . 111
2.45 Evolution of the y integral along the x direction of the quantity $-\nabla p \nabla \phi_M$, associated to the time- and spanwise-averaged flow solutions at $Re = 50\,000$ for $\alpha = 1.5°$ and $\alpha = 2°$ . . . 111
2.46 Spatial distribution of the convective and Reynolds stress terms, associated to the time- and spanwise-averaged flow solutions at $Re = 50\,000$ for $\alpha = 1.5°$ and $\alpha = 2°$ . . . 112
2.47 Spatial distribution of the quantities $2\phi_M Q_p$ and $2\phi_M Q_n$, associated to the time- and spanwise-averaged flow solutions at $Re = 50\,000$ for $\alpha = 1.5°$ and $\alpha = 2°$ . . . 112
2.48 Evolution of the y integral along the x direction of the quantities $2\phi_M Q_p$ and $2\phi_M Q_n$, associated to the time- and spanwise-averaged flow solutions at $Re = 50\,000$ for $\alpha = 1.5°$ and $\alpha = 2°$ . . . 113

3.1 Hydrodynamic mean flow linear stability analysis: spectrum at $Re = 50\,000$ and $\alpha = 0°$ . . . 126
3.2 Vortex shedding eigenmode of hydrodynamic mean flow linear stability analysis at $Re = 50\,000$ and $\alpha = 0°$. 127

3.3 Two stable low frequency eigenmodes of hydrodynamic mean flow linear stability analysis at $Re = 50\,000$ and $\alpha = 0^\circ$ . . . 127
3.4 Fluid–structure mean flow linear stability analysis: spectrum at $Re = 50\,000$ and $\alpha = 0^\circ$ . . . 128
3.5 Evolution of the eigenvalue solutions with the nonlinear Newton iterations . . . 129
3.6 Evolution of the eigenvalue solutions on the complex plane with the nonlinear Newton iterations . . . 130
3.7 Variation of the growth rate of the divergence eigenvalues with K_s: comparison between Krylov–Schur and explicit prediction methods . . . 130
3.8 Mapping of the fluid transfer function, the solid transfer function and their sum on the complex plane . . . 132
3.9 Evolution of the eigenvalue solutions on the complex plane with the nonlinear Newton iterations, superimposed to the residual isocontours . . . 134
3.10 Fluid–structure mean flow linear stability analysis: spectrum at $Re = 50\,000$ and $\alpha = 0^\circ$ with a comparison between the exact and quasi-steady approximation at order 2 . . . 136
3.11 Mapping of the real and imaginary parts of the fluid transfer function: exact solution and approximations via a rational function . . . 137
3.12 Evolution of the fluid transfer function along the s_r and s_i axes: comparison between exact and ration approximation methods . . . 138
3.13 Fluid–structure mean flow linear stability analysis: spectrum at $Re = 50\,000$ and $\alpha = 0^\circ$ with a comparison between the exact and rational function approximation methods . . . 140

4.1 Time-averaged flow solution from two-dimensional simulations at $Re = 50\,000$ and $\alpha = 0^\circ$ . . . 143
4.2 Evolution of the reconstructed angular displacement, aerodynamic moment coefficient and pressure field, based on their time-averaged quantity plus an infinitesimal perturbation associated to the divergence and flutter eigenmodes at $Re = 50\,000$ and $\alpha = 0^\circ$ . . . 144
4.3 Influence of the structural stiffness on the FSI eigenvalues . . . 145
4.4 Influence of the structural damping on the FSI eigenvalues . . . 146
4.5 Influence of the structural inertia and elastic centre on the FSI eigenvalues . . . 147
4.6 Influence of the Reynolds number on the FSI eigenvalues . . . 148
4.7 Influence of the airfoil geometry on the FSI eigenvalues . . . 148
4.8 Fluid–structure mean flow linear stability analyses: spectrum comparison between analyses around mean flow solutions from 2D and 3D simulations at $Re = 50\,000$ and $\alpha = 0^\circ$ . . . 150
4.9 Fluid–structure mean flow linear stability analyses: spectrum comparison between classical and Reynolds stress formulations at $Re = 50\,000$ and $\alpha = 0^\circ$ . . . 150
4.10 Floquet multipliers on the complex plane for the Floquet FSI analysis at $Re = 20\,000$, $\alpha = 0^\circ$ and $K_s = 0$ . . . 151
4.11 Fluid component of the divergence Floquet eigenmode at $Re = 20\,000$, $\alpha = 0^\circ$ and $K_s = 0$ . . . 152
4.12 Fluid component of the flutter Floquet eigenmode at $Re = 20\,000$, $\alpha = 0^\circ$ and $K_s = 0$ . . . 153
4.13 Mean and first harmonic components of the fluid component of the divergence Floquet eigenmode at $Re = 20\,000$, $\alpha = 0^\circ$ and $K_s = 0$ . . . 153
4.14 Evolution of the solid components of the divergence Floquet eigenmode and the corresponding aerodynamic moment coefficient, over one vortex shedding period at $Re = 20\,000$, $\alpha = 0^\circ$ and $K_s = 0$ . . . 154
4.15 Comparison between the divergence eigenmode of a mean flow analysis and the mean component of the divergence eigenmode of the Floquet FSI analysis, at $Re = 20\,000$, $\alpha = 0^\circ$ and $K_s = 0$ . . . 155

4.16 Comparison between the exponential growth of the angular displacement observed in nonlinear FSI simulations at $Re = 20000$ and $K_s = 0$ with the divergence eigenvalues of mean flow and Floquet linear analyses . . . 156

5.1 Quasi-steady equilibrium positions for mean flow solutions from 2D simulations at $Re = 20000$: evolution of the aerodynamic moment coefficient with the angle of attack and evolution of the equilibrium angle of attack with the structural stiffness . . . 159
5.2 Regime R_1: time history of the angle of attack, the angular velocity and the aerodynamic moment coefficient for a two-dimensional coupled time-marching simulation at $Re = 20000$ and $K_s = 1.390$ . . . 161
5.3 Regime R_1: phase diagrams at $Re = 20000$ and $K_s = 1.390$ . . . 162
5.4 Regime R_2: time history of the angle of attack, the angular velocity and the aerodynamic moment coefficient for a two-dimensional coupled time-marching simulation at $Re = 20000$ and $K_s = 0.347$ . . . 164
5.5 Regime R_2: instantaneous fields of a two-dimensional coupled time-marching simulation at $Re = 20000$ and $K_s = 0.347$ . . . 164
5.6 Regime R_2: phase diagrams at $Re = 20000$ and $K_s = 0.347$ . . . 165
5.7 Regimes R_1 and R_2: three-dimensional phase diagrams of α–Ω–m_z at $Re = 20000$ for $K_s = 1.390$ and $K_s = 0.347$ . . . 166
5.8 Regime R_3: time history of the angle of attack, the angular velocity and the aerodynamic moment coefficient for a two-dimensional coupled time-marching simulation at $Re = 20000$ and $K_s = 0.087$ . . . 167
5.9 Regime R_3: spectral density estimation of the angle of attack, the angular velocity and the aerodynamic moment coefficient for a two-dimensional coupled time-marching simulation at $Re = 20000$ and $K_s = 0.087$ 168
5.10 Regime R_3: phase diagrams at $Re = 20000$ and $K_s = 0.087$ . . . 169
5.11 Regime R_3: instantaneous fields on the ascending and descending phases of the angle of attack of a two-dimensional coupled time-marching simulation at $Re = 20000$ and $K_s = 0.087$ . . . 170
5.12 Regime R_4: time history of the angle of attack, the angular velocity and the aerodynamic moment coefficient for a two-dimensional coupled time-marching simulation at $Re = 20000$ and $K_s = 0$ . . . 171
5.13 Regime R_4: spectral density estimation of the angle of attack, the angular velocity and the aerodynamic moment coefficient for a two-dimensional coupled time-marching simulation at $Re = 20000$ and $K_s = 0$ . . . 172
5.14 Regime R_4: phase diagrams at $Re = 20000$ and $K_s = 0$ . . . 173
5.15 Regime R_5: time history and spectral density estimation of the angle of attack and the aerodynamic moment coefficient for a two-dimensional coupled time-marching simulation at $Re = 20000$ and $K_s = 0.078$ . . . 174
5.16 Bifurcation diagram of K_s as function of the pitch amplitude oscillation for $Re = 20000$ . . . 176
5.17 Phase diagrams of α–Ω at $Re = 20000$ for different K_s values . . . 177
5.18 Three-dimensional phase diagrams of α–Ω–m_z at $Re = 20000$ for different K_s values . . . 178
5.19 Equilibrium points for $Re = 50000$: evolution of the two-dimensional mean aerodynamic moment coefficient with the angle of attack . . . 180
5.20 Transition between regimes R_4 and R_6: time history and phase diagram of the angular displacement versus the angular velocity for $Re \geq 50000$ and $K_s^{dim} = 0.3\text{Nm}$ . . . 181
5.21 Evolution of the averaged maximum and minimum pitch amplitude and the pitch angular frequency with the Reynolds number, associated to the laminar separation flutter phenomenon, for two-dimensional coupled time-marching simulation for $K_s^{dim} = 0.3\text{Nm}$ . . . 182
5.22 Instantaneous fields of two-dimensional coupled time-marching simulations for $K_s^{dim} = 0.3\text{Nm}$ at $Re = 50000$, $Re = 64000$, $Re = 80000$ and $Re = 117500$ . . . 182

6.1 Equilibrium points for $Re = 20000$: evolution of the two-dimensional mean aerodynamic moment coefficient with the angle of attack . . . 186
6.2 Classical formulation of the mean flow linear stability analysis at $Re = 20000$ and $\overline{\alpha}_2 = 3.44°$, corresponding to a structural stiffness of $K_s = 0.087$ . . . 187
6.3 Classical formulation of the mean flow linear stability analysis at $Re = 20000$: evolution of the growth rate and frequency of the divergence and flutter modes with K_s . . . 189
6.4 Spatial distribution of the streamwise and cross-stream components of the divergence of the Reynolds stress for two incidences and their corresponding difference . . . 190
6.5 Comparison between classical and Reynolds stress formulations of the mean flow linear stability analysis at $Re = 20000$ and $\overline{\alpha}_2 = 3.44°$, corresponding to a structural stiffness of $K_s = 0.087$ . . . 191
6.6 Comparison between classical and Reynolds stress formulations of the mean flow linear stability analysis at $Re = 20000$: evolution of the growth rate and frequency of the divergence and flutter modes with K_s . . . 192
6.7 Floquet multipliers on the complex plane for the Floquet FSI analysis at $Re = 20000$ on three secondary equilibrium points . . . 193
6.8 Visualisation of the instantaneous flutter Floquet eigenmode for $Re = 20000$, $\overline{\alpha}_2 = 3.44°$ and $K_s = 0.087$ . . . 194
6.9 Equilibrium points for $Re = 50000$: evolution of the aerodynamic moment coefficient of the time- and spanwise-averaged flow solutions with the angle of attack . . . 196
6.10 Classical formulation of the mean flow linear stability analysis at $Re = 50000$ and different secondary equilibrium positions . . . 198
10 Mean flow FSI linear stability analysis of the RANS mean flow using the SA-BC model at $Re = 50000$ and $\alpha = 0°$ . . . 203

C.1 Evolution of angle of attack of the critical Reynolds number, for which an unstable mode in a base flow linear stability analysis emergences . . . 215
C.2 Preliminary results on the base flow linear stability analysis at $Re = 6000$ and $\alpha = 0°$ . . . 216
C.3 Sensitivity field associated to the leading eigenmode of a stability analysis conducted at $Re = 6000$ and $\alpha = 0°$ 216
C.4 Hydrodynamic Floquet stability analysis at $\alpha = 5°$ . . . 217
C.5 Hydrodynamic Floquet stability analysis at $\alpha = 6°$ . . . 218

E.1 Two-dimensional triangular mesh around the NACA0012 airfoil for the RANS computations . . . 227
E.2 Evolution of the RANS equations residual with the nonlinear Newton iterations . . . 228
E.3 Variation of the abscissa of the upper boundary layer separation point and variation the drag coefficient with $\tilde{\nu}^\infty$ on the RANS Spalart–Allmaras model . . . 229
E.4 Variation of the C_f distribution with $\tilde{\nu}^\infty$ on the RANS Spalart–Allmaras model and corresponding ν_t/ν fields 229
E.5 Validation of the Spalart–Allmaras model on the Eppler E387 airfoil . . . 230
E.6 Effect of the τ_{SUPG} definition on the RANS FSI spectrum . . . 231
E.7 Effect of the h_K definition on the RANS FSI spectrum at $Re = 50000$ and $\alpha = 0°$ . . . 231
E.8 Spanwise vorticity field of the RANS mean flow for $Re = 50000$ and $\alpha = 0°$, using the SA model with $\tilde{\nu}^\infty = 0$. The yellow dots over the airfoil surface represent the separation points . . . 233
E.9 Quantity ν_t/ν and the production term of the SA model, for the RANS mean flow at $Re = 50000$ and $\alpha = 0°$, using the SA model with $\tilde{\nu}^\infty = 0$ . . . 233
E.10 Comparison of the C_f and $-C_p$ distributions between the RANS mean flow using the SA model with $\tilde{\nu}^\infty = 0$ and the mean flow issued from 3D simulations for $Re = 50000$ and $\alpha = 0°$ . . . 233

E.11 Spanwise vorticity field of the RANS mean flow for $Re = 50\,000$ and $\alpha = 0°$, using the SA-BC model. The yellow dots over the airfoil surface represent the separation points 234
E.12 Quantity ν_t/ν and the production term of the SA model, for the RANS mean flow at $Re = 50\,000$ and $\alpha = 0°$, using the SA-BC model 234
E.13 Intermittency function and the product of the intermittency function with the production term of the SA model for a RANS mean flow for $Re = 50\,000$ and $\alpha = 0°$, using the SA-BC model 234
E.14 Comparison of the C_f and $-C_p$ distributions between the RANS mean flow using the SA-BC model and the mean flow issued from 3D simulations for $Re = 50\,000$ and $\alpha = 0°$ 235
E.15 Hydrodynamic linear stability analysis of the RANS mean flow: spectrum for $Re = 50\,000$ and $\alpha = 0°$ using the SA model with $\tilde{\nu}^\infty = 0$, and using the SA-BC model 235
E.16 Streamwise velocity and $\hat{\tilde{\nu}}$ SA model variable of the vortex shedding eigenmode from a hydrodynamic mean flow linear around the RANS SA-BC mean flow at $Re = 50\,000$ and $\alpha = 0°$ 235
E.17 Mean flow FSI linear stability analysis of the RANS mean flow using the SA-BC model: spectrum for $Re = 50\,000$ and $\alpha = 0°$ 236
E.18 Streamwise velocity and $\hat{\tilde{\nu}}$ SA model variable of the divergence eigenmode from a mean flow FSI linear stability analysis around the RANS SA-BC mean flow at $Re = 50\,000$ and $\alpha = 0°$ 237
E.19 Streamwise velocity and $\hat{\tilde{\nu}}$ SA model variable of the flutter eigenmode from a mean flow FSI linear stability analysis around the RANS SA-BC mean flow at $Re = 50\,000$ and $\alpha = 0°$ 237
E.20 Quasi-laminar mean flow FSI linear stability analysis of the RANS mean flow using the SA-BC model: spectrum for $Re = 50\,000$ and $\alpha = 0°$ 237
E.21 m_z evolution with the incidence of the RANS mean flow for $Re = 50\,000$, using the SA model with $\tilde{\nu}^\infty = 0$ . . 238
E.22 m_z evolution with the incidence of the RANS mean flow for $Re = 50\,000$, using the SA-BC model 239
E.23 Comparison of the m_z^p and C_p distributions over the upper surface of the airfoil between the mean flow using a SA-BC model, using the "improved" SA-BC, where $\tilde{\nu}^\infty = 0.672\nu$ and the 3D results 239
E.24 m_z evolution with the incidence of the RANS mean flow for $Re = 50\,000$, using a modified SA-BC model, where $\tilde{\nu}^\infty = 0.672\nu$ 240

List of tables

1.1 Nominal dimensional fluid–structure parameters . . . 23
1.2 Structural dimensional and nondimensional parameters for different Reynolds numbers . . . 24
1.3 Fluid–structure nondimensional parameters for different Reynolds numbers . . . 25
1.4 Numerical values of the transfer functions associated to the solid motion of the structure for three Reynolds numbers at the corresponding vortex shedding frequencies . . . 30
1.5 Simplex number of 2D and 3D meshes along with the size of the P_2, P_1, and Taylor–Hood FEM spaces . . . 49
1.6 Convergence of the two-dimensional mesh with respect to the time-marching and mean flow properties and to the mean flow FSI eigenvalues . . . 63
1.7 Convergence of the time- and spanwise-averaged flow properties and mean flow FSI eigenvalues for the three-dimensional simulations . . . 63
1.8 Effect of the lateral boundary condition of the 3D computations on the global coefficients and on the abscissa of the boundary layer separation point of the time- and spanwise-averaged flow . . . 64
1.9 Effect of the SUPG stabilisation on the eigenvalues of a mean flow FSI linear stability analysis . . . 67
1.10 Three-dimensional time-marching simulation performance . . . 68
1.11 Influence of the preconditioner inversion strategy on the three-dimensional time-marching simulations . . . 69

2.1 Values of the period, angular frequency and Strouhal number associated to the vortex shedding for different Reynolds numbers at $\alpha = 0^\circ$. The last column also reports the abscissa of the time-averaged boundary layer separation point . . . 73
2.2 Comparison between two- and three-dimensional simulations at $Re = 50\,000$ as function of the angle of attack 102

3.1 Hydrodynamic linear stability analysis of the mean flow: eigenvalues for $Re = 50\,000$ and $\alpha = 0^\circ$ . . . 125
3.2 FSI linear stability analysis of the mean flow: divergence and flutter eigenvalues for $Re = 50\,000$ and $\alpha = 0^\circ$ 128
3.3 Initial guesses and converged eigenvalues of the Newton procedure . . . 129
3.4 Added coefficients of the quasi-steady approximation for the three first orders at $Re = 50\,000$ and $\alpha = 0^\circ$ . . . 135
3.5 Summary of eigenvalues predicted by the quasi-steady approximation for the three first orders at $Re = 50\,000$ and $\alpha = 0^\circ$ . . . 135
3.6 Constants associated to the Y^f approximation . . . 137
3.7 Exact and approximative values of the fluid transfer function Y^f at the divergence and flutter eigenvalues location . . . 139
3.8 Comparison of the FSI eigenvalues between the exact and the Y^f approximation methods based on one and two poles . . . 139

4.1 Summary of the vortex shedding, divergence and flutter eigenmodes for the FSI linear stability analysis of the mean flow at $Re = 50\,000$ and $\alpha = 0^\circ$ . . . 143
4.2 Divergence and flutter eigenvalues of a mean flow FSI spectrum at $Re = 50\,000$ and $\alpha = 0^\circ$, with a mean flow issued from 2D simulations and issued from 3D simulations . . . 150
4.3 Comparison between the classical and the Reynolds stress formulations: divergence and flutter eigenvalues of a mean flow FSI spectrum at $Re = 50\,000$ and $\alpha = 0^\circ$ . . . 150
4.4 Divergence and flutter Floquet multipliers and corresponding eigenvalues for $Re = 20\,000$, $\alpha = 0^\circ$ and $K_s = 0$ 151
4.5 Solid components and the associated aerodynamic moment coefficient of the divergence and flutter eigenmodes for a Floquet FSI linear stability analysis at $Re = 20\,000$, $\alpha = 0^\circ$ and $K_s = 0$ . . . 152
4.6 Mean and first harmonic components of the solid components and the corresponding aerodynamic moment coefficient of the divergence Floquet eigenmode for $Re = 20\,000$, $\alpha = 0^\circ$ and $K_s = 0$ . . . 154
4.7 Comparison between nonlinear and linear analyses for $Re = 20\,000$, $\alpha = 0^\circ$ and $K_s = 0$ . . . 155
4.8 Comparison between the exponential growth of the nonlinear FSI simulation and the unstable divergence eigenvalues from the mean flow FSI and Floquet FSI linear stability analyses at $Re = 20\,000$, $\alpha = 0^\circ$ and $K_s = 0$ . . . 156
4.9 Comparison between nonlinear simulations and linear analyses for $Re = 20\,000$ and $\alpha = 0^\circ$ . . . 156

5.1 Equilibrium positions of a NACA0012 airfoil at $Re = 20\,000$ as function of the structural stiffness . . . 160
5.2 Comparison of the values of H_θ and H_Ω, evaluated at the vortex shedding frequency, for the theoretical estimation and for the nonlinear simulations at $Re = 20\,000$ and $K_s = 1.390$ . . . 161
5.3 Comparison of the values of H_θ and H_Ω, evaluated at the vortex shedding frequency, for the theoretical estimation and for the nonlinear simulations at $Re = 20\,000$ and $K_s = 0.347$ . . . 164
5.4 Comparison of the values of H_θ and H_Ω, evaluated at the two vortex shedding frequencies, for the theoretical estimation and for the nonlinear simulations at $Re = 20\,000$ and $K_s = 0.087$ . . . 167
5.5 Values of the low frequency and the vortex shedding frequencies for a two-dimensional coupled time-marching simulation at $Re = 20\,000$ and $K_s = 0.087$ . . . 168
5.6 Values of H_θ and H_Ω, evaluated at the two vortex shedding frequencies, for the nonlinear simulations at $Re = 20\,000$ and $K_s = 0$ . . . 171
5.7 Values of the low frequency and the vortex shedding frequencies for a two-dimensional coupled time-marching simulation at $Re = 20\,000$ and $K_s = 0$ . . . 172
5.8 Summary of the first four nonlinear FSI regimes found at $Re = 20\,000$ as function of the structural stiffness K_s 175
5.9 Summary of the values of H_θ and H_Ω for the structural stiffness values on the quasi-periodic branch of nonlinear FSI solutions . . . 179

6.1 Classical formulation of the mean flow linear stability analysis at $Re = 20\,000$: summary of the divergence and flutter eigenvalues for three different second equilibrium positions. Comparison with the frequency of the nonlinear simulations found for the quasi-periodic and chaotic branches . . . 188
6.2 Summary of the Floquet multipliers, eigenvalues, solid components of the eigenmodes and aerodynamic moment coefficients for the flutter mode at $Re = 20\,000$ for the three equilibrium positions considered . . . 195

E.1 Triangle number of a typical RANS mesh along with the size of the P_2, P_1, and RANS FEM spaces . . . 227
E.2 Convergence of the RANS mean flow properties and RANS FSI eigenvalues for the SA-BC model . . . 228
E.3 Effect of the τ_{SUPG} definition on the RANS FSI eigenvalues . . . 231

E.4 Effect of the h_K definition on the RANS FSI eigenvalues 231
E.5 Summary of the divergence and flutter eigenvalues obtained with the RANS FSI and the RANS FSI quasi-laminar approaches 236

Nomenclature

$\mathbb{1}$ identity matrix

Roman symbols

A amplitude

c airfoil chord

C_D drag coefficient

C_f friction coefficient

C_L lift coefficient

C_p pressure coefficient

D space dimension & cylinder diameter

D_s structural damping

$\boldsymbol{e}_x, \boldsymbol{e}_y, \boldsymbol{e}_z$ basis of absolute reference frame

$\boldsymbol{e}_X, \boldsymbol{e}_Y, \boldsymbol{e}_Z$ basis of relative reference frame

f frequency

$\boldsymbol{f}$ forcing term & linearisation of divergence of Reynolds stress tensor

$\boldsymbol{g}$ divergence of Reynolds stress tensor

h characteristic cell length

H_θ, H_Ω transfer functions

I_s moment of inertia around elastic centre

K_s structural stiffness

L Jacobian matrix

$\boldsymbol{m}$ aerodynamic moment vector

m_z spanwise aerodynamic moment

M Mach number

M mass matrix

$\boldsymbol{n}$ normal to boundary

N_{MPI} number of MPI processes

N_z number of spanwise planes

p fluid pressure

q test function

$\boldsymbol{q}$ state vector

$\hat{\boldsymbol{q}}$ eigenmode

Q quantity associated to the Q-criterion

$\boldsymbol{R}, R$ residual

R resolvent operator

Re Reynolds number

$\mathbb{R}$ rotation matrix

s complex variable & grad-div stabilisation

$\boldsymbol{S}$ strain rate tensor

St Strouhal number

t time

T period

$\boldsymbol{u} = [u, v, w]^T$ absolute fluid velocity vector on absolute frame

$\boldsymbol{U} = [U, V, W]^T$ absolute fluid velocity vector on relative frame

U^∞ reference velocity

$\boldsymbol{v}$ test function

$\boldsymbol{x} = [x, y, z]^T$, $\boldsymbol{X} = [X, Y, Z]^T$ absolute and relative position vectors

Y transfer function

Greek symbols

α angle of attack

$\alpha_0, \alpha_1, \alpha_2$ BDF scheme coefficients

β spanwise wavenumber

β_1, β_2 BDF scheme coefficients

γ relaxation factor

Γ domain boundary

ϵ small parameter

ζ damping factor

θ angular displacement

λ growth rate

λ_z spanwise wavelength

μ fluid dynamic viscosity coefficient & Floquet multiplier

ν fluid kinematic viscosity coefficient

ρ fluid density

σ eigenvalue

$\boldsymbol{\sigma}$ stress tensor

τ stabilisation parameter

ϕ angular phase of complex quantity & potential function

$\mathbf{\Phi}$, Ψ trial/expansion functions

ω angular frequency

Ω fluid domain & angular velocity

$\mathbf{\Omega}$ vorticity field & angular velocity vector

$\Omega_x, \Omega_y, \Omega_z$ vorticity field components

$\mathbf{\Omega}^r$ rotation tensor

Subscripts

$\bullet_a$ added

$\bullet_{AC}$ aerodynamic centre

$\bullet_b$ base

$\bullet_d$ separation

$\bullet_{dof}$ degrees of freedom

$\bullet_{ele}$ element

$\bullet_{EC}$ elastic centre

$\bullet_f$ fluid

$\bullet_{ft}$ fast time scale

$\bullet_{GD}$ grad-div

$\bullet_i$ imaginary

$\bullet_{in}$ inlet boundary

$\bullet_{lat}$ lateral boundary

$\bullet_{LF}$ low frequency

$\bullet_{LSF}$ laminar separation flutter

$\bullet_M$ moment

$\bullet_n$ negative & natural

$\bullet_{nl}$ nonlinear

$\bullet_{out}$ upper, lower and outlet boundaries

$\bullet_p$ positive

$\bullet_{QS}$ quasi-steady

$\bullet_r$ reattachment & resonance & real

$\bullet_s$ structure

$\bullet_{sh}$ shift

$\bullet_{sl}$ slow time scale

$\bullet_{SUPG}$ Streamline Upwind/Petrov–Galerkin

$\bullet_t$ time

$\bullet_{VS}$ vortex shedding

$\bullet_w$ wing/airfoil

$\bullet_\theta/\bullet_\Omega$ relative to angular displacement/velocity

Superscripts

$\bullet^{'}$ perturbation

$\bullet^0$ mean component

$\bullet^{1/4}$ quarter-chord

$\bullet^1$ first harmonic component

$\bullet^{dim}$ dimensional

$\bullet^{down}$ lower surface

$\bullet^{EC}$ elastic centre

$\bullet^f$ friction & fluid

$\bullet^h$ discrete

$\bullet^H$ Hermitian transpose

$\bullet^i$ input

$\bullet^o$ output

$\bullet^p$ pressure

$\bullet^s$ structure

$\bullet^S$ strong form

$\bullet^t$ airfoil thickness

$\bullet^{up}$ upper surface

$\bullet^\theta/\bullet^\Omega$ relative to angular displacement/velocity

Introduction

Aeroelastic phenomena have strongly shaped the course of the aircraft evolution since the earliest days of flight. One of the first incidents associated to aeroelastic phenomena was the failed attempted flight of Professor Samuel Langley at the beginning of the 20th century, on its tandem monoplane, illustrated in figure 1a. Langley's failure has been attributed to the overall lack of structural rigidity, especially torsional rigidity of the wing and fuselage. Later on, other structural failures were observed in the early days of aircraft design, namely during the flights of the First World War German airplanes Albatros D.III and Fokker D.VIII. In these cases, the structural cracks that often resulted on the airplanes' crash, had their origin on the divergent twist of the wing's aircraft during flight, notably over a dive manoeuvre (Garrick *et al.*, 1981).

The appearance of these aeroelastic instabilities was a direct consequence of the aircraft design evolution, by seeking better rate-of-climb and manoeuvrability, higher velocity and autonomy, in detriment of a more solid structural construction, where these incidents could have been potentially avoided. The reason why this happened and, most importantly, the solution to these failures only arrived during the 1930s with the pioneer works of Glauert (1930), Theodorsen (1935) and von Kármán *et al.* (1938). Their investigation shed a light on the understanding of the main features associated to the aeroelastic phenomena encountered on the early aircraft designs.

The subsequent works of Collar (1946) enabled to view aeroelasticity as a physical phenomenon resulting from

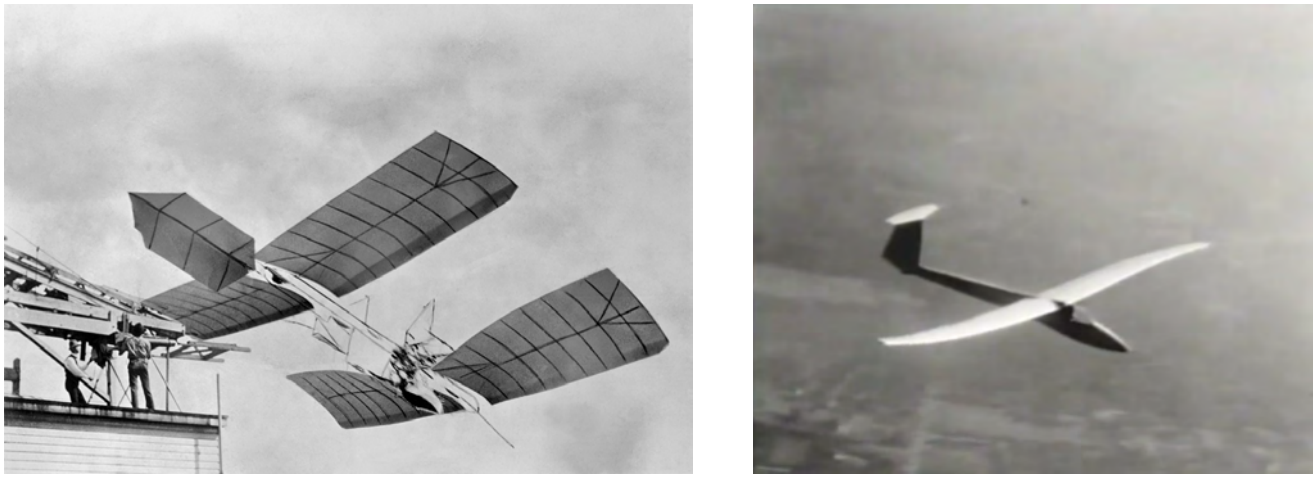

(a) **(b)**

Figure 1 – *On the left, first attempt of Professor Langley to launch its Aerodrome aircraft (Auriti et al., 2004). On the right, in-flight aeroelastic tests performed with the SB-9 glider in 1970 (from Akaflieg Braunschweig website).*

the interaction of aerodynamic, elastic and inertial forces from a flow field acting on a structure. More generally, this *fluid–structure* interaction is present in a wide range of domains, from the motion of insects, fish and birds to flows around turbomachinery blades, flexible pipes, bridges, buildings and aircraft.

Most aeroelastic phenomena are of an undesirable character, compromising not only the long term durability of the wing structure, but also the operational safety, flight performance, design effectiveness and energy efficiency of the aircraft. However, in recent years, the beneficial effects of aeroelasticity have received greater attention, *e.g.*, with the exploitation of the morphing capacities of the aircraft's wing to create aerodynamically efficient designs for multiple flight regimes. Further, aeroelastic instabilities can also be exploited for energy production. For example, this is the case in marine engineering, where numerous researches are devoted to exploit the excitation of oscillation modes on flexible membranes by a current and/or a wave for energy harvesting (Achour, 2022).

The need for a lightweight design of aircraft often results in flexible structures, prone to deformation under load. Such deformations change the aerodynamic load distribution, which in turn changes back the deformations. This interacting feedback process may lead to numerous aeroelastic instabilities, namely to *flutter*, illustrated in figure 1b, a self-excited oscillation, often destructive, wherein energy from the fluid flow is absorbed by the structure. In this thesis, we are particularly interested in describing and understanding these different fluid–structure instabilities that may arise in wings whose boundary layer is mostly laminar. This laminarity is desired from the aircraft design perspective, with the aim of reducing the skin friction drag and therefore reducing the aviation's climate impact and carbon footprint of Humanity on environment.

Divergence and flutter instabilities

Aeroelastic instabilities are generally categorised into two very different categories, namely *static instabilities* and *dynamic instabilities* (Bisplinghoff *et al.*, 1955), depending on whether the behaviour is non-oscillatory or oscillatory. Both kinds of instabilities are illustrated in figure 2 in the simplest case where the structure is modelled by a rigid wing mounted on a torsion spring.

One example of a static instability is the ***divergence instability***, illustrated in figure 2a. This instability arises whenever the aerodynamic moment exerted by the flow onto the wing cannot be counterbalanced by the elastic stiffness of the structure (Fung, 2008), resulting in a non-oscillatory deviation of the wing incidence, α, from its equilibrium position.

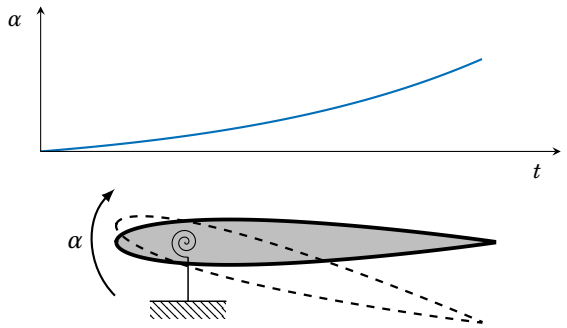

(a) *Divergence instability, characterised by a non-oscillatory deviation from the equilibrium position.*

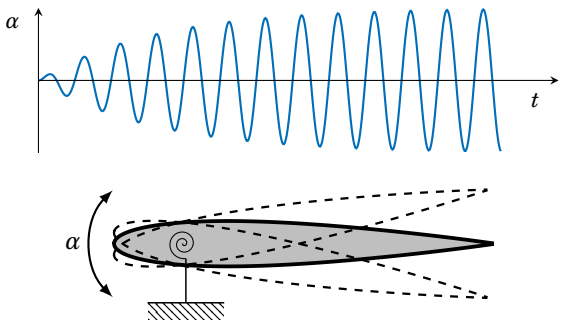

(b) *Flutter instability, characterised by an oscillatory deviation from the equilibrium position towards a limit cycle.*

Figure 2 – *Schematic representation of the divergence and flutter instabilities of a NACA0012 airfoil with a pitch degree of freedom.*

Its occurrence can be simply predicted using a *static criterion*, stating that a divergence instability occurs whenever the total stiffness (including structural stiffness and *aerodynamic stiffness*) is negative. At lower flight speeds, the presence of a torsion spring has a small effect on the wing dynamics, often leading to a different equilibrium state of the wing incidence, which in this case is stable. However, at higher flight speeds, the presence of a torsion spring and its effect may become so serious as to lead to large amplitude oscillations, to render a control surface ineffective, or even to reverse the sense of control. In the case of Langley's airplane or the German fighters, this phenomenon led to the fatal failure of the structure. For modern aircraft, the critical flight speeds at which divergence sets in are usually higher than those of other aeroelastic instabilities, as for the flutter instability, described next.

Flutter is a classical example of a dynamic instability, illustrated in figure 2b. This instability arises in situations where the *aerodynamic damping* is negative, and sufficiently strong to counterbalance the structural damping (which is always positive, for the structural model considered here), leading to a total negative damping scenario. In these situations, one finds, at the leading order, an oscillatory behaviour of the structure. Indeed, the aerodynamic forces exerted on the wing depend on its unsteady motion and not only on its instantaneous incidence. In particular, this aerodynamic force contains an aerodynamic damping which is proportional to the rotational velocity of the wing.

Based on a linear approach, it is known that flutter instability appears at a certain aircraft velocity, often called critical reduced velocity or critical flutter speed. Close to that threshold, the nonlinear limit cycle oscillations appear for either lower or upper reduced velocities, depending on the nature of the bifurcation (Thomas *et al.*, 2002; Moulin *et al.*, 2022). In the case of a soft or supercritical bifurcation scenario, flutter can only appear for velocities higher than the critical flutter speed, whereas for a hard or subcritical bifurcation scenario, nonlinear oscillations may appear below the linear threshold if disturbances are sufficiently large.

The major types of flutter encountered on aircraft can often be analysed in terms of idealised models having only a small number of degrees of freedom. An even greater simplification is the replacement of the three-dimensional wing model by an equivalent two-dimensional airfoil model, where several types of flutter can be investigated and categorised, as the coupled-mode flutter, the transonic flutter, the stall flutter, the single-degree-of-freedom pitching flutter or the laminar separation flutter. The present thesis will focus on the last type of flutter. Prior to this, we will review the literature devoted to the other types of flutter.

Coupled-mode flutter, also called classical or coalescence flutter, is a phenomenon where at least two structural normal modes (classically the bending and torsion modes) are coupled and excited through the time-dependent aerodynamic loads (Hancock *et al.*, 1985). The phenomenon was firstly treated using linear unsteady inviscid formulations, valid on a high chord-based Reynolds number and fully attached flow framework, predicting the critical conditions for the generic case of a two-degree-of-freedom pitch-plunge wing (Theodorsen, 1935; Sears, 1941). This phenomenon was also reported and treated by Rocard (1943), describing the coupling of the bending and torsion modes on a clamped wing. In subsequent works, Barmby *et al.* (1951) extended Theodorsen theory to swept wings, while Yates Jr. (1966) extended it to subsonic, supersonic and hypersonic flows, both validating the theoretical results with experiments. While flutter for low subsonic attached flows can, in general, be accurately predicted with these seminal linearised theories, such methods fail for separated or transonic flows where the traditional small-disturbance formulation is inherently nonlinear (see, for example, Ueda *et al.* (1984)). This nonlinear behaviour is not particular to the classical flutter, but can also be found for example in laminar separation flutter or transonic flutter phenomena.

Several studies have tried to better understand the nonlinear regime of flutter phenomena. The nonlinearity sources can be either structural or aerodynamic. In the structural side, the main sources are: (i) geometric, where the system response is altered due to the significant changes in the initial shape of the structure; (ii) damping, where the damping forces of the structure contribute to the nonlinear response. For example, Lee *et al.* (1999) studied the effect of a cubic structural restoring force on the flutter characteristics of a two-dimensional airfoil placed in an incompressible flow and,

more recently, Patil *et al.* (2004) carried out a nonlinear aeroelastic analysis for high-aspect-ratio wings. Concomitantly, the main sources of aerodynamic nonlinearities are: (i) flow separation, either due to an increase of the angle of attack of a wing or to a laminar separation of the boundary layer; (ii) appearance of a shock in the transonic flow regime, where the discontinuity in the pressure distribution interacts with the boundary layer, causing separation. As an example, Bendiksen (2011) made a review on unsteady transonic aerodynamics and its relevance on understanding the flutter, divergence, and control reversal phenomena of transonic aircraft. Beedy *et al.* (2003) developed a nonlinear method of stall flutter analysis based on an ONERA aerodynamic model (Tran *et al.*, 1980).

Unlike the classical flutter, ***stall flutter*** is a self-excited limit cycle oscillation caused by the interaction of a dynamic stall event with the inertial and elastic characteristics of a wing. In its turn, dynamic stall is defined as an unsteady aerodynamic phenomenon, characterised by the abrupt loss of aerodynamic loads (lift and/or pitching moment) due to flow separation on wings undergoing unsteady motions (Halfman *et al.*, 1951). Stall flutter is a nonlinear dynamic phenomenon that can even be found when considering only the torsional degree of freedom (Corke *et al.*, 2015). This phenomenon can be encountered in a variety of situations, such as helicopter rotor blades (Tang *et al.*, 1992), wind turbine blades (Hansen *et al.*, 2006) or flexible wings (Razak *et al.*, 2011).

Concerning the experimental literature, Amandolese *et al.* (2013) studied the dynamical response of a two-degree-of-freedom flat plate undergoing classical coupled-mode flutter in a wind tunnel at low-to-moderate Reynolds number ($Re \approx 2.5 \times 10^4$). Dimitriadis *et al.* (2009) studied a NACA0012 airfoil undergoing stall flutter oscillations in a low-speed wind tunnel, characterising the local bifurcation behaviour of the dynamic system. Razak *et al.* (2011) investigated the stall flutter of a rectangular wing through pressure, acceleration, and Particle Image Velocimetry (PIV) measurements, finding that the dynamic stall mechanism has significant influence on the occurrence and on the characteristics of stall flutter oscillations.

In addition to the previous aeroelastic phenomena, one can find the ***Single-Degree-Of-Freedom (SDOF) pitching flutter***, which is a flutter instability that appears for *attached* flows around an airfoil oscillating in the pitch direction with an amplitude of approximatively $\alpha = 0.5^\circ$. This type of flutter was first discovered by Glauert (1930) and subsequently investigated by Kiergan *et al.* (1942) and Smilg (1949) for attached potential flows under a two-dimensional incompressible hypothesis. Additionally, this phenomenon was reported for supersonic regimes by Garrick *et al.* (1946). Runyan (1951) and Runyan *et al.* (1952) further explored the effect of the compressibility on subsonic regimes and the position of the axis of rotation. These works included a set of experimental results, confirming the existence of a SDOF pitching flutter for unswept wings with very high values of inertia.

Figure 3 illustrates the instability zone predicted by the linearised theory, for three different Mach numbers. These results show a destabilising trend for when the Mach number is increased. Further, it was noted that the reduction of the wing's aspect ratio was strongly stabilising, as well as the increase of the structural damping. Despite the initial interest on this flutter phenomenon, the case was considered only as an academic case study and with little practical interest, since it required the moment of inertia to be several orders of magnitude higher than the one typically found on an aircraft (Bisplinghoff *et al.*, 1955, p. 617).

The extension of the linearised theory to the compressible inviscid *attached* flows was only accomplished several years later by Jones *et al.* (1997) which noted that thicker airfoils may achieve SDOF flutter under more realistic conditions. The extension to viscous flows was investigated in Kakkavas (1998), using a URANS model, closed with a Baldwin–Lomax model (Baldwin *et al.*, 1978), for a Reynolds number of 10^6. Among their findings, they note that viscous flow effects had a stabilising influence, reducing the possibility of SDOF flutter.

At the same time, the SDOF pitching flutter was also observed for transonic and low supersonic speeds regimes.

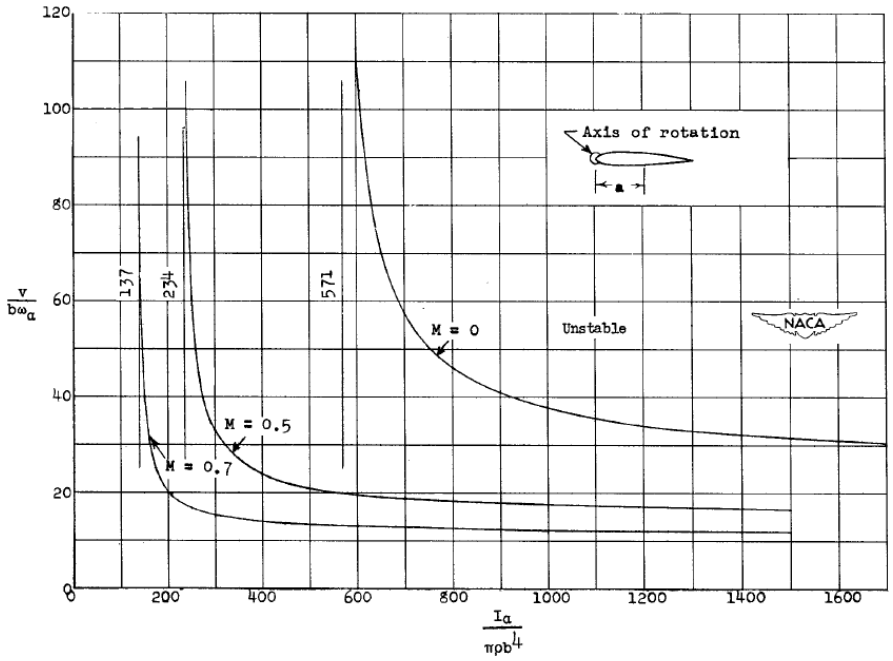

Figure 3 – *Graphic extracted from Runyan (1951), plotting the critical reduced velocity for the SDOF pitching flutter versus the moment of inertia about the leading edge of a wing for various Mach numbers. For each case, the unstable region is located on the right of the corresponding curve. The vertical asymptotes, on the left limit of the unstable zone, indicate the smallest value of the inertia parameter at which the oscillation can occur.*

Experimental evidence of this phenomenon at the bottom of the transonic dip[1] was obtained during the late 1950s and into the 1960s in wind tunnel tests by Bratt *et al.* (1954) and Bratt *et al.* (1962). A recent review is presented in section 7 of Bendiksen (2011) on the general features of the transonic SDOF pitching flutter. Recently, Gao *et al.* (2016), studied this phenomenon with a reduced-order model, arguing that transonic flutter, differently from the classical flutter, emerge from the coupling of a structural and a fluid mode. Transonic SDOF flutter can also be observed in control surfaces (Lambourne, 1968), denoted "buzz", characterised by a self-excited and sudden vibration of the aileron yielding large amplitudes, potentially leading to permanent damage of the aircraft structure.

In this thesis, we will investigate and describe a similar flutter phenomenon, also characterised by only the pitch degree of freedom, but observed for subsonic regimes (in particular incompressible regimes) and for lower Reynolds numbers, where the separation of the boundary layer plays an important role. The phenomenon was recently discovered and labelled *laminar separation flutter*. To introduce this phenomenon, we first proceed to a physical description of the transitional flow regime around a NACA0012 airfoil.

Transitional flow regime

For conventional commercial aircraft wings, usually in transonic regimes and whose Reynolds number exceeds a million, a turbulent flow regime is readily triggered from upstream locations near the leading edge, leading to a boundary layer that remains attached to the wing's surface for a relatively high range of angles of attack. However, for lower

[1] Transonic dip represents a flight envelope region where a sharp drop of the critical flutter speed is found as the flow reaches a transonic regime.

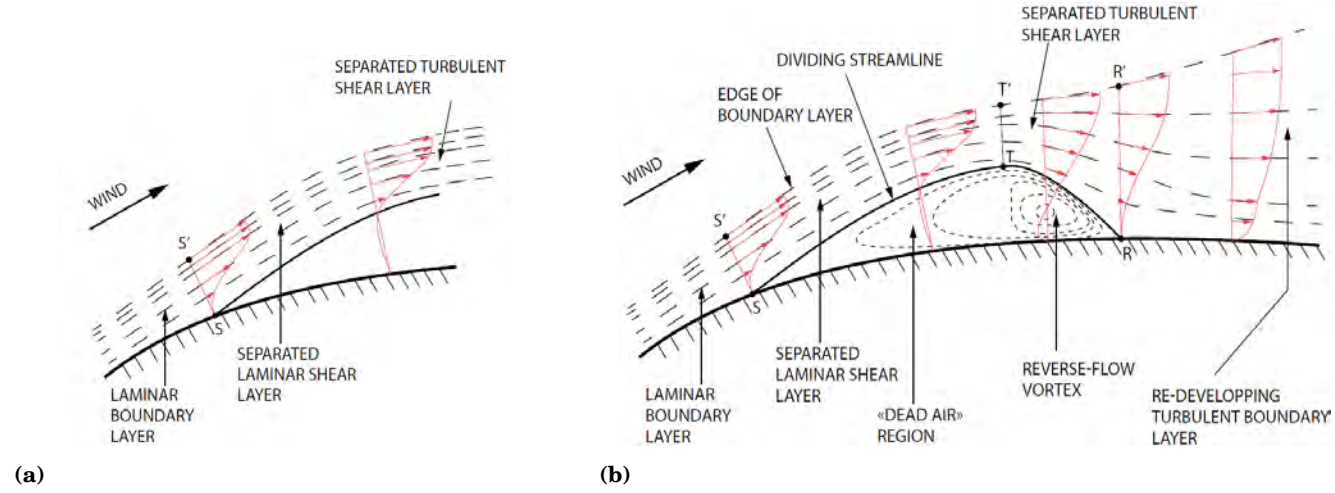

Figure 4 – *Schematic illustration of a two-dimensional laminar boundary layer separation (left) and of a laminar separation bubble (right). Adapted from Busquet (2020).*

Reynolds and Mach numbers, corresponding for instance to the flight regimes of drones and gliders, the transition location moves downstream, originating a laminar boundary layer over a considerable portion of the wing. For a low-to-moderate Reynolds number range, $10^4 \leq Re \leq 10^6$, the boundary layer is characterised by the coexistence of laminar, transition and turbulent regions, where complex viscous phenomena can occur, such as the formation of a laminar separation bubble (Mueller, 1951).

Laminar separation bubble

Laminar boundary layer separation over an airfoil describes the phenomenon where a laminar attached boundary layer separates from the surface of the airfoil. This results from a strong adverse pressure gradient in the streamwise direction, present downstream of the point of minimum pressure. After separation, the resulted shear flow is usually very unstable and prone to transition to a turbulent state, as a result of the amplification of velocity disturbances present immediately after the separation. As for example described in Busquet (2020), two scenarios can be encountered. The first case is illustrated in figure 4a. The laminar separation of the boundary layer occurs at the section $\overline{SS'}$. The separation point, S, represents an inflection point beyond which the flow velocity close to the airfoil surface has an upstream direction. On the separated boundary layer, a transition of the flow field to a turbulent state can occur. In this scenario, the boundary layer remains separated up to the end of the surface. As a consequence, a large wake is formed downstream the trailing edge, which is usually associated to large values of aerodynamic resistance/drag. In a second scenario, illustrated in figure 4b, the rise in pressure of the shear flow due to turbulent mixing is sufficiently high to cause the reattachment of the separated flow, at the point R, located before the trailing edge. From the section $\overline{RR'}$ onwards, a turbulent attached boundary layer is formed. The region formed under the separated shear layer, between the airfoil surface and the dividing streamline, is termed ***Laminar Separation Bubble*** (LSB). Figure 4b presents a classical model of the time-averaged structure of a laminar separation bubble, proposed by Horton (1968). The transition of the separated shear layer is reduced to the section $\overline{TT'}$, rather than a spatial region, in order to simplify the exposure.

As an example of the latter scenario, we present in figure 5 the distribution of the friction and pressure coefficients along the airfoil surfaces for a time- and spanwise-averaged solution of a Direct Numerical Simulation (DNS) at $Re = 50\,000$

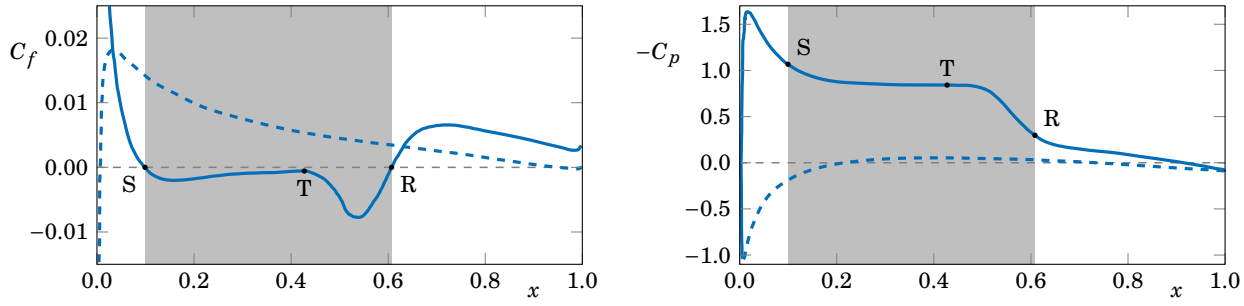

Figure 5 – *Time- and spanwise-averaged distributions of the friction coefficient C_f (left) and the pressure coefficient C_p (right) associated to DNS simulations at $Re = 50\,000$ and $\alpha = 5°$, from Jones et al. (2008). The solid and dashed blue lines represent the distribution along the upper and lower surfaces, respectively. The separation and reattachment points are noted S and R, respectively. The transition point is graphically estimated and noted T. The grey zone for $0.099 < x < 0.607$ represents the region where the laminar separation bubble is present.*

and $\alpha = 5°$, from Jones *et al.* (2008). The presence of a laminar separation bubble is observed in the upper surface of the airfoil, represented by the solid blue line. At these conditions, the flow transitions to (well resolved in the simulations) turbulence, with a laminar separation bubble forming on the first half of the airfoil ($0.099 < x < 0.607$). The separation and reattachment points are characterised by a null friction stress at the wall. The recirculation region on the LSB can be divided into two sub-regions relative to the average position of transition. The first sub-region is located between the separation point S and the transition location T and is characterised by a slow-moving reverse flow. As a result, the streamwise pressure gradient is nearly zero, resulting in a plateau on the pressure distribution of the airfoil upper surface. Concomitantly, the friction coefficient is characterised by the slightly negative value. This region is usually called the "dead air" region. The second sub-region is located between the averaged transition position T and the reattachment point R. This region is characterised by a vortical structure with a strong circulation, called *reverse-flow vortex*. This recirculation causes a drop in the friction coefficient upstream of the reattachment point. The abrupt reattachment of the shear layer leads to a rapid increase in surface pressure.

Laminar separation bubbles appear in numerous aerodynamic applications, such as low Reynolds number flying vehicles, high-altitude long-endurance unmanned aerial vehicles (Shimoyama *et al.*, 2017), Mars exploration aerial vehicles (Anyoji *et al.*, 2014) or dynamic stall characteristics of wings (Chen *et al.*, 2021), to cite a few. The existence of a laminar separation bubble for a certain airfoil shape is dependent on the Reynolds number, angle of attack and freestream turbulence level. In fact, the LSB on an airfoil can be eliminated completely by enforcing transition upstream of the point of separation (*e.g.*, Lei *et al.* (2020)). In many applications, this is not desirable since it results in a turbulent boundary layer over a large portion of the airfoil, leading to an increase of the skin friction coefficient and larger values of the total drag coefficient.

The interest on separation bubbles firstly arose from their occurrence on the upper surface of an airfoil at incidence, playing an important role on its stalling characteristics (Jones, 1934). In particular, the LSB was associated to a thin-airfoil stall occurrence (McCullough *et al.*, 1951), characterised by a laminar flow separation near the leading edge with reattachment at a point which moves progressively rearward, towards the trailing edge, with the increase of the angle of attack.

Classically, the laminar separation bubbles were classified into two types: *short* and *long* bubbles (Owen *et al.*, 1955). Short bubbles were defined as possessing a bubble length approximately 10^2 times the displacement thickness of the boundary layer at the separation point, corresponding only to a few percent points of the airfoil chord. On the other hand,

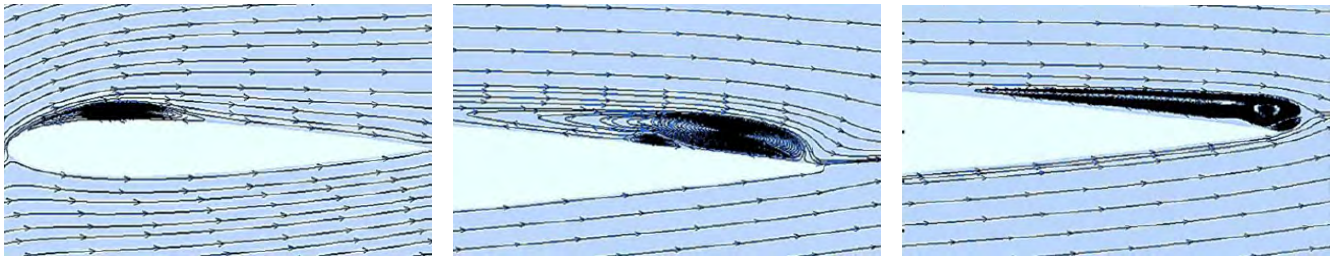

(a) **(b)** **(c)**

Figure 6 – *Representation of different types of laminar separation bubbles: a short bubble (left), a long bubble (centre) and a trailing-edge bubble (right), from Xia* et al. *(2021).*

long bubbles were defined as having a length of order 10^4 times the displacement thickness of the boundary layer at the separation point, corresponding to more than 20% of the entire airfoil. One of the earliest studies on the issue was conducted by Tani (1964), who observed that the length of short bubbles decreased with the angle of attack at small incidences until a critical state was reached, where the bubble suddenly increases in length. This sudden transition from short to long bubbles, or even to a fully separated state of the boundary layer with no reattachment is known as a bubble "bursting".

An example of the structure of short and long bubbles is shown in figures 6a and 6b, extracted from a recent review of the aerodynamic characteristics of a flow field over different airfoils at low Reynolds number (Xia *et al.*, 2021). In addition to these two types of laminar separation bubbles, a third type of bubble was recently introduced in the literature by Bai *et al.* (2016), the trailing-edge LSB, presented in figure 6c (also referred as open bubble, *e.g.*, in ElAwad *et al.* (2019)). They reported the presence of a trailing-edge LSB for a symmetric SD8020 airfoil at $Re = 40\,000$. The trailing-edge LSB precedes the emergence of a long LSB as the angle of attack increases. This type of bubble can also be found in the previous publications, although categorised as a long LSB or just as a separated flow regime (*e.g.*, Kojima *et al.* (2013)). The trailing-edge LSB is topologically different from the classic long LSB. The former is characterised by a main vortex located above the trailing edge, in contrast to the reverse-flow vortex of a long LSB, located above the upper surface of the airfoil. Additionally, the separated shear layer above a trailing-edge LSB does not present a time-averaged reattachment point, in contrast to the long LSB shear layer, that reattaches before the trailing edge. In the present thesis, the emergence of a laminar separation bubble will be investigated for different time- and spanwise-averaged solutions of Direct Numerical Simulations over a NACA0012 airfoil at different fixed incidences, discussing, among other topics, its impact on global coefficients such as the aerodynamic moment. The next paragraphs introduce the characteristics of these global coefficients on a low-to-moderate Reynolds number.

Negative lift and aerodynamic moment at small angles of attack

In the low-to-moderate Reynolds number regime, the laminar boundary layer separation phenomenon has been associated to a counter-intuitive behaviour of the global coefficients, such as drag, lift and aerodynamic moment coefficients, as function of the angle of attack. We illustrate this phenomenon in figure 7, by the drag and lift evolutions with the angle of attack, from the literature (Ohtake *et al.*, 2007; Mueller *et al.*, 1982). Concerning the drag coefficient, the presence of a laminar boundary layer on a considerable part of the airfoil enables one to obtain a much lower skin friction component, when compared to the values obtained with a turbulent boundary layer found in the general aviation and commercial transport aircraft. This leads to the presence of a low drag regime for a range of angles of attack, due to a predominance of

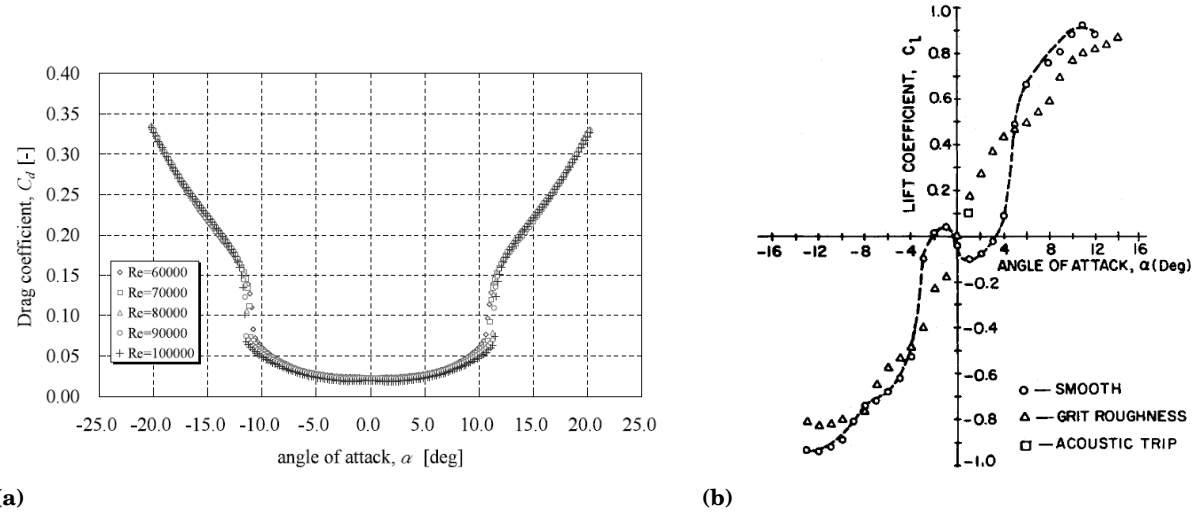

(a) **(b)**

Figure 7 – *On the left, evolution of the drag coefficient with the angle of attack for different Reynolds numbers, from the experiments of Ohtake et al. (2007). On the right, evolution of the lift coefficient with the angle of attack for* $Re = 130\,000$*, from the experiments of Mueller et al. (1982). In this case, three sets of data are plotted: the circles represent the unperturbed experiments, where a negative lift is observed on the range* $0° < \alpha < 3°$*, the triangles represent the experiments where the boundary layer was tripped at the leading edge, and the square, where the flow was acoustically excited.*

the laminar flow, often called "drag bucket". This phenomenon can be observed in figure 7a, on the range $-11° \lesssim \alpha \lesssim 11°$. Concerning the lift coefficient evolution (figure 7b), one can readily note the presence of an initial negative region of this coefficient for an incidence range well bellow the stall angles. This nonlinear behaviour could not be predicted using linear theories, such as the inviscid thin-airfoil theory, which predicts a linear evolution of the lift coefficient, with a positive slope of 2π. Mueller *et al.* (1982) were the first team to experimentally describe this phenomenon, for the symmetric NACA66$_3$-018 airfoil at $Re = 130\,000$. They found this negative region of the lift coefficient in the range $0° < \alpha < 3°$, followed by a change in sign as the angle of attack increases. Bellow and above this Reynolds number, no negative lift was observed. This nonlinear behaviour is represented by the black line and the circles marks. The phenomenon was completely removed by addition of surface roughness (triangle marks) and also by acoustic excitation (square mark). With these modifications on the flow, no laminar boundary layer separation is found. The results of Mueller *et al.* (1982), associated to this nonlinear behaviour of the lift global coefficient, appeared isolated in the literature at the time.

The same observations were only described in the recent years for a NACA0012 airfoil. Ohtake *et al.* (2007) observed this phenomenon in a low-speed wind tunnel, for Reynolds numbers between $Re = 25\,000$ and $Re = 70\,000$. One year later, Yonemoto *et al.* (2008) investigated this phenomenon using two-dimensional Navier–Stokes computations, proposing that the emergence of a negative lift is due to a reverse flow on the upper surface at the trailing edge, that accelerates the boundary layer on the lower surface. A review on the basic understanding of airfoil characteristics at low Reynolds numbers is presented in Winslow *et al.* (2018), where this phenomenon was reported. A comparison between the experimental and numerical results on the literature for different airfoils was carried out by Tank *et al.* (2017a,b), and studied by Pranesh *et al.* (2019) on the NACA0012 airfoil using two-dimensional RANS computations, with a SST k–ω closure model, used in conjunction with a γ–Re_θ transition model.

As reported in Pranesh *et al.* (2019), the flow field around the NACA0012 airfoil at $Re = 50\,000$ and $\alpha = 0°$ is characterised by a laminar separated boundary layer, that transitions while separated, and does not reattach. As the

angle of attack increases, the separation point moves upstream. For $\alpha = 4°$, the turbulent separated boundary layer reattaches, forming a long LSB on the upper surface. They further report that an increase of α beyond $4°$ resulted in a shorter LSB, moving towards the leading edge. Finally, we note that this change in the topology of the flow field as the incidence increases has a similar effect on the evolution of the aerodynamic moment coefficient, which was also reported in the cited literature.

The above considerations were made for fixed airfoil configurations, where no structure was taken into account. In this thesis, we will investigate a fluid–structure instability, the laminar separation flutter, in which the laminar separation and the negative aerodynamic moment phenomena play an important role on the structure oscillations. In that way, we continue in the next section our discussion on this type of fluid–structure instability.

Laminar separation flutter

The pioneer experimental investigation of Poirel *et al.* (2008) reported a new aeroelastic phenomenon, labelled ***Laminar Separation Flutter*** (LSF), described as the self-sustained pitch oscillation of an airfoil mounted on a torsional spring system. These oscillations, reported on a NACA0012 airfoil for the Reynolds number range of $45\,000 \leq Re \leq 130\,000$, are characterised by a Strouhal frequency around $St_{LSF} = 0.06$ (based on the airfoil chord) and a maximum amplitude of oscillation of $\alpha_{max} \approx 5.5°$, around the equilibrium position at $\alpha = 0°$. The authors suggested that the loss of stability of the airfoil at its equilibrium position and, consequently, the dynamics of the pitch oscillations, were governed by the laminar separation of the boundary layer over the airfoil, either due to a trailing edge separation or to the presence of a laminar separation bubble.

The phenomenon was numerically reproduced by Poirel *et al.* (2011), where two-dimensional coupled time-marching aeroelastic simulations were performed for $50\,000 < Re < 150\,000$. The authors adopted a purely two-dimensional laminar fluid model and a URANS fluid model, the latter associated to a SST k–ω turbulence model with a low-Reynolds-number correction. The investigation confirmed that the laminar separation of the boundary layer near the trailing edge plays a critical role in initiating and sustaining the pitch oscillations. For this reason, the phenomenon is labelled as *laminar separation flutter*. The authors also showed that the turbulence viscosity tends to inhibit the existence of the instability. In subsequent studies, this instability was investigated by Barnes *et al.* (2016, 2018), where Implicit Large-Eddy Simulations (ILES), coupled with the structural dynamics, were performed. Among the findings, the authors found the existence of the flutter limit cycle oscillation beyond the initial Reynolds number range investigated by Poirel *et al.* (2008), $77\,000 \leq Re \leq 200\,000$, at which the pitch instability was observed after imposing an initial disturbance on the airfoil incidence. They also reported a reduction on the size of the LSB with the increase of the Reynolds number.

The different phenomena associated to the flow dynamics on the limit cycle oscillation of the LSF are explored in figure 8a, taken from Barnes *et al.* (2016). The figure represents different instantaneous flow fields during half of a flutter oscillation period, between the maximum and minimum incidences, *i.e.*, during a pitch-down phase. The flow fields are associated to the lower airfoil surface, with the same phenomena appearing on the upper airfoil surface for the pitch-up phase. During the first stages of the flutter oscillation period, illustrated by the first instantaneous flow fields in the figure, a laminar separation is formed on the rear portion of the wing. Eventually, as the angular displacement continues to decrease, the separated shear layer becomes unstable, transitions to turbulence, and reattaches at the trailing edge. This process imparts a brief spike in the moment coefficient which tends to damp the limit cycle oscillation. The long laminar separation bubble is then observed up to the minimum incidence instant, characterised by the presence of spanwise coherent boundary layer vortices, as displayed in the figure. This flow pattern alternates between the upper and lower surfaces in subsequent strokes.

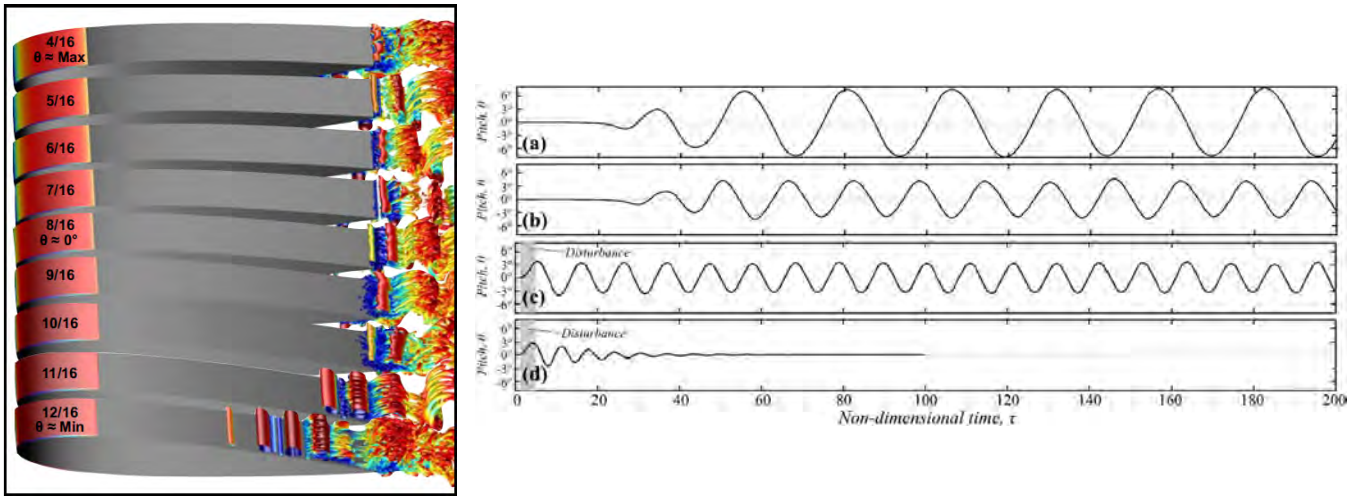

(a) **(b)**

Figure 8 – *On the left, three-dimensional view of instantaneous Q-criterion isosurfaces from ILES simulations of the lower airfoil surface for* $Re = 77\,000$ *and* $K_s^{dim} = 0.3$Nm*, at several phases of the pitch-down motion, between the maximum and minimum incidences (Barnes* et al.*, 2016). On the right, time history of the pitching oscillations at* $Re = 77\,000$ *for* $K_s^{dim} = 0.003$*,* 0.3*,* 1 *and* 3Nm *(Barnes* et al.*, 2019). An initial disturbance on the structural model was introduced on the two last cases.*

The influence of the structural stiffness on the LSF phenomenon was investigated in more detail in Barnes *et al.* (2019) for $Re = 77\,000$ and $Re = 110\,000$, where the LSF is shown to persist over several orders of magnitude of structural rigidity. Figure 8b, taken from this reference, presents the time history of the angular displacement for different values of the structural stiffness, K_s^{dim}. The simulations were initiated from a time-marching solution at a static angle of $\alpha = 0°$. For the lower values of K_s^{dim}, represented on the top evolutions, the self-sustained oscillations appear readily after a few convective time units. A first exponential growth of the incidence is observed, followed by the limit cycle oscillations, whose maximum amplitude decreases with the increase of K_s^{dim}. In the two last time evolutions, for higher values of K_s^{dim}, an initial disturbance on the aerodynamic moment was introduced at the beginning of the simulations in order to prompt the limit cycle oscillations. As noted by the authors, this perturbation was introduced in the "Cases which do not oscillate on their own [...]". This suggests the existence of different stable solutions for the same values of structural stiffness. In the last time evolution, the value of the structural stiffness is sufficiently high to cause the airfoil to remain on its equilibrium position at $\alpha = 0°$.

The authors further concluded that the effect of the structural rigidity at a fixed Reynolds number exhibited a similar behaviour as the effect of Reynolds number at a fixed stiffness. More precisely, both parameters influence the timing of transition events relative to the pitch limit cycle, with, for example at high stiffness values, a turbulent reattachment that occurs at a later phase of the cycle. Further, as the stiffness increased, the LSB was reported to increasingly be dominated by laminar—rather than turbulent—reattachment. This shift in the flow structure resulted in an increasingly nonlinear behaviour of the aerodynamic moment over the flutter oscillation. Likewise, the same effects were observed to occur when the Reynolds number was decreased at a fixed stiffness in Barnes *et al.* (2018).

Finally, although the phenomenon was initially identified considering a single degree of freedom, the pitching, several subsequent analyses also detected it in cases with two degrees of freedom, pitching and heaving. These studies include the experiments of Poirel *et al.* (2012, 2014), numerical LES simulations from Yuan *et al.* (2013), among others.

In all the above references, the lower Reynolds number limit of the LSF oscillations was reported to be around $Re \approx 50\,000$. Below this value, the literature reports negligible incidence oscillations of the FSI configuration around $\alpha = 0^\circ$. With that in mind, in this thesis we will investigate both the nonlinear regimes for the Reynolds number range where the LSF was reported in the literature, as well as the nonlinear regimes that arise for lower Reynolds numbers, which precede the LSF oscillations. This investigation will be performed with a fluid–structure time-marching scheme, where the fluid will be modelled by the two-dimensional Navier–Stokes equations. The parametric space will be explored by varying both the structural stiffness and the Reynolds number. The onset of these fluid–structure oscillations will also be investigated in a linear stability analysis framework, presented in the next paragraphs.

Fluid–structure linear stability analysis

Linear Stability Analysis (LSA) theory has been of central importance in fluid mechanics ever since the observation that the property of a flow state being a solution of the governing equations is no guarantee that it will actually be realised in practice. The linear stability theory started on a hydrodynamic framework at the late 19^{th} century with the controlled experiments of Reynolds (Reynolds, 1883) and the works of Rayleigh (1879) and Kelvin (1887). The concept of linear stability was later extended to coupled fluid–structure systems, where the primordial aim was to delimit the flight envelope of military and commercial aircraft cruise flights, whose Reynolds number often exceeds a million (Bisplinghoff *et al.*, 1955; Clark *et al.*, 2004).

The notion of stability is intimately related to the evolution of an infinitesimal perturbation imposed to an equilibrium point of a dynamic system. In particular, in a modal approach, used in this thesis, we are interested on the long-term evolution of these perturbations that are decomposed as the sum of linearly independent modes. The linear stability of an equilibrium point is then obtained from a spectral analysis of the linearised equations governing the dynamic system. A stable equilibrium point is one where a perturbation decays in time and the system returns to its equilibrium state. On the other hand, considering an unstable equilibrium point, this same perturbation grows exponentially in time, eventually leading the system to a different attractor solution (which may be for instance another stable equilibrium point, a limit cycle, or a chaotic attractor) (Schmid *et al.*, 2012).

A classical example of hydrodynamic instability is the emergence of a vortex shedding behind a rigid circular cylinder immersed in a low Reynolds number flow. This instability arises from a Hopf bifurcation (Provansal *et al.*, 1987; Sreenivasan *et al.*, 1987), for a Reynolds number around 46.7. Below this threshold, the flow is steady in time. In contrast, above this threshold, an unsteady von Kármán vortex wake is observed. The bifurcation threshold is predicted via a LSA around an equilibrium state that corresponds to the steady solution of the Navier–Stokes equations, also known as *base flow* solution. After the onset of the vortex shedding, the physics of the flow is usually described via a LSA around the *mean flow* state, rather than the base flow, as the former more accurately predicts some of the flow characteristics, *e.g.*, the vortex shedding frequency (Barkley, 2006; Sipp *et al.*, 2007). A further increase in the Reynolds number results in secondary instabilities leading to three-dimensional vortices, which can be investigated via hydrodynamic Floquet linear stability analyses, where the dynamic equilibrium state corresponds to the periodic flow solution vibrating at the frequency of the vortex shedding (Barkley *et al.*, 1996; Williamson, 1996a). In the context of this thesis, both hydrodynamic mean flow and Floquet analyses around a NACA0012 airfoil at $\alpha = 0^\circ$ will be performed. The former will be used to understand the role of the fluid modes on the FSI instabilities, while the latter will be used to investigate the onset of three-dimensional perturbations on the wing's spanwise direction.

Concerning fluid–structure systems, a classical benchmark on the low Reynolds number regime is the case of the spring-mounted circular cylinder, where vortex-induced vibrations may be observed below the fixed cylinder threshold (Cossu

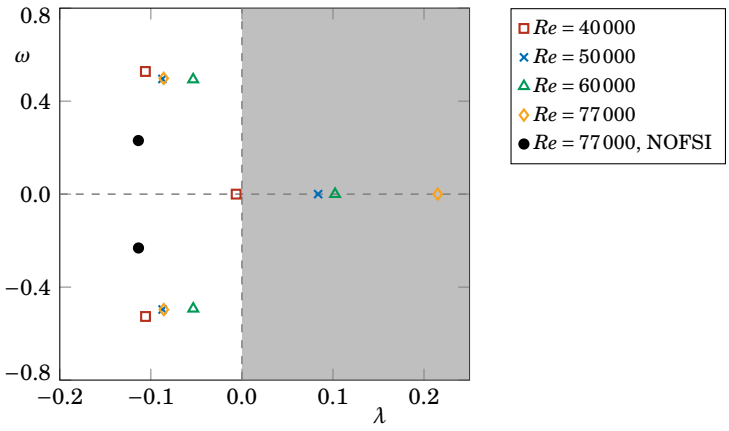

Figure 9 – *Aeroelastic eigenvalues of a mean flow LSA for different Reynolds numbers at* $\alpha = 0°$ *and* $K_s^{dim} = 0.15$Nm*. A complex pair of low frequency eigenvalues associated to a hydrodynamic analysis for a stationary wing at* $Re = 77\,000$ *and* $\alpha = 0°$*, is also plotted, noted NOFSI. All results are from Negi* et al. *(2021).*

et al., 2000; Meliga *et al.*, 2011; Zhang *et al.*, 2015b; Navrose *et al.*, 2016; Kou *et al.*, 2017; Sabino *et al.*, 2020). Below the fixed cylinder threshold, even if the flow by itself and the structure do not present intrinsic instability mechanisms, their mutual interaction may result in unstable scenarios. In particular, due to the presence of the additional degree of freedom of the structure, the fluid–structure instabilities were shown to be triggered for Reynolds numbers as low as 20. Among other fluid–structure studies, Assemat *et al.* (2012); Tchoufag *et al.* (2014a,b) examined the case of two-dimensional rigid bodies falling or rising freely in a viscous fluid, Pfister *et al.* (2020); Furquan *et al.* (2021) carried out a LSA on a flexible splitter plate attached to a rigid circular cylinder and Moulin *et al.* (2021) investigated the case of a rectangular plate mounted on heave and torsion springs.

After a primary bifurcation leading to a time-periodic limit cycle, fluid–structure systems may also be affected by secondary instabilities. The latter may be detected using a Floquet linear stability analysis, which represents a generalisation of the base/mean flow analyses presented above. In this case, rather than investigating the long-term perturbation evolution of a steady state, we study the growth or decay of a perturbation over one oscillation period. If the system is unstable, perturbations will grow progressively shifting the system away from its periodic equilibrium. In this case, the system is expected to transition to a behaviour which remains periodic, with the same period or with a doubled period, or to a quasi-periodic behaviour. Regarding the literature, Elston *et al.* (2004) employed this method to determine the onset of two-dimensional symmetry breaking in a quiescent fluid of an oscillating circular cylinder. More recently, Jallas *et al.* (2017) studied the symmetry breaking in time-periodic propulsive wakes for imposed flapping airfoils. Benetti Ramos *et al.* (2021) investigated the role of linear mechanisms in the emergence of nonlinear horizontal self-propelled states of a heaving foil in a quiescent fluid.

Concerning the low-to-moderate Reynolds number regime and, in particular, the linear stability studies investigating the laminar separation flutter phenomenon, the literature is rather scarce. The only study was conducted by Negi *et al.* (2021), performing a mean flow fluid–structure LSA over a NACA0012 airfoil configuration with a torsional degree of freedom. The mean flow fields were obtained from time- and spanwise-averaged solutions of DNS simulations at $\alpha = 0°$. They have shown that the spontaneous onset of the laminar separation flutter is due to a linearly unstable mode of the coupled fluid–structure interaction problem.

One of their main results is reproduced in figure 9, where the FSI eigenvalues are sketched in a spectrum representa-

tion for different Reynolds numbers. The growth rate of the eigenvalues, λ, is represented on the horizontal axis, while their corresponding frequency, ω, can be found on the vertical axis. An eigenvalue is deemed unstable if its growth rate is positive: $\lambda > 0$. Negi *et al.* (2021) concluded that the onset of pitch oscillations is caused by the emergence of a purely real eigenvalue, between the Reynolds numbers 40 000 and 50 000 (for a structural stiffness of $K_s^{dim} = 0.15$Nm). However, the divergence mode is only expected to lead to a diverging behaviour instability (as sketched in figure 2a), and not to an oscillating behaviour (as sketched in figure 2b). Hence, these results alone are unable to explain the existence of the self-sustained oscillations associated to the LSF, since no frequency is associated to the divergence mode.

In their investigation, Negi *et al.* (2021) suggested that the frequency selection of the self-sustained oscillations came from the linearly stable low frequency mode, whose frequency ($\omega \approx 0.5$) was in accordance with the frequency of the LSF observed experimentally. In that way, they concluded that "[...] the observed LCO frequency is likely to arise due to the nonlinear modification of the linearly stable aeroelastic mode, while the onset itself is caused by the divergence instability with zero frequency.". They also compared the FSI results with the results from a hydrodynamic analysis, present in the figure, highlighting the fact that no unstable modes were found when the pitching degree of freedom of the structure was not considered.

In light of these results, the present thesis will readdress the laminar separation phenomenon with different linear stability analysis strategies. In a first part, we will study the onset of the static instability of the airfoil configuration at $\alpha = 0\,^\circ$, associated to the presence of this linearly unstable divergence mode. We will extend the investigation from a mean flow analysis to the FSI Floquet analysis, where the presence of the divergence mode is studied for a periodic equilibrium state. Further, the influence of the low frequency modes of the hydrodynamic spectrum will be investigated in order to better understand the role of the additional torsional degree of freedom and to construct a simplified model to predict the fluid–structure eigenmodes. In a second part, both linear stability analyses will be used to explore the stability of a secondary equilibrium position of the fluid–structure system that may exist for $\alpha \neq 0\,^\circ$.

Organisation of the manuscript

The remaining pages of this thesis are divided in six chapters, organised as follows:

- Chapter 1 introduces in detail the fluid and structure models used in this thesis. First, the non-dimensional Navier–Stokes equations are expressed on a non-inertial reference frame. This is followed by the presentation of the dimensional and non-dimensional equations governing the pitch motion of the right body airfoil. Then, the formulation associated to the FSI Floquet linear stability analysis is introduced, along with the considered hypotheses. Two variants of the mean flow LSA are derived, where we highlight the simplifications made with respect to the Floquet formulation. The technical details on the finite element spatial discretisation of the Navier–Stokes equations are provided, as well as the details of the SUPG and grad-div stabilisation techniques employed. The different time-marching schemes used through this thesis are then introduced. Finally, preliminary results concerning the validation of some key aspects of the numerical implementation presented above are explored. This chapter is mostly meant to offload the rest of the manuscript from the cumbersome technical details, *e.g.*, the derivation of the Navier–Stokes equations on a non inertial reference frame or the derivation of the Floquet and mean flow linear stability analyses.

- In chapter 2, we describe the flow field around a NACA0012 profile wing and the corresponding aerodynamic forces acting on it from a Reynolds number of $Re = 1\,000$ to $Re = 65\,000$, at different angles of attack. No interaction between the fluid and the wing is taken into account as the wing incidence is fixed to a static position for each

simulation. In a first part, we consider the flow as being model by the two-dimensional Navier–Stokes equations, where we explore the onset of a vortex shedding on the wake of a NACA0012 airfoil and the notions of base and mean flow solutions. We then characterise the emergence of the three-dimensional instabilities in the airfoil spanwise direction, by the means of a hydrodynamic Floquet stability analysis. In a second part, we characterise both instantaneous and spectral properties associated to three-dimensional Direct Numerical Simulations carried out at $Re = 50\,000$ for five angles of attack, between 0° and 2°. In particular, time- and spanwise-averaged solutions are obtained from these simulations, that are later used for the mean flow stability analyses. In a third part, we present an alternative approach to evaluate the aerodynamic moment of the airfoil, based on the spatial distribution of the different terms of the Navier–Stokes equations, rather than the classic approach based on the stress integration over the fluid–solid interface.

- Chapter 3 is dedicated to the presentation and implementation of different methods for the computation of the FSI eigenpairs of the mean flow linear stability problem. The first type of methods is based on the exact formulation of the mean flow eigenvalue problem, where the inversion of the fluid–structure Jacobian is obtained by solely inverting the fluid Jacobian and by some additional matrix-vector product operations. The second type of methods is based on several relevant simplifications of the original problem. In particular, the results of the exact formulation are first compared to a quasi-steady formulation, where classic aeroelastic added coefficients are computed. Then, the FSI eigenmodes are approximated with the help of a rational function expansion solely based on the most relevant hydrodynamic eigenvalues.

- Chapter 4 explores the linear stability of the coupled fluid–structure system on the primary equilibrium position at $\alpha = 0^\circ$. We start by characterising the emergence of the divergence eigenmode, responsible for the departure of the structure from this equilibrium position. This analysis is based on the mean flow formulations present in the first chapter. We then investigate the influence of the structure parameters on both divergence and flutter eigenmodes, as well as the influence of the elastic centre position, Reynolds number and airfoil thickness. The FSI eigenmodes obtained with a mean flow from two-dimensional computations are then compared to the ones obtained with a time- and spanwise-averaged flow from three-dimensional computations. Finally, the emergence of the primary FSI instability is analysed via a Floquet FSI analysis, where a comparison with the results of the mean flow analyses and a comparison with the fluid–structure behaviour found for nonlinear time-marching simulations are carried out.

- Chapter 5 aims at investigating the different nonlinear behaviours arising in the present fluid–structure system, considering a two-dimensional model. First, we illustrate the different equilibrium positions admissible by the structure, retrieved from the quasi-steady mean aerodynamic moment curve evolution with the angle of attack. Secondly, we use nonlinear simulations of the coupled FSI problem to identify different possible regimes. By varying the structural stiffness and keeping the Reynolds number constant, we identify five different regimes. Third, a bifurcation diagram is sketched, highlighting different stable branches for the same values of structural stiffness. In particular, for a finite range of structural stiffness values, a bistable behaviour is identified characterised by the coexistence of chaotic and quasi-periodic solutions. Finally, we explore the different regimes appearing for $Re \geq 50\,000$, keeping the structural parameters constant, that ultimately lead to the global limit cycle oscillations referred to as laminar separation flutter.

- At the end of this thesis, in chapter 6, we revisit the different mean flow and Floquet linear stability analyses to investigate the stability of a secondary equilibrium position that may exist for certain values of structural stiffness. In a first part, we investigate the stability of these second equilibrium positions. In particular, we are interested

in predicting the emergence of the quasi-periodic solutions reported in the previous chapter. In a second part, we perform mean flow FSI analyses for the secondary equilibrium positions of the time- and spanwise-averaged solutions issued from three-dimensional simulations.

Chapter 1

Problem description and numerical tools

The characteristics of a flow field and the generated aerodynamic forces and moments on a body immersed in it are generally assessed by either experimental essays or by the means of numerical simulations. When these aerodynamic forces and moments are strong enough, they can induce deformations and displacements on the structure, which must be taken into account when modelling a fluid–structure problem. In the present thesis, we study this fluid–structure interaction via numerical simulations. In that way, this chapter is divided in five parts. In a first part, the mathematical formulation associated to the present problem is presented. The flow field is described by the two-/three-dimensional incompressible Navier–Stokes equations, the latter referred to as Direct Numerical Simulations (DNS). In a second part, the formulation associated to the rigid-body model is presented, with a spanwise torsional degree of freedom of the wing. In a third part, we summarise the fluid–structure formalism, introducing the slow and fast time scales and studying the solid response to a harmonic forcing. These developments serve as basis for the derivation of the linearised fluid–structure equations, introduced in a fourth part. The linearisation is first based on the fast time scale dynamics, with a Floquet FSI and mean flow FSI linear stability analyses. Then, an alternative derivation is made for the mean flow FSI stability analysis, based on the slow time scale dynamics. In a fifth part, the spatial discretisation, based on the Finite Element Method (FEM), and the time discretisations of the aforementioned equations are detailed, along with a description of the meshing procedure and the numerical details associated to the numerical stabilisation. The chapter ends with the presentation of several preliminary results associated to the numerical validation.

We start this chapter by introducing the inertial and non-inertial frames of reference in which the different formulations are based on.

1.1 Incompressible flow model

1.1.1 Inertial and non-inertial reference frames

A number of challenging problems arises when treating the coupling between a structure and the fluid flow, namely the fact that the domain occupied by the fluid is time-dependent. Several methods can be found in the literature in order to take into account this displacement, *e.g.*, the Immersed Boundary Methods (IBM) (Mittal *et al.*, 2005) or the Arbitrary Lagrangian–Eulerian (ALE) methods (Donea *et al.*, 2004). For a rigid-body configuration, as considered throughout this thesis, the flow field is modelled in a frame of reference attached to the body, such that the fluid–solid interface does not depend on the time (Mougin *et al.*, 2002). This reference frame is usually non-inertial due to the rigid-body motion.

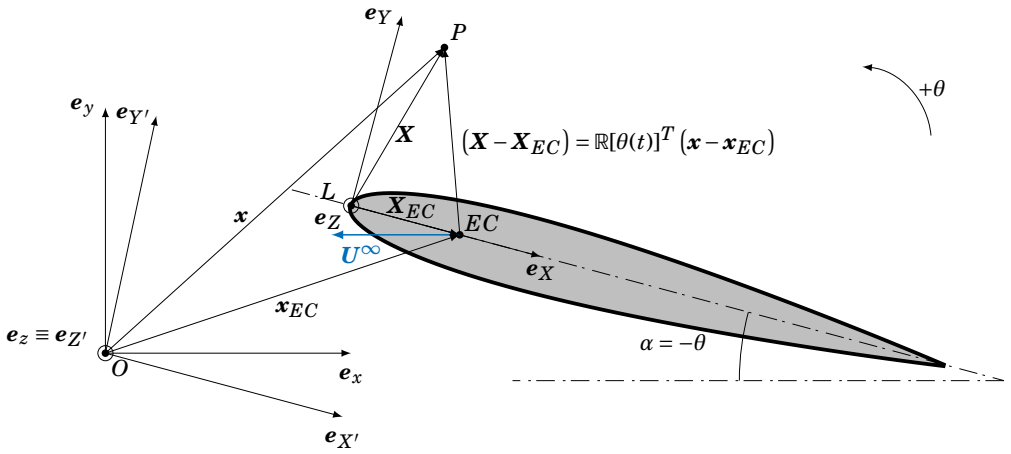

Figure 1.1 – *Schematic illustration of the transformation between the inertial and non-inertial frames, with the reference airfoil velocity vector, $\boldsymbol{U}^\infty$, in blue.*

The implementation of this last approach starts with the introduction of three orthonormal direct Cartesian reference frames. First, an absolute reference frame, noted $\mathscr{R}_a = (O, \boldsymbol{e}_x, \boldsymbol{e}_y, \boldsymbol{e}_z)$, assumed inertial and where the fluid is at rest far away from the wing, is defined, with an arbitrary origin O. At the same time, a second reference frame, noted $\mathscr{R}_{r'} = (O, \boldsymbol{e}_{X'}, \boldsymbol{e}_{Y'}, \boldsymbol{e}_{Z'})$, is defined, following the wing's rotation. Finally, a third reference frame, noted $\mathscr{R}_r = (L, \boldsymbol{e}_X, \boldsymbol{e}_Y, \boldsymbol{e}_Z)$, is introduced, following both wing's rotation and translation, with L the mid-span point at the leading edge of the wing. The last two references are referred to as relative or non-inertial reference frames.

The Cartesian coordinates of a generic point P can be represented in the frames $\mathscr{R}_a$ and $\mathscr{R}_r$, using $\boldsymbol{x} = [x, y, z]^T$ and $\boldsymbol{X}(t) = [X(t), Y(t), Z(t)]^T$, respectively, with $t \geq 0$ the time variable. We note that the position vector $\boldsymbol{X}(t)$ is time-dependent, since the reference frame $\mathscr{R}_r$ is non-inertial. The connection between the inertial and rotated frames is accomplished with the help of the rotation matrix, noted as $\mathbb{R}[\theta(t)]$. For a rotation around a spanwise axis passing through the point EC, this matrix only depends on the absolute angular displacement of the relative frame, θ, which depend on the time, t. The angular displacement is positive in the anticlockwise direction, whereas the angle of incidence or angle of attack, α, is positive in the clockwise direction, having $\theta = -\alpha$. In this way, the relation between $\boldsymbol{x}$ and $\boldsymbol{X}$ is given by:

$$(\boldsymbol{X} - \boldsymbol{X}_{EC}) = \mathbb{R}[\theta(t)]^T (\boldsymbol{x} - \boldsymbol{x}_{EC}) \quad \text{with} \quad \mathbb{R}[\theta(t)] = \begin{bmatrix} \cos[\theta(t)] & -\sin[\theta(t)] & 0 \\ \sin[\theta(t)] & \cos[\theta(t)] & 0 \\ 0 & 0 & 1 \end{bmatrix}, \tag{1.1}$$

where $\boldsymbol{x}_{EC}$ and $\boldsymbol{X}_{EC}$ represent the absolute and relative positions of the wing's elastic centre axis, respectively, around which the rotation is performed. This transformation can be visualised with the help of figure 1.1. The next sections are dedicated to the derivation of the fluid equations, projected on the non-inertial frame of reference that follows the rotation of the wing, but not its translation.

1.1.2 Inertial frame formulation

Physically, the general motion of a non-reactive continuum fluid is governed by a set of partial differential equations, commonly called Navier–Stokes equations (Landau *et al.*, 1987). For an incompressible fluid, where the fluid density ρ is

constant, this set of equations can be posed in a nondimensional form[1], with respect to the inertial frame $\mathscr{R}_a$, as:

$$\frac{\partial \boldsymbol{u}}{\partial t} + (\boldsymbol{u}\cdot\nabla)\boldsymbol{u} - \nabla\cdot\boldsymbol{\sigma}(\boldsymbol{u}, p) = \boldsymbol{0}, \tag{1.2a}$$

$$\nabla\cdot\boldsymbol{u} = 0, \tag{1.2b}$$

where $\boldsymbol{u}(\boldsymbol{x}, t) = [u, v, w]^T$ is the absolute fluid velocity and $\boldsymbol{\sigma}(\boldsymbol{u}, p)$ the stress tensor, depending on the fluid pressure, $p(\boldsymbol{x}, t)$, with $\boldsymbol{x} \in \Omega_{f,t}$. The fluid domain $\Omega_{f,t}$, represented in the absolute frame of reference, is considered to be moving due to the displacement of the fluid–solid interface. These equations were first described by Navier (1827), but their adequate physical justification was given only later on the work of Stokes (1845).

We assume an isotropic Newtonian fluid, where the viscous stress varies linearly with the velocity rate. The fluid dynamic viscosity coefficient, μ, is considered to be a positive constant, not varying with temperature and pressure—and hence with the position. Furthermore, the temperature of the fluid is also considered constant and Stokes' hypothesis is considered to hold[2]. With these hypotheses, the stress tensor is given by

$$\boldsymbol{\sigma}(\boldsymbol{u}, p) = -p\mathbb{1} + \frac{2}{Re}\boldsymbol{S}(\boldsymbol{u}),$$
$$\boldsymbol{S}(\boldsymbol{u}) = \frac{1}{2}\left(\nabla\boldsymbol{u} + (\nabla\boldsymbol{u})^T\right),$$

where $\boldsymbol{S}$ is the strain rate tensor and $\mathbb{1}$ the identity operator. The Reynolds number, used to characterise the ratio between the inertial and viscous forces within the fluid, is defined as $Re = \rho U^\infty c/\mu$, with U^∞ the reference velocity and c the constant chord of the unswept wing. The Reynolds number can also be written in terms of the fluid kinematic viscosity coefficient, $\nu = \mu/\rho$, as $Re = U^\infty c/\nu$. The values U^∞ and c are both fixed at 1. Therefore, the Reynolds number is varied by modifying the values of ν.

The pressure field is defined up to a constant and this constant is fixed in the numerical description (section 1.7). In the case of an incompressible flow, the pressure gradient corresponds to a more relevant physical quantity, representing a force per unit volume. Indeed, the pressure field in incompressible flows is not a thermodynamic variable and can be viewed, from an optimisation point of view, as a Lagrange multiplier associated with the isochoric constraint (equation 1.2b), which constrains the velocity field to remain divergence-free.

The problem is considered closed after taking into account the initial and boundary conditions. Physically, this means that, at infinity, the flow field tends to an unperturbed flow field at rest, with a velocity that tends to zero, while at the wing surface, Γ_w, the fluid velocity tends to the wing velocity such that the velocity continuity at the interface is respected (no-slip condition). These conditions can be posed as

$$\boldsymbol{u}(\boldsymbol{x}, 0) = \boldsymbol{u}_0(\boldsymbol{x}) \qquad \boldsymbol{x} \in \Omega_{f,t}, \tag{1.3a}$$

$$\boldsymbol{u}(\boldsymbol{x}, t) \to \boldsymbol{0} \qquad \|\boldsymbol{x}\| \to \infty, \tag{1.3b}$$

$$\boldsymbol{u}(\boldsymbol{x}, t) = \boldsymbol{u}_w \qquad \boldsymbol{x} \in \Gamma_w(t), \tag{1.3c}$$

with $\boldsymbol{u}_0$ the given initial fluid velocity at $t = 0$ (respecting the boundary conditions and the divergence-free condition and hence prescribing the initial pressure) and $\boldsymbol{u}_w$ the wing velocity. The wing velocity $\boldsymbol{u}_w$ is composed by a component

[1] The nondimensional Navier–Stokes equations are derived from their dimensional form, using dimensional analysis (Buckingham, 1914). The demonstration can be found in most of the introductory fluid mechanics books (*e.g.*, White (1991), pp. 81–89).

[2] Stating these hypotheses, the classical energy equation and the thermodynamic relations connecting the thermodynamic variables (density, specific internal energy and temperature) and the pressure are not considered in this thesis.

coming from the wing translation, given by $\boldsymbol{U}^{\infty} = -U^{\infty}\boldsymbol{e}_x$ (see blue arrow in figure 1.1), and a component coming from the wing rotation, detailed later. As stated previously, we note that $\Omega_{f,t}$ and Γ_w are both time-dependent. This situation can pose a series of numerical complications, as the ill-posedness of the time derivative at a point sufficiently near the interface between the fluid and the wing. To circumvent this time-dependency, the above equations are projected into the non-inertial frame, rotating with the wing, but with no translation velocity. This operation is conducted in two steps:

- In a first step, the space operators are rewritten with an explicit dependency on the relative space position, *i.e.*, not depending explicitly on the absolute coordinates, $\boldsymbol{x}$, but on the relative ones, $\boldsymbol{X}$;
- In a second step, the resulting system of equations is projected into the relative frame of reference rotating with the wing, $\mathscr{R}_{r'}$.

1.1.3 Space derivatives on the non-inertial frame

The explicit dependence on the state variables on space coordinates of the system $\mathscr{R}_r$ is written as $\boldsymbol{u}(\boldsymbol{x},t) = \boldsymbol{u}(\boldsymbol{X},t)$ and $p(\boldsymbol{x},t) = p(\boldsymbol{X},t)$. Further, the projection of the absolute velocity into the relative frames, $\boldsymbol{U}(\boldsymbol{X},t)$, is defined with the help of the rotation matrix in equation 1.1, yielding:

$$\boldsymbol{U}(\boldsymbol{X},t) = \mathbb{R}^T \boldsymbol{u}(\boldsymbol{X},t).$$

Each space derivative operation present in equations 1.2 can then be rewritten as (see appendix A for the detailed derivations):

$$\begin{aligned}
\text{Space derivative w.r.t. } \boldsymbol{x} &\Rightarrow \text{Space derivative w.r.t. } \boldsymbol{X} \\
(\boldsymbol{u}\cdot\nabla)\boldsymbol{u} &\Rightarrow \mathbb{R}[(\boldsymbol{U}\cdot\nabla)\boldsymbol{U}]\,, \\
\nabla\cdot\boldsymbol{\sigma}(\boldsymbol{u},p) &\Rightarrow \mathbb{R}[\nabla\cdot\boldsymbol{\sigma}(\boldsymbol{U},p)]\,, \\
\nabla\cdot\boldsymbol{u} &\Rightarrow \nabla\cdot\boldsymbol{U}\,,
\end{aligned}$$

where henceforward, the gradient operator, ∇, represents the space derivative with respect to the relative space coordinates, $[X,Y,Z]^T$.

1.1.4 Time derivative on the non-inertial frame

Concerning the time derivative, one can write

$$\partial_t[\boldsymbol{u}(\boldsymbol{x},t)]\Big|_{\boldsymbol{x}} = \partial_t[\boldsymbol{u}(\boldsymbol{X}(t),t)]\Big|_{\boldsymbol{x}} = \partial_t[\boldsymbol{u}(\boldsymbol{X},t)]\Big|_{\boldsymbol{X}} + \left(\frac{\mathrm{d}(\boldsymbol{X}-\boldsymbol{X}_{EC})}{\mathrm{d}t}\bigg|_{\boldsymbol{x}}\cdot\nabla\right)\boldsymbol{u}(\boldsymbol{X},t),$$

where the term $\mathrm{d}(\boldsymbol{X}-\boldsymbol{X}_{EC})/\mathrm{d}t$ represents the frame velocity vector projected on the relative frame. Since the domain is not deformable, $\mathrm{d}(\boldsymbol{X}-\boldsymbol{X}_{EC})/\mathrm{d}t$ also corresponds to the velocity of any point on the domain. Furthermore, if these points are considered to be on the wing surface, this term will also correspond to the wing velocity. Using equation 1.1, it can be developed[3] as

$$\frac{\mathrm{d}(\boldsymbol{X}-\boldsymbol{X}_{EC})}{\mathrm{d}t} = -\boldsymbol{\Omega}\times(\boldsymbol{X}-\boldsymbol{X}_{EC}) - \dot{\boldsymbol{X}}_{EC}\,, \tag{1.4}$$

[3] See Identity 5, in appendix A.

where $\dot{\boldsymbol{X}}_{EC}$ represents a velocity field, corresponding to the pure translation velocity of the frame (and the wing), on the relative frame, and $\boldsymbol{\Omega}(t) = [0, 0, \Omega(t)]^T$ its angular velocity vector, with a sole component on the $\boldsymbol{e}_z$-direction. The former is defined as

$$\dot{\boldsymbol{X}}_{EC} \equiv \boldsymbol{U}^{\infty} = -U^{\infty}\boldsymbol{e}_x = -U^{\infty}(\cos(\theta)\boldsymbol{e}_X - \sin(\theta)\boldsymbol{e}_Y)\,.$$

Injecting the previous developments into the Navier–Stokes momentum equation, one arrives to:

$$\frac{\partial \boldsymbol{u}}{\partial t} - \left(\left[\boldsymbol{\Omega}\times(\boldsymbol{X}-\boldsymbol{X}_{EC}) + \dot{\boldsymbol{X}}_{EC}\right]\cdot\nabla\right)\boldsymbol{u} + \mathbb{R}[(\boldsymbol{U}\cdot\nabla)\boldsymbol{U}] - \mathbb{R}[\nabla\cdot\boldsymbol{\sigma}(\boldsymbol{U},p)] = \boldsymbol{0}\,.$$

We can identify the rigid-body velocity field $\boldsymbol{U}_w$, defined in every point in space, corresponding to the motion of the relative frame with respect to the inertial frame, as

$$\boldsymbol{U}_w = \boldsymbol{\Omega}\times(\boldsymbol{X}-\boldsymbol{X}_{EC}) + \dot{\boldsymbol{X}}_{EC}\,,$$

where the first term accounts for the angular velocity, whereas the second term accounts for the translation velocity.

The final stage passes through the projection of the governing equations into the relative frame:

$$\mathbb{R}^T\frac{\partial \boldsymbol{u}}{\partial t} - \mathbb{R}^T[(\boldsymbol{U}_w\cdot\nabla)\boldsymbol{u}] + \mathbb{R}^T\mathbb{R}[(\boldsymbol{U}\cdot\nabla)\boldsymbol{U}] - \mathbb{R}^T\mathbb{R}[\nabla\cdot\boldsymbol{\sigma}(\boldsymbol{U},p)] = \boldsymbol{0}\,.$$

The development of the time derivative reads

$$\mathbb{R}^T\frac{\partial \boldsymbol{u}}{\partial t} = \frac{\partial \mathbb{R}^T\boldsymbol{u}}{\partial t} - \boldsymbol{u}\frac{\mathrm{d}\mathbb{R}^T}{\mathrm{d}t} = \frac{\partial \boldsymbol{U}}{\partial t} - \frac{\mathrm{d}\mathbb{R}^T}{\mathrm{d}\theta}\frac{\mathrm{d}\theta}{\mathrm{d}t}\boldsymbol{u} = \frac{\partial \boldsymbol{U}}{\partial t} + \boldsymbol{\Omega}\times\boldsymbol{U}\,,$$

where an additional term appears, $\boldsymbol{\Omega}\times\boldsymbol{U}$, which is associated to the rotational acceleration of the wing. The term associated to the rigid-body velocity field $\boldsymbol{U}_w$ is simplified as

$$\begin{aligned}\mathbb{R}^T([\boldsymbol{U}_w\cdot\nabla]\boldsymbol{u}) &= \nabla\cdot\left[\mathbb{R}^T\boldsymbol{u}\otimes\boldsymbol{U}_w\right] - \mathbb{R}^T\boldsymbol{u}\cancelto{0}{(\nabla\cdot\boldsymbol{U}_w)} = \nabla\cdot[\boldsymbol{U}\otimes\boldsymbol{U}_w] = [\boldsymbol{U}_w\cdot\nabla]\boldsymbol{U} + \boldsymbol{U}\cancelto{0}{(\nabla\cdot\boldsymbol{U}_w)}\\ \Rightarrow \mathbb{R}^T([\boldsymbol{U}_w\cdot\nabla]\boldsymbol{u}) &= [\boldsymbol{U}_w\cdot\nabla]\boldsymbol{U}\,.\end{aligned}$$

1.1.5 Non-inertial frame formulation

Finally, the previous developments lead to the incompressible Navier–Stokes equations projected on the relative frame

$$\frac{\partial \boldsymbol{U}}{\partial t} + \boldsymbol{\Omega}\times\boldsymbol{U} + ([\boldsymbol{U}-\boldsymbol{U}_w]\cdot\nabla)\boldsymbol{U} - \nabla\cdot\boldsymbol{\sigma}(\boldsymbol{U},p) = \boldsymbol{0}\,, \tag{1.5a}$$

$$\nabla\cdot\boldsymbol{U} = 0\,, \tag{1.5b}$$

with $\boldsymbol{X}\in\Omega_f$, where Ω_f is the fixed reference domain with respected to the relative frame, not depending on time. The fluid velocity, $\boldsymbol{U}(\boldsymbol{X},t) = [U,V,W]^T$, represents the absolute velocity field as function of the relative coordinates, $\boldsymbol{X} = [X,Y,Z]^T$, and projected into the non-inertial frame, rotating with the wing, but with no translation velocity. As

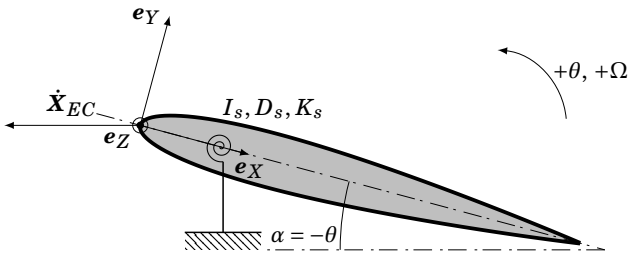

Figure 1.2 – *Schematic illustration of the damped spring-mounted NACA0012 airfoil.*

present in equations 1.3, the initial and boundary conditions are posed as

$$\boldsymbol{U}(\boldsymbol{X},0)=\boldsymbol{U}_0(\boldsymbol{X}) \qquad \boldsymbol{X}\in\Omega_f\,, \tag{1.6a}$$

$$\boldsymbol{U}(\boldsymbol{X},t)\to\boldsymbol{0} \qquad \|\boldsymbol{X}\|\to\infty, \tag{1.6b}$$

$$\boldsymbol{U}(\boldsymbol{x},t)=\boldsymbol{U}_w \qquad \boldsymbol{X}\in\Gamma_w\,, \tag{1.6c}$$

where this time, the fluid–solid interface, Γ_w, does not vary with time. Hence, we recover the formulation of the equations given in Mougin *et al.* (2002), associated to a rigid-body motion. When comparing with the Navier–Stokes equations written in an inertial frame of reference, two additional terms appear: the rotational acceleration $\boldsymbol{\Omega}\times\boldsymbol{U}$ and a modification of the convective velocity by the rigid-body velocity field, defined as

$$\boldsymbol{U}_w=\boldsymbol{\Omega}\times(\boldsymbol{X}-\boldsymbol{X}_{EC})+\dot{\boldsymbol{X}}_{EC} \quad \text{with} \quad \dot{\boldsymbol{X}}_{EC}=U^\infty[-\cos(\theta),\sin(\theta),0]^T\,.$$

Note that this formulation should not be confused with the more classical formulation in terms of relative velocities in a relative frame, which features a Coriolis term in the form $2\boldsymbol{\Omega}\times\boldsymbol{U}$ (see, *e.g.*, Landau *et al.* (1987), p. 40). This term should not be confused with the non-inertial terms appearing in the present formulation.

1.2 Torsion rigid-body model

The inherent complexity of a flexible airplane structure can be modelled by a two-dimensional airfoil section, a NACA0012 airfoil of chord c, whose geometry generation is detailed in appendix A. The airfoil is considered as a rigid body, allowed to rotate around its elastic centre, $\boldsymbol{X}_{EC}$. The pitching motion is characterised by the instantaneous angular displacement, or pitch angle, $\theta(t)$, and by the angular velocity, $\Omega(t)$, both considered positive for a nose-down displacement. As stated before, the angle of attack is defined simply as $\alpha=-\theta$. The motion being purely two-dimensional, $\Omega(t)$ represents the $\boldsymbol{e}_z$-component of the vectorial angular velocity $\boldsymbol{\Omega}=\Omega\boldsymbol{e}_z$. The schematic representation of the airfoil mounted on a torsional spring is presented in figure 1.2.

The temporal evolution of the airfoil can be described by a simple damped harmonic oscillator, governed by the first-order dimensional system:

$$I_s^{dim}\frac{\mathrm{d}\Omega}{\mathrm{d}t}+D_s^{dim}\Omega+K_s^{dim}\theta=m_z^{dim}(\boldsymbol{U},p)\,, \tag{1.7a}$$

$$\frac{\mathrm{d}\theta}{\mathrm{d}t}-\Omega=0\,, \tag{1.7b}$$

where I_s^{dim}, D_s^{dim} and K_s^{dim} are the dimensional moment of inertia around the elastic centre position, structural damping

X_{EC}(% of chord)	ρ(kg/m^2)	μ(Ns/m^2)	c(m)	I_s^{dim}(kgm^2 or Nms^2)	D_s^{dim}(Nms)	K_s^{dim}(Nm)
0.186	1.189	1.85×10^{-5}	0.156	0.00135	0.002	0.15

Table 1.1 – *Nominal dimensional fluid–structure parameters, along with the reference values used by Poirel et al. (2008) for retrieving the nondimensional fluid–structure parameters.*

and structural stiffness per unit span, respectively, and m_z^{dim} the dimensional $\boldsymbol{e}_z$-component of the aerodynamic moment, $\boldsymbol{m}^{dim} = m_z^{dim}\boldsymbol{e}_z$ per unit span, measured around the elastic centre. The latter is defined as

$$\boldsymbol{m}^{dim}(\boldsymbol{U},p) = \int_{\Gamma_w} (\boldsymbol{X}-\boldsymbol{X}_{EC})\times(\boldsymbol{\sigma}(\boldsymbol{U},p)\cdot\boldsymbol{n}_w)\,\mathrm{d}\Gamma_w\,, \tag{1.8}$$

where $\mathrm{d}\Gamma_w$ is an infinitesimal increment along the airfoil's boundary with $\boldsymbol{n}_w$ its outward unit normal vector. As an alternative to the definition based on a surface integral, we explore in section 2.3 (page 104) a definition of the pressure component of the aerodynamic moment based on a volume integral. The pressure component is demonstrated to be dominant in the present scenarios, when compared to the friction component.

We note that the fluid interaction with the solid motion is taken into account by the aerodynamic moment, which depends on the fluid state variables, $[\boldsymbol{U},p]^T$. The initial conditions for the first order system 1.7 are usually set as $[\theta,\Omega]^T=[0,0]^T$ for $t=0$. Following the present convention, a positive moment corresponds to a moment that forces the airfoil to pitch-down, decreasing the angle of attack, α. In all the developments present in this thesis, we assume that all the structural parameters are zero or positive quantities. The nominal structural parameters are present in table 1.1, in accordance with the experimental values used in Poirel *et al.* (2008).

In this thesis, the structural equations are made nondimensional using the reference parameters taken into account by Poirel *et al.* (2008) and reported in table 1.1. Note that these reference values are only used to retrieve the nondimensional structure parameters that are then considered throughout this thesis, since that, for the nondimensionalisation of the fluid equations, U^∞ and c were fixed at 1. In that way, the nondimensional version of the system 1.7 is given by:

$$I_s\frac{\mathrm{d}\Omega}{\mathrm{d}t} + D_s\Omega + K_s\theta = m_z(\boldsymbol{U},p), \tag{1.9a}$$

$$\frac{\mathrm{d}\theta}{\mathrm{d}t} - \Omega = 0\,. \tag{1.9b}$$

The relation between the dimensional and nondimensional aforementioned variables is defined as

$$I_s = \frac{I_s^{dim}}{\frac{1}{2}\rho c^4}\,,\quad D_s = \frac{D_s^{dim}}{\frac{1}{2}\rho U^\infty c^3}\,,\quad K_s = \frac{K_s^{dim}}{\frac{1}{2}\rho U^{\infty 2}c^2}\,,\quad m_z = \frac{m_z^{dim}}{\frac{1}{2}\rho U^{\infty 2}c^2}\,. \tag{1.10}$$

For the simplified case where the structure is in vacuum, the movement is governed by the homogeneous ordinary differential equation $I_s\ddot{\theta}+D_s\dot{\theta}+K_s\theta=0$. The general solution of this equation can be search in a normal form $\theta = \left(\mathrm{e}^{\sigma_s t}+\mathrm{c.c.}\right)/2$, where σ_s represents the fundamental decay (real part) and frequency (imaginary part) of the structure, defined as

$$\sigma_s = \lambda_s + \omega_s\mathrm{i} \quad\text{with}\quad \lambda_s = -\frac{D_s}{2I_s} \quad\text{and}\quad \omega_s = \pm\sqrt{\frac{K_s}{I_s}-\lambda_s^2}\,. \tag{1.11}$$

The dimensional value of σ_s is given by $\sigma_s^{dim} = \sigma_s U^\infty/c$. The numerical values of σ_s^{dim} and σ_s for the current nominal

	σ_s	f_s	ω_n	ζ
Dimensional value	0.74074 + 10.51487i	1.67349	10.54093	—
Nondimensional value at $Re = 10\,000$	0.11586 + 1.64461i	0.26175	1.64869	0.07027
Nondimensional value at $Re = 20\,000$	0.05793 + 0.82231i	0.13087	0.82434	0.07027
Nondimensional value at $Re = 50\,000$	0.02317 + 0.32892i	0.05235	0.32974	0.07027

Table 1.2 – *Structural dimensional and nondimensional parameters for different Reynolds numbers.*

parameters are reported in table 1.2. Any positive value of the damping coefficient results into a negative structural growth rate ($\lambda_s < 0$) damping any structure oscillation, which returns to a stable equilibrium position. We further define the frequency of the structure as $f_s = \omega_s/(2\pi)$, also reported in table 1.2 (with $f_s^{dim} = f_s U^\infty/c$). Here, ω_s is assumed real, corresponding to the case studied in this thesis. The different regimes that may arise on a structure in vacuum are described in the following paragraphs, for completeness of the manuscript.

We can rewrite the structure equation in terms of the damping ratio, ζ, and the natural frequency of the structure, ω_n, defined as

$$\zeta = \frac{D_s}{2I_s\omega_n} = \frac{D_s}{2\sqrt{K_s I_s}} \quad \text{and} \quad \omega_n = \sqrt{\frac{K_s}{I_s}}.$$

Their numerical values for the current nominal parameters are reported in table 1.2 (with $\omega_n^{dim} = \omega_n U^\infty/c$). The damping ratio corresponds to ratio between the actual damping D_s and the critical damping ratio $2\sqrt{K_s I_s}$ (when $D_s = 2\sqrt{K_s I_s}$, we have $\zeta = 1$), while the natural frequency corresponds to the frequency at which the system would oscillate if the damping coefficient was zero. Therefore, the structure equation can be written as

$$\frac{\mathrm{d}^2\theta}{\mathrm{d}t^2} + 2\zeta\omega_n\frac{\mathrm{d}\theta}{\mathrm{d}t} + (\omega_n)^2\theta = \frac{1}{I_s}m_z(\boldsymbol{U}, p). \tag{1.12}$$

With the definitions of ζ and ω_n, the eigenvalues of the structure (in vacuum) can be categorised into four cases:

- first, if the system is *undamped* ($\zeta = 0$), the eigenvalues are complex conjugate and located on the imaginary axis, with $\omega_s = \omega_n$;
- second, if $0 < \zeta < 1$, the system is referred to as *underdamped*, and the eigenvalues are complex conjugate, lying on the stable side of the spectrum ($\lambda_s < 0$). The eigenvalue frequency and growth rate are given by $\omega_s = \pm\omega_n\sqrt{1-\zeta^2}$ and $\lambda_s = -\zeta\omega_n$, respectively. The quantity $\zeta\omega_n$ is usually termed attenuation;
- third, if $\zeta = 1$, the eigenvalues coincide on the real axis, having a zero frequency and a growth rate of $\lambda_s = -\omega_n$. The system is referred to as *critically damped*;
- forth, if $\zeta > 1$, the eigenvalues are positioned at two distinct locations of the real axis, on the stable side of the spectrum: $\lambda_s = -\left(\zeta - \sqrt{\zeta^2-1}\right)\omega_n$ and $\lambda_s = -\left(\zeta + \sqrt{\zeta^2-1}\right)\omega_n$. For $\zeta \geq 1$, the spring-damped system exhibits an exponential decay behaviour in the time domain is referred to as *overdamped*. In the limit as ζ tends to infinity, one of the eigenvalues will approach the origin, while the other one will tend to $-\infty$.

Considering the reference values given in table 1.1, the nondimensional structural parameters depend upon the Reynolds number as follows:

$$I_s = 3.8343, \quad D_s = 0.0888(Re/10^5)^{-1}, \quad K_s = 0.1042(Re/10^5)^{-2}.$$

Re	I_s	D_s	K_s	St_s	St_f	St_s^t	St_f^t
10 000	3.83428	0.88846	10.42220	0.26175	2.50627	0.03141	0.30075
20 000	3.83428	0.44423	2.60555	0.13087	3.35578	0.01570	0.40269
50 000	3.83428	0.17769	0.41689	0.05235	4.87173	0.00628	0.58460

Table 1.3 – *Fluid–structure nondimensional parameters for different Reynolds numbers, along with the structural and fluid Strouhal numbers. The last two columns are based on the airfoil thickness.*

The values of the nondimensional structure parameters are given in table 1.3 for three Reynolds numbers. Similarly, the structural frequency, f_s^{dim}, can be represented by a structural Strouhal number, also depending upon the Reynolds number as:

$$St_s = \frac{f_s^{dim} c}{U^\infty} = 0.0262(Re/10^5)^{-1}.$$

This Strouhal number can be compared to the Strouhal number characterising vortex shedding phenomenon, St_f. The latter is estimated to be on the range

$$St_f \approx [2-5].$$

Table 1.3 reports these two Strouhal numbers for three Reynolds numbers, with St_f associated to the vortex shedding of two-dimensional simulations at $\alpha = 0^\circ$ (explored in chapter 2). By comparing St_s and St_f, we infer that the problem is characterised by two different time scales. Additionally, we report these values based on the airfoil thickness, noted St_s^t and St_f^t. In view of the different order of magnitude between the solid and fluid frequencies, one can expect the fluid–structure dynamics to be decomposed into a *fast time scale*, corresponding to the vortex shedding, and a *slow time scale* corresponding to motion of the airfoil. This decomposition is further justified and explored in the following sections in order to be exploited in the linear stability analyses.

1.3 Fluid–structure formalism

One of the main goals of the present thesis is to access the stability of a fluid flow around an airfoil, taking into account their interaction. For that, several points are discussed in this section. First, we introduce a triple decomposition of the state variables, isolating the slow and fast time scale dynamics of the present fluid–structure system. Second, we study the response of the structure to a harmonic forcing in order to make some hypotheses concerning the fast time scale dynamics of the structure. Finally, we end this section by explaining the equilibrium positions admissible by the fluid–structure system. All these considerations serve as basis for the linear stability analyses, introduced in subsequent sections. Since the analyses are made in a two-dimensional domain, the $\boldsymbol{e}_z$-component of the different vectorial quantities is omitted from the notation. We recall the nonlinear fluid–structure system:

$$\frac{\partial \boldsymbol{U}}{\partial t} + \Omega[\boldsymbol{e}_z \times \boldsymbol{U}] + ([\boldsymbol{U} - \boldsymbol{U}_w]\cdot\nabla)\boldsymbol{U} - \nabla\cdot\boldsymbol{\sigma}(\boldsymbol{U}, p) = \boldsymbol{0}, \tag{1.13a}$$

$$\nabla\cdot\boldsymbol{U} = 0, \tag{1.13b}$$

$$I_s \frac{\mathrm{d}\Omega}{\mathrm{d}t} + D_s\Omega + K_s\theta = m_z(\boldsymbol{U}, p), \tag{1.13c}$$

$$\frac{\mathrm{d}\theta}{\mathrm{d}t} - \Omega = 0, \tag{1.13d}$$

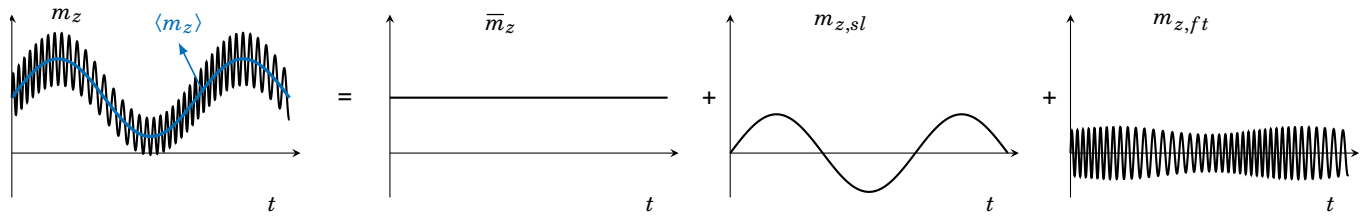

Figure 1.3 – *Illustration of the triple decomposition of the aerodynamic moment coefficient, with m_z and its phase average, $\langle m_z \rangle$, on the left. The former corresponds to the sum of the mean component, $\overline{m}_z$, the slow time scale fluctuations, $m_{z,sl}$, and the fast time scale fluctuations, $m_{z,ft}$, such that $m_z = \overline{m}_z + m_{z,sl} + m_{z,ft}$.*

where $\boldsymbol{U} = [U, V]^T$ is the fluid velocity and $\boldsymbol{U}_w$ the rigid-body velocity field defined as

$$\boldsymbol{U}_w(\boldsymbol{X}, t) = \Omega(t)[\boldsymbol{e}_z \times (\boldsymbol{X} - \boldsymbol{X}_{EC})] + U^\infty[-\cos(\theta(t)), \sin(\theta(t))]^T . \tag{1.14}$$

The initial and physical boundary conditions read

$$\boldsymbol{U}(\boldsymbol{X}, 0) = \boldsymbol{U}_0(\boldsymbol{X}) \qquad \boldsymbol{X} \in \Omega_f , \tag{1.15a}$$

$$\boldsymbol{U}(\boldsymbol{X}, t) \to \boldsymbol{0} \qquad \|\boldsymbol{X}\| \to \infty , \tag{1.15b}$$

$$\boldsymbol{U}(\boldsymbol{x}, t) = \boldsymbol{U}_w \qquad \boldsymbol{X} \in \Gamma_w . \tag{1.15c}$$

In the previous section, we have observed that the problem is characterised by two very different time scales: a fast time scale associated the flow dynamics (vortex shedding on the airfoil wake) and a slow time scale characterising the motion of the structure. Further, we note that in many situations the flow dynamics can be considered as a *periodic* phenomenon. With that in mind, we proceed to the formal introduction of the triple decomposition of the state variables.

1.3.1 Triple decomposition of the state variables

In this paragraph, we introduce the formalism associated to the separation of the slow and fast time scales present in our fluid–structure problem. Inspired in Hussain *et al.* (1970); Reynolds *et al.* (1972), we introduce a triple decomposition of the fluid and solid fluctuating variables as

$$[\,\boldsymbol{U},\ p\,]^T(\boldsymbol{X}, t) = \left[\,\overline{\boldsymbol{U}},\ \overline{p}\,\right]^T(\boldsymbol{X}) + [\,\boldsymbol{U}_{sl},\ p_{sl}\,]^T(\boldsymbol{X}, t) + [\,\boldsymbol{U}_{ft},\ p_{ft}\,]^T(\boldsymbol{X}, t), \tag{1.16a}$$

$$[\,\theta,\ \Omega\,]^T(t) \quad = \left[\,\bar{\theta},\ 0\,\right]^T \quad + [\,\theta_{sl},\ \Omega_{sl}\,]^T(t) \quad + [\,\theta_{ft},\ \Omega_{ft}\,]^T(t), \tag{1.16b}$$

where the notation $\bar{\bullet}$ is associated to a mean (time-averaged) quantity, the subscript $\bullet_{sl}$ is associated to the slow time scale fluctuations and the subscript $\bullet_{ft}$ is associated to the fast time scale fluctuations. We note that the mean component of the angular velocity is zero, since $\mathrm{d}\bar{\theta}/\mathrm{d}t \equiv 0$. This decomposition, used by the aforementioned references on a turbulent flow framework, is justified here by the incommensurability of frequencies of the slow and fast time scales.

This decomposition can be visualised on the aerodynamic moment coefficient, m_z, with the help of figure 1.3. The phase average of m_z is represented by the blue line. Although we are interested in considering the fast fluctuation as a periodic signal, the fast fluctuation can be, in a general case, a random signal. To take into account this behaviour in the illustrations, the fast fluctuations are represented by a periodic signal, modulated both in amplitude and frequency.

We also define a *phase average* (*e.g.*, for m_z) as

$$\langle m_z(t)\rangle = \lim_{N\to\infty} \frac{1}{N} \sum_{n=0}^{N} m_z(t + nT_{sl}), \tag{1.17}$$

where T_{sl} represents the period of the slow time scale oscillation. The phase average represents the average of the values of m_z at a particular phase of the slow time scale cycle, fixed by t. The phase average can also be constructed as the sum of the time average and the slow time scale fluctuating components as

$$[\,\langle \boldsymbol{U}\rangle,\ \langle p\rangle\,]^T(\boldsymbol{X},t) = \left[\,\overline{\boldsymbol{U}},\ \overline{p}\,\right]^T(\boldsymbol{X}) + [\,\boldsymbol{U}_{sl},\ p_{sl}\,]^T(\boldsymbol{X},t), \tag{1.18a}$$

$$[\,\langle \theta\rangle,\ \langle \Omega\rangle\,]^T(t) \quad = \left[\,\overline{\theta},\ 0\,\right]^T \qquad + [\,\theta_{sl},\ \Omega_{sl}\,]^T(t). \tag{1.18b}$$

On the other hand, we can define the mean plus the fast time fluctuations, using the notation $\tilde{\bullet}$, as

$$[\,\tilde{\boldsymbol{U}},\ \tilde{p}\,]^T(\boldsymbol{X},t) = \left[\,\overline{\boldsymbol{U}},\ \overline{p}\,\right]^T(\boldsymbol{X}) + [\,\boldsymbol{U}_{ft},\ p_{ft}\,]^T(\boldsymbol{X},t), \tag{1.19a}$$

$$[\,\tilde{\theta},\ \tilde{\Omega}\,]^T(t) \quad = \left[\,\overline{\theta},\ 0\,\right]^T \qquad + [\,\theta_{ft},\ \Omega_{ft}\,]^T(t). \tag{1.19b}$$

Some useful properties that follow from the definitions of time and phase average for two generic f and g scalar quantities are

$$\langle f_{ft}\rangle = 0, \qquad \overline{f}_{ft} = 0, \qquad \overline{f}_{sl} = 0, \qquad \langle f_{sl} g_{ft}\rangle = 0.$$

The first property states that the phase average of the fast fluctuations is zero. The second and third properties state that the time average of either slow or fast time scale components is zero. The last property states that the phase average of the product between slow and fast time scale signals is zero.

To illustrate this last property, used in several derivations of the subsequent sections, we sketch on figure 1.4 the slow and fast time scale components of the simplified signal used previously, along with their product. The representation is made in the time domain, on the top figures, and in the frequency domain, on the lower figures, obtained from a Fast Fourier Transform (FFT) of the different signals. The phase average of the different signals is represented by the dashed blue lines. As expected, the phase average of $m_{z,sl}$ coincides with its signal, while phase-averaging $m_{z,ft}$ gives a function that is null for any t. This is due to the fact that the frequencies of the slow and fast time scales are incommensurable. Similarly, the phase average of $m_{z,sl}m_{z,ft}$ also gives a null function in time. To better understand why, we observe the frequency content of the different signals. The FFT of $m_{z,sl}$ presents a single peak at a very low frequency, while the FFT of $m_{z,ft}$ presents a range of significant peaks at a very high frequency. The presence of this range of peaks, rather than a single peak, is associated to the modulation made on the original periodic fast time scale signal. Further, this FFT is symmetric with respect to the original periodic signal frequency, highlighted by vertical dashed line. The FFT of the product $m_{z,sl}m_{z,ft}$, which can be obtained by the periodic convolution of the frequency content of $m_{z,sl}$ and $m_{z,ft}$ is presented on the lower right figure. The result corresponds to the linear combination of the low frequency of $m_{z,sl}$ with the different high frequencies of $m_{z,ft}$. Due to the difference in the order of magnitude of the frequencies associated to $m_{z,sl}$ and $m_{z,ft}$, the result presents a range of peaks only in the high frequency zone. Since the phase average of a fast time scale signal is zero, this corroborates the last property of the previous equation: $\langle f_{sl} g_{ft}\rangle = 0$.

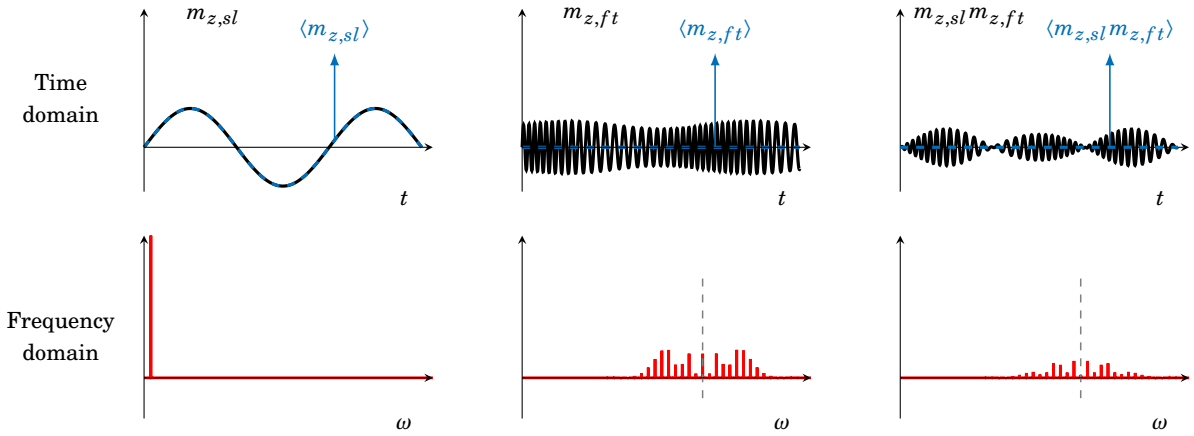

Figure 1.4 – *Illustration of the slow and fast time scale components of a signal (left and centre figures, respectively), e.g., the aerodynamic moment coefficient, on the time and frequency domains (top and bottom figures, respectively), along with their product in the time domain, corresponding to their convolution in the frequency domain (right figures). The phase average of the different signals is represented by the dashed blue lines in the top figures. The vertical dashed lines in the frequency domain figures represent the frequency of the original periodic signal that was then modulated to generate the fast time scale fluctuation.*

1.3.2 Response of the structure to a harmonic forcing

In the following paragraphs, we study the response of the structure to a harmonic forcing. In particular, we quantity the contributions of the fast time scale fluid oscillations on the structure dynamics, namely on the angular displacement and velocity, $[\theta, \Omega]^T$. The oscillations of the fluid components, associated to the vortex shedding, usually correspond to a high forcing frequency, when compared with the fundamental frequency of the structure, f_s. In particular, the fluid oscillations are reflected in the aerodynamic moment, $m_z(\boldsymbol{U}, p)$, which corresponds to the forcing term in the structure equation. These quantities are in general nonperiodic. However, for the sake of simplicity, we consider aerodynamic moment coefficient, the angular displacement and the angular velocity as periodic in time, and dominated by the fundamental component vibrating at the frequency ω_f, such that:

$$\theta = \frac{\hat{\theta}\mathrm{e}^{\mathrm{i}\omega_f t} + \text{c.c.}}{2}, \quad \Omega = \frac{\mathrm{i}\omega_f \hat{\theta}\mathrm{e}^{\mathrm{i}\omega_f t} + \text{c.c.}}{2} \quad \text{and} \quad m_z = \frac{\hat{m}_z \mathrm{e}^{\mathrm{i}\omega_f t} + \text{c.c.}}{2}. \tag{1.20}$$

Injecting the above decompositions on the structural equation 1.12 leads to

$$\frac{\mathrm{d}^2}{\mathrm{d}t^2}\left(\hat{\theta}\mathrm{e}^{\mathrm{i}\omega_f t}\right) + 2\zeta\omega_n \frac{\mathrm{d}}{\mathrm{d}t}\left(\hat{\theta}\mathrm{e}^{\mathrm{i}\omega_f t}\right) + \omega_n^2\left(\hat{\theta}\mathrm{e}^{\mathrm{i}\omega_f t}\right) = \frac{1}{I_s}\left(\hat{m}_z \mathrm{e}^{\mathrm{i}\omega_f t}\right).$$

By isolating the displacement term, one obtains

$$\hat{\theta} = \frac{1}{I_s\left(-\omega_f^2 + 2\omega_f\omega_n\zeta\mathrm{i} + \omega_n^2\right)}\hat{m}_z. \tag{1.21}$$

We note that, when the frequencies ω_f and ω_n are significantly different, as discussed in the previous section, the denominator on the right-hand side of 1.21 has a high value and the harmonic content present in m_z is not reflected in θ. Therefore, the fast time scale fluctuations on the aerodynamic moment only conduct to small fast time scale fluctuations

of the pitching angle, *i.e.*, there is no resonant interaction between the fast time scale fluctuations of the aerodynamic moment and the fast time scale component of the airfoil oscillation, the amplitude of the latter being consequently very small.

To illustrate the relation between $\hat{\theta}$ and $\hat{m}_z$, we define the transfer function $H_\theta(\omega_f)$ as

$$H_\theta(\omega_f) \equiv \frac{\hat{\theta}}{\hat{m}_z} = \frac{1}{I_s\left(-\omega_f^2 + 2\omega_f\omega_n\zeta\mathrm{i} + \omega_n^2\right)} \quad \text{such that} \quad \left|H_\theta(\omega_f)\right| = \frac{1}{I_s\sqrt{\left(\omega_n^2 - \omega_f^2\right)^2 + \left(2\omega_f\omega_n\zeta\right)^2}}, \tag{1.22}$$

which represents a low-pass filter of second order. With this function, we estimate the magnitude of the solid displacement induced by the fluctuations of the aerodynamic moment. We sketch in figure 1.5 the magnitude of $H_\theta(\omega_f)$ (in its dimensional form) as function of the forcing frequency[4], which represents any forcing frequency of the flow dynamics. A dimensional representation is chosen in order to be independent of the Reynolds number.

We first observe a resonance peak near the point where the fluid frequency, ω_f, corresponds to the structural frequency, ω_s. In this region, we identified the natural frequency of the structure, ω_n, with a vertical line. The exact value of the resonant frequency is slightly inferior to ω_s and ω_n and can be found by computing the frequency corresponding to the maximum of $\left|H_\theta(\omega_f)\right|$. For that, we differentiate $\left|H_\theta(\omega_f)\right|$ with respect to ω_f and set the result to zero. After some algebra (see Meirovitch (2001), p. 115), the resonant frequency ω_r and corresponding $|H_\theta(\omega_r)|$ are given by

$$\omega_r = \omega_n\sqrt{1-2\zeta^2} \quad \text{and} \quad |H_\theta(\omega_r)| = \frac{1}{2\zeta\omega_n^2 I_s\sqrt{1-\zeta^2}},$$

with the dimensional numerical values of $\omega_r^{dim} = 10.489\mathrm{s}^{-1}$ and $\left|H_\theta^{dim}(\omega_r)\right| = 47.552(\mathrm{Nm})^{-1}$. One can note that, as ζ tends to zero, the magnitude of $H_\theta(\omega_r)$ tends to infinity, while ω_r tends to ω_n. On the other hand, one can note from the first equality of the above equations that the resonant peak disappears for $\zeta \geq 1/\sqrt{2} \approx 0.707$[5].

From the resonating frequency, a decay of $\left|H_\theta(\omega_f)\right|$ is observed. The decay is hyperbolic in a linear plot and is linear with a negative slope in a log-log plot, the latter case being represented in the figure. The slope has a value of -40dB per decade[6], characteristic of second order transfer functions. The coloured dots represent transfer function value at the vortex shedding frequencies ω_{VS} for two-dimensional simulations at $\alpha = 0°$ (explored in chapter 2), whose Strouhal numbers are reported in table 1.3. The gain associated to $\left|H_\theta(\omega_f = \omega_{VS})\right|$ (in its dimensional form), obtained at the different frequencies, is reported in table 1.4. We can observe that this gain is *small*. In that way, we henceforward assume that the fast time scale component of the angular displacement are associated to an infinitesimal amplitude $A_\theta \ll 1$.

The same exercise can be made for the angular velocity, Ω, where we denote its transfer function as $H_\Omega(\omega_f)$. The magnitude of the corresponding transfer function can be directly calculated as $\left|H_\Omega(\omega_f)\right| = \left|\omega_f H_\theta(\omega_f)\right|$, due to the relation $\Omega = \mathrm{d}\theta/\mathrm{d}t$. These values are reported in the last column of table 1.4. One can note that gain associated to the transfer function of H_Ω at the vortex shedding frequencies is non negligible, although it decreases as the Reynolds number increases. Despite these results, the terms associated to the fast fluctuations of Ω are neglected in the following developments, as an approximation. The presence of the Ω_{ft} terms is observed and discussed for the nonlinear simulations (chapter 5), in order to measure the strength of this hypothesis. The amplitude associated to Ω_{ft} is termed A_Ω. In that

[4] This representation is termed Bode magnitude diagram, in electrical engineering and control theory.

[5] For the value of $\zeta = 1/\sqrt{2}$, the filter is termed Butterworth filter.

[6] A decade corresponds to a ratio of 10 on a logarithmic scale between two frequencies. The decibel is defined as $1\mathrm{dB} = 20\log(H_1/H_2)$, with H_1 and H_2 two different amplitudes of the transfer function.

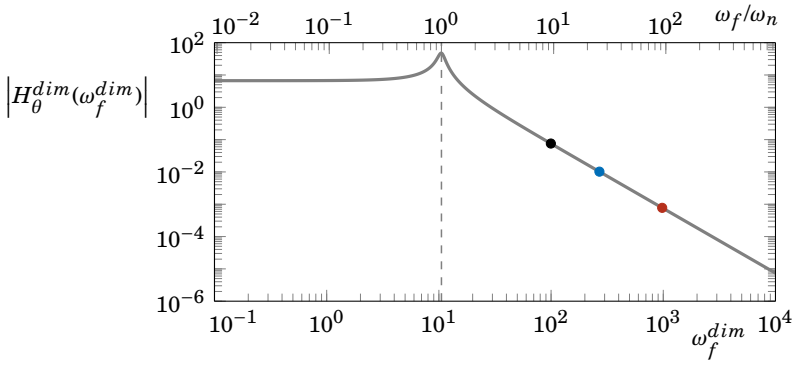

Re	$\left\|H_\theta^{dim}(\omega_{VS}^{dim})\right\|$	$\left\|H_\Omega^{dim}(\omega_{VS}^{dim})\right\|$
10 000	0.07560	7.61140
20 000	0.01020	2.75007
50 000	0.00077	0.75347

Figure 1.5 & Table 1.4 – *Evolution of the magnitude of the transfer function H_θ^{dim} with the forced frequency. The vortex shedding frequency for three Reynolds numbers is represented by the three dots: $Re = 10\,000$ (black), $Re = 20\,000$ (blue) and $Re = 50\,000$ (red). The vertical dashed line represents the natural frequency of the structure, ω_n^{dim}. On the right, the table reports the numerical values of the magnitude of the transfer functions H_θ^{dim} (units:* 1/(Nm)*) and H_Ω^{dim} (units:* 1/(Nms)*) for the three Reynolds numbers at the corresponding vortex shedding frequencies.*

way, we henceforward assume that the fast time scale components of the solid variables $[\theta_{ft}, \Omega_{ft}]^T$ are associated to A_θ and A_Ω, having

$$[\,\theta,\ \Omega\,]^T(t) = \left[\,\bar{\theta},\ 0\,\right]^T + [\,\theta_{sl},\ \Omega_{sl}\,]^T(t) + \left[\,A_\theta\theta_{ft},\ A_\Omega\Omega_{ft}\,\right]^T(t). \tag{1.23}$$

At the same time, since the structure does not respond to fast time scale fluctuations of the aerodynamic moment, this term *is neglected on the solid motion equation*, and is henceforward associated to a small amplitude A, having

$$m_z(\boldsymbol{U}, p) = m_z(\langle \boldsymbol{U} \rangle, \langle p \rangle) + A m_z\big(\boldsymbol{U}_{ft}, p_{ft}\big),$$

where we assume the aerodynamic moment to be a linear operator (valid on an incompressible flow framework). Further, due to the linearity of the aerodynamic moment, we have $m_z(\langle \boldsymbol{U} \rangle, \langle p \rangle) = \langle m_z(\boldsymbol{U}, p) \rangle$.

Finally, we note that the above transfer functions are adimensionalised as

$$H_\theta = H_\theta^{dim} \frac{1}{2}\rho U^{\infty 2} c^2 \quad \text{and} \quad H_\Omega = H_\Omega^{dim} \frac{1}{2}\rho U^{\infty} c^3 .$$

The values of H_θ and H_Ω are computed in chapter 5 for different values of K_s and compared with the actual ratios $\hat{\theta}/\hat{m}_z$ and $\hat{\Omega}/\hat{m}_z$ given by their harmonic content on the nonlinear FSI temporal simulations.

1.3.3 Quasi-steady equilibrium positions of the fluid–structure system

In this paragraph, we define the quasi-steady equilibrium positions admissible by the present fluid–structure system. These points are given by the structural equation, where the aerodynamic moment is associated to the time-averaged flow field obtained for static incidence simulations. From equation 1.13c, the quasi-steady equilibrium positions must respect the equation

$$K_s \bar{\theta} = m_z\left(\overline{\boldsymbol{U}}, \bar{p}\right). \tag{1.24}$$

We can see that the previous equality can give us the values of a nonzero aerodynamic moment that counterbalances the moment generated by the torsional spring. Alternatively, one can define the admissible equilibrium angles of incidence as

$\bar{\theta} = m_z\left(\overline{\boldsymbol{U}}, \bar{p}\right)/K_s$. For the case $K_s = 0$, the quasi-steady equilibrium angles of incidence correspond to the configurations where the aerodynamic moment is also null.

The above equality gives us a first equilibrium angle at $\bar{\theta} = 0\,^\circ$, admissible for any value of the structure stiffness. We denote this point as the primary equilibrium position. Then, depending on the value of K_s, a second equilibrium angle, characterising a secondary equation position, can be found. These points are introduced in the subsequent chapters. In the present thesis, several DNS were performed at fixed incidences, explored in chapter 2. The number of simulations was limited, due to their computational time cost. In these cases, the structural stiffness that ensures the equilibrium of a FSI configuration can be retrieved by posing $K_s = m_z\left(\overline{\boldsymbol{U}}, \bar{p}\right)/\bar{\theta}$. Again, for the case $\bar{\theta} = 0\,^\circ$, any structural stiffness will ensure that the null incidence is a solution of the FSI configuration.

1.4 Linear stability analyses based on fast time scale dynamics

The linear mechanisms responsible by the onset of self-sustained pitch oscillations can be determined by investigating the nature of small amplitude perturbations of particular state field. For that, we derive in this section the formulation associated to fluid–structure linear stability analyses, based on the fast time scale dynamics. The general idea is to apply a linear stability approach to the present FSI system in order to characterise the evolution of the perturbations that may arise along the slow time scale, considering either the fast-oscillating state (Floquet analysis) or the mean state (mean flow analysis) as the base solution. For that, in a first part, we introduce the governing equations of the fast time scale dynamics, by neglecting the slow time scale fluctuations of all state variables. In a second part, we introduce the linearised equations of the nonlinear FSI system. In a third part, we introduce the Floquet FSI linear stability analysis formalism. Finally, in a forth part, we derive the mean flow FSI linear stability analysis formalism from the Floquet equations, highlighting the terms that are neglected. This last formalism is labelled classical formulation, in contrast with the Reynolds stress formulation introduced in a subsequent section.

1.4.1 Equations governing a periodic flow

In this paragraph, we describe the governing equations associated to the fast time scale dynamics of a flow field around an airfoil at a fixed incidence. The solution of these equations corresponds to the periodic flow solution around which the Floquet linear stability analysis is carried out, as presented in a subsequent paragraph. For that, we assume a periodic flow, oscillating with a fast time scale frequency and we neglect the slow time scale oscillations. This is accomplished by assuming a small amplitude of the fast time scale fluctuations as A_{sl}, having the fluid–solid state variables decomposed as

$$[\,\boldsymbol{U},\ p,\ \theta,\ \Omega\,]^T = [\,\tilde{\boldsymbol{U}},\ \tilde{p},\ \tilde{\theta},\ \tilde{\Omega}\,]^T + A_{sl}[\,\boldsymbol{U}_{sl},\ p_{sl},\ \theta_{sl},\ \Omega_{sl}\,]^T. \tag{1.25}$$

We start by injecting the decomposition 1.25 into the rigid-body velocity field definition (equation 1.14), having

$$\begin{aligned}
\boldsymbol{U}_w &= \tilde{\Omega}[\boldsymbol{e}_z \times (\boldsymbol{X} - \boldsymbol{X}_{EC})] + U^\infty\left[-\cos\left(\tilde{\theta}\right), \sin\left(\tilde{\theta}\right)\right]^T + A_{sl}\Omega_{sl}[\boldsymbol{e}_z \times (\boldsymbol{X} - \boldsymbol{X}_{EC})] + A_{sl}\theta_{sl}U^\infty\left[\sin\left(\tilde{\theta}\right), \cos\left(\tilde{\theta}\right)\right]^T \\
&= U^\infty\left[-\cos\left(\bar{\theta}\right), \sin\left(\bar{\theta}\right)\right]^T + A_\Omega\Omega_{ft}[\boldsymbol{e}_z \times (\boldsymbol{X} - \boldsymbol{X}_{EC})] + A_\theta\theta_{ft}U^\infty\left[\sin\left(\bar{\theta}\right), \cos\left(\bar{\theta}\right)\right]^T + A_{sl}U_{w,sl} \\
&\approx U^\infty\left[-\cos\left(\bar{\theta}\right), \sin\left(\bar{\theta}\right)\right]^T + A_{sl}U_{w,sl}\,.
\end{aligned}$$

In the last line of the above developments, we neglect the fast time oscillations of $\tilde{\theta}$ and $\tilde{\Omega}$ (as discussed in section 1.3.2), represented in red, while we represent in grey the terms associated to the slow time scale variations. By neglecting the

latter term, where A_{sl} intervenes, we conclude that the angular displacement is time-independent (equal to $\bar{\theta}$) and the angular velocity is zero, which implies that the rigid-body velocity field is approximated by a time-independent field, corresponding to a translation velocity, noted $\overline{\boldsymbol{U}}_w$. Next, we inject the decomposition 1.25 into the momentum and mass equations of the system 1.13, having

$$\begin{aligned}
\frac{\partial \boldsymbol{U}}{\partial t} + \Omega[\boldsymbol{e}_z \times \boldsymbol{U}] + ([\boldsymbol{U} - \boldsymbol{U}_w]\cdot\nabla)\boldsymbol{U} - \nabla\cdot\boldsymbol{\sigma}(\boldsymbol{U}, p) = \frac{\partial \tilde{\boldsymbol{U}}}{\partial t} + \left(\left[\tilde{\boldsymbol{U}} - \overline{\boldsymbol{U}}_w\right]\cdot\nabla\right)\tilde{\boldsymbol{U}} - \nabla\cdot\boldsymbol{\sigma}(\tilde{\boldsymbol{U}}, \tilde{p}) + A_{sl}\left(\frac{\partial \boldsymbol{U}_{sl}}{\partial t} - \nabla\cdot\boldsymbol{\sigma}(\boldsymbol{U}_{sl}, p_{sl})\right) \\
+ A_{sl}\left(\Omega_{sl}[\boldsymbol{e}_z \times \tilde{\boldsymbol{U}}] + \left(\left[\tilde{\boldsymbol{U}} - \overline{\boldsymbol{U}}_w\right]\cdot\nabla\right)\boldsymbol{U}_{sl} + ([\boldsymbol{U}_{sl} - \boldsymbol{U}_{w,sl}]\cdot\nabla)\tilde{\boldsymbol{U}}\right) \\
+ A_{sl}^2\left(\Omega_{sl}[\boldsymbol{e}_z \times \boldsymbol{U}_{sl}] + ([\boldsymbol{U}_{sl} - \boldsymbol{U}_{w,sl}]\cdot\nabla)\boldsymbol{U}_{sl}\right) \\
+ A_\Omega\Omega_{ft}\left([\boldsymbol{e}_z \times \tilde{\boldsymbol{U}}] + A_{sl}[\boldsymbol{e}_z \times \boldsymbol{U}_{sl}]\right), \\
\nabla\cdot\boldsymbol{U} = \nabla\cdot\tilde{\boldsymbol{U}} + A_{sl}\nabla\cdot\boldsymbol{U}_{sl}\,.
\end{aligned}$$

By neglecting the A_Ω and A_{sl} terms, the momentum and mass equations become

$$\frac{\partial \tilde{\boldsymbol{U}}}{\partial t} + \left(\left[\tilde{\boldsymbol{U}} - \overline{\boldsymbol{U}}_w\right]\cdot\nabla\right)\tilde{\boldsymbol{U}} - \nabla\cdot\boldsymbol{\sigma}(\tilde{\boldsymbol{U}}, \tilde{p}) = \boldsymbol{0} \qquad \text{and} \qquad \nabla\cdot\tilde{\boldsymbol{U}} = 0\,.$$

The same procedure can be made for the structural equation 1.13c, having

$$I_s\frac{\mathrm{d}\Omega}{\mathrm{d}t} + D_s\Omega + K_s\theta - m_z(\boldsymbol{U}, p) = K_s\bar{\theta} - m_z\left(\overline{\boldsymbol{U}}, \bar{p}\right) + A_{sl}\left(I_s\frac{\mathrm{d}\Omega_{sl}}{\mathrm{d}t} + D_s\Omega_{sl} + K_s\theta_{sl} - m_z(\boldsymbol{U}_{sl}, p_{sl})\right).$$

After neglecting the A_{sl} terms, we note that aerodynamic moment present on the structure equation is time-independent, being associated to the mean component of the flow field for a fixed incidence $\bar{\theta}$.

Gathering both fluid and solid equations, the system governing a periodic flow vibrating on a fast time scale frequency can be put in the form

$$\frac{\partial \tilde{\boldsymbol{U}}}{\partial t} + \left(\left[\tilde{\boldsymbol{U}} - \overline{\boldsymbol{U}}_w\right]\cdot\nabla\right)\tilde{\boldsymbol{U}} - \nabla\cdot\boldsymbol{\sigma}(\tilde{\boldsymbol{U}}, p) = \boldsymbol{0}, \tag{1.26a}$$

$$\nabla\cdot\tilde{\boldsymbol{U}} = 0, \tag{1.26b}$$

$$K_s\bar{\theta} = m_z\left(\overline{\boldsymbol{U}}, \bar{p}\right). \tag{1.26c}$$

This system of equations is associated to the periodic state vector $\left[\tilde{\boldsymbol{U}}, \tilde{p}, \bar{\theta}, 0\right]^T$. The solution of this system represents a periodic flow solution around an airfoil with the incidence fixed by the ratio between the quasi-steady aerodynamic moment and the structural stiffness, such that $\bar{\theta} = m_z\left(\overline{\boldsymbol{U}}, \bar{p}\right)/K_s$, as discussed in section 1.3.3. For the case $K_s = 0$, the equilibrium incidence corresponds to the configurations where the moment is also null.

1.4.2 Linearised equations

In the following paragraphs, we present the linearisation of the nonlinear FSI equations. For that, we start by decomposing the fluid–solid state variables $[U, V, p, \theta, \Omega]^T$ as a base equilibrium state solution and an infinitesimal perturbation:

$$[\,\boldsymbol{U},\ p,\ \theta,\ \Omega\,]^T = [\,\boldsymbol{U}_b,\ p_b,\ \theta_b,\ \Omega_b\,]^T + \epsilon[\,\boldsymbol{U}',\ p',\ \theta',\ \Omega'\,]^T,$$

with $\epsilon \ll 1$. The above base equilibrium state is decomposed into a mean component and a fast and slow time scale components, such that

$$[\,\boldsymbol{U}_b,\ p_b,\ \theta_b,\ \Omega_b\,]^T = \left[\,\overline{\boldsymbol{U}}_b,\ \overline{p}_b,\ \bar{\theta}_b,\ 0\,\right]^T + [\,\boldsymbol{U}_{ft,b},\ p_{ft,b},\ A_\theta\theta_{ft,b},\ A_\Omega\Omega_{ft,b}\,]^T + A_{sl}\,[\,\boldsymbol{U}_{sl,b},\ p_{sl,b},\ \theta_{sl,b},\ \Omega_{sl,b}\,]^T.$$

Neglecting the terms associated to A_θ, A_Ω and A_{sl}, one obtains a base equilibrium state that is governed by the equations 1.26, describing a periodic flow at fixed incidence. With respect to equations 1.26, one has the following equivalence:

$$[\,\boldsymbol{U}_b,\ p_b,\ \theta_b,\ \Omega_b\,]^T = \left[\,\tilde{U},\ \tilde{p},\ \bar{\theta},\ 0\,\right]^T.$$

Since that, with the above simplifications, θ_b is time-independent, we henceforward denoted it as $\bar{\theta}_b$. As showed, the slow time scale fluctuations are not taken into account in the periodic flow equations. However, no hypotheses are made regarding the time scales associated to the perturbation.

Injecting these decompositions into the FSI governing equations 1.13 and retaining the terms at order ϵ, we obtain a linearised system that satisfies

$$\frac{\partial \boldsymbol{U}'}{\partial t} + \Omega'[\boldsymbol{e}_z \times \boldsymbol{U}_b] + \left([\boldsymbol{U}' - \boldsymbol{U}'_w]\cdot\nabla\right)\boldsymbol{U}_b + \left(\left[\boldsymbol{U}_b - \overline{\boldsymbol{U}}_w\right]\cdot\nabla\right)\boldsymbol{U}' - \nabla\cdot\boldsymbol{\sigma}(\boldsymbol{U}', p') = \boldsymbol{0}, \tag{1.27a}$$

$$\nabla\cdot\boldsymbol{U}' = 0, \tag{1.27b}$$

$$I_s\frac{\mathrm{d}\Omega'}{\mathrm{d}t} + D_s\Omega' + K_s\theta' = m_z(\boldsymbol{U}', p'), \tag{1.27c}$$

$$\frac{\mathrm{d}\theta'}{\mathrm{d}t} - \Omega' = 0. \tag{1.27d}$$

The first two equations represent the linearised momentum and mass equations governing the fluid velocity and pressure perturbations. They are coupled to the structure perturbation via three terms: first, the bulk term $\Omega'[\boldsymbol{e}_z \times \boldsymbol{U}_b]$, that modifies the production of fluid perturbation in the momentum equation via a perturbation of the airfoil angular velocity; second, the bulk term $\boldsymbol{U}'_w\cdot\nabla\boldsymbol{U}_b$, that also modifies the production of fluid perturbation by modifying the perturbed convective velocity; third, a term in the boundary condition at the airfoil surface Γ_w, where we impose $\boldsymbol{U}' = \boldsymbol{U}'_w$. The third and forth equations represent the linearised structural equations, which are inherently linear. They are coupled to the fluid variables via the aerodynamic moment associated to the fluid perturbation. The linearisation of the rigid-body velocity is given by

$$\boldsymbol{U}'_w = \Omega'[\boldsymbol{e}_z \times (\boldsymbol{X} - \boldsymbol{X}_{EC})] + U^\infty\left[\sin\left(\bar{\theta}_b\right), \cos\left(\bar{\theta}_b\right)\right]^T\theta',$$

where the following trigonometric developments were used

$$\cos\left(\bar{\theta}_b + \epsilon\theta'\right) = \cos\left(\bar{\theta}_b\right)\cos\left(\epsilon\theta'\right) - \sin\left(\bar{\theta}_b\right)\sin\left(\epsilon\theta'\right) \approx \cos\left(\bar{\theta}_b\right) - \epsilon\sin\left(\bar{\theta}_b\right)\theta',$$

$$\sin\left(\bar{\theta}_b + \epsilon\theta'\right) = \sin\left(\bar{\theta}_b\right)\cos\left(\epsilon\theta'\right) + \cos\left(\bar{\theta}_b\right)\sin\left(\epsilon\theta'\right) \approx \sin\left(\bar{\theta}_b\right) + \epsilon\cos\left(\bar{\theta}_b\right)\theta'.$$

1.4.3 Floquet FSI linear stability analysis

The linearised FSI system 1.27 can be represented in a compact form as

$$\frac{\partial \boldsymbol{q}'}{\partial t} = L\left(\boldsymbol{q}_b(\boldsymbol{X},t)\right)\boldsymbol{q}', \tag{1.28}$$

where $\boldsymbol{q}_b(\boldsymbol{X},t) = \left[\boldsymbol{U}_b(\boldsymbol{X},t), p_b(\boldsymbol{X},t), \bar{\theta}_b, 0\right]^T$ is the periodic flow vector and $\boldsymbol{q}'(\boldsymbol{X},t) = \left[\boldsymbol{U}'(\boldsymbol{X},t), p'(\boldsymbol{X},t), \theta'(t), \Omega'(t)\right]^T$ the fluid–solid perturbation. Since the flow around which we conduct our analysis is T-periodic, the linear operator $L\left(\boldsymbol{q}_b\right)$ is also T-periodic. Thus, according to Floquet theory (Floquet, 1883), the solution of the linear system 1.28 can be found, in a modal approach, as a superposition of Floquet form signals as

$$\boldsymbol{q}'(\boldsymbol{X},t) = \frac{\hat{\boldsymbol{q}}(\boldsymbol{X},t)\mathrm{e}^{\sigma t} + \text{c.c.}}{2}, \tag{1.29}$$

where $\hat{\boldsymbol{q}}$ is a T-periodic function, called Floquet eigenmodes of $L\left(\boldsymbol{q}_b\right)$, and $\sigma = \lambda + \omega\mathrm{i}$ is the complex Floquet exponent. The Floquet eigenmode is formed from a fluid and a solid components as $\hat{\boldsymbol{q}} = \left[\hat{\boldsymbol{q}}_f, \hat{\theta}, \hat{\Omega}\right]^T$, with $\hat{\boldsymbol{q}}_f = \left[\hat{U}, \hat{V}, \hat{p}\right]^T$. The Floquet eigenmode is associated to the fast time scale, whereas σ can be associated to either slow or fast time scales, depending on its frequency. The real part of the Floquet exponent, λ quantifies the growth/decay of an infinitesimal perturbation that may develop around the periodic flow solution, while the imaginary part, ω, represents its frequency. It is usual to describe the Floquet growth/decay over a period T via the Floquet multipliers[7] $\mu = \mathrm{e}^{\sigma T}$. A Floquet multiplier represents the complex amplitude gain of the periodic Floquet eigenmode over one period, *i.e.*, $\hat{\boldsymbol{q}}(\boldsymbol{X}, t+T) = \mu\hat{\boldsymbol{q}}(\boldsymbol{X},t)$. The polar decomposition of a Floquet multiplier reads $\mu = |\mu|\,\mathrm{e}^{\phi\mathrm{i}}$, where the modulus $|\mu|$ quantifies the growth/decay of the corresponding Floquet eigenmode over the period and ϕ represents its phase shift over the same period. The stability of the periodic flow is then addressed by considering the modulus of the Floquet multipliers. A Floquet eigenmode is stable (respectively, unstable) when the corresponding Floquet multiplier lies inside (respectively, outside) the unit circle $|\mu| < 1$ (respectively, $|\mu| > 1$) on the complex plane. When one Floquet eigenmode becomes unstable, the time-periodic flow becomes unstable.

Additionally, when a Floquet multiplier is real ($\phi = 0$), the Floquet eigenmode is synchronous and the perturbation evolves in time with the period of the flow without a phase shift. On the other hand, when a Floquet multiplier is complex ($\phi \neq 0$), the Floquet eigenmode is asynchronous and the perturbation evolves in time with the period of the flow and a phase shift of ϕ at each period.

Injecting the Floquet form decomposition into the linearised FSI equations 1.27, one arrives to the periodic eigenvalue problem

$$\sigma\hat{\boldsymbol{U}} + \frac{\partial\hat{\boldsymbol{U}}}{\partial t} + \hat{\Omega}[\boldsymbol{e}_z \times \boldsymbol{U}_b] + \left([\hat{\boldsymbol{U}} - \hat{\boldsymbol{U}}_w]\cdot\nabla\right)\boldsymbol{U}_b + \left(\left[\boldsymbol{U}_b - \overline{\boldsymbol{U}}_w\right]\cdot\nabla\right)\hat{\boldsymbol{U}} - \nabla\cdot\boldsymbol{\sigma}\left(\hat{\boldsymbol{U}}, \hat{p}\right) = \boldsymbol{0}, \tag{1.30a}$$

$$\nabla\cdot\hat{\boldsymbol{U}} = 0, \tag{1.30b}$$

$$I_s\left(\sigma\hat{\Omega} + \frac{\mathrm{d}\hat{\Omega}}{\mathrm{d}t}\right) + D_s\hat{\Omega} + K_s\hat{\theta} - m_z\left(\hat{\boldsymbol{U}}, \hat{p}\right) = 0, \tag{1.30c}$$

$$\sigma\hat{\theta} + \frac{\mathrm{d}\hat{\theta}}{\mathrm{d}t} - \hat{\Omega} = 0, \tag{1.30d}$$

[7] The same Greek letter μ is used for the fluid dynamic viscosity coefficient, introduced in section 1.1.2, which is a real constant, and the complex valued Floquet multiplier. However, as they represent distinct quantities, we hope no confusion is made.

with

$$\hat{\boldsymbol{U}}_w = \hat{\Omega}[\boldsymbol{e}_z \times (\boldsymbol{X} - \boldsymbol{X}_{EC})] + U^{\infty}\left[\sin\left(\bar{\theta}_b\right), \cos\left(\bar{\theta}_b\right)\right]^T \hat{\theta}\,.$$

These equations describe the evolution of periodic eigenmodes associated to a perturbation that may arise around the fast time scale periodic solution (with the period being associated to the vortex shedding frequency).

Spectral components of the Floquet eigenmodes

The harmonic content of a Floquet eigenmode can be obtained through time-integration of the linearised equations, where the term $-\lambda \mathsf{M}\hat{\boldsymbol{q}}$ is added to the right-hand side of equation 1.28, having

$$\mathsf{M}\frac{\partial \hat{\boldsymbol{q}}}{\partial t} = \mathsf{L}\left(\boldsymbol{q}_b(\boldsymbol{X}, t)\right)\hat{\boldsymbol{q}} - \lambda \mathsf{M}\hat{\boldsymbol{q}}\,. \tag{1.31}$$

The matrix M, as it will see later, is associated to the spatial discretisation of the Navier–Stokes equations, while L is the discretisation of the fluid–structure Jacobian matrix. The time-integration is performed over one vortex shedding cycle, using as initial condition the instantaneous Floquet eigenmode solution associated to one particular instant of the periodic flow limit cycle. The growth rate of the Floquet eigenmode λ being known, the right-hand side term appropriately counteracts the temporal growth (respectively decay) of the unstable (respectively stable) Floquet eigenmode. From this time-integration, one can obtain the mean and first harmonic components of the Floquet eigenmode, which are denoted $\hat{\boldsymbol{q}}^0$ and $\hat{\boldsymbol{q}}^1$, respectively. These components are computed and discussed in section 4.3.2.

1.4.4 Mean flow FSI linear stability analysis: classical formulation

In the following paragraphs, we derive the equations associated to the fluid–structure linear stability analysis around a mean flow state. The aim is to characterise the fluid–structure linear perturbations, associated to any time scale frequency, that may arise around the mean component of the flow solution. This derivation is done from the Floquet stability equations, in order to understand which terms are neglected in this analysis. The present mean flow stability formalism is labelled classical formulation, in contrast with the Reynolds stress formulation introduced in a subsequent section.

We start from the Floquet FSI eigenvalue problem and we decompose the Floquet eigenmodes into a time-averaged component plus a harmonic content as

$$\begin{aligned}
\hat{\boldsymbol{U}}(\boldsymbol{X}, t) &= \overline{\hat{\boldsymbol{U}}}(\boldsymbol{X}) + \delta\hat{\boldsymbol{U}}(\boldsymbol{X}, t),\\
\hat{p}(\boldsymbol{X}, t) &= \overline{\hat{p}}(\boldsymbol{X}) + \delta\hat{p}(\boldsymbol{X}, t),\\
\hat{\theta}(t) &= \overline{\hat{\theta}} + \delta\hat{\theta}(t),\\
\hat{\Omega}(t) &= \overline{\hat{\Omega}} + \delta\hat{\Omega}(t).
\end{aligned}$$

The same decomposition is applied to the fluid components of the periodic flow, already present in equation 1.19, such that:

$$[\,\boldsymbol{U}_b,\, p_b\,]^T(\boldsymbol{X}, t) = \left[\,\overline{\boldsymbol{U}}_b,\, \overline{p}_b\,\right]^T(\boldsymbol{X}) + [\,\boldsymbol{U}_{b,ft},\, p_{b,ft}\,]^T(\boldsymbol{X}, t).$$

We inject the above decompositions in the different terms of the system 1.30 (*i.e.*, in the Floquet LSA equations). Concerning the fluid equations, we separate the linearised terms that do not depend on the periodic flow from the

rotational term and the two convective terms:

$$\sigma\hat{\boldsymbol{U}}+\frac{\partial\hat{\boldsymbol{U}}}{\partial t}-\nabla\cdot\boldsymbol{\sigma}\left(\hat{\boldsymbol{U}},\hat{p}\right)=\sigma\overline{\hat{\boldsymbol{U}}}-\nabla\cdot\boldsymbol{\sigma}\left(\overline{\hat{\boldsymbol{U}}},\overline{\hat{p}}\right)+\sigma\delta\hat{\boldsymbol{U}}+\frac{\partial\delta\hat{\boldsymbol{U}}}{\partial t}-\nabla\cdot\boldsymbol{\sigma}\left(\delta\hat{\boldsymbol{U}},\delta\hat{p}\right),$$

$$\hat{\Omega}\left[\boldsymbol{e}_z\times\boldsymbol{U}_b\right]=\overline{\hat{\Omega}}\left[\boldsymbol{e}_z\times\overline{\boldsymbol{U}}_b\right]+\delta\hat{\Omega}\left[\boldsymbol{e}_z\times\overline{\boldsymbol{U}}_b\right]+\overline{\hat{\Omega}}\left[\boldsymbol{e}_z\times\boldsymbol{U}_{b,ft}\right]+\delta\hat{\Omega}\left[\boldsymbol{e}_z\times\boldsymbol{U}_{b,ft}\right],$$

$$\left(\left[\hat{\boldsymbol{U}}-\hat{\boldsymbol{U}}_w\right]\cdot\nabla\right)\boldsymbol{U}_b=\left(\left[\overline{\hat{\boldsymbol{U}}}-\overline{\hat{\boldsymbol{U}}}_w\right]\cdot\nabla\right)\overline{\boldsymbol{U}}_b+\left(\left[\overline{\hat{\boldsymbol{U}}}-\overline{\hat{\boldsymbol{U}}}_w\right]\cdot\nabla\right)\boldsymbol{U}_{b,ft}+\left(\left[\delta\hat{\boldsymbol{U}}-\delta\hat{\boldsymbol{U}}_w\right]\cdot\nabla\right)\overline{\boldsymbol{U}}_b+\left(\left[\delta\hat{\boldsymbol{U}}-\delta\hat{\boldsymbol{U}}_w\right]\cdot\nabla\right)\boldsymbol{U}_{b,ft},$$

$$\left(\left[\boldsymbol{U}_b-\overline{\boldsymbol{U}}_w\right]\cdot\nabla\right)\hat{\boldsymbol{U}}=\left(\left[\overline{\boldsymbol{U}}_b-\overline{\boldsymbol{U}}_w\right]\cdot\nabla\right)\overline{\hat{\boldsymbol{U}}}+\left(\left[\overline{\boldsymbol{U}}_b-\overline{\boldsymbol{U}}_w\right]\cdot\nabla\right)\delta\hat{\boldsymbol{U}}+\left(\boldsymbol{U}_{b,ft}\cdot\nabla\right)\overline{\hat{\boldsymbol{U}}}+\left(\boldsymbol{U}_{b,ft}\cdot\nabla\right)\delta\hat{\boldsymbol{U}},$$

$$\nabla\cdot\hat{\boldsymbol{U}}=\nabla\cdot\overline{\hat{\boldsymbol{U}}}+\nabla\cdot\delta\hat{\boldsymbol{U}}.$$

The first terms of the right-hand side of each equation, in black, correspond to the linearised contributions that are time-independent, *i.e.*, where only the time-averaged component of the Floquet eigenmode is retained. At the same time, we grouped, with a grey colour, three types of terms: (i) the terms that correspond to the linear harmonic contributions of the Floquet eigenmode (on the terms that do not depend on $\boldsymbol{U}_b$); (ii) the terms that correspond to the interaction between the mean flow and the harmonic content of the Floquet eigenmodes (on the rotational and on the two convective terms); (iii) the terms that correspond to the interaction between the harmonics of the periodic flow and the mean components of the Floquet eigenmodes (on the rotational and on the two convective terms). The red terms correspond to the interactions between the harmonic contributions of the periodic flow and of the Floquet eigenmodes.

After time-averaging the above terms, the grey terms vanish and the momentum equation reads

$$\sigma\overline{\hat{\boldsymbol{U}}}+\overline{\hat{\Omega}}\left[\boldsymbol{e}_z\times\overline{\boldsymbol{U}}_b\right]+\left(\left[\overline{\hat{\boldsymbol{U}}}-\overline{\hat{\boldsymbol{U}}}_w\right]\cdot\nabla\right)\overline{\boldsymbol{U}}_b+\left(\left[\overline{\boldsymbol{U}}_b-\overline{\boldsymbol{U}}_w\right]\cdot\nabla\right)\overline{\hat{\boldsymbol{U}}}-\nabla\cdot\boldsymbol{\sigma}\left(\overline{\hat{\boldsymbol{U}}},\overline{\hat{p}}\right)$$
$$+\overline{\delta\hat{\Omega}\left[\boldsymbol{e}_z\times\boldsymbol{U}_{b,ft}\right]}+\overline{\left(\left[\delta\hat{\boldsymbol{U}}-\delta\hat{\boldsymbol{U}}_w\right]\cdot\nabla\right)\boldsymbol{U}_{b,ft}}+\overline{\left(\boldsymbol{U}_{b,ft}\cdot\nabla\right)\delta\hat{\boldsymbol{U}}}=\boldsymbol{0}. \tag{1.32}$$

The first line of the above equation corresponds to the contribution of the time-averaged components of the Floquet eigenmode to the eigenproblem momentum equation. In the second line, three terms appear. The first term is associated to the time-averaged interaction between the harmonics of the Floquet eigenmode angular velocity and the harmonics of the periodic flow. The second and third terms correspond to the interaction between the harmonics of the Floquet eigenmode velocity field and the harmonics of the periodic flow. For the mean flow FSI linear stability analysis, we assume that all three terms present in the second line of equation 1.32 are negligible. After the above simplifications, we arrive to the momentum and mass equations associated to the mean flow FSI linear stability analysis:

$$\sigma\overline{\hat{\boldsymbol{U}}}+\overline{\hat{\Omega}}\left[\boldsymbol{e}_z\times\overline{\boldsymbol{U}}_b\right]+\left(\left[\overline{\hat{\boldsymbol{U}}}-\overline{\hat{\boldsymbol{U}}}_w\right]\cdot\nabla\right)\overline{\boldsymbol{U}}_b+\left(\left[\overline{\boldsymbol{U}}_b-\overline{\boldsymbol{U}}_w\right]\cdot\nabla\right)\overline{\hat{\boldsymbol{U}}}-\nabla\cdot\boldsymbol{\sigma}\left(\overline{\hat{\boldsymbol{U}}},\overline{\hat{p}}\right)=\boldsymbol{0},$$

$$\nabla\cdot\overline{\hat{\boldsymbol{U}}}=0.$$

The same procedure of injecting the Fourier decomposition into the Floquet eigenproblem can be applied for the solid

equations 1.30c and 1.30d, whose terms do not depend on the periodic flow. In that way, we obtain:

$$I_s\left(\sigma\hat{\Omega}+\frac{\mathrm{d}\hat{\Omega}}{\mathrm{d}t}\right)+D_s\hat{\Omega}+K_s\hat{\theta}-m_z\left(\hat{\boldsymbol{U}},\hat{p}\right)=I_s\sigma\overline{\hat{\Omega}}+D_s\overline{\hat{\Omega}}+K_s\overline{\hat{\theta}}-m_z\left(\overline{\hat{\boldsymbol{U}}},\overline{\hat{p}}\right)+I_s\left(\sigma\delta\hat{\Omega}+\frac{\mathrm{d}\left(\delta\hat{\Omega}\right)}{\mathrm{d}t}\right)+D_s\delta\hat{\Omega}+K_s\delta\hat{\theta}-m_z\left(\delta\hat{\boldsymbol{U}},\delta\hat{p}\right),$$

$$\sigma\hat{\theta}+\frac{\mathrm{d}\hat{\theta}}{\mathrm{d}t}-\hat{\Omega}=\sigma\overline{\hat{\theta}}-\overline{\hat{\Omega}}+\sigma\delta\hat{\theta}+\frac{\mathrm{d}\delta\hat{\theta}}{\mathrm{d}t}-\delta\hat{\Omega}.$$

Once again, the first terms of the right-hand side of each equation, in black, correspond to the linearised contributions of the Floquet eigenmode solid components that are time-independent, whereas, in grey, we have their harmonic contributions. After time averaging the above equations, all the grey terms vanish.

After the above simplifications, the eigenproblem associated to a mean flow FSI linear stability analysis can be written as

$$\sigma\overline{\hat{\boldsymbol{U}}}+\overline{\hat{\Omega}}\left[\boldsymbol{e}_z\times\overline{\boldsymbol{U}}_b\right]+\left(\left[\overline{\hat{\boldsymbol{U}}}-\overline{\hat{\boldsymbol{U}}}_w\right]\cdot\nabla\right)\overline{\boldsymbol{U}}_b+\left(\left[\overline{\boldsymbol{U}}_b-\overline{\boldsymbol{U}}_w\right]\cdot\nabla\right)\overline{\hat{\boldsymbol{U}}}-\nabla\cdot\boldsymbol{\sigma}\left(\overline{\hat{\boldsymbol{U}}},\overline{\hat{p}}\right)=\boldsymbol{0}, \tag{1.33a}$$

$$\nabla\cdot\overline{\hat{\boldsymbol{U}}}=0, \tag{1.33b}$$

$$I_s\sigma\overline{\hat{\Omega}}+D_s\overline{\hat{\Omega}}+K_s\overline{\hat{\theta}}-m_z\left(\overline{\hat{\boldsymbol{U}}},\overline{\hat{p}}\right)=0, \tag{1.33c}$$

$$\sigma\overline{\hat{\theta}}-\overline{\hat{\Omega}}=0, \tag{1.33d}$$

with the time-averaged component of the linearisation of the rigid-body velocity field defined as

$$\overline{\hat{\boldsymbol{U}}}_w=\overline{\hat{\Omega}}[\boldsymbol{e}_z\times(\boldsymbol{X}-\boldsymbol{X}_{EC})]+U^{\infty}\left[\sin\left(\bar{\theta}_b\right),\cos\left(\bar{\theta}_b\right)\right]^T\overline{\hat{\theta}}.$$

Similar to the Floquet FSI analysis, the mean flow eigenpair $(\overline{\hat{\boldsymbol{q}}},\sigma)$ (solution of the system 1.33) is part of the mean flow perturbation, written in the form of a global mode as

$$\boldsymbol{q}'(\boldsymbol{X},t)=\frac{\overline{\hat{\boldsymbol{q}}}(\boldsymbol{X})\mathrm{e}^{\sigma t}+\mathrm{c.c.}}{2}, \tag{1.34}$$

where $\overline{\hat{\boldsymbol{q}}}$ is a complex time-independent eigenmode representing the spatial distribution of the perturbation, associated to the eigenvalue $\sigma=\lambda+\omega\mathrm{i}$. The mean flow eigenmode is formed from a fluid and a solid components as $\overline{\hat{\boldsymbol{q}}}=\left[\overline{\hat{\boldsymbol{q}}}_f,\overline{\hat{\theta}},\overline{\hat{\Omega}}\right]^T$, with $\overline{\hat{\boldsymbol{q}}}_f=\left[\overline{\hat{U}},\overline{\hat{V}},\overline{\hat{p}}\right]^T$. The real part λ represents the growth rate of the mean flow perturbation, indicating if the perturbation linearly grows (unstable perturbation, with $\lambda>0$) or decays (stable perturbation, with $\lambda<0$) in time, whereas the imaginary part ω corresponds to the frequency at which the eigenmode oscillates. The case $\lambda=0$ describes a marginally stable scenario, where a perturbation neither is amplified nor damped. On the other hand, the cases where $\omega=0$ correspond to static eigenmodes, which diverge or converge linearly, but without oscillating.

As indicated earlier, the present system of equations is identified as the classical formulation. The mean flow eigenvalue problem can be put in a matrix form $\sigma\mathsf{M}\overline{\hat{\boldsymbol{q}}}=\mathsf{L}\overline{\hat{\boldsymbol{q}}}$:

$$\sigma\begin{bmatrix}\mathsf{M}_f & \boldsymbol{0} & \boldsymbol{0}\\ \boldsymbol{0} & 1 & 0\\ \boldsymbol{0} & 0 & I_s\end{bmatrix}\begin{bmatrix}\overline{\hat{\boldsymbol{q}}}_f\\ \overline{\hat{\theta}}\\ \overline{\hat{\Omega}}\end{bmatrix}=\begin{bmatrix}\mathsf{L}_f\left(\overline{\boldsymbol{U}}_b\right) & \boldsymbol{v}_\theta & \boldsymbol{v}_\Omega\\ \boldsymbol{0} & 0 & 1\\ \boldsymbol{m}^T & -K_s & -D_s\end{bmatrix}\begin{bmatrix}\overline{\hat{\boldsymbol{q}}}_f\\ \overline{\hat{\theta}}\\ \overline{\hat{\Omega}}\end{bmatrix}, \tag{1.35}$$

where M_f is the fluid mass operator, later associated to the spatial discretisation, L_f the fluid Jacobian operator and $\boldsymbol{v}_\theta$, $\boldsymbol{v}_\Omega$ the linearised vector components of the solid motion. We note that the fluid–structure Jacobian matrix is non-hermitian, *i.e.*, $\mathsf{L} \neq \mathsf{L}^H$. Therefore, the above eigenproblem corresponds to a right generalised non-Hermitian eigenvalue problem. The term "right" comes from the fact that the eigenvectors $\bar{\hat{\boldsymbol{q}}}$ are the right eigenvectors of the present problem. The term "generalised" comes from the presence of a matrix M, different from the identify matrix. Further, as detailed below, this matrix is singular, due to the zero coefficients of M_f on the degrees of freedom of the pressure component.

The vector $\boldsymbol{v}_\theta$ represents a unitary linear angular displacement of the airfoil structure, whereas $\boldsymbol{v}_\Omega$ represents a unitary linear angular velocity, both on an anticlockwise direction. The fluid mass and Jacobian operators are defined as:

$$\mathsf{M}_f = \begin{bmatrix} \mathbb{1} & \mathbf{0} \\ \mathbf{0} & 0 \end{bmatrix} \quad \text{and} \quad \mathsf{L}_f \bar{\hat{\boldsymbol{q}}}_f = - \begin{bmatrix} \left(\bar{\hat{\boldsymbol{U}}}\cdot\nabla\right)\bar{\boldsymbol{U}}_b + \left(\left[\bar{\boldsymbol{U}}_b - \bar{\boldsymbol{U}}_w\right]\cdot\nabla\right)\bar{\hat{\boldsymbol{U}}} - \nabla\cdot\boldsymbol{\sigma}\left(\bar{\hat{\boldsymbol{U}}}, \bar{\hat{p}}\right) \\ \nabla\cdot\bar{\hat{\boldsymbol{U}}} \end{bmatrix},$$

while the linearised vectors $\boldsymbol{v}_\theta$, $\boldsymbol{v}_\Omega$ are defined as

$$\boldsymbol{v}_\theta = U^\infty \left(\begin{bmatrix} \sin\left(\bar{\theta}_b\right) \\ \cos\left(\bar{\theta}_b\right) \end{bmatrix} \cdot\nabla \right) \bar{\boldsymbol{U}}_b \quad \text{and} \quad \boldsymbol{v}_\Omega = - \begin{bmatrix} -\bar{V}_b \\ \bar{U}_b \end{bmatrix} + \left(\begin{bmatrix} -(Y - Y_{EC}) \\ (X - X_{EC}) \end{bmatrix} \cdot\nabla \right) \bar{\boldsymbol{U}}_b ,$$

with the physical boundary conditions applied on the left-hand side of the system 1.35 as

$$\bar{\hat{\boldsymbol{U}}}(\boldsymbol{X}) \to \mathbf{0} \qquad \|\boldsymbol{X}\| \to \infty, \tag{1.36a}$$

$$\bar{\hat{\boldsymbol{U}}}(\boldsymbol{X}) = \mathbf{1} \qquad \boldsymbol{X} \in \Gamma_w, \tag{1.36b}$$

$$\boldsymbol{v}_\theta = -U^\infty [\sin(\bar{\theta}_b), \cos(\bar{\theta}_b)]^T \qquad \boldsymbol{X} \in \Gamma_w, \tag{1.36c}$$

$$\boldsymbol{v}_\Omega = -[-(Y - Y_{EC}), (X - X_{EC})]^T \qquad \boldsymbol{X} \in \Gamma_w. \tag{1.36d}$$

1.5 Linear stability analysis based on slow time scale dynamics

In this section, we concentrate our attention on the slow time scale dynamics of the fluid–structure system. Therefore, we introduce in a first part the equations governing the slow time scale dynamics of our problem. In a second and third parts, we linearise these equations in order to arrive to the equations associated to the mean flow state at a fixed incidence and to the mean flow FSI linear stability eigenproblem. This formulation of the stability equations is denoted Reynolds stress formulation, due to the fact that we take into account the variation of the Reynolds stress terms with respect to the state variables, as discussed in the following paragraphs.

1.5.1 Equations governing the slow time scale dynamics

In the following paragraphs, we describe the governing equations associated to the phase-averaged state variables. For that, we recall that the fluid–solid variables are decomposed into a phase-averaged and a fast time scale contributions as

$$[\,\boldsymbol{U},\, p,\, \theta,\, \Omega\,]^T = [\,\langle\boldsymbol{U}\rangle,\, \langle p\rangle,\, \langle\theta\rangle,\, \langle\Omega\rangle\,]^T + [\,\boldsymbol{U}_{ft},\, p_{ft},\, A_\theta\theta_{ft},\, A_\Omega\Omega_{ft}\,]^T. \tag{1.37}$$

We start by injecting this decomposition into the rigid-body velocity field definition (equation 1.14), having

$$\boldsymbol{U}_w = \Omega[\boldsymbol{e}_z \times (\boldsymbol{X} - \boldsymbol{X}_{EC})] + U^{\infty}[-\cos(\theta), \sin(\theta)]^T = \langle\Omega\rangle[\boldsymbol{e}_z \times (\boldsymbol{X} - \boldsymbol{X}_{EC})] + U^{\infty}[-\cos(\langle\theta\rangle), \sin(\langle\theta\rangle)]^T$$
$$+ A_\Omega \Omega_{ft}[\boldsymbol{e}_z \times (\boldsymbol{X} - \boldsymbol{X}_{EC})] + A_\theta \theta_{ft} U^{\infty}[\sin(\langle\theta\rangle), \cos(\langle\theta\rangle)]^T,$$

which can be written as

$$\begin{aligned}\boldsymbol{U}_w &= \langle\boldsymbol{U}_w\rangle + A\boldsymbol{U}_{w,ft} \\ &= \langle\boldsymbol{U}_w\rangle + A_\theta \boldsymbol{U}^{\theta}_{w,ft} + A_\Omega \boldsymbol{U}^{\Omega}_{w,ft},\end{aligned}$$

where we separate the fast time scale contributions of the angular displacement and velocity. The black terms correspond to the slow time scale contributions, while the red terms correspond to the fast time scale contributions, associated to the small amplitudes A_θ and A_Ω. For clarify, the following trigonometric developments were used on the translation velocity component:

$$\cos\left(\langle\theta\rangle + A_\theta\theta_{ft}\right) = \cos(\langle\theta\rangle)\cos\left(A_\theta\theta_{ft}\right) - \sin(\langle\theta\rangle)\sin\left(A_\theta\theta_{ft}\right) \approx \cos(\langle\theta\rangle) - A_\theta\theta_{ft}\sin(\langle\theta\rangle),$$
$$\sin\left(\langle\theta\rangle + A_\theta\theta_{ft}\right) = \sin(\langle\theta\rangle)\cos\left(A_\theta\theta_{ft}\right) + \cos(\langle\theta\rangle)\sin\left(A_\theta\theta_{ft}\right) \approx \sin(\langle\theta\rangle) + A_\theta\theta_{ft}\cos(\langle\theta\rangle).$$

Next, we inject the decomposition 1.37 into the momentum and mass equations of the system 1.13. For a better understanding of the decomposition, we separate the linear terms of the momentum equation, from the nonlinear terms, having

$$\frac{\partial \boldsymbol{U}}{\partial t} - \nabla\cdot\boldsymbol{\sigma}(\boldsymbol{U}, p) = \frac{\partial\langle\boldsymbol{U}\rangle}{\partial t} - \nabla\cdot\boldsymbol{\sigma}(\langle\boldsymbol{U}\rangle, \langle p\rangle) + \frac{\partial\left(\boldsymbol{U}_{ft}\right)}{\partial t} - \nabla\cdot\boldsymbol{\sigma}\left(\boldsymbol{U}_{ft}, p_{ft}\right),$$
$$([\boldsymbol{U} - \boldsymbol{U}_w]\cdot\nabla)\boldsymbol{U} = ([\langle\boldsymbol{U}\rangle - \langle\boldsymbol{U}_w\rangle]\cdot\nabla)\langle\boldsymbol{U}\rangle + ([\langle\boldsymbol{U}\rangle - \langle\boldsymbol{U}_w\rangle]\cdot\nabla)\boldsymbol{U}_{ft} + \left([\boldsymbol{U}_{ft} - A\boldsymbol{U}_{w,ft}]\cdot\nabla\right)\langle\boldsymbol{U}\rangle + \left(\boldsymbol{U}_{ft}\cdot\nabla\right)\boldsymbol{U}_{ft} - A\left(\boldsymbol{U}_{w,ft}\cdot\nabla\right)\boldsymbol{U}_{ft},$$
$$\Omega[\boldsymbol{e}_z \times \boldsymbol{U}] = \langle\Omega\rangle[\boldsymbol{e}_z \times \langle\boldsymbol{U}\rangle] + \langle\Omega\rangle\left[\boldsymbol{e}_z \times \boldsymbol{U}_{ft}\right] + A_\Omega\boldsymbol{\Omega}_{ft}[\boldsymbol{e}_z \times \langle\boldsymbol{U}\rangle] + A_\Omega\boldsymbol{\Omega}_{ft}\left[\boldsymbol{e}_z \times \boldsymbol{U}_{ft}\right],$$
$$\nabla\cdot\boldsymbol{U} = \nabla\cdot\langle\boldsymbol{U}\rangle + \nabla\cdot\boldsymbol{U}_{ft}.$$

The first terms of the right-hand side of each equation, in black, correspond to the phase-averaged contributions, evolving on the slow time scale. The grey terms correspond to the fast time scale contributions (on the linear terms) and to the interaction between the slow and fast time scale contributions (on the nonlinear terms). The red terms correspond to the nonlinear contributions depending exclusively on the fast time scale terms. After phase-averaging the above terms, the grey terms vanish (since they correspond to the phase average of a fast time scale signal or to the phase average of a product between a fast and a slow time scale signals) and the momentum equation reads

$$\frac{\partial\langle\boldsymbol{U}\rangle}{\partial t} + \langle\Omega\rangle[\boldsymbol{e}_z \times \langle\boldsymbol{U}\rangle] + ([\langle\boldsymbol{U}\rangle - \langle\boldsymbol{U}_w\rangle]\cdot\nabla)\langle\boldsymbol{U}\rangle - \nabla\cdot\boldsymbol{\sigma}(\langle\boldsymbol{U}\rangle, \langle p\rangle) = -\left\langle\left(\boldsymbol{U}_{ft}\cdot\nabla\right)\boldsymbol{U}_{ft}\right\rangle$$
$$+ A_\theta\left\langle\left(\boldsymbol{U}^{\theta}_{w,ft}\cdot\nabla\right)\boldsymbol{U}_{ft}\right\rangle + A_\Omega\left\langle\left(\boldsymbol{U}^{\Omega}_{w,ft}\cdot\nabla\right)\boldsymbol{U}_{ft}\right\rangle - A_\Omega\left\langle\boldsymbol{\Omega}_{ft}\left[\boldsymbol{e}_z \times \boldsymbol{U}_{ft}\right]\right\rangle.$$

By taking $A_\theta = A_\Omega = 0$ (as discussed in section 1.3.2), we neglect the red terms present in the second line of the above equation, corresponding to the effect of the fast time scale solid fluctuations onto the slow time scale dynamics. However,

the red term of the first line is not neglected. This term corresponds to the effect of the fast time scale flow fluctuations onto the slow time scale dynamics, in the form of the divergence of the Reynolds stress tensor. This term can be rewritten as $\left\langle \nabla\cdot\left[\boldsymbol{U}_{ft}\otimes\boldsymbol{U}_{ft}\right]\right\rangle$.

The same procedure of injecting the decomposition 1.37 into the nonlinear FSI equations system can be applied to the solid equations 1.13c and 1.13d, whose terms are linear. In that way, we obtain:

$$I_s\frac{\mathrm{d}\Omega}{\mathrm{d}t}+D_s\Omega+K_s\theta-m_z(\boldsymbol{U},p)=I_s\frac{\mathrm{d}\langle\Omega\rangle}{\mathrm{d}t}+D_s\langle\Omega\rangle+K_s\langle\theta\rangle-\langle m_z(\boldsymbol{U},p)\rangle+A_\Omega\left(I_s\frac{\mathrm{d}\Omega_{ft}}{\mathrm{d}t}+D_s\Omega_{ft}\right)+A_\theta K_s\theta_{ft}-Am_z(\boldsymbol{U}_{ft},p_{ft}),$$

$$\frac{\mathrm{d}\theta}{\mathrm{d}t}-\Omega=\frac{\mathrm{d}\langle\theta\rangle}{\mathrm{d}t}-\langle\Omega\rangle+A_\theta\frac{\mathrm{d}\theta_{ft}}{\mathrm{d}t}-A_\Omega\Omega_{ft}.$$

After phase-averaging the above terms, the grey terms vanish. In that way, the fluid–solid equations governing the slow time scale dynamics can be put in the form

$$\frac{\partial\langle\boldsymbol{U}\rangle}{\partial t}+\langle\Omega\rangle\left[\boldsymbol{e}_z\times\langle\boldsymbol{U}\rangle\right]+\left(\left[\langle\boldsymbol{U}\rangle-\langle\boldsymbol{U}_w\rangle\right]\cdot\nabla\right)\langle\boldsymbol{U}\rangle-\nabla\cdot\boldsymbol{\sigma}(\langle\boldsymbol{U}\rangle,\langle p\rangle)=-\left\langle\nabla\cdot\left[\boldsymbol{U}_{ft}\otimes\boldsymbol{U}_{ft}\right]\right\rangle, \tag{1.38a}$$

$$\nabla\cdot\langle\boldsymbol{U}\rangle=0, \tag{1.38b}$$

$$I_s\frac{\mathrm{d}\langle\Omega\rangle}{\mathrm{d}t}+D_s\langle\Omega\rangle+K_s\langle\theta\rangle=m_z(\langle\boldsymbol{U}\rangle,\langle p\rangle), \tag{1.38c}$$

$$\frac{\mathrm{d}\langle\theta\rangle}{\mathrm{d}t}-\langle\Omega\rangle=0. \tag{1.38d}$$

This set of equations is very similar to the original nonlinear system 1.13, excepting the forcing term on the right-hand side of the momentum equation. This system is used in the following paragraphs to derive the equations associated to the Reynolds stress formulation of the FSI linear stability analysis around a mean flow solution.

1.5.2 Mean flow FSI linear stability analysis: Reynolds stress formulation

In the following paragraphs, we derive the equations associated to the mean flow state and the linear stability equations. For that, we start by decomposing the slow time scale fluid–solid variables $[\langle U\rangle,\langle V\rangle,\langle p\rangle,\langle\theta\rangle,\langle\Omega\rangle]^T$ as a base equilibrium state solution and an infinitesimal perturbation:

$$[\,\langle\boldsymbol{U}\rangle,\,\langle p\rangle,\,\langle\theta\rangle,\,\langle\Omega\rangle\,]^T=[\,\boldsymbol{U}_b,\,p_b,\,\theta_b,\,\Omega_b\,]^T+\epsilon[\,\boldsymbol{U}',\,p',\,\theta',\,\Omega'\,]^T,$$

with $\epsilon\ll 1$. The above base equilibrium state corresponds to the mean flow solution obtained for fixed incidence simulations at $\bar{\theta}_b$, having

$$[\,\boldsymbol{U}_b,\,p_b,\,\theta_b,\,\Omega_b\,]^T=\left[\,\overline{\boldsymbol{U}}_b,\,\bar{p}_b,\,\bar{\theta}_b,\,0\,\right]^T.$$

We inject the above decomposition into the momentum and mass equations of the slow time scale equations, given by system 1.38. For a better understanding of the decomposition, we separate the linear terms on the momentum equation,

from the nonlinear terms (the rotational, convection and Reynolds stress terms), having

$$\frac{\partial \langle \boldsymbol{U} \rangle}{\partial t} - \nabla \cdot \boldsymbol{\sigma}(\langle \boldsymbol{U} \rangle, \langle p \rangle) = -\nabla \cdot \boldsymbol{\sigma}\left(\overline{\boldsymbol{U}}_b, \overline{p}_b\right) + \epsilon \left[\frac{\partial \boldsymbol{U}'}{\partial t} - \nabla \cdot \boldsymbol{\sigma}\left(\boldsymbol{U}', p'\right) \right],$$

$$\langle \Omega \rangle [\boldsymbol{e}_z \times \langle \boldsymbol{U} \rangle] = \epsilon \Omega' \left[\boldsymbol{e}_z \times \overline{\boldsymbol{U}}_b \right] + \epsilon^2 \Omega' \left[\boldsymbol{e}_z \times \boldsymbol{U}' \right],$$

$$([\langle \boldsymbol{U} \rangle - \langle \boldsymbol{U}_w \rangle] \cdot \nabla) \langle \boldsymbol{U} \rangle = \left(\left[\overline{\boldsymbol{U}}_b - \overline{\boldsymbol{U}}_{w,b} \right] \cdot \nabla \right) \overline{\boldsymbol{U}}_b + \epsilon \left[([\boldsymbol{U}' - \boldsymbol{U}'_w] \cdot \nabla) \overline{\boldsymbol{U}}_b + \left(\left[\overline{\boldsymbol{U}}_b - \overline{\boldsymbol{U}}_{w,b} \right] \cdot \nabla \right) \boldsymbol{U}' \right] + \epsilon^2 ([\boldsymbol{U}' - \boldsymbol{U}'_w] \cdot \nabla) \boldsymbol{U}',$$

$$-\left\langle \nabla \cdot [\boldsymbol{U}_{ft} \otimes \boldsymbol{U}_{ft}] \right\rangle = -\nabla \cdot \overline{[\boldsymbol{U}_{ft} \otimes \boldsymbol{U}_{ft}]} - \epsilon \boldsymbol{f}(\boldsymbol{U}', p', \theta', \Omega'),$$

$$\nabla \cdot \langle \boldsymbol{U} \rangle = \nabla \cdot \overline{\boldsymbol{U}}_b + \epsilon \nabla \cdot \boldsymbol{U}'.$$

In black, one finds the leading order terms, associated to the mean flow equation, while in grey, one finds the terms at orders ϵ and ϵ^2. In the forth line, we present the decomposition associated to the Reynolds stress term, with the time-averaged component at the leading order, in black, and the linearised component, in grey, represented by the variable $\boldsymbol{f}$, defined in a subsequent paragraph.

The same procedure can be made for the structure equation 1.38c, having

$$I_s \frac{\mathrm{d} \langle \Omega \rangle}{\mathrm{d}t} + D_s \langle \Omega \rangle + K_s \langle \theta \rangle - m_z(\langle \boldsymbol{U} \rangle, \langle p \rangle) = K_s \bar{\theta}_b - m_z\left(\overline{\boldsymbol{U}}_b, \overline{p}_b\right) + \epsilon \left(I_s \frac{\mathrm{d}\Omega'}{\mathrm{d}t} + D_s \Omega' + K_s \theta' - m_z\left(\boldsymbol{U}', p'\right) \right).$$

Mean flow governing equations

Gathering the leading order terms present in the above fluid and solid decompositions, one arrives to the equations governing the mean flow state at a fixed incidence:

$$\left(\left[\overline{\boldsymbol{U}}_b - \overline{\boldsymbol{U}}_{w,b} \right] \cdot \nabla \right) \overline{\boldsymbol{U}}_b - \nabla \cdot \boldsymbol{\sigma}\left(\overline{\boldsymbol{U}}_b, \overline{p}_b\right) + \nabla \cdot \overline{[\boldsymbol{U}_{ft} \otimes \boldsymbol{U}_{ft}]} = \boldsymbol{0}, \tag{1.39a}$$

$$\nabla \cdot \overline{\boldsymbol{U}}_b = 0, \tag{1.39b}$$

$$K_s \bar{\theta}_b = m_z\left(\overline{\boldsymbol{U}}_b, \overline{p}_b\right). \tag{1.39c}$$

The term $\nabla \cdot \overline{[\boldsymbol{U}_{ft} \otimes \boldsymbol{U}_{ft}]}$ corresponds to the divergence of the Reynolds stress tensor. If the nonlinearity is *sufficiently small*, the Reynolds stress tensor can be neglected and equations 1.39 are reduced to the base flow equations, describing a steady solution of the Navier–Stokes equations.

Mean flow FSI eigenproblem equations

The perturbation $\left[\boldsymbol{U}', p', \theta', \Omega'\right]^T$ is written in the form of a global mode as in equations 1.29 and 1.34:

$$\boldsymbol{q}'(\boldsymbol{X}, t) = \frac{\hat{\bar{\boldsymbol{q}}}(\boldsymbol{X}) \mathrm{e}^{\sigma t} + \text{c.c.}}{2}.$$

With this definition, and gathering the terms at order ϵ in the above decompositions, one arrives to the equations of the mean flow FSI eigenvalue problem, written as

$$\sigma\overline{\hat{\boldsymbol{U}}} + \overline{\hat{\Omega}}\left[\boldsymbol{e}_z \times \overline{\boldsymbol{U}}_b\right] + \left(\left[\overline{\hat{\boldsymbol{U}}} - \overline{\hat{\boldsymbol{U}}}_w\right]\cdot\nabla\right)\overline{\boldsymbol{U}}_b + \left(\left[\overline{\boldsymbol{U}}_b - \overline{\boldsymbol{U}}_w\right]\cdot\nabla\right)\overline{\hat{\boldsymbol{U}}} - \nabla\cdot\boldsymbol{\sigma}\left(\overline{\hat{\boldsymbol{U}}}, \overline{\hat{p}}\right) = -\boldsymbol{f}\left(\overline{\hat{\boldsymbol{U}}}, \overline{\hat{p}}, \overline{\hat{\theta}}, \overline{\hat{\Omega}}\right), \tag{1.40a}$$

$$\nabla\cdot\overline{\hat{\boldsymbol{U}}} = 0, \tag{1.40b}$$

$$I_s\sigma\overline{\hat{\Omega}} + D_s\overline{\hat{\Omega}} + K_s\overline{\hat{\theta}} - m_z\left(\overline{\hat{\boldsymbol{U}}}, \overline{\hat{p}}\right) = 0, \tag{1.40c}$$

$$\sigma\overline{\hat{\theta}} - \overline{\hat{\Omega}} = 0. \tag{1.40d}$$

The red term corresponds to the linearisation of the phase-averaged component of the fast time scale Reynolds stress contribution, which is viewed here as a forcing term. The difference between the two mean flow eigenproblem formulations (equations 1.33 and 1.40) is precisely this term. In its general form, this term depends on all the fluid–solid state variables. Denoting $\boldsymbol{g} = \nabla\cdot\overline{[\boldsymbol{U}_{ft}\otimes\boldsymbol{U}_{ft}]}$, the linearised term can be explicitly written as:

$$\boldsymbol{f}\left(\overline{\hat{\boldsymbol{U}}}, \overline{\hat{p}}, \overline{\hat{\theta}}, \overline{\hat{\Omega}}\right) = \overline{\hat{\boldsymbol{U}}}\left.\frac{\partial\boldsymbol{g}}{\partial\boldsymbol{U}}\right|_{\boldsymbol{U}=\overline{\boldsymbol{U}}_b} + \overline{\hat{p}}\left.\frac{\partial\boldsymbol{g}}{\partial p}\right|_{p=\overline{p}_b} + \overline{\hat{\theta}}\left.\frac{\partial\boldsymbol{g}}{\partial\theta}\right|_{\theta=\overline{\theta}_b} + \overline{\hat{\Omega}}\left.\frac{\partial\boldsymbol{g}}{\partial\Omega}\right|_{\Omega=\overline{\Omega}_b}.$$

We note that, if one uses a RANS formulation, rather than the Navier–Stokes formulation present in this chapter, the Reynolds stress tensor is a function of the state variables due to the Boussinesq approximation (cf. equation E.7). Consequently, the linearisation of the RANS modelling explicitly takes into account the first term, while the other terms do not exist (due to the fact that the modelling only depends on $\boldsymbol{U}$). In that way, a RANS formulation presents a methodological advantage, when compared to the present formulation, independently of choice for the model closure. The different aspects associated to the RANS model are explored in appendix E and serve as basis for future works. For the Navier–Stokes formulation, we considerer that this term only depends on the angular displacement component $\overline{\hat{\theta}}$. Further, we estimate this contribution via a finite difference scheme for two fixed angular displacements, such that

$$\boldsymbol{f}\left(\overline{\hat{\boldsymbol{U}}}, \overline{\hat{p}}, \overline{\hat{\theta}}, \overline{\hat{\Omega}}\right) \approx \boldsymbol{f}\left(\overline{\hat{\theta}}\right) = \overline{\hat{\theta}}\left.\frac{\partial\boldsymbol{g}}{\partial\theta}\right|_{\theta=\overline{\theta}_b} \approx \overline{\hat{\theta}}\frac{\boldsymbol{g}(\overline{\theta}_b + \delta\overline{\theta}_b) - \boldsymbol{g}(\overline{\theta}_b)}{\delta\overline{\theta}_b}. \tag{1.41}$$

The influence of this term in the mean flow linear stability results is analysed in sections 4.2.5 (149) and 6.1.2 (190). This new formulation for the mean flow problem can be put in a matrix form $\sigma\mathsf{M}\overline{\hat{\boldsymbol{q}}} = \mathsf{L}\overline{\hat{\boldsymbol{q}}}$, like equation 1.35, as

$$\sigma\begin{bmatrix}\mathsf{M}_f & \boldsymbol{0} & \boldsymbol{0}\\ \boldsymbol{0} & 1 & 0\\ \boldsymbol{0} & 0 & I_s\end{bmatrix}\begin{bmatrix}\overline{\hat{\boldsymbol{q}}}_f\\ \overline{\hat{\theta}}\\ \overline{\hat{\Omega}}\end{bmatrix} = \begin{bmatrix}\mathsf{L}_f\left(\overline{\boldsymbol{U}}_b\right) & \boldsymbol{v}_\theta^f & \boldsymbol{v}_\Omega\\ \boldsymbol{0} & 0 & 1\\ \boldsymbol{m}^T & -K_s & -D_s\end{bmatrix}\begin{bmatrix}\overline{\hat{\boldsymbol{q}}}_f\\ \overline{\hat{\theta}}\\ \overline{\hat{\Omega}}\end{bmatrix}, \tag{1.42}$$

where the term $\boldsymbol{v}_\theta^f$ corresponds to $\boldsymbol{v}_\theta^f = \boldsymbol{v}_\theta - \boldsymbol{f}$.

1.6 Quasi-steady fluid approximation

Up until now, the linear stability analyses rely on an exact linearisation. Thus, all the couplings between the fluid and structural perturbations are taken into account. In this section, a first estimation of the eigenvalues of either Floquet

or mean flow FSI linear stability analyses is achieved using a quasi-steady approximation of the fluid flow state on the linear formulations. The aim is to identify the linear mechanisms at play in the destabilisation of the fully coupled modes using a simpler approach. In a quasi-steady approximation, the fluid time scale of the linearised problem is assumed to be slow compared to the solid time scale. The fluid–solid eigenvalue problem can then be reduced to a solid vibration problem where the fluid effect is taken into account with added inertia, added damping and added stiffness coefficients, as is stated in classical aeroelasticity (Dowell, 2004).

We start by explicitly writing the fluid component of the mean flow eigenvector (from the classical formulation) as function of the angular displacement. For that, we rearrange the first line of the matrix system 1.35, arriving to

$$\bar{\hat{\boldsymbol{q}}}_f = \left(\sigma \mathsf{M}_f - \mathsf{L}_f\right)^{-1} \cdot \left(\boldsymbol{v}_\theta \bar{\hat{\theta}} + \boldsymbol{v}_\Omega \bar{\hat{\Omega}}\right).$$

The matrix inversion represents the fluid resolvent operator, noted

$$\mathsf{R}_f(\sigma) = \left(\sigma \mathsf{M}_f - \mathsf{L}_f\right)^{-1}.$$

With these developments, we can eliminate the fluid variable from the system 1.35, obtaining an equivalent nonlinear eigenvalue problem of reduced-size, which can be posed as

$$\left(\sigma \begin{bmatrix} 1 & 0 \\ 0 & I_s \end{bmatrix} + \begin{bmatrix} 0 & -1 \\ K_s & D_s \end{bmatrix}\right) \begin{bmatrix} \bar{\hat{\theta}} \\ \bar{\hat{\Omega}} \end{bmatrix} = \begin{bmatrix} 0 & 0 \\ \boldsymbol{m}^T \mathsf{R}_f(\sigma) \boldsymbol{v}_\theta & \boldsymbol{m}^T \mathsf{R}_f(\sigma) \boldsymbol{v}_\Omega \end{bmatrix} \begin{bmatrix} \bar{\hat{\theta}} \\ \bar{\hat{\Omega}} \end{bmatrix}. \tag{1.43}$$

Noting that $\bar{\hat{\Omega}} = \sigma \bar{\hat{\theta}}$, we obtain an equation for $\bar{\hat{\theta}}$ only

$$\left(I_s \sigma^2 + D_s \sigma + K_s\right) \bar{\hat{\theta}} = \boldsymbol{m}^T \mathsf{R}_f(\sigma) (\boldsymbol{v}_\theta + \sigma \boldsymbol{v}_\Omega) \bar{\hat{\theta}}. \tag{1.44}$$

Note that the above equation still represents the exact mean flow linear stability analysis described previously for the classical formulation. The right-hand side represents how a linear rigid-body displacement influences the solid modal problem after having "travelled" in the fluid. The term $(\boldsymbol{v}_\theta + \sigma \boldsymbol{v}_\Omega)\bar{\hat{\theta}}$ represents the linearised forcing present in the fluid, due to the pitch oscillations of the structure. This forcing is composed by the contribution $\boldsymbol{v}_\theta$, representing a unitary angular displacement perturbation, and by the contribution $\boldsymbol{v}_\Omega$, representing a unitary angular velocity perturbation. The term $\mathsf{R}_f(\sigma)$ represents the linearised fluid response to this forcing term, transforming the forcing into a fluid perturbation. Finally, the term $\boldsymbol{m}^T$ extracts the constraints exerted by the fluid onto the solid at the fluid–solid interface, represented by the aerodynamic moment associated to the linearised fluid response to the forcing term.

In a quasi-steady approximation, where the fluid time scale is assumed to be slow compared to the solid time scale, we can approximate the resolvent operator by a Taylor expansion around $\sigma = 0$ (as done recently in Pfister *et al.* (2020)). In this way, the right-hand side of the above equation can be developed as

$$\boldsymbol{m}^T \left(\sigma \mathsf{M}_f - \mathsf{L}_f\right)^{-1} (\boldsymbol{v}_\theta + \sigma \boldsymbol{v}_\Omega) \bar{\hat{\theta}} \tag{1.45a}$$

$$\approx \boldsymbol{m}^T \left[-\mathsf{L}_f^{-1} - \sigma \mathsf{L}_f^{-1} \mathsf{M}_f \mathsf{L}_f^{-1} - \sigma^2 \left(\mathsf{L}_f^{-1} \mathsf{M}_f\right)^2 \mathsf{L}_f^{-1} + \dots\right] (\boldsymbol{v}_\theta + \sigma \boldsymbol{v}_\Omega) \bar{\hat{\theta}} \tag{1.45b}$$

$$\approx \boldsymbol{m}^T \left[-\mathsf{L}_f^{-1} \boldsymbol{v}_\theta - \left(\mathsf{L}_f^{-1} \boldsymbol{v}_\Omega + \mathsf{L}_f^{-1} \mathsf{M}_f \mathsf{L}_f^{-1} \boldsymbol{v}_\theta\right) \sigma - \left(\left(\mathsf{L}_f^{-1} \mathsf{M}_f\right)^2 \mathsf{L}_f^{-1} \boldsymbol{v}_\theta + \mathsf{L}_f^{-1} \mathsf{M}_f \mathsf{L}_f^{-1} \boldsymbol{v}_\Omega\right) \sigma^2 + \dots\right] \bar{\hat{\theta}}. \tag{1.45c}$$

This development can be put in a synthetic way as $-I_a\sigma^2 - D_a\sigma - K_a$, where I_a, D_a and K_a are the added inertia, added damping and added stiffness coefficients, respectively, defined as

$$K_a = \boldsymbol{m}^T \mathsf{L}_f^{-1} \boldsymbol{v}_\theta \,,$$

$$D_a = D_a^\theta + D_a^\Omega = \boldsymbol{m}^T \mathsf{L}_f^{-1} \mathsf{M}_f \mathsf{L}_f^{-1} \boldsymbol{v}_\theta + \boldsymbol{m}^T \mathsf{L}_f^{-1} \boldsymbol{v}_\Omega \,,$$

$$I_a = I_a^\theta + I_a^\Omega = \boldsymbol{m}^T \left(\mathsf{L}_f^{-1} \mathsf{M}_f\right)^2 \mathsf{L}_f^{-1} \boldsymbol{v}_\theta + \boldsymbol{m}^T \mathsf{L}_f^{-1} \mathsf{M}_f \mathsf{L}_f^{-1} \boldsymbol{v}_\Omega \,.$$

Concerning the added damping and added inertia coefficients, we separate the contributions associated to the angular displacement perturbation from the ones coming from an angular velocity perturbation. In that way, problem 1.44 is approximated as

$$\left[(I_s + I_a)\sigma^2 + (D_s + D_a)\sigma + (K_s + K_a)\right] \bar{\theta} = 0 \,. \tag{1.46}$$

The added inertia, I_a, may be understood as the inertia added to the oscillating system due to the fact that the accelerating structure moves a certain volume of surrounding fluid as it moves through it. In a similar way, one may consider that the volume of surrounding fluid displaced by the oscillating structure increases the damping and the stiffness of the system by a factor of D_a and K_a, respectively. The magnitude of these effects depends on the structure geometry and physical properties of the fluid and are evaluated in chapter 3.

We denote a quasi-steady approximation of order 2 when all the added coefficients are taken into account, an approximation of order 1 when only the terms D_a and K_a are taken into account and an approximation of order 0 when only K_a is taken into account. For $\bar{\theta} \neq 0$, the solution of the above second order scalar equation, denoted σ_{QS}, reads

$$\sigma_{QS} = -\frac{D_s + D_a}{2(I_s + I_a)} \pm \sqrt{\left(\frac{D_s + D_a}{2(I_s + I_a)}\right)^2 - \frac{K_s + K_a}{I_s + I_a}} \,. \tag{1.47}$$

When the quantity inside the square root is negative, σ_{QS} corresponds to a pair of complex conjugate eigenvalues. On the other hand, if the quantity inside the square root is positive, the quasi-steady approximation will predict two static modes.

In a quasi-steady approximation, a relation between the added stiffness and the static slope of the aerodynamic moment versus the incidence can be made. Indeed, the moment around the position $\bar{\theta}_b + \epsilon\theta'$ can be written as

$$m_z\left(\bar{\theta}_b + \epsilon\theta'\right) = m_z\left(\bar{\theta}_b\right) + \epsilon m_z^\theta \theta' \quad \text{with} \quad m_z^\theta = \left.\frac{\partial m_z}{\partial \theta}\right|_{\theta=\bar{\theta}_b} \,.$$

Here, we neglect the dependence of the aerodynamic moment variation with the angular velocity and acceleration. By supposing the perturbation as being written in a normal form in the above equation, $\theta' = \left(\bar{\theta} \mathrm{e}^{\sigma t} + \text{c.c.}\right)/2$, the linearised structure equation reads:

$$\sigma^2 I_s \bar{\theta} + \sigma D_s \bar{\theta} + K_s \bar{\theta} = m_z^\theta \bar{\theta} \,,$$

where on the left-hand side we find the added stiffness term $K_a = -m_z^\theta$.

In this case, a stability criterion can be written in terms of stiffness and added stiffness coefficients. For the limiting case $D_s = 0$, which can be viewed as a conservative approximation of the actual problem, the quasi-steady approximation can predict the presence of an unstable static eigenvalue in terms of K_s and m_z^θ:

$$\text{if } -(K_s + K_a) > 0 \Leftrightarrow K_s < m_z^\theta : \quad \text{Existence of an unstable static eigenvalue.} \tag{1.48}$$

Due to the problem symmetry with respect the angular displacement, $\alpha = -\theta$, the above relation can be rewritten as

$$\text{if } K_s < -m_z^\alpha : \quad \text{Existence of an unstable static eigenvalue.} \tag{1.49}$$

1.7 Numerical discretisation

After the presentation of the mathematical models for describing the physics of the flow and structure behaviours, this section introduces the numerical tools employed for the discretisation of the present problem. In a first part, we introduce the space discretisation of the incompressible Navier–Stokes equations, where no degree of freedom is associated to the structure, as an example of the models presented before, whereas in a second part, we present the time discretisation associated to the two- and three-dimensional time-marching schemes. The time discretisation could alternatively be performed using time spectral methods, not explored in this manuscript (see Moulin (2020); Benetti Ramos (2020)).

In this regard, we first introduce the numerical boundary conditions considered. Next, we introduce the weak formalism associated to the Navier–Stokes equations. This is followed by the mesh generation details, the domain decomposition and the description of the Finite Element Method (FEM) used to derive the semi-discrete (continuous in time, discrete in space) formulation of the present problem. We then define the numerical stabilisations associated to this discretisation and finish by describing the different time-marching scheme discretisations.

Exact solutions of the Navier–Stokes equations are only possible for few particular cases which frequently represent coarse simplifications of reality[8]. In most cases, only an approximative numerical solution is possible to achieve. The resolution of these challenges is often associated to the branch of fluid mechanics called *Computational Fluid Dynamics* (CFD).

Various numerical methods can be found on the literature for the discretisation and resolution of the Navier–Stokes equations. The most common ones are the Finite Difference Methods (Strikwerda, 1984), the Finite Volume Methods (Eymard *et al.*, 2000), the Finite Element Methods (Girault *et al.*, 1979; Rannacher, 2000) and Spectral Element Methods (Canuto *et al.*, 2006). Mesh-free methods, including Vortex Methods (Cottet *et al.*, 2000) and Smoothed Particle Hydrodynamics (Li *et al.*, 2002) can also be found on the literature. All these methods have their own advantages and disadvantages, making them more or less suitable for the discretisation of a given problem. In the present manuscript, the discretisation and resolution of our problem is made with the help of a Finite Element Method, a procedure for obtaining an approximative numerical solution for general problems based on their weak formulation and a decomposition of the domain into a finite number of elements, as described in the following paragraphs.

1.7.1 Boundary conditions on the numerical domain

Before presenting the weak formulation of the incompressible Navier–Stokes equations, we introduce the numerical boundary conditions implemented. The unbounded physical domain is restricted upstream by an inlet frontier, labelled Γ_{in}, and restricted on the remaining space directions by an outlet, upper and lower frontiers, labelled Γ_{out}. For the three-dimensional computations, an additional frontier is created on the lateral sides of the wing, denoted Γ_{lat}. As previously noted, the airfoil/wing surface is denoted Γ_w on the two-/three-dimensional domain. The position of these different borders can be seen in figure 1.6. Since the airfoil is considered to move forward on a resting fluid, we shall impose a null fluid velocity at Γ_{in} and a continuity velocity requirement at the fluid–solid interface, Γ_w. At Γ_{out}, we

[8] For the three-dimensional incompressible Navier–Stokes system of equations, and given some initial conditions, mathematicians have not yet proved that smooth solutions always exist for all time. This is called the Navier–Stokes existence and smoothness problem, one of the seven Millennium Prize Problems stated by the Clay Mathematics Institute (Jaffe, 2006).

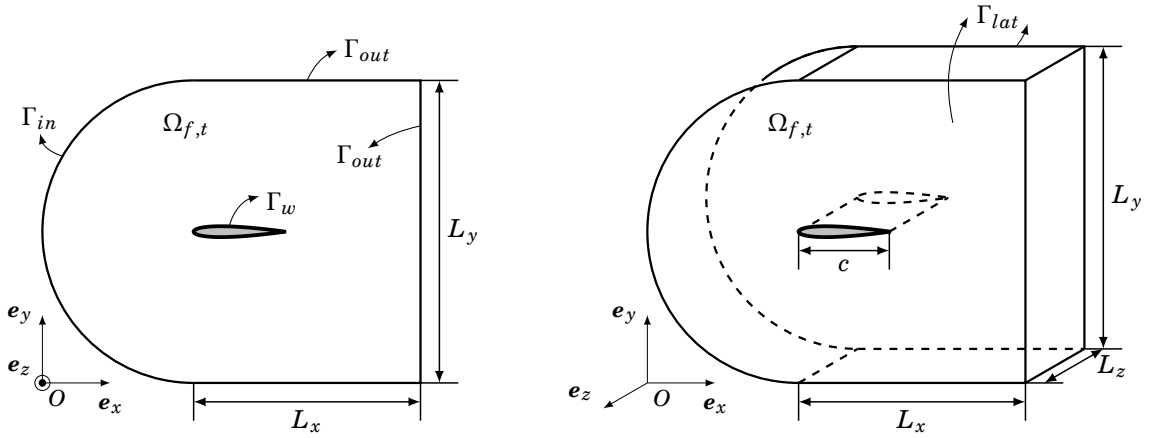

Figure 1.6 – *Schematic illustration of the computational domain for the two-dimensional (left) and the three-dimensional (right) simulations.*

impose a natural stress-free condition (a Neumann boundary condition). Finally, at Γ_{lat}, we impose a symmetric condition for the normal velocity component, W, and a natural stress-free condition along the remaining space directions. Therefore, the problem 1.13, is numerically closed with

$$\boldsymbol{U}(\boldsymbol{X},t)=\boldsymbol{0} \qquad \boldsymbol{X}\in\Gamma_{in}\,, \tag{1.50a}$$

$$\boldsymbol{U}(\boldsymbol{X},t)=\boldsymbol{U}_w \qquad \boldsymbol{X}\in\Gamma_{w}\,, \tag{1.50b}$$

$$\boldsymbol{\sigma}(\boldsymbol{U},p)\cdot\boldsymbol{n}_\infty=\boldsymbol{0} \qquad \boldsymbol{X}\in\Gamma_{out}\cup\Gamma_{lat}\,, \tag{1.50c}$$

$$W(\boldsymbol{X},t)=0 \qquad \boldsymbol{X}\in\Gamma_{lat}\,, \tag{1.50d}$$

with $\boldsymbol{n}_\infty$ the outward unit normal vector of the Γ_{out} and Γ_{lat} borders. The general dimensions of the domain are fixed at $L_x=10$, $L_y=30$ and $L_z=0.2$.

1.7.2 Weak formulation

Originally, the weak formulation has been introduced by mathematicians to investigate the behaviour of the solution of partial differential equations, and to prove its existence and uniqueness. Later on, numerical schemes have been based on this formulation, leading to an approximate solution. The weak formulation is also called the variational formulation, where the solution satisfies a minimum of energy. Mathematically, the state variables $\boldsymbol{U}$ and p of equations 1.5 are defined in the trial functional spaces, $\mathcal{V}_{\boldsymbol{U}}^2$ and $\mathcal{V}_p^1$, which can be written as:

$$\boldsymbol{U}\in\mathcal{V}_{\boldsymbol{U}}^2 \quad \text{with} \quad \mathcal{V}_{\boldsymbol{U}}^2=\left\{\boldsymbol{a}\in\left[\mathscr{H}^2\left(\Omega_f\right)\right]^D \;\middle|\; \boldsymbol{a}|_{\Gamma_{in}}=\boldsymbol{0}\ \wedge\ a_z|_{\Gamma_{lat}}=0\right\}, \tag{1.51a}$$

$$p\in\mathcal{V}_p^1 \quad \text{with} \quad \mathcal{V}_p^1=\left\{b\in\mathscr{H}^1\left(\Omega_f\right)\right\}, \tag{1.51b}$$

where $\mathscr{H}^1$ and $\mathscr{H}^2$ represent the Sobolev spaces[9], D the space dimension and a_z the $\boldsymbol{e}_z$-component of $\boldsymbol{a}$. As noted previously, the pressure field is determined up to constant. If only Dirichlet conditions are used to close equations 1.5, an additional condition for fixing the constant has to be introduced in the definition of the space $\mathscr{V}_p^1$, *e.g.*, that the integral of the pressure over the entire domain should vanish for all time t (Volker, 2016, p. 20). In the present case, the pressure constant is fixed naturally by the use of Neumann conditions, as described in the following paragraphs.

Concomitantly, we define the test functions $\boldsymbol{v}$ and q in the test functional spaces $\mathscr{V}_{\boldsymbol{v}}^1$ and $\mathscr{L}^2$ as

$$\boldsymbol{v} \in \mathscr{V}_{\boldsymbol{v}}^1 \quad \text{with} \quad \mathscr{V}_{\boldsymbol{v}}^1 = \left\{ \boldsymbol{a} \in \left[\mathscr{H}^1\left(\Omega_f\right)\right]^D \;\middle|\; \boldsymbol{a}|_{\Gamma_{in}\cup\Gamma_w} = \boldsymbol{0} \;\wedge\; a_z|_{\Gamma_{lat}} = 0 \right\}, \tag{1.52a}$$

$$q \in \mathscr{L}^2, \tag{1.52b}$$

where the test function $\boldsymbol{v}$ is set to zero on all Dirichlet conditions, where the solution is known. The weak formulation can be obtained by multiplying equations 1.5a and 1.5b by the test functions $\boldsymbol{v}$ and q, respectively, followed by their integration over the domain Ω_f, yielding

$$\int_{\Omega_f} \left[\frac{\partial \boldsymbol{U}}{\partial t} + \boldsymbol{\Omega} \times \boldsymbol{U} + ([\boldsymbol{U} - \boldsymbol{U}_w]\cdot\nabla)\boldsymbol{U} + \nabla p - \frac{2}{Re}\nabla\cdot\boldsymbol{S}(\boldsymbol{U}) \right] \cdot \boldsymbol{v} + [\nabla\cdot\boldsymbol{U}]\, q \, \mathrm{d}\Omega_f = 0 \,.$$

Applying the integration by parts to the stress tensor terms results[10]

$$\int_{\Omega_f} \nabla p \cdot \boldsymbol{v} \, \mathrm{d}\Omega_f = -\int_{\Omega_f} p \nabla\cdot\boldsymbol{v} \, \mathrm{d}\Omega_f + \overbrace{\int_{\Gamma_{in}\cup\Gamma_w} p\boldsymbol{v}\cdot\boldsymbol{n} \, \mathrm{d}\Gamma}^{=0,\ \text{since } \boldsymbol{v}=\boldsymbol{0}} + \overbrace{\int_{\Gamma_{out}} p\boldsymbol{v}\cdot\boldsymbol{n}_\infty \, \mathrm{d}\Gamma}^{=0,\ \text{Neumann condition}} ,$$

$$-\int_{\Omega_f} \frac{2}{Re}[\nabla\cdot\boldsymbol{S}(\boldsymbol{U})]\cdot\boldsymbol{v} \, \mathrm{d}\Omega_f = \int_{\Omega_f} \frac{2}{Re}\boldsymbol{S}(\boldsymbol{U}) : \boldsymbol{S}(\boldsymbol{v}) \, \mathrm{d}\Omega_f - \underbrace{\int_{\Gamma_{in}\cup\Gamma_w} \frac{2}{Re}[\boldsymbol{S}(\boldsymbol{U})\cdot\boldsymbol{n}]\cdot\boldsymbol{v} \, \mathrm{d}\Gamma}_{=0,\ \text{since } \boldsymbol{v}=\boldsymbol{0}} - \underbrace{\int_{\Gamma_{out}} \frac{2}{Re}[\boldsymbol{S}(\boldsymbol{U})\cdot\boldsymbol{n}_\infty]\cdot\boldsymbol{v} \, \mathrm{d}\Gamma}_{=0,\ \text{Neumann condition}} ,$$

with $\boldsymbol{n}$ corresponding to $\boldsymbol{n}_w$ or $\boldsymbol{n}_\infty$ on Γ_w or Γ_{in}, respectively. As the test function $\boldsymbol{v}$ is supposed with compact form on *all* Dirichlet conditions, the terms associated to the border integrals over Γ_{in} and Γ_w are identically equal to zero. Additionally, the sum of both integrals over Γ_{out} vanishes due to the Neumann condition of the present problem. Therefore, in order to impose a homogeneous Neumann condition on FEM, one has nothing to do, hence the name "do nothing" condition that is sometimes used in the literature[11]. Finally, one can note that the integral over Γ_{out} on the first equation contains a contribution from the pressure. This fixes the constant associated to the definition of the pressure field.

The weak formulation is posed as

$$\int_{\Omega_f} \left[\frac{\partial \boldsymbol{U}}{\partial t} + \boldsymbol{\Omega} \times \boldsymbol{U} + ([\boldsymbol{U} - \boldsymbol{U}_w]\cdot\nabla)\boldsymbol{U} \right] \cdot \boldsymbol{v} - p\nabla\cdot\boldsymbol{v} + \frac{2}{Re}\boldsymbol{S}(\boldsymbol{U}) : \boldsymbol{S}(\boldsymbol{v}) + [\nabla\cdot\boldsymbol{U}]\, q \, \mathrm{d}\Omega_f = 0 \,. \tag{1.53}$$

[9] Sobolev space $\mathscr{H}^p$ is a space of functions equipped with a norm that is a combination of $\mathscr{L}^p$-norms (Lebesgue space norms) of the function together with its derivatives up to the order p.

[10] To simply the explanation, the integrals over the lateral boundary Γ_{lat} are omitted as they correspond to Dirichlet and Neumann conditions, exemplified by the integrals over the other boundaries.

[11] While homogeneous Neumann conditions appear naturally in FEM formulation, other methods as spectral collocation or finite difference methods must enforce this conditions explicitly, which may pollute the accuracy some time discretisations, as the fractional step methods, presented in section 1.7.7 of Guermond *et al.* (2006), p. 6036.

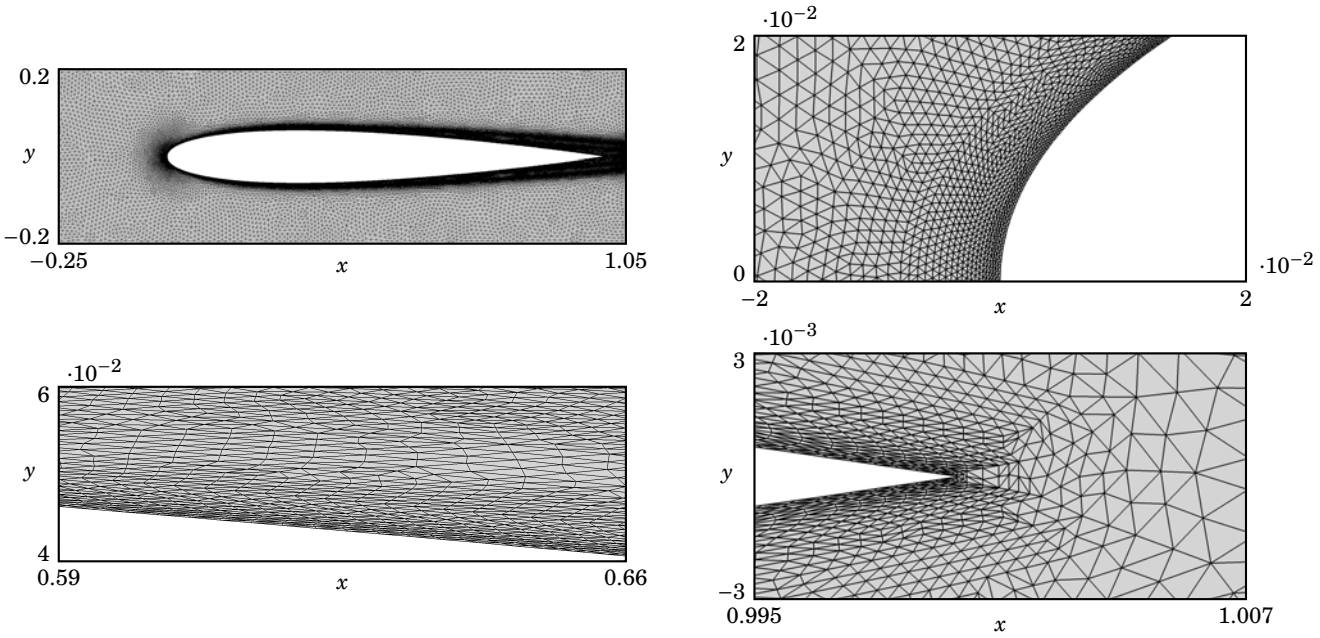

Figure 1.7 – *Two-dimensional triangular mesh around the NACA0012 airfoil, at $\alpha = 0\,°$, on the top left, with the following close-up views: near airfoil surface around mid-chord, on the bottom left, near the leading edge, on the top right, and near the trailing edge, on the bottom right.*

The integration by parts operation reduces the order of the maximum derivative of the problem and $\boldsymbol{U}$ no longer has to belong to $\mathcal{V}_{\boldsymbol{U}}^2$, since equation 1.53 only involves first derivatives of $\boldsymbol{U}$. Also, p no longer has to belong to $\mathcal{V}_p^1$, since no derivatives are required for the pressure variable. Therefore, the problem can be restricted to the search of functions $\boldsymbol{U} \in \mathcal{V}_{\boldsymbol{U}}^1$ and $p \in \mathscr{L}^2$ with

$$\mathcal{V}_{\boldsymbol{U}}^1 = \left\{ \boldsymbol{a} \in \left[\mathscr{H}^1\left(\Omega_f\right)\right]^D \;\middle|\; \boldsymbol{a}|_{\Gamma_{in}} = \boldsymbol{0} \;\wedge\; a_z|_{\Gamma_{lat}} = 0 \right\}.$$

The solution set has been expanded, hence the denomination weak form. If a solution of this weak form exists, then its uniqueness is proven by the Lax–Milgram theorem (Boldo *et al.*, 2017), key ingredient used to build the Finite Element Method.

1.7.3 Mesh generation

Before discussing the Finite Element Method used for the numerical discretisation of the above weak formulation, we introduce the notions regarding the domain discretisation. Consider the partition of the fluid domain Ω_f into a finite number N_{ele} of closed disjoint[12] D-dimensional elements $\mathscr{K}$, forming a discrete domain Ω_f^h, such that

$$\Omega_f^h = \bigcup_{e=1}^{N_{ele}} \mathscr{K}_e \,.$$

[12]This means that, for $l \neq k \Rightarrow \mathscr{K}_l \cap \mathscr{K}_k = \emptyset \oplus \mathscr{K}_l \cap \mathscr{K}_k = \{1 \text{ vertex}\} \oplus \mathscr{K}_l \cap \mathscr{K}_k = \{1 \text{ edge}\}$, with the $\oplus$ notation representing the exclusive disjunction, allowing only one of the equalities to be true at a time.

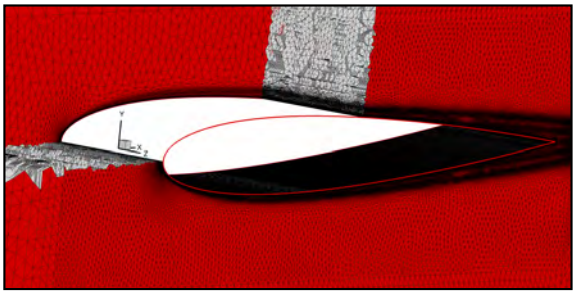

2D mesh: triangle number	155 752
2D P_2 space size	312 576
2D P_1 space size	78 412
2D $[P_2]^2/P_1$ space size	703 564
3D mesh: tetrahedron number	42 053 040
3D P_2 space size	56 576 256
3D P_1 space size	7 135 492
3D $[P_2]^3/P_1$ space size	176 864 260

Figure 1.8 & Table 1.5 – *On the left, visualisation of the three-dimensional mesh, at $\alpha = 0°$. The red faces represent two YX planes at $Z = -0.1$ and $Z = 0.1$. On the right, the simplex number of the 2D and 3D meshes along with the size of the P_2, P_1, and Taylor–Hood FEM spaces. The number of tetrahedra on the 3D mesh corresponds to $3N_z$ times the number of triangles on the 2D mesh.*

The meshing procedure is based on a Delaunay triangulation procedure, accomplished by the software *FreeFem++* (Hecht, 2012)[13], which is an open-source software used to solve partial differential equations, based on a Finite Element Method discretisation, described in the next section. The elements $\mathscr{K}_e$ are restricted to simplex elements by the *FreeFem++* software, either to triangles for two-dimensional or to tetrahedra for three-dimensional meshes.

The *FreeFem++* software makes possible a local adaptation based on several user defined fields, which allows for an efficient discretisation technique and an unstructured mesh generation. The adaptation algorithm is described in Hecht (1998). The resulted mesh has a grid-point distribution determined by a metric matrix based on the Hessian of one or several user defined fields. The precision of the adaptation (and hence the grid-point density) can be controlled by specifying the desired interpolation error of the fields on the new mesh. Further parameters can be stipulated, as the minimum and maximum edge sizes and the anisometric coefficient of the elements of the considered mesh.

The three-dimensional mesh is constructed by disposing several copies of the two-dimensional mesh along the spanwise direction. The latter is generated in two steps. An example for $\alpha = 0°$ is present in figure 1.7. The same procedure is done for the remaining incidences. In a first step, an initial mesh is generated, with a fine refinement on the wake region and with the presence of 10 cell layers of fixed thickness around the airfoil surface. These layers are used to enforce a constant height (in the normal direction to the airfoil surface) of the mesh simplexes, close to the airfoil. The height of the first cell is fixed to $2 \cdot 10^{-4}$, with an expansion ratio of 1.15, so that $y^+ \sim O(1)$ for the flow regimes in the present manuscript. With this mesh, a first estimation of the two-dimensional flow field at different instances is made. In a second step, a rectangular region around the airfoil is established (represented by the domain in the upper left of figure 1.7), in which the initial mesh is adapted to several instantaneous flow fields at different time instances. The details around the leading edge, trailing edge and at a middle point over the upper surface are present on the zooms of figure 1.7. The different layers created on the initial mesh around the airfoil force the adaptation procedure to produce triangles whose vertices remain on theses layers, fixing the maximum height of each layer. The objective of these layers is to keep an isotropic character in the normal direction of the wall, while having an anisotropic behaviour along the airfoil surface direction. This effect is clearly seen on the bottom left figure, which represents a close-up on the upper surface of

[13]The *FreeFem++* version used to obtain the results of the present thesis is the 4.400002, found on https://github.com/FreeFem/FreeFem-sources/commit/7a6f53a44649aba87bb6d8179a062f7fe6da5a09.

the airfoil. The anisotropic factor given to the *FreeFem++* adaptation routine has a value of 10, while the interpolation error is fixed at 0.008. As stated before, the general dimensions of the domain are fixed at $L_x = 10$, $L_y = 30$ and $L_z = 0.2$.

The three-dimensional tetrahedral meshes are then obtained by an extrusion in the spanwise direction, *i.e.*, by disposing several copies of a two-dimensional mesh along the spanwise direction. This procedure initially generates a triangular prism for each triangle of two adjacent planes, which is then divided in three tetrahedral. In that way, the number of tetrahedra on the three-dimensional mesh corresponds to $3N_z$ times the number of triangles on the two-dimensional mesh. The nominal number of planes is fixed at $N_z = 90$. A sliced view near the airfoil is present in figure 1.8. The number of simplex elements and degrees of freedom associated to the polynomial bases, described in the following paragraphs, is present in table 1.5.

1.7.4 MPI implementation and domain decomposition

The numerical resolution of the different problems of this thesis benefits from a MPI[14] standard, associated to the partition of the space discretisation. Each partition, obtained from a domain decomposition, is associated to a different process[15].

Domain decomposition, in the context of parallel computing, refers to the partitioning of the computational work among multiple cores. In the present case, the global mesh is decomposed into N_{MPI} submeshes, each one assigned to a separate MPI process. The choice of the number of subdomains has a significant effect on the computational time. As N_{MPI} increases, the computational time tends to decrease, since the work is distributed by a higher number of processes. However, the increase of N_{MPI} also increases the number of communications to be made between the neighbouring subdomains. In that sense, the overall computational time can be minimised for an optimal choice of N_{MPI}. This value can be obtained theoretical for fairly simple scenarios (Chan *et al.*, 1995). However, for practical scientific computing problems that commonly involve complex domains, no generic rule can be found for its prediction.

Along with the concern on the number of subdomains, one must also avoid a load imbalance in case of a vast difference in the relative sizes of the subdomains. In this regard, the operation of decomposing the domain into N_{MPI} subdomains, called partitioning, is often performed in such a way that the resulting subdomains require comparable amounts of computational effort, with minimal communication costs for handling the subdomain interfaces. This operation is often done in a "pre-processing" step before the numerical computations and can be accomplished using a graph partitioning software, such as Chaco (Hendrickson *et al.*, 1994), PT-SCOTCH (Chevalier *et al.*, 2008) or, as in the present case, ParMETIS (Karypis *et al.*, 1998).

1.7.5 Space discretisation: Finite Element Method

Although the Finite Element Method (FEM) was firstly used by structural engineers in the early 1940s (Courant, 1943), it was introduced in the fluid mechanics community in the late 1970s (Babuška, 1973; Pironneau, 1989). The idea of FEM is to build up a solution to a differential equation from a sequence of local approximations. In that sense, the approximations are noted $\boldsymbol{U}^h \approx \boldsymbol{U}$, $p^h \approx p$, $\boldsymbol{v}^h \approx \boldsymbol{v}$, $q^h \approx q$. We define the subspaces $\mathcal{V}_{\boldsymbol{U}}^{1,h} \subset \mathcal{V}_{\boldsymbol{U}}^{1}$, $\mathcal{L}^{2,h} \subset \mathcal{L}^2$ and $\mathcal{V}_{\boldsymbol{v}}^{1,h} \subset \mathcal{V}_{\boldsymbol{v}}^{1}$ where the discrete solutions of equation 1.53 can be searched and the test functions defined. Note that, since the Lax–Milgram theorem is valid for the continuous formulation of the problem, it is also valid for its discrete version. The

[14] Message Passing Interface (MPI) is an *ad hoc* standard for writing parallel programs that defines an application programmer interface (API) implementing the message-passing programming model (Padua, 2011, p. 1184).

[15] Typically, for maximum performance, each process, responsible for a fraction of the space domain, is assigned to a single CPU core. This assignment happens at runtime through the agent that starts the MPI program, *mpirun* for the present case.

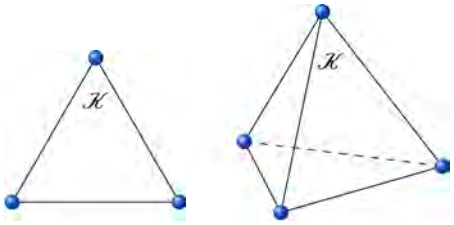

(a) *Degrees of freedom for a continuous piecewise linear finite element space* P_1.

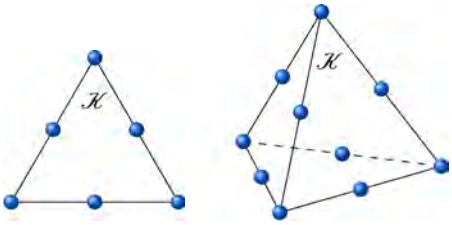

(b) *Degrees of freedom for a continuous piecewise quadratic finite element space* P_2.

Figure 1.9 – *Two- and three-dimensional standard element cells: illustration of the number of degrees of freedom for the* P_1 *and* P_2 *finite element spaces.*

semi-discrete form of the weak formulation is therefore written as

$$\int_{\Omega_f^h} \left[\frac{\partial \boldsymbol{U}^h}{\partial t} + \boldsymbol{\Omega} \times \boldsymbol{U}^h + \left(\left[\boldsymbol{U}^h - \boldsymbol{U}_w^h \right] \cdot \nabla \right) \boldsymbol{U}^h \right] \cdot \boldsymbol{v}^h - p^h \nabla \cdot \boldsymbol{v}^h + \frac{2}{Re} \boldsymbol{S}\left(\boldsymbol{U}^h \right) : \boldsymbol{S}\left(\boldsymbol{v}^h \right) + \left[\nabla \cdot \boldsymbol{U}^h \right] q^h \, \mathrm{d}\Omega_f^h = 0 . \tag{1.54}$$

The discretisation of the rigid-body velocity field, noted $\boldsymbol{U}_w^h$, follows exactly the same reasoning as the discretised fluid velocity $\boldsymbol{U}^h$. The discrete variables $\boldsymbol{U}^h$ and p^h are now represented as a truncated series expansion, for instance[16],

$$\boldsymbol{U}^h(\boldsymbol{X}, t) = \sum_{i=1}^{N_{dof}^{\boldsymbol{U}}} \hat{\boldsymbol{U}}_i^h(t) \odot \boldsymbol{\Phi}_i(\boldsymbol{X}) \qquad \text{and} \qquad p^h(\boldsymbol{X}, t) = \sum_{i=1}^{N_{dof}^{p}} \hat{p}_i^h(t) \Psi_i(\boldsymbol{X}),$$

where $\boldsymbol{\Phi}_i = \left[\Phi_i^U, \Phi_i^V, \Phi_i^W \right]^T$ and Ψ_i are analytic functions called trial (or expansion) functions, consisting of piecewise polynomial functions[17], and $\hat{\boldsymbol{U}}_i^h$ and $\hat{p}_i^h$ are the unknown coefficients for the velocity and pressure solutions. The variables $N_{dof}^{\boldsymbol{U}}$ and N_{dof}^{p} represent the number of unknowns of the problem (with a total of N_{dof}), depending on both the number of elements N_{ele} and the order of the basis function. Upon convergence, as $N_{dof} \to \infty$, the approximative solution $\left[\boldsymbol{U}^h, p^h \right]^T$ approaches the exact solution $[\boldsymbol{U}, p]^T$.

The choice of the basis functions for the velocity and pressure is constrained by the inf-sup or Ladyzhenskaya–Babuška–Brezzi (known as LBB) condition (see, for instance, Brezzi *et al.* (1991)) in order to guarantee a stable approximation. Indeed, the coupling of velocity and pressure in incompressible flow problems does not allow the straightforward use of arbitrary pairs of finite element spaces. Several stable pairs of finite element spaces have been proposed in the literature, as the MINI basis for simplex elements $[P_{1+b}]^D/P_1$ (piecewise-linear polynomials enriched with local cubic bubble functions for the discrete velocity and piecewise-linear polynomials for the discrete pressure, see Arnold *et al.* (1984)) or the Taylor–Hood basis $[P_{k+1}]^D/P_k$ with $k \geqslant 1$ (the degree of the discrete velocity is one order superior to the one of the discrete pressure, see Hood *et al.* (1974)). Note that both basis ensure that the pressure is approximated by a continuous function. The Taylor–Hood bases are among the most popular, mainly due to its easy implementation compared to other inf-sup pairs (Volker, 2016, p. 99). We opted for the Taylor–Hood basis $[P_2]^D/P_1$, whose standard representation is present in figure 1.9. For a two-dimensional problem, one obtains, for each cell, 3 degrees of freedom

[16] The notation $\boldsymbol{a} \odot \boldsymbol{b}$ stands for the Hadamard or element-wise product, in this case, between two vectors $\boldsymbol{a}$ and $\boldsymbol{b}$, where each element of the result product is the product of elements of the original two vectors.

[17] In practice, each element is mapped into a standard element of unitary size, where local trial functions are defined. The global trial functions are then constructed using a parametric transformation between the "physical" cell and the reference unit cell (Karniadakis *et al.*, 2013, p. 38).

for the pressure and 6 degrees of freedom per velocity component, whereas for a three-dimensional problem, one has 4 degrees of freedom for the pressure and 10 degrees of freedom per velocity component. Finally, we note that the inf-sup requirement can be circumvented by using a proper numerical stabilisation, given for example by the Pressure Stabilisation Petrov–Galerkin (PSPG) methods (Hughes *et al.*, 1986, 1987), not used in this thesis. The number of degrees of freedom associated to each computation made are present in table 1.5 (and in table E.1, page 227 for the RANS computations).

We initially consider the Galerkin method (known as the Bubnov–Galerkin method) for the choice of the test functions. In this method, the test functions are chosen to be in the bases used to define the trial functions, such that

$$\boldsymbol{v}^h(\boldsymbol{X}) = \sum_{j=1}^{N_{dof}^{\boldsymbol{U}}} \boldsymbol{\Phi}_j(\boldsymbol{X}) \qquad \text{and} \qquad q^h(\boldsymbol{X}) = \sum_{j=1}^{N_{dof}^{p}} \Psi_j(\boldsymbol{X}).$$

A broader class of the Galerkin method, known as the Petrov–Galerkin methods is discussed in section 1.7.6, where the test functions and the trial functions are not found on the same bases.

Injecting the above decompositions into equation 1.54, one obtains the following discretised problem

$$\begin{bmatrix} \mathsf{M}^{\boldsymbol{U}} & 0 \\ 0 & 0 \end{bmatrix} \frac{\partial}{\partial t} \begin{bmatrix} \hat{\boldsymbol{U}}^h \\ \hat{p}^h \end{bmatrix} + \mathsf{R}\left(\hat{\boldsymbol{U}}^h, \hat{p}^h\right) = 0, \tag{1.55}$$

with $\mathsf{M}^{\boldsymbol{U}}$ the mass matrix operator, whose entries are given by

$$\mathsf{M}^{\boldsymbol{U}}_{ij} = \int_{\Omega_f^h} \boldsymbol{\Phi}_i \boldsymbol{\Phi}_j \, \mathrm{d}\Omega_f^h. \tag{1.56}$$

The residual operator R is defined as

$$\mathsf{R}\left(\hat{\boldsymbol{U}}^h, \hat{p}^h\right) = \begin{bmatrix} \mathsf{A}^{\boldsymbol{\Omega}} \odot \hat{\boldsymbol{U}}^h + \mathsf{C}\hat{\boldsymbol{U}}^h + \mathsf{D}\hat{\boldsymbol{U}}^h - \mathsf{B}^T \hat{p}^h \\ \mathsf{B}\hat{\boldsymbol{U}}^h \end{bmatrix},$$

with the entries of the different discrete operators given by

$$\mathsf{A}^{\boldsymbol{\Omega}}_i = \int_{\Omega_f^h} \boldsymbol{\Omega} \times \boldsymbol{\Phi}_i \, \mathrm{d}\Omega_f^h, \quad \mathsf{D}_{ij} = \int_{\Omega_f^h} \boldsymbol{S}(\boldsymbol{\Phi}_i) : \boldsymbol{S}(\boldsymbol{\Phi}_j) \, \mathrm{d}\Omega_f^h, \quad \mathsf{B}_{ij} = \int_{\Omega_f^h} \Psi_j \nabla \cdot \boldsymbol{\Phi}_i \, \mathrm{d}\Omega_f^h.$$

The treatment of the nonlinear convection term C usually passes through a linearised approximation, depending on the problem to be solved. Its treatment on the different time-marching schemes used in this thesis is detailed in subsequent paragraphs. Each integral over the discretised domain is further decomposed into a sum of integrals over each element $\mathscr{K}$. Then, the integrals are evaluated numerically on each element, using a Gauss quadrature integration, available on the *FreeFem++* software.

Numerical treatment of the boundary conditions

We have seen how the natural Neumann conditions directly appear on the variational formulation. Concerning the Dirichlet conditions, present at the airfoil surface, on the inlet and on the lateral boundaries of the three-dimensional domain, they are enforced on each degree of freedom of the boundary x_i, after the assembly of equation 1.55, typically in

a matrix form $\mathsf{A}\boldsymbol{x} = \boldsymbol{b}$. This is done by imposing the value of the condition, g, on the corresponding degree of freedom of the $\boldsymbol{b}$ vector, as $b_i = g$, and setting all coefficients of the i^{th} line of A to zero, excepting the diagonal value, that is set to 1. In that way, the degree of freedom x_i is forced to the value g on the boundary condition, as desired.

1.7.6 Numerical stabilisations: Streamline Upwind/Petrov–Galerkin (SUPG) and grad-div

One of the flaws of the standard Galerkin formulation in FEM discretisation is the generation of spurious node to node oscillations for high Reynolds number problems. These oscillations come from three main sources:

- from the convective term, where oscillations may contaminate the velocity field for high advection problems (*i.e.*, where the local Reynolds number, based on the characteristic length of the cell, is high);
- from a possible singularity on the discretised pressure equation, leading to pressure oscillations, associated to a choice of velocity and pressure finite element pairs that does not satisfy the inf-sup condition. This is usually treated with a suitable choice of finite element pair or with a PSPG stabilisation (see chapter 6 of Bodnár *et al.* (2020) for a recent review on the subject);
- from the discrete violation of the divergence-free constraint, caused by a poor resolution of the pressure variable, leading to large errors on both velocity and pressure fields.

In the context of variational formulations and weighted residual methods, several strategies to attenuate/suppress these oscillations can be found in the literature, see for example Braack *et al.* (2007) for a review of these techniques. In this thesis, we implement a Streamline Upwind/Petrov–Galerkin (SUPG) and a grad-div stabilisations, in order to address the first and third points presented above. The second point is solved by a correct choice of a finite element pair, satisfying the inf-sup condition. The SUPG stabilisation was not necessary for the time-marching Navier–Stokes computations, but was imperative for the RANS computations to converge (see appendix E). Concerning the grad-div stabilisation, it was deemed necessary for both fluid models. Further, both stabilisations where used in the stability analyses presented in sections 1.4 and 1.5. For this sake, a linearisation of the SUPG and grad-div must be computed. Their formal definition is present in appendix A, section A.4. In the next paragraphs, we detail the formulation associated to the stabilisation techniques used.

SUPG stabilisation

Historically, the SUPG method was introduced by Brooks *et al.* (1982) for stabilising convection diffusion equations with a dominance of the convective term. Later, the stabilisation of the stationary Navier–Stokes equations appeared with Hansbo *et al.* (1990), Lube *et al.* (1990) and Franca *et al.* (1992). The need for a SUPG stabilisation is related to the inability to capture the small scales on the velocity field for a given mesh cell. To circumvent the problem, one could over-refine the mesh, which would lead to an excessive refined mesh. The other option consists in adding a control parameter, that depends on the strong residual of the momentum equation (plus the Spalart–Allmaras equation, for the RANS model, see appendix E) on each cell, to the left-hand side of the Galerkin finite element formulation in equation 1.54. This control term reads

$$\sum_{e=1}^{N_{ele}} \int_{\mathcal{K}_e} \tau_{SUPG} \mathsf{R} \cdot \left[\left(\left[\boldsymbol{U}^h - \boldsymbol{U}_w^h \right] \cdot \nabla \right) \boldsymbol{v}^h \right] \, \mathrm{d}\mathcal{K}_e \,, \tag{1.57}$$

where R represents the strong semi-discretised residual of equation 1.5a (or equations E.8 and E.9 for RANS computations) and $\tau_{SUPG} \geqslant 0$ represents the nonnegative scalar value, called intrinsic time or SUPG parameter, different for each

mesh element and possibly dependent on the fluid velocity and viscosity at that element. This term is approximated by piecewise constant functions, belonging to the P_0 finite element space. Since this additional term is based on the strong residual of the problem's equations, it vanishes as the numerical solution approaches the exact analytical solution, leading to a consistent formulation.

The addition of the above term can also be interpreted as the use of a different class of weighting functions on the FEM, defined as,

$$\boldsymbol{v}^h_{SUPG} = \boldsymbol{v}^h + \tau_{SUPG}\left(\left[\boldsymbol{U}^h - \boldsymbol{U}^h_w\right]\cdot\nabla\right)\boldsymbol{v}^h\,.$$

The additional term represents a streamline upwind contribution. Compared to the standard Galerkin method, this new weighting function, $\boldsymbol{v}^h_{SUPG}$, is no longer continuous across the inter-element boundaries. The resulting procedure is known as Petrov–Galerkin formulation. The addition of this term results on a nonsymmetrical mass matrix, represented in equation 1.56, which can be problematic for some linear solvers.

In regards to the stabilisation parameter τ_{SUPG}, different definitions were used in the literature. In this work, two different definitions were used. The first one was proposed by Tezduyar *et al.* (1992):

$$\tau_{SUPG,1} = \frac{h_K}{2\left\|\boldsymbol{U}^h\right\|_K}\xi(Re_K) \quad \text{with} \quad \xi(Re_K) = \begin{cases} Re_K, & 0 \leqslant Re_K \leqslant 3 \\ 1 & Re_K > 3 \end{cases} \quad \text{and} \quad Re_K = \frac{\left\|\boldsymbol{U}^h\right\|_K h_K}{2\nu}\,, \tag{1.58}$$

where $\left\|\boldsymbol{U}^h\right\|_K$ corresponds to the element-wise fluid velocity norm, h_K represents the characteristic length of the element and Re_K the local Reynolds number. This definition is used in the RANS computations (appendix E). The second definition, used in the two- and three-dimensional simulations, was proposed in Codina (2000); Sari *et al.* (2018) and reads

$$\tau_{SUPG,2} = \left[\left(\frac{2\left\|\boldsymbol{U}^h\right\|_K}{h_K}\right)^2 + \left(\frac{4\nu}{h_K^2}\right)^2\right]^{-1/2}\,. \tag{1.59}$$

The characteristic length can also have different definitions. For elements that are highly stretched in one particular direction (anisotropic meshes), this definition becomes paramount. Mittal (2000) compared different definitions of h_K on the SUPG stabilisation of the Navier–Stokes flows, one based on the maximum edge length of each element, one based on their minimum edge length and one based on the element length along the streamwise direction. Although, their study was performed at Reynolds numbers of $10 \leqslant Re \leqslant 100$, they concluded that the maximum edge definition produced overly diffused solutions, while the one based on the velocity-magnitude produced oscillatory solutions close to the solid boundary.

Other works have also analysed the effect of h_K, as Förster *et al.* (2009); Micheletti *et al.* (2003); Sari *et al.* (2018) with no definitive definition. In the present thesis, we considered two definitions of h_K. The first one is based on the work of Franceschini (2019),

$$h_{K,1} = \sqrt{2}\frac{A_K}{\max(h_{edge})}\,, \tag{1.60}$$

with A_K the cell area and h_{edge} the size of the different cell edges. The second one corresponds to the minimum edge size

$$h_{K,2} = \min(h_{edge})\,. \tag{1.61}$$

The tests on the different definitions of τ_{SUPG} and h_K are present in section E.2.5 (page 232). For the results present in this thesis, we use the definition $\tau_{SUPG,1}$ for the RANS simulations and $\tau_{SUPG,2}$ for the Navier–Stokes formulation, and we use the definition $h_{K,2}$ for both fluid models.

Grad-div stabilisation

While dominating advection flows can lead to numerical instabilities addressed by the SUPG stabilisation, there is another source of numerical oscillations in the finite element discretisation of incompressible flows related to a possible poor resolution of the pressure field, leading to a loss of accuracy on the velocity approximation and ultimately to a non-compliance of the discrete divergence-free condition, *i.e.*, of the conservation of mass. One of the options proposed in the literature to correct this lack of mass conservation passes through the introduction of a penalty term in the Galerkin finite element formulation, referred to as grad-div (also called Least Square on Incompressibility Constraint (LSIC)). Its inclusion in incompressible flow problems was first accomplished around the same time as the τ_{SUPG} term, by Franca *et al.* (1988); Hansbo *et al.* (1990); Franca *et al.* (1992); Kobel'kov (1995), and later studied for example in Codina (2000); Olshanskii (2002); Olshanskii *et al.* (2009); Sari *et al.* (2018); Fiordilino *et al.* (2018). The grad-div term, added to equation 1.54, reads

$$s_{GD} = \sum_{e=1}^{N_{ele}} \int_{\mathcal{K}_e} \tau_{GD} \left(\nabla\cdot\boldsymbol{U}^h\right)\left(\nabla\cdot\boldsymbol{v}^h\right) \mathrm{d}\mathcal{K}_e \,, \tag{1.62}$$

where $\tau_{GD} \geqslant 0$ is a nonnegative scalar value, called grad-div coefficient, different for each mesh element, as the τ_{SUPG} parameter, defined as

$$\tau_{GD} = \frac{(h_K/c_0)^2}{4D\tau_{SUPG}} \,,$$

where c_0 is a constant corresponding to the velocity space interpolation order (here, fixed at $c_0 = 2$) and D the space dimension.

Note that when expressed into a strong form instead of a variational form, the grad-div stabilisation is a vector quantity, added to the left-hand side of the Navier–Stokes momentum equation, with the form

$$\boldsymbol{s}_{GD}^S = \nabla\left[\tau_{GD}\left(\nabla\cdot\boldsymbol{U}^h\right)\right] .$$

This strong form justifies the name "grad-div" for this stabilisation.

In the following paragraphs, we present the schemes associated to the time discretisation, where the grad-div term is used. In order to simplify the presentation, we reconsider the strong formulation of the Navier–Stokes equations, where the term $\boldsymbol{s}_{GD}^S$ appears.

Finally, we note that the divergence-free condition can be numerically achieved using pressure-robust space discretisations to define the basis functions, *e.g.*, the Scott–Vogelius element spaces (Scott *et al.*, 1985; Kean *et al.*, 2021). However, this choice is followed by several restrictions in the mesh generation and therefore this option was not studied in this thesis.

1.7.7 Time discretisation of the three-dimensional Navier–Stokes equations

Along with a space discretisation, the time-marching simulations require a temporal numerical scheme to advance in time. We present the time discretisation here by applying it to the strong form of the Navier–Stokes equations 1.5 with $\boldsymbol{\Omega} = 0$, since the wing is in a static position. The rigid-body velocity field $\boldsymbol{U}_w$ is therefore fixed for each angle of attack. This numerical scheme will be used for the computations that are presented in chapter 2. The time discretisation is implemented using a linearised implicit backward differentiation formula (BDF) of 2$^{\text{nd}}$ order (Curtiss *et al.*, 1952;

Quarteroni *et al.*, 1991):

$$\frac{\alpha_0}{\Delta t}\boldsymbol{U}^{k+1} + \left(\boldsymbol{U}^{\star}\cdot\nabla\right)\boldsymbol{U}^{k+1} - \nabla\cdot\boldsymbol{\sigma}\left(\boldsymbol{U}^{k+1}, p^{k+1}\right) + \boldsymbol{s}_{GD}^{S}\left(\boldsymbol{U}^{k+1}\right) = \boldsymbol{f}^{k+1}, \tag{1.63a}$$

$$\nabla\cdot\boldsymbol{U}^{k+1} = 0, \tag{1.63b}$$

with $\boldsymbol{X} \in \Omega_f$, where $\Delta t > 0$ is the time step, k the current time step iteration, $\boldsymbol{f}^{k+1}$ a source term and $\boldsymbol{U}^{\star}$ the convective velocity extrapolated from the previous time steps. The last two terms are defined as

$$\boldsymbol{f}^{k+1} = -\left(\frac{\alpha_1}{\Delta t}\boldsymbol{U}^{k} + \frac{\alpha_2}{\Delta t}\boldsymbol{U}^{k-1}\right),$$

$$\boldsymbol{U}^{\star} = \beta_1\left(\boldsymbol{U}^{k} - \boldsymbol{U}_w\right) + \beta_2\left(\boldsymbol{U}^{k-1} - \boldsymbol{U}_w\right).$$

In all simulations, we adapt the time step such that the Courant–Friedrichs–Lewy (CFL) number is found around 0.66. The constants α_0, α_1, α_2, β_1 and β_2 correspond to the BDF coefficients and take the values of $\alpha_0 = 1$, $\alpha_1 = -1$, $\alpha_2 = 0$, $\beta_1 = 1$, $\beta_2 = 0$ for the first time iteration—corresponding to a BDF method of 1$^{\text{st}}$ order—and $\alpha_0 = 3/2$, $\alpha_1 = -2$, $\alpha_2 = 1/2$, $\beta_1 = 2$, $\beta_2 = -1$ otherwise—corresponding to a BDF method of 2$^{\text{nd}}$ order.

In order to efficiently solve the system 1.63 at each time step, we implemented an incremental projection algorithm, where the velocity and pressure variables are solved in different substeps of the k^{th} time iteration. This separation comes from the numerical difficulty of solving incompressible flows, where these variables are coupled by the incompressibility constraint. The interest in using projection methods to overcome this problem started in the late 1960s with the works of Chorin (1968) and Témam (1969). Further, these methods are not specific to the BDF scheme used in this thesis. A recent review by Guermond *et al.* (2006) addressed the different projection methods available on the literature. The present implementation passes through a pressure-correction scheme, composed of two main substeps. In the first substep, the pressure is treated explicitly and an intermediate velocity $\tilde{\boldsymbol{U}}$ is calculated by solving the momentum equations only. As the incompressibility constraint is not taken into account in this substep, the obtained velocity is not divergent-free. Only in the second substep, this velocity is projected into the pressure space, obtaining, first, a correction for the velocity field and, second, the pressure field.

The time-discrete momentum equation solved in the first substep can be put as

$$\frac{\alpha_0}{\Delta t}\tilde{\boldsymbol{U}} + \left(\boldsymbol{U}^{\star}\cdot\nabla\right)\tilde{\boldsymbol{U}} - \frac{1}{Re}\nabla^2\left(\tilde{\boldsymbol{U}}\right) + \boldsymbol{s}_{GD}^{S}\left(\tilde{\boldsymbol{U}}\right) = \boldsymbol{f}^{k+1} - \nabla p^{k}, \tag{1.64}$$

or, in a matrix form:

$$\mathsf{A}\boldsymbol{x} = \boldsymbol{b} \Leftrightarrow \begin{bmatrix} \mathsf{L}(U^{k+1}) + s_{GD}^{S,xx} & s_{GD}^{S,xy} & s_{GD}^{S,xz} \\ s_{GD}^{S,yx} & \mathsf{L}(V^{k+1}) + s_{GD}^{S,yy} & s_{GD}^{S,yz} \\ s_{GD}^{S,zx} & s_{GD}^{S,zy} & \mathsf{L}(U^{k+1}) + s_{GD}^{S,zz} \end{bmatrix} \begin{bmatrix} \tilde{U} \\ \tilde{V} \\ \tilde{W} \end{bmatrix} = \begin{bmatrix} f_x^{k+1} - \partial_x p^k \\ f_y^{k+1} - \partial_y p^k \\ f_z^{k+1} - \partial_z p^k \end{bmatrix}, \tag{1.65}$$

where L represents the first three terms of the left-hand side of equation 1.64 and $s_{GD}^{S,\bullet\bullet}$ the different components of the grad-div term, that depend on each velocity component. One can see that the latter terms are responsible for coupling the different velocity components of the first substep system. This system is solved using a Generalised Minimum Residual (GMRES) method (Saad *et al.*, 1986), preconditioned on the right side by a the block lower triangular version of the matrix

in equation 1.65 (see appendix B for more details on this class of methods):

$$\mathsf{A}\mathsf{P}^{-1}\mathsf{P}\boldsymbol{x} = \boldsymbol{b} \Leftrightarrow \begin{cases} \mathsf{A}\mathsf{P}^{-1}\boldsymbol{y} = \boldsymbol{b} \\ \mathsf{P}\boldsymbol{x} \quad = \boldsymbol{y} \end{cases} \quad \text{with} \quad \mathsf{P} = \begin{bmatrix} \mathsf{L}(U^{k+1}) + s_{GD}^{S,xx} & \mathbf{0} & \mathbf{0} \\ s_{GD}^{S,yx} & \mathsf{L}(V^{k+1}) + s_{GD}^{S,yy} & \mathbf{0} \\ s_{GD}^{S,zx} & s_{GD}^{S,zy} & \mathsf{L}(U^{k+1}) + s_{GD}^{S,zz} \end{bmatrix}. \tag{1.66}$$

The relative tolerance of the unpreconditioned residual is set to 10^{-9} with a fixed restart parameter of 25. We note that the addition of the grad-div terms couples the velocity components, decreasing the sparsity of the matrix to invert and making the preconditioning more difficult. A comparison of the GMRES performance between the cases with and without the grad-div stabilisation is present in the preliminary results, in section 1.8.4. In contrast, we note that the preconditioner is diagonally dominant when the time step is small, hence, its performance is expected to increase as Δt decreases. This behaviour is not explored in the numerical tests since one of the advantage of the linearised implicit discretisation (com- pared to semi-implicit discretisation, where the nonlinear convection term is treated explicitly) is their numerical stability with respect to larger time steps.

The inverse of the preconditioner matrix is accomplished via a forward substitution process, where the inverse of each diagonal block is performed. The inverse of each diagonal block is approximated by a block Jacobi, where each block—associated to an individual domain of a MPI process—is solved via an incomplete LU factorisation, ILU(l), where the fill level set to $l = 1$. This last parameter changes the amount of coefficients of the original matrix taken into account in the factorisation. Increasing l leads to a more exact factorisation, with an increase on the computational time. Different inverse strategies are tested in section 1.8.4.

Concerning the second substep, we use a Standard Incremental Pressure-Correction (SIPC) scheme (van Kan, 1986). With this scheme, the velocity and pressure fields are corrected by solving the system:

$$\frac{\alpha_0}{\Delta t}\boldsymbol{U}^{k+1} - \frac{\alpha_0}{\Delta t}\tilde{\boldsymbol{U}} + \nabla\cdot(p^{k+1} - p^k) = \mathbf{0}, \tag{1.67a}$$

$$\nabla\cdot\boldsymbol{U}^{k+1} = 0. \tag{1.67b}$$

Taking the divergence of equation 1.67a and noting $\mathrm{d}P = p^{k+1} - p^k$ the pressure correction, one arrives to

$$\frac{\alpha_0}{\Delta t}\nabla\cdot\tilde{\boldsymbol{U}} = \nabla^2\mathrm{d}P, \tag{1.68}$$

with the corrections given by

$$p^{k+1} = p^k + \mathrm{d}P,$$

$$\boldsymbol{U}^{k+1} = \tilde{\boldsymbol{U}} + \frac{\Delta t}{\alpha_0}\nabla\cdot\mathrm{d}P.$$

The system 1.68 represents a Laplace equation, which is solved via a left preconditioned Conjugate Gradient (CG) (Málek *et al.*, 2015) iterative method, taking advantage of the positive-definite character of the discrete Laplace matrix to inverse. The absolute tolerance of the unpreconditioned residual is set to 10^{-8} and the preconditioner corresponds to a Geometric Algebraic Multigrid (GAMG) (Stüben, 2001) preconditioner, with a smoothed aggregation algorithm.

1.7.8 Time discretisation of the two-dimensional FSI equations

In this section, we present the time discretisation used for the two-dimensional coupled time-marching simulations, described by the nonlinear set of equations 1.13. This numerical scheme is used for the computations that are presented in chapter 5. The coupled system is solved via a fully implicit temporal discretisation, using a backward differentiation formula (BDF) of 2$^{\text{nd}}$ order (Curtiss *et al.*, 1952; Quarteroni *et al.*, 1991):

$$\frac{\alpha_0 \boldsymbol{U}^{k+1} + \alpha_1 \boldsymbol{U}^{k} + \alpha_2 \boldsymbol{U}^{k-1}}{\Delta t} + \Omega^{k+1}\left[\boldsymbol{e}_z \times \boldsymbol{U}^{k+1}\right] + \left(\left[\boldsymbol{U}^{k+1} - \boldsymbol{U}_w^{k+1}\right]\cdot\nabla\right)\boldsymbol{U}^{k+1} - \nabla\cdot\boldsymbol{\sigma}\left(\boldsymbol{U}^{k+1}, p^{k+1}\right) + \boldsymbol{s}_{GD}^{S}\left(\boldsymbol{U}^{k+1}\right) = \boldsymbol{0}, \tag{1.69a}$$

$$\nabla\cdot\boldsymbol{U}^{k+1} = 0, \tag{1.69b}$$

$$I_s \frac{\alpha_0 \Omega^{k+1} + \alpha_1 \Omega^{k} + \alpha_2 \Omega^{k-1}}{\Delta t} + D_s \Omega^{k+1} + K_s \theta^{k+1} = m_z\left(\boldsymbol{U}^{k+1}, p^{k+1}\right), \tag{1.69c}$$

$$\frac{\alpha_0 \theta^{k+1} + \alpha_1 \theta^{k} + \alpha_2 \theta^{k-1}}{\Delta t} - \Omega^{k+1} = 0. \tag{1.69d}$$

In all simulations, we adapt the time step such that the Courant–Friedrichs–Lewy (CFL) number is found between 5 to 10. This nonlinear set of equations is solved with the help of a Newton–Raphson method (see for example Deuflhard (2011) for a review on these methods). This class of methods has become a popular strategy for solving large systems of nonlinear equations in the field of CFD due to its ability to provide deep convergence levels for stiff systems such as the ones found in the discretisation of the Navier–Stokes equations. In short, the Newton methods represent a class of iterative root-finding algorithms which produces successively better approximations to the roots of the considered system of equations, given a *reasonably* close initial guess, which is the case in the current application.

At each time iteration k, the solution at the Newton iteration $i+1$ is computed as $\boldsymbol{q}^{i+1,k+1} = \boldsymbol{q}^{i,k+1} + \delta\boldsymbol{q}$. By injecting this decomposition on equations 1.69, one arrives to a linear system which can be posed in the form:

$$\left.\frac{\partial \boldsymbol{R}}{\partial \boldsymbol{q}}\right|_{\boldsymbol{q}=\boldsymbol{q}^{i,k+1}} \delta\boldsymbol{q} = -\boldsymbol{R}\left(\boldsymbol{q}^{i,k+1}\right).$$

The superscript $\bullet^i$ will be dropped, in order to simplify the notation. The state vector correction $\delta\boldsymbol{q}$ is computed by solving the corresponding linearised system, posed in a matrix form as

$$\begin{bmatrix} \mathsf{L}_f & \boldsymbol{v}_\theta & \boldsymbol{v}_\Omega \\ \boldsymbol{0} & \frac{1}{\Delta t} & -1 \\ \boldsymbol{m}^T & K_s & \left(\frac{I_s}{\Delta t} + D_s\right) \end{bmatrix} \begin{bmatrix} \delta\boldsymbol{q}_f \\ \delta\theta \\ \delta\Omega \end{bmatrix} = - \begin{bmatrix} \boldsymbol{R}_f \\ \boldsymbol{R}_\theta \\ \boldsymbol{R}_\Omega \end{bmatrix}, \tag{1.70}$$

where the right-hand side terms $\boldsymbol{R}_f = \left[\boldsymbol{R}_f^U, \boldsymbol{R}_f^p\right]^T$, $\boldsymbol{R}_\theta$ and $\boldsymbol{R}_\Omega$ are the time-discrete residuals, posed as

$$\boldsymbol{R}_f^{\boldsymbol{U}} = \frac{\alpha_0 \boldsymbol{U}^{k+1} + \alpha_1 \boldsymbol{U}^k + \alpha_2 \boldsymbol{U}^{k-1}}{\Delta t} + \Omega^{k+1}\left[\boldsymbol{e}_z \times \boldsymbol{U}^{k+1}\right] + \left(\left[\boldsymbol{U}^{k+1} - \boldsymbol{U}_w^{k+1}\right]\cdot\nabla\right)\boldsymbol{U}^{k+1} - \nabla\cdot\boldsymbol{\sigma}\left(\boldsymbol{U}^{k+1}, p^{k+1}\right) + \boldsymbol{s}_{GD}^S\left(\boldsymbol{U}^{k+1}\right),$$

$$\boldsymbol{R}_f^p = \nabla\cdot\boldsymbol{U}^{k+1},$$

$$\boldsymbol{R}_\theta = \frac{\alpha_0 \theta^{k+1} + \alpha_1 \theta^k + \alpha_2 \theta^{k-1}}{\Delta t} - \Omega^{k+1},$$

$$\boldsymbol{R}_\Omega = \frac{\alpha_0 \Omega^{k+1} + \alpha_1 \Omega^k + \alpha_2 \Omega^{k-1}}{\Delta t} + D_s\Omega^{k+1} + K_s\Omega^{k+1} - \boldsymbol{m}^T\boldsymbol{q}_f^{k+1},$$

for $\boldsymbol{X} \in \Omega_f$ and $\Delta t > 0$. The boundary conditions associated to the right-hand side of equation 1.70 are posed as

$$\boldsymbol{U}^{k+1}(\boldsymbol{X}) = \boldsymbol{0} \qquad \boldsymbol{X} \in \Gamma_{in}, \tag{1.71a}$$

$$\boldsymbol{U}^{k+1}(\boldsymbol{X}) = \boldsymbol{U}_w^{k+1} \qquad \boldsymbol{X} \in \Gamma_w, \tag{1.71b}$$

$$\boldsymbol{\sigma}\left(\boldsymbol{U}^{k+1}, p^{k+1}\right)\cdot\boldsymbol{n}_\infty = \boldsymbol{0} \qquad \boldsymbol{X} \in \Gamma_{out}. \tag{1.71c}$$

The terms L_f, $\boldsymbol{v}_\theta$, $\boldsymbol{v}_\Omega$ correspond to the linearised operators around the state vector $\boldsymbol{q}^{k+1}$, which are posed as

$$\mathsf{L}_f\delta\boldsymbol{q}_f = \begin{bmatrix} \frac{\alpha_0\delta\boldsymbol{U}}{\Delta t} + \Omega^{k+1}[\boldsymbol{e}_z \times \delta\boldsymbol{U}] + \left(\left[\boldsymbol{U}^{k+1} - \boldsymbol{U}_w^{k+1}\right]\cdot\nabla\right)\delta\boldsymbol{U} + (\delta\boldsymbol{U}\cdot\nabla)\boldsymbol{U}^{k+1} - \nabla\cdot\boldsymbol{\sigma}(\delta\boldsymbol{U}, \delta p) + \boldsymbol{s}_{GD}^S(\delta\boldsymbol{U}) \\ \nabla\cdot\delta\boldsymbol{U} \end{bmatrix},$$

$$\boldsymbol{v}_\theta = -U^\infty\left(\begin{bmatrix} \sin\left(\theta^{k+1}\right) \\ \cos\left(\theta^{k+1}\right) \end{bmatrix}\cdot\nabla\right)\boldsymbol{U}^{k+1},$$

$$\boldsymbol{v}_\Omega = \begin{bmatrix} -V^{k+1} \\ U^{k+1} \end{bmatrix} - \left(\begin{bmatrix} -(Y - Y_{EC}) \\ X - X_{EC} \end{bmatrix}\cdot\nabla\right)\boldsymbol{U}^{k+1},$$

for $\boldsymbol{X} \in \Omega_f$ and $\Delta t > 0$. The boundary conditions associated to the left-hand side of equation 1.70 are posed as

$$\delta\boldsymbol{U}(\boldsymbol{X}) = \boldsymbol{0} \qquad \boldsymbol{X} \in \Gamma_{in}, \tag{1.72a}$$

$$\delta\boldsymbol{U}(\boldsymbol{X}) = \boldsymbol{1} \qquad \boldsymbol{X} \in \Gamma_w, \tag{1.72b}$$

$$\boldsymbol{\sigma}(\delta\boldsymbol{U}, \delta p)\cdot\boldsymbol{n}_\infty = \boldsymbol{0} \qquad \boldsymbol{X} \in \Gamma_{out}, \tag{1.72c}$$

$$\boldsymbol{v}_\theta = -U^\infty\left[\sin\left(\theta^{k+1}\right), \cos\left(\theta^{k+1}\right)\right]^T \qquad \boldsymbol{X} \in \Gamma_w, \tag{1.72d}$$

$$\boldsymbol{v}_\Omega = -\left[-(Y - Y_{EC}), (X - X_{EC})\right]^T \qquad \boldsymbol{X} \in \Gamma_w. \tag{1.72e}$$

The convergence of the Newton is achieved when the absolute residual respect $\|\boldsymbol{R}(\boldsymbol{q})\| < 10^{-14}$.

1.7.9 Modular approach for fluid–structure Jacobian inversion

Using several linear algebra manipulations, the inversion of the full Jacobian matrix can be based solely on the inversion of the fluid Jacobian, L_f. The final result can be related to the Schur complement of the fluid Jacobian[18].

We start by decomposing the fluid correction state vector into three components:

$$\delta \boldsymbol{q}_f = -\left(\delta \boldsymbol{q}_{f,f} + \delta \boldsymbol{q}_\theta \delta\theta + \delta \boldsymbol{q}_\Omega \delta\Omega\right),$$

referred to as the "intrinsic" fluid component, $\delta \boldsymbol{q}_{f,f}$, and the "coupled" fluid components, $\delta \boldsymbol{q}_\theta$ and $\delta \boldsymbol{q}_\Omega$. From the first equation of the system 1.70,

$$\delta \boldsymbol{q}_f = -\mathsf{L}_f^{-1}\left(\boldsymbol{R}_f + \boldsymbol{v}_\theta \delta\theta + \boldsymbol{v}_\Omega \delta\Omega\right),$$

one can identify the three fluid systems to solve in order to obtain the aforementioned components of $\delta \boldsymbol{q}_f$:

$$\delta \boldsymbol{q}_{f,f} = \mathsf{L}_f^{-1}\boldsymbol{R}_f,$$

$$\delta \boldsymbol{q}_\theta = \mathsf{L}_f^{-1}\boldsymbol{v}_\theta,$$

$$\delta \boldsymbol{q}_\Omega = \mathsf{L}_f^{-1}\boldsymbol{v}_\Omega.$$

The corrections on the solid variables come from the second and third lines of the system 1.70, which is posed as

$$\begin{bmatrix} \frac{1}{\Delta t} & -1 \\ K_s + \tilde{K}_a & \left(\frac{I_s}{\Delta t} + D_s + \tilde{D}_a\right) \end{bmatrix} \begin{bmatrix} \delta\theta \\ \delta\Omega \end{bmatrix} = - \begin{bmatrix} \boldsymbol{R}_\theta \\ \boldsymbol{R}_\Omega + \boldsymbol{m}^T \delta \boldsymbol{q}_{f,f} \end{bmatrix},$$

where $\tilde{K}_a$ and $\tilde{D}_a$ are terms similar to the added stiffness and to the added damping coefficients, defined as

$$\tilde{K}_a = \boldsymbol{m}^T \delta \boldsymbol{q}_\theta,$$
$$\tilde{D}_a = \boldsymbol{m}^T \delta \boldsymbol{q}_\Omega.$$

Numerically, the solution obtained with these linear algebra manipulations is only accurate if the matrix L_f is well-conditioned. For this reason, the Newton method based on the solid-reduced eigenproblem developed in chapter 3 mainly targets the fluid–structure eigenvalues (see section 3.2.3, page 121). For completeness of the above paragraphs, the Schur component of the matrix L_f is defined as

$$\mathsf{S} = \begin{bmatrix} \frac{1}{\Delta t} & -1 \\ K_s & \left(\frac{I_s}{\Delta t} + D_s\right) \end{bmatrix} - \begin{bmatrix} 0 \\ \boldsymbol{m}^T \end{bmatrix} \mathsf{L}_f^{-1} \begin{bmatrix} \boldsymbol{v}_\theta & \boldsymbol{v}_\Omega \end{bmatrix}.$$

1.7.10 Time discretisation of the linearised two-dimensional FSI equations

We present in this section the method implemented for time-marching the linearised FSI equations, described by the system 1.27. This is used for the computation of the leading eigenvalues of the Floquet FSI linear stability analysis, detailed in appendix B, with the results present in chapters 4 and 6.

[18] In electrical engineering, this linear algebra manipulation is referred to as network reduction or Kron reduction (Bergen *et al.*, 2000, sec. 9.3).

The linearised system, represented by equations 1.27, is solved via a fully implicit temporal discretisation, using a backward differentiation formula (BDF) of 2$^{\text{nd}}$ order (Curtiss *et al.*, 1952; Quarteroni *et al.*, 1991):

$$\frac{\alpha_0 \boldsymbol{U}'^{k+1} + \alpha_1 \boldsymbol{U}'^{k} + \alpha_2 \boldsymbol{U}'^{k-1}}{\Delta t} + \Omega'^{k+1}\left[\boldsymbol{e}_z \times \boldsymbol{U}_b^{k+1}\right] + \left(\left[\boldsymbol{U}'^{k+1} - \boldsymbol{U}_w'^{k+1}\right]\cdot\nabla\right)\boldsymbol{U}_b^{k+1} + \left(\left[\boldsymbol{U}_b^{k+1} - \overline{\boldsymbol{U}}_w\right]\cdot\nabla\right)\boldsymbol{U}'^{k+1} - \nabla\cdot\boldsymbol{\sigma}\left(\boldsymbol{U}'^{k+1}, p'^{k+1}\right) + \boldsymbol{s}_{GD}^{S}\left(\boldsymbol{U}'^{k+1}\right) = \boldsymbol{0}, \tag{1.73a}$$

$$\nabla\cdot\boldsymbol{U}'^{k+1} = 0, \tag{1.73b}$$

$$I_s\frac{\alpha_0\Omega'^{k+1} + \alpha_1\Omega'^{k} + \alpha_2\Omega'^{k-1}}{\Delta t} + D_s\Omega'^{k+1} + K_s\theta'^{k+1} = m_z\left(\boldsymbol{U}'^{k+1}, p'^{k+1}\right), \tag{1.73c}$$

$$\frac{\alpha_0\theta'^{k+1} + \alpha_1\theta'^{k} + \alpha_2\theta'^{k-1}}{\Delta t} - \Omega'^{k+1} = 0. \tag{1.73d}$$

Note that, since the flow around which the linearisation was carried out is periodic, evolving in time, its corresponding terms are also implicit, namely the velocity component $\boldsymbol{U}_b^{k+1}$. If one denotes $\left[\delta\boldsymbol{q}_f, \delta\theta, \delta\Omega\right]^T = \left[\boldsymbol{U}'^{k+1}, p'^{k+1}, \theta'^{k+1}, \Omega'^{k+1}\right]^T$, the time-discretised linear system can be put in a matrix form as

$$\begin{bmatrix} \mathsf{L}_f & \boldsymbol{v}_\theta & \boldsymbol{v}_\Omega \\ \boldsymbol{0} & \frac{1}{\Delta t} & -1 \\ \boldsymbol{m}^T & K_s & \left(\frac{I_s}{\Delta t} + D_s\right) \end{bmatrix} \begin{bmatrix} \delta\boldsymbol{q}_f \\ \delta\theta \\ \delta\Omega \end{bmatrix} = - \begin{bmatrix} \boldsymbol{R}_f \\ \boldsymbol{R}_\theta \\ \boldsymbol{R}_\Omega \end{bmatrix}, \tag{1.74}$$

where the right-hand side terms $\boldsymbol{R}_f = \left[\boldsymbol{R}_f^U, \boldsymbol{R}_f^p\right]^T$, $\boldsymbol{R}_\theta$ and $\boldsymbol{R}_\Omega$ are posed as

$$\boldsymbol{R}_f^U = \frac{\alpha_1\boldsymbol{U}'^{k} + \alpha_2\boldsymbol{U}'^{k-1}}{\Delta t},$$

$$\boldsymbol{R}_f^p = 0,$$

$$\boldsymbol{R}_\theta = \frac{\alpha_1\theta'^{k} + \alpha_2\theta'^{k-1}}{\Delta t},$$

$$\boldsymbol{R}_\Omega = \frac{\alpha_1\Omega'^{k} + \alpha_2\Omega'^{k-1}}{\Delta t},$$

for $\boldsymbol{X} \in \Omega_f$ and $\Delta t > 0$. The boundary conditions associated to the right-hand side of equation 1.74 are posed as

$$\boldsymbol{U}'^{k+1}(\boldsymbol{X}) = \boldsymbol{0} \quad \boldsymbol{X} \in \Gamma_{in}, \tag{1.75a}$$

$$\boldsymbol{U}'^{k+1}(\boldsymbol{X}) = \boldsymbol{0} \quad \boldsymbol{X} \in \Gamma_{w}, \tag{1.75b}$$

$$\boldsymbol{\sigma}\left(\boldsymbol{U}'^{k+1}, p'^{k+1}\right)\cdot\boldsymbol{n}_\infty = \boldsymbol{0} \quad \boldsymbol{X} \in \Gamma_{out}. \tag{1.75c}$$

The terms L_f, $\boldsymbol{v}_\theta$, $\boldsymbol{v}_\Omega$ correspond to the linearised operators around the periodic state $\left[\boldsymbol{U}_b^{k+1}, \bar{\theta}_b, 0\right]^T$, which are posed

as

$$\mathsf{L}_f \boldsymbol{q}_f'^{k+1} = \begin{bmatrix} \frac{\alpha_0 \boldsymbol{U}'^{k+1}}{\Delta t} + \left(\left[\boldsymbol{U}'^{k+1}\right]\cdot\nabla\right)\boldsymbol{U}_b^{k+1} + \left(\left[\boldsymbol{U}_b^{k+1} - \overline{\boldsymbol{U}}_w\right]\cdot\nabla\right)\boldsymbol{U}'^{k+1} - \nabla\cdot\boldsymbol{\sigma}\left(\boldsymbol{U}'^{k+1}, p'^{k+1}\right) + \boldsymbol{s}_{GD}^{S}\left(\boldsymbol{U}'^{k+1}\right) \\ \nabla\cdot\boldsymbol{U}'^{k+1} \end{bmatrix}$$

$$\boldsymbol{v}_\theta = -U^\infty \left(\begin{bmatrix} \sin\left(\bar{\theta}_b\right) \\ \cos\left(\bar{\theta}_b\right) \end{bmatrix} \cdot\nabla \right) \boldsymbol{U}_b^{k+1},$$

$$\boldsymbol{v}_\Omega = \begin{bmatrix} -V_b^{k+1} \\ U_b^{k+1} \end{bmatrix} - \left(\begin{bmatrix} -(Y - Y_{EC}) \\ X - X_{EC} \end{bmatrix} \cdot\nabla \right) \boldsymbol{U}_b^{k+1},$$

for $\boldsymbol{X} \in \Omega_f$ and $\Delta t > 0$. The boundary conditions associated to the left-hand side of equation 1.74 are posed as

$$\boldsymbol{U}'^{k+1}(\boldsymbol{X}) = \boldsymbol{0} \qquad \boldsymbol{X} \in \Gamma_{in}, \tag{1.76a}$$

$$\boldsymbol{U}'^{k+1}(\boldsymbol{X}) = \boldsymbol{1} \qquad \boldsymbol{X} \in \Gamma_{w}, \tag{1.76b}$$

$$\boldsymbol{\sigma}\left(\boldsymbol{U}'^{k+1}, p'^{k+1}\right)\cdot\boldsymbol{n}_\infty = \boldsymbol{0} \qquad \boldsymbol{X} \in \Gamma_{out}, \tag{1.76c}$$

$$\boldsymbol{v}_\theta = -U^\infty \left[\sin\left(\bar{\theta}_b\right), \cos\left(\bar{\theta}_b\right)\right]^T \qquad \boldsymbol{X} \in \Gamma_{w}, \tag{1.76d}$$

$$\boldsymbol{v}_\Omega = -\left[-(Y - Y_{EC}), (X - X_{EC})\right]^T \qquad \boldsymbol{X} \in \Gamma_{w}. \tag{1.76e}$$

The inversion of the fluid–solid Jacobian present in system 1.74 is based solely on the inversion of the fluid Jacobian, as explained in section 1.7.9.

1.8 Preliminary results: numerical validation

This first set of results aims to numerically validate the different methods presented previously. In that way, different numerical aspects of the two- and three-dimensional simulations are discussed: the mesh convergence, the influence of the lateral boundary condition, the influence of the numerical stabilisation and the impact on the performance of different resolution strategies of the velocity substep on the SIPC scheme.

Computations were conducted on “Sator”, an ONERA supercomputer. This cluster is composed by 620 nodes, each one with two CPU processors Intel Xeon “Broadwell” E5-2680v4, with a clock rate of 2.4GHz. Each processor has 14 cores, making a total of 28 cores per node.

1.8.1 Mesh convergence

The mesh convergence is firstly done on the two-dimensional case, at $Re = 50\,000$ and $\alpha = 0°$. Table 1.6 summarises the details of the five meshes compared and their associated results. We start by comparing the amplitude of oscillation of the lift signal, C_L^1, on the time-marching simulation, followed by the indicators associated to the mean flow solution, the drag coefficient, C_D, the recirculation length, L_{recirc}, and the position of the upper surface separation, X_d^{up}. The last two columns correspond to the numerical values of the divergence and flutter FSI eigenvalues (from a linear analysis using the classical formulation, around a mean flow from 2D simulations), for the set of nominal structural parameters indicated in section 1.2, table 1.1. The description of these eigenvalues is made in the subsequent chapters 3, 4 and 6. The robustness of the results is observed by varying the space resolution and the domain size of the different meshes.

Mesh	# triangles	Δy^1	L_x	L_y	C_L^1	C_D	L_{recirc}	X_d^{up}	Div. mode	Flutter mode
M_0^{2D}	103 284	$4\cdot10^{-4}$	10	30	0.024212	0.020658	0.064372	0.698125	0.208479	$-0.144575+0.539988$i
$\boldsymbol{M_1^{2D}}$	155 752	$2\cdot10^{-4}$	10	30	0.024002	0.020647	0.064903	0.698588	0.208568	$-0.144496+0.540228$i
M_2^{2D}	239 732	$1\cdot10^{-4}$	10	30	0.023644	0.020635	0.065479	0.699387	0.208661	$-0.144555+0.540391$i
M_3^{2D}	198 176	$2\cdot10^{-4}$	20	30	0.023941	0.020649	0.064882	0.698588	0.208560	$-0.143634+0.540807$i
M_4^{2D}	203 396	$2\cdot10^{-4}$	10	60	0.023704	0.020640	0.065162	0.698588	0.208388	$-0.139083+0.526076$i

Table 1.6 – *Convergence of the two-dimensional mesh with respect to the time-marching and mean flow properties and to the mean flow FSI eigenvalues at* $Re = 50\,000$ *and* $\alpha = 0°$. *Concerning the physical description these FSI eigenvalues, see chapter 4.*

A first comparison is made between meshes M_0^{2D}, M_1^{2D} and M_2^{2D}, where the height of the first cell around the airfoil is successively divided by two. A second comparison is made between the meshes M_1^{2D} and M_3^{2D}, where the influence of the airfoil distance to the outlet boundary is investigated. Finally, a third comparison is made between the meshes M_1^{2D} and M_4^{2D}, where the influence of the airfoil distance to the upper, lower and inlet boundaries is investigated.

Concerning for example the values of C_L^1, the absolute differences are of order 10^{-4}. The same can be said for the mean flow indicators, with absolute differences of order 10^{-5}, 10^{-3} and 10^{-4} for the drag, recirculation length and separation location, respectively, revealing an overall good agreement of the results. The main differences are observed between the meshes M_1^{2D} and M_2^{2D}, where the height of the first wall cell varies. Concerning the mean flow FSI eigenvalues, the higher variations appear on the frequency of the flutter eigenvalue. In this case, the distance to the upper, lower and inlet boundaries appear to have the most influence, where the absolute error on the flutter frequency between meshes M_1^{2D} and M_4^{2D} is of 0.014152. In regards to the present results, mesh M_1^{2D} is considered to provide the adequate spatial resolution for the current simulations. The same tests were conducted for the remaining angles of attack studied.

The three-dimensional discretisation was obtained by an extrusion of the 2D mesh in the spanwise direction. The convergence of the mean flow and FSI eigenvalues with respect to the averaged time (*i.e.*, the time during which the mean flow was computed) and the number of planes, N_z, is depicted in table 1.7, for the case $Re = 50\,000$ and $\alpha = 1.5°$. The number of spanwise planes was found to have a small influence in the present results, with the bigger discrepancies

Averaged time	N_z	C_D	C_L	$U(1.2, 0.05)$	Flutter mode	Mode from coalesced div. modes
37.25	60	0.023824	0.055870	0.920767	$-0.076053+0.405422$i	$-0.322608+0.167439$i
7.25	90	0.023406	0.048295	0.919270	$-0.073922+0.407158$i	$-0.293129+0.176473$i
17.25	90	0.023465	0.046626	0.920188	$-0.074141+0.408924$i	$-0.289391+0.174183$i
27.25	90	0.023450	0.047374	0.920630	$-0.079202+0.407900$i	$-0.285979+0.172037$i
37.25	90	0.023440	0.048416	0.920680	$-0.080360+0.406060$i	$-0.285003+0.172186$i

Table 1.7 – *Convergence of the time- and spanwise-averaged flow properties and mean flow FSI eigenvalues for the three-dimensional simulations at* $Re = 50\,000$ *and* $\alpha = 1.5°$, *with the averaged time and number of planes in the spanwise direction.*

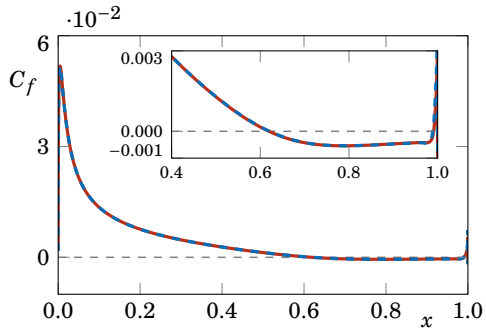

	Periodic BC	Symmetric BC	Absolute error
C_D	0.021093	0.021021	$7.2{\cdot}10^{-5}$
C_L	−0.026578	−0.025904	$6.7{\cdot}10^{-4}$
m_z	−0.011496	−0.011343	$1.5{\cdot}10^{-4}$
X_d^{up}	0.619973	0.621336	$1.4{\cdot}10^{-3}$

Figure 1.10 & Table 1.8 – *Comparison of the upper surface friction coefficient distribution, C_f, associated to the time- and spanwise-averaged flow between two computations at $Re = 50\,000$ and $\alpha = 0.5°$: a first one with lateral periodic boundary conditions (solid red curve) and a second one with a symmetric boundary condition on the W velocity component (dashed blue curve). On the right, comparison of several global coefficients and abscissa of the boundary layer separation point, X_d^{up}, between these two computations.*

on the C_L coefficient and on the stable eigenvalue from the coalesced divergence eigenvalues. Concerning the averaged time convergence, the indicators associated to the mean flow solution, C_D, C_L and the streamwise velocity on the point $(1.2, 0.05)$, have an absolute error of order 10^{-5}, 10^{-3} and 10^{-5}, respectively. Concerning the results associated to the FSI eigenvalue, the same reasoning can be made, so that we can conclude that the mean flow is averaged during a sufficient amount of time.

1.8.2 Influence of the lateral boundary condition on the three-dimensional computations

A comparison between two types of lateral boundary conditions is made for the three-dimensional case at $Re = 50\,000$ and $\alpha = 0.5°$. We consider a first computation where a periodic boundary condition is imposed by setting

$$[\boldsymbol{U}, p](X, Y, Z = L_z, t) = [\boldsymbol{U}, p](X, Y, Z = -L_z, t)\,,$$

and a second computation, where a symmetric boundary condition on the W velocity component is imposed (see equation 1.50d). The comparison is made on the extracted mean flow. As depicted in the figure 1.10, the C_f distributions of the mean flow over the upper surface of the airfoil field coincide for both computations. The same observation can be made for the global coefficients, present in table 1.8, where the absolute error does not surpass the 10^{-3} order of magnitude. We conclude that, with respect to the mean flow characteristics, the choice of the lateral boundary conditions does not affect the results.

In this thesis, the choice of symmetric conditions, rather than periodic conditions is due to particular numerical difficulty, associated to the *FreeFem++* software. The difficulty is related to the fact that, every degree of freedom where the periodic condition has to be imposed should be on the same MPI process, and therefore, on the same domain partition. This constraint strongly deteriorates the performance of the simulations. In that sense, we choose to apply symmetric boundary conditions to the lateral boundaries of the domain.

1.8.3 Influence of the SUPG and grad-div stabilisations

The two-dimensional field representations of the SUPG and grad-div stabilisations, τ_{SUPG} and τ_{GD}, respectively, are depicted in figure 1.11, for $Re = 50\,000$ and $\alpha = 0°$. The higher values of these fields are present near the inlet region,

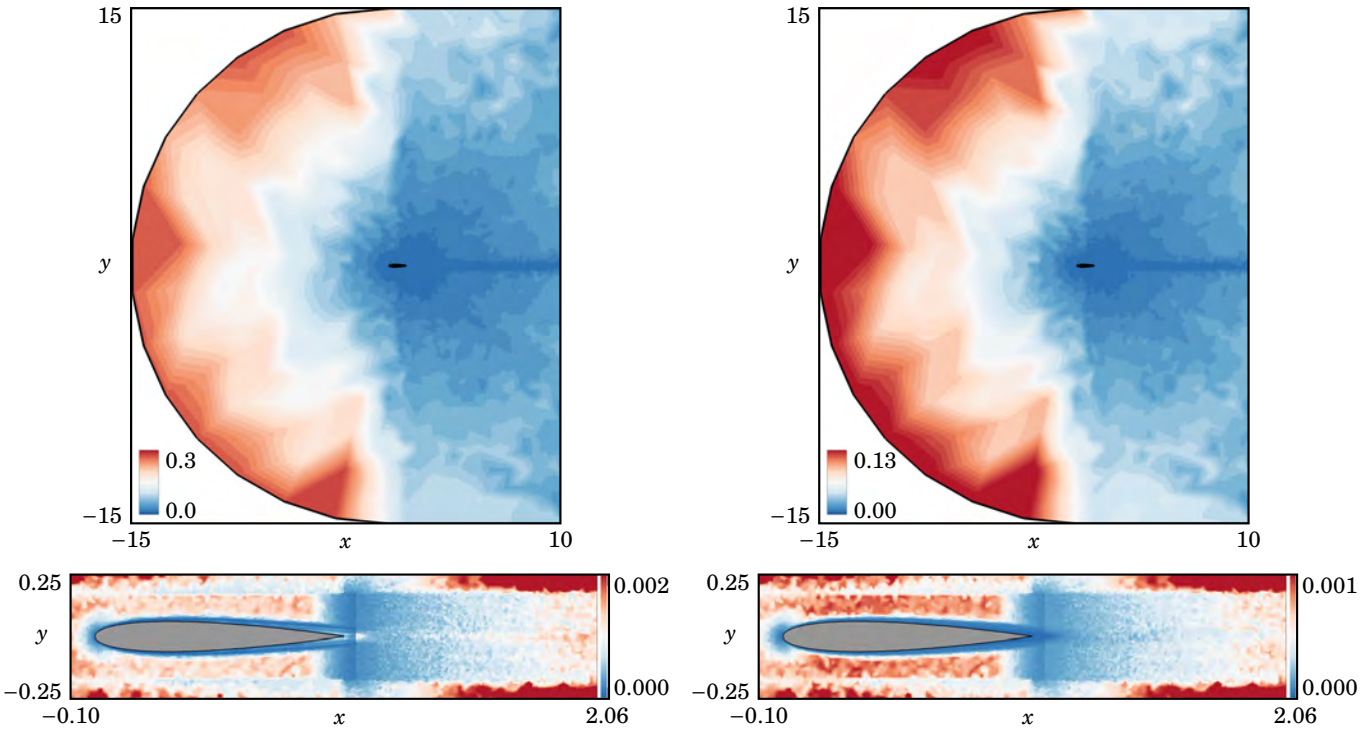

Figure 1.11 – *Spatial structure of the τ_{SUPG} (left) and the τ_{GD} (right) fields, with a close-up representation near the airfoil on the bottom plots, for $Re = 50\,000$ and $\alpha = 0°$.*

where the mesh is coarser, with a maximum value of 0.282 for τ_{SUPG} and 0.141 for τ_{GD}. Near the airfoil, the stabilisation is around 10^3 times smaller, associated to the fact that a finer mesh is used in this region in order to capture the desired physical phenomena. As explained before, the grad-div is used in the time-marching simulations, whereas both SUPG and grad-div are used in the eigenvalue problem simulations. We first present the influence of the grad-div on the three-dimensional simulation, followed by the influence of SUPG on the eigenvalue problem.

The impact of the grad-div stabilisation is explored by sketching the discrete divergence of the there-dimensional velocity field, present in figure 1.12. The fields are computed using discontinuous piecewise-linear finite element functions (P_1^{dc}) as the discrete divergence corresponds to the space derivative of continuous piecewise-quadratic finite element functions. The figure represents an isosurface of $\nabla{\cdot}\boldsymbol{U}^h = 2$ on the upper plots, along with a contour field corresponding to $Z = 0$ on the lower plots. The left side corresponds to a computation without considering τ_{GD}, whereas on the right side, τ_{GD} is taken into account. The violation of the discrete mass conservation is mainly observed near the leading edge and on the wake of the wing, with a clear distinction between the two computations. The maximum values of $\nabla{\cdot}\boldsymbol{U}^h$ are attained at the beginning of the wing's wake and have values of 207.98 and 42.26 for the computations without and with τ_{GD}, respectively.

The importance of the SUPG stabilisation on a mean flow FSI linear stability analysis is depicted in figure 1.13, using the classical formulation. The analysis is made around a mean flow from 2D simulations at $Re = 50\,000$ and $\alpha = 0°$. We present the results on a spectrum representation (introduced in the next chapter) for the nominal values of the structural parameters (see table 1.1).

The eigenvalues computed without SUPG stabilisation, represented by the black crosses, are mostly composed of

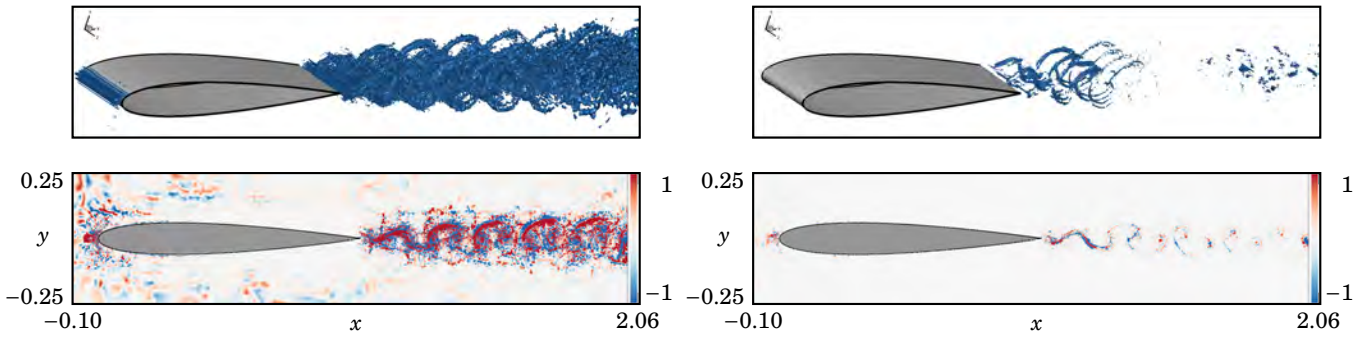

Figure 1.12 – *Effect of the grad-div stabilisation on the three-dimensional simulations for* $Re = 50\,000$, $\alpha = 0°$ *and* $N_z = 60$, *illustrated by the isosurface of* $\nabla{\cdot}\boldsymbol{U}^h = 2$ *of a snapshot and the corresponding contour at* $Z = 0$, *without* τ_{GD} *(left) and with* τ_{GD} *(right).*

spurious eigenvalues, that remain on the stable side of the spectrum (excluding the two unstable eigenvalues with $\lambda > 0$, corresponding to physical eigenmodes). The value of these spurious eigenvalues varies with the numerical discretisation: either with the mesh, or with the choice of the finite element pair for the fluid variables. Further, as depicted in the zoom near the origin, present on the left side of the figure, the physical eigenvalues of interest are mixed with all the remaining spurious ones, rendering their analysis difficult. One of the methods to discern the physical from the spurious eigenvalues is to run several computations, usually increasing the mesh refinement, and select the eigenvalues that show a convergence behaviour towards a fixed value. The observation of the eigenmode field associated to each eigenvalue also constitutes a qualitative way of selecting the physical modes, as the structure of the spurious eigenmodes is mostly located near the boundary regions. An alternative way of proceeding passes through the addition of a SUPG stabilisation to the linear formulations, whose results are represented by the red triangles. As present in the figure, most of the spurious modes are damped, leading to a more clear picture of the spectrum. Most important, the SUPG spectrum near the origin only presents the physical modes, enabling the physical discussion present in the next chapter. The influence

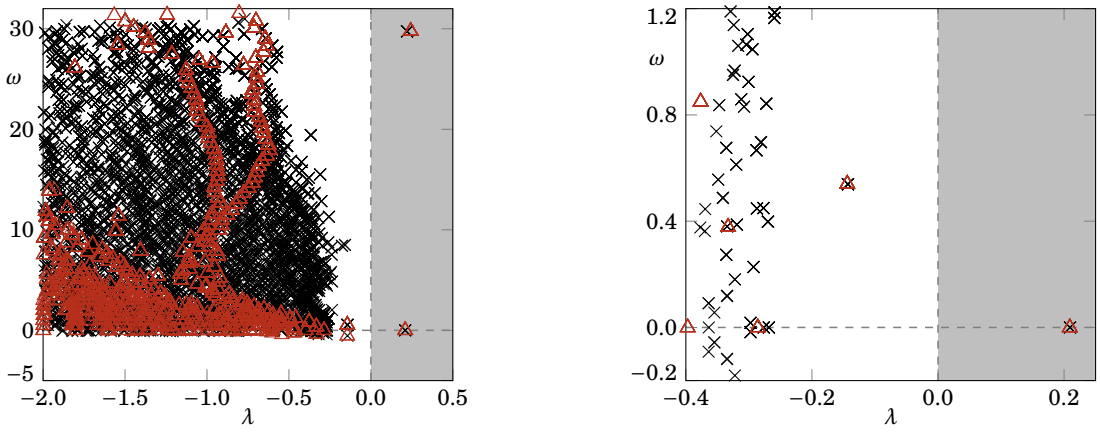

Figure 1.13 – *Comparison between the results of a mean flow FSI linear stability analysis around a mean flow from 2D simulations at* $Re = 50\,000$ *and* $\alpha = 0°$ *without SUPG stabilisation (black crosses) and with SUPG stabilisation (red triangles). On the left, a general view and, on the right, a close-up of the same spectrum near the origin.*

	Divergence mode	Flutter mode
Without SUPG	0.209414	$-0.142875 + 0.539014\mathrm{i}$
With SUPG	0.209065	$-0.143952 + 0.540529\mathrm{i}$
Error	$3.49{\cdot}10^{-4}$	$1.077{\cdot}10^{-3} + 1.515{\cdot}10^{-3}\mathrm{i}$

Table 1.9 – *Influence of the SUPG stabilisation on the divergence and flutter eigenvalues of a mean flow FSI linear stability analysis around a mean flow from 2D simulations for* $Re = 50\,000$ *and* $\alpha = 0°$. *Last line depicts the absolute error of the real and imaginary parts of the eigenvalues.*

of the SUPG stabilisation on the numerical values of the two eigenmodes of interest is present in table 1.9, where the absolute error of the real and imaginary parts is at most of order of magnitude 10^{-3}.

Finally, we note that the use of the SUPG stabilisation is also beneficial for the computation of the fluid eigenspectrum. In particular, this way of identifying the physical eigenvalues enables to have a clear approximation of the fluid transfer function Y^f via a rational approximation, as presented in section 3.

1.8.4 Influence of the three-dimensional time discretisation parameters

A general view of the performance of the three-dimensional time-marching simulations is discussed in the present paragraph, for $Re = 50\,000$, $\alpha = 0°$ and $N_z = 60$. The assembly of all the required matrices is performed via the *FreeFem++* software, while their factorisation and inversion are performed using the *FreeFem++* interface with the PETSc library tools (Balay *et al.*, 2022).

The CPU time spent on each stage of a time iteration is depicted in table 1.10, for four different tests. The first test is conducted without the grad-div stabilisation, whereas the other three tests differ on the number of processors considered, while using the grad-div stabilisation. This information is contained in the first two lines of table 1.10. The third line concerns the CPU time spent on the assembly of the preconditioner matrix used in the first substep of the SIPC scheme, present in equation 1.66. As this matrix does not significantly vary between iterations, its construction is not required at each time step. In fact, the reconstruction of the preconditioner is based on the deterioration of its relative performance, which in the present tests, where a transient regime was already surpassed, never occurs. Its contribution is therefore not taken into account for the total time per iteration on the last line of the table. This represents a relative gain in performance, as the time of the preconditioner assembly would represent around 60% of the total time of a time iteration for the first test.

The forth line corresponds to the CPU time spent on the assembly of the matrix used in the matrix-vector product during the GMRES iterative method, in the first substep of the SIPC scheme, present in equation 1.65. As only the convection and grad-div coefficient terms vary between time iterations, only these terms are recomputed. The diffusion and pressure terms of the matrix are computed at the beginning the simulation once. The fifth line corresponds to the averaged number of GMRES iterations on the first substep resolution, where the CPU times associated to the matrix application and preconditioner inversion are present in the sixth and seventh lines. For the case where grad-div is not taken into account, the associated matrix 1.65 is reduced to a block diagonal matrix. The preconditioner in equation 1.66 is therefore mathematically equivalent to the associated matrix and one one GMRES iteration is expected to occur. However, the approximation is made during the inversion of each block, which is accomplished by an incomplete LU factorisation, as described in section 1.7.7. This fact explains the number of GMRES iterations of the test one.

The total time spent on the first substep of the SIPC scheme is then depicted. This corresponds to 14% of the total

	Test 1	Test 2	Test 3	Test 4
Grad-div	No	Yes	Yes	Yes
N_{MPI}	560	560	840	1120
Preconditioner assembly (not taken into account)	11.693 s	11.864 s	8.551 s	6.584 s
Convection/Grad-div matrix assembly	3.565 s	3.638 s	2.603 s	1.988 s
# GMRES iterations	6	16	18	18
1 Matrix application	0.045 s	0.108 s	0.083 s	0.062 s
1 Preconditioner inversion	0.089 s	0.107 s	0.077 s	0.054 s
Total time step 1	1.092 s	3.972 s	3.279 s	2.374 s
Total time step 2	0.732 s	0.710 s	0.769 s	0.637 s
Total time step 3	0.532 s	0.493 s	0.343 s	0.282 s
Post-treatment	1.927 s	1.927 s	1.330 s	1.050 s
Total time per time iteration	7.848 s	10.740 s	8.325 s	6.331 s

Table 1.10 – *Comparison of the three-dimensional time-marching simulation performance for one time iteration, for four test cases (varying the inclusion of the grad-div stabilisation and the number of MPI processes), at* $Re = 50\,000$*,* $\alpha = 0^\circ$ *and* $N_z = 60$*. The preconditioner assembly time is not taken into account on the total time per time iteration, as it is not done at each time iteration.*

time for the test 1, compared to 37% for the test 2. The only difference between the two computations is the use of the grad-div stabilisation, which renders the matrix 1.65 non diagonal and decreases the performance of the lower triangular preconditioner. This is also related to the number of GMRES iterations, which triplicated with the addition of the grad-div stabilisation.

The second and third substeps correspond to the pressure equation resolution and velocity correction, not depending on the use of the stabilisation. The penultimate line corresponds to the post-treatment routines, where the time-averaged flow and harmonics are computed[19], the solution at the current instant is written in disk and the global variables, such as C_L and C_D, are computed.

The influence of the GMRES preconditioner used in the first substep of the SIPC scheme is depicted in table 1.11 for the case test two. The bottleneck of this operation is associated to the inversion of the preconditioner. A first naive choice would be to perform a LU factorisation of each diagonal block. However, for the three-dimensional simulations, this is not possible due to the amount of memory required by this operation.

The next step is to approximate each diagonal block of the matrix 1.66 by a block Jacobi, where each block—associated to an individual domain—is solved either via a LU or an incomplete LU factorisation, ILU(l), where the fill level representing the amount of coefficients of the original matrix taken into account. The comparison between these different approaches is detailed in the remaining lines of table 1.11. The comparison is made in terms of the number of GMRES iterations, and CPU times associated to one diagonal block inversion and to the GMRES solver. For $l = 0$, the

[19]The average in the spanwise direction, when needed, is computed on a different post-treatment simulation.

	# GMRES iters.	CPU time on 1 diagonal block inversion	CPU time on GMRES solver
LU	Not enough memory		
BJacobi + LU	13	$1.30 \cdot 10^{-1}$ s	8.726 s
BJacobi + ILU(0)	Diverge		
BJacobi + ILU(1)	16	$2.60 \cdot 10^{-2}$ s	3.972 s
BJacobi + ILU(2)	13	$5.94 \cdot 10^{-2}$ s	5.042 s
BJacobi + ILU(3)	13	$1.11 \cdot 10^{-1}$ s	7.381 s

Table 1.11 – *Influence of the preconditioner inversion strategy on one time iteration for* $Re = 50\,000$*,* $\alpha = 0°$*,* $N_z = 60$ *and* $N_{MPI} = 560$*.*

preconditioner inversion is not well enough approximated in order to correctly solve the system. By increasing the fill level, the incomplete factorisation tends to the exact factorisation and, for $l = 1$, the GMRES converges in 16 iterations. The increase of the fill level to 2 and 3 leads to the same number of GMRES iterations as to the LU factorisation. However, the time spent on each diagonal block inversion increases significantly. In view of these results, the level fill is set to 1, reflecting the best compromise between the number of GMRES iterations and the preconditioner inversion CPU time.

Finally, we estimate the CPU time spent on the DNS simulation at $Re = 50\,000$ and $\alpha = 0°$. The computation was performed with 560 MPI processes, corresponding to the test 2 on table 1.10, as it represented a good equilibrium between the number of nodes used, 20, and the number of nodes available on the ONERA cluster, 620. This simulation was performed for a total physical time of 230 time units. With a total CPU time per time iteration around 10.74s and a time step of 0.001 time units, we estimate that this simulation took approximatively 2 470 200, *i.e.*, around 28.59 days.

Chapter 2

Flow around a fixed NACA0012 profile wing

This chapter is devoted to the description of the flow field around a NACA0012 profile wing and the corresponding aerodynamic forces acting on it from a Reynolds number of $Re = 1\,000$ to $Re = 65\,000$, at different angles of attack. This chapter is divided in three parts. We start by describing the emergence of the vortex shedding phenomenon on the rear of the airfoil for $\alpha = 0^\circ$, followed by the description of the flow field characteristics as function of the Reynolds number and incidence. We then characterise the emergence of the negative aerodynamic moment and lift coefficients associated to the base and mean flow fields. This analysis is carried out with a two-dimensional Navier–Stokes model. Finally, we characterise the emergence of the three-dimensional instabilities on the spanwise direction, by the means of a classic purely-hydrodynamic Floquet stability analysis. In a second part, we characterise both instantaneous and spectral properties associated to three-dimensional Direct Numerical Simulations (DNS) carried out at $Re = 50\,000$ for five angles of attack, between 0° and 2°. In a third part, we proceed to evaluate the aerodynamic moment as function of the incidence, based on the spatial distribution of the different terms of the Navier–Stokes equations, rather than the classic approach based on the stress integration over the fluid–solid interface.

2.1 Two-dimensional flow description

2.1.1 Emergence of a vortex shedding at $\alpha = 0^\circ$

The vortex shedding phenomenon is characterised by an alternating emission of vortex structures at the rear of a body from one side to the other, forming a von Kármán vortex street. This shedding generates alternating low-pressure zones on the structure giving rise to fluctuating forces and moments acting on the body. The emergence of this phenomenon is well documented for the case of a circular cylinder (a blunt/bluff body), resulting from a supercritical Hopf bifurcation (Provansal *et al.*, 1987; Dušek *et al.*, 1994). In the case of an airfoil at low incidences (a streamlined body), few studies have been done specifically on the emergence of the vortex shedding. For example, Elimelech *et al.* (2005, 2007) reported the onset of the vortex shedding for a NACA0009 airfoil at $Re \approx 20\,000$ for $\alpha = 0^\circ$. For the thicker NACA0012 airfoil, this fluid instability is expected to appear at a lower Re. We studied this onset using two-dimensional time-marching simulations.

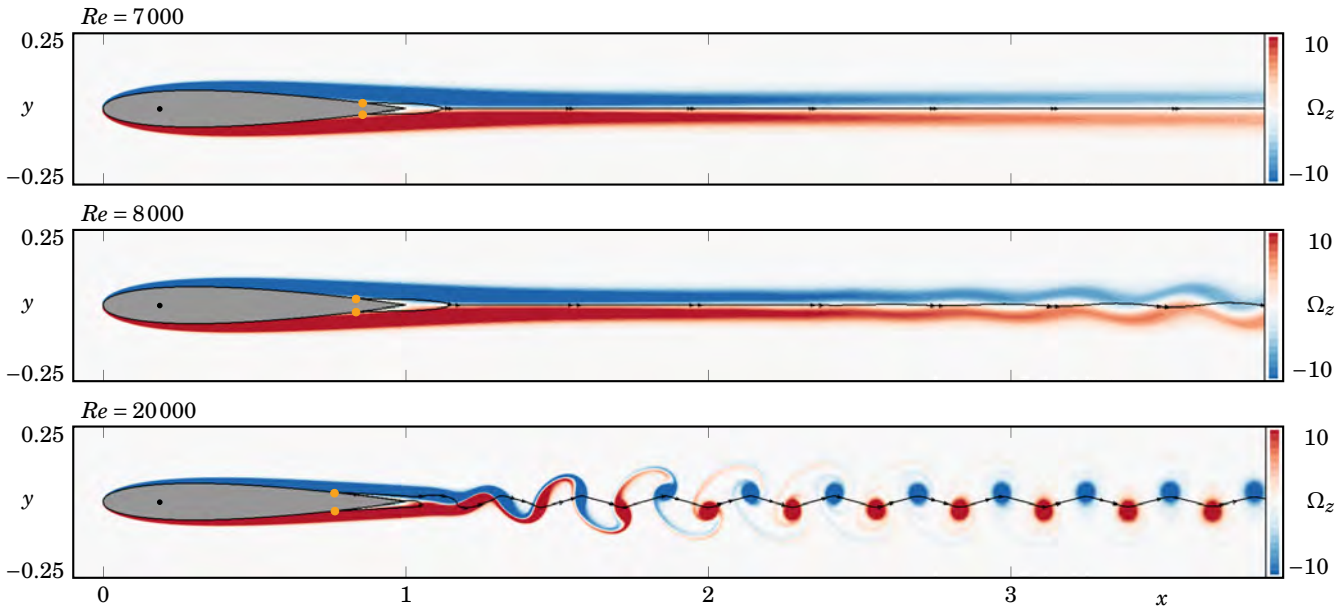

Figure 2.1 – *Spanwise vorticity field of two-dimensional instantaneous flow solutions at* $\alpha = 0°$ *for:* $Re = 7000$ *(top),* $Re = 8000$ *(centre) and* $Re = 20000$ *(bottom). The highlighted streamlines delineate the recirculation zone at the rear of the airfoil. The yellow dots over the airfoil surface represent the separation points.*

The vorticity[1] field associated to an instantaneous solution at different Reynolds numbers for $\alpha = 0°$ is present in figure 2.1. In all three considered Reynolds numbers, the flow field exhibits a boundary layer separation in both upper and lower surfaces of the airfoil. At $Re = 7000$, the flow field is steady in time, corresponding to a steady solution of the Navier–Stokes equations. This solution is usually called the *base flow* solution. Since the flow is symmetric in the $\boldsymbol{e}_y$-direction with respect to the airfoil chord line, the separation points on both upper and lower surfaces of the airfoil are located at the same abscissa, $X_d = 0.857$. For $Re = 8000$, one can observe a small oscillation of the flow field around $x \approx 3$, with a period of $T = 0.433$, corresponding to an angular frequency of $\omega_{VS} = 14.480$ and a Strouhal[2] of $St_{VS} = 2.305$ (cf. table 2.1). We therefore estimate the appearance of the vortex shedding around $Re = 8000$. When based on the thickness of the airfoil, rather than the chord, one obtains a thickness Strouhal of $St^t_{VS} = 0.276$, which is around 2.3 times greater than the Strouhal associated to the vortex shedding threshold of the cylinder benchmark at $Re = 46.7$ (Provansal *et al.*, 1987; Sreenivasan *et al.*, 1987; Fabre *et al.*, 2019a). The high convective character of this instability near the threshold region, illustrates the numerical difficulty in estimating this threshold for $\alpha = 0°$. As one approaches the threshold, the computational outlet boundary should be located far enough of the rear of the airfoil to not interfere with the convective instability. For these simulations, the outlet distance was increased to $L_x = 20$. However, no studies were further conducted in order to converge this value.

The instability threshold is usually predicted via a purely-hydrodynamic linear stability analysis around the base flow solution, as classically done for the case of the circular cylinder (see *e.g.*, Fabre *et al.* (2019a), for a recent review). However, a crucial difference between these two cases exists, namely the body shape, corresponding to a streamline shape for the airfoil and to a bluff shape for the cylinder. As a consequence, the perturbations associated to these two cases present a

[1] Vorticity is a vectorial quantify, defined as the curl of the velocity, $\boldsymbol{\Omega} = \left[\Omega_x, \Omega_y, \Omega_z\right]^T = \nabla \times \boldsymbol{U}$.

[2] Strouhal is defined as $St = \frac{c\omega/(2\pi)}{U^\infty}$, with c and U^∞ the airfoil chord and reference velocity, introduced in chapter 1.

Re	Period T	Angular frequency ω_{VS}	Strouhal number St_{VS}	Mean separation point X_d
3300	—	—	—	1.000
7000	—	—	—	0.857
8000	0.433	14.480	2.305	0.835
10000	0.333	18.868	3.003	0.817
20000	0.298	21.085	3.356	0.765
50000	0.207	30.354	4.831	0.700

Table 2.1 – *Values of the period, angular frequency and Strouhal number associated to the vortex shedding for different Reynolds numbers at $\alpha = 0°$. The last column also reports the abscissa of the time-averaged boundary layer separation point. For the first two Re, no vortex shedding characteristics are reported, since the flow is steady in time. The first Re corresponds to the emergence of the separation point at the trailing edge.*

very different structure, with the ones associated to the airfoil at $\alpha = 0°$ being highly convected. Their structure is similar to the global perturbations found in shear layer instabilities (Tammisola, 2012; Canton *et al.*, 2017). Since the instability is highly convected downstream, the position of the outlet boundary condition influences the obtained results that we did not manage to converge. Lesshafft (2017) discussed the possible emergence of artificial eigenmodes in truncated flow domains, issued from a numerical feedback of the pressure signal from the outlet to upstream positions. Appendix C reports the attempts in predicting the threshold of a NACA0012 airfoil at low incidences via a linear stability analysis around the base flow, and sheds a light in the possible alternatives and modifications that can be adopted in future works to overcome the present difficulties. Finally, we note that, as the angle of attack increases, the convective character of the linear perturbations disappears and the threshold can be predicted via the classic base flow linear stability analysis approach. This is related to the fact that, as the angle of attack increases, the length of the airfoil in the transverse direction to the flow increases, progressively transforming the streamline shape of the airfoil into a bluff shape, similar to the cylinder.

With the increase of the Reynolds number, the vortex shedding tends to appear closer to the trailing edge of the airfoil, with an increased frequency, as observed in the case at $Re = 20000$, on the bottom of figure 2.1. In this case, the angular frequency has a value of $\omega_{VS} = 21.085$ (cf. table 2.1). The flow at this incidence and Reynolds number presents a *periodic*

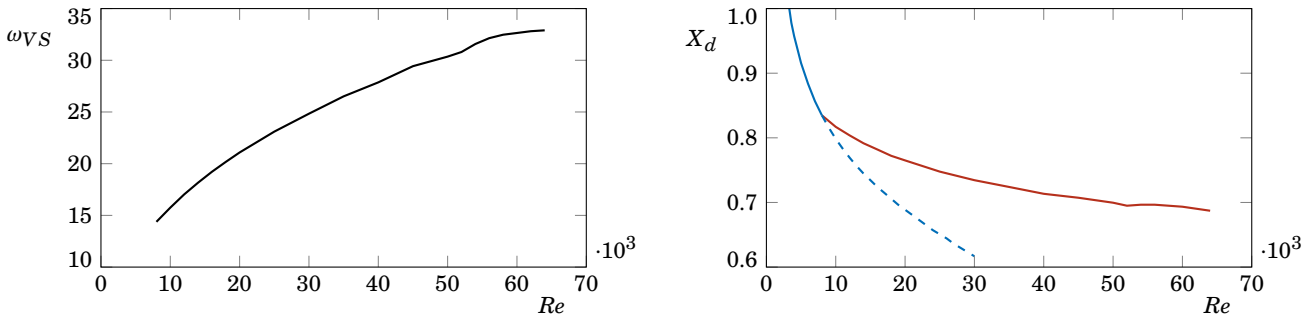

Figure 2.2 – *On the left, evolution of the vortex shedding frequency present on two-dimensional unsteady simulations with the Reynolds number at $\alpha = 0°$. On the right, evolution of the abscissa of the boundary layer separation point on the airfoil surface at $\alpha = 0°$, with the Reynolds number for two-dimensional stable base flow (solid blue), unstable base flow (dashed blue) and mean flow (solid red) solutions.*

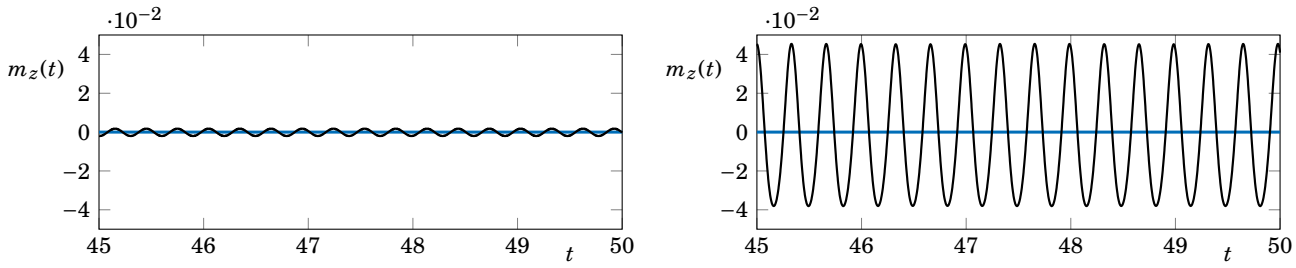

Figure 2.3 – *Time history of the aerodynamic moment coefficient around* $X_{EC} = 0.186$ *for* $Re = 20\,000$ *at* $\alpha = 0°$ *(left) and* $\alpha = 3.64°$ *(right), with the angular frequencies of* $\omega_{VS} = 21.085$ *and* $\omega_{VS} = 18.868$*, respectively. The blue line represents the mean value.*

behaviour in time. This periodicity can be observed in the alternating shed of the vortex structures at the trailing edge of the airfoil, as well as in the evolution of aerodynamic moment coefficient in time, as present on the left of figure 2.3. In this latter case, the oscillations occur around the null mean value, with an amplitude of $\pm 1.88 \cdot 10^{-3}$.

The evolution of the vortex shedding frequency with the Reynolds numbers for $\alpha = 0°$ is sketched on the left of figure 2.2, where one can note that vortex shedding frequency increases as Re increases. This is associated to the increase of the momentum and kinetic energy on the flow and consequent decrease of the boundary layer thickness around the airfoil as the Reynolds number increases.

The presence of the vortex shedding phenomenon enables one to compute a time-averaged quantity, denoted *mean flow*, which takes into account the unsteadiness of the flow field. Note that above the threshold corresponding to the onset of the unsteadiness, the steady solution of the Navier–Stokes equations, *i.e.*, the *base flow* solution, still exists. However, above the threshold, this solution is unstable and cannot be obtained using classical time-stepping simulations. On the other hand, it can be computed directly as a fixed point of the time-independent Navier–Stokes equations. In this thesis, we compute the base flow solutions using a Newton method, following the classical approach in stability analysis of fluid flows (see for instance in Fabre *et al.* (2019a)).

On the right of figure 2.2, one can find the evolution of the abscissa of the boundary layer separation point on the airfoil surface as function of the Reynolds number, for base and mean flow solutions at $\alpha = 0°$. Since that, for $\alpha = 0°$, the flow field is symmetric in the $\boldsymbol{e}_y$-direction with respect to the airfoil chord line, this coordinate characterises the separation of the boundary layer on both upper and lower surfaces of the airfoil. The separation points associated to the base flow solution are represented by the blue line, with a solid representation for the stable base flow solutions and a dashed representation for the unstable ones. At the same time, the separation points associated to the mean flow solutions are represented by the solid red line. The latter curve starts at $Re = 8\,000$, corresponding to the vortex shedding threshold at $\alpha = 0°$, since that, below this Re, both base and mean flow solutions coincide.

The separation of the boundary layer appears at $Re = 3\,300$, on the base flow curve, *i.e.*, before the vortex shedding unsteadiness. This separation point moves upwards with the Reynolds number. For $Re = 8\,000$, corresponding to the onset of the vortex shedding oscillations, the separation is located at $X_d = 0.835$. From this point, the blue and red curves divergence from each other, with the base flow predicting an earlier separation when compared to the mean flow solution. This is associated to the unsteadiness of the flow, taken into account for the computation of the mean flow, which increases the momentum on the boundary layer and forces the mean separation point to be located at a rearward position, when compared to base flow separation point. From $Re = 45\,000$ to $Re = 65\,000$, the mean flow separation point has a roughly constant value, with a $X_d = 0.707$ for $Re = 45\,000$ and $X_d = 0.687$ for $Re = 65\,000$. Finally, we also note that the value of

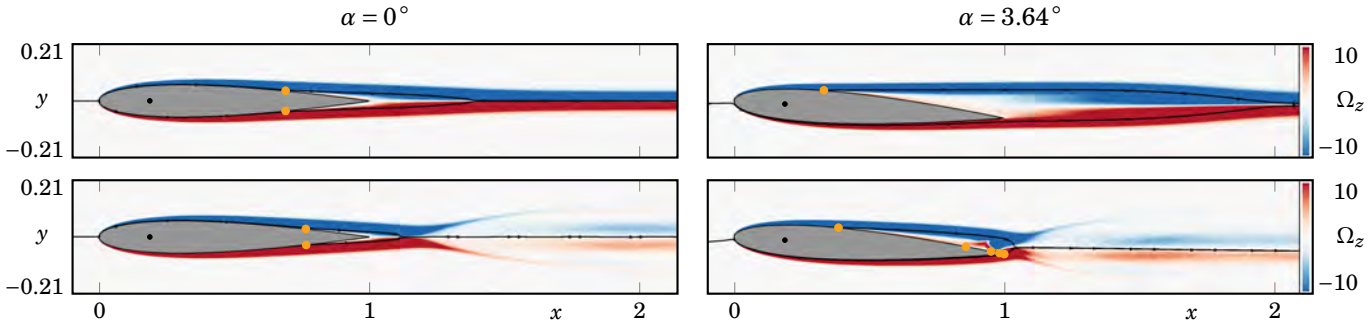

Figure 2.4 – *Spanwise vorticity field of two-dimensional base flow (top) and mean flow (bottom) solutions at* $Re = 20\,000$ *for* $\alpha = 0°$ *(left) and for* $\alpha = 3.64°$ *(right).*

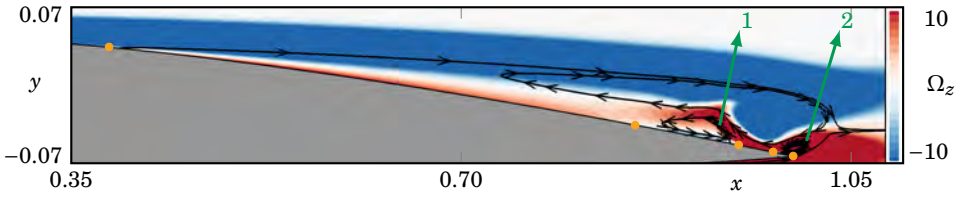

Figure 2.5 – *Spanwise vorticity field of mean flow solution at* $Re = 20\,000$ *for* $\alpha = 3.64°$*: close-up on the recirculation zone of the upper surface. The yellow dots over the airfoil surface represent the different separation and reattachment points.*

X_d does not vary significantly in time. For example, for $Re = 50\,000$ and $\alpha = 0°$, the difference between the maximum and minimum abscissa values of the separation points in time is of order 10^{-3}.

2.1.2 Flow field description for $\alpha \geq 0°$

In the following paragraphs, we analyse the influence of the increase in the angle of attack on the base and mean flow solutions, for a fixed Reynolds number. We start by analysing the evolution in time of the aerodynamic moment coefficient, evaluated around $X_{EC} = 0.186$ for $Re = 20\,000$ and two different angles of attack, $\alpha = 0°$ and $\alpha = 3.64°$. The results are present in figure 2.3. We start by noting that, for both angles, the mean aerodynamic moment, represented by the blue curve, is zero. In contrast, the amplitude of the oscillations has drastically increase between these two angles. For $\alpha = 0°$, the amplitude is $\pm 1.88 \cdot 10^{-3}$, while for $\alpha = 3.64°$, we have the minimum and maximum values of $-3.80 \cdot 10^{-2}$ and $4.55 \cdot 10^{-2}$, respectively. Despite the fact that the signal remains periodic in time between these two incidences (with a slight decrease of the vortex shedding frequency), the harmonic content increases as the angle of attack increases. This increase in the harmonic content is responsible for the difference between the minimum and maximum values of the time signal for $\alpha = 3.64°$, even if the mean value is zero.

The spanwise vorticity associated to the base and mean flow fields at $Re = 20\,000$ and two different angles of attack is present in figure 2.4 ($\alpha = 0°$ and $\alpha = 3.64°$). For both angles, the base flow solutions, on the left, present an unrealistic large recirculation length, when compared to the mean flow solutions, on the right. The account for the unsteadiness on the mean flow computations can be noted on the deviated vorticity zones at the rear of the airfoil. This deviation is associated to the presence of the Reynolds stress tensor terms in the mean flow solution, resulting in shorter recirculation zones.

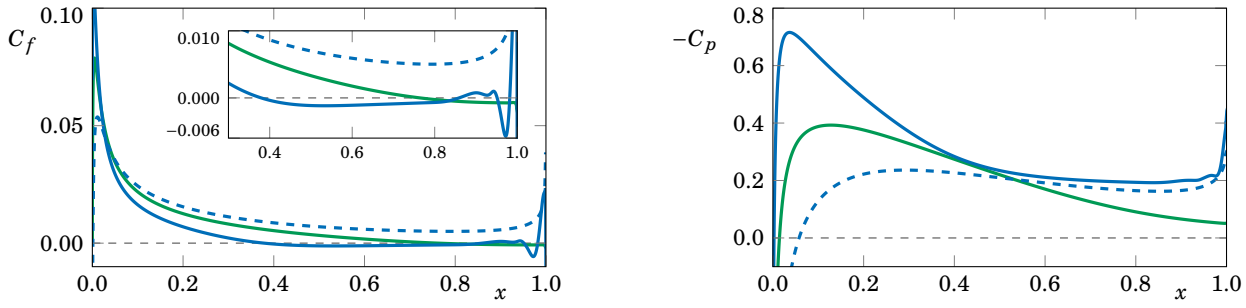

Figure 2.6 – *Distributions of the friction, C_f, and pressure, C_p coefficients of two-dimensional mean flow solutions along the upper (solid) and lower (dashed) surfaces of the airfoil at $Re = 20\,000$ for $\alpha = 0^\circ$ (green) and $\alpha = 3.64^\circ$ (blue).*

A close-up near the trailing edge for the mean flow solution at $\alpha = 3.64^\circ$ is made in figure 2.5. One can firstly note that the main separated boundary layer of the upper surface, whose separation point is located at $X_d^{up} = 0.397$, has not reattached. On the other hand, the boundary layer of the lower airfoil surface does not present any separation. This recirculation is characteristic of a trailing-edge laminar separation bubble (LSB), presented on the Introduction of this thesis (see figure 6). This type of LSB is topologically different from the classic long LSB, mainly due to the fact that the separated boundary layer does not reattach. As a consequence, the main vortex of the recirculation bubble is located above the trailing edge, in contrast to the vortex associated to a long LSB, which is usually placed closer to the upper surface of the airfoil and has a flattened shape. Additionally, we report the presence of two secondary recirculation bubbles, circulating in the anticlockwise direction, identified as 1 and 2 by the green arrows in the figure. They are located on the ranges $0.860 < x < 0.951$ and $0.982 < x < 1$, respectively. The recirculation bubble labelled 1 marks the end of the "dead air" region, located on the range $0.397 \lesssim x \lesssim 0.860$, characterised by low fluid velocities and a roughly constant (and negative) friction coefficient.

The evolution of the mean friction, C_f, and mean pressure, C_p, coefficients along the upper and lower surfaces of the airfoil, for the same Re and α parameters, is present in figure 2.6. The upper surface distributions are represented by the solid line, while the lower ones are represented by the dashed lines. No dashed line is observed for $\alpha = 0^\circ$, since the upper and lower distributions coincide. For $\alpha = 0^\circ$ (green curve), both lower and upper surfaces present a maximum depression point, located at $x = 0.128$, where $-C_p$ is maximum, followed by an adverse pressure gradient regime, up to the trailing edge. In the cases where the adverse pressure gradient is strong enough, a separation point appears, characterised by a null friction tension. In the present situation, one can observe this separation point at $X_d = 0.765$, on the C_f zoom, when the sign of the green curve changes. The fact that the boundary layer does not reattach can also be confirmed by the fact that the C_f distribution remains negative until the trailing edge.

Concerning the case at $\alpha = 3.64^\circ$ (blue curve), the separation point on the upper airfoil surface moved upwards to $X_d^{up} = 0.379$, when compared to $\alpha = 0^\circ$. This is a consequence of the higher adverse pressure gradient, which for this angle starts at $x = 0.037$. The presence of the two secondary recirculation bubbles on the upper surface, identified in figure 2.5, can be identified in the behaviour of the C_f curve, in the second half of the airfoil, where it changes sign at the separation and reattachment points previously reported. The plateau of negative values of C_f in the range $0.397 \lesssim x \lesssim 0.860$ is characteristic of the "dead air" region. In this region, a plateau of $-C_p$ can also be discerned. Concerning the boundary layer over the lower surface, the separation no longer exists, when compared to the case at $\alpha = 0^\circ$, with a pressure coefficient roughly constant for $x > 0.3$.

The transition between the two angles described above can be observed in figure 2.7, where C_f and $-C_p$ are sketched

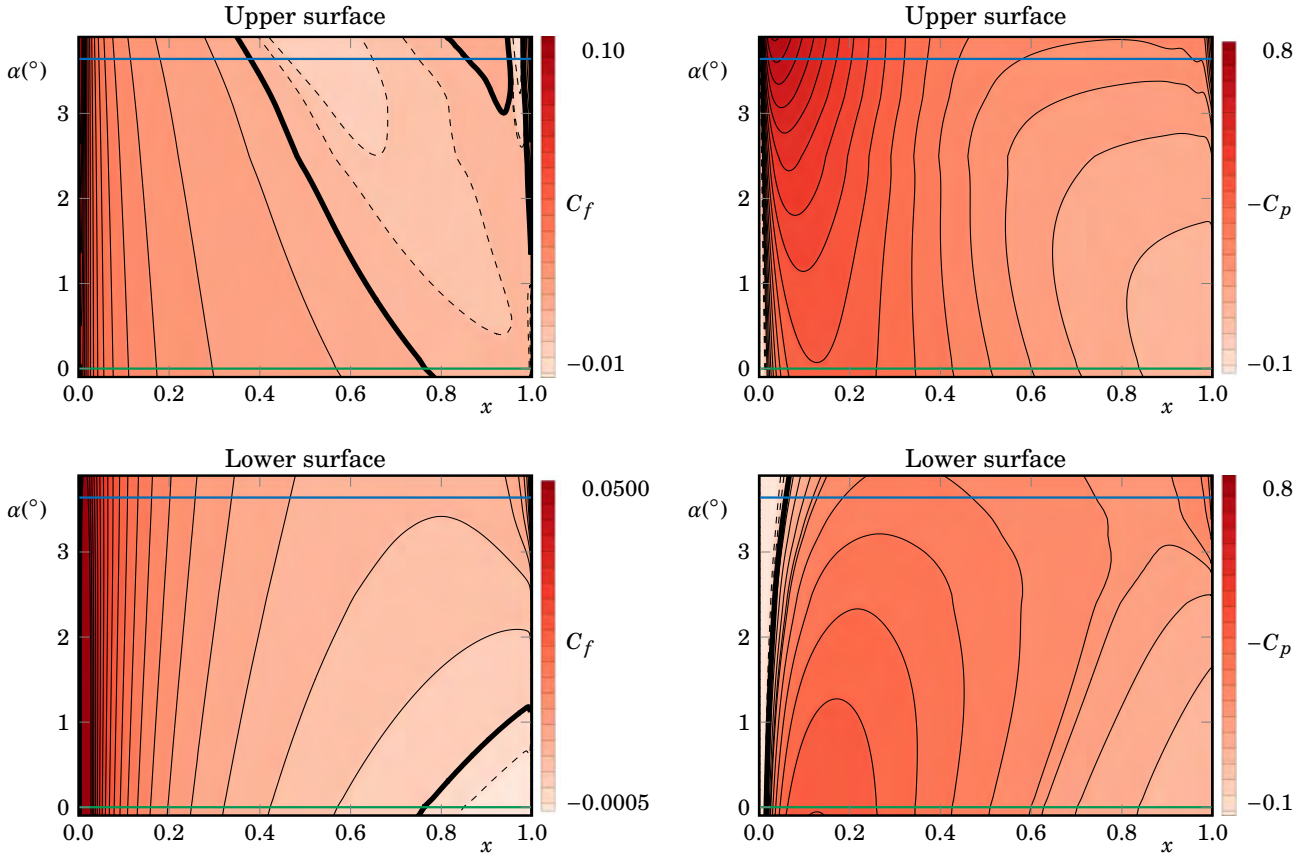

Figure 2.7 – *Colour map of the distributions of the friction, C_f, and pressure, C_p coefficients of two-dimensional mean flow solutions along the upper and lower surfaces of the airfoil (top and bottom figures, respectively) at $Re = 20\,000$ as function of the angle of attack. The horizontal green and blue lines correspond to $\alpha = 0°$ and $\alpha = 3.64°$, respectively.*

as function of the angle of attack. The angles analysed in the previous paragraphs are represented by the horizontal green and blue lines. Concerning the upper surface, one can note the displacement of the separation point upwards (on the C_f graphic). The same occurs to the maximum depression point, whose intensity increases with the angle of attack (in the $-C_p$ graphic). The emergence of the two smaller recirculation bubbles can also be observed on the C_f map. The recirculation bubble labelled 1 emerges at $\alpha = 3.01°$, while the recirculation bubble labelled 2, near the trailing edge, emerges earlier at $\alpha = 1.34°$. Concerning the lower surface, one can observe the separation point moving forward, on the C_f map, with its extinction at $\alpha = 1.18°$. In the $-C_p$ map, one can observe the decrease of the maximum depression intensity with the angle of attack, whose position moves forward.

2.1.3 Characterisation of the base and mean aerodynamic efforts for $\alpha \geq 0°$

In this section, we continue our analysis by describing the behaviour of the global aerodynamic forces and moments as function of the incidence and Reynolds number. As explained in section 1.3.2, in the presence of a high frequency vortex shedding, the aerodynamic forces exerted on the body comprise both a mean component, which can be directly extracted from the *mean flow*, and an unsteady component, oscillating at the high frequency of the vortex shedding. This unstable

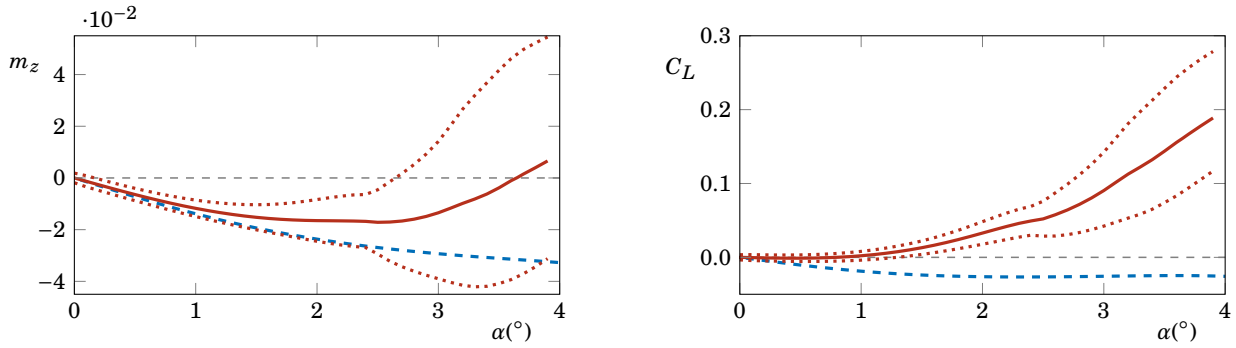

Figure 2.8 – *Evolution of the aerodynamic moment around $X_{EC} = 0.186$ and lift coefficients with the angle of attack for two-dimensional base flow (dashed blue) and mean flow (solid red) solutions at $Re = 20\,000$. The dotted red curves are associated to the minimum and maximum values of the m_z and C_L signals.*

component is observed to be periodic for the lower incidences. However, this periodic behaviour ceases to exist as the angle of attack increases. This lost of periodicity is demonstrated at the end of this section for the case at $Re = 50\,000$. At the same time, we have also justified that the motion of an airfoil with a pitch degree of freedom is mostly sensitive to the mean component of the aerodynamic moment coefficient, for the range of parameters of interest in this thesis. Hence, in the present section, we document the behaviour of the mean aerodynamic efforts (aerodynamic moment and lift coefficients), in particular their dependency on the incidence angle and on the Reynolds number.

As previously noted, each time-stepping simulation is performed for a fixed angle of attack. In this section, we stick to the reference value $X_{EC} = 0.186$ for the elastic centre, the nominal value used in this thesis (as indicated in section 1.2, table 1.1). Different values of X_{EC} are considered in the next section.

We consider first the effect of varying the incidence α for a fixed Reynolds number of $Re = 20\,000$. Figure 2.8 displays both the aerodynamic moment and the lift coefficients as function of α. The values associated to the unstable base flow solutions are represented by the blue dashed lines. The mean flow values are represented by the solid red curves, with the amplitude of the oscillations represented by the dotted lines envelope. For this value of Re, the base flow is found to be unstable in all the incidence range, including at $\alpha = 0°$, in accordance with the vortex shedding onset predicted at $Re = 8\,000$. However, the base flow solution still exists as an unstable solution of the Navier–Stokes equations, and can be computed using a Newton method, as explained previously. In the corresponding efforts (dashed blue line), we observe that the moment coefficient remains negative for the incidence range considered, tending to a constant value. The lift coefficient presents the same tendency.

The mean flow results (red curves) are computed using time-stepping simulations, followed by a time-average post processing. Observation of the figure leads to the following findings. First, one finds that the unsteady efforts vary considerably around the mean value, with this variation increasing as the incidence increases. In particular, one can note that the amplitude of the oscillation of the aerodynamic moment has same order of magnitude as its mean value. Secondly, one observes that the efforts obtained from the mean flow are rather different from the ones obtained from the unstable base flow. This deviation is not surprising, since the base flow is no longer relevant after the onset of unsteadiness, and very different from the mean flow solution, as previously observed in figure 2.4. The third important observation is that the mean aerodynamic moment m_z becomes a growing function of α just after the onset of oscillation, crossing zero at $\alpha = 3.64°$ and becoming positive for higher values of α.

Considering the lift coefficient associated to the mean flow solutions, one also observes a small region, $0° < \alpha < 0.8°$,

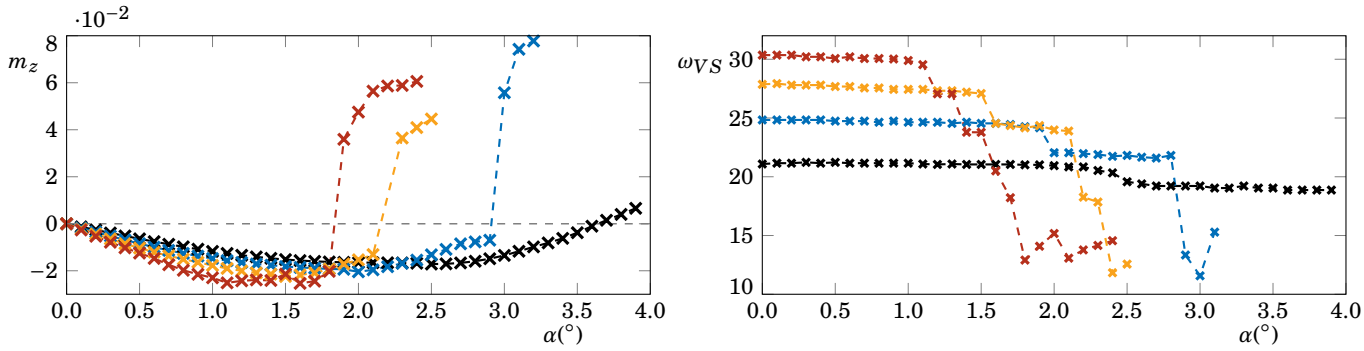

Figure 2.9 – *On the left, evolution of the aerodynamic moment coefficient around* $X_{EC} = 0.186$ *with the angle of attack for two-dimensional mean flow solutions at* $Re = 20\,000$ *(black),* $Re = 30\,000$ *(blue),* $Re = 40\,000$ *(yellow) and* $Re = 50\,000$ *(red). On the right, evolution of the vortex shedding frequency with the angle of attack for two-dimensional unsteady simulations.*

with negative values. This surprising phenomenon was firstly observed by Mueller *et al.* (1982) on a symmetric NACA66$_3$-018 airfoil at $Re = 130\,000$. More recently, the same observations were found for a transitional Reynolds number regime on a NACA0012 airfoil (Ohtake *et al.*, 2007; Yonemoto *et al.*, 2008; Tank *et al.*, 2017a,b; Pranesh *et al.*, 2019), as reported on the Introduction of this thesis. Additionally, the same phenomenon was found by Jallas (2018) for a flapping airfoil configuration (see figure 4.2, page 109). The initial negative aerodynamic moment and lift coefficients was associated to the laminar separation of the boundary layer. Further, this unusual behaviour disappears for larger values of α where the lift coefficient becomes positive in accordance with the usual expectation and the predictions of the potential theory. The change in sign of these coefficients for larger incidences was associated to the reattachment of the separated boundary layer, forming a laminar separation bubble. The negative lift coefficient region was completely removed by addition of surface roughness or acoustic excitation, on the experiments, or via transition of the boundary layer before separation, on the numerical computations. With these modifications, the flow readily transitions to a turbulent state while attached, exhibiting no separation afterwards. Finally, we observe that the amplitude of the oscillations (red dotted curves) varies significantly with the incidence. In particular, we observe a change in the amplitude growth rate at $\alpha = 2.4^\circ$, mainly on the lower limit of the oscillations. As it will be discussed next, this change is also associated to a decrease on the frequency of the vortex shedding oscillations.

We document on the left of figure 2.9, the variation of m_z associated to the mean flow with respect to α for larger values of the Reynolds number. As stated before, the mean flow solutions are obtained from the time averaging of two-dimensional time-marching simulations. For a fixed Reynolds number, the simulations are carried out by increasing the angle of attack, with a step of 0.1°, starting from $\alpha = 0^\circ$ and initialising the next simulation with the instantaneous solution of the previous incidence. The aerodynamic moment associated to each mean flow computation is represented by a cross in figure 2.9, for four different Reynolds numbers. One can firstly note that the slope at $\alpha = 0^\circ$, associated to an aerodynamic stiffness, while negative, increases (in absolute value) as the Reynolds number increases. The relation between this slope and a quasi-steady approximation was introduced in chapter 1, page 42, to predict the present of an unstable static eigenvalue for the FSI configuration equilibrium at $\alpha = 0^\circ$. Since the slope is negative, we can predict from the criterion presented in equation 1.49 that an undamped system will have an unstable static eigenvalue if this slope is higher (in absolute value) than the structural stiffness considered. Further, it can be inferred that the static instability of the equilibrium point at $\alpha = 0^\circ$ is further destabilised as the Reynolds number increases. The complete stability analysis of the equilibrium point at $\alpha = 0^\circ$ is investigated in chapters 3 and 4 using linear stability analysis.

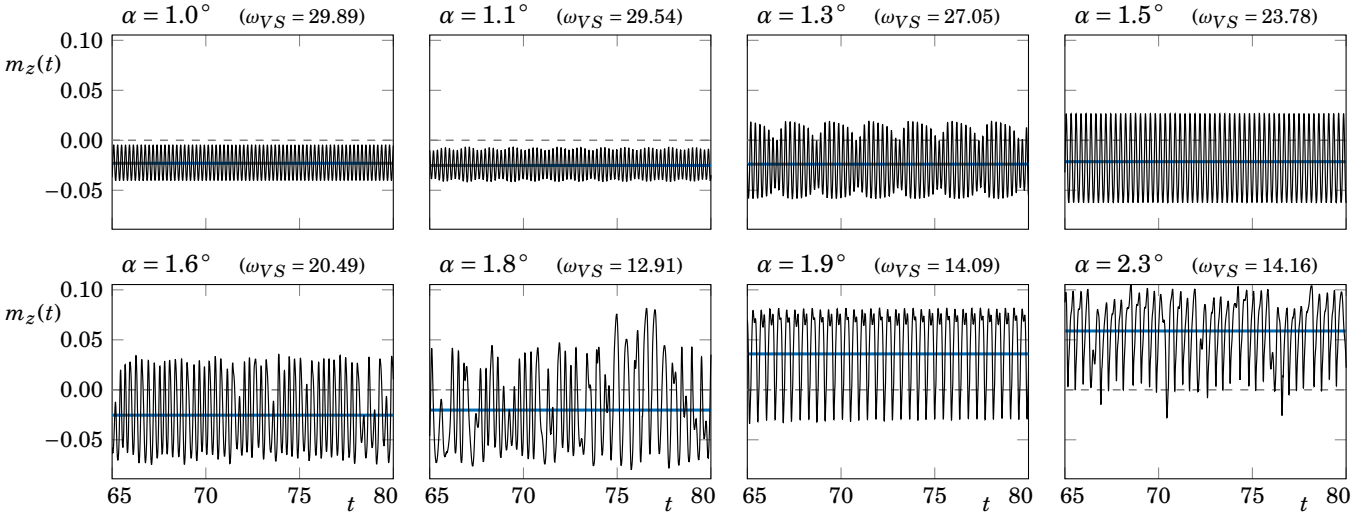

Figure 2.10 – *Time history of the aerodynamic moment coefficient around* $X_{EC} = 0.186$ *for* $Re = 50\,000$ *at different angles of attack. The blue line represents the mean value.*

A second equilibrium point is reached, when mean aerodynamic moment is again zero, for a different incidence. For the already discussed case at $Re = 20\,000$, this point occurs at $\alpha = 3.64°$. The linear stability around this point is discussed in chapter 6. We note that, as the Reynolds number increases, a discontinuity emerges near the end of each curve, where the mean aerodynamic moment passes suddenly from a negative to a positive value. Therefore, the task of finding a second equilibrium point for a mean flow solution from two-dimensional simulations at $Re > 20\,000$ is nontrivial. The case at $Re = 20\,000$ becomes a pertinent case due to the absence of this discontinuity, that appears outside the incidence range considered. One can further note that, as the Reynolds number increases, the jump between a negative and a positive value of the m_z occurs at lower incidences.

The jump in the m_z coefficient is associated to a period-doubling of the vortex shedding phenomenon. The evolution of the vortex shedding frequency ω_{VS} with the incidence for the different Reynolds numbers considered is present on the right of figure 2.9. Concerning the first part of the curves (before the jump in m_z), we first confirm that, for a fixed incidence, the vortex shedding frequency increases as the Re increases (as observed in figure 2.2 for $\alpha = 0°$). Secondly, we note that the frequency is approximately constant with the incidence. However, a slight decrease on ω_{VS} is observed in all curves when the minimum m_z is reached. This decrease in frequency occurs at the same incidence as the change in the behaviour of the amplitude of the global coefficients m_z and C_L, reported in figure 2.8. For example, for the case at $Re = 20\,000$, the minimum of m_z is found around $\alpha = 2.4°$, where the frequency decreases from $\omega_{VS} = 20.334$ at $\alpha = 2.4°$ to $\omega_{VS} = 19.573$ at $\alpha = 2.5°$. Finally, we note that, in the zone of the m_z jump, ω_{VS} decreases until reaching values that approximately correspond to half of the vortex shedding frequency before the jump. For example, for the case at $Re = 50\,000$, the frequency of the vortex shedding passes from $\omega_{VS} = 29.54$ at $\alpha = 1.1°$, evaluated before the jump, to the value of $\omega_{VS} = 14.09$ at $\alpha = 1.9°$. This period-doubling phenomenon was also found recently by Marquet *et al.* (2022) for a NACA0012 airfoil in stall conditions at $Re = 5\,000$ and $\alpha \approx 8°$.

To better understand why this m_z jump and period-doubling occurs, we sketch the evolution of the instantaneous aerodynamic moment as function of time for eight different incidences at $Re = 50\,000$ in figure 2.10. The first case, at $\alpha = 1°$, presents a periodic flow with a negative mean value. This scenario is found for the range $|\alpha| \leq 1°$. This point is located before the jump in the mean aerodynamic moment, having a frequency of $\omega_{VS} = 29.89$. For the next case,

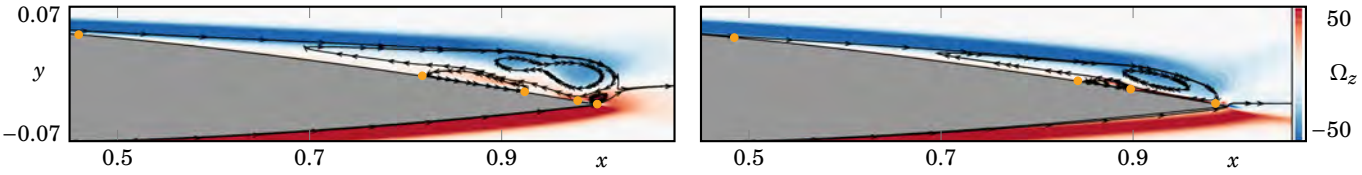

Figure 2.11 – *Spanwise vorticity field near the trailing edge of two-dimensional mean flow solutions at* $Re = 50\,000$ *for* $\alpha = 1.8°$ *(left) and* $\alpha = 1.9°$ *(right).*

at $\alpha = 1.1°$, the signal becomes quasi-periodic, while keeping the roughly the same amplitude as the previous case. However, for $\alpha = 1.3°$, the amplitude of the quasi-periodic signal increases, and, for $\alpha = 1.5°$, the signal regains its periodic character. Then, suddenly, the signal becomes chaotic (cases $1.6°$ and $1.8°$). This chaoticity is associated to the fact that the separated boundary layer of the upper surface of the airfoil, associated to the instantaneous flow fields, switches between a reattachment and a no reattachment scenario at the end of the trailing edge. For a higher incidence case, the reattachment of the instantaneous boundary layer is observed for all time instants. This is the case for $\alpha = 1.9°$. In this case, the quasi-periodicity is retrieved, but with a double period when compared with the period of the periodic signal before this transition. For higher angles, as the case at $\alpha = 2.3°$, the signal loses again its periodic/quasi-periodic behaviour. We note that the flow at this Reynolds number is three-dimensional, as explored in the following section. In a subsequent section, we also show that the aerodynamic moment of a mean flow solution coming from three-dimensional simulations does not present this jump. Further, we show that the vortex shedding frequency decreases continuously with the angle of attack.

Finally, we sketch the mean flow solution near the trailing edge before and after the discontinuity on the aerodynamic moment coefficient curve, for the case at $Re = 50\,000$, in figure 2.11. The angles before and after the jump correspond to $\alpha = 1.8°$ and $\alpha = 1.9°$, respectively. The case at $\alpha = 1.8°$, when the moment coefficient is still negative, presents boundary layer on the upper surface that separates at $X_d^{up} = 0.458$ and does not reattach to the airfoil. This situation is similar to the case at $Re = 20\,000$ and $\alpha = 3.64°$, analysed in figure 2.4. This is typical of a trailing-edge laminar separation bubble, as presented on the Introduction of this thesis, in figure 6, where the main vortex structure of the recirculation zone is located above the trailing-edge. We also note the presence of two secondary bubbles, circulating in the anticlockwise direction. On the other hand, the case at $\alpha = 1.9°$, which presents a positive moment coefficient, has a boundary layer on the upper surface that separates at $X_d^{up} = 0.483$ and reattaches at $X_r^{up} = 0.980$, characteristic of a long laminar separation bubble. In this case, we note that the secondary bubble located below the main recirculation vortex has a smaller size, while the secondary bubble at the trailing edge ceased to exist on the attached flow, as observed in the figure. This drastic change in the topology of the mean flow solution explains the sudden jump on the m_z–α curves. Further, we expect to find a hysteresis behaviour near this topological change, which could be investigated with a series of simulations carried out by decreasing the angle of attack and initialising the next simulation with the instantaneous solution of the previous incidence. However, no further investigations were conducted in this direction and we leave this exploration for a future work.

2.1.4 Characterisation of the aerodynamic stiffness at $\alpha = 0°$

As discussed previously, the variation of the mean aerodynamic moment as function of the angle of incidence considering a *fixed* airfoil configuration is directly related to the possible occurrence of a *static instability* of the coupled fluid–solid system. More specifically, we have justified in section 1.6 that the aerodynamic moment associated to the *mean*

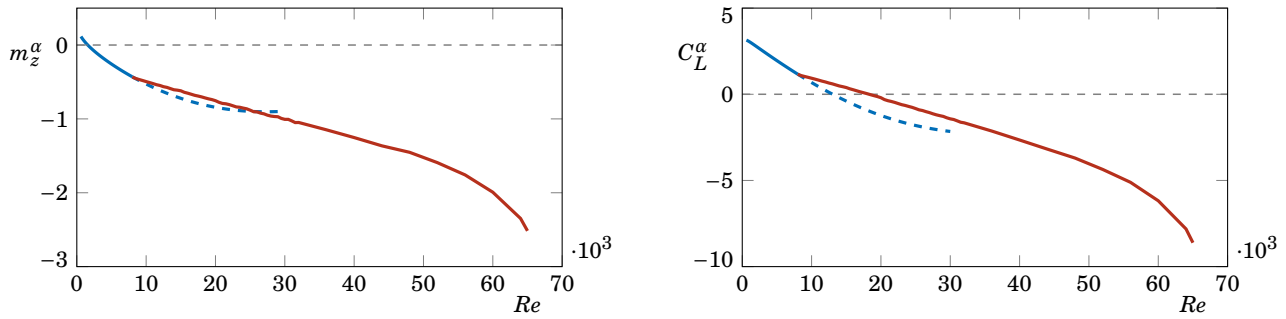

Figure 2.12 – *Evolution of aerodynamic moment stability derivative m_z^α (left) and lift stability derivative C_L^α (right) for $\alpha = 0°$, with the Reynolds number. The solid blue lines are associated to stable base flow solutions, the dashed blue lines to unstable base flow solutions and the solid red lines to mean flow solutions.*

flow can be used to build a quasi-steady model predicting the evolution of the coupled system over the slow time scale. This model is able to give a first approximation of the static instability that may be present in the coupled fluid–solid system. In this model, the key quantity is $m_z^\alpha = \partial m_z/\partial\alpha$, which can be interpreted as an aerodynamic stiffness coefficient. This quantity is also called a stability derivative or control derivative.

In some of the figures of the previous sections, where we sketch the evolution of the aerodynamic moment with α, the equilibrium solutions of the FSI configuration correspond to the values of α that respect the equality $\alpha = -m_z\left(\overline{\boldsymbol{U}}, \overline{p}\right)/K_s$ (equation 1.24, page 30). At the same time, the quantity m_z^α correspond to the slope of the curves at different angles. In this section, we restrict to the equilibrium solution corresponding to $\alpha = 0°$ and examine the m_z^α dependency on the Reynolds number. This will provide simple arguments to predict the onset of a *static instability*. Note that a similar discussion could be made considering the value of m_z^α for the nonzero equilibrium solutions. We come back to this point in chapter 6.

We thus plot in figure 2.12 the evolution of m_z^α (slope of the aerodynamic moment curve at $\alpha = 0°$) with the Reynolds number. This evolution is documented for the stable and unstable base flow solutions, represented by the solid and dashed blue curves, respectively, and for the mean flow solutions, represented by the solid red curves. We also document the evolution of C_L^α, which corresponds to the slope of the lift coefficient curve at $\alpha = 0°$. Concerning the slope of the aerodynamic moment, we first observe that it is positive for the initial values of Re, on the range $Re \lesssim 1500$. From this point, the value of m_z^α remains negative for the remaining Re considered. We note that the change in sign of this quantity is observed while the base flow solution is still stable, before the onset of the vortex shedding unsteadiness. The divergence of the base and mean flow curves is observed from $Re = 8000$ onwards, with a base flow prediction that tends to a constant value and a mean flow prediction that continues to decrease. The same qualitative behaviour can be found for the C_L^α–Re curve. However, at the vortex shedding onset, this quantity is still positive, crossing the zero value at a different Reynolds number for the base and mean flows. We report that, for $Re = 50000$, we obtain a value of $m_z^\alpha = -1.5223$. This value is analysed in chapter 3, when discussing the quasi-steady approximation.

The above considerations are valid for an aerodynamic centre located at the nominal value of $X_{EC} = 0.186$. For this value, we have seen that the aerodynamic stiffness indicates a possible static instability from $Re \gtrsim 1500$ onwards. We now address the question of the effect of X_{EC} on this static instability criterion.

To address the general case, we can first recognise that the necessary criterion for static instability on m_z^α can be reformulated in a different way. For this, we can refer to the *aerodynamic centre* X_{AC}, defined as the point along the chord around which the mean aerodynamic moment is independent of the angle of attack, *i.e.*, m_z^α is constant. Alternatively,

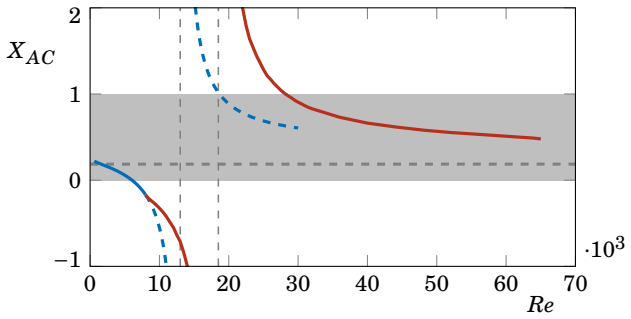

Figure 2.13 – *Evolution of the aerodynamic centre location, X_{AC}, with the Reynolds number for two-dimensional stable base flow (dashed blue), stable base flow (solid blue) and mean flow (solid red) solutions at $\alpha = 0\,^\circ$. The grey zone represents the streamwise abscissa range occupied by the airfoil. The vertical dashed lines correspond to the asymptotic values for base and mean flow solutions at $Re = 13\,000$ and $Re = 18\,500$, respectively. The horizontal dashed line represents the nominal value of the elastic centre $X_{EC} = 0.186$.*

this point is can be defined as the point of application of the mean aerodynamic efforts. For a symmetric airfoil, since the mean aerodynamic moment at $\alpha = 0\,^\circ$ is null, the aerodynamic centre corresponds to the situation where m_z^α is also null.

With that in mind, the criterion can be reformulated as follows: the equilibrium position is stable whenever C_L^α is positive and the elastic centre is placed before the aerodynamic centre ($X_{EC} < X_{AC}$), and unstable when the elastic centre is placed after the aerodynamic centre ($X_{EC} > X_{AC}$). When C_L^α becomes negative, the equilibrium position is unstable for every X_{EC}, as a small increment in α results in a decrease of C_L, inducing a negative vertical velocity and reinforcement of the angular rotation of the airfoil in the clockwise direction. The location of the aerodynamic centre can be deduced from the values of the aerodynamic moment and lift stability derivatives as follows:

$$(X_{EC} - X_{AC}) = \frac{m_z^\alpha}{C_L^\alpha}\,. \tag{2.1}$$

The variation of the aerodynamic centre position, X_{AC}, with Re is depicted in figure 2.13. The solid and dashed blue lines correspond to the variation of X_{AC} associated to the stable and unstable base flow solutions, while the solid red line is associated the aerodynamic centre position of the mean flow solutions. The base and mean flow curves coincide for $Re < 8\,000$, as the flow is steady in time. From this point, at which the base flow becomes unstable, the base and mean curves diverge from each other. We represent the nominal value of the elastic centre $X_{EC} = 0.186$ by the horizontal dashed line.

Concerning the base flow curve, it is first noted that for $Re \lesssim 1500$, the nominal elastic centre $X_{EC} = 0.186$ is located behind the aerodynamic centre X_{AC}, confirming the previous results, where a positive m_z^α was found. In this regime, one finds a stable equilibrium position for $X_{EC} = 0.186$. As the Reynolds number increases, X_{AC} moves upwards, being at the leading edge for $Re = 6\,000$. For the range, $6\,000 < Re < 13\,000$, the aerodynamic centre associated to the base flow is located behind the leading edge ($X_{AC} < 0$).

Concerning the base flow solution, a singularity on the location of X_{AC} is found at $Re = 13\,000$, where its value passes from a position ahead of the airfoil to a position behind the airfoil. Concerning the mean flow curve, the results are qualitatively similar. The singularity is found at a higher Re number, $Re = 18\,500$. From this point, the aerodynamic centre is located behind the airfoil, moving upwards as the Reynolds number increases. The singularity can be understood by inspecting equation 2.1. For a nonzero value of m_z^α, the behaviour of the quantity $(X_{EC} - X_{AC})$ is governed by the

behaviour of C_L^α, depicted in figure 2.12. As reported earlier, C_L^α changes sign from positive to negative at $Re = 13\,000$ and $Re = 18\,500$ for the base and mean flow, respectively. In this way, the quantity $(X_{EC} - X_{AC})$ changes sign from negative to positive at the same Reynolds numbers.

2.1.5 Emergence of three-dimensional structures: hydrodynamic Floquet analysis

Up until now, we investigated the flow field around a NACA0012 airfoil as function of the Re and α parameters via two-dimensional time-marching simulations, without questioning if the flow is in reality two- or three- dimensional. To address this question, we investigate in this section the emergence of three-dimensional perturbations on the instantaneous flow field by the means of a linear Floquet analysis for $\alpha = 0°$. This follows the classical Floquet analysis, applied to purely-hydrodynamic configurations, present in Barkley *et al.* (1996).

Method and bibliographical elements

In the previous sections, we showed that the two-dimensional flow field was periodic in time at $\alpha = 0°$, for the Re number range considered. Taking advantage of this property, we investigate the emergence of three-dimensional perturbations on periodic flow field solutions at $\alpha = 0°$ by the means of a Floquet analysis (Floquet, 1883), for different values of Reynolds numbers. This analysis was firstly used by Barkley *et al.* (1996) to study the onset of three-dimensional structures on the periodic wake of a cylinder. More recently, Tsiloufas *et al.* (2009) performed a Floquet analysis around a massive separated flow at $400 \geq Re \geq 600$ at $\alpha = 20°$ on a NACA0012 airfoil, while He *et al.* (2017) performed similar analyses on different NACA airfoils. Deng *et al.* (2017) also used this analysis to investigate the case of a NACA0015 airfoil in post-stall conditions ($\alpha = 12.5°$ and $\alpha = 15°$).

We note that the Floquet analysis present here aims at investigating three-dimensional perturbations on a purely-hydrodynamic configuration, in contrast to the FSI Floquet analysis, introduced in chapter 1 and explored in the subsequent chapters 4 and 6, where the airfoil structure has a pitch degree of freedom. Similarly to the developments present in section 1.4.3, the Floquet multipliers, μ, are complex numbers quantifying the growth/decay and frequency of infinitesimal perturbations that may develop on top of an established periodic limit cycle oscillation. This time, the infinitesimal perturbations are posed as

$$\boldsymbol{q}'(X, Y, Z, t) = \frac{\hat{\boldsymbol{q}}_\beta(X, Y, t)\mathrm{e}^{\sigma t + \mathrm{i}\beta Z} + \text{c.c.}}{2},$$

where $\hat{\boldsymbol{q}}_\beta = \left[\hat{U}_\beta, \hat{V}_\beta, \hat{W}_\beta, \hat{p}_\beta\right]^T$ is the Floquet eigenmode, corresponding to a T-periodic function, $\beta = 2\pi/\lambda_z$ is the forcing spanwise wavenumber and λ_z is the corresponding spanwise wavelength. The Floquet multipliers are then retrieved from the identity $\mu = \mathrm{e}^{\sigma T}$. The numerical tool used to compute the most unstable Floquet eigenpairs is described in appendix B.

In order to have a better understanding of the phenomenon, we review the main results of Floquet analysis for the circular cylinder, whose wake undergoes transition to three-dimensionality via three distinct modes: modes A, B and C. The mode A (Williamson, 1996a,b) instability emerges naturally with the onset of the three-dimensionality for $Re \gtrsim 180$ and is characterised by spatially periodic streamwise vortex structures, with a spanwise wavelength of approximately $\lambda_z \approx 4D$, where D is the cylinder diameter. For $Re \gtrsim 230$, a gradual shift of energy from the mode A to the mode B is observed, as the Reynolds number increases. Mode B instability is characterised by a distinctly smaller wavelength, around $\lambda_z \approx 1D$. Finally, mode C instability is observed in a circular cylinder when the flow is excited via a control wire placed in the wake, parallel to cylinder axis (Yildirim *et al.*, 2013). The spanwise wavelength is around $\lambda_z \approx 2D$. Additionally, a quasi-periodic mode is found on the literature (Blackburn *et al.*, 2005), appearing around $Re \approx 380$, not

discussed in the following.

One of the differences between these three modes, is the arrangement of the streamwise vortices from one braid of the vortex shedding structure to the other. Mode A is characterised by an odd RT-symmetry, where R denotes the reflection about the wake axis ($y = 0$) and T denotes the translation in time by $T/2$. Mathematically, this property can be expressed in terms of the streamwise vorticity as:

$$\Omega_x(X, Y, t) = -\Omega_x(X, -Y, t + T/2). \tag{2.2}$$

Therefore, mode A instability has a staggered arrangement of the streamwise vortices. In contrast, mode B is characterised by an even RT-symmetry, which can be posed mathematically as

$$\Omega_x(X, Y, t) = \Omega_x(X, -Y, t + T/2). \tag{2.3}$$

In this case, the spanwise structures are arranged in-line. On the other hand, mode C does not have a RT-symmetry. Instead, it exhibits a period-doubling, *i.e.*, the spatial arrangement of the streamwise vortices is the same every $2T$ time units. Mathematically, this can be posed as

$$\Omega_x(X, Y, t) = -\Omega_x(X, Y, t + T). \tag{2.4}$$

Since both modes A and B preserve the T-symmetry of the periodic flow, they become unstable by crossing the unit circle with a Floquet exponent of $\mu = 1$. In contrast, since mode C introduces a period-doubling on the periodic flow, it becomes unstable for a Floquet exponent of $\mu = -1$.

Concerning the three-dimensional transition around a NACA0012 airfoil, Jones *et al.* (2008) reported that the three-dimensionality transition for $Re = 50\,000$ and $\alpha = 5^\circ$ occurs via a mode resembling the mode B instability of the circular cylinder. A similar conclusion was made by Hoarau *et al.* (2003) at $\alpha = 20^\circ$ for $Re = 800$ and $Re = 1\,200$. For a NACA0015 airfoil, Deng *et al.* (2017) found that the transition takes place via a mode C instability for $(\alpha, Re) = (12.5^\circ, 1082)$ and $(\alpha, Re) = (15^\circ, 730)$, with $\lambda_z = 1.38d$ and $\lambda_z = 1.62d$, d being the characteristic dimension transverse to the freestream, $d = c \sin\alpha$. Finally, Samuthira Pandi *et al.* (2019) reported the onset of the three-dimensionality of an Eppler 61 airfoil at $\alpha = 10^\circ$ to be around $Re = 1\,280.9$ via a mode C instability and hairpin vortex structures with $\lambda_z = 1.34$.

Results

We start our analysis at $Re = 30\,000$ and $\alpha = 0^\circ$. In figure 2.14a, we present a Floquet spectrum, where 20 Floquet multipliers were computed for the spanwise wavenumber $\beta = 50$. This corresponds to the value of $\lambda_z = 0.126$. A single Floquet multiplier is found in the unstable zone ($|\mu| > 0$). This Floquet multiplier is highlighted by the bigger black circle and corresponds to a synchronous Floquet eigenmode, with no imaginary part. The corresponding spanwise velocity of the Floquet eigenmode, $\hat{W}_\beta$, is presented in figure 2.14c. This field is associated to an arbitrary instant of the periodic limit cycle oscillation around which the stability analysis is carried out. The spanwise vorticity of this instant is represented by the black isocontour lines, with the negative and positive values represented by the dashed and solid lines, respectively. We observe that the Floquet eigenmode is mostly located on the cores of the vortex shedding and on the secondary streamwise vorticity zones.

This analysis can be carried out for different values of β. In that sense, figure 2.14b presents the evolution of the modulus of the synchronous leading Floquet multiplier as function of the forcing wavenumber β. We are able to identify a small range $35 \lesssim \beta \lesssim 60$, for which the leading Floquet multipliers are unstable. This means that the periodic

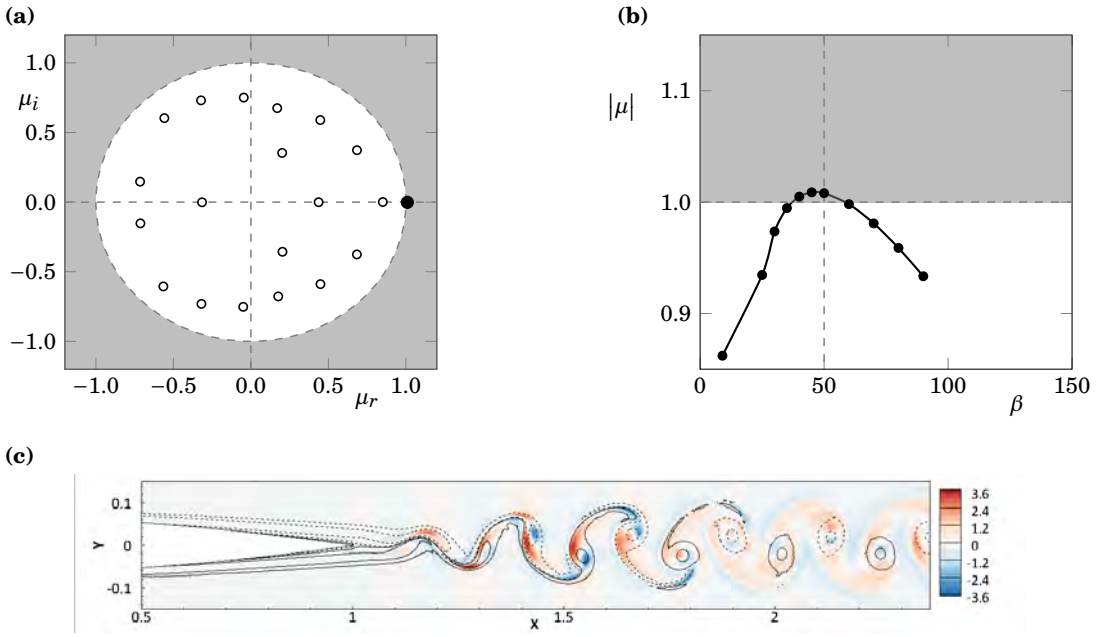

Figure 2.14 – *Floquet analysis around periodic flow solution at* $Re = 30\,000$ *and* $\alpha = 0°$. *(a)* 20 *Floquet multipliers computed for the spanwise wavenumber* $\beta = 50$, *represented on the complex plane* (μ_r, μ_i). *The unstable region outside the unit circle* $|\mu| > 1$ *is represented by the grey zone. The black bigger circle corresponds to the leading synchronous Floquet multiplier. (b) Absolute value of the leading Floquet multiplier,* $|\mu|$, *as a function of the spanwise wavenumber,* β. *(c) Instantaneous spanwise velocity* $\hat{W}_\beta$ *(colours) of the leading Floquet eigenmode for* $\beta = 50$. *The black isocontours represent the spanwise vorticity of the corresponding instant of the periodic flow* ($\Omega_z = \pm 4$ *and* $\Omega_z = \pm 16$).

two-dimensional flow becomes unstable to spanwise infinitesimal disturbances for a spanwise wavenumber within this range.

Returning to the case at $\beta = 50$, corresponding to $\lambda_z = 0.126$, the wavelength can be based on a characteristic length on the transverse direction to the freestream (the airfoil thickness), $\lambda_z = 0.12\lambda_z^t$, having $\lambda_z^t = 1.04$. When comparing with the values reported earlier for the circular cylinder case, one finds that this value is in good agreement with the wavelength found for the mode B. The signature of the mode B can also be discerned on the spatial structure of the Floquet eigenmode. Based on the equality 2.3, associated to the even RT-symmetry property of the mode B, one can note that the vorticity surrounding a particular vortex shedding core can be found for the adjacent core but on the symmetric position with respect to x-axis.

The range for which the leading Floquet multiplier is unstable is identified for different Reynolds numbers in figure 2.15. We can firstly note that as the Reynolds number increases, the range of wavenumbers for which the periodic flow solution is unstable increases. One can also note that the wavenumber of the most unstable Floquet multiplier remains constant at $\beta = 50$ with the increase of the Reynolds number. Further, we observe for $Re = 50\,000$ the emergence of a second Floquet multiplier branch at a higher wavenumber, extending the unstable region. The branch could already be identified for $Re = 45\,000$, even if all the corresponding Floquet multipliers are stable. The Floquet multipliers associated to this new branch are also synchronous. For this new branch, at $Re = 50\,000$, the most unstable Floquet multiplier is found for a wavenumber of $\beta = 90$, having $\lambda_z = 0.069$ ($\lambda_z^t = 0.582$).

The comparison between the eigenmodes of the two branches is made at $\beta = 50$. For that, we sketch the spanwise velocity of the corresponding Floquet eigenmodes, $\hat{W}_\beta$, for the two branches in figure 2.16. As in the previous eigenmode representation, the spanwise vorticity associated to an instant of the periodic flow is represented by the black isocontour lines. The topology of the synchronous eigenmode associated to the first branch, in figure 2.16a, resembles the eigenmode previously described at $Re = 30\,000$, presenting values mostly on the cores of the vortex shedding and on the secondary streamwise vortices. As stated before, this mode is comparable to the mode B of the circular cylinder case.

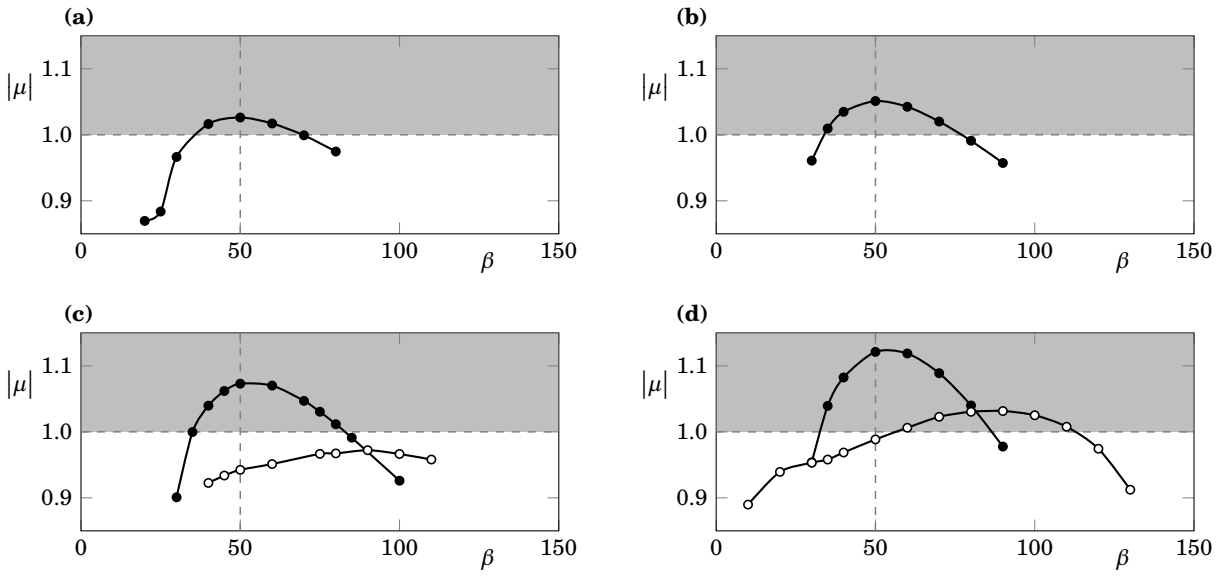

Figure 2.15 – *Absolute value of the Floquet multiplier, $|\mu|$, as a function of the spanwise wavenumber, β, for $\alpha = 0°$ and four Reynolds numbers: (a) $Re = 35\,000$, (b) $Re = 40\,000$, (c) $Re = 45\,000$ and (d) $Re = 50\,000$. The white circles in (c) and (d) correspond to a second branch of synchronous Floquet multipliers, unstable for $Re = 50\,000$.*

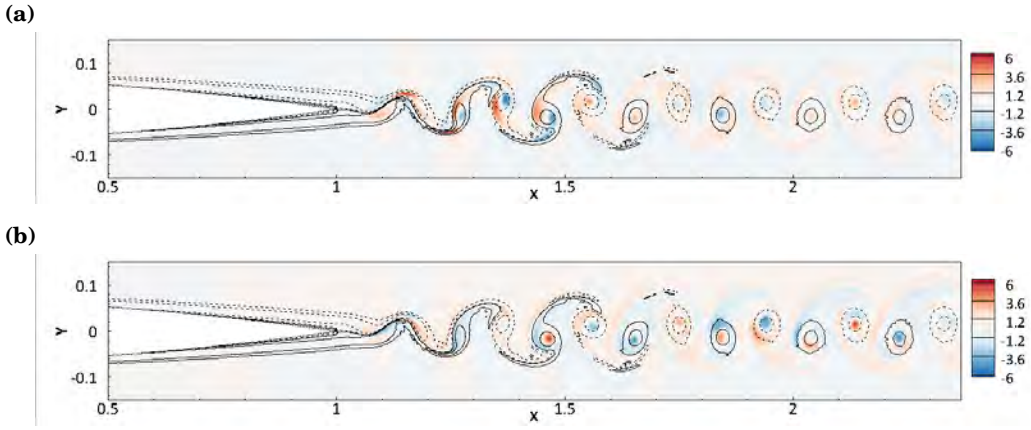

Figure 2.16 – *Instantaneous spanwise velocity $\hat{W}_\beta$ of (a) the first synchronous Floquet eigenmode and (b) the second synchronous Floquet eigenmode at $\beta = 50$ for $Re = 50\,000$ and $\alpha = 0°$. The black isocontours represent the spanwise vorticity of the corresponding instant of the periodic flow ($\Omega_z = \pm 4$ and $\Omega_z = \pm 16$).*

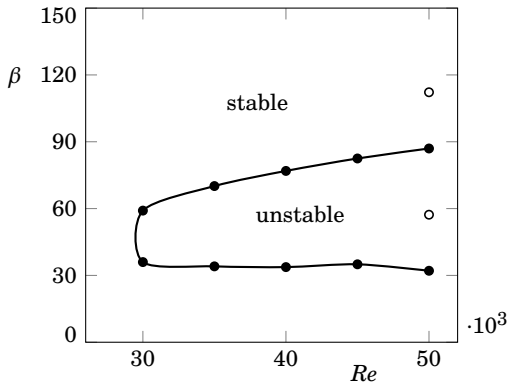

Figure 2.17 – *Neutral curve in the parameter space $Re - \beta$ for the first (black circles) and second (white circles) synchronous Floquet eigenmodes at $\alpha = 0°$.*

Similarly, the synchronous eigenmode associated to the second branch, present in figure 2.16b presents values of $\hat{W}_\beta$ mostly on the cores of the spanwise vortices and on the secondary streamwise vortices. However, this time we discern an odd RT-symmetry, characteristic of the mode A. Based on the equality 2.2, one can note that the vorticity surrounding a particular vortex shedding core can be found for the adjacent core but on the symmetric position with respect to the x-axis and with the opposite sign. Even if the odd RT-symmetry can be found on both the present eigenmode and on the mode A of the cylinder case, the spanwise wavelengths are not similar, since the mode A of the cylinder presents a value of $\lambda_z \approx 4D$, while the present case presents a wavelength based on the airfoil thickness of $\lambda_z^t = 0.582$.

Finally, taking into account the marginally stable Floquet eigenvalues for each Reynolds number, a neutral curve can be sketched, as presented in figure 2.17. This curve separates two regions, where each point is characterised by the parameters (Re, β): a first region, stable, where three-dimensional perturbations are not excited; and a second region, where the two-dimensional periodic flow is unstable to spanwise infinitesimal disturbances. We note that the region of instability increases as the Reynolds number increases. Additionally, we represent the marginal Floquet eigenvalues of the second branch by the white filled circles, at $Re = 50\,000$. The inclusion of this second branch on the neutral curve extends the upper limit of β. The inclusion of more data near the value of $Re = 50\,000$ is suggested for future investigations, in order to better characterise this the neutral curve in this region. Further, we expect the eigenvalue of this second branch to be dominant as the Reynolds numbers increases beyond the value of $Re = 50\,000$.

The Floquet analysis for $\alpha > 0°$ is briefly discussed in appendix C, where some additional results are reported for $\alpha = 5°$ and $\alpha = 6°$. We obtained the emergence of synchronous Floquet eigenmodes for lower Reynolds numbers as the incidence increased. This reasoning is in accordance with the results of Deng *et al.* (2017) and Samuthira Pandi *et al.* (2019), who reported the emergence of three-dimensional instabilities at high angles of attack for lower Reynolds numbers.

2.2 Three-dimensional flow description: Direct Numerical Simulations

In the previous section, we reported the emergence of three-dimensional instabilities on the spanwise direction, associated to a two-dimensional periodic flow, for a closed spanwise wavelength. These instabilities emerged around $Re = 30\,000$ for $\alpha = 0°$. Based on these findings, one can expect the flow field to be three-dimensional for higher Reynolds numbers. In that way, in this section, we proceed to investigate the three-dimensional flow field by the means of Direct

Numerical Simulations (DNS). These simulations are conducted at $Re = 50\,000$, still considering fixed-wing configurations with constant values of the incidence α. We start by describing the instantaneous flow field at $\alpha = 0°$, both in the time and frequency domains. The same exercise is then performed for angles of attack up to $2°$, with a step of $0.5°$.

Recently, DNS has been used to study the flow around the symmetric NACA0012 profile wing by Shan *et al.* (2005), considering a Reynolds number of $Re = 100\,000$ and an angle of attack of $\alpha = 4°$. They found that the vortex shedding from the separated free shear layer was due to a Kelvin–Helmholtz instability. At a higher Reynolds number, $Re = 400\,000$, and $\alpha = 5°$, Hosseini *et al.* (2016) performed the DNS to study the boundary-layer development around a NACA0012 profile wing under strong adverse pressure gradients. For the same Reynolds number as the present study, $Re = 50\,000$, but for larger incidences ($9.25°$ and $12°$) the same case was analysed by Rodríguez *et al.* (2013), finding that the massive separation on the suction side of the wing was caused by a combination of leading-edge and trailing-edge stall. Jones *et al.* (2008) studied the linear stability of the laminar separation bubble present in the time-averaged flow field at the same Reynolds number, for $\alpha = 5°$ and $M = 0.4$ (Mach number), suggesting that the two-dimensional vortex shedding behaviour is absolutely unstable to three-dimensional perturbations, similar to mode B instability observed in the circular cylinder. At $\alpha = 0°$, Jones *et al.* (2006) studied the behaviour of the NACA0012 airfoil from $Re = 10\,000$ to $Re = 50\,000$, for different Mach numbers. They reported that the flow around the airfoil was dominated by vortex shedding from an unstable wake from around $Re = 7\,000$. At $Re = 50\,000$, they report an additional high-amplitude low-frequency oscillation for certain values of the Mach number, which is also found on the incompressible simulation present in the following paragraphs, at $\alpha = 0°$.

2.2.1 Instantaneous flow description at $Re = 50\,000$ and $\alpha = 0°$

We start by describing the results for $\alpha = 0°$. The DNS simulation was initialised from an instantaneous two-dimensional solution extruded in the spanwise direction. After surpassing a transient regime, the instantaneous flow fields are plotted via the quantity Q, a widely used method for visualise and classify three-dimensional flow structures[3]. This quantity was defined in Hunt *et al.* (1988) as

$$Q = \frac{1}{2}\left(\|\boldsymbol{\Omega}^r\|^2 - \|\boldsymbol{S}\|^2\right), \tag{2.5}$$

where $\boldsymbol{\Omega}^r$ and $\boldsymbol{S}$ correspond to the antisymmetric (rotation tensor) and symmetric (shear strain tensor) parts of $\nabla \boldsymbol{U}$, respectively. Accordingly, this quantity represents the local balance between rotation and shear strain rate magnitudes (Kolář, 2007). The Q-criterion corresponds to the representation of a fixed value of Q.

Figure 2.18 – *Visualisation of the instantaneous vorticity structures of a DNS snapshot by the means of a Q-isosurface, with $Q = 75$, coloured by the spanwise vorticity Ω_z (left) and the streamwise vorticity Ω_x (right) at $Re = 50\,000$ and $\alpha = 0°$.*

[3]The use of the vorticity is not considered suitable for the identification of a vortex as it cannot distinguish between pure shearing motions and the actual swirling motion of a vortex (Jeong *et al.*, 1995).

Figure 2.18 presents the flow field at a particular time instant. The vortex identification is made via an isocontour at $Q = 75$. We first note the presence of the spanwise vortex structures, shed from the trailing edge of the airfoil at an angular frequency of $\omega_{VS} = 30.610$ ($T = 0.205$). Additionally, smaller structures are present around these main vortices, associated to the three-dimensionality of the flow field, owning a hairpin form. In other to better visualise all these structures, the Q-criterion is coloured by the spanwise vorticity, on the left, and by the streamwise, vorticity on the right. The main vortex shedding structures are easily identified on the left figure. The alternating coloured pattern is associated to the sense of rotation of each vortex, with the red ones (positive spanwise vorticity) being shed from the lower surface and the blue ones (negative spanwise vorticity) being shed from the upper surface of the airfoil. The hairpin structures, in white, can more easily be discerned on the right figure, where the Q-criterion was coloured by the streamwise vorticity. These structures are formed at the trailing edge of the airfoil, resulting from the instability of the primary spanwise vortices.

Time history of the velocity components and force coefficients

The time history of the streamwise and cross-stream velocities at one point located at $(x, y, z) = (2, 0.1, 0.05)$ is present in figure 2.19 for 370 vortex shedding periods. A simple moving average over five vortex shedding oscillations is computed for the presented time window and represented by the blue line. One can note that the simple moving average of the streamwise velocity is always below 1, with an overall mean of $\overline{U} = 0.995$, while the cross-stream velocity has a mean value of $\overline{V} = 0.00864$. We also note that the maximum values of both signals present an alternating pattern, varying between a higher and a lower value. This behaviour presents a periodicity of $2T$, being associated to the frequency $\omega_{VS}/2$.

In addition to the phenomena associated to ω_{VS} and $\omega_{VS}/2$, a low frequency can be discerned on both time histories, with an angular oscillation of $\omega_{LF} = 0.825$ ($T_{LF} = 7.315$). The period of this low frequency oscillation corresponds to approximately 37 vortex shedding periods. For the velocities on this point, the influence of the low frequency is mainly

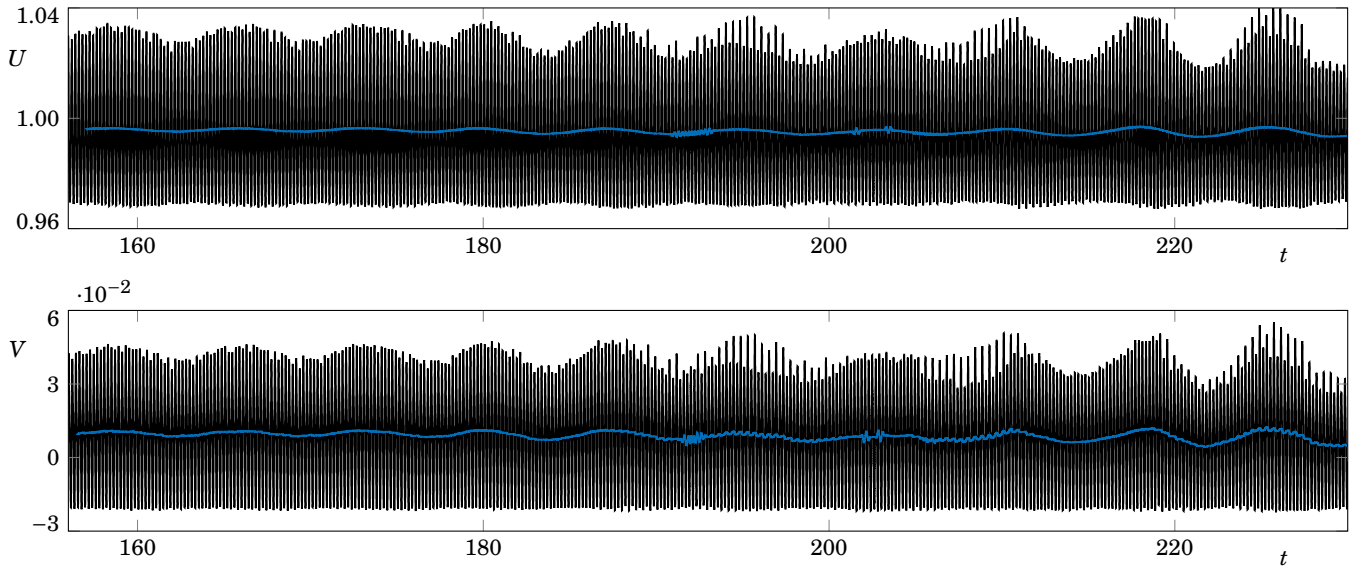

Figure 2.19 – *Time history of the streamwise and cross-stream velocities, U and V, at* $(x, y, z) = (2, 0.1, 0.05)$ *for the DNS simulation at* $Re = 50\,000$ *and* $\alpha = 0°$. *The blue line represents the simple moving average over five vortex shedding periods.*

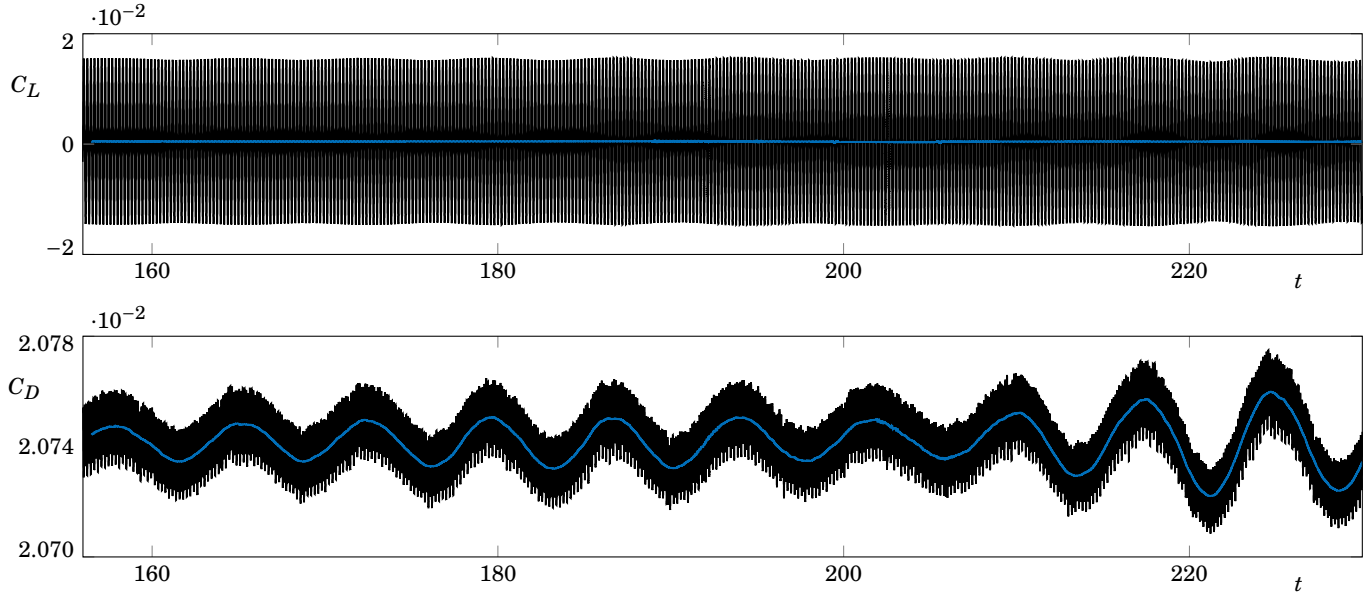

Figure 2.20 – *Time history of the lift and drag coefficients for the DNS simulation at* $Re = 50\,000$ *and* $\alpha = 0°$. *The blue line represents the simple moving average over five vortex shedding periods.*

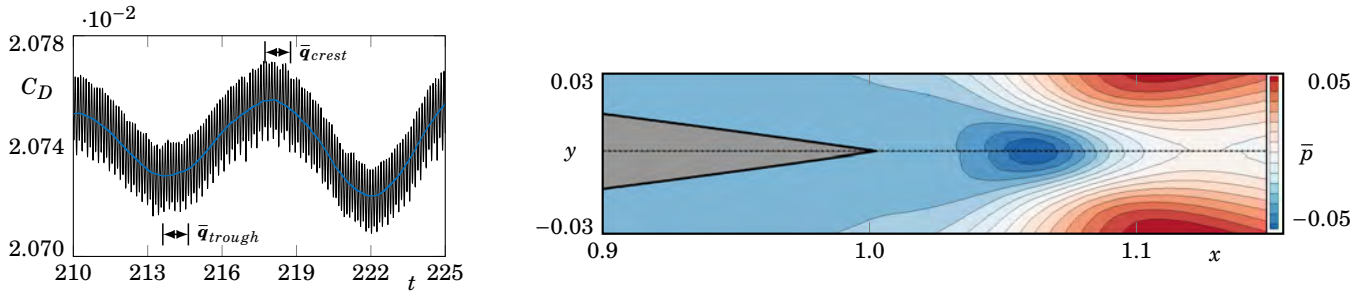

Figure 2.21 – *On the left, time history of the drag coefficient for the DNS simulation at* $Re = 50\,000$ *and* $\alpha = 0°$, *highlighting the low frequency oscillation and two regions where the time- and spanwise-averaged flow solutions where computed, denoted by* $\overline{\boldsymbol{q}}_{trough}$ *and* $\overline{\boldsymbol{q}}_{crest}$. *On the right, pressure fields associated to* $\overline{\boldsymbol{q}}_{trough}$, *on the lower half of the plot, and to* $\overline{\boldsymbol{q}}_{crest}$, *on the upper half of the plot.*

observed in the maximum values of each vortex shedding cycle.

This low frequency can be also discerned on the time history of the global coefficients C_L and C_D, presented in figure 2.20. This time, the simple moving average associated to the lift coefficient does not vary in time, presenting a mean C_L value of zero and a root mean square of $C_L^{RMS} = 0.0105$. The maximum lift coefficient amplitude is found on the crest of the low frequency cycle, with a value of $C_{L,max}^{crest} = 0.0156$, while in the trough the maximum corresponds to $C_{L,max}^{trough} = 0.0146$, corresponding to a difference of 10^{-3}.

Contrary to the lift coefficient, the evolution of C_D presents a different behaviour. The drag coefficient signal is characterised by an overall mean of 0.020741. However, the simple moving average does not have a constant value, with a maximum and minimum values of 0.020760 and 0.020722, respectively. The oscillation of the simple moving average associated to the drag coefficient indicates that the low frequency oscillation of the flow field is associated to a respiration

of the recirculation zone on the rear of the airfoil. This phenomenon resembles to the meandering reported on a circular cylinder by Lehmkuhl *et al.* (2013) at $Re = 3900$.

To further understand this phenomenon, a close-up on the last 15 time units of the drag coefficient time history is reproduced on the left of figure 2.21. Two different time- and spanwise-averaged solutions were computed during five vortex shedding cycles, a first located on the trough of the low frequency cycle, denoted $\overline{\boldsymbol{q}}_{trough}$, and a second one located on the crest, denoted $\overline{\boldsymbol{q}}_{crest}$. On the right of figure 2.21, a close-up near the trailing edge of these mean flow solutions is presented, with the pressure quantity being compared. The mean flow $\overline{\boldsymbol{q}}_{trough}$ is represented in the lower half of the figure, while $\overline{\boldsymbol{q}}_{crest}$ is represented in the upper half, with a dashed-dotted line separating the two pressure fields. We note the presence of a negative pressure zone after the trailing edge, associated to the presence of a time- and spanwise-averaged recirculation zone. We also note that a small discrepancy of the isocontour lines along the axis $y = 0$. This discrepancy shows that the mean recirculation zone associated to $\overline{\boldsymbol{q}}_{crest}$ is smaller, when compared with the mean recirculation zone associated to $\overline{\boldsymbol{q}}_{trough}$. This difference in the pressure fields between the two mean flow solutions illustrates the respiration of the recirculation zone on the rear of the airfoil. For a future work, it would be pertinent to study the possible interaction between this low frequency and the frequency of the structure, for a configuration where the pitch degree of freedom is taken into account.

Hairpin description

We concentrate our attention on the hairpin structures present around the main vortex shedding structures, that were identified on the right of figure 2.18. In figure 2.22, we present a close-up view near the trailing edge of three different instants, with a three-dimensional view on the left and a top view on the right, separated by $T/2$ time units, identified as instants A, B and C. The hairpin structures are highlighted on the top view of instant A, with two pairs of hairpin structures present on the upper part of the wake, and two other pairs present on the lower part of the wake. Firstly, one can note that the flow field is qualitatively periodic, with a period T, by comparing the instants A and C. Additionally, one can observe from the highlighted upper and lower hairpins pairs, that an odd RT-symmetry is present. Following equation 2.2, this means that the legs of the upper and lower hairpins located at the same spanwise coordinate, have an opposite streamwise vorticity value. The spanwise wavelength is estimated to be $\lambda_z = 0.1036$, which corresponds to $\lambda_z^t = 0.8635$ when based on the thickness of the airfoil. These values are obtained from a time-averaged flow, explored in a subsequent paragraph. When comparing these attributes with the Floquet eigenmodes reported in section 2.1.5, we conclude that this flow topology corresponds to the onset of three-dimensional perturbations from a synchronous Floquet eigenmode of the second branch, associated to modes of type A. On this branch of Floquet eigenmodes, an odd RT-symmetry was also found. Further, the most unstable Floquet eigenmode presented a spanwise wavelength of $\lambda_z^t = 0.582$, coherent with the spanwise wavelength of the hairpin structures presented here.

In figure 2.22, one can notice a black line, aligned with the z-axis, located at $(x, y) = (1.2, 0.02)$. We proceed to evaluate the time variation of the cross-stream vorticity on this line, for eight vortex shedding periods. The results are present in figure 2.23. The black isocontour lines represent the Q-criterion at $Q = 75$ used in the previous figures. One can firstly note that only the spanwise vortices shed from the upper surface of the airfoil cross the chosen proben line. This can be inferred from the nearly vertical Q-isocontour lines, found at each T time units, for example readily before and after the instant B.

The corresponding cross-stream vorticity on the instants A, B and C of the previous figure are highlighted by the vertical dashed lines. The intersection of the secondary vortex structures with the considered probe line is illustrated by the small Q-isocontour circles, present at each $T/2$ time units. For example, one can note that the probe line at instants A and C intersects the upper hairpin legs. This can be clearly seen in the three-dimensional view present in figure 2.22.

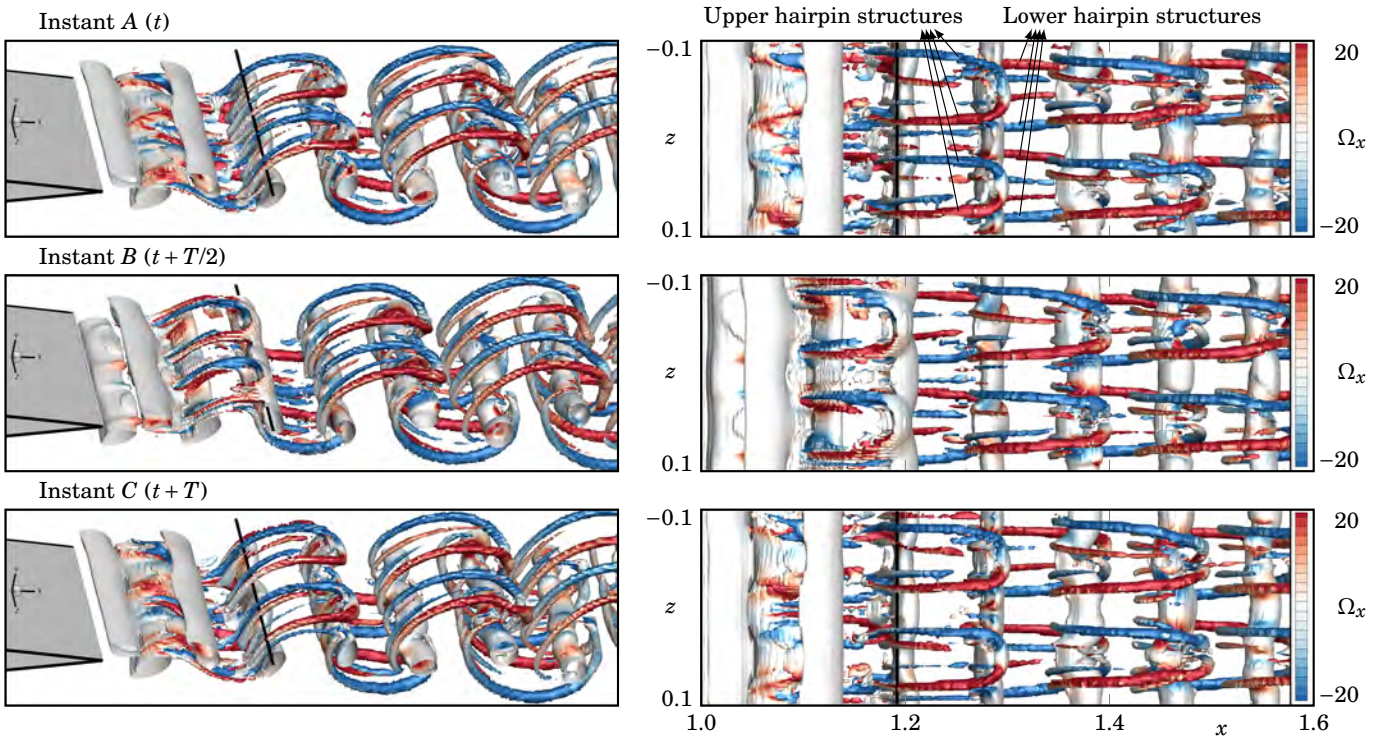

Figure 2.22 – *Three-dimensional view (left) and top view (right) of three DNS instantaneous flow solutions at* $Re = 50\,000$ *and* $\alpha = 0°$*, on the rear of the airfoil, for: the time* t *(top), the time* $t + T/2$ *(centre) and the time* $t + T$ *(bottom). The visualisation is made via a* Q*-isosurface, with* $Q = 75$*, coloured by streamwise vorticity,* Ω_x*. The solid black line along the z-direction, located at* $(x, y) = (1.2, 0.02)$*, is associated to the time history extraction of figure 2.23.*

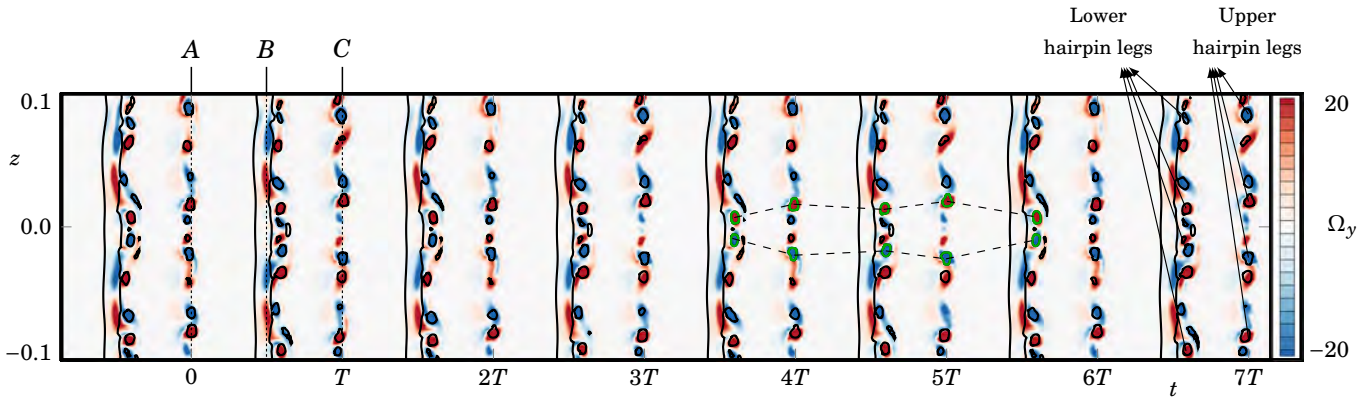

Figure 2.23 – *Time history of the cross-stream vorticity,* Ω_y *along an axis oriented in the z-direction, located at* $(x, y) = (1.2, 0.02)$*. The black isocontours represent the* Q*-isocontour for* $Q = 75$*. The vertical dashed lines correspond to the three instants present in figure 2.22, distanced of* $T/2$ *time units The isocontours highlighted in green and connected by dashed lines, on the zone* $3T < t < 6T$*, illustrate the* $2T$ *periodicity of the spanwise hairpin length.*

Further, we note that around instant B, the legs of the lower hairpins have not cross the probe line yet.

This figure also enables one to track the position of the hairpins legs as function of the time, in particular their spanwise position. When comparing the position of the hairpins legs at the different instants, one can note a small oscillation on their spanwise location. This oscillation is highlighted by the dashed lines connecting the green isocontours, for the centre hairpin legs on the zone $3T < t < 6T$. Despite the fact that the flow structure is qualitatively periodic with a period T, this small oscillation on λ_z shows a periodicity of $2T$. The different frequency components of the flow field are further analysed in the following paragraphs.

Additionally, we also report the presence of several other smaller structures. These structures appear in general in pairs and are located between the legs of each main hairpin and in between adjacent hairpins. They rotate in the opposite sense of the adjacent vortices.

2.2.2 Spectral flow description at $Re = 50\,000$ and $\alpha = 0°$

As a complement of the time analysis, the spectral representation enables a better understand of the fundamental frequencies and corresponding harmonics present in different flow quantities. The signals described previously are here characterised in the frequency space, using a spectral density estimation. The estimation is made using a Welch's method (Welch, 1967), in order to reduce the noise obtained from a simple FFT. The Welch's method estimates the spectral density of a signal by dividing it into several overlapping segments, performing a FFT on each segment of the data multiplied by a tapering function, and averaging the results. The zero frequency, associated to a mean value in the time domain, is removed from the spectral representation for clarity. For the following spectral representations, the signal is divided into two segments, using 60% of overlap and a Hann tapering function. For further details, the reader in invited to consult the origin article (Welch, 1967).

Figure 2.24 presents a spectral density estimation of the streamwise velocity and lift coefficient histories. The velocity spectrum is characterised by an initial peak corresponding to the low frequency $\omega_{LF} = 0.825$, followed by the peaks associated to the vortex shedding frequency, with the fundamental frequency being $\omega_{VS} = 30.610$. The first of these peaks appears at $\omega_{VS}/2$. In the time analysis, this period-doubling property can be discerned in two occasions. Firstly, on the streamwise and cross-stream velocity evolutions (figure 2.19), where an alternating pattern of the maximum values of both signals was noted, presenting a periodicity of $2T$. Secondly, on the variation of the spanwise wavelength of the hairpin structures, on figure 2.23. The peak at $\omega_{VS}/2$ is followed by the fundamental frequency at ω_{VS}, characteristic of

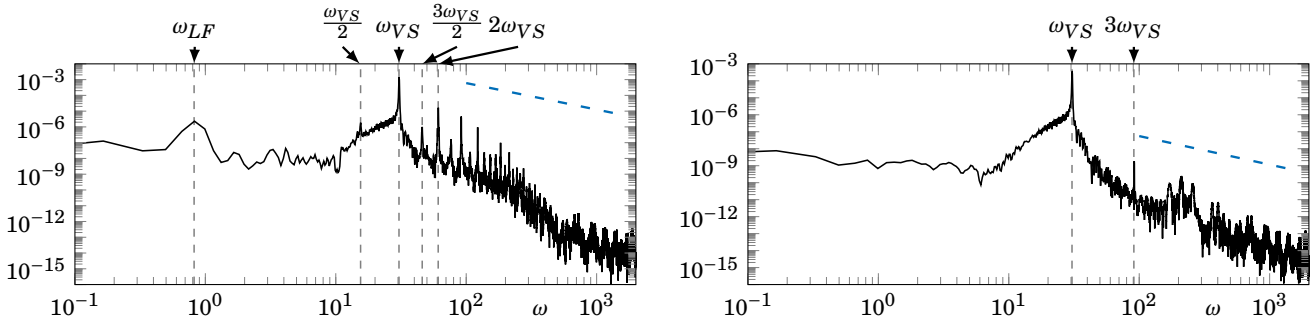

Figure 2.24 – *Spectral density estimation of the streamwise velocity U at $(x, y, z) = (2, 0.1, 0.05)$ (left) and of the lift coefficient C_L (right) for the DNS simulation at $Re = 50\,000$ and $\alpha = 0°$. The dashed blue lines correspond to the $-5/3$ slope. The dashed grey lines highlight the low frequency, the vortex shedding frequency and its harmonics ($\omega_{LF} = 0.825$ and $\omega_{VS} = 30.610$).*

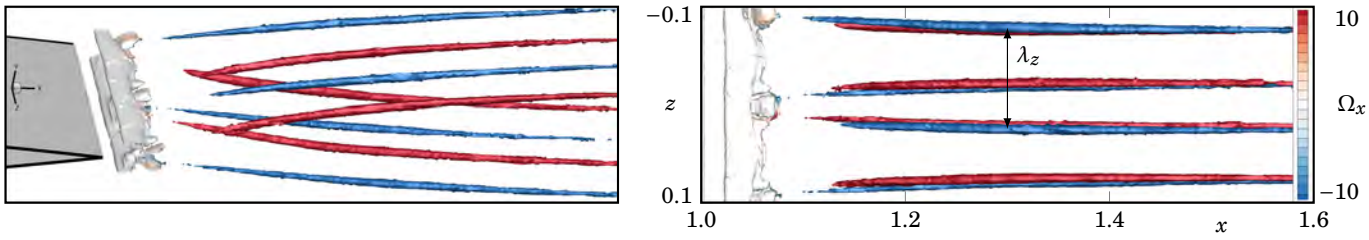

Figure 2.25 – *Three-dimensional representation of the time-averaged flow solution for the DNS simulation at* $Re = 50\,000$ *and* $\alpha = 0°$*, with a Q-isosurface at* $Q = 50$*, coloured by the streamwise vorticity,* Ω_x*, with a three-dimensional view (left) and a top view (right).*

the vortex shedding phenomenon. The following peaks, with a lower amplitude, correspond to the combination of the former to frequencies, *e.g.*, $\omega_{VS}/2 + \omega_{VS} = 3\omega_{VS}/2$.

The spectrum of C_L presents a less informative content, as only the fundamental frequency ω_{VS} and its harmonic $3\omega_{VS}$ have an important value. This is associated to the fact that the lift coefficient is a global quantity, integrated over the airfoil surface, which tends to present more smooth and clean results, in contrast to the velocity value at one point in space.

The dashed blue lines correspond to the Kolmogorov law, which states that homogeneous and isotropic turbulence energy decays with the frequency at a logarithmic rate of −5/3. As can be seen in the figures, the −5/3 rate of decay is relatively well approximated for the considered frequency range.

We proceed to the computation of the three-dimensional time-averaged flow. Figure 2.25 presents a close-up near the trailing edge and a top view of a Q-isosurface at $Q = 50$, coloured by the streamwise vorticity. Firstly, a close isosurface near the trailing edge can be discerned on each side of the airfoil, corresponding to the time-averaged recirculation zone. These isosurfaces are mainly coloured in white, as they are dominated by spanwise vorticity and not streamwise vorticity. In contrast, the red and blue values of the streamwise vorticity can be seen in the time-averaged hairpin structures. The odd RT-symmetry can again be seen here, since that for the same spanwise coordinate, the time-averaged hairpin structures on the lower and upper parts of the wake have opposite spanwise vorticity signs. The top view, on the right, enables one to compute the time-averaged spanwise wavelength of the hairpin structures. The evaluation is made at $x = 1.3$, as the spanwise position of the time-averaged hairpin structures does not vary substantially downstream this abscissa. The spanwise wavelength of these time-averaged structures is $\lambda_z = 0.1036$ ($\lambda_z^t = 0.8635$).

In addition to the average in time, we compute the first fundamental harmonic of the flow field, based on the vortex

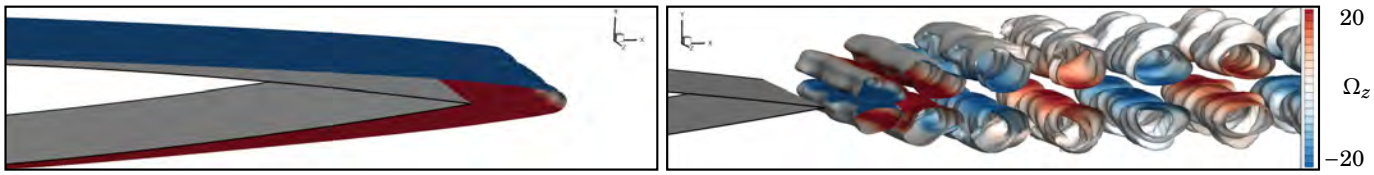

Figure 2.26 – *Three-dimensional representation of the time-averaged and real part of the first harmonic flow solution for the DNS simulation at* $Re = 50\,000$ *and* $\alpha = 0°$*, with an isosurface of streamwise velocity* $\overline{U} = 0.5$ *for the time-averaged flow solution (left) and* $\left\|\overline{U}\right\| = 0.05$ *for the first harmonic (right). The isosurfaces are coloured by the spanwise vorticity,* Ω_z*.*

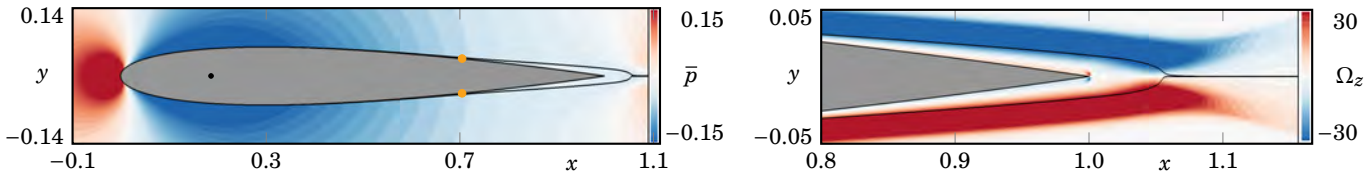

Figure 2.27 – *Time- and spanwise-averaged flow solution at* $Re = 50\,000$ *and* $\alpha = 0°$*: the pressure field around the airfoil (left) and the spanwise vorticity near the trailing edge (right).*

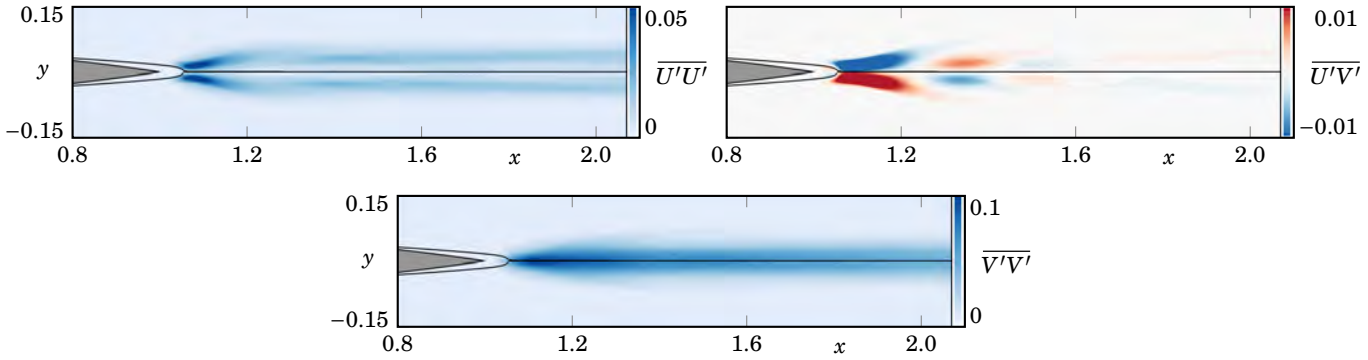

Figure 2.28 – *Fields of the spanwise-averaged Reynolds stress components* $\overline{U'U'}$*,* $\overline{U'V'}$ *and* $\overline{V'V'}$ *at* $Re = 50\,000$ *and* $\alpha = 0°$*. The streamlines enclose the recirculation zone.*

shedding frequency ω_{VS}. In this approximation, we neglect the lower frequency ω_{LF} and we suppose that the flow is periodic in time, with a period T. Figure 2.26 presents an isosurface of streamwise velocity for the time-averaged flow, on the left, and for the real part of the fundamental harmonic, on the right. This time, the isosurfaces are coloured by the spanwise vorticity. In both figures 2.25 and 2.26, one can see that the time-averaged flow is not constant along the spanwise direction.

The time-averaged flow can be further averaged in the spanwise direction in order to obtain a two-dimensional representation of the mean flow, referred to as the time- and spanwise-averaged flow. The pressure field and spanwise vorticity of this quantity are represented in figure 2.27. We first observe, on the left plot, that the laminar boundary layer starting at the leading edge, presents a separation point at $X_d = 0.706$, represented by the yellow dots over the upper and lower airfoil surfaces. However, the boundary layer remains separated by the end of the airfoil, forming a recirculation zone on the rear, enclosed by the black streamlines. Concerning the right plot, the spanwise vorticity shows a negative vorticity on the separated boundary layer of the upper surface, indicating that the flow is locally rotating in the clockwise direction, while in the red zone, below the lower airfoil surface, the flow is rotating in the anticlockwise direction.

The time- and spanwise-averaged components of the Reynolds stress tensor are also predicted. The time-averaged Reynolds stress tensor is accessed via the identify $\overline{\boldsymbol{U}' \otimes \boldsymbol{U}'} = \overline{\boldsymbol{U} \otimes \boldsymbol{U}} - \overline{\overline{\boldsymbol{U}} \otimes \overline{\boldsymbol{U}}}$, where the first term of the right-hand side is computed during the DNS simulation and the second term is obtained during the post-processing phase. The resulting quantity is then averaged in the spanwise direction. Figure 2.28 presents the $\overline{U'U'}$, $\overline{U'V'}$ and $\overline{V'V'}$ spanwise-averaged components of the Reynolds stress tensor. As the tensor is averaged in the spanwise direction, the Reynolds stress components where W' intervenes are not plotted. The black isocontour lines enclose the recirculation zone, present at the rear of the trailing edge of the time- and spanwise-averaged solution. Qualitatively, the predicted Reynolds shear stress shows agreement with the experimental data reported in the literature (*e.g.*, in Lee *et al.* (2005)) in terms of pattern

shape. The Reynolds stress are mainly present on the region of the vortex shedding formation, readily after the end of the recirculation zone on the rear of the airfoil. The components $\overline{U'U'}$ and $\overline{V'V'}$ present a symmetry with respect to the x-axis, while the component $\overline{U'V'}$ present an antisymmetric property with respect to the same axis.

2.2.3 Instantaneous and spectral flow descriptions at $Re = 50\,000$ and $\alpha > 0°$

Our analysis continues at the same Reynolds number, for incidences higher that 0°. The instantaneous vorticity structures for four different incidences are present in figure 2.29. The flow fields for the incidences of 0.5° and 1° present a coherent vortex shedding emission, as the angle $\alpha = 0°$. However, the hairpin vortices present a more disordered organisation. The angles 1.5° and 2° present a turbulent region on the wake of the airfoil, with no recognisable pattern on the wake of the airfoil. One can note that an instantaneous three-dimensional recirculation bubble has emerged on the second half of the upper surface of the airfoil. A zoom near the trailing edge is made in figure 2.30, where these two different regimes can be observed, one for $\alpha \leq 1$ and the other for $\alpha \geq 1.5$.

The time history and corresponding spectral density estimation of the streamwise velocity located at $(x, y, z) = (2, 0.1, 0.05)$ are presented in figure 2.31 for the angles $\alpha = 0.5°$ and $\alpha = 2°$. One can start by noticing that the low oscillation frequency found for the angle $\alpha = 0°$ has disappeared. The streamwise velocity signal at $\alpha = 0.5°$ oscillates at a fundamental frequency $\omega_{VS} = 29.914$, inferior to the case at $\alpha = 0°$. The secondary peak at $\omega_{VS}/2$ is still present, as in the case at $\alpha = 0°$. However, the remaining peaks observed at $\alpha = 0°$ are no longer discerned at $\alpha = 0.5°$, since the flow

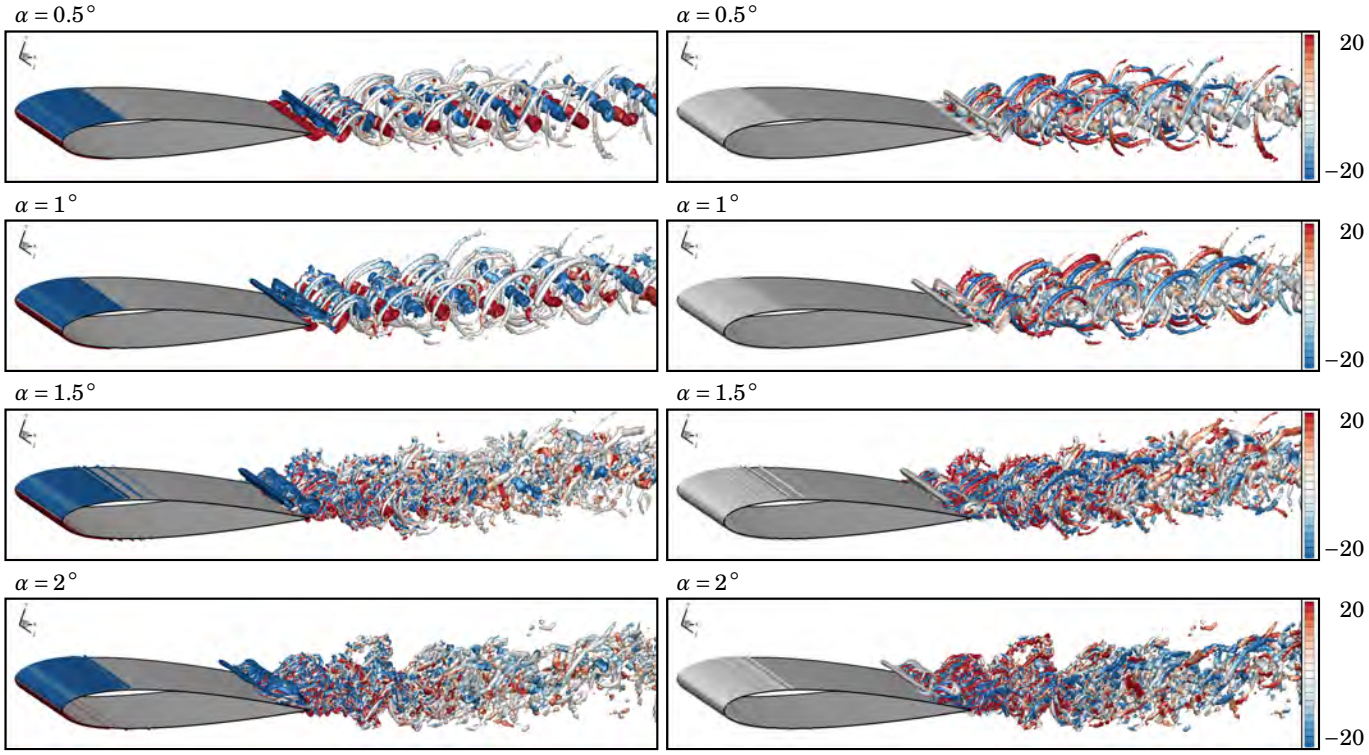

Figure 2.29 – *Visualisation of the instantaneous vorticity structures of DNS snapshots by the means of Q-isosurface, with $Q = 75$, coloured by the spanwise vorticity Ω_z (left) and the streamwise vorticity Ω_x (right) at $Re = 50\,000$ and $\alpha > 0°$.*

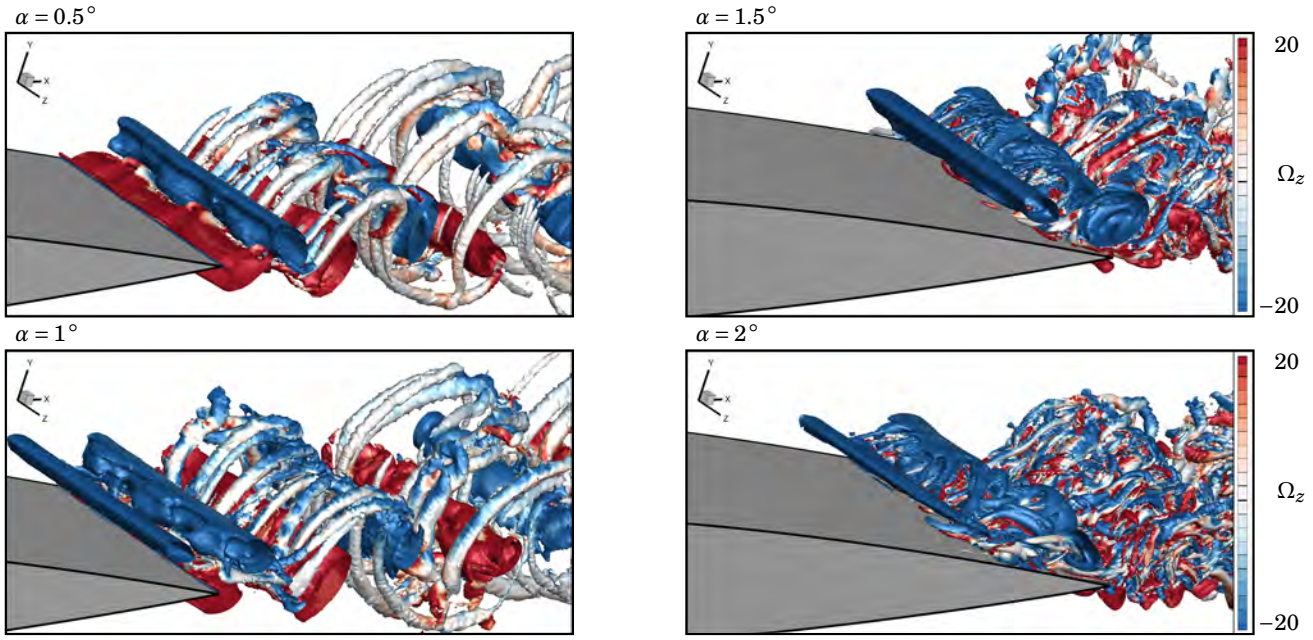

Figure 2.30 – *Visualisation of the instantaneous vorticity structures of DNS snapshots by the means of Q-isosurface, with $Q = 75$, coloured by the spanwise vorticity at $Re = 50\,000$ and $\alpha > 0°$: zoom near trailing edge of the wing.*

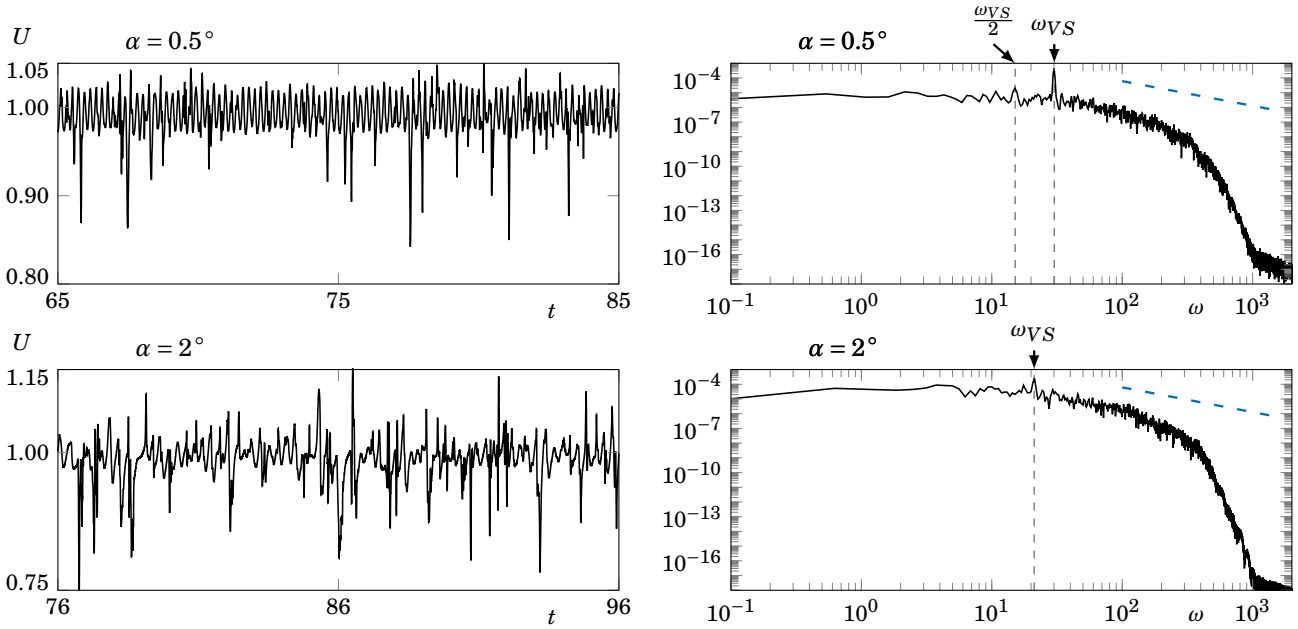

Figure 2.31 – *Time history (left) and corresponding spectral density estimation (right) of the streamwise velocity at $(x, y, z) = (2, 0.1, 0.05)$ for $Re = 50\,000$, $\alpha = 0.5°$ (top) and for $\alpha = 2°$ (bottom). The dashed blue lines correspond to the $-5/3$ slope. The dashed grey lines highlight the vortex shedding frequency and its harmonics ($\omega_{VS} = 29.914$ for $\alpha = 0.5°$ and $\omega_{VS} = 21.136$ for $\alpha = 2°$).*

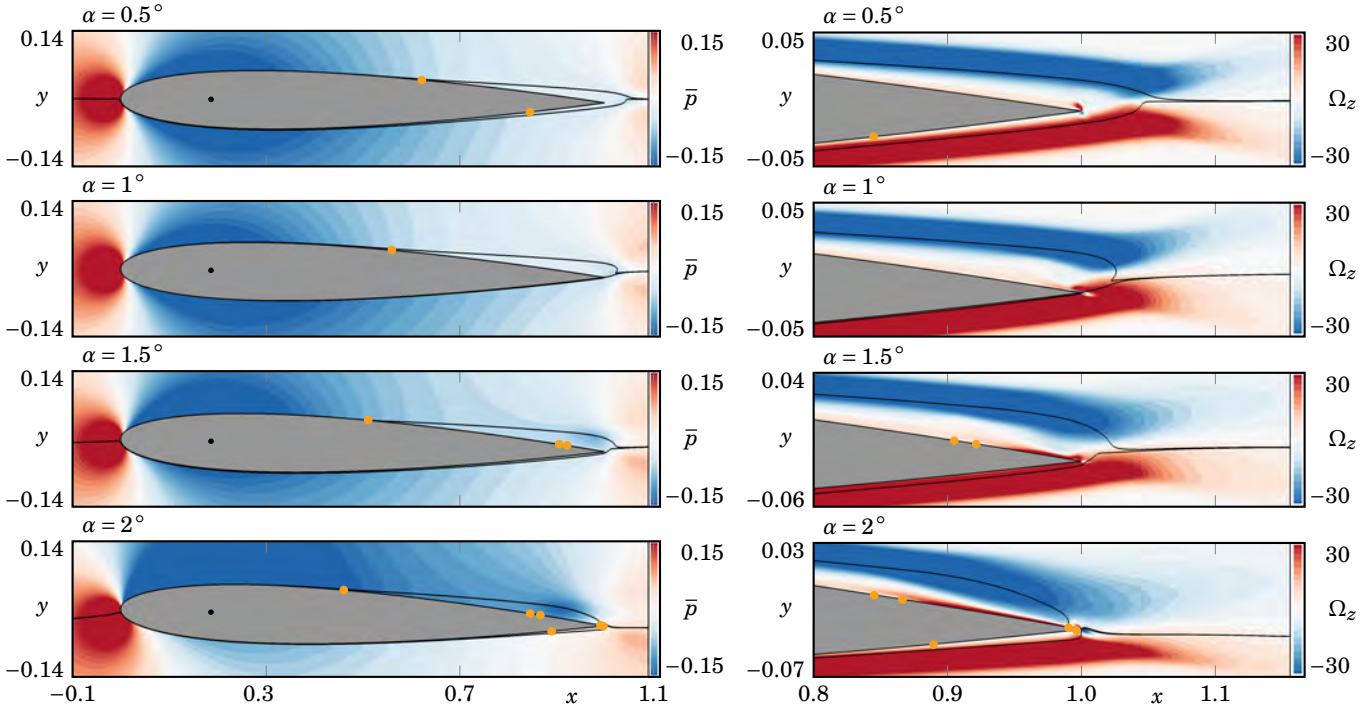

Figure 2.32 – *Time- and spanwise-averaged flow solution at* $Re = 50\,000$ *and* $\alpha > 0°$*: the pressure field around the airfoil (left) and the spanwise vorticity near the trailing edge (right).*

presents a more chaotic behaviour, characteristic of a turbulent flow.

For $\alpha = 2°$, the streamwise velocity signal presents a fundamental frequency with a lower value with respect to the previous incidences ($\omega_{VS} = 21.136$). Contrary to $\alpha = 0°$ and $\alpha = 0.5°$, the temporal signal of the streamwise velocity has lost its main periodic characteristics, as the turbulence level increased substantially with the increase of the angle of attack. Additionally, one can note that the Kolmogorov law, represented by the dashed blue lines is respected up to a frequency around 400 for both angles of attack, suggesting the presence of a cut-off frequency associated to the characteristic size of the mesh elements.

The time- and spanwise-averaged flow fields for $\alpha > 0°$ are presented in figure 2.32, with the separation and possible reattachment points represented by the yellow dots. Concomitantly, the corresponding C_f and C_p distributions over the airfoil are presented in figure 2.33. The solid lines correspond to the distributions over the upper surface, while the dashed lines correspond to the distributions over the lower surface.

The yellow line represents the case at $\alpha = 0°$, with a separation point on both upper and lower surfaces of the airfoil at $X_d = 0.706$, where the C_f has a change in sign. As the angle increases to $\alpha = 0.5°$ (red lines), the separation position of the boundary layer on the upper surface moves upwards ($X_d^{up} = 0.621$), while the separation position associated to the boundary layer on the lower surface moves forward ($X_d^{down} = 0.845$). At $\alpha = 1°$ (blue lines), the boundary layer on the lower surface of the airfoil remains attached (C_f always positive), while the separation position on the upper airfoil surface continues to move upwards ($X_d^{up} = 0.560$). As the boundary layer on the upper surface does not reattach, a recirculation zone is formed in the rear of airfoil. This topology is characteristic of a trailing-edge laminar separation bubble, which was already previously found in the mean flow fields issued from two-dimensional simulations. The same scenario is found for $\alpha = 1.5°$ (green lines). However, this incidence presents a significant drop on the C_f distribution at

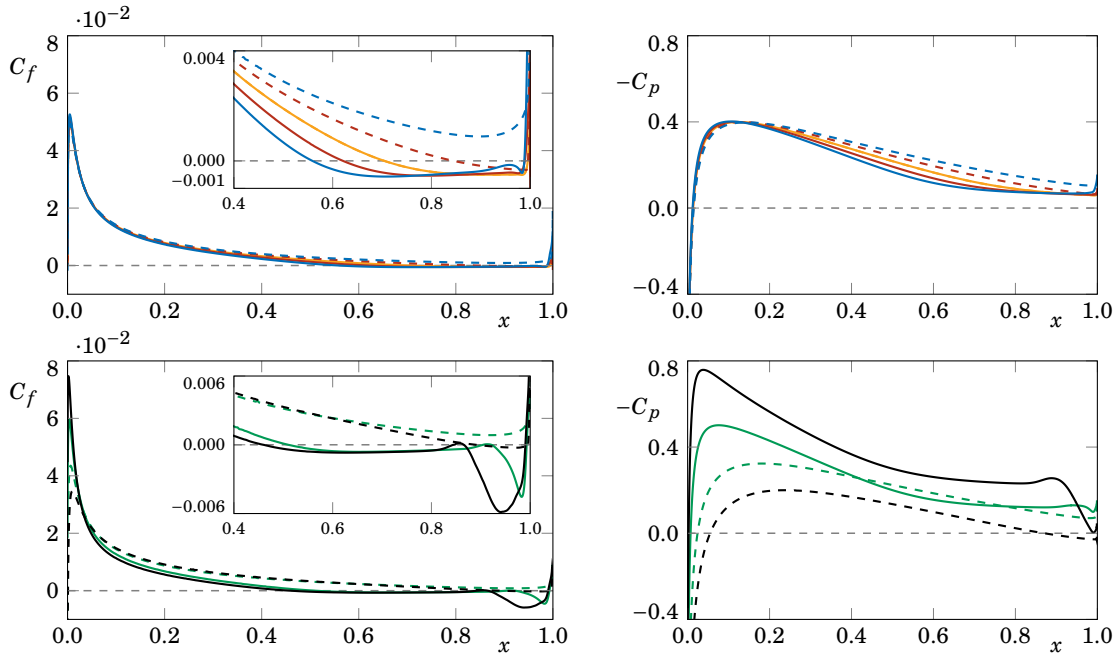

Figure 2.33 – *Distributions of the friction, C_f, and pressure, C_p coefficients of time- and spanwise-averaged flow solutions along the upper (solid) and lower (dashed) surfaces of the airfoil at $Re = 50\,000$ and different incidences: $\alpha = 0°$ (yellow), $\alpha = 0.5°$ (red), $\alpha = 1°$ (blue), $\alpha = 1.5°$ (green) and $\alpha = 2°$ (black).*

the end of the upper surface, associated to the emergence of a big recirculation in the clockwise direction. This drop on the C_f distribution is intensified for $\alpha = 2°$ (black lines). For this last angle, a reattachment of the boundary layer on the upper surface is observed at $X_r^{up} = 0.990$, forming a long laminar separation bubble.

The emergence of a smaller bubble inside the main recirculation zone is observed for the angles $\alpha = 1.5°$ and $\alpha = 2°$. This zone is bounded on figure 2.32 by the yellow dots inside the main recirculation and can also be discerned on the C_f distributions, right before the drop of C_f near the airfoil trailing edge, where the C_f distribution has a small range of positive values. At the same time, a smaller recirculation bubble appears on the lower surface, at $\alpha = 2°$, for the range $0.89 \leq x \leq 1$.

The C_p distribution is also presented, on the right side of figure 2.33. For the angles $\alpha = 0.5°$ and $\alpha = 1°$, one can note that the lower surface $-C_p$ distributions (dashed lines) are located above the upper surfaces distributions (solid lines), for $x \gtrsim 0.2$. This means that, for these angles, it is the lower surface that corresponds to the suction side. This unusual behaviour is associated to the negative lift coefficient found for small incidences, already discussed for the mean flow solutions issued from two-dimensional simulations. The peak value of $-C_p$ on the upper surface, where the fluid velocity is maximum along the airfoil surface, remains approximately constant, as well as its streamwise position, located at $x \approx 0.1$. However, for the angles $\alpha = 1.5°$ and $\alpha = 2°$, this peak drastically moves upwards, accompanied by an increase of its magnitude. For $\alpha = 1.5°$, corresponding to the green curve, the $-C_p$ distribution of the upper and lower surfaces still presents a range $0.42 \leq x \leq 0.78$ where the lower surface corresponds to the suction surface. However, for $\alpha = 2°$, this is no longer the case, with the lower and upper surfaces corresponding to the so-called pressure and suction surfaces, respectively. Additionally, the upper surface $-C_p$ distribution for this last angle presents a roughly constant plateau on the separated zone, with an increase of $-C_p$ around $X \approx 0.9$, corresponding to the depression caused by the laminar

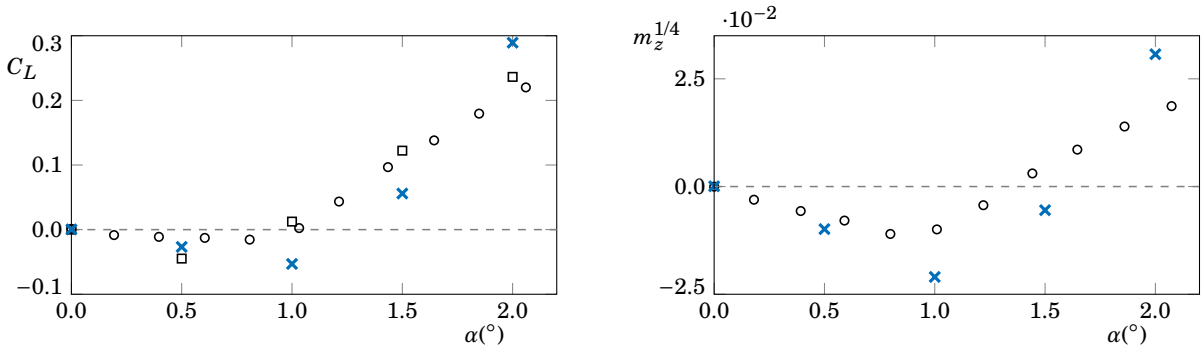

Figure 2.34 – *Evolution of the lift and quarter-chord aerodynamic moment coefficients with the angle of attack for the time- and spanwise-averaged flow solutions at* $Re = 50\,000$*. The comparison is made between the present results (blue crosses), the experimental data from Ohtake* et al. *(2007) (black circles) and the experimental data from Tank* et al. *(2017a) (black squares).*

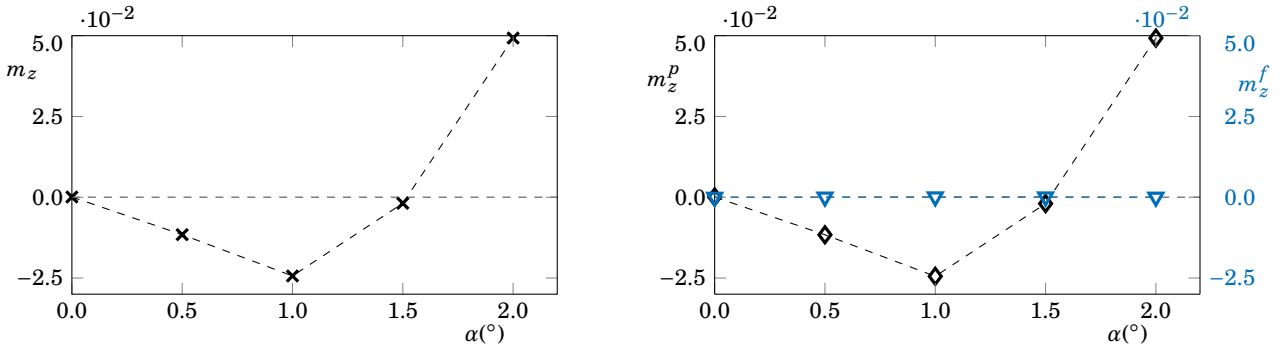

Figure 2.35 – *Evolution of the aerodynamic moment coefficient around* $X_{EC} = 0.186$*, on the left, and the corresponding pressure (black diamonds) and friction (blue triangles) components, on the right, with the angle of attack, for the time- and spanwise-averaged flow solutions at* $Re = 50\,000$*.*

separation bubble.

The C_L and $m_z^{1/4}$ global coefficients, resulting from the integration of the local contributions of the lift and moment coefficients along both surfaces, are presented in figure 2.34, as function of the angle of attack. A comparison is made with experimental data from the recent studies of Ohtake *et al.* (2007) and Tank *et al.* (2017a,b). The present data shows qualitative agreement with the experimental data reported in the literature, with some discrepancies on the values. The negative C_L and $m_z^{1/4}$ tendency is captured on the present simulations, in accordance with the literature data. Concerning the C_L behaviour, we obtain a negative value for the angles $\alpha = 0.5°$ and $\alpha = 1°$. This is in accordance with the inversion of the pressure and suction sides of the $-C_p$ distribution, discussed in the previous paragraph. For $\alpha = 1°$, we obtain a lift coefficient that is still negative, while the literature reports a nearly null value. For $\alpha > 1°$, the lift coefficient changes sign, being positive and increasing as the angle of attack increases. The same behaviour is found for the quarter-chord aerodynamic moment coefficient, $m_z^{1/4}$. In this case, the moment is negative for $\alpha \leq 1.5°$ and positive for $\alpha = 2°$.

The behaviour of the aerodynamic moment with α is also found for the aerodynamic moment around the elastic centre $X_{EC} = 0.186$. The results are present in figure 2.35. On the left plot, one can note that m_z is negative for the range $\alpha \leq 1.5°$. Additionally, we separate the pressure and friction contributions to the aerodynamic moment coefficient, noted

m_z^p and m_z^f, respectively, represented on the right plot. One can note that the overall behaviour of m_z is governed by its pressure component. The friction component, represented with the same scale by the blue coloured symbols, presents nearly trivial values for all considered incidences. With that in mind, we present in section 2.3 an insight of the m_z–α behaviour, based solely on the decomposition of the pressure component and its evaluation in terms of volume integrals, rather than in terms of surface integrals, as done up until this point. Prior to this analysis, we present a comparison between the two- and three-dimensional results for $Re = 50\,000$.

2.2.4 Comparison between two- and three-dimensional results for $Re = 50\,000$

In the following paragraphs, we compare several features of the two- and three-dimensional simulations at $Re = 50\,000$. We start by comparing the values of the vortex shedding frequency, ω_{VS}, as the angle of attack increases, present in table 2.2. Concerning the two-dimensional results, this quantity was already plotted on the right side of figure 2.9. We first observe that in both 2D and 3D simulations, ω_{VS} decreases as the angle of attack increases. Further, for the angles $\alpha = 0°$, $\alpha = 0.5°$ and $\alpha = 1.5°$ the 3D vortex shedding frequency is very well approximated by the corresponding value of the 2D simulations. The bigger discrepancy is found for $\alpha = 2°$, where for the 2D simulations, we observed the period doubling phenomenon. This phenomenon in not observed in the 3D simulations, even if a decrease of ω_{VS} is observed as the incidence increases.

We also report in table 2.2 the aerodynamic moment coefficient associated to the mean flow solutions issued from 2D and 3D simulations These values were already plotted in figures 2.9 and 2.35. Both curves present a negative region for the smaller incidences, with a very food agreement of the numerical values for $\alpha \leq 1°$. However, the m_z results associated to the 2D simulations present a discontinuity behaviour around $\alpha \approx 1.8°$, already described previously. This discontinuity is not found in the m_z results issued from the 3D simulations. We also report the abscissa of the separation and reattachment points of the boundary layer on the upper surface as function of the angle of attack. The reattachment point only exists for the case at $\alpha = 2°$, associated to the presence of a long laminar separation bubble. We observe a very good agreement on the separation points for all the incidences considered. This can be associated to the fact that, in this region of the space, the flow is mainly two-dimensional, even in the three-dimensional simulations. The reattachment point for the case at $\alpha = 2°$ also presents a very good agreement between the two simulations.

We continue the comparison between the two- and three-dimensional simulations in figure 2.36, where, on the left

	α	0°	0.5°	1°	1.5°	2°
2D	ω_{VS}	30.354	30.150	29.891	23.782	15.172
	m_z	0	−0.01249	−0.02300	−0.02140	0.04751
	X_d^{up}	0.700	0.613	0.557	0.505	0.478
	X_r^{up}	—	—	—	—	0.987
3D	ω_{VS}	30.610	29.914	26.611	23.961	21.136
	m_z	0	−0.01157	−0.02435	−0.00187	0.04927
	X_d^{up}	0.706	0.621	0.560	0.511	0.460
	X_r^{up}	—	—	—	—	0.990

Table 2.2 – *Comparison between two- and three-dimensional simulations at Re = 50 000 as function of the angle of attack: vortex shedding oscillation frequency, ω_{VS}, mean flow aerodynamic moment, m_z, and abscissa of the separation and reattachment points of the upper boundary layer, X_d^{up} and X_r^{up}.*

side, we sketch the C_f distribution over the upper surface of the airfoil for the different considered incidences and, on the right side, we plot the difference between pressure fields of the mean flow solutions issued from 2D and 3D simulations. Concerning the C_f distributions, we observe that the curves associated to the 2D simulations (black curves) are in very good agreement with the 3D results (green curves). For the lower incidences, the superposition of both curves is observed for the entire abscissa along the airfoil. The main differences are observed for the angles $\alpha = 1.5°$ and $\alpha = 2°$, for $x \gtrsim 0.85$.

Concerning the difference between the pressure fields, the main differences are located around the trailing edge, where a close-up is made on the right side of figure 2.36. Additionally, we sketch the streamlines enclosing the recirculation zone of the mean flow solutions from 3D simulations with solid black lines. The streamlines of the mean flow solutions from 2D simulations are not presented as they are very similar to the ones sketched. Concerning the case at $\alpha = 0°$, the main

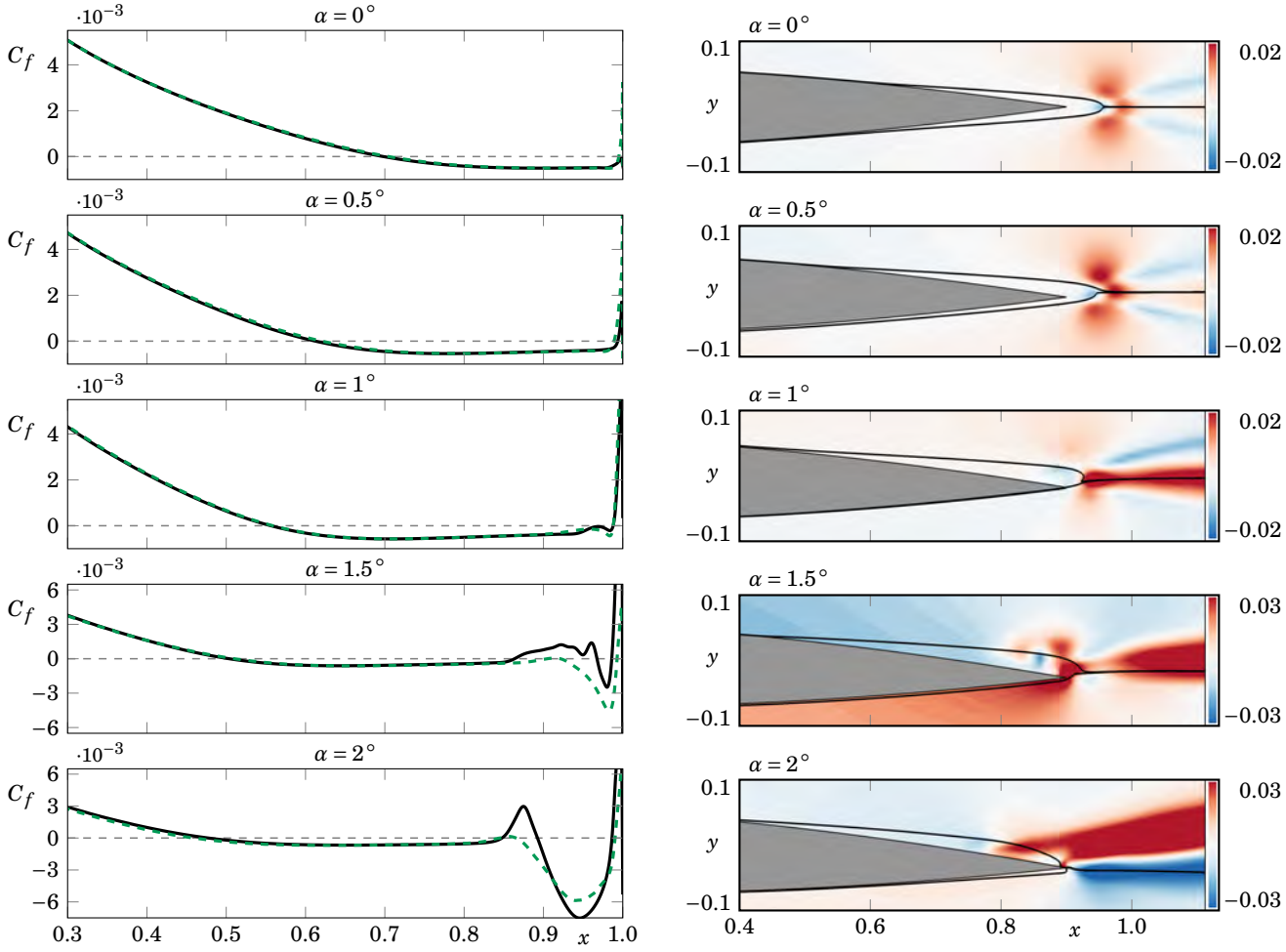

Figure 2.36 – *Comparison between the two- and three-dimensional mean flow solutions at* $Re = 50\,000$ *as function of the angle of attack: on the left, a close-up on the* C_f *distribution over the upper surface on the second half of the airfoil for the mean flow solutions issued from 2D simulations (solid black) and from 3D simulations (dashed green). On the right, difference between the pressure fields of the mean flow solutions from 2D and 3D simulations. The solid black lines represent the streamlines enclosing the recirculation zone for a mean flow issued from 3D simulations.*

differences are located outside the recirculation zone. These differences increase with the angle of attack, but remain outside the recirculation zone for $\alpha \leq 1^\circ$. As a consequence, the values of the aerodynamic moment coefficient of the mean flow solutions from 2D and 3D simulations present a relatively small difference, as discussed in table 2.2. The case at $\alpha = 1.5^\circ$ presents a difference both located at the rear of the recirculation zone and around the airfoil. As a consequence, the differences on the aerodynamic moment coefficient are bigger. For the case at $\alpha = 2^\circ$, the differences are again mainly located outside the recirculation zone, with relatively higher values when compared with the lower incidences.

We conclude that the unsteady characteristics of the two- and three-dimensional simulations present significant differences, not only on the vortex shedding frequency, discussed in this section, but also on the spatial distribution of the flow solutions, presented in the previous sections. On the other hand, we conclude that the time- and spanwise-averaged mean flow solution issued from 3D simulations is well approximated by the mean flow solution from 2D simulations, in particular for the lower incidences.

2.3 Decomposition of the pressure component on the mean aerodynamic moment

2.3.1 Mathematical formulation

The aim of this section is to quantitatively correlate specific volume contributions of the Navier–Stokes equations, such as the convective and the Reynolds stress terms, to the behaviour of the aerodynamic moment coefficient. This is accomplished by defining the moment acting on the airfoil not as a surface integral, but as a volume integral, that takes into account the spatial distribution of the flow structures. This approach is based on a force decomposition method, recently used in the works of Zhang *et al.* (2015a) and Menon *et al.* (2021a). One of the first works discussing this idea, Quartapelle *et al.* (1983), showed that the forces and moments acting on a body immersed in a fluid flow could be written as integrals of the velocity field and its derivatives by projecting the Navier–Stokes equations onto the gradient of an auxiliary harmonic potential. This approach is discussed in the following paragraphs.

The mean aerodynamic moment coefficient generated by the airfoil is given by the sum of its pressure and friction components as:

$$\boldsymbol{m} = \boldsymbol{m}^p + \boldsymbol{m}^f \,, \tag{2.6}$$

with the $\boldsymbol{e}_z$-components noted as $m_z = m_z^p + m_z^f$. Hitherto, their value was computed using a surface integral, present in equation 1.8 (page 23), and adimensionalised using the last expression of equations 1.10. In this section, we present an equivalent formulation, based on volume integrals, in order to evaluate these quantities.

The evolution of m_z^p and m_z^f with the angle of attack is illustrated on the right of figure 2.35. As discussed previously, the total evolution of the mean aerodynamic moment coefficient is mainly governed by its pressure component, m_z^p. With that in mind, we henceforward concentrate our attention on the decomposition of this pressure component. The pressure component of the mean aerodynamic moment coefficient along the $\boldsymbol{e}_z$-axis can be computed with the integration of the pressure stress along the airfoil surface as

$$m_z^p = \int_{\Gamma_w} [(\boldsymbol{X} - \boldsymbol{X}_{EC}) \times (-p\boldsymbol{n}_w)] \cdot \boldsymbol{e}_z \, \mathrm{d}\Gamma_w \,. \tag{2.7}$$

In order to express the same quantity in terms of a volume integral, the first step consists in multiplying the Navier–Stokes momentum equation associated to the mean flow (equation 1.39a, page 41) by the gradient of a potential function ϕ,

followed by an integration of the result over the volume Ω:

$$-\int_{\Omega}\nabla p\nabla\phi\,\mathrm{d}\Omega=\int_{\Omega}[(\boldsymbol{U}\cdot\nabla)\boldsymbol{U}]\cdot\nabla\phi\,\mathrm{d}\Omega+\int_{\Omega}-\frac{1}{Re}\Delta\boldsymbol{U}\cdot\nabla\phi\,\mathrm{d}\Omega+\int_{\Omega}\nabla\cdot\left[\overline{\boldsymbol{U}'\otimes\boldsymbol{U}'}\right]\cdot\nabla\phi\,\mathrm{d}\Omega,\tag{2.8}$$

where, on the left-hand side, we isolate the pressure component, and, on the right-hand side, the convective, diffusive and Reynolds stress components. The notation $\bar{\bullet}$, identifying $\left[\overline{\boldsymbol{U}},\overline{p}\right]^T$ as a mean flow solution, is dropped to simplify the notation. The boundary conditions are also modified in order to simplify the discussion, such that the velocity at the airfoil surface is considered zero, while the far field velocity is equal to $U^{\infty}\left[\cos\left(\bar{\theta}\right),-\sin\left(\bar{\theta}\right)\right]^T$. In that way, the rigid-body velocity field drops from the convective term in equation 1.39a.

We further decompose the pressure term as

$$-\int_{\Omega}\nabla p\nabla\phi\,\mathrm{d}\Omega=\int_{\Omega}p\Delta\phi\,\mathrm{d}\Omega-\int_{\Gamma_w}p\nabla\phi\cdot\boldsymbol{n}_w^{in}\,\mathrm{d}\Gamma_w-\int_{\Gamma_{\infty}}p\nabla\phi\cdot\boldsymbol{n}_{\infty}\,\mathrm{d}\Gamma_{\infty},\tag{2.9a}$$

$$=\int_{\Omega}p\Delta\phi\,\mathrm{d}\Omega+\int_{\Gamma_w}p\nabla\phi\cdot\boldsymbol{n}_w\,\mathrm{d}\Gamma_w-\int_{\Gamma_{\infty}}p\nabla\phi\cdot\boldsymbol{n}_{\infty}\,\mathrm{d}\Gamma_{\infty},\tag{2.9b}$$

where $\boldsymbol{n}_w^{in}$ represents the unit normal vector pointing outward of the fluid, *i.e.*, inward of the profile. At the same time, $\boldsymbol{n}_w=-\boldsymbol{n}_w^{in}$ is the outward of the profile unit normal vector, $\Gamma_{\infty}=\Gamma_{in}\cup\Gamma_{out}$ is the far field boundary and $\boldsymbol{n}_{\infty}$ its outward unit normal vector. The potential function, $\phi=\phi_M$, associated to the definition of the aerodynamic moment coefficient, satisfies

$$\begin{cases}\Delta\phi_M=0 & \text{in }\Omega,\quad(2.10a)\\ \nabla\phi_M\cdot\boldsymbol{n}_w=-[(\boldsymbol{X}-\boldsymbol{X}_{EC})\times\boldsymbol{n}_w]\cdot\boldsymbol{e}_z & \text{in }\Gamma_w,\quad(2.10b)\\ \phi_M=0 & \text{in }\Gamma_{\infty}.\quad(2.10c)\end{cases}$$

Note that ϕ_M represents a potential angular displacement around the elastic centre. The same reasoning could have been made for the lift and drag coefficients, by choosing the appropriate boundary condition of the potential function along the airfoil, in equation 2.10b. With the definition of ϕ_M, equation 2.9b can be simplified as

$$-\int_{\Omega}\nabla p\nabla\phi_M\,\mathrm{d}\Omega=\int_{\Gamma_w}[(\boldsymbol{X}-\boldsymbol{X}_{EC})\times(-p\boldsymbol{n}_w)]\cdot\boldsymbol{e}_z\,\mathrm{d}\Gamma_w=m_z^p.\tag{2.11}$$

This equation gives a different way of computing the pressure component of the mean aerodynamic moment coefficient, by the means of a volume integral.

Further, from equation 2.8, one can note that m_z^p can be obtained as a sum of different moment-producing mechanisms:

$$m_z^p = m_z^{p,conv} + m_z^{p,diff} + m_z^{p,ReStress} \quad \text{with} \begin{cases} m_z^{p,conv} = \displaystyle\int_\Omega [(\boldsymbol{U}\cdot\nabla)\boldsymbol{U}]\cdot\nabla\phi_M \,\mathrm{d}\Omega\,, & (2.12a) \\ m_z^{p,diff} = \displaystyle\int_\Omega -\frac{1}{Re}\Delta\boldsymbol{U}\cdot\nabla\phi_M \,\mathrm{d}\Omega\,, & (2.12b) \\ m_z^{p,ReStress} = \displaystyle\int_\Omega \nabla\cdot\left[\overline{\boldsymbol{U}'\otimes\boldsymbol{U}'}\right]\cdot\nabla\phi_M \,\mathrm{d}\Omega\,. & (2.12c) \end{cases}$$

As noted by Jeong *et al.* (1995) and recently by Menon *et al.* (2021b), the convection term can be rewritten in terms of the quantity Q, defined in equation 2.5 (page 89). Using integration by parts (see section A.3, for the complete demonstration), one obtains:

$$\begin{aligned} \int_\Omega [(\boldsymbol{U}\cdot\nabla)\boldsymbol{U}]\cdot\nabla\phi_M \,\mathrm{d}\Omega &= \cancelto{0}{\int_\Gamma \phi_M [(\boldsymbol{U}\cdot\nabla)\boldsymbol{U}]\,\mathrm{d}\Gamma}\,, - \int_\Omega \phi_M \nabla\cdot[(\boldsymbol{U}\cdot\nabla)\boldsymbol{U}]\,\mathrm{d}\Omega \\ &= \int_\Omega 2\phi_M Q \,\mathrm{d}\Omega\,. \end{aligned} \tag{2.13a}$$

This contribution is interpreted as a vortex-induced term and can be further decomposed into a Q positive part and a Q negative part as:

$$\int_\Omega 2\phi_M Q \,\mathrm{d}\Omega = \int_\Omega 2\phi_M Q_p \,\mathrm{d}\Omega + \int_\Omega 2\phi_M Q_n \,\mathrm{d}\Omega\,, \quad \text{with} \quad Q_p = (Q \geq 0)Q \quad \text{and} \quad Q_n = (Q < 0)Q\,. \tag{2.14}$$

The term with Q_p is associated to the spatial regions that contributes to the moment via the rotation of the flow, whereas the term with Q_n is associated to the spatial regions that contributes to the moment via the shear strain of the flow.

In the following sections, we describe the results at $Re = 50\,000$, for $\alpha = 0.5°$ and $\alpha = 1°$ in a first part. We then proceed to the analysis of the angles $\alpha = 1.5°$ and $\alpha = 2°$.

2.3.2 Results for $\alpha = 0.5°$ and $\alpha = 1°$

In equation 2.11, we demonstrated that the pressure component of the aerodynamic moment coefficient can be computed via the traditional integration of the pressure efforts along the wall, or via a volume integral, where the gradient of the potential function ϕ_M intervenes. The spatial distribution of the term $-\nabla p\nabla\phi_M$, present inside the volume integral, is plotted in figure 2.37, for the angles $\alpha = 0.5°$ and $\alpha = 1°$. The important values of this quantity are mainly present at the leading edge and at the trailing edge. We recall that a volume integral of this field equates for the pressure component of the aerodynamic moment, m_z^p. We first note that the upper and lower side contributions on the leading edge appear to qualitatively equilibrate each other, with a spatial structure resembling to a dipole. However, such conclusion is hard to make for the trailing edge zone, where for both angles, the upper side is mainly dominated by a negative contribution, whereas the lower side is dominated by positive contributions.

In order to better quantify the regions that contributes to this term, we perform the integral of this quantity along the cross-stream direction, for different values along the streamwise direction. In other words, the volume integral is decomposed into its two spatial variables, x and y, and the integral is only performed along the y-direction. Then,

the resulting quantity is plotted as function of the x coordinate. The results are present in figure 2.38, for the range $-0.5 \leq x \leq 1.5$. Outside this range, the contributions are trivial, as observed by the tendency of the curves. The integration of these curves results in the scalar quantity m_z^p, as expected.

We first note that the leading edge contribution has negligible values, as suspected before. However, a small negative contribution is present along the entire chord length, starting readily after the leading edge. Then, a negative peak followed by a positive peak appear on the trailing zone. The amplitude of these peaks increases with the angle of attack. In view of these results, we attribute the initial negative moment to this slight difference between the pressure gradient of the boundary layer contributions to the aerodynamic moment on the lower and upper airfoil surfaces.

We continue our reasoning by separating the above spatial quantity into three main contributions, coming from the convection, the Reynolds stress and the diffusion terms of the Navier–Stokes momentum equation (as present in equation 2.12). The convective and Reynolds stress terms are depicted in figure 2.39, for $\alpha = 0.5°$ and $\alpha = 1°$. The diffusive term is not plotted due to its negligible values, when compared with the presented terms. Concerning the convective term, we observe that, at the leading edge, the convective term presents the dipole resemblance found for the $-\nabla p \nabla \phi_M$ spatial structure. However, at trailing edge, both the convective and Reynolds stress terms present significant values. The former

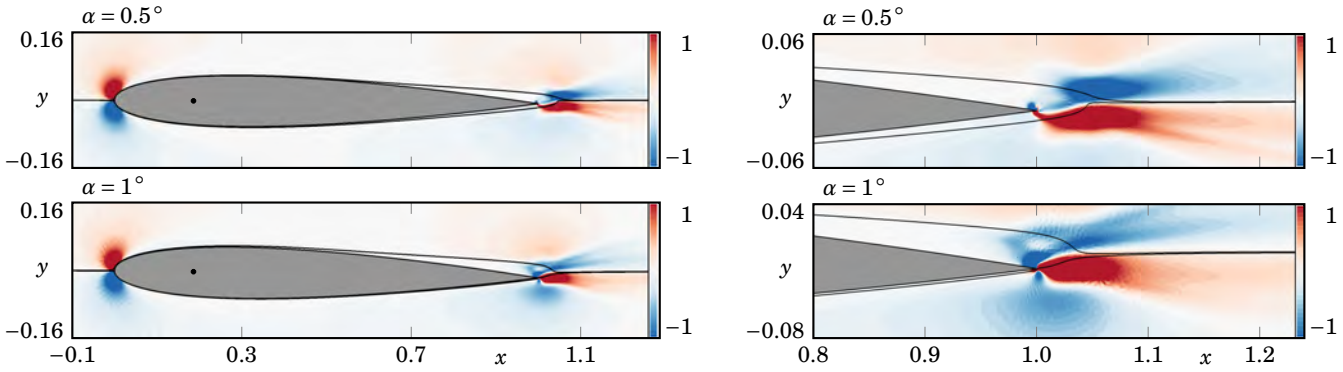

Figure 2.37 – *Spatial distribution of the quantity $-\nabla p \nabla \phi_M$, associated to the time- and spanwise-averaged flow solutions at $Re = 50\,000$ for $\alpha = 0.5°$ (top) and $\alpha = 1°$ (bottom): view around the airfoil (left) and close-up near the trailing edge (right).*

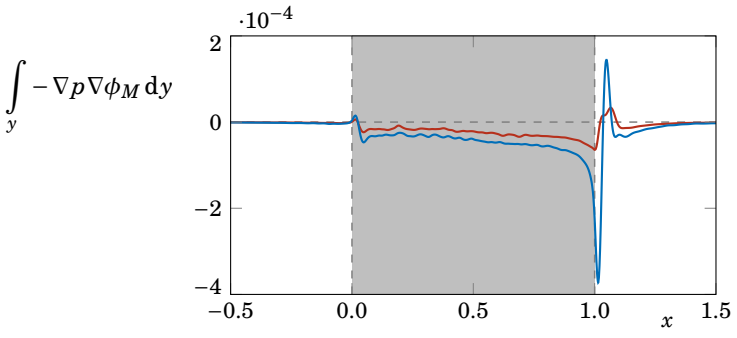

Figure 2.38 – *Evolution of the y integral along the x direction of the quantity $-\nabla p \nabla \phi_M$, associated to the time- and spanwise-averaged flow solutions at $Re = 50\,000$ for $\alpha = 0.5°$ (red) and $\alpha = 1°$ (blue). The grey zone represents the x coordinate range occupied by the airfoil.*

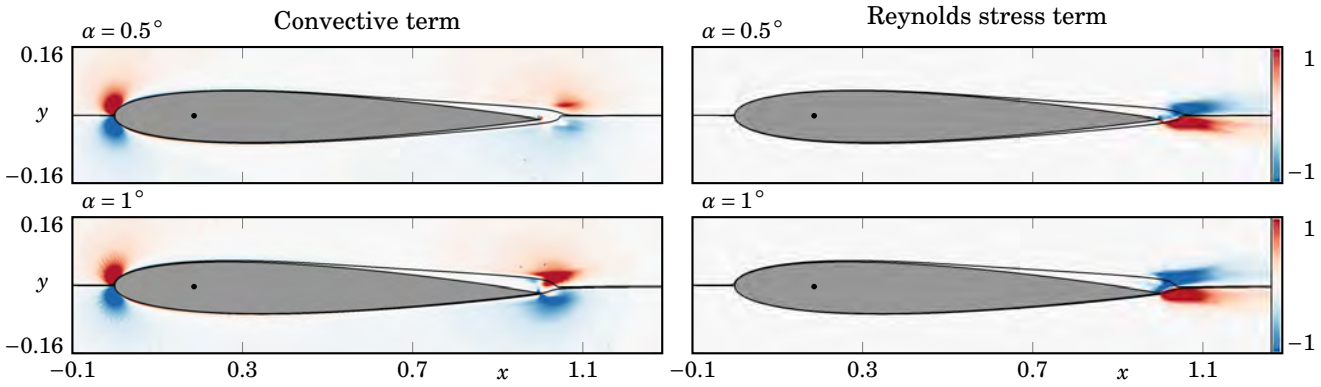

Figure 2.39 – *Spatial distribution of the convective and Reynolds stress terms, associated to the time- and spanwise-averaged flow solutions at* $Re = 50\,000$ *for* $\alpha = 0.5°$ *and* $\alpha = 1°$.

presents mainly positive values for $y > 0$ and negative values for $y < 0$, while the Reynolds stress contributes on the other sense, with negative and positive values for $y > 0$ and $y < 0$, respectively. Observing figure 2.37, we conclude that the trailing edge zone of $-\nabla p \nabla \phi_M$ follows the blue-red pattern dictated by the Reynolds stress term. It is worth noting that the shape pattern of the Reynolds stress term is similar to the Reynolds stress tensor component $\overline{U'V'}$, present in figure 2.28.

We proceed to the volume integration of each of the three terms, contributing to the pressure component of the aerodynamic moment coefficient. The results are depicted in figure 2.40. The same scale is used for all the plotted quantities for a better comparison. On the left, we present the sum of the three contributions, noted m_z^p, along with the convective contribution, noted $m_z^{p,conv}$. On the right, we plot the Reynolds stress and diffusive contributions, $m_z^{p,ReStress}$ and $m_z^{p,diff}$, respectively. The diffusive term has a global negligible contribution, as its spatial form already indicated. In contrast, the Reynolds stress terms also present a negligible contribution after the domain integration, albeit the presence of non negligible terms in their spatial representation. From the left plot, we conclude that the dominant term for the pressure component of the aerodynamic moment coefficient is the convective term, which dictates the increasingly

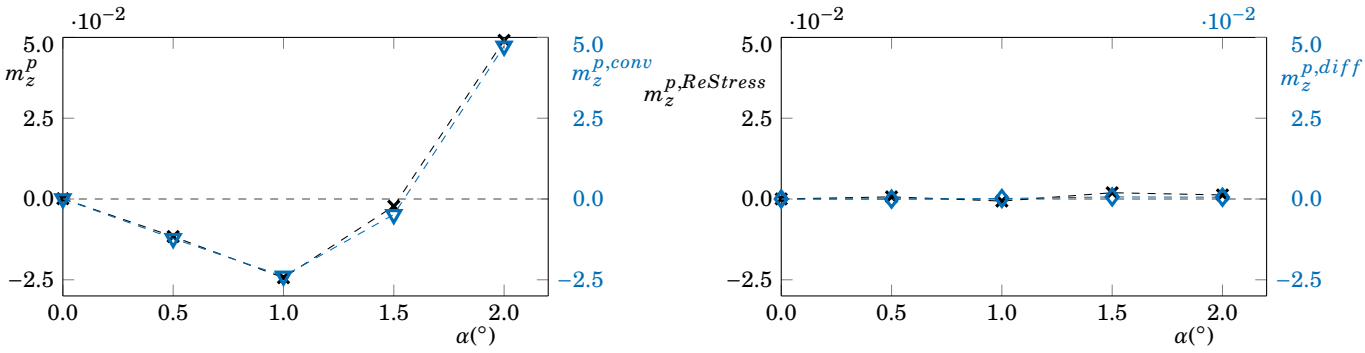

Figure 2.40 – *Evolution of the three volume integrated terms of the pressure component of the aerodynamic moment coefficient around* $X_{EC} = 0.186$ *with the angle of attack, associated to the time- and spanwise-averaged flow solutions at* $Re = 50\,000$*: their sum* m_z^p *(black crosses), the convective term* $m_z^{p,conv}$ *(blue triangles), the Reynolds stress term* $m_z^{p,ReStress}$ *(black crosses) and diffusive term* $m_z^{p,diff}$ *(blue diamonds).*

negative values for $\alpha = 0.5°$, $\alpha = 1°$. The remaining values for $\alpha > 1°$ are discussed in a subsequent part.

We proceed to further decompose the convective term into a contribution coming from the rotation of the flow, $2\phi_M Q_p$, and a part coming from the shear strain, $2\phi_M Q_n$. As these two terms complement each other (cf. equation 2.14), we represent both contributions on the same plot, in figure 2.41. The blue-red colouring represents the spatial structure of $2\phi_M Q_p$, associated to rotational flow zones, whereas the orange-purple colouring represents the spatial structure of $2\phi_M Q_n$, associated to shear strain flow zones. We first note that the contributions at the leading edge are given by the term $2\phi_M Q_n$. This is due to the fact that, in this zone, we observe the deviation of the streamlines associated to the presence of the airfoil. The blue-red contribution appears right after, inside the boundary layer that separates around the mid-chord, up to the trailing edge, with positive values on the upper side and negative values on the lower side. The lower side contribution of $2\phi_M Q_p$ (in blue) has nontrivial values along all the boundary layer up to the trailing edge. On the other hand, the upper side contribution of $2\phi_M Q_p$ (in red) presents a zone around $x \approx 0.7$, where it ceases to exist. The value matches the position of the boundary layer separation on the upper surface previously reported ($X_d^{up} = 0.621$

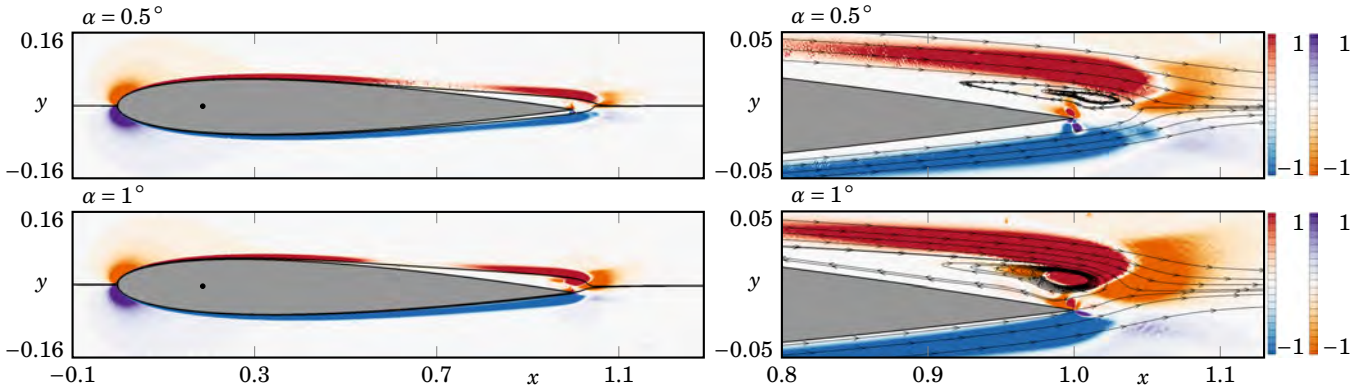

Figure 2.41 – *Spatial distribution of the quantities $2\phi_M Q_p$ (blue-red colouring) and $2\phi_M Q_n$ (orange-purple colouring), associated to the time- and spanwise-averaged flow solutions at $Re = 50\,000$ for $\alpha = 0.5°$ (top) and $\alpha = 1°$ (bottom): view around the airfoil (left) and close-up near the trailing edge (right).*

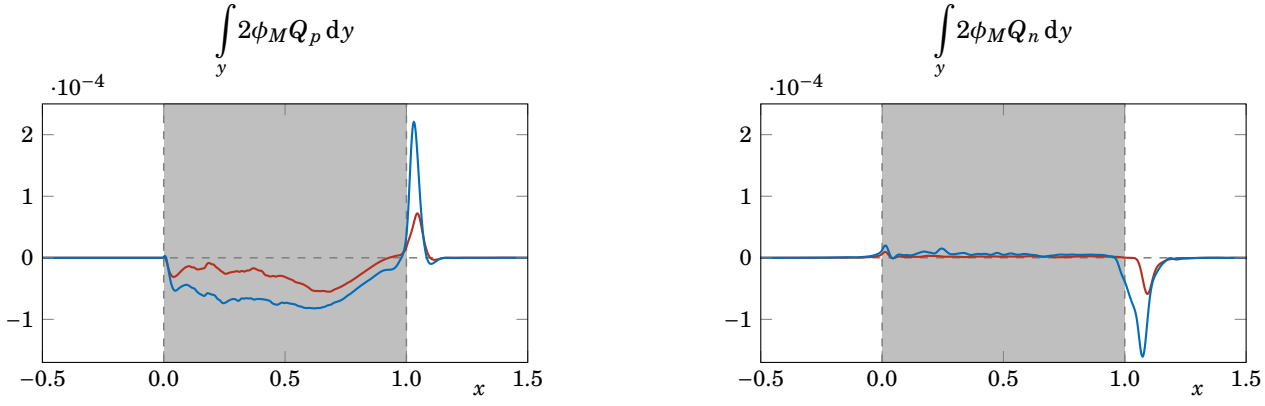

Figure 2.42 – *Evolution of the y integral along the x direction of the quantities $2\phi_M Q_p$ and $2\phi_M Q_n$, associated to the time- and spanwise-averaged flow solutions at $Re = 50\,000$ for $\alpha = 0.5°$ (red) and $\alpha = 1°$ (blue). The grey zone represents the x coordinate range occupied by the airfoil.*

for $\alpha = 0.5°$ and $X_d^{up} = 0.560$ for $\alpha = 1°$, see table 2.2). A significant negative contribution of $2\phi_M Q_n$ (in orange) appears at $x \approx 1.05$. The close-up on the right side of figure 2.41 enables to associate this zone to the deviation of the streamlines coming from the separated boundary layer on the upper surface.

In order to quantify the contributions along the streamwise direction, the quantities $2\phi_M Q_p$ and $2\phi_M Q_n$ are integrated on the y-direction and plotted as function of the x coordinate, as done previously. The results are present in figure 2.42. To what concerns $2\phi_M Q_p$, on the left, this term presents a negative contribution from the leading edge up to the emergence of the recirculation zone at the end of the airfoil. Here, a positive peak emerges, associated to the rotation of the flow on the separated boundary layer. The magnitude of the peak increases as the angle of attack increases, a consequence of the higher rotational character of the flow on this region. To what concerns $2\phi_M Q_n$, a negligible contribution is reported up to the end of the airfoil. From there, a negative peak appears, related to the orange colour observed in figure 2.41. Similarly to the other peaks, its magnitude increases with the increase of the angle of attack.

The total contribution of these two terms is accessed from the integration over the entire volume, present in figure 2.43, as function of the incidence. The rotation and the shear stress terms appear to have the same importance for the angles $\alpha = 0.5°$, $\alpha = 1°$. Both terms are negative, contributing for the initial negative aerodynamic moment found for these small incidences. We proceed to investigate the angles $\alpha = 1.5°$ and $\alpha = 2°$.

2.3.3 Results for $\alpha = 1.5°$ and $\alpha = 2°$

We concentrate our attention on the higher angles $\alpha = 1.5°$ and $\alpha = 2°$, where the pressure component of the moment ceases to decrease and becomes positive. In a first part, we present the spatial distribution of the term $-\nabla p \nabla \phi_M$ on figure 2.44. The contributions are mainly located at the leading and trailing edges of the airfoil, as for the lower angles investigated previously. The leading edge zone continues to present a positive zone and a negative zone on the upper and lower airfoil sides, respectively, that qualitatively appear to balance each other. On the trailing edge, a more complex scenario is found, with a significant positive contribution that dominates the recirculation zone and is intensified as the angle increases.

The values of the cross-stream integration of $-\nabla p \nabla \phi_M$ as function of the x coordinate are present in figure 2.45. Contrary to the lower incidences, a non negligible contribution is found at the leading edge. In this zone, two peaks, one positive followed by a negative one, are present. The magnitude of the peaks increases with the angle of attack. For $\alpha = 1.5°$, a negative plateau follows these initial oscillations up to the trailing edge. At the trailing edge, a positive peak is present. For the case $\alpha = 2°$, the peaks at the leading edge are followed by an increase of the cross-stream integral up

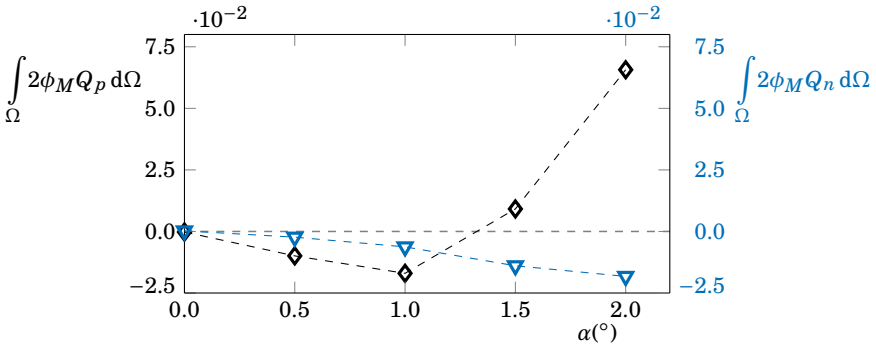

Figure 2.43 – *Evolution of volume integrated contributions from $2\phi_M Q_p$ (black diamonds) and $2\phi_M Q_n$ (blue triangles) with the angle of attack at $Re = 50\,000$.*

to a maximum value at the trailing edge.

As done previously, we sketch the convective and Reynolds stress terms, associated to the decomposition of $-\nabla p \nabla \phi_M$ in figure 2.46. The leading edge continues to be dominated by the convective term, while at the trailing edge, both terms are significant. Further, at the trailing edge, the convective term presents a positive contribution on the separated boundary layer of the upper surface and a smaller negative contribution on the lower side. On the other hand, the Reynolds stress term presents again a similar pattern shape as the Reynolds stress tensor component $\overline{U'V'}$, in figure 2.28. Additionally, the Reynolds stress terms present negative values inside the laminar separation bubble, which can be also found on the spatial distribution of $-\nabla p \nabla \phi_M$.

The evolution of the volume integration of the different contributions to m_z^p with the angle of attack is present in figure 2.40, as discussed previously. The case at $\alpha = 1.5°$ presents nearly zero values for all contributions, making difficult to understand which contribution is relevant. However, the case at $\alpha = 2°$ establishes again the convective component as the one that dominates the behaviour of the pressure component of the aerodynamic moment. Since that m_z^p is dominated by the convective term, we once again divide this term into its rotation contribution and its shear stress contribution. The spatial structures of $2\phi_M Q_p$ and $2\phi_M Q_n$ are present in figure 2.47 for the angles $\alpha = 1.5°$ and $\alpha = 2°$. The leading

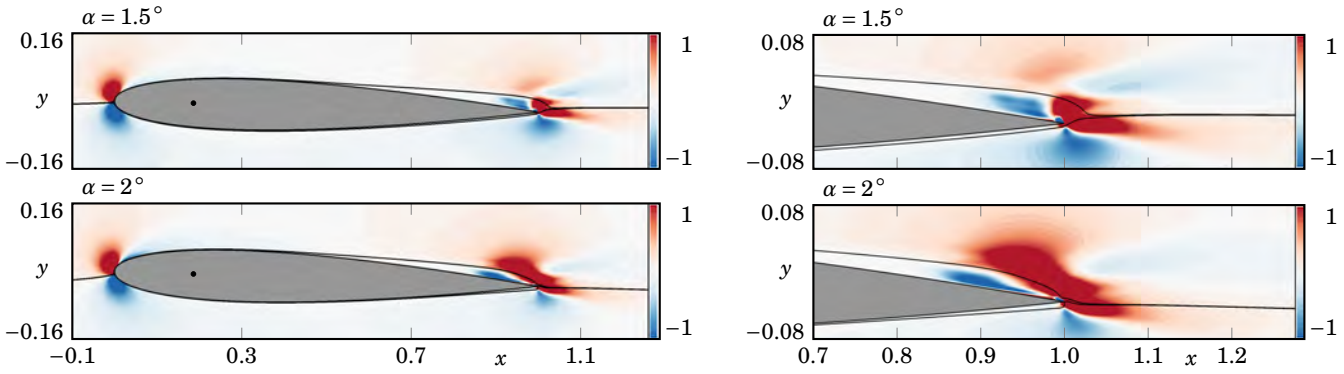

Figure 2.44 – *Spatial distribution of the quantity $-\nabla p \nabla \phi_M$, associated to the time- and spanwise-averaged flow solutions at $Re = 50\,000$ for $\alpha = 1.5°$ (top) and $\alpha = 2°$ (bottom): view around the airfoil (left) and close-up near the trailing edge (right).*

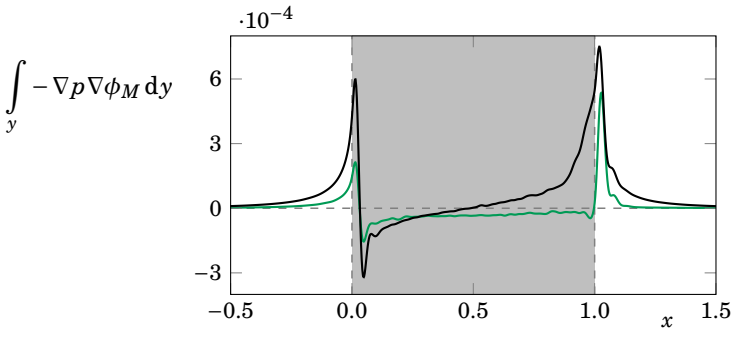

Figure 2.45 – *Evolution of the y integral along the x direction of the quantity $-\nabla p \nabla \phi_M$, associated to the time- and spanwise-averaged flow solutions at $Re = 50\,000$ for $\alpha = 1.5°$ (green) and $\alpha = 2°$ (black). The grey zone represents the x coordinate range occupied by the airfoil.*

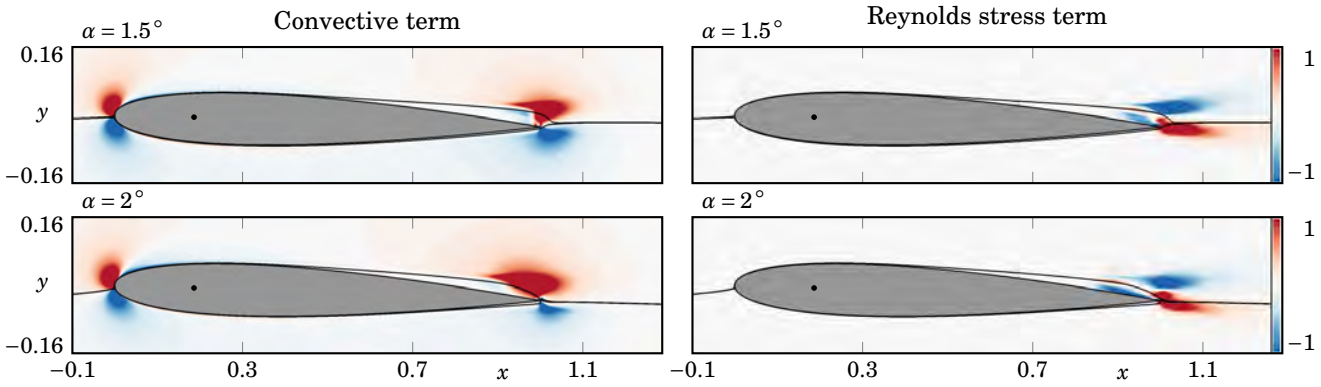

Figure 2.46 – *Spatial distribution of the convective and Reynolds stress terms, associated to the time- and spanwise-averaged flow solutions at* $Re = 50\,000$ *for* $\alpha = 1.5°$ *and* $\alpha = 2°$.

edge is again firstly dominated by a dipole structure coming from the term $2\phi_M Q_n$ (orange-purple colouring), followed by the contributions of $2\phi_M Q_p$ at the emergence of the boundary layer. This time, the positive contribution of $2\phi_M Q_p$ (in red) dominates the entire boundary layer on the upper side, including the separated zone, while the lower side is dominated by a negative contribution (in blue). On the trailing edge zone, different contributions are found, with a positive contribution, coming from the rotational term (in red) at the centre of the laminar separation bubble. The remaining laminar separation bubble presents either no contribution, in the "dead air" region, or a negative contribution coming from the shear stress term (in orange).

The values of the cross-stream integration of the above terms as function of the x coordinate are present in figure 2.48. Unlike the lower angles, a first positive peak is found on the $2\phi_M Q_p$ at the leading edge, followed by a negative region between the leading and trailing edge zones. In this latter zone, both angles exhibit a positive peak. Further, for the angle $\alpha = 2°$ (black curve), this positive peak is followed by a negative one, with a lower intensity. Concerning the evolution of $2\phi_M Q_n$, it presents the same behaviour as the lower angles, with a nearly trivial contribution along the entire airfoil and a negative peak at the trailing edge. This latter contribution is a consequence of the deviation of the streamlines at the

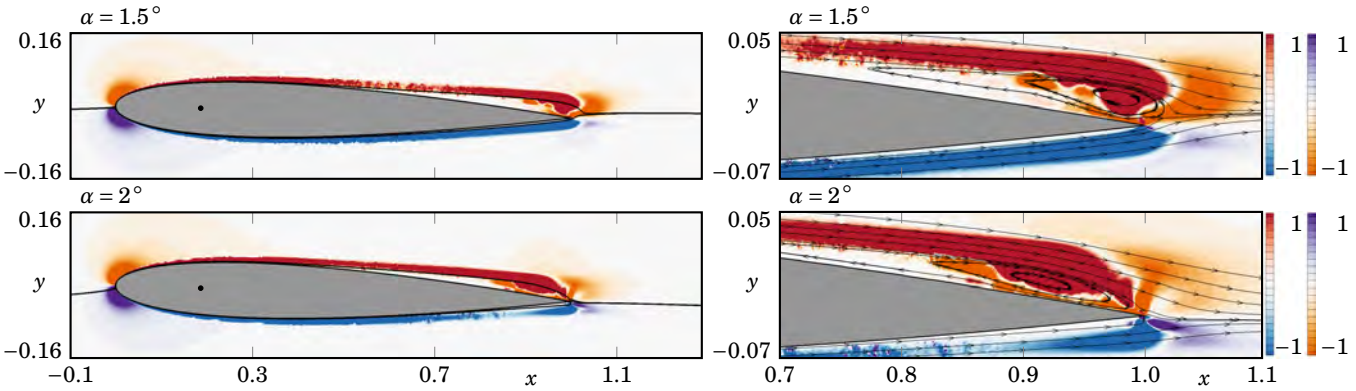

Figure 2.47 – *Spatial distribution of the quantities* $2\phi_M Q_p$ *(blue-red colouring) and* $2\phi_M Q_n$ *(orange-purple colouring), associated to the time- and spanwise-averaged flow solutions at* $Re = 50\,000$ *for* $\alpha = 1.5°$ *(top) and* $\alpha = 2°$ *(bottom): view around the airfoil (left) and close-up near the trailing edge (right).*

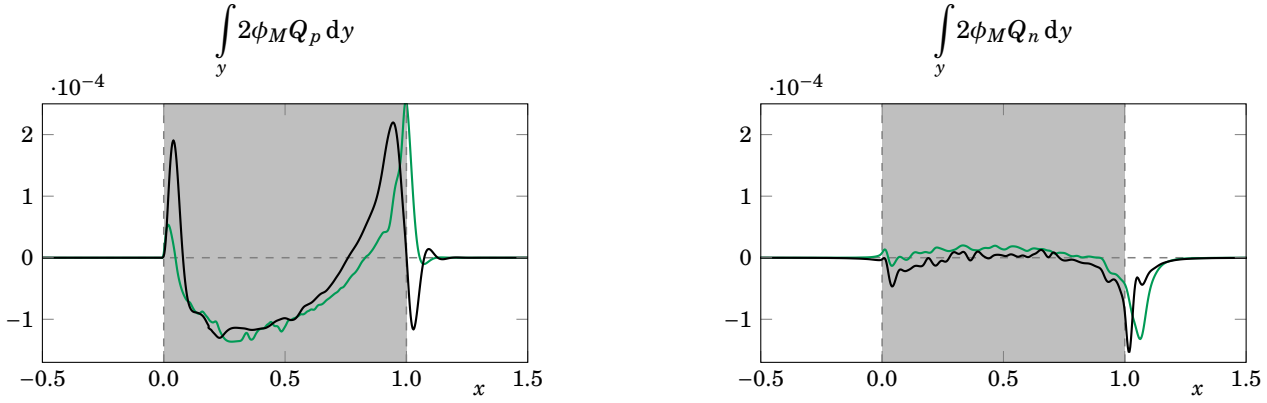

Figure 2.48 – *Evolution of the y integral along the x direction of the quantities $2\phi_M Q_p$ and $2\phi_M Q_n$, associated to the time- and spanwise-averaged flow solutions at $Re = 50\,000$ for $\alpha = 1.5°$ (green) and $\alpha = 2°$ (black). The grey zone represents the x coordinate range occupied by the airfoil.*

trailing edge, as illustrated on the right side of figure 2.47 in the orange coloured zone.

The values of the volume integrations of $2\phi_M Q_p$ and $2\phi_M Q_n$ are present in figure 2.43. In the case $\alpha = 1.5°$, both contributions are significant. Their sum, corresponding to the value of m_z^p, has a slightly negative value. Concerning the case at $\alpha = 2°$, one can observe that the rotational term dominates over the shear stress term. We can conclude that the change in the m_z^p behaviour towards the positive values is a consequence of the convective term contribution, in particular the part that accounts for the rotation of the flow field, as a consequence of the emergence of a laminar separation bubble.

Chapter 3

Methods for mean flow FSI linear stability analyses

One of the objectives of this thesis is the investigation of the linear perturbations that may arise on a FSI configuration, which may explain the onset of nonlinear pitch oscillations of a NACA0012 airfoil. In this regard, this chapter is consecrated to the presentation and implementation of different methods associated to the linear stability analysis of a FSI system around a time-averaged fluid–solid state. The chapter is organised as follows. In a first part, we present a brief introduction of the different approaches found in the literature to solve an eigenvalue problem. In a second part, we revisit the classical formulation of the mean flow eigenvalue problem for fluid–structure problems, presenting the different methods used to solve the considered problem: a first type of methods, based on the exact formulation of the eigenvalue problem and a second type of methods where several relevant simplifications are considered in order to render the original problem simpler to solve. In particular, we introduce a method for approximating the FSI eigenvalues with a rational function based on the eigenvalues of the hydrodynamic eigenproblem. In a third part, we implement and compare the different methods for estimating the eigenvalues and corresponding eigenmodes around a mean flow solution at $Re = 50\,000$ and $\alpha = 0\,^\circ$.

3.1 Introduction

Linear stability theory has been of central importance in fluid mechanics ever since the observation that the property of a flow state being a solution of the governing equations is no guarantee that it will actually be realised in practice. The linear stability theory started on a hydrodynamic framework at the late 19^{th} century with the controlled experiments of Reynolds (Reynolds, 1883) and the works of Rayleigh (1879) and Kelvin (1887). The first investigations were based on local stability theory, adapted to problems where the flow has a single inhomogeneous spatial direction (generally perpendicular to the advection direction). This approach was well suited for describing the perturbations present in parallel flows. However, the advances in computer power and numerical tools allowed for an increase in the flow complexity, extending the linear stability analysis to two- and three-dimensional flow perturbations (Theofilis, 2003; Chomaz, 2005; Sipp *et al.*, 2010).

In a linear stability problem, the linearised initial value problem describing how infinitesimal disturbances temporally evolve on top of a steady reference state is converted into an eigenvalue problem for the (possibly complex) eigenvalues of normal modes with an exponential temporal behaviour. Two main approaches are found in the literature to

numerically solve the above resulting eigenvalue problem. The first one is denominated "time-stepping" or "matrix-free" approach (Loiseau *et al.*, 2018). In this approach, the Jacobian matrix, associated to the linearisation of the governing equations, is not fully assembled. Instead, one only needs to evaluate the matrix-vector product in order to generate a Krylov basis from which the spectral properties of the Jacobian are approximated. This matrix-vector product operation is usually embedded on pre-existing unsteady nonlinear solvers, as part of the time-stepping procedure. This represents an advantage, since this procedure is usually efficiently designed for the unsteady simulations. However, one of the disadvantages is the slow convergence towards the approximative eigenpairs, associated the small values for the time-step required to converge (Tuckerman *et al.*, 2000).

The second approach present in the literature to numerically solve an eigenvalue problem is denoted "matrix-forming" or "matrix-based" (Sipp *et al.*, 2010; Iorio *et al.*, 2014). In this case, the Jacobian matrix is usually assembled as a sparse matrix and inverted using existing parallel libraries that implement a direct sparse LU factorisation (such as UMFPACK (Davis, 2002), SuperLU (Li, 2005) or MUMPS (Amestoy *et al.*, 2001)). This method has the disadvantage of running into computational difficulties as the size of the Jacobian matrix increases, associated to the time-consuming step for its assembling or the memory requirements for its LU factorisation, especially for large-scale problems. On the other hand, this approach has the advantage of converging towards the leading eigenvalues within a few iterations (depending on the methods used to solve the eigenvalue problem, see next section).

In this thesis, we apply this "matrix-based" approach to the case of a fluid–structure eigenvalue problem. However, as we will see, the fluid–structure Jacobian is not fully assembled. Instead, we present a modular approach, where the inversion of the fluid–structure Jacobian is solely based on the assembling and inversion of the fluid Jacobian. With that in mind, we start by describing the numerical tools used to compute the eigenpairs of the present problem.

3.2 Methods for mean flow analyses in fluid–structure problems

In this section, we present the different methods used to solve the mean flow FSI linear eigenproblem. We recall that two different formulations were presented in chapter 1 for the mean flow eigenproblem: a classical formulation and a Reynolds stress formulation. Since we are only interested in describing the different methods used to solve any of the formulations, we base the discussion of the present chapter in the classical formulation. In that way, we recall, from equation 1.35 (page 37), that mean flow FSI eigenvalue problem can be put in a matrix form $\sigma \mathsf{M}\overline{\boldsymbol{q}} = \mathsf{L}\overline{\boldsymbol{q}}$. The notation $\hat{\bullet}$ is dropped for this chapter to render the equations cleaner:

$$\sigma \begin{bmatrix} \mathsf{M}_f & \mathbf{0} & \mathbf{0} \\ \mathbf{0} & 1 & 0 \\ \mathbf{0} & 0 & I_s \end{bmatrix} \begin{bmatrix} \overline{\boldsymbol{q}}_f \\ \bar{\theta} \\ \overline{\Omega} \end{bmatrix} = \begin{bmatrix} \mathsf{L}_f\left(\overline{\boldsymbol{U}}_b\right) & \boldsymbol{v}_\theta & \boldsymbol{v}_\Omega \\ \mathbf{0} & 0 & 1 \\ \boldsymbol{m}^T & -K_s & -D_s \end{bmatrix} \begin{bmatrix} \overline{\boldsymbol{q}}_f \\ \bar{\theta} \\ \overline{\Omega} \end{bmatrix}, \tag{3.1}$$

where σ is a complex eigenvalue associated to the eigenmode $\overline{\boldsymbol{q}} = \left[\overline{\boldsymbol{q}}_f, \bar{\theta}, \overline{\Omega}\right]^T$ with $\overline{\boldsymbol{q}}_f = \left[\overline{U}, \overline{V}, \overline{p}\right]^T$ the velocity and pressure fields and $\bar{\theta}$ and $\overline{\Omega}$ the pitching angle and velocity, respectively. $\overline{U}_b$ represents the velocity field of the mean flow solution. When analysing the fluid–structure stability of the mean flow, one looks for the eigenvalue with largest real part. Indeed, if one of eigenvalues of the above problem has a positive real part ($\mathrm{Re}(\sigma) \equiv \lambda > 0$), the mean flow is unstable, while it remains stable if all eigenvalues have a negative real part.

In the following, we describe several methods to compute these eigenvalues. In section 3.2.1, we briefly introduce a Krylov–Schur method relying on a shift-and-invert transformation that allows to compute any eigenvalue σ in the spectrum, independently of its frequency $\mathrm{Im}(\sigma) \equiv \omega$. Both the high frequency eigenvalues associated to the flow dynamics

and the low frequency eigenvalues associated to the solid dynamics can thus be retrieved. The implementation of a modular technique avoiding the assembly of the fluid–structure Jacobian and relying on the assembly/factorisation of the hydrodynamic Jacobian is further described. Next, we introduce three methods that specifically target the computation of the solid eigenvalues by reformulating the linear eigenvalue problem 3.1 as a nonlinear eigenvalue problem, after elimination of the flow variables. The first method is simply based on the resolution of this nonlinear eigenvalue problem using a Newton–Raphson method (section 3.2.3). The second method relies on a quasi-steady approximation, already presented in section 1.6, based on the separation of the fluid and solid time scales of the linearised problem (section 3.2.4). The third method relies on the approximation of the resolvent operator (more precisely, the fluid transfer function, as detailed next) as a sum of rational functions (section 3.2.5).

3.2.1 Method for computing the full eigenvalue spectrum

Krylov–Schur subspace iterative method and shift-and-invert transformation

Several methods can be found in the literature to access the eigenvalues of a matrix system. For small- to medium-sized dense matrices, their complete spectrum can be calculated via classical algorithms present in common libraries, such as LAPACK (Anderson *et al.*, 1999). However, for very large and (typically) sparse matrices, found typically in eigenvalue problems, the choice of the method used to access to their spectrum depends on mathematical properties of the system and on the trade-off between efficiency and accuracy. Further, one is often interested in a restrict number of eigenvalues, and not on the complete spectrum. Amongst the first methods employed to solve sparse matrix eigenvalue problems, one can find the Power Iteration or the Rayleigh Quotient Iteration, capable of converging to a single eigenpair. The generalisation of these methods enabled to simultaneously reach several eigenpairs, with for example the Subspace/Simultaneous Iteration method (Bauer, 1957; Duff *et al.*, 1993). However, a much better performance can be achieved by subspace-based methods, where the solution is approximated on a low-dimensional subspace of the original problem. In this category, one can find the Lanczos methods (Lanczos, 1950; Saad, 2011), for generalised Hermitian eigenvalue problems, or the Arnoldi methods (Arnoldi, 1951; Lehoucq *et al.*, 1996; Sorensen, 1992) and Krylov–Schur subspace methods (Stewart, 2001, 2002), for generalised non-Hermitian eigenvalue problems. In the present thesis, the eigenvalues of the system 3.1 are computed via a Krylov–Schur subspace algorithm, available through the SLEPc library tool (Hernandez *et al.*, 2005).

The aforementioned methods provide approximations of the desired eigenvalues within a reasonable number of iterations, when they represent well-separated extremal eigenvalues. Nevertheless, in many cases the desired eigenvalues are not well separated or do not represent the extremal eigenvalues of the system, which can cause an excessive slow convergence of the iterative methods, or even their divergence. To circumvent the problem, a spectral transformation of the system can be employed (also referred to as preconditioning (Saad, 2011, chap. 8)), so that these poorly separated eigenvalues are transformed into well-separated extremal eigenvalues of the new transformed system. Among the most popular spectral transformations, one finds the Cayley (Cliffe *et al.*, 1993) and the shift-and-invert transformations (Christodoulou *et al.*, 1988), the latter used in the present thesis.

The shift-and-invert transformation analytically modifies the original eigenvalue spectrum to facilitate the extraction of the certain eigenvalues that are close to a given shift s, in absolute value. The transformation reads

$$(\mathsf{L} - s\mathsf{M})^{-1}\mathsf{M}\overline{\boldsymbol{q}} = (\sigma - s)^{-1}\overline{\boldsymbol{q}} = \sigma_{sh}\overline{\boldsymbol{q}}\,, \tag{3.2}$$

where σ_{sh} is the shifted eigenvalue of the transformed problem. With this transformation, the eigenvalues closest to the target shift s become dominant and with a better separation from the remaining eigenvalues than in the original spectrum. In other words, the shifted eigenvalues with largest magnitude will correspond to the original eigenvalues σ

that are closest to the targeted shift value, set as an input. Note that the eigenvectors are not altered.

The resolution of the shift-and-invert system using an iterative algorithm, based on the Krylov–Schur subspace of the matrix $(\mathsf{L}-s\mathsf{M})^{-1}\mathsf{M}$, requires the following operations:

- The matrix-vector product with the matrix M, which can be performed in a matrix-free style, where the matrix M_f is assembled;
- The solution $\overline{\boldsymbol{q}}^o$ of the linear system $(\mathsf{L}-s\mathsf{M})\overline{\boldsymbol{q}}^o = \overline{\boldsymbol{q}}^i$ for any right-hand side vector $\overline{\boldsymbol{q}}^i$.

With this method, one can compute any eigenvalue of the system 3.1, by varying the shift value, and the number of demanded eigenvalues.

Modular inversion of the fluid–structure Jacobian

The bottleneck of this implementation passes through the resolution of the second step. The straightforward way to solve it is by assembling and inverting the complete fluid–solid Jacobian shifted matrix, which we will refer it as the *full-assembly method*. However, a more efficient technique passes through solely assemble and invert the fluid Jacobian shifted matrix, which we will refer it as the *modular method*. The latter method is described in section 1.7.9 to time-marching the unsteady FSI Navier–Stokes equations, and it is here recalled for the inversion of the shifted Jacobian.

We start by expanding the equation $(\mathsf{L}-s\mathsf{M})\overline{\boldsymbol{q}}^o = \overline{\boldsymbol{q}}^i$ as

$$\begin{bmatrix} \mathsf{L}_f - s\mathsf{M}_f & \boldsymbol{v}_\theta & \boldsymbol{v}_\Omega \\ \mathbf{0} & -s & 1 \\ \boldsymbol{m}^T & -K_s & -(D_s + sI_s) \end{bmatrix} \begin{bmatrix} \overline{\boldsymbol{q}}_f^o \\ \overline{\theta}^o \\ \overline{\Omega}^o \end{bmatrix} = \begin{bmatrix} \overline{\boldsymbol{q}}_f^i \\ \overline{\theta}^i \\ \overline{\Omega}^i \end{bmatrix}. \tag{3.3}$$

The fluid component, $\overline{\boldsymbol{q}}_f^o$, can be decomposed as

$$\overline{\boldsymbol{q}}_f^o = \overline{\boldsymbol{q}}_{f,f}^o - \overline{\theta}^o\,\overline{\boldsymbol{q}}_{f,\theta}^o - \overline{\Omega}^o\,\overline{\boldsymbol{q}}_{f,\Omega}^o. \tag{3.4}$$

By injecting this decomposition into the fluid equation, *i.e.*, the first line of equation 3.3, one obtains that the "intrinsic" fluid component $\overline{\boldsymbol{q}}_{f,f}^o$ satisfies

$$\left(\mathsf{L}_f - s\mathsf{M}_f\right)\overline{\boldsymbol{q}}_{f,f}^o = \overline{\boldsymbol{q}}_f^i, \tag{3.5}$$

while the "coupled" fluid components, $\overline{\boldsymbol{q}}_{f,\theta}^o$ and $\overline{\boldsymbol{q}}_{f,\Omega}^o$, satisfy

$$\left(\mathsf{L}_f - s\mathsf{M}_f\right)\overline{\boldsymbol{q}}_{f,\theta}^o = \boldsymbol{v}_\theta, \tag{3.6a}$$

$$\left(\mathsf{L}_f - s\mathsf{M}_f\right)\overline{\boldsymbol{q}}_{f,\Omega}^o = \boldsymbol{v}_\Omega. \tag{3.6b}$$

Note that the problem 3.5 depends on the input vector $\overline{\boldsymbol{q}}^i$, unlike the linear problems 3.6 that can thus be solved once for all, prior to the iterative eigenvalue algorithm. By injecting now the decomposition 3.4 into the solid equations, *i.e.*, the second and third lines of problem 3.3, one obtains

$$\begin{bmatrix} -s & 1 \\ -(K_s + \tilde{K}_a) & -(D_s + \tilde{D}_a + sI_s) \end{bmatrix} \begin{bmatrix} \overline{\theta}^o \\ \overline{\Omega}^o \end{bmatrix} = \begin{bmatrix} \overline{\theta}^i \\ \overline{\Omega}^i - \left(\boldsymbol{m}^T\,\overline{\boldsymbol{q}}_{f,f}^o\right) \end{bmatrix}, \tag{3.7}$$

where the complex coefficients $\tilde{K}_a$ and $\tilde{D}_a$ are terms similar to the added stiffness and to the added damping coefficients, defined as

$$\tilde{K}_a = \boldsymbol{m}^T \bar{\boldsymbol{q}}^o_{f,\theta}\,, \tag{3.8a}$$

$$\tilde{D}_a = \boldsymbol{m}^T \bar{\boldsymbol{q}}^o_{f,\Omega}\,. \tag{3.8b}$$

In summary, the solution of the coupled fluid–solid system 3.3 is divided into two stages: a first stage independent of the input vector of the system 3.3, that can be solved before entering the Krylov–Schur subspace iterative process; and a second stage, to be solved iteratively. The first stage is composed by the following steps:

- Computation of the "coupled" fluid components $\bar{\boldsymbol{q}}^o_{f,\theta}$ and $\bar{\boldsymbol{q}}^o_{f,\Omega}$ from equations 3.6;
- Computation of the added coefficients $\tilde{K}_a$ and $\tilde{D}_a$ from equations 3.8.

On the other hand, the second stage is composed by the three following steps:

- Resolution of the fluid problem 3.5 to obtain the "intrinsic" fluid component $\bar{\boldsymbol{q}}^o_{f,f}$;
- Resolution of the solid problem 3.7 to obtain the solid components $\left[\bar{\theta}^o, \bar{\Omega}^o\right]^T$;
- Assemblage of the total fluid component $\bar{\boldsymbol{q}}^o_f$ using equation 3.4.

The sparse matrices L_f and M_f are assembled using the software *FreeFem++* (Hecht, 2012). The LU factorisation of the shifted matrix is performed in parallel via the tool MUMPS (Amestoy *et al.*, 2001), available through the SLEPc library tool (Hernandez *et al.*, 2005).

3.2.2 Definition of the fluid and solid transfer functions

In this section, we define two transfer functions that take into account the contributions of the fluid and solid components for the linear eigenvalue problem. For that, we start by noting that the fluid component of the mean flow eigenvector can be written as function of the solid components (first line of the equation 3.1) as

$$\bar{\boldsymbol{q}}_f = \mathsf{R}_f(\sigma)\left(\boldsymbol{v}_\theta \bar{\theta} + \boldsymbol{v}_\Omega \bar{\Omega}\right), \tag{3.9}$$

where we have introduced the fluid resolvent operator, defined as

$$\mathsf{R}_f(\sigma) = \left(\sigma \mathsf{M}_f - \mathsf{L}_f\right)^{-1}. \tag{3.10}$$

The fluid resolvent operator, already introduced in section 1.6, is an operator that, for an input perturbation associated to an eigenvalue σ, outputs the linearised response of the fluid. We note that the input has two contributions, one from an angular displacement perturbation, proportional to $\bar{\theta}$ and a second contribution from an angular velocity perturbation, proportional to $\bar{\Omega}$. The two contributions to the linear perturbation are noted

$$\bar{\boldsymbol{q}}^\theta_f = \mathsf{R}_f(\sigma)\boldsymbol{v}_\theta\,,$$
$$\bar{\boldsymbol{q}}^\Omega_f = \mathsf{R}_f(\sigma)\boldsymbol{v}_\Omega\,,$$

so that the fluid eigenmode component can be written as

$$\bar{\boldsymbol{q}}_f = \bar{\boldsymbol{q}}^\theta_f \bar{\theta} + \bar{\boldsymbol{q}}^\Omega_f \bar{\Omega}\,. \tag{3.11}$$

As seen in section 1.6, the system 3.1 can be written as a *nonlinear* eigenvalue problem of reduced size as

$$\left(\sigma\begin{bmatrix}1 & 0\\ 0 & I_s\end{bmatrix}+\begin{bmatrix}0 & -1\\ K_s & D_s\end{bmatrix}\right)\begin{bmatrix}\bar{\theta}\\ \bar{\Omega}\end{bmatrix}=\begin{bmatrix}0 & 0\\ \boldsymbol{m}^T\bar{\boldsymbol{q}}_f^{\theta}(\sigma) & \boldsymbol{m}^T\bar{\boldsymbol{q}}_f^{\Omega}(\sigma)\end{bmatrix}\begin{bmatrix}\bar{\theta}\\ \bar{\Omega}\end{bmatrix}. \tag{3.12}$$

The above system represents a *nonlinear* eigenvalue problem, since the quantities $\bar{\boldsymbol{q}}_f^{\theta}(\sigma)$ and $\bar{\boldsymbol{q}}_f^{\Omega}(\sigma)$ depend on the resolvent operator, which depends on the eigenvalue σ. On the right-hand side, $\boldsymbol{m}^T\bar{\boldsymbol{q}}_f^{\theta}=m_z^{\theta}$ is the (complex) moment generated by the linear flow response $\bar{\boldsymbol{q}}_f^{\theta}$ to a unitary angular displacement perturbation, while $\boldsymbol{m}^T\bar{\boldsymbol{q}}_f^{\Omega}=m_z^{\Omega}$ is the moment generated by the linear flow response $\bar{\boldsymbol{q}}_f^{\Omega}$ to a unitary angular velocity perturbation. The sum of these two contributions gives the total aerodynamic moment associated to the eigenmode $\bar{\boldsymbol{q}}_f$, which writes

$$m_z\left(\bar{\boldsymbol{q}}_f\right)=m_z^{\theta}\bar{\theta}+m_z^{\Omega}\bar{\Omega}\quad\text{with}\quad\begin{cases}m_z^{\theta}=\boldsymbol{m}^T\bar{\boldsymbol{q}}_f^{\theta}\\ m_z^{\Omega}=\boldsymbol{m}^T\bar{\boldsymbol{q}}_f^{\Omega}\end{cases}. \tag{3.13}$$

The right-hand side of problem 3.12 can also be formulated by defining a fluid transfer function $Y^f(s)$, defined here as the ratio between the (complex) aerodynamic moment m_z and the (complex) angular displacement $\bar{\theta}$. The parameter s represents a complex value, that corresponds to the fluid–structure eigenvalue when $s=\sigma$. The introduction of this transfer function is inspired on the concept impedance, used in previous publications (Fabre *et al.*, 2019b, 2020; Sabino *et al.*, 2020), where it is not the angular displacement, but the angular velocity that is used. Here, the use of the angular displacement is preferable as it more easily enables to separate the contributions to the aerodynamic moment from the linear response of the angular displacement from the angular velocity. Using the definition of the aerodynamic moment in equation 3.13, $Y^f(s)$ can be expanded as

$$Y^f(s)=\frac{\boldsymbol{m}^T\bar{\boldsymbol{q}}_f}{\bar{\theta}}=\frac{m_z}{\bar{\theta}}=\frac{m_z^{\theta}\bar{\theta}+m_z^{\Omega}\bar{\Omega}}{\bar{\theta}}=\frac{\boldsymbol{m}^T\mathsf{R}_f(s)\left(\boldsymbol{v}_{\theta}\bar{\theta}+\boldsymbol{v}_{\Omega}\bar{\Omega}\right)}{\bar{\theta}}=\boldsymbol{m}^T\mathsf{R}_f(s)\left(\boldsymbol{v}_{\theta}+\boldsymbol{v}_{\Omega}s\right). \tag{3.14}$$

With this definition, the eigenproblem 3.12 can be written as

$$\left(s^2I_s+sD_s+K_s\right)\bar{\theta}=Y^f(s).$$

Likewise, one can define a structure transfer function, $Y^s(s)$, as the ratio between the moment generated by the structure and the angular displacement:

$$Y^s(s)=-s^2I_s-sD_s-K_s. \tag{3.15}$$

Therefore, the linear fluid–structure equation is rewritten as

$$-Y^s(s)=Y^f(s). \tag{3.16}$$

We further note that, $Y^f(s)$ and $Y^s(s)$ can be divided into a real and imaginary parts, $Y^f=Y_r^f+Y_r^f\mathrm{i}$ and $Y^s=Y_r^s+Y_r^s\mathrm{i}$, with the latter given by

$$Y_r^s(s)=-(s_r^2-s_i^2)I_s-s_rD_s-K_s,$$

$$Y_i^s(s)=-2s_rs_iI_s-s_iD_s.$$

3.2.3 Newton method for a reduced-size nonlinear eigenproblem

In this paragraph, we present an alternative method to compute the eigenvalues of the fluid–structure eigenproblem. The method is based on the reduced-size problem, which is solved via a nonlinear iterative procedure. The method is particularly effective for the computation of the solid eigenvalues, as noted at the end of the section 1.7.9 (page 60), since the system that has to be inverted is ill-conditioned (the fluid Jacobian matrix) for the eigenvalues that are not affected by the presence of the structure (*e.g.*, the high frequency eigenvalues).

From the definitions of the fluid and solid transfer functions, $Y^f(s)$ and $Y^s(s)$, we note that the values of the complex parameter s for which the sum of transfer functions vanishes correspond to fluid–structure eigenvalues σ, such that the problem 3.12 can be written as

$$R_{FSI}(\sigma) = Y^f(\sigma) + Y^s(\sigma) = 0\,. \tag{3.17}$$

This equation can solved via a Newton–Raphson iterative procedure, similar to the one discussed in section 1.7.8, with which we converge individually to the desired eigenvalues, depending on the initial guess. At each k iteration of the Newton procedure, the value of σ can be computed by posing $\sigma^{k+1} = \sigma^k + \gamma_{Newton}\delta\sigma$, where $0 < \gamma_{Newton} \leq 1$ is a relaxation parameter and $\delta\sigma$ is the eigenvalue variation during each Newton iteration. The latter can be found after the linearisation of equation 3.17, such that:

$$\delta\sigma = \left[2I_s\sigma^k + D_s - \left.\frac{\mathrm{d}Y^f}{\mathrm{d}\sigma}\right|_{\sigma^k}\right]^{-1}\left(R_{FSI}(\sigma^k)\right), \tag{3.18}$$

with

$$\left.\frac{\mathrm{d}Y^f}{\mathrm{d}\sigma}\right|_{\sigma^k} = \boldsymbol{m}^T\left[\left.\frac{\mathrm{d}\mathsf{R}_f}{\mathrm{d}\sigma}\right|_{\sigma^k}\left(\boldsymbol{v}_\theta + \sigma^k\boldsymbol{v}_\Omega\right) + \mathsf{R}_f(\sigma^k)\boldsymbol{v}_\Omega\right]. \tag{3.19}$$

The derivative of the resolvent operator with respect to σ, present in this last expression, is found by inserting the decomposition $\sigma = \sigma_0 + \delta\sigma$ into its definition:

$$\begin{aligned}
\mathsf{R}_f(\sigma) &= \left(\sigma\mathsf{M}_f - \mathsf{L}_f\right)^{-1} \\
&= \left(\sigma_0\mathsf{M}_f + \delta\sigma\mathsf{M}_f - \mathsf{L}_f\right)^{-1} \\
&= \left[\left(\sigma_0\mathsf{M}_f - \mathsf{L}_f\right)\left(\mathbb{1} + \delta\sigma\left(\sigma_0\mathsf{M}_f - \mathsf{L}_f\right)^{-1}\mathsf{M}_f\right)\right]^{-1} \\
&= \left(\mathbb{1} + \delta\sigma\mathsf{R}_f(\sigma_0)\mathsf{M}_f\right)^{-1}\mathsf{R}_f(\sigma_0) \\
&= \left(\mathbb{1} - \mathsf{R}_f(\sigma_0)\mathsf{M}_f\delta\sigma + \left(\mathsf{R}_f(\sigma_0)\mathsf{M}_f\right)^2(\delta\sigma)^2 + \ldots\right)\mathsf{R}_f(\sigma_0) \\
&= \mathsf{R}_f(\sigma_0) \underbrace{- \mathsf{R}_f(\sigma_0)\mathsf{M}_f\mathsf{R}_f(\sigma_0)}_{\left.\mathrm{d}\mathsf{R}_f/\mathrm{d}\sigma\right|_{\sigma_0}}\delta\sigma + \left(\mathsf{R}_f(\sigma_0)\mathsf{M}_f\right)^2\mathsf{R}_f(\sigma_0)(\delta\sigma)^2 + \ldots\,.
\end{aligned} \tag{3.20}$$

The parameter γ_{Newton} is set to 0.3 in the first five iterations to circumvent the fact that the initial solution is not sufficiently close to the final solution.

Concerning the computation of the eigenmodes, we note that, if the eigenvalue σ is known, the solid components of the eigenmode can be retrieved from the eigenvectors of the reduced-size system 3.12. In this process, the eigenmode can be normalised with respect to the angular displacement, forcing $\left|\overline{\theta}\right| = \sqrt{\overline{\theta}^H\overline{\theta}} = 1$. The fluid component is then retrieved from equality 3.9.

Explicit method for the structural divergence instability

From equation 3.17, a simplified method can be formulated to compute the possible static eigenvalues as function of the structural stiffness, without passing through the Newton iterations. Hitherto, the structural equation was viewed as an implicit definition of the eigenvalue as function of the structural parameters and of the transfer function $Y^f(\sigma)$. However, one can rewrite the structure equation 3.17, such that it becomes an explicit function of σ, when solved for the only term independent of σ, the structural stiffness, K_s. More precisely, if one assumes the existence of a real eigenvalue $\sigma = \lambda$, one arrives to:

$$K_s = Y^f(\lambda) - \lambda^2 I_s - \lambda D_s \,. \tag{3.21}$$

With this method, the real eigenvalue λ is viewed as parameter. By fixing its value, one can compute $Y^f(\lambda)$ (exactly or approximatively) and thus obtain a value for K_s via equation 3.21. By repeating this procedure for several values of λ, one can map K_s as a function of the growth rate of this static eigenvalue. The divergence instability for a given K_s can finally be determined. This method is clearly adapted when performing a parametric investigation (*i.e.*, varying K_s).

3.2.4 Quasi-steady approximation method

Hitherto, the eigenvalues of the present fluid–structure problem were computed without any assumption on the fluid. The quasi-steady approximation relies on the assumption that, in the linearised problem, the fluid time scale is slow compared to the solid time scale. The fluid–solid eigenvalue problem can then be reduced to a solid vibration problem where the fluid effect is taken into account with added inertia, added damping and added stiffness coefficients, as explained in section 1.6. In summary, the problem 3.1 is approximated as

$$(I_s + I_a)\sigma_{QS}^2 + (D_s + D_a)\sigma_{QS} + (K_s + K_a) = 0\,,$$

where K_a, D_a and I_a are the added stiffness, the added damping and the added inertia coefficients, defined as

$$K_a = \boldsymbol{m}^T \mathsf{L}_f^{-1} \boldsymbol{v}_\theta \,, \tag{3.22a}$$

$$D_a = D_a^\theta + D_a^\Omega = \boldsymbol{m}^T \mathsf{L}_f^{-1} \mathsf{M}_f \mathsf{L}_f^{-1} \boldsymbol{v}_\theta + \boldsymbol{m}^T \mathsf{L}_f^{-1} \boldsymbol{v}_\Omega \,, \tag{3.22b}$$

$$I_a = I_a^\theta + I_a^\Omega = \boldsymbol{m}^T \left(\mathsf{L}_f^{-1}\mathsf{M}_f\right)^2 \mathsf{L}_f^{-1} \boldsymbol{v}_\theta + \boldsymbol{m}^T \mathsf{L}_f^{-1} \mathsf{M}_f \mathsf{L}_f^{-1} \boldsymbol{v}_\Omega \,. \tag{3.22c}$$

We denote a quasi-steady approximation of order 2 when all the added coefficients are taken into account, an approximation of order 1 when only the terms D_a and K_a are taken into account and an approximation of order 0 when only K_a is taken into account. The solution of the above second order scalar equation reads

$$\sigma_{QS} = -\frac{D_s + D_a}{2(I_s + I_a)} \pm \sqrt{\left(\frac{D_s + D_a}{2(I_s + I_a)}\right)^2 - \frac{K_s + K_a}{I_s + I_a}} \,. \tag{3.23}$$

This method presents a first approximation of the eigenvalues of the structure. The results based on this approximation are reported in section 3.3.5.

3.2.5 Rational function approximation of the fluid transfer function

The computation of the fluid–structure eigenvalues involves the computation of the fluid transfer function, which in turn involves the calculation of the resolvent operator. For that, an inversion of the linearised fluid operator is needed, which represents the most consuming step of the fluid transfer function computation. An alternative to the exact calculation of this inversion is presented in this section. The objective is to approximate the fluid–structure eigenvalues based on the approximation of the fluid transfer function. In this thesis, several attempts were made in order to approximate the fluid transfer function. In a first part, a Taylor expansion of the fluid transfer function was implemented. The results were not satisfactory, since the exact behaviour of the fluid transfer function resembles to a rational function. The theoretical development and results are summarised in appendix D. In a second part, we try to approximate the fluid transfer function by a rational function, based on the eigenvalues of the fluid eigenproblem, as explained in the following.

The use of rational functions to approximate unsteady aerodynamic loads dates back to the 1940s, with the work of Jones (1940) on the approximation of the Theodorsen function Theodorsen (1935). In its works, Jones built a rational approximation by placing two poles along the real axis of the s-plane, idealising the time delays inherent to the unsteady aerodynamic loadings. Following this work, similar approaches are found on the literature (Roger *et al.*, 1975; Roger, 1977; Vepa, 1977; Edwards, 1979), some of them based on a least squares technique to minimise the difference between the rational expansion and a set of known data of the aerodynamic loads. The rational approximation is designed to fit these data along the imaginary axis of the s-plane and is then extrapolated to the entire s-plane. Much of the relevant literature is summarised by Karpel (1981, 1982), whose own contribution was to develop a transfer function representation of minimum order for a given level of accuracy for simple harmonic aerodynamic loads. In this thesis, the rational function approximation is based on the fluid eigenvalue problem, as detailed next.

We want to approximate $Y^f(s) = \boldsymbol{m}^T \bar{\boldsymbol{q}}_f(s)/\bar{\theta}$, where $\bar{\boldsymbol{q}}_f$ is the linearised fluid component response to a solid displacement, given by equation 3.9 and rewritten as

$$\bar{\boldsymbol{q}}_f = \mathsf{R}_f(s)(\boldsymbol{v}_\theta + s\boldsymbol{v}_\Omega)\bar{\theta}\,. \tag{3.24}$$

Moreover, the purely-hydrodynamic problem, admits an eigenpair $(\bar{\boldsymbol{q}}_0, \sigma_0)$, solution of the homogeneous problem:

$$\left(\sigma_0 \mathsf{M}_f - \mathsf{L}_f\right)\bar{\boldsymbol{q}}_0 = \boldsymbol{0}\,. \tag{3.25}$$

The eigenvalue σ_0 corresponds to a pole of the transfer function Y^f. This means that the left-hand side operator is singular, which is a requirement for the existence of a nontrivial solution $\bar{\boldsymbol{q}}_0$. In the vicinity of the fluid eigenvalue σ_0, the complex parameter s can be expanded as

$$s = \sigma_0 + \epsilon\sigma_1 + \epsilon^2\sigma_2 + \dots\,, \tag{3.26}$$

where $\epsilon \ll 1$ is a small (real) parameter indicating that the development is valid close to the eigenvalue σ_0. On the other hand, the ratio between the flow component $\bar{\boldsymbol{q}}_f$ and the angle $\bar{\theta}$ is expanded as

$$\frac{\bar{\boldsymbol{q}}_f}{\bar{\theta}} = \frac{1}{\epsilon}\bar{\boldsymbol{q}}_0 + \bar{\boldsymbol{q}}_1 + \epsilon\bar{\boldsymbol{q}}_2 + \epsilon^2\bar{\boldsymbol{q}}_3 + \dots\,, \tag{3.27}$$

where the leading term scales as $\mathcal{O}(1/\epsilon)$. This scaling reflects that the eigenvalue σ_0 is a pole of the fluid transfer function $Y^f(s)$ that diverge when s tends towards σ_0. By injecting the previous expansions into equation 3.24, one obtains, at the

leading orders:

$$\mathcal{O}\left(\frac{1}{\epsilon}\right): \quad (\sigma_0 \mathsf{M}_f - \mathsf{L}_f)\bar{\boldsymbol{q}}_0 = \boldsymbol{0}, \tag{3.28a}$$

$$\mathcal{O}(1): \quad (\sigma_0 \mathsf{M}_f - \mathsf{L}_f)\bar{\boldsymbol{q}}_1 = (\boldsymbol{v}_\theta + \sigma_0 \boldsymbol{v}_\Omega) - \sigma_1 \mathsf{M}_f \bar{\boldsymbol{q}}_0, \tag{3.28b}$$

and, for the Y^f approximation:

$$Y^f(s) = \frac{1}{\epsilon} Y_0 + Y_1 \ldots, \tag{3.29}$$

where Y_0 and Y_1 are given by $Y_0 = \boldsymbol{m}^T \bar{\boldsymbol{q}}_0$ and $Y_1 = \boldsymbol{m}^T \bar{\boldsymbol{q}}_1$. Equation 3.28a represents a homogeneous system, associated to the fluid eigenvalue problem. The arbitrary magnitude and phase of the $\bar{\boldsymbol{q}}_0$ modes are fixed by imposing the normalisation condition $\bar{\boldsymbol{q}}_0^H \mathsf{M}_f \bar{\boldsymbol{q}}_0 = 1$, with the superscript $\bullet^H$ representing the Hermitian transpose. On the other hand, equation 3.28b represents a nonhomogeneous system forced by two terms: the first one involves the unitary angular displacement and velocity fields, while the second one is proportional to the fluid eigenmode $\bar{\boldsymbol{q}}_0$. Since the operator on the left-hand side is singular, the right-hand side terms must belong the kernel this operator, in order to respect the solvability condition. Following the works of Crouch *et al.* (1993) (see also Pham *et al.* (2018); McCloughan *et al.* (2020)), this condition can be replaced by an orthogonality condition, which can be put as $\bar{\boldsymbol{q}}_0^H \mathsf{M}_f \bar{\boldsymbol{q}}_1 = 0$. Then the latter problem is solved, using an augmented matrix system by adding the orthogonality condition[1] as an extra equation of the system, and declaring σ_1 as an extra unknown, which can be put in the form:

$$\begin{bmatrix} (\sigma_0 \mathsf{M}_f - \mathsf{L}_f) & \mathsf{M}_f \bar{\boldsymbol{q}}_0 \\ \bar{\boldsymbol{q}}_0^H \mathsf{M}_f & 0 \end{bmatrix} \begin{bmatrix} \bar{\boldsymbol{q}}_1 \\ \sigma_1 \end{bmatrix} = \begin{bmatrix} \boldsymbol{v}_\theta + \sigma_0 \boldsymbol{v}_\Omega \\ 0 \end{bmatrix}. \tag{3.30}$$

Pham *et al.* (2018) proved that the system 3.30 is nonsingular, leading to a unique solution, while Crouch *et al.* (1993) demonstrated that the system respects the solvability condition, also called Fredholm alternative (Olver, 2014, p. 350). This augmented method has the advantage of not requiring the adjoint eigenmodes of the fluid system.

By solving the above augmented problem, we obtain the vector $\bar{\boldsymbol{q}}_1$ as well as the complex scalar σ_1. To obtain the development of the transfer function, we further note that, by neglecting the second order terms in the expansion 3.26, we obtain that the small parameter satisfies $\epsilon = (s - \sigma_0)/\sigma_1$. Once injected in the expansion 3.29 of the fluid transfer function Y^f, we obtain the approximation based on one sided-pole as

$$Y^f(s;\sigma_0) = \frac{\sigma_1}{s - \sigma_0} Y_0 + Y_1. \tag{3.31}$$

The above approximation is valid around the eigenvalue σ_0, but we should also consider the existence of the complex conjugate σ_0^*. The development of the transfer function taking into account both poles writes

$$Y^f(s;\sigma_0,\sigma_0^*) = Y^f(s;\sigma_0) + Y^f(s;\sigma_0^*). \tag{3.32}$$

In fact, the transfer function satisfies $Y(s;\sigma_0^*) = Y^*(s;\sigma_0)$, *i.e.*, the terms Y_0 and Y_1 associated to the pole σ_0^* are the complex conjugate of the terms associated to σ_0.

Following the notation that will be introduced in section 3.3.1, we proceed to the approximation of the Y^f function

[1] A different orthogonality condition was tested, $\bar{\boldsymbol{q}}_0^{+,H} \mathsf{M}_f \bar{\boldsymbol{q}}_1 = 0$, with $\bar{\boldsymbol{q}}_0^{+,H}$ the fluid adjoint eigenmode of the adjoint LSA problem, obtaining the same results.

based on two fluid eigenvalues, denoted σ_{f1} and σ_{f2}, arriving to

$$Y^f(s;\sigma_{f1},\sigma^*_{f1},\sigma_{f2},\sigma^*_{f2}) = Y^f(s;\sigma_{f1}) + Y^f(s;\sigma^*_{f1}) + Y^f(s;\sigma_{f2}) + Y^f(s;\sigma^*_{f2}). \tag{3.33}$$

We note that the terms of order $\mathcal{O}(1/\epsilon)$ have a singularity behaviour around their corresponding pole, whereas the terms Y_1, associated to the order $\mathcal{O}(1)$, are complex constants, independent of the distance to the poles. Further, we note that the sum $Y_1(\sigma_0)+Y_1(\sigma_0^*)$ for each contribution of a complex pair of a poles represents a real quantity.

We concluded in the results section that, the order $\mathcal{O}(1)$ terms, which represent a constant, tended to deviate the approximation from the exact solution. Therefore, we substituted the Y_1 terms by a constant C, designed to calibrate the model at one point of the complex plane, such that the approximation of $Y^f(s)$ reads:

$$Y^f(s;\sigma_{f1},\sigma^*_{f1},\sigma_{f2},\sigma^*_{f2}) = \frac{\sigma_{1,f1}}{s-\sigma_{f1}}Y_0(\sigma_{f1}) + \frac{\sigma^*_{1,f1}}{s-\sigma^*_{f1}}Y_0(\sigma^*_{f1}) + \frac{\sigma_{1,f2}}{s-\sigma_{f2}}Y_0(\sigma_{f2}) + \frac{\sigma^*_{1,f2}}{s-\sigma^2_{f2}}Y_0(\sigma^*_{f2}) + C\,. \tag{3.34}$$

One can note that, in order to obtain the approximation of Y^f in all points of the complex plane, the system 3.30 only needs to be inverted one time for each considered pole (in addition to the exact inversion done for the computation of the calibration constant). This represents a substantial save of computational time with respect to the exact computation of Y^f, since the exact computation needs the inversion of the shifted fluid Jacobian for each position on the complex plane.

With the analytical expression of the approximation of Y^f, given be equation 3.34, the fluid–structure eigenvalues are approximating using the Newton method present previously. For that, the expression of the linearisation of Y^f is needed, which is given, at the Newton iteration k, by

$$\left.\frac{\mathrm{d}Y^f}{\mathrm{d}\sigma}\right|_{s^k} = -\frac{\sigma_{1,f1}}{\left(s^k-\sigma_{f1}\right)^2}Y_0(\sigma_{f1}) - \frac{\sigma^*_{1,f1}}{\left(s^k-\sigma^*_{f1}\right)^2}Y_0(\sigma^*_{f1}) - \frac{\sigma_{1,f2}}{\left(s^k-\sigma_{f2}\right)^2}Y_0(\sigma_{f2}) - \frac{\sigma^*_{1,f2}}{\left(s^k-\sigma^2_{f2}\right)^2}Y_0(\sigma^*_{f2}). \tag{3.35}$$

3.3 Application of the various methods for $Re = 50\,000$ and $\alpha = 0°$

In this section, we implement the different approaches presented previously in section 3.2 to calculate the eigenvalues of a mean flow FSI eigenproblem. The aim is to discuss the methodological aspects of these different approaches. The physical discussion, along with the presentation of the FSI eigenmodes, is considered in the next chapter, in section 4.2. In that way, the mean flow taken into account in this section corresponds to the time-averaged solution of a two-dimensional time-marching computation, presented in the previous chapter, for $Re = 50\,000$ and $\alpha = 0°$.

σ_{f1}	Low frequency eigenvalue 1	$-0.1446 + 0.1992\mathrm{i}$
σ_{f2}	Low frequency eigenvalue 2	$-0.2944 + 0.4441\mathrm{i}$
σ_{f3}	Vortex shedding eigenvalue	$0.2480 + 29.2972\mathrm{i}$

Table 3.1 – *Hydrodynamic linear stability analysis of the mean flow: values of the two least stable low frequency eigenvalues and the unstable vortex shedding eigenvalue for Re = 50 000 and α = 0°.*

3.3.1 Full eigenvalue spectrum: purely-hydrodynamic mean flow analysis

We first present the results of the purely-hydrodynamic mean flow analysis. They are obtained by solving the purely-hydrodynamic eigenvalue problem

$$\sigma \mathsf{M}_f \overline{\boldsymbol{q}}^f = \mathsf{L}_f(\overline{\boldsymbol{U}}_b)\overline{\boldsymbol{q}}^f ,$$

using a Krylov–Schur algorithm and the shift-and-invert strategy described in section 3.2.1. The operator L_f corresponds to the linearisation of the Navier–Stokes equations around the mean flow solution, while $\overline{\boldsymbol{q}}^f$ corresponds to a purely-hydrodynamic eigenmode. This purely-hydrodynamic analysis is relevant for the understanding of the FSI eigenvalues, present in the subsequent sections.

The eigenvalue results are presented on a one-sided spectrum in figure 3.1a, with the growth rate on the horizontal axis and the eigenvalue frequency on the vertical axis. A zoom close to the origin of the graph is plotted in figure 3.1b. The unstable zone, in grey, corresponds to a positive amplification rate. The eigenmodes are normalised to 1 with respect to the discrete inner product such that $\overline{\boldsymbol{q}}^{f,H}\mathsf{M}_f\overline{\boldsymbol{q}}^f = 1$.

The spectrum is characterised by a cloud of stable eigenvalues and a single unstable eigenvalue, labelled 3 and denoted σ_{f3}, vibrating at a frequency of $\omega = 29.30$ (table 3.1). This frequency corresponds to the frequency of the vortex shedding in the wake of the airfoil, detailed in the previous chapter. We note that the spanwise vorticity field of the real part of the corresponding eigenmode, present in figure 3.2, is concentrated on the convected wake region, far from the airfoil.

We turn our attention to the fluid eigenvalues near the origin, namely to the two least stable eigenvalues in that region, labelled 1 and 2 in figure 3.1b and denoted σ_{f1} and σ_{f2}, respectively. The real and imaginary parts of the velocity and pressure fields of the eigenmode associated to σ_{f1} are present in figure 3.3. A similar spatial structure is found for the low frequency eigenmode associated to σ_{f2}. In contrast to the vortex shedding eigenmode, the low frequency eigenmodes do not exhibit a high frequency oscillating spatial structure. While the $\overline{U}$ component display non negligible values in the far wake, the $\overline{V}$ and $\overline{p}$ components are located near the airfoil. Furthermore, the $\overline{U}$ and $\overline{p}$ components present an antisymmetric structure with respect to the airfoil chord line, whereas the $\overline{V}$ component is symmetric. Although stable,

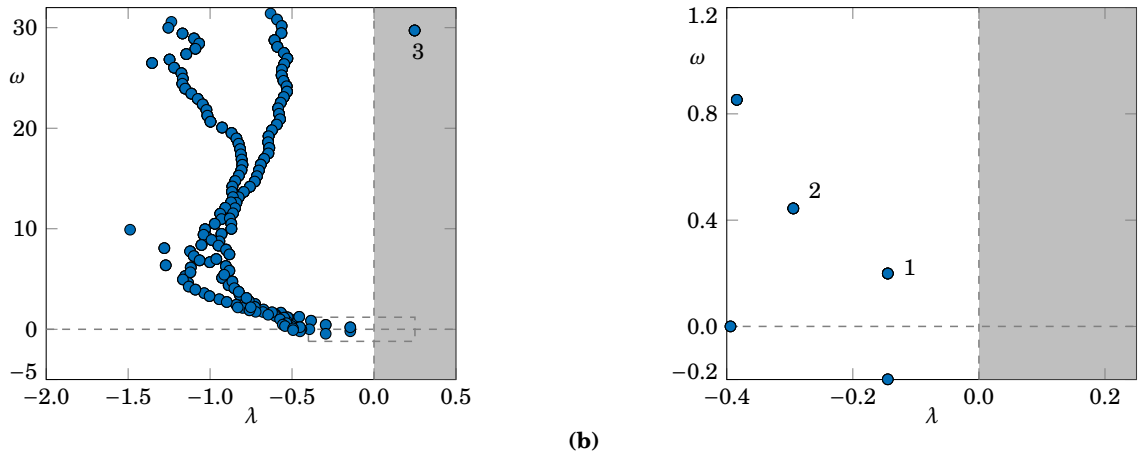

(a) **(b)**

Figure 3.1 – *Spectrum of a hydrodynamic mean flow linear stability analysis at Re* = 50 000 *and* $\alpha = 0°$. *On the left, general view, highlighting an unstable eigenvalue,* σ_{f3}, *labelled* 3, *with a frequency corresponding to the vortex shedding frequency. On the right, a close-up of the same spectrum near the origin, highlighting the two least stable low frequency eigenvalues,* σ_{f1} *and* σ_{f2}, *labelled* 1 *and* 2.

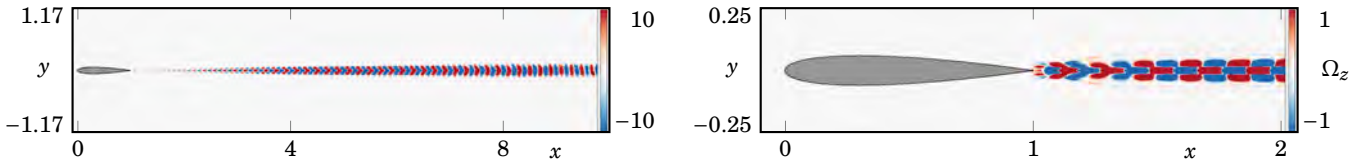

Figure 3.2 – *Real part of the spanwise vorticity field of the vortex shedding eigenmode (left), with a close-up near the airfoil (right).*

the presence of these low frequency eigenmodes is found to have a major influence on the moment associated to the fluid response to the solid motion, as discussed in the subsequent sections.

3.3.2 Full eigenvalue spectrum: mean flow FSI analysis

The first methodological approach for computing the eigenvalues of the mean flow FSI eigenproblem is based on the modular approach of a Krylov–Schur subspace iterative method presented in section 3.2.1. The analysis is carried out for shift values with a real part located at 0.1 and an imaginary part ranging from 0 to 30, with a step of 0.5. The step is decreased to 0.2 for frequency values inferior to 1, near the origin. The eigenvalue solver is set to converge 10 eigenvalues for each shift. This method gives directly the requested eigenvalues as well as the corresponding eigenmodes.

Figure 3.4a shows the one-sided spectrum of the mean flow FSI linear stability analysis. A close-up near the origin is present in figure 3.4b. The structural eigenvalue, calculated with the help of equation 1.11 (page 23), is represented by a black cross. This method enables to compute any desired eigenpairs in the vicinity of a given shift. This represents both an advantage and a disadvantage. The advantage is related to the fact that we can have a clear picture of the spectrum in the region of interest, namely close to the structural eigenvalue. In the present case, we converged to 650 eigenvalues. On the other hand, the method does not enable to distinguish the fluid eigenvalues from the eigenvalues associated to the structure. Additionally, most of the converged eigenvalues will correspond either to spurious modes, associated to the spatial discretisation, or to stable physical modes that are not pertinent for the present FSI study.

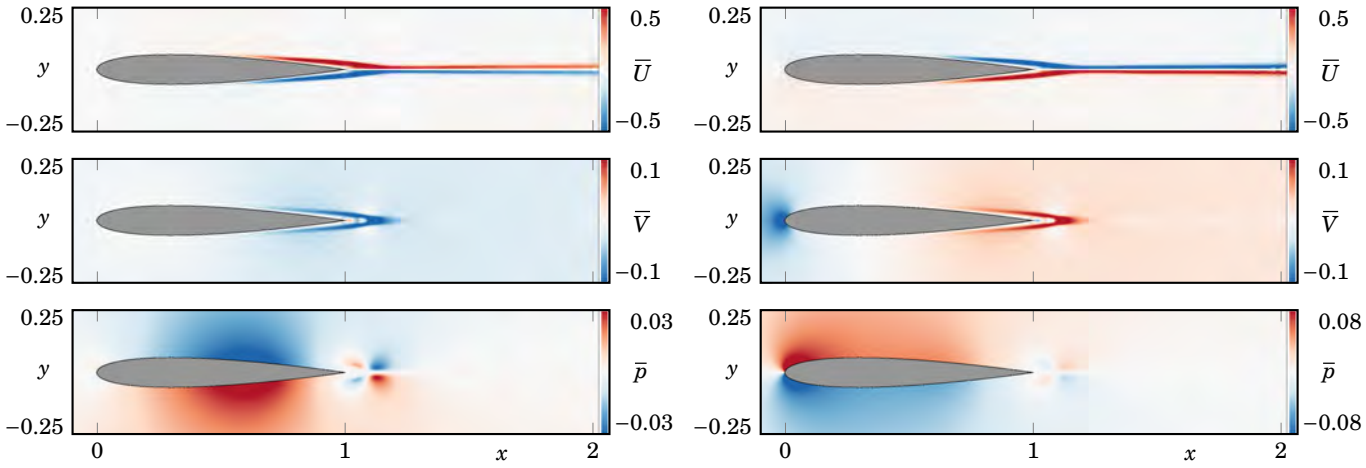

Figure 3.3 – *Velocity and pressure fields of the stable low frequency eigenmode associated to the eigenvalue σ_{f1}: real part (left) and imaginary part (right).*

As for the fluid spectrum detailed previously, an unstable eigenvalue appears at a frequency of 29.30, which is associated to the vortex shedding instability. In contrast, a close observation of the spectrum near the origin, in figure 3.4b, reveals the emergence of two pairs of eigenvalues. The first pair is located along the real axis, presenting no associated frequency, illustrated by the bigger red circles. The unstable eigenmode has a growth rate of $\lambda = 0.2084$, whereas the other static eigenmode is stable, with a growth rate of $\lambda = -0.2862$. The second pair is located at the growth rate of $\lambda = -0.1465$, having a frequency of $\omega = \pm 0.5386$, illustrated by the yellow circles. A summary of these eigenvalues is present in table 3.2.

Although the complete FSI spectrum can be calculated with this method, the influence of the structure can only be noted if we also have access to the fluid spectrum (figure 3.1) and to the structural eigenvalue, represented with a cross in figure 3.4b. This comparison enables us to label the eigenvalue presenting a divergent character as *divergence mode*, and the low frequency eigenmode, possibly at the origin of the flutter oscillations, as *flutter mode*. Further, the interaction between the structure and the fluid cannot be determined only with this method. Different scenarios can arise from this interaction. For example, the effect of the fluid on the structural eigenvalues (black cross) could decrease their frequency such that this complex pair would collide on the real axis and be transformed into the two static eigenvalues (bigger red circles). A different scenario could also happen, where the fluid would tend to increase the frequency of the structural

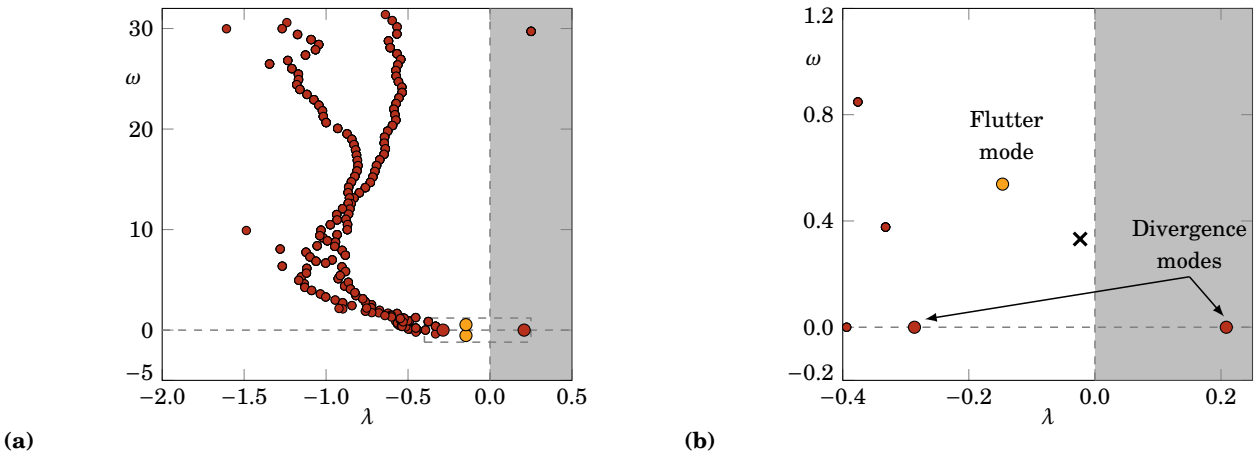

Figure 3.4 – *Spectrum of a fluid–structure mean flow linear stability analysis at Re* = 50 000 *and* $\alpha = 0°$ *for the nominal structure parameters and using the classical formulation. On the left, general view and, on the right, a close-up of the same spectrum near the origin, highlighting the divergence (bigger red circles) and flutter (yellow circles) eigenvalues. The remaining eigenvalues are represented by the smaller red circles. The eigenvalue of the structure equation in vacuum is represented by the black cross.*

Unstable divergence eigenvalue	0.2084
Stable divergence eigenvalue	−0.2863
Flutter eigenvalue	−0.1465 + 0.5386i
Natural structure eigenvalue	−0.0232 + 0.3289i

Table 3.2 – *Divergence and flutter eigenvalues of the complete FSI eigenproblem for Re* = 50 000 *and* $\alpha = 0°$*, compared to the structure equation eigenvalue.*

Initial guess	Converged eigenvalue
0.0000 + 0.0000i	0.2084
−0.1000 + 0.0000i	−0.2863
−0.0232 + 0.3289i	−0.1465 + 0.5386i

Table 3.3 – *Initial guesses and converged eigenvalues of the Newton procedure.*

eigenvalues and to stabilise them, obtaining the flutter eigenvalues, represented by the yellow circles.

From the present results, the association of these modes to the structure is not evident. This is done with the help of the methods explored in the next paragraphs, where we focus our attention on the computation of the solid eigenvalues, that will enable us to clarify the above scenarios.

3.3.3 Newton method for a reduced-size nonlinear eigenproblem

In the previous method, the divergence and flutter eigenvalues have been obtained by computing several eigenvalues of the fluid–structure eigenproblem via a Krylov–Schur method, and have been identified by comparison with the purely-hydrodynamic and purely-solid spectra. We now present the results obtained by solving the reduced-size nonlinear eigenvalue problem with a Newton method, as introduced in section 3.2.3. We will demonstrate how it may help in better understanding the nature of the coupled eigenvalues.

In order to initialise the resolution of the nonlinear system, three guess values are considered, as present in table 3.3, with the objective to retrieve the divergence and flutter eigenvalues. For that, the first two initial guesses are chosen along the real axis, where the imaginary part of the nonlinear residual, R_{FSI}, is already zero.

Figure 3.5 shows the evolution of growth rate λ and frequency ω as a function of the Newton iteration, for the three guess values indicated above. Interestingly, we clearly observe that different converged solutions are obtained depending on the initial solution. When starting with purely real guess values (red curves), the algorithm converges within the first 10 iterations towards a real eigenvalue, that is either the unstable divergence eigenvalue (solid red line) or the stable divergence eigenvalue (dashed red line). Their growth rates ($\lambda = 0.2084$ and $\lambda = -0.2863$) correspond

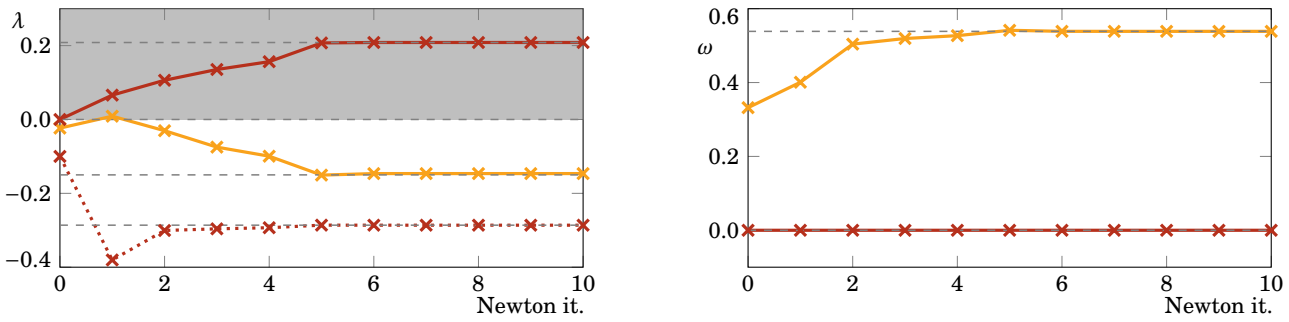

Figure 3.5 – *Evolution of the growth rate (left) and frequency (right) eigenvalue solutions with the nonlinear Newton iterations for three different initial guesses, converging to the stable and unstable divergence modes (dotted and solid red lines) and to the flutter mode (solid yellow line). The initial guess values, two on the real axis and a third one corresponding to the structure eigenvalue, are reported in table 3.3.*

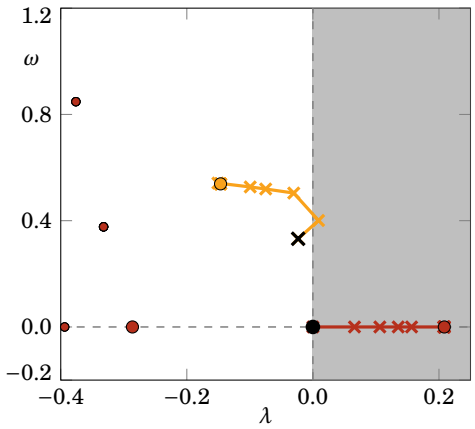

Figure 3.6 – *Evolution of the eigenvalue solutions on the complex plane as the nonlinear Newton procedure converges to the unstable divergence (red circle) eigenvalue and to the flutter (yellow circle). The divergence and flutter eigenvalues are represented by the bigger red and yellow circles, respectively. The remaining FSI eigenvalues are represented by the smaller red circles. The initial guesses are represented by the black circle and the black cross, for the divergence and flutter eigenvalues, respectively, see table 3.3.*

exactly to those obtained with the Krylov–Schur method. Considering now as guess value the complex eigenvalue of the purely-solid eigenproblem, we observe (yellow curve) that it converges towards the flutter eigenvalue, whose growth rate is $\lambda = -0.1465$ and frequency is $\omega = 0.5386$.

To better visualize the path of these eigenvalues towards to divergence and flutter eigenvalues, we sketch the evolution of the first and third guesses on the complex plane in figure 3.6. Concerning the unstable divergence mode, in red, the path is concentrated in the real axis, as noted before, with a monotonic increase of the growth rate up to convergence. Concerning the flutter eigenvalue, in yellow, we note that it goes through the unstable zone $\lambda > 0$ in the first Newton iteration, but restabilises for the next iterations. Although complex, this path clearly indicates that the flutter eigenvalue emerges from the purely-solid (complex) eigenvalue, thus better justifying its denomination as “flutter instability”. The flow interaction tends to decrease its growth rate and increase its frequency. To better understand this, we examine in

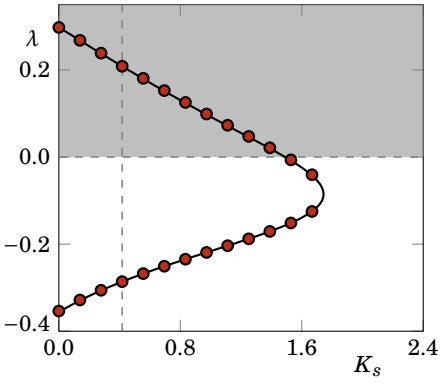

Figure 3.7 – *Variation of the growth rate of the divergence eigenvalues with* K_s*, where the red circles represent the divergence eigenvalues obtained with the Krylov–Schur method and the black line represents the explicit prediction. The vertical dashed line represents the nominal value of* $K_s = 0.417$.

the next paragraph the fluid and solid transfer functions defined in equations 3.14 and 3.15 (page 120).

The behaviour of the divergence eigenvalues can be explicitly mapped as function of the structural stiffness of the airfoil, using the method described in at the end of section 3.2.3. With this method, we impose a static eigenvalue, and search for admissible solutions of the structural stiffness, *i.e.*, for real and positive values of K_s. Figure 3.7 compares the divergence eigenvalues obtained with the Krylov–Schur method, to the static predictions given by the present method. Both methods give the same results for the considered range of λ. In particular, we observe that, for the nominal stiffness value represented by the vertical dashed line, both methods predict a stable and an unstable eigenvalue. We also observe that no admissible values of K_s are found for $\lambda < -0.354 \wedge \lambda > 0.298$.

3.3.4 Description of the fluid and solid transfer functions

To better understand the influence of the fluid and the structure components on the FSI eigenproblem, we propose to analyse the behaviour of the fluid and solid transfer functions on the complex plane. We recall that that these transfer functions are defined for any complex number s as

$$Y^f(s) = \boldsymbol{m}^T \left(s\mathsf{M}_f - \mathsf{L}_f\right)^{-1} (\boldsymbol{v}_\theta + \boldsymbol{v}_\Omega s)\,,$$
$$Y^s(s) = -s^2 I_s - sD_s - K_s\,.$$

The fluid–structure eigenvalues σ correspond to complex values s for which the residual vanishes, *i.e.*, $R_{FSI} = Y^f(\sigma) + Y^s(\sigma) = 0$. Note also that the purely-fluid eigenvalues are poles of the fluid transfer function that is singular at those points.

While the solid transfer function is trivial to compute, the fluid transfer function requires the inversion of the matrix $\left(s\mathsf{M}_f - \mathsf{L}_f\right)$ for several values s, in order to map the complex plane. The computational cost of this method is entirely dominated by the evaluation of this fluid transfer function. Once it is determined, the effect of the solid parameters onto the problem can be quickly accessed. However, the prohibitive number of matrix inversions necessary to map the complex plane makes this method quite inefficient compared to the Newton method discussed before. We will see in the next section (section 3.3.6) how to reduce this computation cost by approximating the fluid transfer function based on few fluid eigenvalues. Here, we rather highlight its interest for better understanding the role played by some purely-fluid eigenvalues on the divergence and flutter eigenvalues.

In figure 3.8, we sketch the fluid and solid transfer functions, along with their sum, R_{FSI}, as function of the complex variable $s = s_r + s_i\mathrm{i}$. The first column represents the Y^f function, the second column represents the Y^s function and the last column represents their sum, R_{FSI}. The isocontours are depicted with thin solid and dashed lines for the positive and negatives values, respectively. The blue and red colours are also used to represent positive and negative values. The thick black curves highlight the zero isocontours of the corresponding function.

We start by analysing the fluid transfer function, present in the first column of figure 3.8. The eigenvalues of the purely-fluid eigenproblem are superposed to the Y^f representation using blue circles. On the bottom left plot, we label the fluid eigenvalues described in section 3.3.1, σ_{f1} and σ_{f2}, as 1 and 2, respectively. In the top left corner, one finds the real part of Y^f, which presents a symmetry with respect to the real axis, with a positive region between the fluid eigenvalue σ_{f1} and the origin. Concomitantly, the zone between the eigenvalues σ_{f2} and σ_{f1} is dominated by negative values, for $s_i \approx 0.4$. This negative region has an upper limit around $s_i \approx 0.8$. The highlighted zero isocontour lines are then separating these positive and negative regions, passing through the fluid eigenvalues, where Y^f is not defined. Concerning the imaginary part of Y^f, it presents an antisymmetric behaviour with respect to the real axis. In a similar way as for the real part, the behaviour of Y_i^f is mainly governed by the fluid eigenvalues σ_{f1} and σ_{f2}. This time, a wide

negative region for a positive s_i is found near the s_i axis. Due to its antisymmetric characteristic, Y_i^f is zero along the s_r axis. We further note that, as Y_i^f is zero along the s_r axis, Y^f is purely real, which means that a moment generated by a

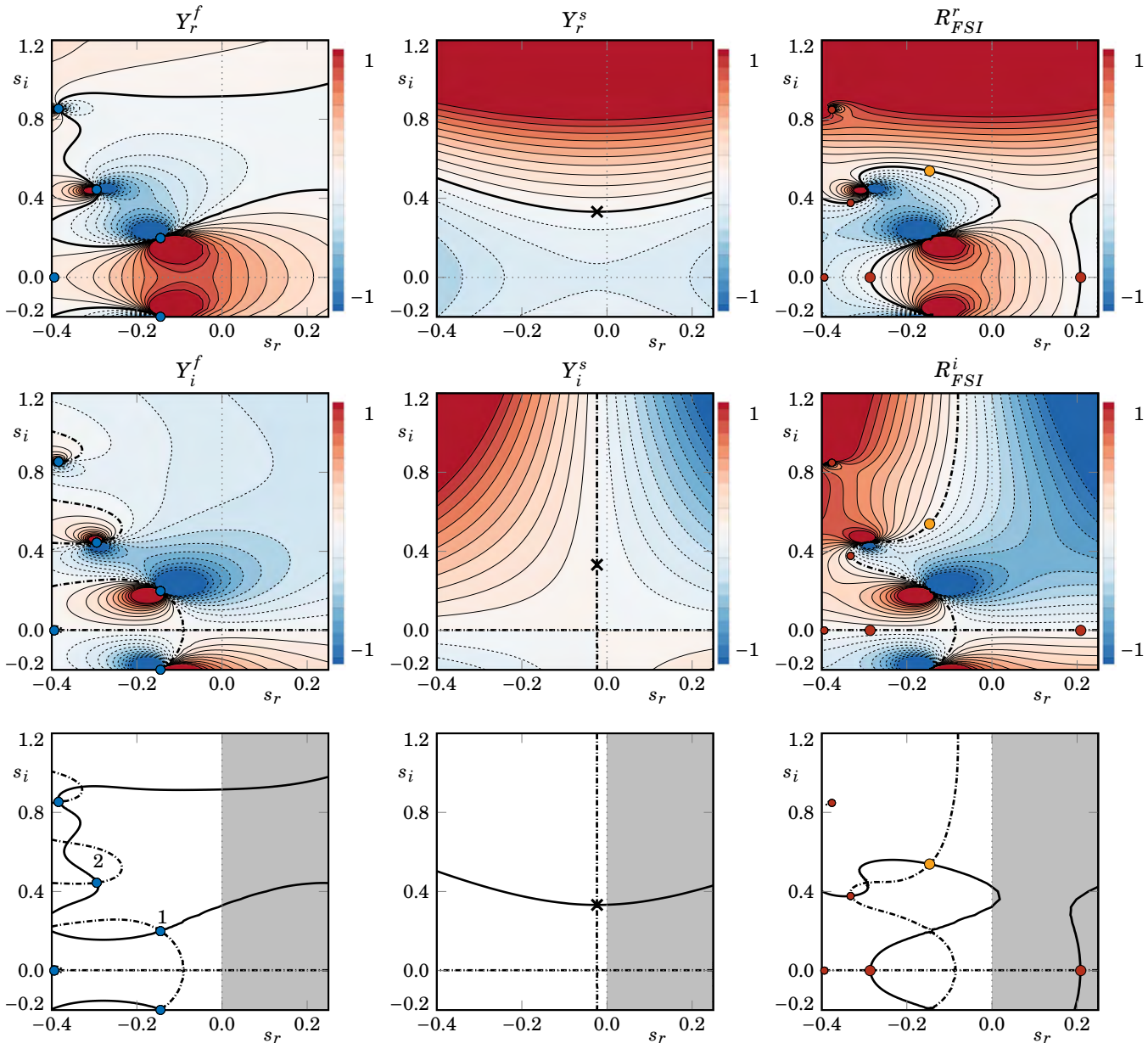

Figure 3.8 – *Mapping of the functions Y^f, Y^s and R_{FSI} on the complex plane. The first row represents their real part, the second row represents their imaginary part and the third row represents the zero isocontours of the real (solid line) and imaginary (dash-dotted lines) parts. The fluid eigenvalues are represented by the blue circles, with the two low frequency eigenvalues labelled 1 and 2 highlighted on the bottom left figure. The divergence and flutter eigenvalues are represented by the bigger red and yellow circles, respectively. The remaining FSI eigenvalues are represented by the smaller red circles. The eigenvalue of the structure equation in vacuum is represented by the black cross.*

static linear fluid response will be purely real as well.

The zero isocontour lines of both Y_r^f and Y_i^f functions are presented in the bottom left of figure 3.8. Most of the intersecting points correspond to purely-fluid eigenvalues (blue circles), where the resolvent operator is singular. Since they are poles of the fluid transfer function, their amplitude is not defined, instead of being zero. The case where both Y_r^f and Y_i^f are zero appears twice in the figure. Based on the definition of the fluid transfer function, $Y^f = \boldsymbol{m}^T \bar{\boldsymbol{q}}_f / \bar{\theta}$, the case where both Y_r^f and Y_i^f are zero corresponds to the situation where a nonzero angular displacement applied to the airfoil does not generate a moment on the structure. This situation can be found on bodies where their inertia tends to zero. Some examples are the fall of tree leaves and the rising of bubbles in a liquid column, as studied for example in Assemat *et al.* (2012).

We turn our attention to the solid transfer function, Y^s. As for the Y^f function, the real and imaginary parts of Y^s exhibit a symmetric and antisymmetric behaviour, respectively. However, these properties are found not only with respect to the s_r axis, but also with respect to a vertical axis at $s_r = -D_s/(2I_s)$. To better understand the reason behind this behaviour, one can explicitly write the real and imaginary parts of Y^s as:

$$Y_r^s(s) = -(s_r^2 - s_i^2)I_s - s_r D_s - K_s\,,$$

$$Y_i^s(s) = -2 s_r s_i I_s - s_i D_s\,.$$

Each one of these equations represents a typical saddle node surface, called a hyperbolic paraboloid, where the saddle node is located at $(s_r, s_i) = (-D_s/(2I_s), 0)$. The intersection of both zero isocontours gives the eigenvalue of the structure equation in vacuum, given in equation 1.11 (page 23) as $\lambda_s = -D_s/(2I_s)$ and $\omega_s = \pm\sqrt{K_s/I_s - \lambda_s^2}$. This solid eigenvalue is represented by the black cross in the figure. Concerning Y_r^s, it can be observed that for the regions close to the $s_r = -D_s/(2I_s)$ axis, the term Y_r^s increases as the magnitude of s_i increases. Concomitantly, close to the $s_i = 0$ axis, the term Y_r^s decreases as the magnitude of s_r increases. The same reasoning can be made for Y_i^s, but along directions that are 45° out-of-phase of the above axes.

Finally, we analyse the sum of the fluid and solid functions, depicted on the third column of figure 3.8. The coloured circles superimposed on the graphs represent the fluid–structure eigenvalues, with the bigger red circles for the divergence eigenvalues and the yellow circles for the flutter eigenvalue. Concerning the real part of R_{FSI}, the region $s_i \gtrsim 0.5$ is dominated by the structure term Y_r^s. In contrast, Y_r^f dominates the behaviour of R_{FSI}^r near the origin, where the structure component is small and the influence of the fluid eigenvalue σ_{f1} is significant. Between these two regions, the behaviour of R_{FSI}^r is nontrivial. Concerning the imaginary part of R_{FSI}, the region $s_i \gtrsim 0.5$ is again dominated by the structure term Y_i^s, while in remaining regions, both fluid and solid transfer functions are significant. The zero isocontour lines of R_{FSI}^r and R_{FSI}^i are found on the bottom right of figure 3.8. The intersections of these lines represent the cases where either R_{FSI} is zero, corresponding to the eigenvalues of the FSI problem, or to cases where R_{FSI} is not defined, corresponding to the fluid eigenvalues. The former case is highlighted by the red and yellow circles. As depicted in the figure, the flutter mode is located on the stable side of the spectrum, whereas one of the two highlighted divergence modes appears on the unstable side.

One can note that the R_{FSI}^r region where the flutter mode is located is mainly dominated by isocontours oriented on the horizontal direction, suggesting that the frequency of the flutter mode is selected from R_{FSI}^r. On the other hand, we note that the R_{FSI}^i region where the flutter mode is located is mainly dominated by isocontours oriented on the vertical direction, suggesting that the growth rate of the flutter mode is selected from R_{FSI}^i.

Further, one can note that a small portion of the zero isocontour of R_{FSI}^r crosses the unstable region, suggesting an admissible unstable flutter mode, depending on the zero isocontour of R_{FSI}^i. However, both fluid and solid components of

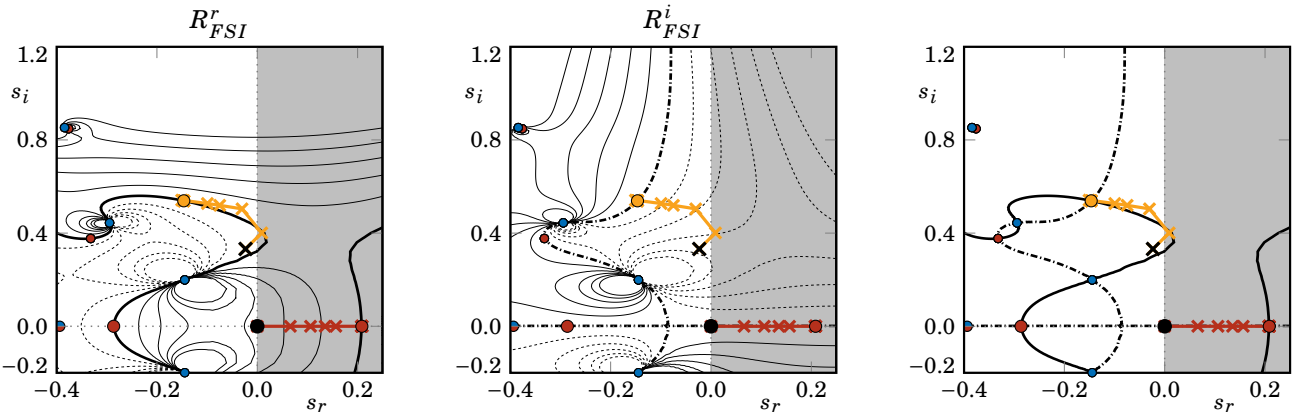

Figure 3.9 – *Evolution of the eigenvalue solutions on the complex plane as the nonlinear Newton procedure converges to the unstable divergence (red circle) eigenvalue and to the flutter (yellow circle). The fluid eigenvalues are represented by the blue circles. The divergence and flutter eigenvalues are represented by the bigger red and yellow circles, respectively. The remaining FSI eigenvalues are represented by the smaller red circles. On the left and centre plots, the isocontour lines of the real and imaginary parts of R_{FSI}, respectively (dotted pattern for the negative isocontours and solid pattern for the zero and positive isocontours). On the right plot, the corresponding zero isocontour lines, with a solid line for the real part and a dash-dotted line for the imaginary part of R_{FSI} The initial guesses are represented by the black circle and the black cross, for the divergence and flutter eigenvalues, respectively, see table 3.3.*

R^i_{FSI} present negative values in the region $s_i > 0$ and $s_r > 0$. This causes the flutter mode to be necessarily located in the stable side of the spectrum.

Concerning the divergence eigenvalue, its growth rate is entirely fixed by the zero isocontour of R^r_{FSI}. This is due to the antisymmetric character of the imaginary parts of both Y^f and Y^s with respect to the s_r axis, their value being zero for $s_i = 0$. One way of stabilising this eigenmode is by varying the zero isocontour line associated to R^r_{FSI}, which in turn can be modified by the Y^s_r behaviour. As detailed in the physical description of these modes, in the next chapter, the Y^s_r behaviour can be modified by varying the stiffness of the structure, K_s.

With the knowledge of the residual behaviour on the complex plane, we turn back our attention to the results presented with the Newton iterative method, in section 3.3.3. In figure 3.9, we superpose the path of the eigenvalues (computed with the iterative Newton algorithm) to isocontours of the residual R_{FSI}. Its real and imaginary parts are displayed on the left and middle figures, while only the zero isocontours are shown on the right figure. Let us first focus on the flutter eigenvalue displayed in yellow and recall that the guess value corresponds to a purely-solid eigenvalue. We note that this guess value is close to a zero isocontour of real residual (left figure). The path of the eigenvalue clearly follows that isocontour because the Newton algorithm looks for zero of the complex residual. For the imaginary part (middle figure), the behaviour is different because the guess value is away from a zero isocontour. In that case, the path of the eigenvalue is roughly normal to the isocontours, illustrating the gradient descent direction chosen by the Newton algorithm. This representation provides a graphical illustration of the role of the purely-fluid eigenvalues on the fluid–structure flutter eigenvalue. The low frequency fluid eigenvalues (blue circles) both tend to push away the initial guess value (black cross) in directions normal to the sum of the dipoles formed around them.

Let us now examine the behaviour of the divergence eigenvalue, highlighted with the red colour. The guess value is here chosen as the origin on the complex plane. The path of the divergence eigenvalue follows the real axis which is a zero isocontour of the imaginary residual (middle figure). This path is oriented into the destabilising direction because the

Quasi-steady order	K_a	D_a^θ	D_a^Ω	D_a	I_a^θ	I_a^Ω	I_a
0	−1.5038	—	—	—	—	—	—
1	−1.5038	5.4354	−0.6874	4.7480	—	—	—
2	−1.5038	5.4354	−0.6874	4.7480	5.3882	2.246	7.6342

Table 3.4 – *Added coefficients of the quasi-steady approximation for the three first orders at Re = 50 000 and α = 0°.*

Quasi-steady order	Eigenvalues σ_{QS}	
0	0.5097	−0.5561
1	0.1920	−1.4766
2	0.1606	−0.5901

Table 3.5 – *Summary of eigenvalues predicted by the quasi-steady approximation for the three first orders at Re = 50 000 and α = 0°.*

isocontours of the real residual (left figure) decrease in that direction. This behaviour is clearly induced by the closest pair of low frequency fluid eigenvalues, thus unravelling its role in the divergence fluid–structure instability. We also remark that choosing a guess value with a lower real part would lead to a convergence towards the stable static eigenvalue.

3.3.5 Quasi-steady approximation results

In this section, we discuss the results associated to the quasi-steady approximation, present in sections 1.6 (page 42) and 3.2.4 (page 122). As a reminder, in the quasi-steady approximation, the structural eigenvalues are approximated by the solution of the following equation:

$$(I_s + I_a)\sigma_{QS}^2 + (D_s + D_a)\sigma_{QS} + (K_s + K_a) = 0\,.$$

We denote a quasi-steady approximation of order 2 when all the added coefficients are taken into account, an approximation of order 1 when only the terms D_a and K_a are taken into account and an approximation of order 0 when only K_a is taken into account. Table 3.4 summarises the added coefficients for these three orders. We first note that these coefficients are real.

Concerning the quasi-steady approximation of order 0, where only the added stiffness is taken into account, several points are noted. First, we note that K_a is negative. Further, as discussed in section 1.6, K_a corresponds to an approximation of the slope at $\alpha = 0°$ of the aerodynamic moment curve as function of the incidence, noted m_z^α. This value was reported in the previous chapter (cf. figure 2.12, page 82), having a value of $m_z^\alpha = -1.5223$. When comparing with the value of the added stiffness ($K_a = -1.5038$) one finds that m_z^α at $\alpha = 0°$ is very well approximated by the quasi-steady approximation. Further, K_a can be interpreted as an aerodynamic stiffness, acting on the opposite sense of the structural stiffness. By neglecting D_s, a stability criterion for the emergence of a static eigenvalue can be posed as (see equation 1.49, page 45)

$$\text{if } K_s < -K_a: \quad \text{Existence of an unstable static eigenvalue.}$$

Since the nondimensional structural stiffness has a value of $K_s = 0.41689$ for $Re = 50\,000$ (see table 1.3, page 1.3), we

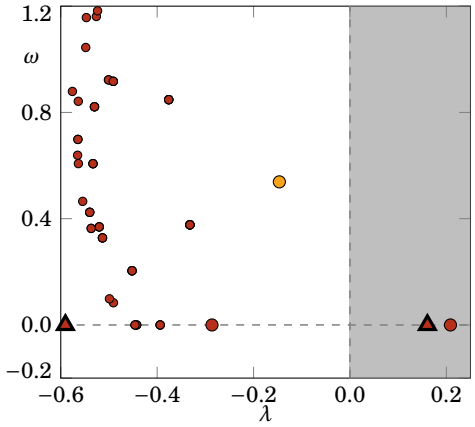

Figure 3.10 – *Comparison between the exact and quasi-steady approximation method at order 2: spectrum of a fluid–structure mean flow linear stability analysis at Re = 50 000 and α = 0° for the nominal structure parameters and using the classical formulation. The exact solution is represented by the circle symbols, highlighting the divergence (bigger red circles) and flutter (yellow circles) eigenvalues. The approximation of the divergence eigenvalues is represented by the red triangles.*

conclude that the presence of an unstable static eigenvalue can be predicted by a the quasi-steady approximation. This loss of total stiffness ($K_s + K_a$) is characteristic of a divergence instability, as discussed on the Introduction of this thesis. The exact value of this prediction is reported in table 3.5. We observe that the quasi-steady approximation estimates a more unstable eigenvalue ($\sigma_{QS} = 0.5097$) than the exact eigenvalue found in the previous sections ($\sigma = 0.2086$). The stable static eigenvalue found in the analysis of the previous sections ($\sigma = -0.2863$) is also found in this quasi-steady approximation ($\sigma_{QS} = -0.5561$), where we also note significant differences between the exact and approximated value.

We also report the added coefficients and resulting eigenvalues for the quasi-steady approximation at orders 1 and 2, in tables 3.4 and 3.5, respectively. Additionally, figure 3.10 gives a graphical comparison between the eigenvalues of a quasi-steady approximation of order 2 and the exact eigenvalues. We start by noting that the added damping coefficient associated to an angular displacement perturbation, D_a^θ, is one order of magnitude larger than the coefficient D_a^Ω, associated to an angular velocity perturbation. Further, they have opposite contributions. Concerning the added inertia contributions, we also found a more important value of the coefficient associated to the angular displacement perturbation. One can note that the prediction for the eigenvalues at the orders 1 and 2 is significantly better than the first prediction at order 0. Interestingly, the order 1 gives a better prediction than the order 2 for the unstable static eigenvalue, when comparing with the exact value of $\sigma = 0.2086$.

With this analysis we conclude that a quasi-steady approximation only gives access to the eigenvalues placed along the real axis, *i.e.*, to the divergence eigenvalues. Therefore, the next approximative method was developed with the aim of also approximating the flutter eigenvalues.

3.3.6 Results for the rational function approximation of the fluid transfer function

In this section, we present the results associated to the approximation of the fluid transfer function as a rational function. This approximation is intended to improve the numerical efficiency of the eigenvalue computation, when compared to the Krylov–Schur and the Newton methods, where the fluid transfer function is exactly computed. The theoretical details of this approximation are present in section 3.2.5 (page 123). The approximation is based on two

Fluid pole	σ_1	Y_0	Y_1	$Y_1 + Y_1^*$	C
$\sigma_{f1} = -0.1446 + 0.1992\mathrm{i}$	$4.4408 + 0.3607\mathrm{i}$	$0.0121 - 0.0199\mathrm{i}$	$0.9536 + 1.0810\mathrm{i}$	1.9072	-0.0327
$\sigma_{f2} = -0.2944 + 0.4441\mathrm{i}$	$-3.6682 + 2.7432\mathrm{i}$	$0.0056 + 0.0069\mathrm{i}$	$0.1748 - 0.0747\mathrm{i}$	0.3496	

Table 3.6 – *Constants associated to the Y^f approximation, for the two fluid poles considered.*

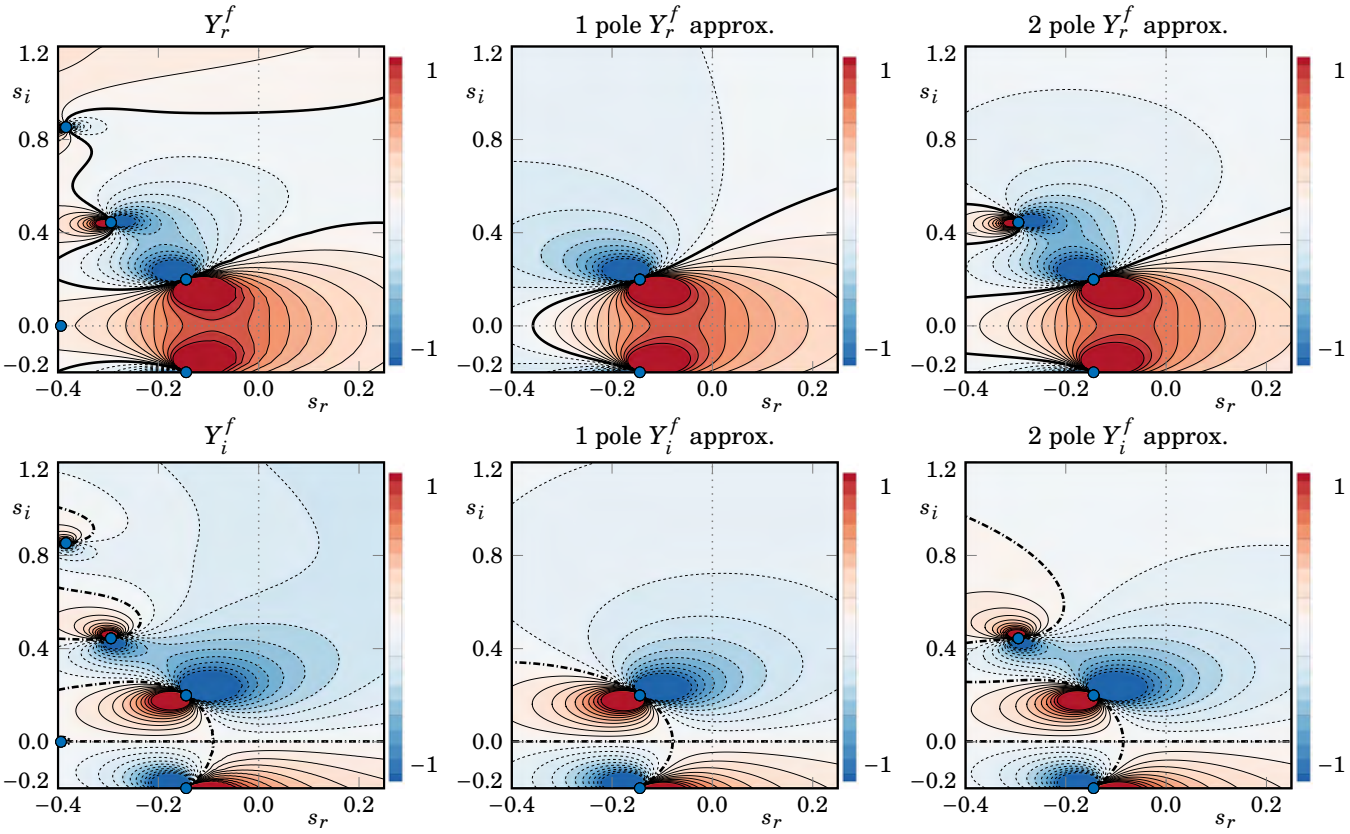

Figure 3.11 – *Mapping of the real and imaginary parts of fluid transfer function Y^f on the complex plane: the exact solution (left), the rational function approximation with one fluid eigenvalue (centre) and with two fluid eigenvalues (right).*

purely-fluid eigenvalues, described in section 3.3.1.

The approximation is given in equations 3.33 and 3.34. The constants σ_1 and Y_0 are associated to the terms at order $\mathcal{O}(1/\epsilon)$, for each pole, while the constant Y_1 is associated to the order $\mathcal{O}(1)$ term. Table 3.6 summarises the values of these constants, as well as the calibration constant C.

The contribution of the order $\mathcal{O}(1)$ terms is given by the column $Y_1 + Y_1^*$, for each pair of complex conjugate poles. As remarked earlier, this term constitutes a real constant. Due to its relative high value, we replace these terms by the constant of calibration C. The calibration constant is chosen such that the model predicts the exact value at the origin of the complex plane, $(s_r, s_i) = (0, 0)$. The position of the calibration is chosen on the s_r axis ($s_i = 0$) in order to obtain a real constant. The value of $s_r = 0$ for the calibration is arbitrary, but it represents a good equilibrium position between

the divergence and flutter eigenvalues that we ultimately want to approximate. The influence of the calibration on the results was not studied.

Figure 3.11 presents the complex mapping of the real and imaginary parts of Y^f, with the exact solution on the left column, a 1 pole approximation on the centre column and a 2 pole approximation on the right column. The 1 pole approximation is based on the fluid eigenvalue σ_{f1} and its complex conjugate. We first note that the 1 pole approximation represents a qualitatively good approximation of the zone near the s_r axis, where the static eigenvalues are present, in particular the divergence mode. However, this approximation is less accurate in the zone $s_i \approx 0.5$, where the flutter mode is expected to be found. Therefore, we consider a 2 pole approximation, based on the fluid eigenvalues σ_{f1} and σ_{f2} (and their complex conjugate), present on the right column of figure 3.11. The addition of this second complex conjugate pair of eigenvalues does not substantially change the behaviour of the Y^f approximation near the s_r axis, while better taking into account the nonlinear character of Y^f on the zone $s_i \approx 0.5$.

To better quantify the accuracy of the 2 pole approximation, we sketch the values of Y_r^f and Y_i^f along the s_r and s_i axes on figure 3.12. Concerning the s_r axis, present on the left, we first note that the Y_i^f, represented by the blue lines, is zero, as expected. On the other hand, Y_r^f, represented by the black lines, presents a good agreement between the exact solution (solid line) and the 2 pole approximation (dashed line). The exact solution presents a discontinuity at $s_r = -0.4$, due to the presence of a fluid eigenvalue. This discontinuity is not found in the 2 pole approximation, as this eigenvalue is not taken into account in the approximation. We also note that the solid and dashed lines cross each other at $s_r = 0$, where the calibration is made. Concerning the s_i axis, presented on the right of figure 3.12, one can note that Y_r^f (black lines), presents a symmetric behaviour with respect to $s_i = 0$, while Y_i^f (blue lines) presents an antisymmetric behaviour. Once again, the approximation is found to be exact at $s_i = 0$, where the calibration is made. The absolute error between the two curves increases with the distance to the origin, which is a consequence of the order truncation of the development and the fact that only two complex conjugate pairs of poles were taken into account.

With an analytic expression for the Y^f approximation (equation 3.34), the fluid–structure eigenvalues can be approximated using the Newton method presented previously. The accuracy of this prediction directly depends on the quality of the Y^f approximation at the divergence and flutter eigenvalues. We note that, since Y^f is approximated, the location of the divergence and flutter eigenvalues is also approximated. However, we can quantify the relative error made on the Y^f approximation at the exact value of these eigenvalues, since we know their exact location. The aim is to understand the effect of this approximation on the final values of the fluid–structure eigenvalues. Table 3.7 summarises

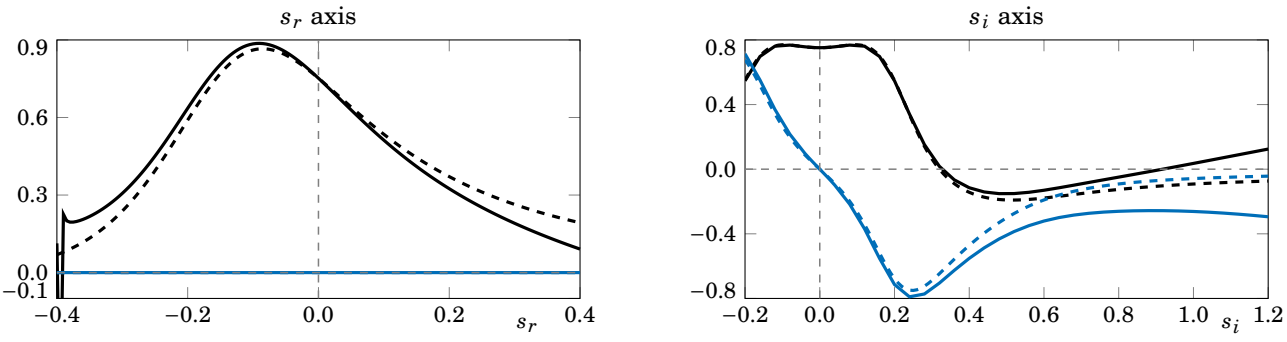

Figure 3.12 – *Evolution of Y_r^f (black) and Y_i^f (blue) along the axes, for the s_r axis (left), where $s_i = 0$, and for the s_i axis (right), where $s_r = 0$. The solid lines represent the exact solution, whereas the dashed lines represent the two pole approximation calibrated on the point $(s_r, s_i) = (0, 0)$.*

	Exact analysis	1 pole approximation	2 pole approximation
Y^f at the divergence eigenvalue	0.3114	0.3422	0.3342
Relative error		9.89%	7.32%
Y^f at the flutter eigenvalue	$-0.3129 + 0.2519$i	$-0.2510 + 0.2705$i	$-0.3335 + 0.1858$i
Relative error		19.81% + 7.35%i	6.57% + 26.22%i

Table 3.7 – *Exact and approximative values of the fluid transfer function Y^f at the divergence and flutter eigenvalues location.*

	Divergence eigenvalue	Flutter eigenvalue
Exact analysis	0.2084	$-0.1465 + 0.5386$i
Approximated analysis (one pole)	0.2420	$-0.1619 + 0.5083$i
Approximated analysis (two poles)	0.2330	$-0.1136 + 0.5422$i
Relative error (one pole)	16.13%	10.54% + 6.67%i
Relative error (two poles)	11.80%	22.45% + 0.67%i

Table 3.8 – *Comparison of the FSI eigenvalues between the exact and the Y^f approximation methods based on one and two poles, along with the relative error of their real and imaginary parts.*

the values of Y^f given by the exact and the approximation analysis, at the divergence and flutter eigenvalues.

Concerning the divergence eigenvalue, with an exact location at $\sigma = 0.2084$, Y^f presents a relative error below 10% for both 1 and 2 pole approximations. The relative error decreases with the increase of the number of poles taken into account. The same tendency is expected to be found on the 1 and 2 pole approximation of the divergence eigenvalue.

Concerning the flutter eigenvalue, with an exact location at $\sigma = -0.1465 + 0.5386$i, the relative error is computed independently for the real and imaginary parts of Y^f. For the real part, we see a decrease of the relative error with the increase of the number of poles taken into account. Interestingly, the opposite behaviour is found for the relative error associated to Y_i^f. From the discussion made in section 3.3.4, we have concluded that the growth rate of the flutter eigenvalue is mainly governed by the imaginary part of R_{FSI} (where Y_i^f is present), whereas the frequency of the flutter eigenvalue is mainly governed by R_{FSI}^r (where Y_r^f is present). Since we found an increase of the relative error of Y_i^f with the increase of poles considered in the approximation, we expect to find the same tendency on the growth rate of the flutter eigenvalue. Likewise, a decrease of the relative error is expected to be found on the frequency of the flutter eigenvalue.

We proceed to the computation of the approximative divergence and flutter eigenvalues, using the Newton method presented previously. Starting from the same guess values as presented in table 3.3, the approximation of the divergence and flutter eigenvalues is found for 1 and 2 pole approximations. The spectrum comparison is present in figure 3.13, with the numerical values and associated relative errors described in table 3.8. Concerning the divergence eigenvalue, we note that the approximation of the fluid transfer function tends to predict a more unstable divergence mode. The relative error associated to this prediction decreases from the 1 pole approximation to the 2 pole approximation, as expected from the reasoning presented in the previous paragraph. Concerning the flutter eigenvalue, we note that the main source of discrepancy is found on its real part. As expected, the increase in the number of poles taken into account increased the relative error of the real part and decreased the error of the imaginary part. The latter presents an excellent agreement with the exact value of the 2 pole approximation, with a relative error inferior to 1%.

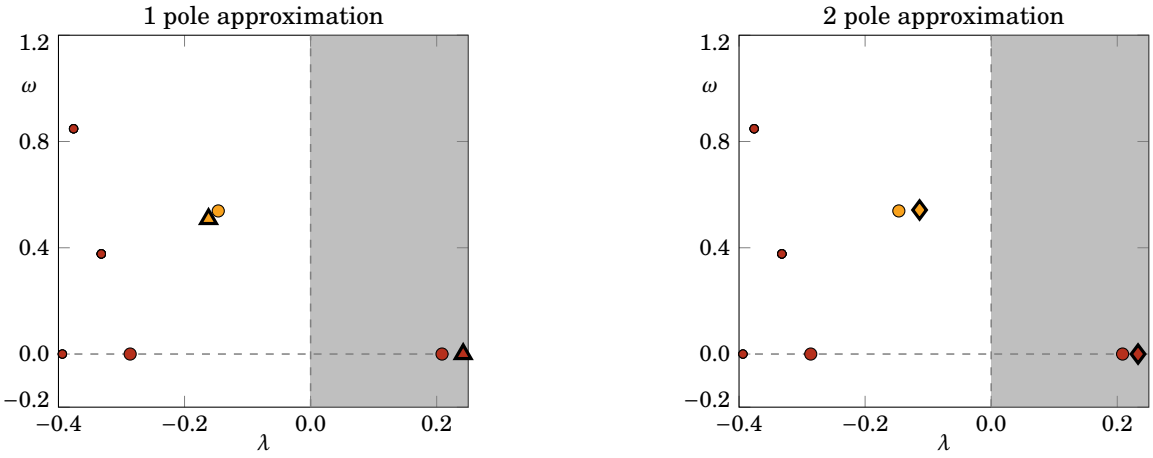

Figure 3.13 – *Comparison between the exact and rational function approximation methods: spectrum of a fluid–structure mean flow linear stability analysis at Re = 50 000 and α = 0° for the nominal structure parameters and using the classical formulation. The exact solution is represented by the circle symbols, highlighting the divergence (bigger red circles) and flutter (yellow circles) eigenvalues. The approximation of the divergence and flutter eigenvalues based on one fluid pole (left) is represented by the red and yellow triangles, respectively, while their approximation based on two fluid poles (right) is represented by the diamond symbols.*

We conclude that the approximation of the transfer function via a sum of rational functions enable us to approximate both divergence and flutter eigenvalues, in contrast with the quasi-steady approximation, when only the divergence eigenvalue is approximated.

Conclusion

This chapter was dedicated to the implementation and comparison of different methods to estimate the eigenvalues and eigenmodes associated to a fluid–structure mean flow linear stability analysis. The first approach, based on a Krylov–Schur method, enabled the computation of any eigenvalue in the spectrum, near an established shift value. The second approach was based on the resolution of an equivalent reduced-size nonlinear eigenvalue problem using a Newton–Raphson method. This enabled the computation of particular eigenvalues near the zone of interest, where the fluid–solid eigenvalues were expected to by present. The influence of the fluid on the fluid–structure eigenvalues was accessed by sketching the behaviour of the fluid transfer function (ratio between the aerodynamic moment associated to the linearised fluid response to the solid motion and the angular displacement) on the complex plane. In the last part of this chapter, the exact value of the fluid transfer function on the complex plane was approximated by a rational function, with which the fluid–structure eigenvalues were approximated.

Chapter 4

Primary aeroelastic instability

In the chapter, we study the linear stability of the coupled fluid–structure system of a rigid NACA0012 airfoil with a pitch degree of freedom. The analysis is centred on the primary FSI instability, for the angle of incidence $\alpha = 0\,^\circ$. In that way, the chapter is organised as follows. In a first part, we describe the emergence of a primary instability of the FSI system, by the means of a mean flow FSI linear stability analysis. In a second part, the emergence of the primary FSI instability is analysed via a Floquet FSI analysis. We end the chapter with a comparison of both methods and a comparison with the fluid–structure behaviour found for nonlinear time-marching simulations.

4.1 Introduction

The linear stability of fluid–solid systems is a classic subject on the aeroelasticity community (Bisplinghoff *et al.*, 1955; Clark *et al.*, 2004). In the earlier years, the primordial aim was to delimit the flight envelope of military and commercial aircraft cruise flights, whose Reynolds number often exceeds a million. In these cases, the turbulent flow regime is readily triggered from upstream locations near the leading edge, leading to a boundary layer that remains attached to the surface for a relatively hight range of angles of attack. In such situations, the prediction for the flutter and divergence instabilities can be based on linearised approaches for the fluid, by considering the flow as inviscid and irrotational, and thus described with potential equations, such as the Theodorsen model (Theodorsen, 1935).

However, as the Reynolds number decreases, the transition location moves downstream, originating a laminar boundary layer over a considerable portion of the wing. For a low-to-moderate Reynolds number range, $10^4 \leq Re \leq 10^6$, the flow regime is characterised by the coexistence of laminar, transition and turbulent regions, where laminar boundary layer region can lead to complex viscous phenomena, such as the formation of a laminar separation bubble (Mueller, 1951).

In this transitional Reynolds number regime, Poirel *et al.* (2008) carried out a wind tunnel experimental investigation of a NACA0012 airfoil mounted on a torsional spring system, demonstrating the existence of self-sustained limit cycle oscillations within the Reynolds number range of $45\,000 \leq Re \leq 130\,000$. The phenomenon is labelled as *Laminar Separation Flutter* (LSF). In this chapter, we perform different linear stability analyses in order to understand the onset of these self-sustained oscillations.

Regarding the global Linear Stability Analysis (LSA), the aim is to evaluate the linear stability character of the dynamical system considered. Accordingly, the solution is decomposed as a sum of a base equilibrium state and a linear perturbation, the latter written as a normal mode with an associated growth rate and frequency. In this thesis,

two different base equilibrium state solutions are considered. For the mean flow analysis, the base equilibrium state corresponds to the time-independent solution, denoted mean flow. On the other hand, for the Floquet analysis, the base equilibrium state corresponds to the periodic solution over one vortex shedding period, denoted periodic flow solution. In both cases, the equilibrium is deemed unstable if at least one eigenmode has a positive growth rate, corresponding to a perturbation that grows in time.

In the case of coupled fluid–structure systems, several configurations have been studied in the past years. To what concerns the very low-Reynolds number regimes, the case of the spring-mounted cylinder represents a classical benchmark. In this case, the phenomenon of the vortex-induced vibrations is studied (Cossu *et al.*, 2000; Meliga *et al.*, 2011; Zhang *et al.*, 2015b; Navrose *et al.*, 2016; Kou *et al.*, 2017; Sabino *et al.*, 2020). Among other studies, Assemat *et al.* (2012); Tchoufag *et al.* (2014a,b) examined the case of two-dimensional rigid bodies falling or rising freely in a viscous fluid, Pfister *et al.* (2020); Furquan *et al.* (2021) carried out a LSA on a flexible splitter plate attached to a rigid circular cylinder and Moulin *et al.* (2021) investigated the case of a rectangular plate mounted on heave and torsion springs. Concerning Floquet FSI analyses, Jallas *et al.* (2017) studied the symmetry breaking in time-periodic propulsive wakes for imposed flapping airfoils. With similar methods, Benetti Ramos (2020); Benetti Ramos *et al.* (2021) investigated the role of linear mechanisms in the emergence of nonlinear horizontal self-propelled states of a heaving foil in a quiescent fluid.

Concerning the laminar separation flutter, the number of linear stability studies is scarce. Negi (2019); Negi *et al.* (2021) performed a mean flow FSI linear stability analysis over a NACA0012 airfoil configuration with a pitch degree of freedom, as the case investigated in this thesis. The mean flow solution was obtained from a time- and spanwise-averaged solution of DNS simulations at $\alpha = 0°$. In their linear stability analysis, they obtained a divergence mode that becomes unstable for $Re \approx 40\,000$ (for the case where $K_s^{dim} = 0.15$Nm). However, with these results alone, one cannot explain the existence of the self-sustained oscillations associated to the LSF, since no frequency is associated to the divergence mode. The explanation came from the linearly stable low frequency mode, whose frequency is in accordance with the frequency of the LSF observed experimentally. In that way, they concluded that "[...] the observed LCO frequency is likely to arise due to the nonlinear modification of the linearly stable aeroelastic mode, while the onset itself is caused by the divergence instability with zero frequency.".

With that in mind, we readdress this problem to study the onset of the static instability of the airfoil configuration at $\alpha = 0°$, associated to the presence of a linearly unstable divergence mode. This is accomplished by the means of two different linear stability formulations of the mean flow eigenproblem, presented in chapter 1, and by the means of a Floquet FSI analysis. The mean flow analyses are performed around a mean flow coming from a time-averaged solution of two-dimensional simulations and from a time- and spanwise-averaged solution of three-dimensional simulations, both at $\alpha = 0°$. At the same time, the Floquet analysis is performed around a periodic two-dimensional limit cycle solution, also at $\alpha = 0°$. In a first part, the Reynolds number is fixed at $Re = 50\,000$, in accordance with the main works found on the literature regarding the laminar separation flutter instability. Subsequently, the influence of the Reynolds number on the fluid–structure eigenvalues is investigated. In the last part, the Floquet analysis is conducted at $Re = 20\,000$, in accordance with the subsequent chapters of this thesis.

4.2 Mean flow analysis of the primary instability at $Re = 50\,000$ and $\alpha = 0°$

We start this section by analysing the eigenmodes of a mean flow FSI linear stability analysis at $Re = 50\,000$ and $\alpha = 0°$. Unlike the previous chapter, mainly focus on the methodology to find the eigenvalues of this problem, the present chapter is rather focused on the physical aspects. This analysis is based on a classical formulation, similar to the one used by Negi *et al.* (2021), which is derived from the Floquet analysis (see section 1.4.4, page 35). The comparison with

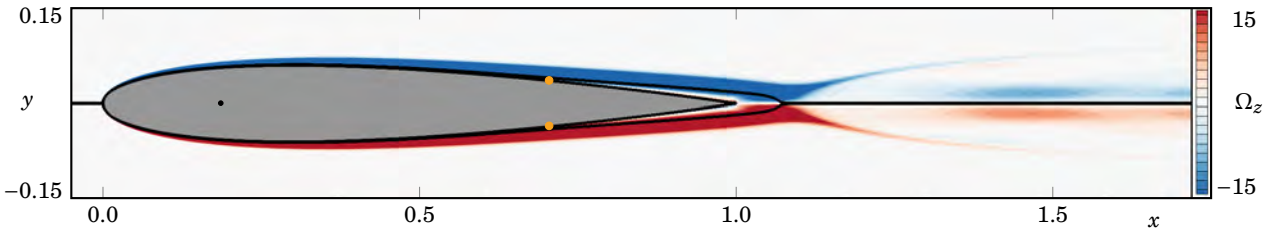

Figure 4.1 – *Spanwise vorticity field of time-averaged flow solution from two-dimensional simulations at Re = 50 000 and α = 0°. The yellow dots over the airfoil surface represent the separation points.*

the Reynolds stress formulation is made in a subsequent section. We start by describing the divergence and flutter eigenmodes, for the nominal values of the structural parameters (cf. table 1.1, page 23), corresponding to the same dimensional parameters employed in Poirel *et al.* (2008) and subsequently used by Negi *et al.* (2021). We then investigate the effect of these parameters on the fluid–structure eigenvalues, followed by the effect of the Reynolds number and the airfoil geometry. These stability analyses are carried out around mean flow solutions issued from two-dimensional time-marching simulations. For that reason, we then proceed to the comparison of these results with a FSI analysis around a time- and spanwise-averaged solution from 3D simulations.

4.2.1 Description of the divergence and flutter eigenmodes

We start by reviewing the spatial distribution of the mean flow solution at $Re = 50\,000$ and $\alpha = 0°$. For that, we present in figure 4.1 the spanwise vorticity field of the mean flow solution. We observe that the vorticity field is mainly concentrated on the boundary layer region, and then on the wake of the airfoil. We also note the influence of the time average of the Reynolds stress components, by observing the deviation of the vorticity field on the wake of the airfoil, readily after the end of the recirculation zone. A deeper description of the mean flow solutions for different parameters was discussed in chapter 2. The present FSI stability analysis is carried out around this mean flow.

The fluid–structure eigenvalues can be recalled from figure 3.4 (page 128), are reported again in table 4.1. The corresponding eigenmodes, noted $\overline{\boldsymbol{q}} = \left[\overline{\boldsymbol{q}}_f, \bar{\theta}, \overline{\Omega}\right]^T$, are normalised with respect to the angular displacement component, verifying $\left|\bar{\theta}\right| = \sqrt{\bar{\theta}^H \bar{\theta}} = 1$. As previously noted, an unstable eigenvalue appears at a frequency of 29.30, which is associated to the hydrodynamic vortex shedding instability. As pointed out, the vorticity field of this eigenmode, present in figure 3.2, is concentrated on a convected wake region, far from the airfoil. Therefore, the eigenmode is expected to have little

	Eigenvalue σ	$\|\overline{\boldsymbol{q}}_f\|$	$\left\|\bar{\theta}\right\|$	$\left\|\overline{\Omega}\right\|$	$\bar{\theta}$	$\overline{\Omega}$
Vortex shedding mode	$0.2480 + 29.2972\mathrm{i}$	$3.5919 \cdot 10^6$	1	29.2970	$0.0175 + 0.9998\mathrm{i}$	$-29.2870 + 0.7607\mathrm{i}$
Divergence mode	0.2084	13.0302	1	0.2084	1	0.2084
Flutter mode	$-0.1465 + 0.5386\mathrm{i}$	39.2050	1	0.5582	$0.9964 + 0.0845\mathrm{i}$	$-0.1915 + 0.5243\mathrm{i}$

Table 4.1 – *Summary of the vortex shedding, divergence and flutter eigenmodes, with the norm of the fluid, $\bar{\theta}$ and $\overline{\Omega}$ components, and the corresponding values of $\bar{\theta}$ and $\overline{\Omega}$, for FSI linear stability analysis of the mean flow at Re = 50 000 and α = 0°.*

influence on the laminar separation flutter onset. Indeed, one can see in table 4.1 that the norm associated to the fluid component of the vortex shedding eigenmode is 5 orders of magnitude larger than the ones associated to the divergence or flutter modes. This fact is in accordance with the conclusions of Poirel *et al.* (2008), where they found no correlation between the pitch response and vortex shedding frequency, and in accordance with Negi *et al.* (2021), where the projection of the solid variables onto the fluid variables was concluded to be close to zero for all the high frequency eigenmodes.

In addition to the vortex shedding eigenmode, a close observation of the spectrum near the origin, in the previous chapter, revealed the emergence of two pairs of eigenvalues associated to the structure. The first pair is located along the real axis, with one eigenvalue on stable side and the other one on the unstable side of the spectrum, presenting no associated frequency. We denoted these eigenmodes as *divergence modes*. The second pair corresponds to a stable complex pair of eigenvalues and were denoted as *flutter modes*. The solid components of these eigenmodes are reported in the last two columns of table 4.1. The frequency of the flutter modes is comparable with the one of the purely-solid eigenvalues. The analytic expression of the real and imaginary parts of the latter is given in equation 1.11 (page 23), with a value of $\sigma_s = -0.0232 + 0.3289\mathrm{i}$.

The perturbation associated to the FSI eigenmodes as function of time can be reconstructed with the help of equation 1.34 (page 37). The perturbed field is retrieved by adding the mean flow state to the perturbation, *i.e.*, $\bar{\boldsymbol{q}}_b + \epsilon \boldsymbol{q}'$, using an arbitrary small value for ϵ. The evolution in time of the angular displacement and associated aerodynamic moment is depicted in figure 4.2 for the divergence mode, on the left, and for the flutter mode, on the right. One can first note that the evolution of the static perturbed variables exhibits no frequency. The exponential growth of the angular displacement is followed by the exponential growth of the moment, which deviates the airfoil from its equilibrium position at $\alpha = 0°$. This deviation can also be seem in the airfoil position on the left bottom plots, where the spatial structure of

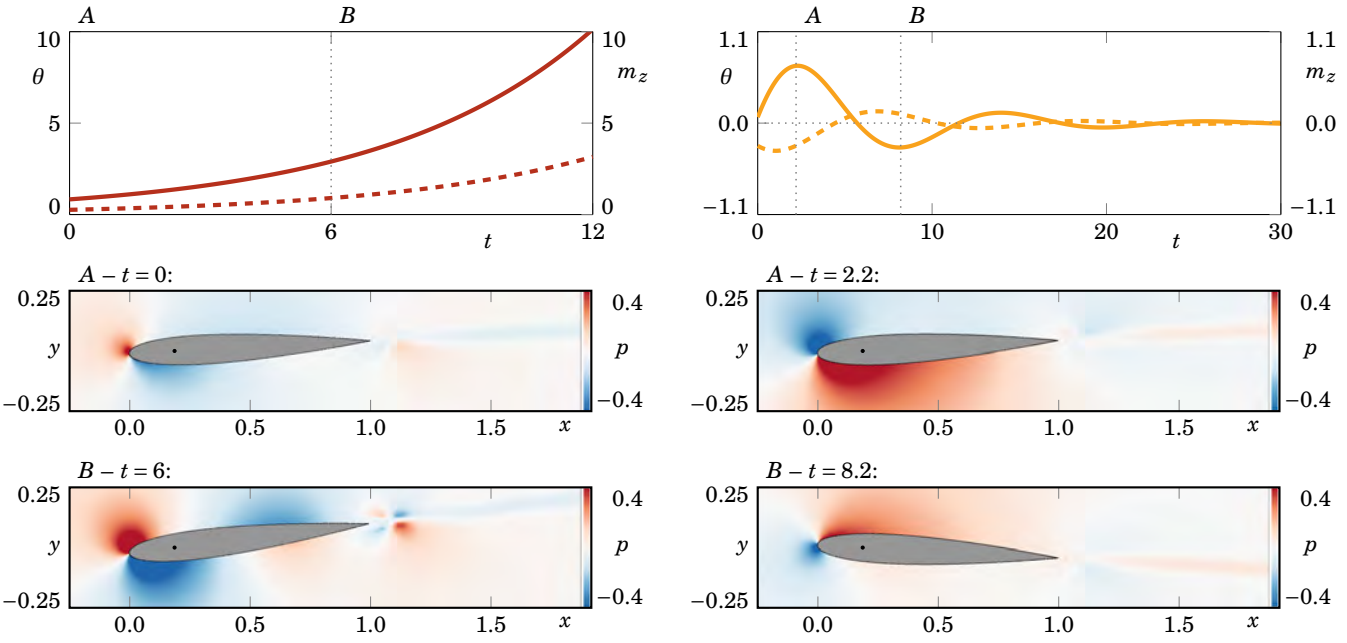

Figure 4.2 – *On top, evolution of the reconstructed angular displacement (solid) and aerodynamic moment coefficient (dashed), based on their time-averaged quantity plus an infinitesimal perturbation associated to the divergence (left) and flutter (right) eigenmodes at* $Re = 50\,000$ *and* $\alpha = 0°$. *On the centre and bottom, the reconstructed pressure field corresponding to two different instants.*

the perturbed pressure field for two instants is present. The amplification of the perturbation can also be seen in the intensification of the pressure fields between the two considered instants.

At the same time, the flutter perturbed state evolution is present on the right of figure 4.2. As the flutter eigenvalue has a negative growth rate, the perturbation decays in time, restoring the equilibrium position of the airfoil at $\alpha = 0°$. The angular displacement and aerodynamic moment are out of phase, presenting a phase shift of $\phi = 141.34°$. This phase shift ensures a restitutive force from the fluid. The decay of the perturbation can also be seen in the spatial decrement of the pressure fields between the two considered instants.

4.2.2 Effect of the structural parameters

In this section, we describe the influence of the stiffness, damping and inertia coefficients on the on the fluid–structure eigenvalues. We start by analysing the influence of the structural rigidity of the airfoil. The evolution of the eigenvalues near the origin with K_s is depicted in figure 4.3a in a spectrum representation. The arrows represent the increase of K_s from a value of $K_s = 0.417$ (corresponding to $K_s^{dim} = 0.15$Nm) to $K_s = 3.335$ (corresponding to $K_s^{dim} = 1.2$Nm). Additionally, figure 4.3b presents the spectrum for three different values of K_s, superimposed to the zero isocontours of the real and imaginary parts of R_{FSI}. We recall that R_{FSI} represents the residual of the reduced-size nonlinear eigenvalue problem, corresponding to the sum of the fluid and solid transfer functions (see equation 3.17, page 121). From the definition of the transfer functions (equations 3.14 and 3.15), we can note that both the fluid transfer function and the imaginary part of Y^s remain constant when K_s changes. Therefore, a change in K_s is only felt on the real part of Y^s and consequently on R^r_{FSI}. For that reason, only one zero isocontour line of R^i_{FSI} is present in figure 4.3b, represented by the black dash-dotted line. On the other hand, the three different coloured solid lines represent the zero isocontour lines of R^r_{FSI} associated to the three values of K_s. This figure helps to understand that the FSI eigenmodes can be found by intersecting the zero isocontour lines of R^r_{FSI}, with the ones from R^i_{FSI}, the latter fixed on the K_s variation.

Concerning the divergence eigenvalues (bigger red circles), one observes that the stable and unstable eigenvalues move

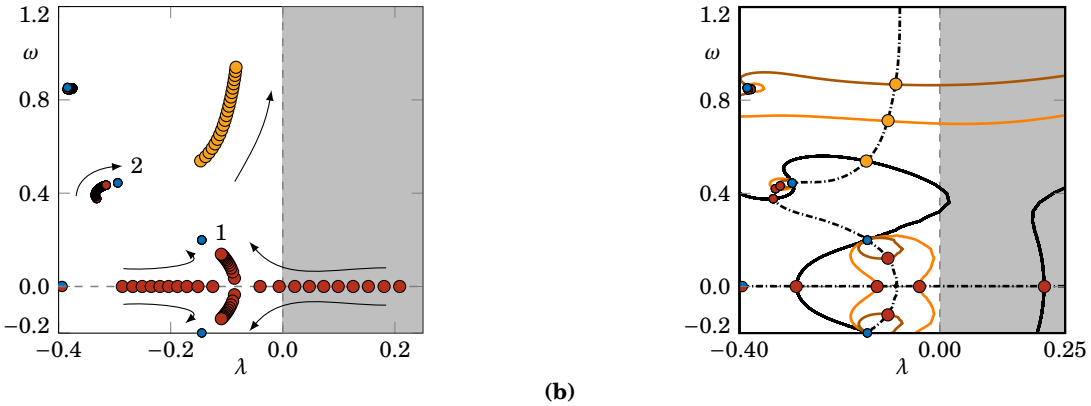

Figure 4.3 – *Influence of the structural stiffness on the FSI eigenvalues: on the left, the spectrum evolution of the eigenvalues for the range* $0.417 \leq K_s \leq 3.335$*, with the bigger red and yellow circles corresponding to the divergence and flutter eigenvalues, respectively, and the smaller blue and red circles to the fluid and remaining FSI eigenvalues, respectively. The increase of* K_s *is represented by the arrows direction. The numbers* 1 *and* 2 *identify the fluid poles described in section 3.3.1. On the right, the zero isocontour lines of the real (solid lines) and imaginary (dash-dotted line) parts of* R_{FSI} *for three values of* K_s*:* $K_s = 0.417$ *(black lines),* $K_s = 1.668$ *(orange lines) and* $K_s = 2.780$ *(brown lines). The imaginary part of* R_{FSI} *does not vary with* K_s*.*

towards each other, as K_s increases. The least stable eigenvalue passes through the marginal state $\lambda = 0$ for a structural stiffness of $K_s = 1.473$. This value is well approximated by the quasi-steady approach (see results in section 3.3.5), in particular by the magnitude of the added stiffness coefficient, $|K_a|$. In a quasi-steady approach, the stability criterion defined in equation 1.48 states that $K_s = -K_a$ for a marginally stable static eigenvalue. The value of $K_a = -1.5038$ is slightly higher, in magnitude, than the marginal value of K_s, indicating that the neglected terms in a quasi-steady approximation have the effect of destabilising the divergence mode. Finally, we note that this value corresponds to a very good approximation of the slope of the aerodynamic moment curve at $\alpha = 0°$ as function of the incidence (m_z^α), as discussed in section 3.3.5.

The coalescence of the two divergence eigenvalues occurs at $\lambda = -0.085$, for $K_s = 1.750$, given rise to a pair of complex conjugate eigenmodes. The growth rate of this coalescence is directly retrieved from the point where the zero isocontour line of R^i_{FSI} also leaves the real axis. As the structural stiffness continues to increase, this pair of stable complex conjugate eigenmodes tends to a fluid pair of complex conjugate eigenvalues, represented by the smaller blue circles. In this case, the fluid eigenvalues correspond to σ_{f1}, identified on section 3.3.1.

Concerning the flutter eigenvalue (yellow circle), one observes an increase of its frequency and growth rate, as K_s increases. From the discussion in section 3.3.4, it was noted that for high frequencies near the axis $\lambda = -D_s/(2I_s)$, the behaviour of R_{FSI} was dominated by the solid component. Therefore, as K_s increases, the growth rate of the flutter mode is expected to approach the value of the structure $\lambda_s = -D_s/(2I_s)$, while the frequency tends to infinity.

We introduce now the variation of the structural damping coefficient on the FSI stability analysis. Unlike the structural stiffness, D_s appears in both real and imaginary parts of R_{FSI}. We start by discussing the behaviour of the divergence mode. For that, the method for predicting non-oscillating modes presented in section 3.2.3 is used. With this method, the existence of static eigenvalues, as the divergence mode, is predicted as function of K_s, for four different values of D_s, as presented in figure 4.4a. The vertical dashed line corresponds to the nominal value of $K_s = 0.417$. For this nominal value, the increase of D_s decreases the growth rate of the unstable divergence mode. Further, the marginal

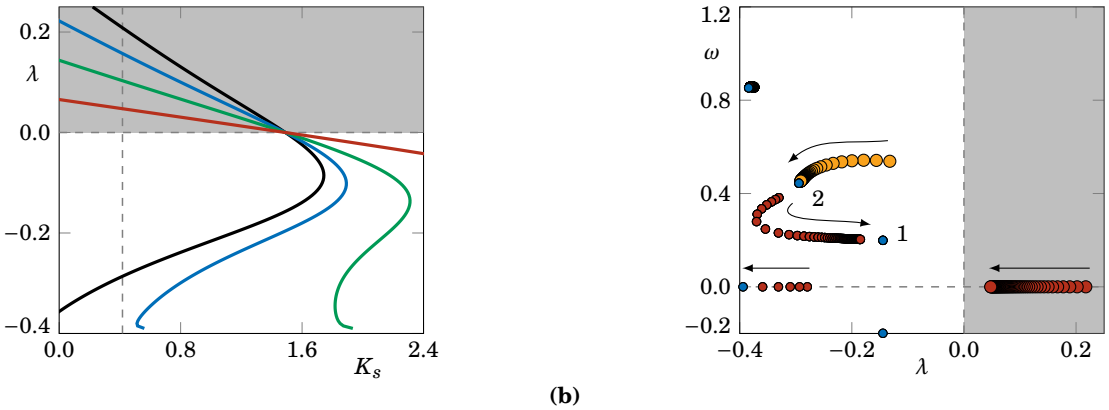

(a) **(b)**

Figure 4.4 – *Influence of the structural damping on the FSI eigenvalues: on the left, the non-oscillating modes prediction for* $D_s = 0.178$ *(black),* $D_s = 1.777$ *(blue),* $D_s = 5.331$ *(green) and* $D_s = 17.769$ *(brown). The vertical dashed line represents the nominal value of* $K_s = 0.417$*. On the right, the spectrum evolution of the eigenvalues for the range* $0 \leq D_s \leq 17.769$*, with the bigger red and yellow circles corresponding to the divergence and flutter eigenvalues, respectively, and the smaller blue and red circles to the fluid and remaining FSI eigenvalues, respectively. The increase of* D_s *is represented by the arrows direction. The numbers* 1 *and* 2 *identify the fluid poles described in section 3.3.1.*

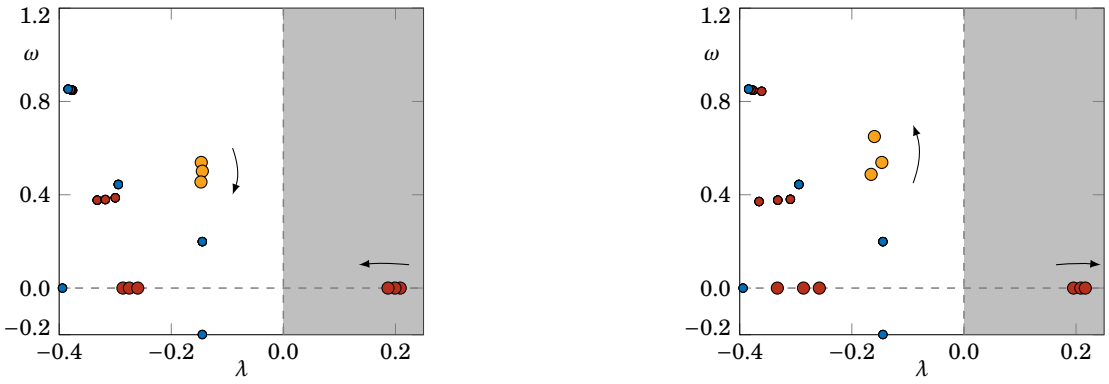

(a) **(b)**

Figure 4.5 – *Influence of the structural inertia and elastic centre on the FSI eigenvalues: on the left, the spectrum representation for three inertia values:* $I_s = 3.834$ *(corresponding to the nominal value),* $I_s = 4.985$ *(corresponding to* 1.3 *times the nominal value) and* $I_s = 6.902$ *(corresponding to* 1.8 *times the nominal value). On the right, the spectrum representation for three elastic centre values:* $X_{EC} = 0$, $X_{EC} = 0.186$ *and* $X_{EC} = 0.25$. *The bigger red and yellow circles correspond to the divergence and flutter eigenvalues, respectively, while the smaller blue and red circles correspond to the fluid and remaining FSI eigenvalues, respectively.*

divergence mode is found on the intersection of all curves with the axis $\lambda = 0$, for the value $K_s = 1.473$. This value was already found in a previous paragraph, when the marginal value of K_s was characterised. From this figure, one can also note that the structural damping does not affect the stable or unstable characteristic of the divergence mode, even if it affects its growth rate.

Finally, the evolution of the eigenvalues near the origin with D_s is depicted in figure 4.4b in a spectrum representation. The arrows represent the increase of D_s from a value of $D_s = 0$ to $D_s = 17.769$ (corresponding to $D_s^{dim} = 0.2$Nms). Concerning the unstable divergence eigenvalue, one can note that as D_s increases, its value tends to the marginal value of $\lambda = 0$. Concerning the flutter eigenvalue, one notes that as D_s increases, its value tends to the fluid eigenvalue σ_{f2}. Therefore, unlike the variation of K_s, the structural damping cannot change the stable or unstable characteristic of the mean flow FSI spectrum.

Lastly, the influence of the structural inertia I_s and the elastic centre X_{EC} are also independently investigated for the nominal values of structural stiffness and damping coefficients. The results are present in figure 4.5. Concerning the variation of I_s, we first note that an increase of the structural inertia tends to stabilise the divergence mode. The flutter mode presents roughly the same growth rate and its frequency decreases with the increase of I_s. Concerning the variation of X_{EC}, we considered three different cases: the case where the elastic centre is fixed at the leading edge, mimicking a rigid flag behaviour, the nominal case $X_{EC} = 0.186$ and the quarter-chord case $X_{EC} = 0.25$. We conclude that the increase of X_{EC} presents the opposite behaviour of the increase of I_s. In particular, we note that that the divergence mode is further destabilised as X_{EC} moves forward. On the other hand, the flutter mode presents a small variation of its growth rate, while the frequency increases with the increase of X_{EC}.

4.2.3 Effect of the Reynolds number and airfoil geometry

In this section, we investigate the behaviour of the fluid–structure eigenvalues, with the Reynolds number variation, as well as with a change in the airfoil geometry, for the nominal structural parameters. We start by analysing the effect of the Reynolds number variation. Figure 4.6a presents the FSI spectrum variation for the range $30\,000 \leq Re \leq 65\,000$.

The spectrum presents a divergence eigenvalue that becomes unstable for a certain value of Re. At the same time, the flutter mode is always located in the stable side of the spectrum and is not greatly affected by the change in the Reynolds number. This behaviour can more clearly be analysed in figure 4.6b, where the growth rate of both divergence and flutter eigenvalues is depicted as function of the Reynolds number. One can see that the divergence eigenvalue becomes unstable for $Re = 32\,000$. As the Reynolds number increases, the growth of the divergence mode continues to increase. For the last to computations at $Re = 60\,000$ and $Re = 65\,000$, the divergence growth rate seems to attain a maximum value. The analysis was not conducted for higher Reynolds numbers, as the mean flow solution from two-dimensional simulations loses the y symmetry for $Re > 65\,000$. Therefore, the approximation of the mean flow solution via the mean flow from two-dimensional simulations seems no longer pertinent. Concerning the flutter eigenvalue, one can observe that its

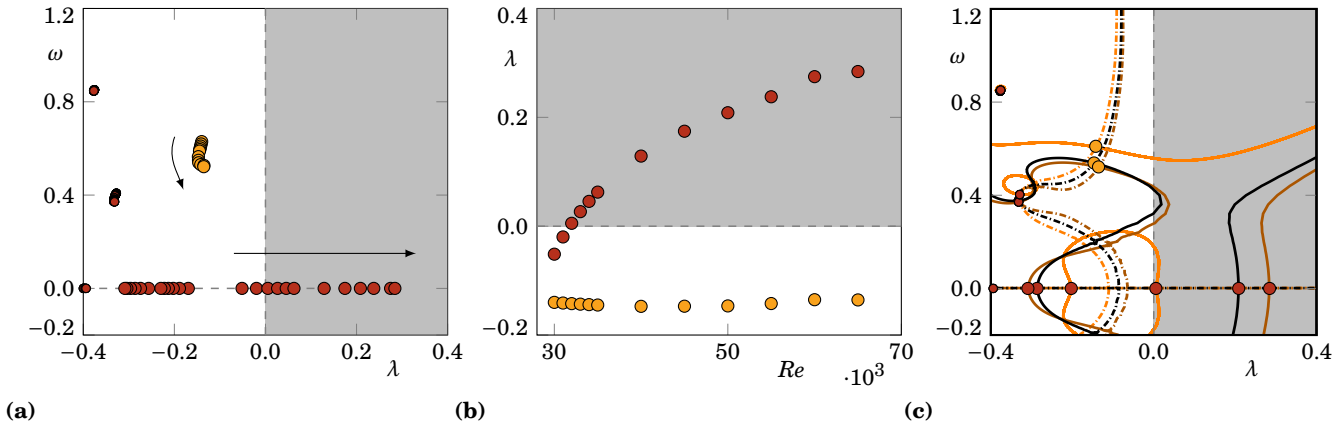

Figure 4.6 – *Influence of the Reynolds number on the FSI eigenvalues for nominal values of the structure parameters: on the left, the spectrum evolution of the eigenvalues for a range* $30\,000 \leq Re \leq 65\,000$*, with the red and yellow circles corresponding to the divergence and flutter eigenvalues, respectively. On the centre, the evolution growth rate of the divergence and flutter eigenvalues with the Reynolds number. On the right, the zero isocontour lines of the real (solid line) and imaginary (dash-dotted line) parts of* R_{FSI} *for three values of Re:* $Re = 32\,000$ *(orange lines),* $Re = 50\,000$ *(black lines) and* $Re = 65\,000$ *(brown lines).*

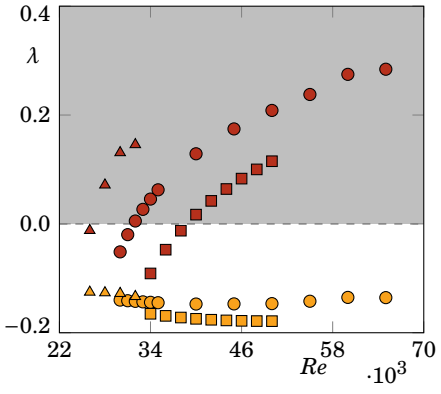

Figure 4.7 – *Influence of the airfoil geometry on the FSI eigenvalues for nominal values of the structure parameters: evolution of the growth rate for the divergence (red) and flutter (yellow) eigenvalues for three airfoil geometries: a NACA0010 (squares), a NACA0012 (circles) and a NACA0014 (triangles).*

growth rate is approximatively constant, through the Re range.

To better understand the position of these eigenvalues on the spectrum as the Reynolds number varies, the zero isocontour of the real and imaginary parts of R_{FSI} is sketched in figure 4.6c for three Reynolds numbers. One can note that the imaginary part of R_{FSI}, represented by the dash-dotted lines, is roughly constant for the three considered Reynolds numbers. This fixes the growth of the flutter mode, as discussed in section 3.3.4. On the other hand, the real part of R_{FSI}, is greatly affected by Re, in particular near the origin. The zero isocontour lines of R^r_{FSI} fix the growth rate of the divergence mode, which is marginally stable for $Re = 32\,000$, in the orange lines, and unstable for the two higher Reynolds numbers.

Finally, the influence of the airfoil geometry on the fluid–structure eigenvalues is presented in figure 4.7. This analysis is considered relevant as several low-Reynolds number UAV's use a symmetric NACA airfoil for their vertical tail (Keane *et al.*, 2017). Three different symmetric airfoils are considered: the nominal case of a NACA0012 airfoil, the thinner case of a NACA0010 airfoil and the thicker case of a NACA0014 airfoil. For the thinner airfoil, the destabilisation of the divergence mode appears at $Re = 39\,000$, corresponding to a higher value with respect to the nominal case. For the thicker airfoil, the divergence mode becomes unstable for $Re = 26\,000$, corresponding to a lower value with respect to the nominal case. The flutter eigenvalue remains on the stable side of the spectrum for the three considered geometries, maintaining a roughly constant growth rate through the Reynolds number range considered. With this analysis, we conclude that the increase of the thickness of the airfoil tends to destabilise both the divergence and the flutter eigenvalues for a fixed value of Re. Concerning the study of asymmetrical airfoils, we note that the primary equilibrium point would not be always at $\alpha = 0°$, depending on the airfoil geometry. This investigation is left for a future work. Further, a change in the geometry should be accompanied by a change in the structural inertia, which was not considered here and is also left for a future work.

4.2.4 Comparison between analyses around a mean flow from 2D and 3D simulations

Hitherto, the mean flow FSI stability analysis was conducted around a mean flow corresponding to the time-averaged solution of two-dimensional simulations. Since the instantaneous flow field is three-dimensional for the considered Reynolds number (as discussed in chapter 2), we perform here a mean flow linear stability analysis with a time- and spanwise-averaged flow solution issued from a DNS simulation at $Re = 50\,000$ and $\alpha = 0°$.

A comparison of the spectrum between the two mean flow analyses is made in figure 4.8. One can observe that both divergence and flutter eigenvalues have a higher growth rate for the mean flow issued from a DNS, when compared with the one coming from 2D simulations. However, the difference is not significant as illustrated by the relative errors of both real and imaginary parts of the eigenmodes in table 4.2. We conclude that the results of a mean flow FSI stability analysis are not significantly influenced by the three-dimensional effects that can be taken into account on the mean flow computation.

4.2.5 Comparison between classical and Reynolds stress formulations of the mean flow stability analyses

Up until now, the mean flow results were performed using the formulation derived from the Floquet analysis, *i.e.*, with the classical formulation (see section 1.4.4, page 35). On the other hand, we presented section 1.5.2 (page 40) an alternative formulation, based on the slow time scale dynamics of the fluid–structure system, denoted Reynolds stress formulation. The results of these two approaches for $Re = 50\,000$ are compared in figure 4.9. On the left-hand side, we compare the eigenvalues near the origin in a spectrum representation, while, on the right-hand side, we report the

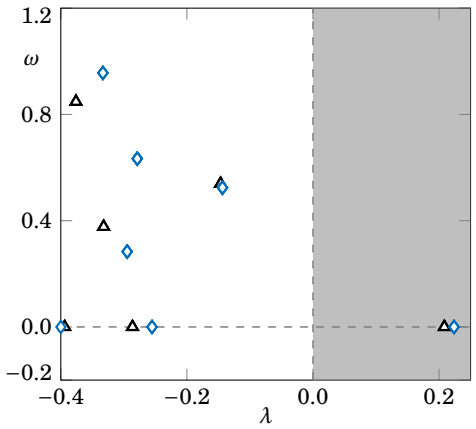

	Divergence eigenvalue	Flutter eigenvalue
△ 2D mean flow	0.2084	−0.1465 + 0.5386i
◇ 3D mean flow	0.2238	−0.1435 + 0.5245i
Relative error	6.88%	2.09% + 2.69%i

Figure 4.8 & Table 4.2 – *On the left, spectrum comparison between analyses around mean flow solutions from 2D (black triangles) and 3D (blue diamonds) simulations at Re = 50 000 and α = 0°, for the nominal structure parameters. On the right, comparison of the corresponding divergence and flutter eigenvalues, along with the relative error of their real and imaginary parts.*

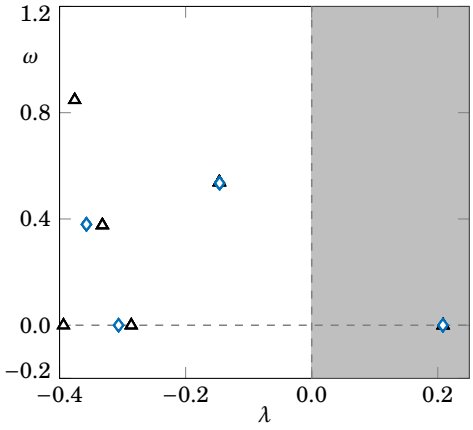

Formulation	Divergence eigenvalue	Flutter eigenvalue
△ Classical	0.2084	−0.1465 + 0.5386i
◇ Reynolds stress	0.2081	−0.1461 + 0.5348i
Relative error	0.14%	0.27% + 0.71%i

Figure 4.9 & Table 4.3 – *On the left, spectrum comparison between classical (black triangles) and Reynolds stress (blue diamonds) formulations at Re = 50 000 and α = 0°, for the nominal structure parameters. On the right, comparison of the corresponding divergence and flutter eigenvalues, along with the relative error of their real and imaginary parts.*

divergence and flutter eigenvalues and corresponding relative error. From the results, we can conclude that the difference between the two approaches is negligible for $\alpha = 0°$. As it will be seen in chapter 6, this difference becomes important for the mean flow linear stability analyses at $\alpha \neq 0°$.

4.3 Floquet analysis of the primary instability at $Re = 20\,000$ and $\alpha = 0°$

In this section, we use the Floquet FSI analysis to investigate the linear fluid–structure stability of a limit cycle oscillation. The limit cycle oscillation corresponds to one period of the vortex shedding phenomenon, for a fixed incidence of $\alpha = 0°$. This analysis is based on the formulation derived in section 1.4.3 (page 34). Contrary to a mean flow FSI

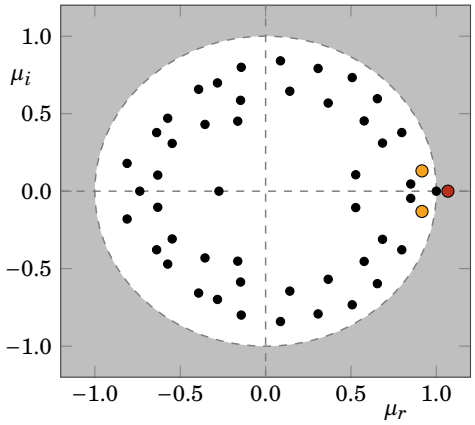

Figure 4.10 – *Floquet multipliers on the complex plane* (μ_r, μ_i) *for the Floquet FSI analysis at* $Re = 20\,000$, $\alpha = 0°$ *and* $K_s = 0$. *The red and yellow circles represent the divergence and flutter Floquet multipliers, respectively, while the remaining Floquet multipliers are represented by the smaller black circles. The unstable region outside the unit circle* $|\mu| > 1$ *is represented by the grey zone.*

analysis, where only the mean component of the limit cycle oscillation is taken into account, the Floquet FSI linear stability analysis is made around a periodic flow solution, taking into account the fast time scale fluid fluctuations.

The study is carried out at $Re = 20\,000$ to keep the coherence with the following chapters, where we conduct the same analysis at a different incidence. Likewise, the structural stiffness was also decreased to a value of $K_s = 0$, justified in the following chapters.

We start by describing the divergence and flutter Floquet eigenmodes, associated to an initial time instant of the vortex shedding period. We then proceed to the characterisation of the divergence Floquet eigenmode during a complete period, with the help of its harmonic decomposition, followed by the comparison of the FSI eigenmodes of both mean flow and Floquet FSI analyses. Finally, a comparison of the growth rate of the divergence mode associated to these analyses is made with respect to the exponential growth rate observed on time-marching FSI nonlinear simulations. The numerical approach used to obtain the Floquet multipliers associated to the present Floquet eigenproblem is detailed in appendix B. As done in the previous sections, the hat notation on the eigenmode is dropped, with respect to chapter 1, to simplify the notation. In that way, the Floquet eigenmodes are noted $\boldsymbol{q} = \left[\boldsymbol{q}_f, \theta, \Omega\right]^T$.

4.3.1 Description of the divergence and flutter Floquet eigenmodes

The stability character of the Floquet FSI eigenmodes is usually accessed via the Floquet multipliers. A Floquet multiplier represents the complex amplitude gain of the periodic Floquet eigenmode over one period T, having $\boldsymbol{q}(\boldsymbol{X}, t+T) = \mu\boldsymbol{q}(\boldsymbol{X}, t)$. A representation of the Floquet multipliers on the complex plane (μ_r, μ_i) is present in figure 4.10 for a periodic

	Floquet multiplier μ	Floquet eigenvalue σ
Divergence mode	1.0679	0.22044
Flutter modes	0.9158 ± 0.1310i	-0.26113 ± 0.4766i

Table 4.4 – *Divergence and flutter Floquet multipliers and corresponding eigenvalues for* $Re = 20\,000$, $\alpha = 0°$ *and* $K_s = 0$.

	θ	Ω	$m_z(\boldsymbol{q}_f)$
Divergence mode	1	0.2176	0.2304
Flutter mode	$0.1238 - 0.9923\mathrm{i}$	$0.4394 + 0.3149\mathrm{i}$	$-0.6929 + 0.5689\mathrm{i}$

Table 4.5 – *Solid components and the associated aerodynamic moment coefficient of the divergence and flutter eigenmodes for a Floquet FSI linear stability analysis at Re = 20 000, α = 0° and $K_s = 0$.*

flow at $\alpha = 0°$ and $Re = 20000$, where we found a period of $T = 0.298$, as reported in the chapter 2. The grey zone corresponds to the unstable region, where the modulus of the Floquet multipliers $|\mu|$ is larger than one. The Floquet multipliers located on the μ_r axis are real and associated to synchronous Floquet eigenmodes, that do not break the time periodicity of the periodic flow solution, while the complex Floquet multipliers introduce a phase shift on the periodic flow solution. The complex Floquet eigenvalue σ can be retrieved using the identity $\mu = \mathrm{e}^{\sigma T}$.

Three Floquet multipliers are highlighted, two of then in yellow corresponding to the flutter Floquet multipliers and a red one corresponding to the divergence Floquet multiplier. A summary of the FSI Floquet eigenvalues is present in table 4.4. The black circles represent the remaining Floquet multipliers, which are stable, excepting a static one, located at $(\mu_r, \mu_i) = (1, 0)$. The latter is associated to the fact that the time derivative of the periodic flow solution, $[\partial \boldsymbol{q}_{f,b}/\partial t, 0, 0]^T$, corresponds to an eigenvector of the Floquet FSI eigenproblem, associated to the eigenvalue $\sigma = 0$.

The results show the presence of an unstable real eigenmode, the divergence mode. This eigenmode is associated to the amplification of the linear perturbation during the vortex shedding period. Since the eigenmode is synchronous, no phase shift of the periodic flow field is observed after the evolution of the associated perturbation during one period. The spatial structure of the divergence eigenmode fluid component is depicted in figure 4.11 for the initial instant of the period. The streamwise velocity field of this divergence mode is displayed with a coloured map. The isocontours of the spanwise vorticity of the periodic flow are superimposed using solid black lines for positive values and dashed black lines for the negative values. The eigenmode is normalised with respect to the angular displacement component, such that $|\theta| = 1$. We note that the spatial structure is mainly located in the wake of the airfoil. In particular, the spatial structure starts by being located near the trailing edge of the airfoil, in the zones dominated by the shear stress in the instantaneous solution of the periodic flow. As the eigenmode is convected, the regions of important values tend to be located at the core of the spanwise vortices. In the case of the divergence mode, all solid components are real, as depicted in table 4.5, along with the associated aerodynamic moment.

Concerning the flutter eigenmode, the corresponding Floquet multiplier is located in the stable region where $|\mu| < 1$. We note that in this case, the Floquet multiplier is complex (see table 4.4), corresponding to an asynchronous eigenmode

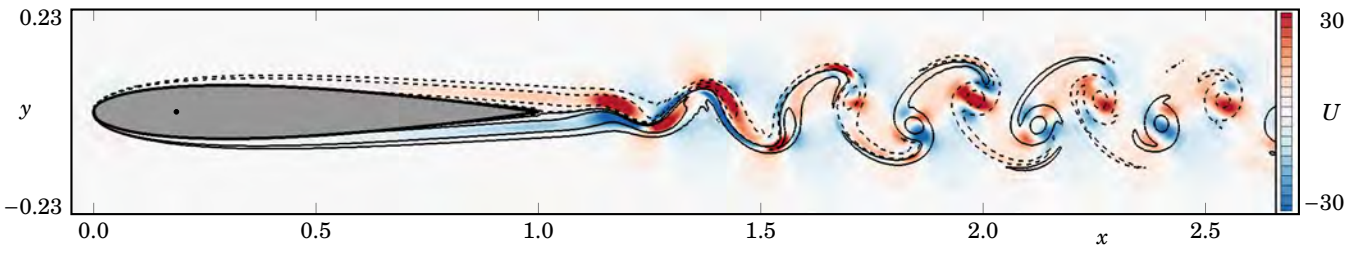

Figure 4.11 – *Instantaneous streamwise velocity field U of the fluid component of the divergence Floquet eigenmode at Re = 20 000, α = 0° and $K_s = 0$. The black isocontours represent the spanwise vorticity of the corresponding instant of the periodic flow ($\Omega_z = \pm 20$ and $\Omega_z = \pm 2$).*

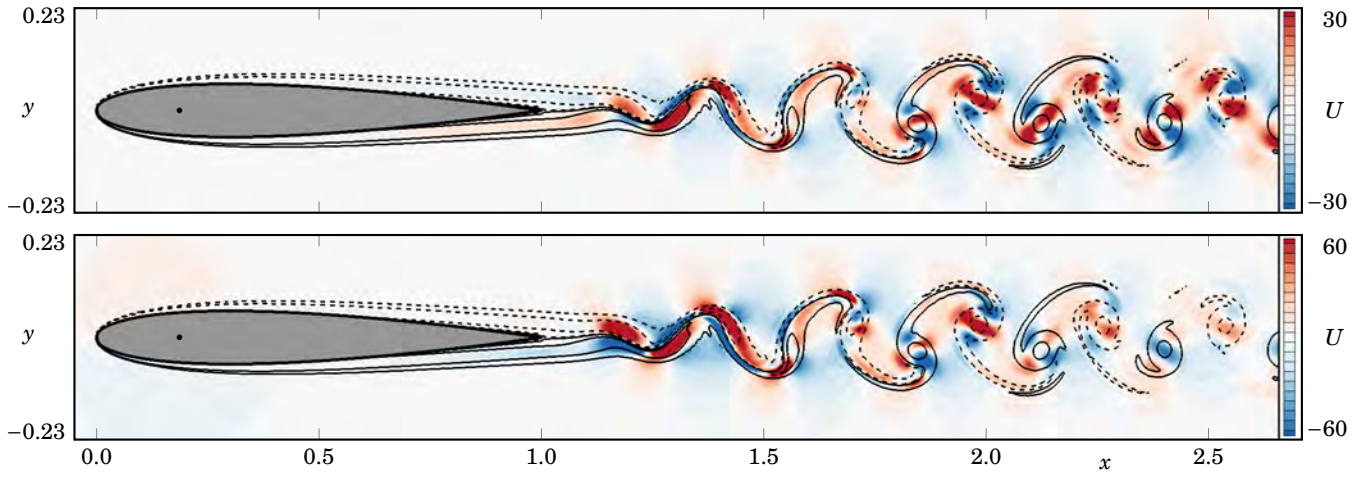

Figure 4.12 – *Instantaneous streamwise velocity field U of the fluid component of the flutter Floquet eigenmode at Re = 20 000, α = 0° and $K_s = 0$: real and imaginary parts on the top and bottom plots, respectively. The black isocontours represent the spanwise vorticity of the corresponding instant of the periodic flow ($\Omega_z = \pm 20$ and $\Omega_z = \pm 2$).*

that introduces a phase shift on the base periodic flow evolution at each period. The solid components of the flutter eigenmode are reported in table 4.5 for the Floquet multiplier with $\mu_i > 0$. The spatial structure of the real and imaginary parts of the fluid component are presented in figure 4.12. Both real and imaginary parts present a similar spatial structure as the divergence eigenmode, with a presence mainly on the wake of the airfoil.

4.3.2 Harmonic content of the divergence Floquet eigenmode over a period

In order to understand the importance of the divergence eigenmode during the complete vortex shedding period, this divergence mode is injected as the initial perturbation of the linearised equations, and a time-integration is performed during one period. The exponential growth rate of the eigenmode is counteracted by an additional term $-\lambda \mathrm{M}\boldsymbol{q}$, added to the linearised equations, as presented in equation 1.31 (page 35).

The mean and first harmonic components of the divergence eigenmode are noted $\boldsymbol{q}^0$ and $\boldsymbol{q}^1$, respectively, with $\boldsymbol{q}^0 = [\boldsymbol{U}^0, p^0, \theta^0, \Omega^0]$ and $\boldsymbol{q}^1 = [\boldsymbol{U}^1, p^1, \theta^1, \Omega^1]$. The spatial structure of the streamwise velocities U^0 and U^1 is presented in figure 4.13. The solid lines correspond to the mean recirculation zone at the rear of the airfoil associated to the periodic flow limit cycle. Concerning the mean component, we observe the deviation of the streamwise velocity field from the streamwise axis for $x \gtrsim 1.2$. The same behaviour is found on the mean flow field (see figure 4.1). For the Floquet

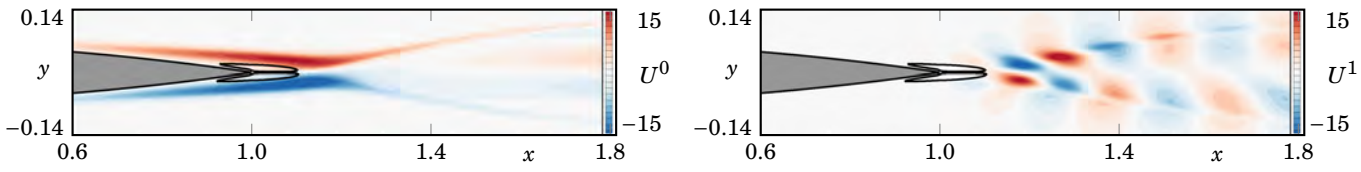

Figure 4.13 – *Spanwise vorticity field of the mean component (left) and the real part of the first harmonic (right) of the fluid component of the divergence Floquet eigenmode at Re = 20 000, α = 0° and $K_s = 0$. The black lines represent the time-averaged recirculation zone.*

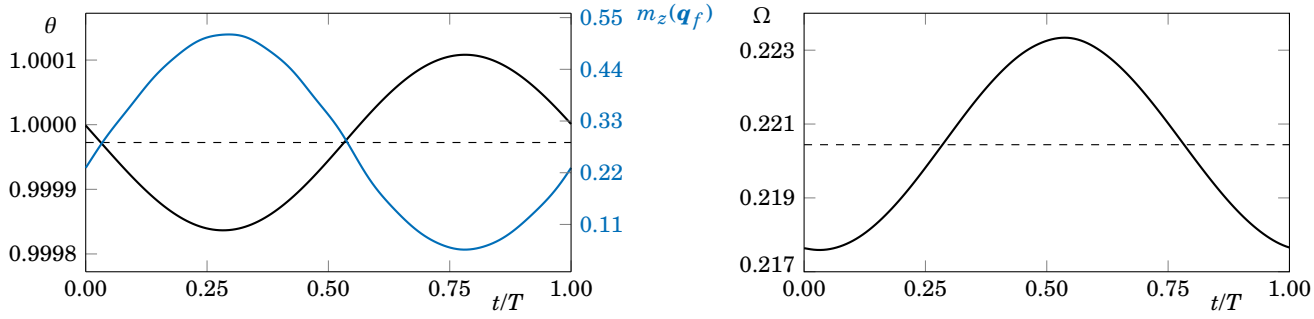

Figure 4.14 – *Evolution of the solid components of the divergence Floquet eigenmode and the corresponding aerodynamic moment coefficient, over one vortex shedding period at Re = 20 000, α = 0° and $K_s = 0$. The dashed horizontal lines represent the mean values.*

	θ	Ω	$m_z(\boldsymbol{q}_f)$
Mean	1	$2.2044 \cdot 10^{-1}$	$2.8431 \cdot 10^{-1}$
1st harmonic	$1.3696 \cdot 10^{-5} + (6.6685 \cdot 10^{-5})$i	$-1.3956 \cdot 10^{-3} + (3.0349 \cdot 10^{-4})$i	$-2.6292 \cdot 10^{-2} + (1.1250 \cdot 10^{-1})$i

Table 4.6 – *Mean and first harmonic components of the solid components and the corresponding aerodynamic moment coefficient of the divergence Floquet eigenmode for Re = 20 000, α = 0° and $K_s = 0$.*

eigenmode, this deviation is associated to the mean component of the flow unsteadiness that is taken into account during the computation of $\boldsymbol{U}^0$.

Concerning the first harmonic component, we observe that U^1 is not symmetric in the cross-stream direction with respect to the x-axis. This loss of symmetry is associated to the nontrivial values of the solid components, in particular the angular displacement, responsible for the deviation of the airfoil from its equilibrium position during one cycle of the vortex shedding oscillation. We further note that the first harmonic spatial structure is non negligible, when compared to the magnitude values of the mean component. This suggests that the terms neglected during the derivation of the mean flow formulation (section 1.4.4) are in fact non-negligible.

The evolution of the solid components and the aerodynamic moment during one period is presented in figure 4.14. The curves start from the previous values reported in table 4.5 for the divergence eigenmode associated to the first instant of the periodic flow. The three curves present a sinusoidal shape. We note that the angular displacement and the aerodynamic moment signals are in antiphase, *i.e.*, with a phase shift of 180°.

Associated to the above signals, the mean and first harmonic component values are present in table 4.6. Concerning θ and Ω, we note that their first harmonic content is almost negligible, when compared to the values of the mean components. In contrast, the first harmonic content of the aerodynamic moment is non-negligible. This is in accordance with the fact that the first harmonic of the fluid eigenmode component (on the right of figure 4.13) is also non-negligible.

4.3.3 Comparison with the mean flow eigenvalues/eigenmodes

We proceed to the comparison between the eigenvalues of both FSI analyses as well as to the comparison between the mean component of the divergence Floquet eigenmode, described previously, and the divergence eigenmode obtained with a mean flow FSI analysis (classical formulation), for the same fluid and structure parameters.

The eigenvalues of both FSI analyses of both analysis are compared in table 4.7. Both analyses present a very good

	Mean flow analysis (classical formulation)	Floquet analysis
Divergence mode	0.21893	0.22044
Flutter modes	-0.23940 ± 0.50841i	-0.26112 ± 0.47663i

Table 4.7 – *Comparison between the FSI eigenvalues from a mean flow analysis and from a Floquet analysis for Re = 20 000, α = 0° and $K_s = 0$.*

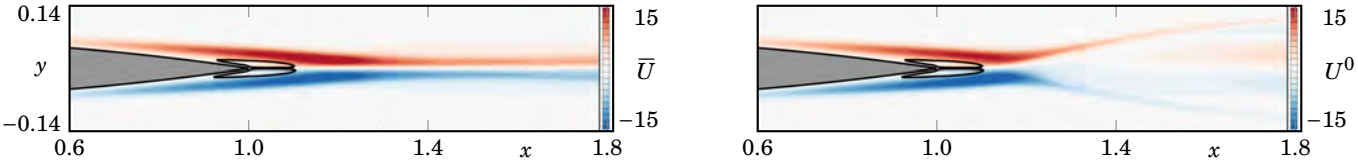

Figure 4.15 – *Comparison of the streamwise velocity field between the divergence eigenmode of a mean flow analysis (left) and the mean component of the divergence eigenmode of the Floquet FSI analysis (right), at Re = 20 000, α = 0° and $K_s = 0$.*

agreement between the different results. The Floquet analysis has a slightly more unstable divergence mode and a more stable flutter mode, when compared to the mean flow analysis.

The differences on the divergence mode are further explored by comparing the mean component of the divergence Floquet eigenmode and the divergence eigenmode of a mean flow FSI analysis. For that, we compare the streamwise velocity of these quantities, in figure 4.15. In the case of the mean flow eigenmode, we recall that the normalisation is such that $\left|\bar{\theta}\right| = \sqrt{\bar{\theta}^H \bar{\theta}} = 1$. In that way, both fields present a unitary angular displacement component. The difference between the two fields can be noted on their spatial structure. The mean flow FSI eigenmode (on the left) has a spatial structure that starts on the second half of the airfoil and continues through the wake. In contrast, the mean component of the Floquet eigenmode (on the right) is deviated on the wake of the airfoil for $x \gtrsim 1.2$. As noted before, the same behaviour is found on the mean flow field (see figure 4.1). The deviation can be attributed to the Reynolds stress components of the periodic flow, that are taken into account on the Floquet analysis. Further, we note that the symmetry break with respect to the x-axis is not visually perceptible for the mean flow eigenmode, whereas it can be discerned for the mean component of the Floquet eigenmode.

4.3.4 Comparison with the nonlinear simulations

We end the chapter with a comparison between the stability results and the two-dimensional nonlinear aeroelastic simulations. These simulations are used in the following chapter to describe the nonlinear dynamics of the coupled system. In this section, we are interested in comparing the exponential growth rate of the angular displacement that can be observed on an initial phase of the nonlinear simulations, with the linear growth rate predicted by the mean flow FSI and Floquet FSI analyses.

Figure 4.16 depicts the evolution in time of the angular displacement in a log scale. The nonlinear simulations are initialised from an instant of a purely-fluid time-marching simulation, with an initial angular displacement and velocity of zero. The exponential growth of θ is illustrated by the dashed red line, with a slope of $\lambda_{nl} = 0.22$. The comparison with the linear analyses is made in table 4.8. Observing the values, we conclude that the divergent behaviour of the airfoil is quite well predicted by the linear analyses conducted in this chapter. Further, we report in table 4.9 the same results for four different values of K_s, used in the next chapter. For the larger value of K_s, no exponential growth is observed in the

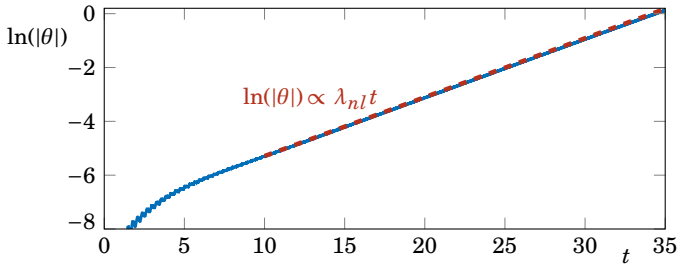

λ_{nl}	0.21910
Mean flow divergence eigenvalue	0.21893
Floquet divergence eigenvalue	0.22044

Figure 4.16 & Table 4.8 – *On the left, exponential growth of the angular displacement observed in nonlinear FSI simulations at* $Re = 20\,000$ *and* $K_s = 0$*. On the right, comparison between the exponential growth of the nonlinear FSI simulation,* λ_{nl}*, and the divergence eigenvalues from mean flow and Floquet linear stability analyses at* $Re = 20\,000$*,* $\alpha = 0°$ *and* $K_s = 0$*.*

K_s^{dim}	K_s	λ_{nl}	Mean Flow divergence eigenvalue	Floquet divergence eigenvalue
0.080	1.390	—	—	—
0.020	0.347	0.12323	0.12362	0.12713
0.005	0.087	0.19619	0.19583	0.19764
0.000	0.000	0.21910	0.21893	0.22044

Table 4.9 – *Comparison between the exponential growth of the nonlinear FSI simulations,* λ_{nl}*, and the unstable divergence eigenvalues from the mean flow FSI and Floquet FSI linear stability analyses at* $Re = 20\,000$ *and* $\alpha = 0°$ *for four different values of structural stiffness.*

nonlinear simulations (as it will be detailed in the next chapter), which is in accordance with the fact that no divergence eigenmode is found. For the remaining values of K_s (0.347, 0.087 and 0), a very good agreement is found between the nonlinear exponential growth of θ and the values of the divergence eigenvalue of the linear analyses.

With the present results in mind, we describe in the next chapter the fluid–structure nonlinear behaviour in time, for different structure parameters and for different Reynolds numbers.

Chapter 5

Nonlinear FSI temporal simulations

In the previous chapter, the onset of a fluid–structure instability on a NACA0012 airfoil mounted on a torsional spring system was characterised via linear analyses. With these tools, a divergence behaviour of the airfoil from the equilibrium position at $\alpha = 0^\circ$ was predicted. Since the governing fluid–structure equations are inherently nonlinear, the unrestrained linear exponential growth of the instability becomes at some point unrealistic. At this point, the influence of the nonlinear terms becomes important, modifying and saturating the perturbation growth.

In this chapter, we perform temporal simulations of the pitching airfoil coupled to the flow equations to investigate the different nonlinear regimes that may arise on the fluid–structure system. In a first part, we illustrate the different equilibrium positions admissible for the fluid–structure system that can be retrieved from the quasi-steady equilibrium positions of the fluid–structure system, given by the aerodynamic moment curve evolution with the angle of attack, for $Re = 20\,000$. In a second part, different nonlinear regimes are identified, varying the structural stiffness and keeping the Reynolds number constant. In a third part, we further explore the existence of self-sustained oscillating states and characterise the vibration amplitude that results from the nonlinear saturation. Herewith, a bifurcation diagram is sketched, where we identify different stable branches for the same values of structural stiffness. Finally, we explore the different regimes appearing for $Re \geq 50\,000$, keeping the structural parameters constant. This increase in the Reynolds number ultimately leads to a global limit cycle oscillation around $\alpha = 0^\circ$, commonly known in the literature as laminar separation flutter.

5.1 Introduction

The present chapter tries to shed light on the emergence of the laminar separation flutter phenomenon, firstly reported in the wind tunnel experimental investigation conducted by Poirel *et al.* (2008). They demonstrated the existence of self-sustained limit cycle oscillations within the Reynolds number range of $45\,000 \leq Re \leq 130\,000$. This limit cycle is characterised by a Strouhal frequency around $St = 0.06$ and a maximum amplitude of oscillation of $\alpha_{max} \approx 5.5^\circ$, around the equilibrium position at $\alpha = 0^\circ$. The authors suggested that the loss of stability of the airfoil at its equilibrium position and, consequently, the dynamics of the pitch oscillations, were governed by the laminar separation of the boundary layer over the airfoil, either due to a trailing edge separation or to the presence of a *Laminar Separation Bubble* (LSB). The presence of the pitch oscillations was demonstrated for three different values of structural stiffness, K_s, including the case of $K_s = 0$, showing that the oscillations are both driven and limited by the aerodynamic forces, and can thus sustain even without the presence a structural spring. These aerodynamic loadings result from the flow behaviour patterns of

laminar separation, transition, and reattachment processes that alternate between either side of the wing.

The phenomenon was numerically reproduced by Poirel *et al.* (2011), where two-dimensional coupled time-marching aeroelastic simulations were performed for $50\,000 < Re < 150\,000$. The authors adopted a purely two-dimensional laminar fluid model and a URANS fluid model, the latter associated to a SST k–ω turbulence model with a low-Reynolds-number correction. The investigation confirmed that the laminar separation of the boundary layer near the trailing edge plays a critical role in initiating and sustaining the pitch oscillations. For this reason, the phenomenon is labelled as *Laminar Separation Flutter* (LSF). The authors also showed that the turbulence viscosity tended to inhibit the existence of the instability. In subsequent studies, this instability was investigated by Barnes *et al.* (2016, 2018), where Implicit Large-Eddy Simulations (ILES), coupled with the structural dynamics, were performed. Among the findings, the authors found the existence of the limit cycle oscillation beyond the initial Reynolds number range investigated by Poirel *et al.* (2008), $77\,000 \leq Re \leq 200\,000$, at which the pitch instability was observed after imposing an initial disturbance on the airfoil incidence. They also reported a reduction on the size of the LSB with the increase of the Reynolds number.

The influence of the structural stiffness was investigated in more detail in Barnes *et al.* (2019) for $Re = 77\,000$ and $Re = 110\,000$, where the LSF is shown to persist over several orders of magnitude of structural rigidity. The effect of the structural rigidity at a fixed Reynolds number exhibited a similar behaviour as the effect of Reynolds number at a fixed stiffness. More precisely, both parameters influence the timing of transition events relative to the pitch limit-cycle, with for example, at high stiffness values, a turbulent reattachment that occurs at a later phase of the cycle.

Finally, although the phenomenon can be observed with only the pitch degree of freedom, several analysis were made afterwards regarding the same case, but considering both pitch and heave degrees of freedom. These studies include the experiments of Poirel *et al.* (2012, 2014), numerical LES simulations from Yuan *et al.* (2013), among others.

Concerning the lower Reynolds number regimes, no studies were found that addressed the different nonlinear regimes that may exist. For the lower limit cases at $Re \approx 50\,000$, the above literature reports negligible oscillations of the FSI configuration around $\alpha = 0°$. In this way, the present chapter aims at investigating the temporal nonlinear behaviour of a NACA0012 airfoil with a pitch degree of freedom on Reynolds numbers regimes below and above 50 000. Related with the subject, Zhu *et al.* (2020) recently performed an experimental study to describe the flow-induced instability of an elastically mounted wing at $Re = 50\,000$. However, the elastic centre was located at mid-chord and the amplitude oscillations were observed up to 120°.

The chapter is organized as follows. In section 5.2, we discuss the quasi-static equilibrium positions admissible by the structure for $Re = 20\,000$, based on the evolution of the mean flow aerodynamic moment curve with the static angle of attack, as a prelude of the nonlinear simulations. In section 5.3, different nonlinear regimes for $Re = 20\,000$ are explored using Navier–Stokes two-dimensional time-marching simulations. Next, in section 5.4, a bifurcation diagram is sketched, mapping the possible stable solutions as function of the structural stiffness. In section 5.5.1, we fix the Reynolds number to 50 000, in order to illustrate the corresponding quasi-static equilibrium points admissible by the structure. Finally, in section 5.5, the nonlinear simulations are used to characterise the different regimes present for $Re \geq 50\,000$.

5.2 Quasi-steady equilibrium positions for mean flow solutions from 2D simulations at $Re = 20\,000$

In the previous chapter, we show that the airfoil equilibrium point at $\alpha = 0°$ could be statically unstable for $Re = 20\,000$, if the structural stiffness is sufficiently low with respect to its nominal value. This is discussed with both mean flow and Floquet FSI analyses (see section 4.3.4, page 155). These analyses are conducted at a null incidence angle, hereafter denoted $\bar{\alpha}_1 = 0°$. We denote this equilibrium state as the primary quasi-steady equilibrium point.

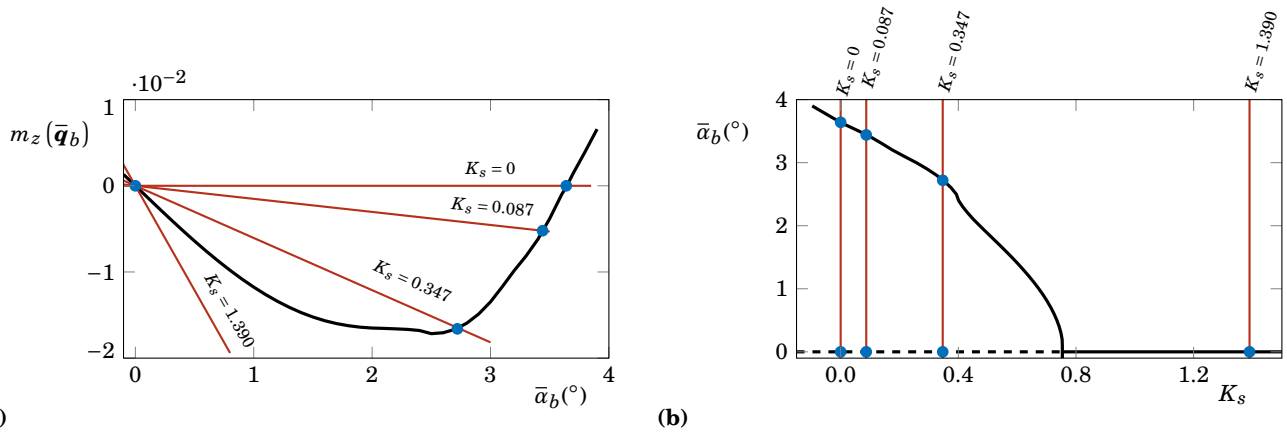

Figure 5.1 – *Quasi-steady equilibrium positions for mean flow from 2D simulations at Re = 20 000. On the left, evolution of the aerodynamic moment coefficient with the angle of attack (black line), associated to fixed incidence simulations at Re = 20 000. On the right, evolution of the admissible equilibrium points with the structural stiffness (black line). The red lines and the blue dots represent the different values of structural stiffness considered and the corresponding quasi-steady equilibrium points, respectively. The highlighted admissible secondary equilibrium positions are $K_s = 0$ ($\overline{\alpha}_2 = 3.64°$), $K_s = 0.087$ ($\overline{\alpha}_2 = 3.44°$) and $K_s = 0.347$ ($\overline{\alpha}_2 = 2.72°$).*

In this section, we demonstrate that, depending on the structural stiffness coefficient, a second point of equilibrium may appear, hereafter denoted $\overline{\alpha}_2$. Formally, both quasi-steady equilibrium points are found from equation 1.24 (page 30), which states that the quasi-steady airfoil incidence, $\overline{\alpha}_b$, is fixed by the ratio between the aerodynamic moment coefficient of a mean flow at this incidence and the structural stiffness, such that

$$\overline{\alpha}_b = -\frac{m_z(\overline{\boldsymbol{q}}_b)}{K_s}. \tag{5.1}$$

In order to illustrate these equilibria, the curve m_z–$\overline{\alpha}_b$, already presented in figure 2.9 (page 79), is revisited in this section in figure 5.1a. We recall that the mean flow is issued from a time-averaged solution of two-dimensional simulations, where for each simulation the airfoil incidence is fixed at $\overline{\alpha}_b$. Four different values of structural stiffness are considered in the following analysis, represented by the red straight lines. We choose these particular values to illustrate the different nonlinear regimes that can be found, as it will be detailed next. We first note that all four red lines intersect the m_z–$\overline{\alpha}_b$ curve at $\overline{\alpha}_b \equiv \overline{\alpha}_1 = 0°$, the primary equilibrium position, represented by one of the blue dots. Then, depending on the value of K_s chosen, a second equilibrium may arise from the intersection of these lines with the mean aerodynamic moment curve. The second equilibrium point can be found for all cases, except for the highest K_s considered, $K_s = 1.390$, where the only intersection with the mean aerodynamic moment curve is located at the origin. For the three other cases, a second equilibrium is found, with an increasing value of $\overline{\alpha}_2$ as K_s decreases.

Alternatively, the equilibrium points can be found by directly sketching the admissible values of K_s as function of $\overline{\alpha}_b$, as presented in figure 5.1b. The computation of these points is based on equation 5.1, represented by the black line. We note that is equation is not defined for $K_s = 0$. In this case, the equilibrium points are such that the associated $m_z(\overline{\boldsymbol{q}}_b)$ is also null. Concerning the values at $\overline{\alpha}_b = 0°$, they correspond to an equilibrium position for every K_s value, since $m_z(\overline{\boldsymbol{q}}_b)$ is null.

Along the axis $\overline{\alpha}_b = 0°$, one finds the primary equilibrium points, $\overline{\alpha}_1$. Based on the primary analysis of the previous chapters, these points are represented by the solid black line in the case of being linearly stable ($K_s \gtrsim 0.75$), or by the

dashed black line in the case where they were found to be linearly unstable. The exact position of this threshold was discussed in the previous chapter, being well approximated by the slope of m_z at $\bar{\alpha}_b = 0°$. The four values of K_s chosen for the following discussion are represented by the vertical red lines.

A summary of the considered values of structural stiffness and the corresponding quasi-steady equilibrium points is present in table 5.1. Finally, we note that, since the airfoil is symmetric, the possible second equilibrium points are also found for the negative values of $\bar{\alpha}_b$, not represented in the previous figures.

5.3 Different FSI nonlinear regimes for $Re = 20\,000$

In this section, we carry out numerical simulations of the pitching airfoil interacting with the two-dimensional flow solution of the incompressible Navier–Stokes equations at $Re = 20\,000$ for the four values of structural stiffness reported in the previous paragraph. The remaining structural parameters are reported in table 1.3 (page 25). All simulations started from an instantaneous solution of a fixed incidence two-dimensional time-marching simulation at $\alpha = 0°$. Therefore, the solid components of the nonlinear simulations were also initialised at $\alpha = 0°$ and $\Omega = 0$. As described in chapter 2, the fixed incidence simulations present a periodic vortex shedding at the rear of the airfoil, vibrating at a *fast* time scale frequency. As expected, this phenomenon is also observed in the fluid–structure nonlinear simulations. Additionally, we describe in the following paragraphs the behaviour of the angular displacement and velocity with time. We note that, depending on the phase of the vortex shedding phenomenon on the instantaneous flow field considered for the initialisation of the nonlinear simulations, the angular displacement could evolve to either positive or negative values. For the initial conditions considered, a positive incidence was always observed on the initial phase of the simulations.

In the following sections, we revisit the definitions of H_θ and H_Ω, introduced in chapter 1 in order to evaluate the effect of the fast time scale oscillations, associated to the vortex shedding frequency, on the solid components. This enables us to evaluate the importance of these terms on the nonlinear simulations. Further, the computation of these terms enables us to discuss the validity of the hypotheses made on the linear stability formulation, where the terms associated to the fast time scale oscillations of the solid components were neglected.

With that in mind, we first define the ratio between the fast time scale harmonic component of the angular displacement and aerodynamic moment coefficient. This ratio can be estimated using equation 1.22 (page 29), which we will denote H_θ^{theory}. At the same time, we can calculate this ratio using the fundamental harmonic components of the angular displacement and aerodynamic moment, α^1 and m_z^1, coming from the nonlinear simulations, which we will denote H_θ^{simul}. In both cases, the fast time scale frequency is fixed by the vortex shedding frequency of the nonlinear simulations, ω_{VS}, having:

$$H_\theta^{theory} = \frac{1}{I_s\left(-\omega_{VS}^2 + 2\omega_{VS}\omega_n\zeta\mathrm{i} + \omega_n^2\right)} \quad \text{and} \quad H_\theta^{simul} = \frac{\alpha^1}{m_z^1},$$

K_s^{dim}(Nm)	0.080	0.020	0.005	0.000
K_s	1.390	0.347	0.087	0.000
$\bar{\alpha}_1$	0.00°	0.00°	0.00°	0.00°
$\bar{\alpha}_2$	—	±2.72°	±3.44°	±3.64°

Table 5.1 – *Primary and secondary equilibrium points, $\bar{\alpha}_1$ and $\bar{\alpha}_2$, respectively, retrieved from the static mean aerodynamic moment curve as function of the angle of attack (see figure 5.1b) for Re = 20 000 as function of the structural stiffness.*

where $\omega_n = \sqrt{K_s/I_s}$ and $\zeta = D_s/(2I_s\omega_n)$. Then, we also define the ratio between the fast time scale harmonic component of the angular velocity and aerodynamic moment coefficient

$$H_\Omega^{theory} = \omega_{VS} H_\theta^{theory} \quad \text{and} \quad H_\Omega^{simul} = \frac{\Omega^1}{m_z^1}.$$

In practice, we will be interested in their magnitude. With that in mind, we proceed to describe the different nonlinear regimes.

5.3.1 Regime R_1: weak oscillations around $\overline{\alpha} = 0°$

In the first case considered, we fix the value of the structural stiffness at $K_s = 1.390$. The time history associated to the angular displacement, angular velocity and aerodynamic moment coefficient is present in figure 5.2. In this case, we observe that the angular displacement oscillates around $\alpha = 0°$, with an amplitude of order 10^{-4}. Therefore, we label the regime where this case is found as a weak oscillation regime around $\overline{\alpha} = 0°$.

The weak oscillations around the zero angle of attack are due to the fact that the value of K_s is sufficiently high, restraining the movement of the structure. This result confirms the stable behaviour of the primary equilibrium point, $\overline{\alpha}_1 = 0°$, predicted by the linear stability results. On the close-up present in the angular displacement figure, we can note a minor deviation from the null value, with an order of magnitude of 10^{-4}. Due to its small value, we neglect this deviation and consider that the mean angular position is at $\alpha = 0°$. Further, we note that all the sketched quantities present periodic behaviour, vibrating at the fundamental frequency of $\omega_{VS} = 21.041$. This value is in very good agreement

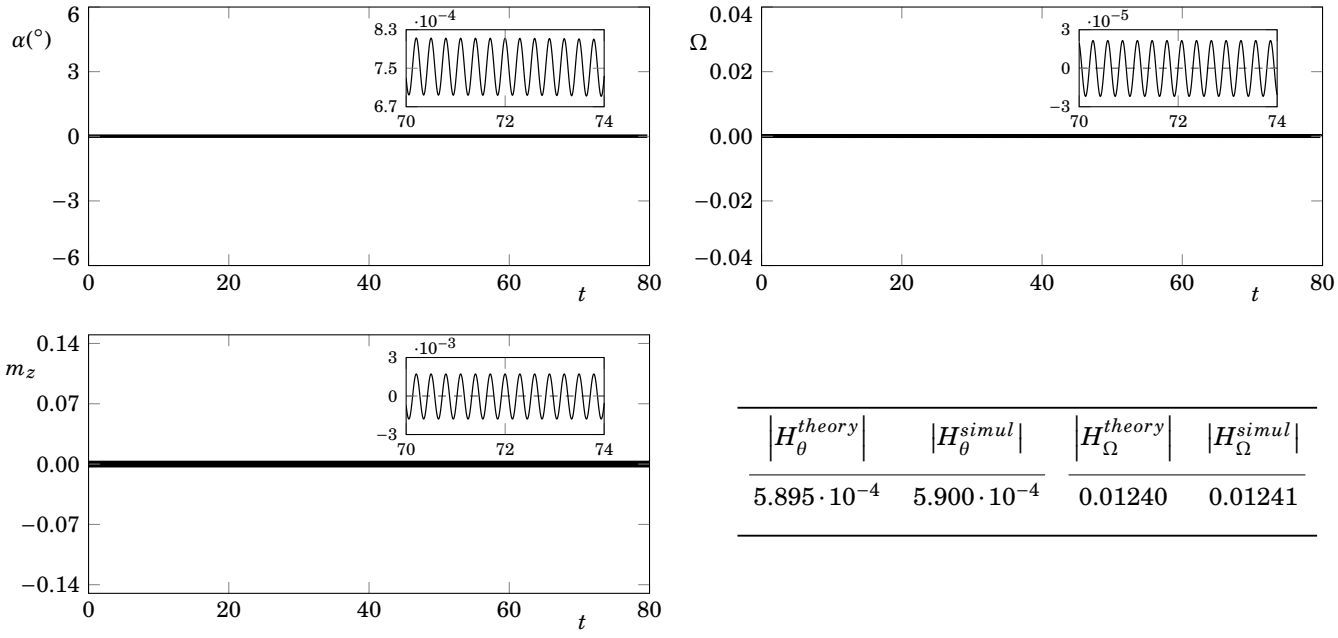

$\lvert H_\theta^{theory} \rvert$	$\lvert H_\theta^{simul} \rvert$	$\lvert H_\Omega^{theory} \rvert$	$\lvert H_\Omega^{simul} \rvert$
$5.895 \cdot 10^{-4}$	$5.900 \cdot 10^{-4}$	0.01240	0.01241

Figure 5.2 & Table 5.2 – *Regime R_1: time history of the angle of attack (top left), the angular velocity (top right) and the aerodynamic moment coefficient (bottom left) for a two-dimensional coupled time-marching simulation at $Re = 20\,000$ and $K_s = 1.390$. The table on the bottom right compares the values of H_θ and H_Ω, evaluated at $\omega_{VS} = 21.041$, the vortex shedding frequency, for the theoretical estimation and for the nonlinear simulations.*

with the vortex shedding frequency found for the static simulations at $\bar{\alpha}_b = 0°$ ($\omega_{VS} = 21.085$, see table 2.1, page 73). Therefore, we conclude that a time-marching simulation carried out at a static angle of $\bar{\alpha}_b = 0°$ represents a very good approximation of the limit cycle oscillation found at $K_s = 1.390$.

We can quantify the importance of the solid vibrations at the vortex shedding frequency on the nonlinear dynamics with the help of the transfer functions H_θ and H_Ω. We report their magnitude in table 5.2, for the theoretical prediction and for the nonlinear simulations. We first note that both the theoretical values and the values coming from the nonlinear simulations are in very good agreement. Second, we observe that the magnitude of the transfer function associated to the fast time scale oscillations of the angular displacement, H_θ, presents an order of magnitude of 10^{-4}, while the magnitude of the transfer function associated to the angular velocity has an order of magnitude 10^{-2}. With these orders of magnitude, we expect the contributions of the fast time fluctuations of the angular displacement to the linear stability analysis formulation to be negligible for the primary equilibrium point. At the same time, we also expect the contributions of the angular velocity to be negligible, even if they present a substantial bigger value. This was confirmed at the end of

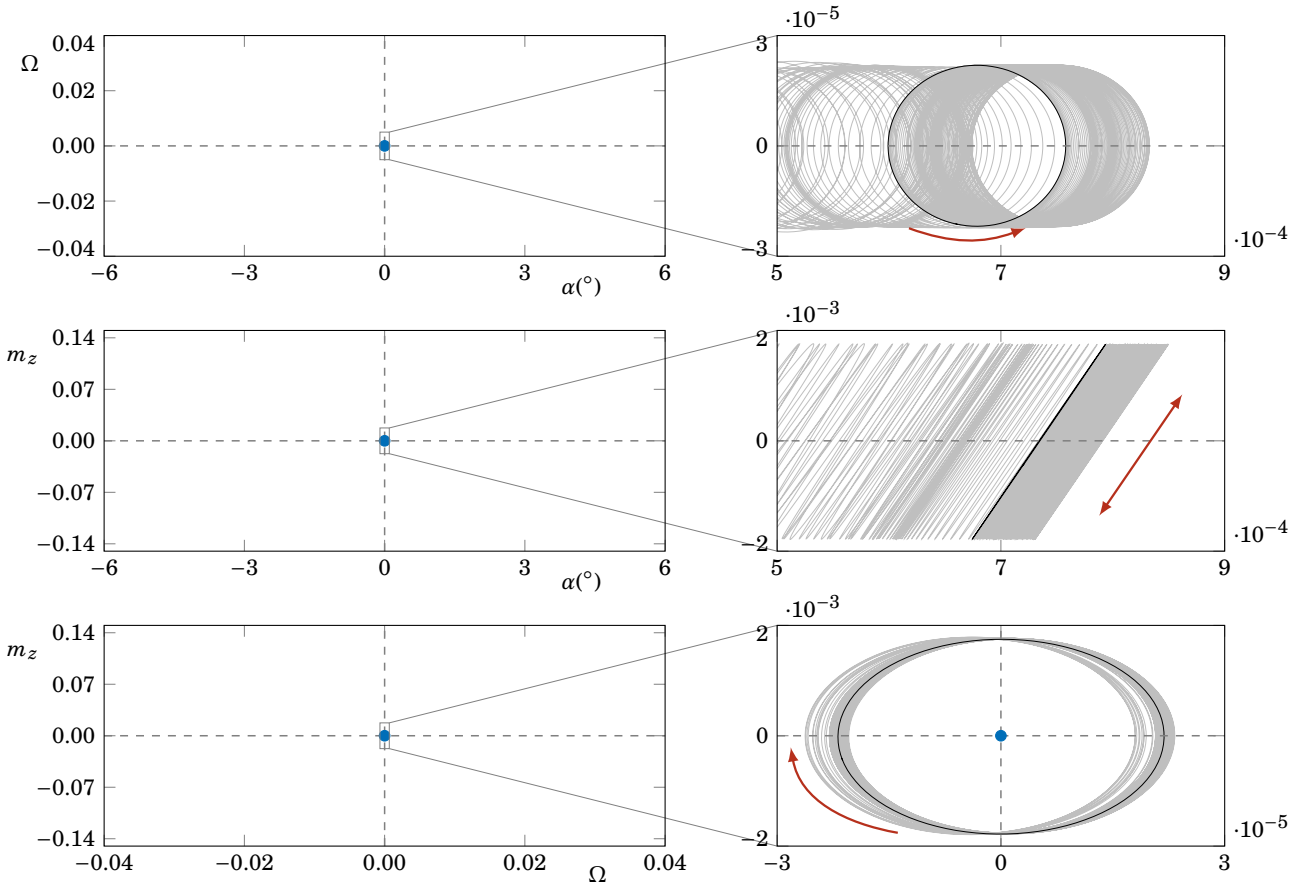

Figure 5.3 – *Regime R_1: phase diagrams at $Re = 20\,000$ and $K_s = 1.390$: angle of attack versus angular velocity, α–Ω, (first row), angle of attack versus aerodynamic moment coefficient, α–m_z, (second row) and angular velocity versus aerodynamic moment coefficient, Ω–m_z, (third row). A general view is present on the left, with a zoom on the right. The transient regime is represented by the grey lines, while the last vortex shedding cycle is represented by the black lines. The blue dots represent the quasi-static equilibrium point, $\bar{\alpha}_1 = 0°$, while the red arrows represent the direction of the time evolution.*

the last chapter, where a good agreement between the nonlinear exponential growth of the angular displacement and the static eigenvalue growth rate of the linear stability analyses was found.

In addition to the time histories present above, we plot in figure 5.3 three phase diagrams based on α, Ω and m_z. We sketch with a black line the last vortex shedding cycle, while the transient behaviour from the initial condition to the converged limit cycle is represented by a grey line. The blue dot represents the primary equilibrium point. We employ on the left side of the figure a scale that we keep constant when analysing the remaining nonlinear regimes, while a zoom at the origin is present in the right side of the figure.

From the zoomed figures, we first note that the α–Ω evolution presents an ellipse form, with their major and minor axes aligned with the figure axes. This indicates us that the time signals of α and Ω are in quadrature, *i.e.*, they have a phase shift of 90°. This value comes naturally from their relation: $\Omega = \mathrm{d}\theta/\mathrm{d}t = -\mathrm{d}\alpha/\mathrm{d}t$. Further, we note that the time direction, represented by the red arrow indicates that the phase diagram evolves on a anticlockwise direction. This is a consequence of considering α and Ω positive when rotating in opposite directions, *i.e.*, α is positive when rotating on the clockwise direction, while Ω is positive when rotating on the anticlockwise direction.

Analysing the zoom on the α–m_z phase diagram, we can conclude that the aerodynamic moment and the angular displacement are in phase, since their evolution over one vortex cycle oscillation (black line) is concentrated on a straight line of slope inferior to 90°. Finally, due to the phase relation between angular displacement and velocity, we obtain a Ω–m_z phase diagram with a quadrature phase evolution. This time, since Ω and m_z are positive when rotating in the same direction (anticlockwise), the phase diagram evolves on a clockwise direction.

A three-dimensional representation of the phase diagram of these three quantities is present in figure 5.7, with a comparison with the case at $K_s = 0.347$, analysed in the following paragraphs.

5.3.2 Regime R_2: weak oscillations around $\overline{\alpha} \neq 0^\circ$

For the second case, we lower the value of the structural stiffness to $K_s = 0.347$. The time history associated to the angular displacement, angular velocity and aerodynamic moment coefficient is present in figure 5.4. In this example, and contrary to the cases in regime R_1, we observe an exponential departure of the structure from its initial condition at $\alpha = 0^\circ$, with no associated frequency. This is in accordance with the linear stability analyses performed in the previous chapter (see table 4.6, page 154), where an unstable static eigenmode was found. After this initial transient regime, we observe that the angular displacement tends to a static position around 2.72°. With a close observation of the zoom present in the angular displacement figure, we actually see that this apparent static position corresponds to a weak oscillation of α, with an amplitude of order 10^{-3}. This oscillation has a periodic behaviour, vibrating at the fundamental frequency of $\omega_{VS} = 19.337$. This high frequency oscillation is also found on the angular velocity and aerodynamic moment time evolutions. As the regime R_1, this regime is considered to be a limit cycle oscillation. This frequency value is in very good agreement with the vortex shedding frequency found for the static simulations at $\overline{\alpha}_b = 2.72^\circ$ ($\omega_{VS} = 19.214$, see figure 2.9, page 79). We also note that this mean equilibrium angle is predicted by the quasi-steady secondary equilibrium point, located at $\overline{\alpha}_2 = 2.72^\circ$ and identified by the horizontal dashed line on the angular displacement evolution.

The final limit cycle oscillation around $\alpha = 2.72^\circ$ is characterised by an angular velocity that oscillates around a null value, as expected. At the same time, the aerodynamic moment signal is also periodic in time, even if we observe that its oscillation amplitude has increased substantially, when compared the value found for the case on the regime R_1. This increase in the aerodynamic moment amplitude oscillations follows the conclusions made in chapter 2, where we report an increase of this amplitude for static time-marching simulations, as the angle increases (see figure 2.8, page 78). The aerodynamic moment tends to a mean value of $\overline{m}_z = -0.0165$, similar to the mean aerodynamic moment of time-marching simulations at the quasi-steady secondary equilibrium point ($m_z(\overline{q}_b) = -0.0167$), confirming the equality in equation 5.1.

The importance of the solid vibrations at the vortex shedding frequency on the nonlinear dynamics is quantified with the help of H_θ and H_Ω, whose magnitude is reported in table 5.3. As for the regime R_1, both the theoretical values and the values coming the nonlinear simulations are in very good agreement, with a slight increase on their numerical values. In view of these results, we expect the contributions coming from the fast time scale solid components to the

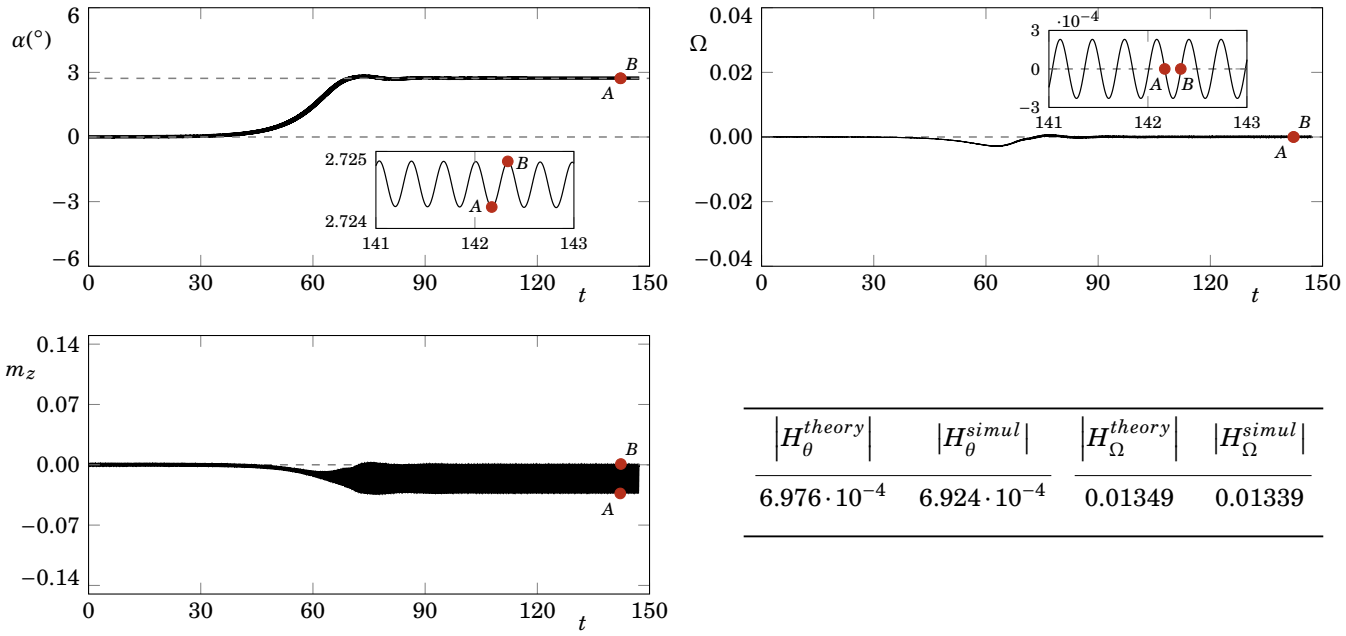

$\lvert H_\theta^{theory} \rvert$	$\lvert H_\theta^{simul} \rvert$	$\lvert H_\Omega^{theory} \rvert$	$\lvert H_\Omega^{simul} \rvert$
$6.976 \cdot 10^{-4}$	$6.924 \cdot 10^{-4}$	0.01349	0.01339

Figure 5.4 & Table 5.3 – *Regime R_2: time history of the angle of attack (top left), the angular velocity (top right) and the aerodynamic moment coefficient (bottom left) for a two-dimensional coupled time-marching simulation at $Re = 20\,000$ and $K_s = 0.347$. On the angle of attack evolution, the horizontal dashed lines represent the quasi-static equilibrium points, $\bar{\alpha}_1 = 0°$ and $\bar{\alpha}_2 = 2.72°$. The red dots highlight the instants A and B. The table on the bottom right compares the values of H_θ and H_Ω, evaluated at $\omega_{VS} = 19.337$, the vortex shedding frequency, for the theoretical estimation and for the nonlinear simulations.*

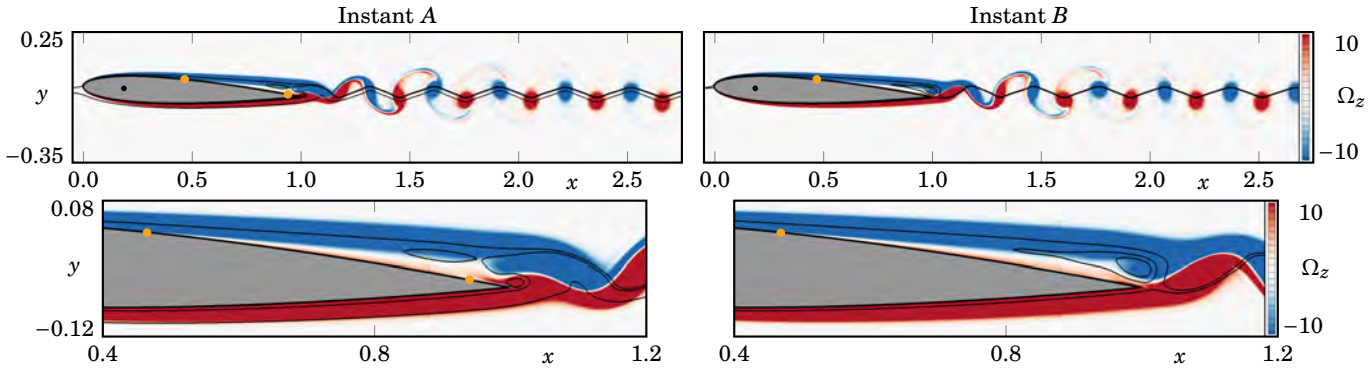

Figure 5.5 – *Regime R_2: spanwise vorticity field of two instants of a two-dimensional coupled time-marching simulation at $Re = 20\,000$ and $K_s = 0.347$, for the instant A (left) and for the instant B (right), identified on figure 5.4. The yellow dots over the airfoil surface represent the different separation and reattachment points.*

linear stability analysis formulation to be negligible for the secondary equilibrium point. The linear stability analysis of this secondary equilibrium point is made in the next chapter.

In figure 5.4 two time instants are highlighted, labelled A and B, corresponding to a maximum and a minimum of the aerodynamic movement magnitude, respectively. The instants are therefore separated by $T/2$ time units, T being the period of the vortex shedding. The instantaneous flow solutions associated to these two instants are illustrated in figure 5.5, by the spanwise vorticity field. A coherent vortex shedding can be observed in both instants on the wake of the airfoil. The black lines, representing different streamlines, illustrate the topology of the flow structure, in particular on the second half of the airfoil, where the boundary layer of the upper surface is separated from $X_d = 0.46$ onwards, on both instants. Both instants present a boundary layer on the upper surface that does not reattach to the airfoil surface. Between the airfoil surface and the separated boundary layer, a main recirculation bubble is formed, rotating on the clockwise direction. Further, instant A presents a reattachment point at $X = 0.94$. This reattachment creates a smaller recirculation bubble, rotating on an anticlockwise direction, formed above the trailing edge.

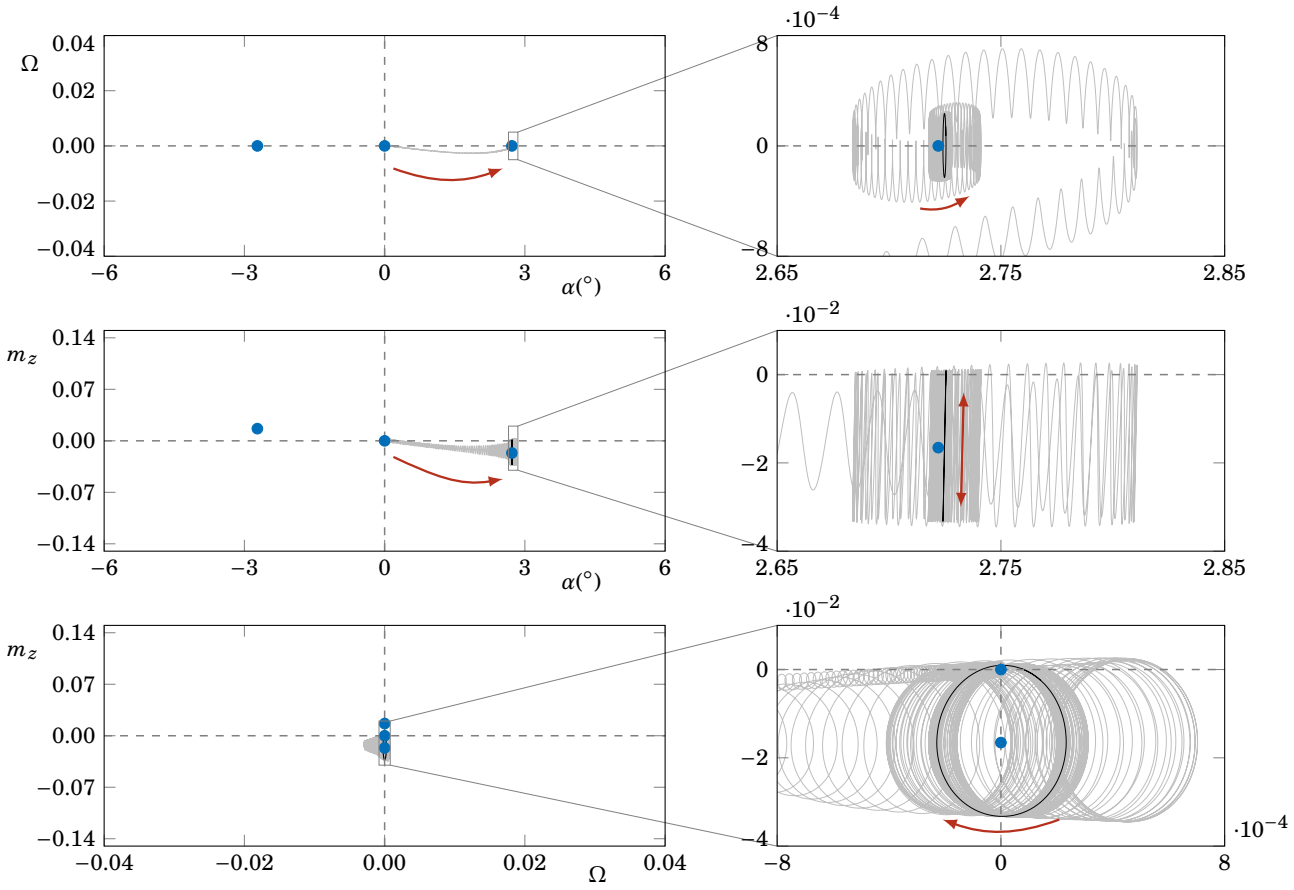

Figure 5.6 – *Regime R_2: phase diagrams at $Re = 20\,000$ and $K_s = 0.347$: angle of attack versus angular velocity, α–Ω, (first row), angle of attack versus aerodynamic moment coefficient, α–m_z, (second row) and angular velocity versus aerodynamic moment coefficient, Ω–m_z, (third row). A general view is present on the left, with a zoom on the right. The transient regime is represented by the grey lines, while the last vortex shedding cycle is represented by the black lines. The blue dots represent the quasi-static equilibrium points, $\bar{\alpha}_1 = 0°$ and $\bar{\alpha}_2 = 2.72°$, while the red arrows represent the direction of the time evolution.*

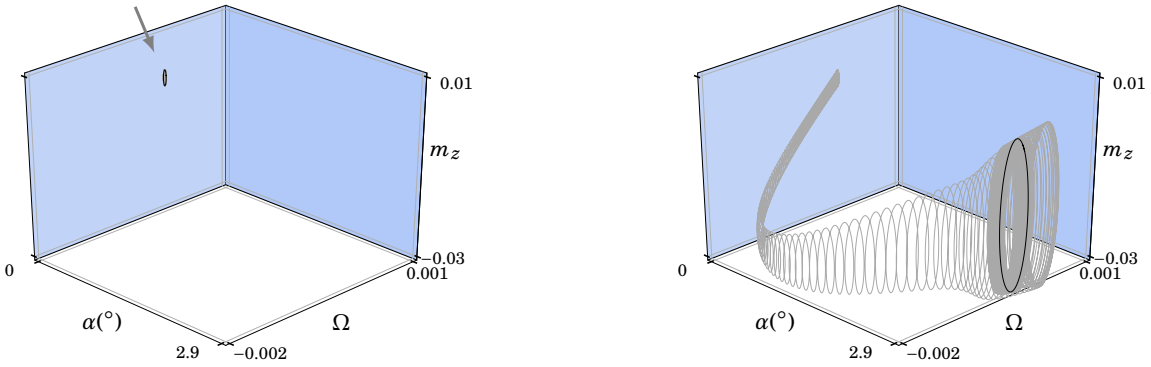

Figure 5.7 – *Regimes R_1 and R_2: three-dimensional phase diagrams of the angle of attack, the angular velocity and the aerodynamic moment coefficient, α–Ω–m_z, at Re = 20 000 for $K_s = 1.390$ (left, corresponding to regime R_1) and $K_s = 0.347$ (right, corresponding to regime R_2). The transient regime is represented by the grey line, while the last vortex shedding cycle is represented by the black line. The small arrow on the left figure highlights the position of the limit cycle.*

In addition to the time histories present above, we plot in figure 5.6 the three phase diagrams based on α, Ω and m_z. As done previously, we sketch with a black line the last vortex shedding cycle, while the transient behaviour from the initial condition to the converged limit cycle is represented by a grey line. This time, the blue dots represent both the primary and secondary equilibrium points.

From the left figures, we can first confirm that the airfoil evolves from the static position at $\alpha = 0°$ towards the angle $\alpha = 2.72°$. As explained before, the angular displacement evolves towards positive values rather than the negative ones due to the choice of the initial instant to initialise the nonlinear simulations and its phase in the vortex shedding cycle. Both positive and negative angular displacement evolutions correspond theoretically to the same phenomenon, due to the symmetry of the problem.

From the right figures, we can obtain the same conclusions regarding the phase shift between α, Ω and m_z as the ones made for the case at $K_s = 1.390$ (regime R_1): α and Ω have a phase shift of 90°, α and m_z are in phase and Ω and m_z also have a phase shift of 90°. We also note that the quasi-steady aerodynamic moment of the second equilibrium point is now negative, respecting equation 5.1.

A three-dimensional representation of the phase diagram of these three quantities is present in figure 5.7. The curve that represents the last vortex shedding cycle (black curve) is in a plane surface, corresponding to a limit cycle oscillation. When comparing the regimes R_1 and R_2, we note that the second limit cycle has a higher amplitude of oscillation in all three directions, in particular in the aerodynamic moment and angular velocity directions.

5.3.3 Regime R_3: strong oscillations around $\overline{\alpha} \neq 0°$

For the third case, we lower the value of the structural stiffness to $K_s = 0.087$. The time history associated to the angular displacement, angular velocity and aerodynamic moment coefficient is present in figure 5.8. Similarly to the case of the previous regime, an initial exponential growth is observed on the initial incidence evolution, corresponding to the departure of the structure from the initial condition at $\alpha = 0°$. A very good agreement is found between this exponential growth and the growth rate of the static eigenmode found on the linear stability analyses of the primary equilibrium point (see table 4.6). However, in contrast to the previous case, we observe that, after this exponential growth, the airfoil starts

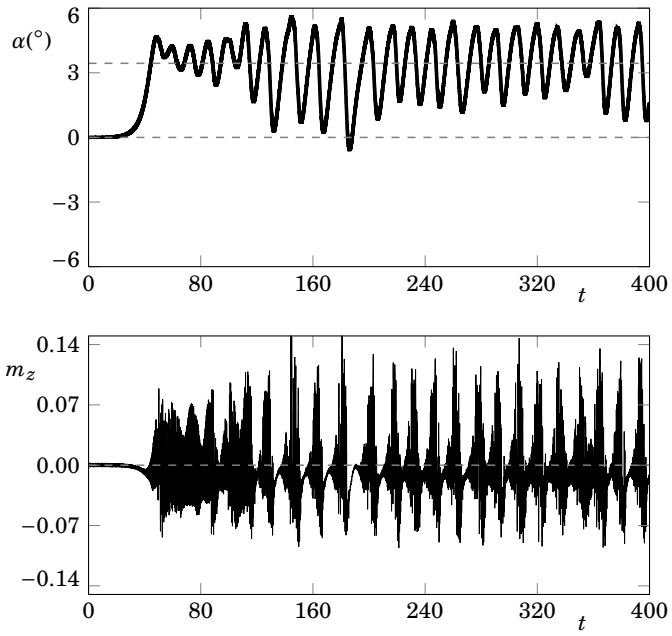

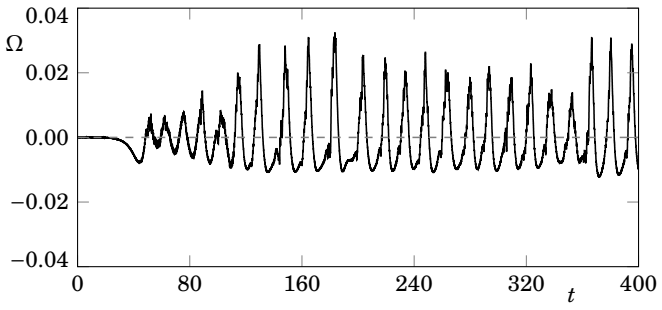

ω_{VS}	$\lvert H_\theta^{theory}\rvert$	$\lvert H_\theta^{simul}\rvert$	$\lvert H_\Omega^{theory}\rvert$	$\lvert H_\Omega^{simul}\rvert$
7.854	$4.457 \cdot 10^{-3}$	$7.852 \cdot 10^{-3}$	0.03410	0.06007
16.151	$1.000 \cdot 10^{-3}$	$1.790 \cdot 10^{-3}$	0.01615	0.02892

Figure 5.8 & Table 5.4 – *Regime R_3: time history of the angle of attack (top left), the angular velocity (top right) and the aerodynamic moment coefficient (bottom left) for a two-dimensional coupled time-marching simulation at $Re = 20\,000$ and $K_s = 0.087$. On the angle of attack evolution, the horizontal dashed lines represent the quasi-static equilibrium points, $\bar{\alpha}_1 = 0°$ and $\bar{\alpha}_2 = 3.44°$. The table on the bottom right compares the values of H_θ and H_Ω, evaluated at $\omega_{VS,1} = 7.854$ and $\omega_{VS,2} = 16.151$, the two vortex shedding frequencies, for the theoretical estimation and for the nonlinear simulations.*

to oscillate around a mean angle of $\bar{\alpha} = 3.34°$. When comparing this mean angle to the quasi-steady secondary equilibrium point, at $\bar{\alpha}_2 = 3.44$, we have a deviation of $0.1°$. Further, the angular displacement oscillations have an amplitude with an order of magnitude of 1 and vibrate at a very low frequency, $\omega_{FSI} = 0.428$, when compared to the vortex shedding frequency present in the aerodynamic moment signal. As detailed in the next paragraphs, the vortex shedding frequency of the FSI simulations varies along the low frequency cycle of the airfoil incidence, on the range $7.854 \lesssim \omega_{VS} \lesssim 16.151$. In a addition to this variation, we note that the frequencies in this range are lower than the frequency found for the static time-marching simulations at $\bar{\alpha}_b = 3.44°$ ($\omega_{VS} = 19.040$, see figure 2.9, page 79).

We can have a better understanding of the frequencies present on the above time signals by sketching them on the frequency space, with the help of a FFT. This is done in figure 5.9. We highlight the low frequency and two vortex shedding frequencies with the vertical dashed lines. The spectral density estimation of the angular displacement (top left) presents a distinct peak at $\omega_{FSI} = 0.428$. For higher frequencies, this spectral density estimation presents a decreasing behaviour as the higher frequencies are not felt by the angular displacement of the structure. In particular, no significant peak is observed at the vortex shedding frequencies highlighted.

Concerning the aerodynamic moment spectrum (bottom left), the low frequency ω_{FSI} also appears as the dominant frequency. However, a wide range of high frequencies is present. We delimit this zone by a lower and higher vortex shedding frequency, representing two local peaks, $\omega_{VS,1} = 7.854$ and $\omega_{VS,2} = 16.151$, respectively. These high frequencies are associated to the vortex shedding phenomenon, that could be already viewed on the temporal evolution of m_z. The wide range of high frequencies is associated to the variation of the vortex shedding frequency along the (low frequency)

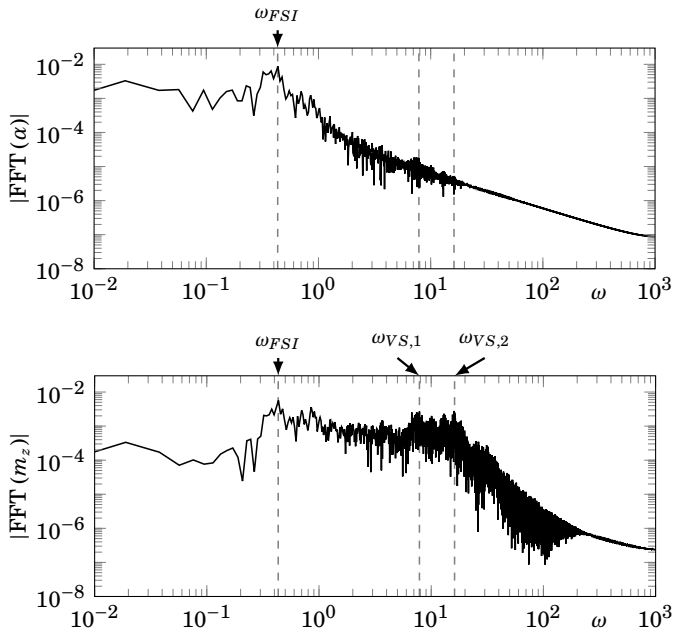

ω_{FSI}	$\omega_{VS,1}$	$\omega_{VS,2}$
0.428	7.854	16.151

Figure 5.9 & Table 5.5 – *Regime R_3: spectral density estimation of the angle of attack (top left), the angular velocity (top right) and the aerodynamic moment coefficient (bottom left), for a two-dimensional coupled time-marching simulation at $Re = 20\,000$ and $K_s = 0.087$. The vertical dashed lines highlight the low frequency and the vortex shedding frequencies, with values reported in the table (bottom right).*

oscillation of the airfoil incidence, as discussed later. In the spectral density estimation of the angular velocity (top right), the three frequencies ω_{FSI}, $\omega_{VS,1}$ and $\omega_{VS,2}$ can be discerned, even if the vortex shedding frequencies present a much lower spectral density estimation value when compared to the one associated to ω_{FSI}.

Due to the presence of these two incommensurable frequencies (ω_{FSI} and ω_{VS}), this regime no longer corresponds to a limit cycle oscillation. Further, with no periodicity or quasi-periodicity on the sketched time signals, and with a wide range of significant frequencies on the spectral representation, we categorise this regime as being a chaotic attractor, also known as a strange attractor. Indeed, some resemblance is found to the Lorenz attractor (Lorenz, 1963), a classical system of ordinary differential equations that presents chaotic solutions for certain parameter values and initial conditions. In the present case, we observed that solution of two different nonlinear simulations, at the same K_s, diverge from each other after some amount of time, even if they start from the same initial condition. This divergence is typical of deterministic chaotic systems, when a small error is introduced either on the initial condition or on the time evolution process. In the present case, the error is likely coming from the numerical resolution and the machine precision approximation.

The values of the spectral density estimation at the two vortex shedding frequencies are used to compute the magnitudes of the transfer functions H_θ^{simul} and H_Ω^{simul}. These values are compared with the theoretical values, $\left|H_\theta^{theory}\right|$ and $\left|H_\Omega^{theory}\right|$, also evaluated at $\omega_{VS,1}$ and $\omega_{VS,2}$, in table 5.4. Contrary to the previous regimes, a small discrepancy is found between the theoretical values and the values obtained from the nonlinear simulations. Further, their magnitude is higher that the ones reported in the previous K_s cases, where no low frequency oscillations were found.

In addition to the time and spectral representations presented, we plot in figure 5.10 the phase diagrams based on α, Ω and m_z, with a two-dimensional representation on the left and the three-dimensional view on the bottom right. The black line represents the last low frequency oscillation, while the grey line represents all the previous time evolution. Since we

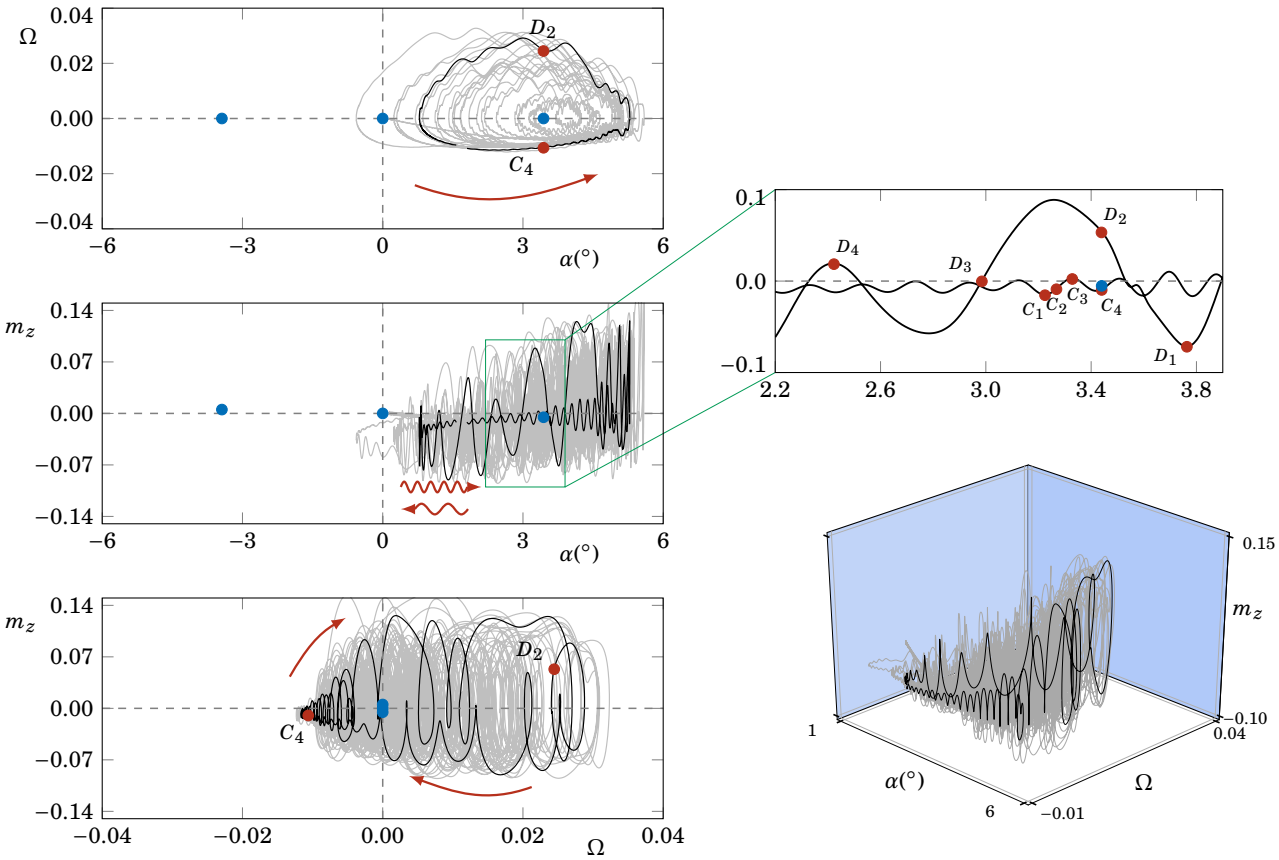

Figure 5.10 – *Regime R_3: phase diagrams at $Re = 20\,000$ and $K_s = 0.087$: angle of attack versus angular velocity, α–Ω, (top left), angle of attack versus aerodynamic moment coefficient, α–m_z, (middle left) and angular velocity versus aerodynamic moment coefficient, Ω–m_z, (bottom left). The transient regime is represented by the grey lines, while the last low frequency cycle is represented by the black lines. The blue dots represent the quasi-static equilibrium points, $\bar{\alpha}_1 = 0°$ and $\bar{\alpha}_2 = 3.44°$, while the red arrows represent the direction of the time evolution. The red dots highlight different instants on the ascending (C instants) and descending (D instants) phases of the angle of attack. On the bottom right, a three-dimensional phase diagram for α–Ω–m_z.*

are in the presence of a chaotic attractor, the black line does not correspond to a closed curve as in the previous limit cycle oscillations. The red dots highlight different time instants, labelled C_i and D_i ($i \in [1, 2, 3, 4]$), whose corresponding flow fields are explored later. These two sets of instants are placed on the ascending and descending phases of the angular displacement evolution in time. In particular, the instants C_4 and D_2 are placed at $\alpha = 3.44°$, the value of the secondary equilibrium angle at this K_s.

The oscillation of the airfoil around the secondary equilibrium position $\bar{\alpha}_2 = 3.44°$ can be clearly observed in the α–Ω phase diagram. Qualitatively, we can note that no fast time oscillations of the black curve are observed in the horizontal direction, coherent with the fact that the frequency spectrum of the angular displacement does not present significant peaks on the high frequency zone (in particular at $\omega_{VS,1}$ and $\omega_{VS,2}$). In contrast, several fast time oscillations are observed in the vertical direction, associated to the harmonic content of the angular velocity spectrum on the high frequency zone.

The phase diagram of α–m_z enables us to identify that the ascending phase of the angular displacement is associated

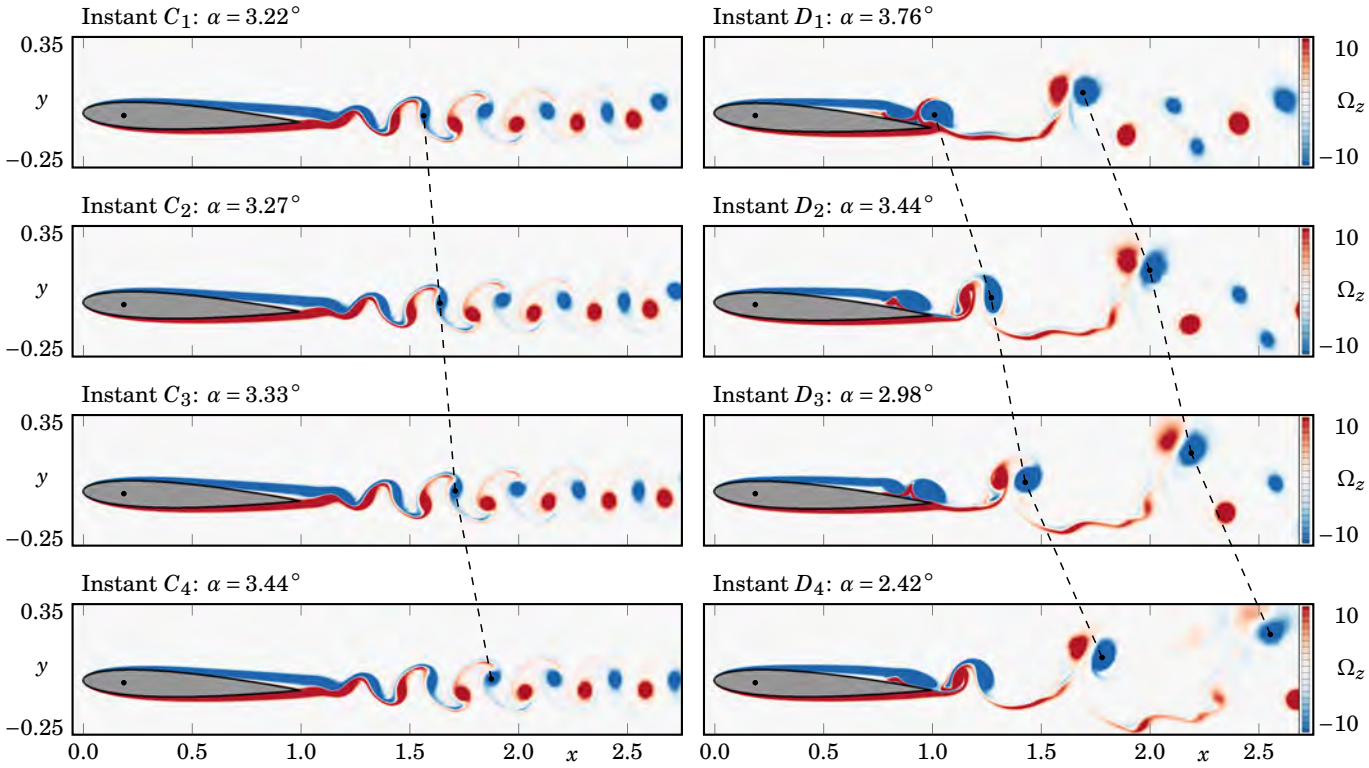

Figure 5.11 – *Regime R_3: spanwise vorticity field of several instantaneous solutions of a two-dimensional coupled time-marching simulation at $Re = 20\,000$ and $K_s = 0.087$. On the left, for the ascending phase of the angle of attack. On the right, for the descending phase of the angle of attack. The position of the instants on a phase diagram is identified on figure 5.10.*

to larger high frequencies (in particular, $\omega_{VS,2}$), while the descending phase is associated to lower high frequencies (in particular, $\omega_{VS,1}$). The time evolution of the black curve can be understood with the red arrows scheme, illustrating the above conclusions. Further, we note that in the descending angular displacement phase, where the lower high frequencies are found, we have larger values of $|\Omega|$, when compared to the ascending phase. As a consequence, the low frequency oscillation is characterised by an ascending phase slower than the descending phase. A close-up near $\alpha = 3.44°$ is made, to identify the location of different instants, analysed in the following paragraph.

Figure 5.11 presents the spanwise vorticity field of two sets of instants. The instants C_1 to C_4, on the left, are located on the ascending phase of the angular displacement. In this case, the flow is characterised by an organised vortex shedding, placed close to the wake axis, similar to the vortex shedding present on the wake of an airfoil at a static incidence (see for instance figure 2.1, page 72). The frequency at which these structures are shed corresponds to the higher frequency of vortex shedding present in the spectrum of m_z ($\omega_{VS,2} = 16.151$). In contrast, the instants D_1 to D_4, on the right, are located on the descending phase of the angular displacement. We note in this case that the vortex shedding has a more disorganised character, with the main vortex structures more distanced from each other and from the wake axis. The frequency at which these structures are shed corresponds to the lower frequency of vortex shedding present in the spectrum of m_z ($\omega_{VS,1} = 7.854$).

When comparing the two vortex shedding frequencies, we observe that $\omega_{VS,1}$ is almost half of $\omega_{VS,2}$. This suggests that, for the period of time that the airfoil incidence is decreasing, we are in the presence of a period-doubling. This

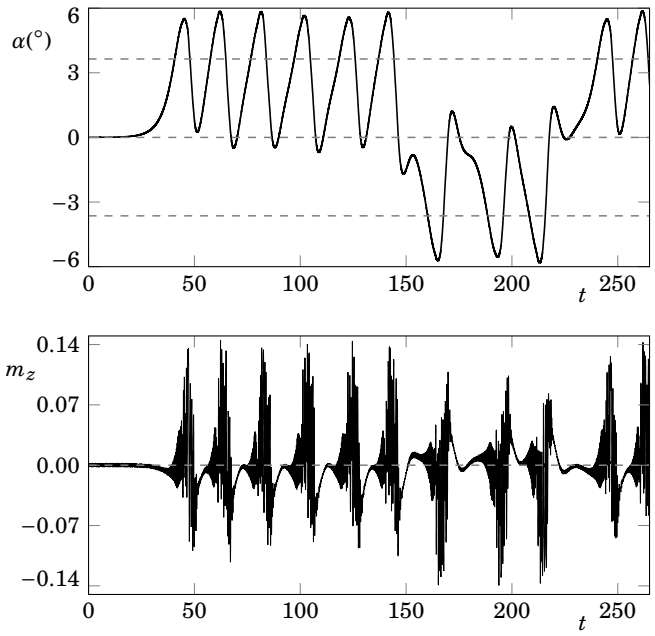

ω_{VS}	$\lvert H_\theta^{theory}\rvert$	$\lvert H_\theta^{simul}\rvert$	$\lvert H_\Omega^{theory}\rvert$	$\lvert H_\Omega^{simul}\rvert$
7.384	—	$5.146 \cdot 10^{-3}$	—	0.03800
10.303	—	$3.437 \cdot 10^{-3}$	—	0.03541

Figure 5.12 & Table 5.6 – *Regime R_4: time history of the angle of attack (top left), the angular velocity (top right) and the aerodynamic moment coefficient (bottom left) for a two-dimensional coupled time-marching simulation at $Re = 20\,000$ and $K_s = 0$. On the angle of attack evolution, the horizontal dashed lines represent the quasi-static equilibrium points, $\bar{\alpha}_1 = 0°$ and $\bar{\alpha}_2 = 3.64°$. The table on the bottom right reports the values of H_θ and H_Ω, evaluated at $\omega_{VS,1} = 7.384$ and $\omega_{VS,2} = 10.303$, the two vortex shedding frequencies, for the nonlinear simulations.*

period-doubling phenomenon was also found recently by Marquet *et al.* (2022) for a NACA0012 airfoil in stall conditions at $Re = 5\,000$ and $\alpha \approx 8°$. Related to the emergence to this phenomenon, we can also categorise the particular pattern formed by the shed of the vortical structures. This is done by comparing the present results to the vast literature on the benchmark case of the oscillating circular cylinder. The different patterns of vortex formation observed for an oscillating cylinder are usually classified as function of the amplitude and frequency of oscillation (Williamson *et al.*, 1988; Govardhan *et al.*, 2000; Williamson *et al.*, 2008). They can be defined, for example, as $2S$ indicating 2 single vortices formed per cycle, $2P$ meaning 2 pairs of vortices formed per cycle and $P+S$ compromising a pair of vortices and a single vortex per cycle. Firstly, observing the instants C_1 to C_4, we can observe the shed of 2 single vortices per cycle. Therefore, we can classify the classic vortex shedding phenomenon as being a $2S$ regime. In contrast, by observing in detail the instants D_1 to D_4, we can observe the shed of 2 pairs of vortices per cycle. In between, a narrow zone of positive vorticity (in red) can be observed. We conclude that, based on the classical identification of the patterns of vortex formation, we are in the presence of a regime in between the P and the $P+S$ modes. We recall that this regime is only observed for a small period of time, when the airfoil incidence is decreasing.

5.3.4 Regime R_4: intermittent switching strong oscillations

For the fourth case, we consider the limiting case of $K_s = 0$. In this case, since no structural stiffness is present, the restoring force acting on the airfoil, counterbalancing the incidence or decrease of the angle of attack, comes entirely from the fluid. The time history associated to the angular displacement, angular velocity and aerodynamic moment coefficient is present in figure 5.12. Similarly to the case of regime R_3, an initial exponential growth is observed on the incidence

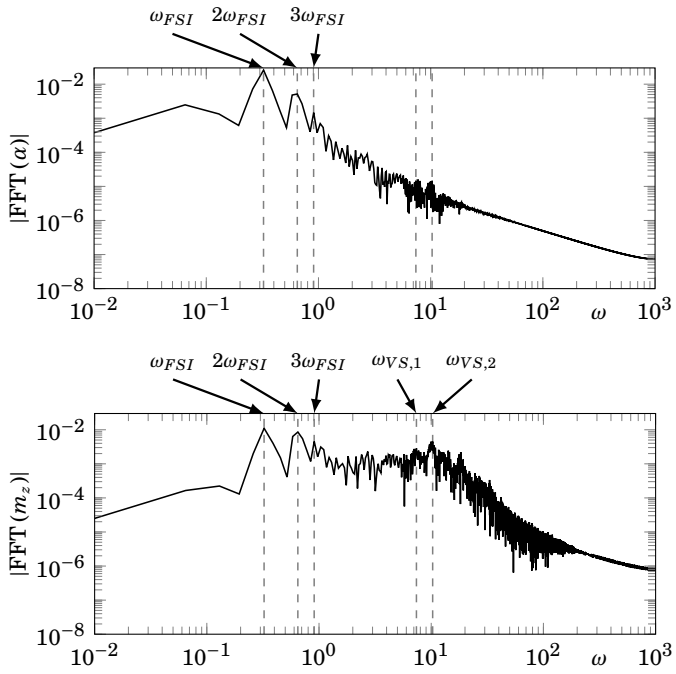

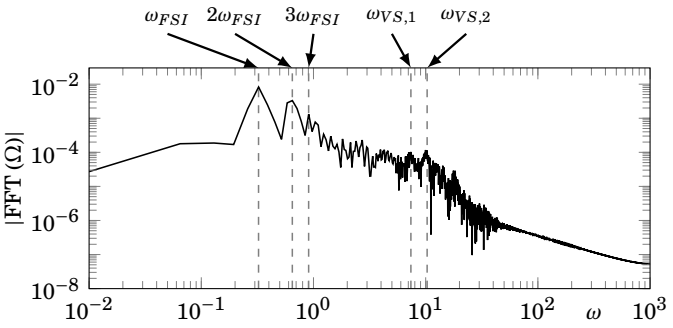

ω_{FSI}	$\omega_{VS,1}$	$\omega_{VS,2}$
0.324	7.384	10.303

Figure 5.13 & Table 5.7 – *Regime R_4: spectral density estimation of the angle of attack (top left), the angular velocity (top right) and the aerodynamic moment coefficient (bottom left), for a two-dimensional coupled time-marching simulation at $Re = 20\,000$ and $K_s = 0$. The vertical dashed lines highlight the low frequency, its harmonics and the vortex shedding frequencies, with values reported in the table (bottom right).*

evolution, corresponding to the departure of the structure from the initial condition at $\alpha = 0\,^\circ$, with a very good agreement between this exponential growth and the growth rate of the static eigenmode found on the linear stability analyses of the primary equilibrium point (see table 4.6). As the angle increases, the nonlinear exponential growth saturates and the airfoil starts to oscillate around a mean angular displacement of $\bar{\alpha} = 2.73\,^\circ$, with a low frequency of $\omega_{FSI} = 0.324$. This mean angle, calculated for the first five low frequency oscillations ($45 < t < 142$), is substantially different from the quasi-steady secondary equilibrium point, $\bar{\alpha}_2 = 3.64\,^\circ$, represented by the horizontal dashed lines in the angular displacement evolution. This low frequency oscillation can also be perceived on the angular velocity and aerodynamic moment evolutions. Additionally, the latter presents a high frequency oscillation, associated to the vortex shedding.

We note that the amplitude of the oscillations is high enough to cause the airfoil incidence to switch from the positive angular displacement oscillations to the negative ones. This intermittent jump of the oscillations between the two attractors, resemblances once again to the Lorenz attractor behaviour, having a chaotic character.

The spectral density estimation of the above time evolutions is present in figure 5.13, with the help of a FFT. This spectral density estimation is made for the time period where the airfoil incidence oscillates around the positive incidence attractor. Concerning the FFT of the angular displacement (top left), we note that the main peaks correspond to the fundamental frequency of the low oscillations ($\omega_{FSI} = 0.324$) and its first and second harmonics. From there, the spectral estimation presents a decreasing behaviour as the higher frequencies are not felt by the angular displacement of the structure. An exception is made for two frequency values on the high frequency range, which we also highlight with the vertical dashed lines. These two frequencies are more clearly identified on the spectral density estimation of the angular velocity (top right) and aerodynamic moment (bottom left). The lower vortex shedding frequency, $\omega_{VS,1} = 7.854$,

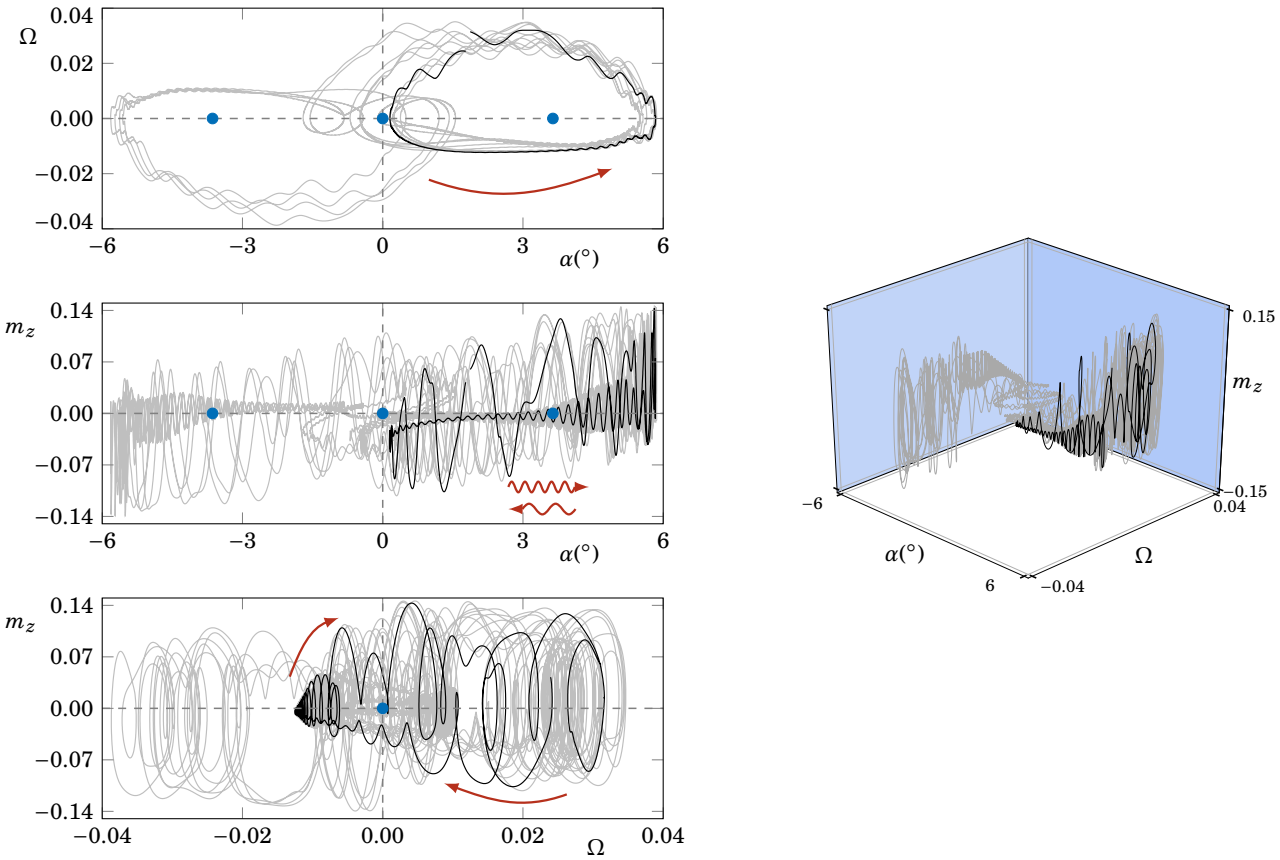

Figure 5.14 – *Regime R_4: phase diagrams at $Re = 20\,000$ and $K_s = 0$: angle of attack versus angular velocity, α–Ω, (top left), angle of attack versus aerodynamic moment coefficient, α–m_z, (middle left) and angular velocity versus aerodynamic moment coefficient, Ω–m_z, (bottom left). The transient regime is represented by the grey lines, while the last low frequency cycle is represented by the black lines. The blue dots represent the quasi-static equilibrium points, $\bar{\alpha}_1 = 0°$ and $\bar{\alpha}_2 = 3.44°$, while the red arrows represent the direction of the time evolution. On the right, a three-dimensional phase diagram for α–Ω–m_z.*

is associated to the descending phase of the airfoil incidence on the low frequency cycle, while the higher vortex shedding frequency, $\omega_{VS,2} = 10.303$, is associated to its ascending phase.

The values of the spectral density estimation at the two vortex shedding frequencies are used to compute the magnitudes of the transfer functions H_θ^{simul} and H_Ω^{simul}. In this case, with K_s equal to zero, the theoretical values are not defined, since the natural frequency of the structure, ω_s, is zero and the damping factor, ζ, tends to infinity as K_s tends to zero. We report the values of H_θ^{simul} and H_Ω^{simul} for the two vortex shedding frequencies, $\omega_{VS,1}$ and $\omega_{VS,2}$ in table 5.6. Their magnitude is higher that the ones reported for regimes R_1 and R_2, where no low frequency oscillations were found. We observe that they have the same magnitude order as the transfer functions associated to the regime R_3.

In addition to the time and spectral representations presented, we plot in figure 5.14 the phase diagrams based on α, Ω and m_z, with a two-dimensional representation on the left and the three-dimensional view on the right. The black line represents the last low frequency oscillation, on the positive side of α, while the grey line represents all the previous time evolution. Since we are in the presence of a chaotic attractor, the black line does not correspond to a closed curve as in the limit cycle oscillation of regimes R_1 and R_2. We can observe that the grey line encircles the two attractors, corresponding

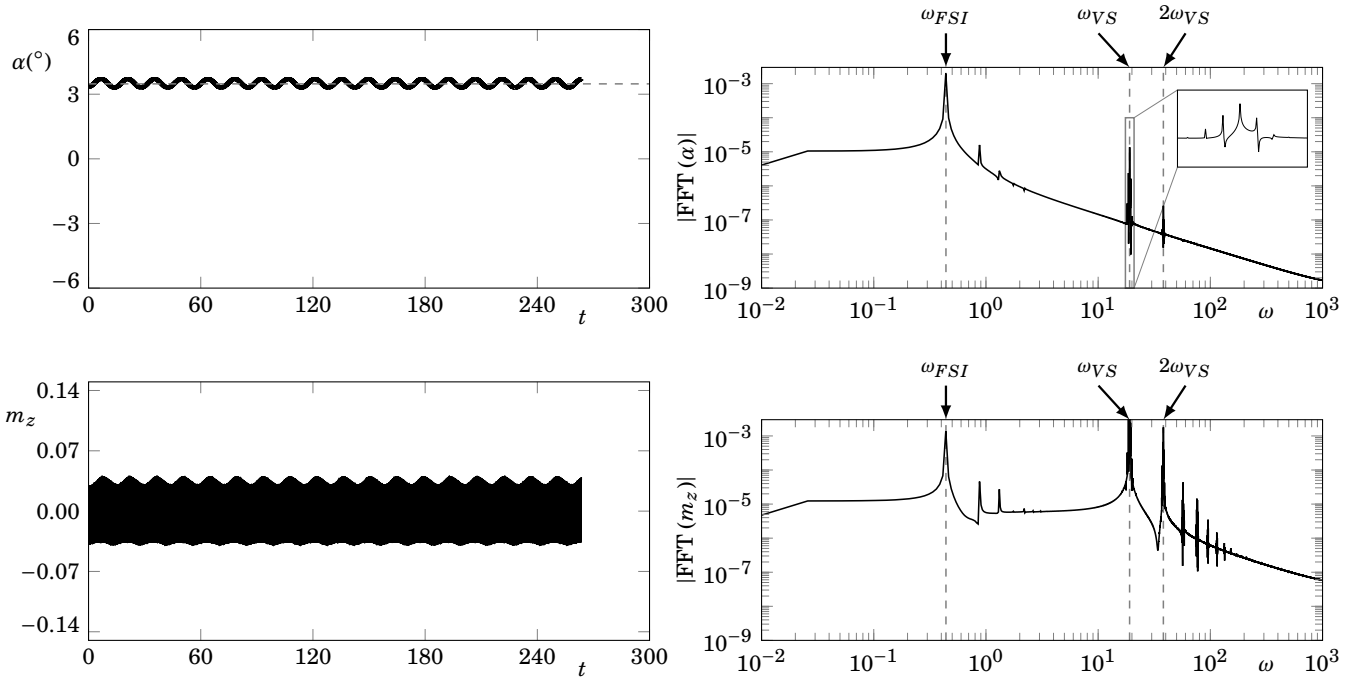

Figure 5.15 – *Regime R_5: time history of the angle of attack and the aerodynamic moment coefficient (left) and corresponding spectral density estimation (right) for a two-dimensional coupled time-marching simulation at $Re = 20\,000$ and $K_s = 0.078$. On the angle of attack evolution, the horizontal dashed lines represent the quasi-static secondary equilibrium point, $\bar{\alpha}_2 = 3.48°$. On the spectral density estimations, the vertical dashed lines highlight the low frequency ($\omega_{FSI} = 0.437$) and the vortex shedding frequency ($\omega_{VS} = 19.067$) and its harmonic.*

to the quasi-steady secondary equilibrium points at $\bar{\alpha}_2 = \pm 3.44°$ (blue dots).

The oscillation of the airfoil around the secondary equilibrium position $\bar{\alpha}_2 = 3.44°$ can be clearly observed in the α–Ω phase diagram. This phase diagram enables us to qualitatively note that no fast time oscillations of the black curve are observed in the horizontal direction, while fast time oscillations are observed in the vertical direction. This is in accordance with the local peaks found on the spectral density estimation of the angular velocity on the high frequency range, in particular at $\omega_{VS,1}$ and $\omega_{VS,2}$.

Concomitantly, the phase diagram of α–m_z enables us to associate the ascending phase of α to the higher high frequency, $\omega_{VS,2}$, while the descending phase is associated to the lower high frequency, $\omega_{VS,1}$. Further, the phase diagram of Ω–m_z enables us to see that the high values of Ω (found on the descending phase of α) are associated to the high amplitude variations of the aerodynamic moment. These high amplitude bursts of the aerodynamic moment could already be seen in its time evolution in figure 5.12.

5.3.5 Regime R_5: quasi-periodic oscillations

In the previous paragraphs, four different regimes for the FSI time-marching simulations are identified, depending on the value of the structural stiffness. In the following paragraphs, we aim at further explore the different solutions that may appear as function of this parameter.

The first four FSI regimes are obtained by initialising the FSI time-marching simulations with an instantaneous

flow solution of a time-marching simulation performed at the static incidence of $\alpha = 0°$. As a consequence, the solid components of the FSI simulations are initialised at a null value, $\alpha = 0°$ and $\Omega = 0$. In these four regimes, two of them present a low frequency oscillation. To find the next regime, a different initialisation technique is used. We start from a FSI solution of the case at $K_s = 0.261$ (regime R_2), where no low frequency oscillation is found and we progressively decrease the value of K_s. With this continuation strategy, both the fluid and the solid components are initialised with the values of the previous FSI time-marching simulation, performed at a higher K_s value.

We start by analysing the case at $K_s = 0.078$. The time history associated to the angular displacement and aerodynamic moment coefficient is present on the left of figure 5.15, with their corresponding spectral density estimation on the right. The angular displacement presents a low frequency oscillation around a nonzero angle of attack of $\bar{\alpha} = 3.48°$ and with moderate amplitude around $0.5°$. In contrast, the aerodynamic moment presents a high frequency oscillation ,which is modulated by a low frequency. In both spectral estimations, two incommensurable frequencies are discerned, a low frequency ω_{FSI}, associated the airfoil oscillation and a high frequency ω_{VS}, associated to the vortex shedding phenomenon. This regime results from the destabilisation of the limit cycle oscillation found on regime R_2. These types of bifurcation are usually denominated as Neimark–Sacker bifurcation (Kuznetsov, 2006). Therefore, due to the presence of these two incommensurable frequencies (ω_{FSI} and ω_{VS}), this regime is labelled as a quasi-periodic oscillation. Additional cases in this regime are considered in the next section, where a global vision of all the regimes for $Re = 20\,000$ is given.

Summary of the five regimes at *Re* = 20 000

In this section we described five regimes associated to the nonlinear dynamics of an airfoil structure with a pitch degree of freedom, immersed in a two-dimensional Navier–Stokes flow. Each regime is associated to a different value of the structural stiffness of the torsional spring. Table 5.8 summarises some figures associated to the different computations. The first two regimes (R_1 and R_2) were characterised by weak incidence oscillations of the structure, at the vortex shedding frequency. In the first regime, these oscillations were observed around the primary equilibrium point $\bar{\alpha}_1 = 0°$, while in the second regime the airfoil incidence oscillated around the secondary equilibrium point $\bar{\alpha}_2 = 2.72°$. In contrast, the last three regimes (R_3, R_4 and R_5) presented large amplitude oscillations of the airfoil incidence, at a low frequency. The first lines of table 5.8 compare the fundamental frequency of this oscillation, ω_{FSI}, with the frequency of the structure in vacuum, ω_s (given by equation 1.11, page 23). The comparison can only be made for the regimes R_3 and R_5, where the same order of magnitude is found between these two frequencies, with a larger values for the FSI time-marching simulations.

Regime	R_1	R_2	R_3	R_4	R_5
K_s^{dim}(Nm)	0.080	0.020	0.005	0.000	0.0045
K_s	1.390	0.347	0.087	0.000	0.078
Solid frequency in vacuum ω_s	0.602	0.301	0.139	—	0.130
Nonlinear low frequency ω_{FSI}	—	—	0.428	0.324	0.437
Quasi-steady secondary equilibrium $\bar{\alpha}_2$	—	2.72°	3.44°	3.64°	3.48°
Mean incidence of nonlinear simulations $\bar{\alpha}$	0.00°	2.72°	3.34°	2.73°	3.50°

Table 5.8 – *Summary of the first four nonlinear FSI regimes found at Re* = 20 000 *as function of the structural stiffness K_s: comparison between the structural frequency in vacuum, ω_s, and the FSI oscillations, ω_{FSI} and comparison between the quasi-steady second equilibrium position and the averaged incidence obtained from the two-dimensional coupled simulations.*

Table 5.8 also compares the second equilibrium angle, obtained in section 5.2, with the averaged incidence of the FSI time-marching simulations. The comparison is pertinent for the four last regimes where a departure from $\alpha = 0°$ was observed. For the regimes R_2 and R_5, the values present a very good agreement. In contrast, in regimes R_3 and R_4, where the chaotic behaviour is found, a deviation from the prediction $\bar{\alpha}_2$ started to appear.

5.4 Bifurcation diagram of the nonlinear dynamics for $Re = 20\,000$ as function of the structural stiffness

In this section, we aim at mapping the different regimes in a bifurcation diagram as function of the structural stiffness. For that, we sketch in figure 5.16 a bifurcation diagram with the averaged minimum and maximum amplitudes associated to the different FSI simulations carried out for $Re = 20\,000$. In the horizontal axis, one finds the bifurcation parameter, K_s, while in the vertical axis, one finds different quantities associated to the angular displacement, as explained next. The first four values of K_s studied previously are highlighted by the vertical dashed lines. Due to the symmetry of the present problem, the results found on the range $\alpha > 0°$ for the regimes R_2, R_3 and R_5 are symmetrised to the range $\alpha < 0°$.

We start by representing with the black curve the admissible equilibrium positions, given by the structure equation for static incidences. This curve is already presented in figure 5.1b, with its numerical values given by equation 5.1. Next, we represent by the blue crosses the results from the FSI time-marching oscillations initialised from the fixed incidence solution at $\alpha = 0°$. In the cases where no low frequency oscillations are found (*i.e.*, the cases with a high value of K_s, regimes R_1 and R_2), the crosses represent the minimum and maximum values of the angular displacement over the high frequency oscillation cycle. As noted in figures 5.2 and 5.4, these oscillations have a very small amplitude. As a consequence, for a fixed K_s value, the maximum and minimum values are almost superposed. In contrast, for the regimes

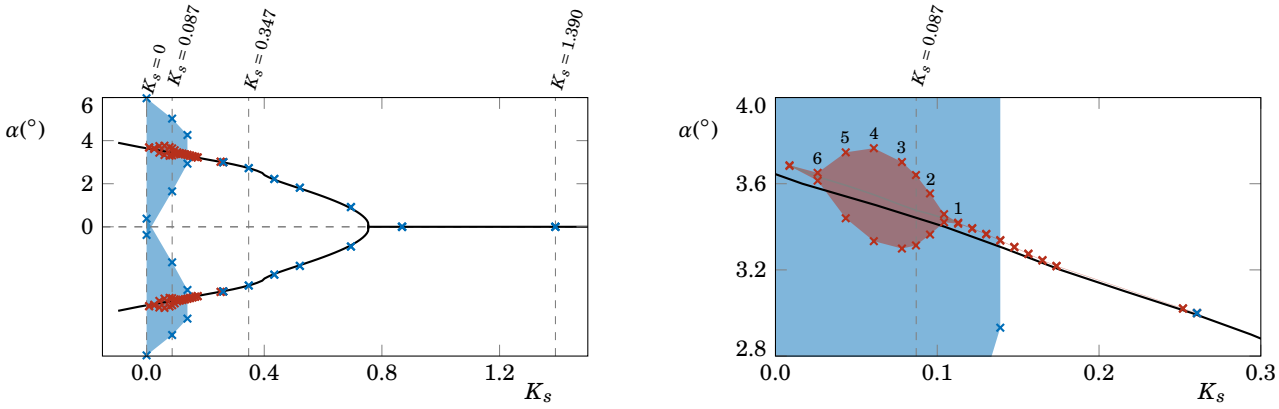

Figure 5.16 – *Bifurcation diagram, representing the variation of the averaged maximum and minimum pitch amplitude on the low frequency oscillations with the structural stiffness for $Re = 20\,000$. The blue crosses represent the pitch amplitude oscillations of the nonlinear simulations started from a static position solution at $\alpha = 0°$ and $\Omega = 0$. The red crosses represent the pitch amplitude oscillations of the nonlinear simulations, where a continuation strategy is implemented, decreasing K_s, with the initial condition corresponding to the instantaneous solution from the previous nonlinear simulation. The vertical dashed lines represent the four cases analysed previously. The black line corresponds to the admissible equilibrium points predicted from the quasi-steady aerodynamic moment coefficient curve, see figure 5.1b. On the right, the numbers 1 to 6 identify the structural stiffness values of the red branch analysed in figures 5.17 and 5.18.*

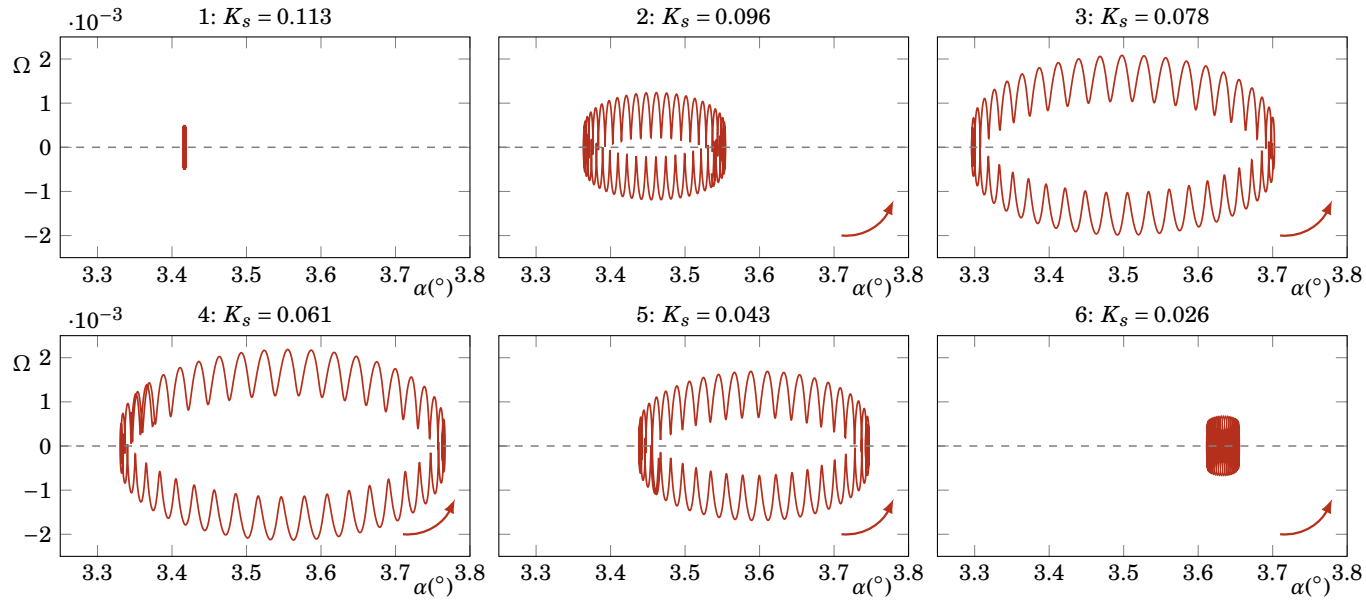

Figure 5.17 – *Phase diagrams of the angular displacement versus the angular velocity, α–Ω, at Re = 20 000 for the different K_s values identified by the numbers 1 to 6 on figure 5.16. The red lines correspond to one low frequency oscillation cycle, while the red arrows represent the direction of the time evolution.*

R_3 and R_4, where a low frequency oscillation of α is found, the crosses represent its averaged minimum and maximum values. These oscillations have a large amplitude, as seen in the previous section, represented by the blue shaded region.

The FSI solutions associated to the second initialisation strategy, where a continuation between FSI simulations is made, are represented by the red crosses. These solutions can be seen in the general view, on the left, or in the zoom made on the right of figure 5.16. The continuation strategy is started from the case at $K_s = 0.261$ and ends at $K_s = 0.009$.

As the K_s is decreased in the red branch, we start by noting that the obtained solutions do not present significant oscillations of the angular displacement, corresponding to the regime R_2. This is observed in the range between the first initial solution ($K_s = 0.261$) and the red crosses labelled 1 ($K_s = 0.113$). In this K_s range, we have a first set of solutions, in the blue crosses, corresponding to the chaotic regime R_3, with large incidence oscillations at a low frequency, and a second set of solutions, in the red crosses, corresponding to the limit cycle regime R_2, with small incidence oscillations vibrating at the frequency of the vortex shedding. We also note that the red crosses are placed slightly above the static equilibrium curve, in black.

As the value of the structural stiffness continues to decrease, we observe the emergence of an oscillation of the angular displacement. These oscillations, represented by the red shaded region, are associated to a low frequency oscillation, with a frequency value around $\omega_{FSI} = 0.44$. The amplitude of the oscillations increases up to the K_s value number 4 and decreases between the K_s values 4 and 6. The last pair of red crosses, at $K_s = 0.009$ represents again a limit cycle oscillation, where no low frequency is present and all quantities oscillate at the vortex shedding frequency. In contrast to the chaotic behaviour found on solutions of the blue branch, the solutions on the red branch, presenting a low frequency oscillation, represent the quasi-periodic regime R_5 described previously. In view of this results, we conclude that for this K_s range, we observe the coexistence of chaotic and quasi-periodic solutions for the same values of the structural parameters.

This quasi-periodicity is associated to the two incommensurable frequencies ω_{VS} and ω_{FSI}. The phase diagram α–Ω

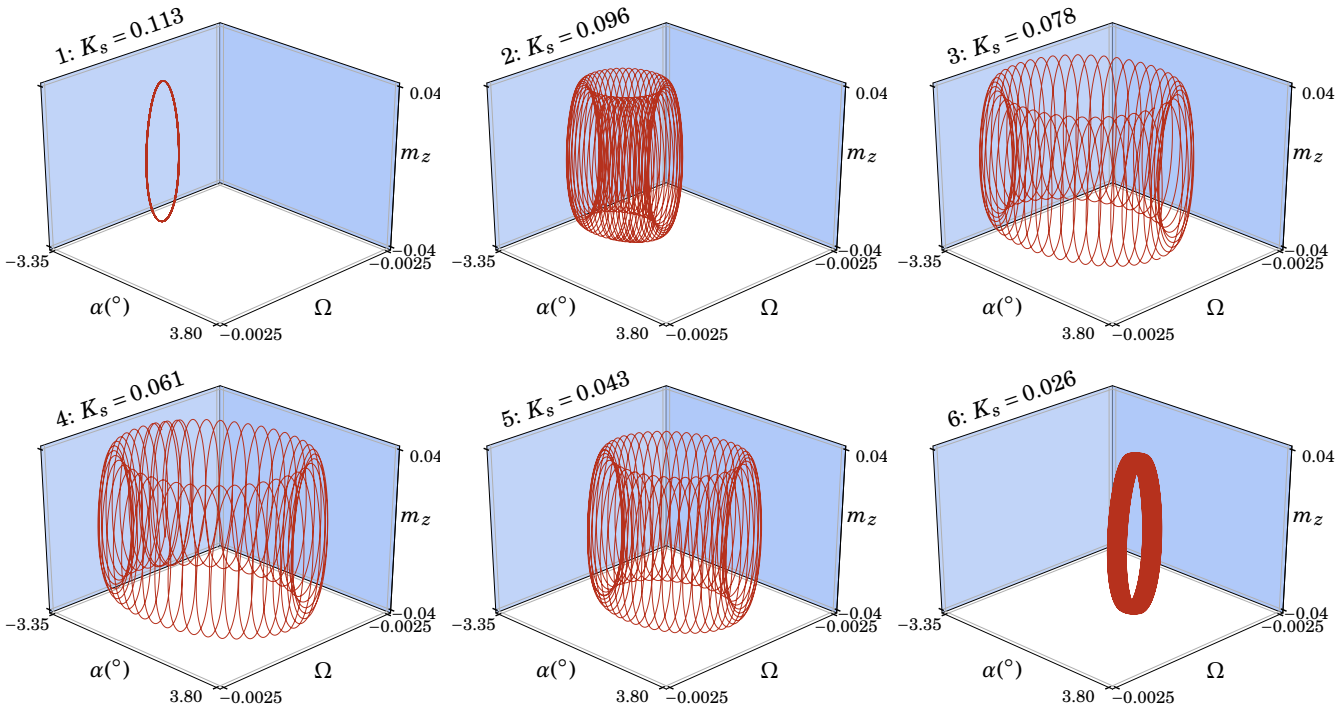

Figure 5.18 – *Three-dimensional phase diagrams of the angular displacement, the angular velocity and the aerodynamic moment coefficient, α–Ω–m_z, at Re = 20 000 for the different K_s values identified by the numbers 1 to 6 on figure 5.16. The red line corresponds to one low frequency oscillation cycle, that evolves over a toric surface for the numbers 2 to 6.*

for the K_s values corresponding to labels 1 to 6 is present in figure 5.17. The red line illustrates the evolution of α and Ω over one low frequency oscillation cycle. The first case ($K_s = 0.113$) still represents a periodic limit cycle oscillation, as the case of regime R_2 presented previously, where the low frequency is not present yet. The quasi-periodicity can then be viewed on the solutions 2 to 6, where the fast time scale oscillations (associated to ω_{VS}) are mainly observed in the vertical direction, *i.e.*, on the signal of the angular velocity. Further, we note that the fast time scale oscillation presents the same harmonic form in both the ascending and descending phases of the angular incidence, in contrast with the chaotic regimes, where two different frequencies were found for these two phases.

The variation of α, Ω and m_z and their dependence can be simultaneously viewed in the three-dimensional phase diagram, as present in figure 5.18. In the first case ($K_s = 0.113$), the periodic limit cycle oscillation can be found on a plane surface, *i.e.*, in a two-dimensional phase space. At the same time, the solutions with lower K_s values, corresponding to the quasi-periodic oscillations, evolve along the three phase space directions. Their trajectory in the phase space corresponds to a curve that can be found along the surface of a torus. Due to the incommensurability between the low and high frequencies, the ending point of this curve never corresponds to its starting point. We can see that the dimensions of the toric surface increases from the solutions 2 to 4 and decreases from the solutions 4 to 6.

Finally, table 5.9 summarises the values of the magnitude of the transfer functions H_θ and H_Ω, computed for the theoretical prediction and for the nonlinear simulations, both evaluated at the vortex shedding frequency, also reported. These values enable us to have an idea if the solid contributions associated to the fast time scale vibrations will have an effect on the linear stability analyses, in particular, on the linear stability analysis made for the secondary equilibrium

	K_s^{dim}(Nm)	K_s	ω_{FSI}	ω_{VS}	$\left\|H_\theta^{theory}\right\|$	$\left\|H_\theta^{simul}\right\|$	$\left\|H_\Omega^{theory}\right\|$	$\left\|H_\Omega^{simul}\right\|$
1	0.0065	0.113	—	19.124	0.00070	0.00071	0.01348	0.01369
2	0.0055	0.096	0.434	19.082	0.00071	0.00072	0.01360	0.01383
3	0.0045	0.078	0.437	19.067	0.00070	0.00071	0.01353	0.01374
4	0.0035	0.061	0.441	19.028	0.00073	0.00079	0.01381	0.01484
5	0.0025	0.043	0.442	19.001	0.00072	0.00074	0.01370	0.01409
6	0.0015	0.026	0.442	18.963	0.00073	0.00072	0.01378	0.01354

Table 5.9 – *Summary of the values of H_θ and H_Ω for the structural stiffness values identified by the numbers* 1 *to* 6 *on figure 5.16, on the red branch, evaluated at the vortex shedding frequency, for the theoretical estimation and for the nonlinear simulations.*

point, present in the next chapter.

We first note that both the theoretical values and the values coming the nonlinear simulations are in very good agreement. Second, we observe that the magnitude of the transfer function associated to the fast time scale oscillations of the angular displacement, H_θ, presents an order of magnitude of 10^{-4}, while the magnitude of the transfer function associated to the angular velocity has an order of magnitude 10^{-2}. With these orders of magnitude, we expect the contributions of the fast time fluctuations of the angular displacement to the linear stability analysis formulation to be negligible for the secondary equilibrium point. At the same time, we also expect the contributions of the angular velocity to be negligible, even if they present a substantial bigger value.

5.5 Reynolds number effect on the FSI nonlinear dynamics for fixed structural parameters

In the remaining part of this chapter, we investigate the different nonlinear solutions appearing at $Re \geq 50\,000$. The aim is to characterise and understand the onset of an additional regime, labelled R_6, the laminar separation flutter, characterised by a global oscillation of the airfoil around a zero angle of incidence. This analysis is made by fixing the structural parameters and by varying Reynolds number. In a first part, we describe difficulties in finding the quasi-steady equilibrium points from a two-dimensional mean flow curve at $Re = 50\,000$. In a second part, the results from the nonlinear simulations are presented for $Re \geq 50\,000$ and compared with the literature.

5.5.1 Quasi-steady equilibrium positions for mean flow solutions from 2D simulations at $Re = 50\,000$

In this section, we try to identify the different quasi-steady equilibrium points from the mean flow curve at $Re = 50\,000$. For that, we apply the same reasoning made in section 5.2 for $Re = 20\,000$ to the case at $Re = 50\,000$. The curve m_z–$\bar{\alpha}_b$ already presented in figure 2.9, page 79, is revisited in this section in figure 5.19. The different black marks represent the different time-marching computations made at fixed incidences. Three values of structural stiffness are represented by the red slopes, corresponding to the values used in the experimental investigation of Poirel *et al.* (2008). As noted in chapter 2, the m_z–$\bar{\alpha}_b$ curve presents a strong discontinuity from $\alpha = 1.8°$ to $\alpha = 1.9°$, associated to a change in the topology of the flow. For this reason, the task of finding the second equilibrium position becomes extremely difficult for the two-dimensional simulations. However, for the time- and spanwise-averaged solution issued from the three-dimensional

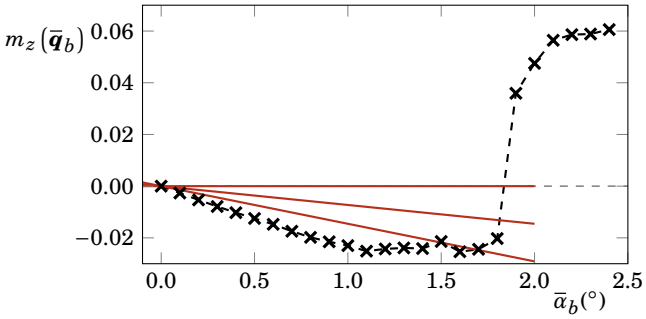

Figure 5.19 – *Evolution of the two-dimensional mean aerodynamic moment coefficient, associated to fixed incidence simulations, with the angle of attack (black line), for* $Re = 50\,000$*. The red lines represent the values of structural stiffness used in Poirel* et al. *(2008):* $K_s^{dim} = 0$*,* 0.15 *and* 0.3Nm.

simulations, no discontinuity is observed, and the second equilibrium positions are well retrieved, and further explored in chapter 6, section 6.3.

5.5.2 Regime R_6: laminar separation flutter

In this section, we carry out two-dimensional coupled time-marching simulations for different values of Reynolds number. In this regard, an initial Reynolds number of $Re = 50\,000$ is considered, corresponding to the experimental value of Poirel *et al.* (2008), where the phenomenon was systematically studied and reported for the first time in the literature. The Reynolds number is progressively increased to $Re = 128\,200$, corresponding to the value of the upper limit for the laminar separation flutter reported by Poirel *et al.* (2008). The structural parameters taken into account in this section are reported in table 1.1 (page 23), except for the value of K_s^{dim}. The latter is fixed at $K_s^{dim} = 0.3$Nm in order to have a comparison with the literature data for the considered Reynolds number range.

The simulations for $Re \leq 80\,000$ are started from instantaneous solutions at the corresponding Reynolds number of fixed two-dimensional time-marching simulations at $\alpha = 0°$, as done in section 5.3. For $Re > 80\,000$, a continuation strategy is used, where the FSI simulations are started from the instantaneous FSI solutions at the previous Reynolds number.

The divergent departure of the airfoil from its equilibrium position $\alpha = 0°$ was studied in chapter 4. This divergent behaviour is found for the different simulations carried out in this section. Figure 5.20 presents the angular displacement evolution and the phase diagram α–Ω for four different Reynolds numbers, where the divergent behaviour is found on the first three cases. In the first case, at $Re = 50\,000$, the airfoil oscillations occur around two nonzero angular positions, mainly located in the zones $\alpha > 0°$ and $\alpha < 0°$. The time evolution occurring on the zone $\alpha < 0°$ is highlighted by the green line. This case is similar to the case analysed in section 5.3.4 at $Re = 20\,000$ and $K_s = 0$, corresponding to the regime R_4. For some low frequency oscillation cycles, the incidence amplitude is large enough to cause the oscillations jump from the positive to the negative incidence regions. As the Reynolds number increases, this amplitude is expected to increase. Further, for a critical Reynolds number, the positive and negative incidence low frequency cycles are expected to collide, giving rise to a global oscillation around the zero angle of incidence. This regime is labelled R_6 and corresponds to the laminar separation flutter phenomenon.

The collision of two limit cycles that merge into a bigger limit cycle is often obtained from a homoclinic bifurcation. This type of bifurcation was studied for example in simpler nonlinear dynamical systems, as the Van der Pol oscillator (Datta, 2017). In view of the present data, we suggest that the emergence of the laminar separation flutter with the Reynolds

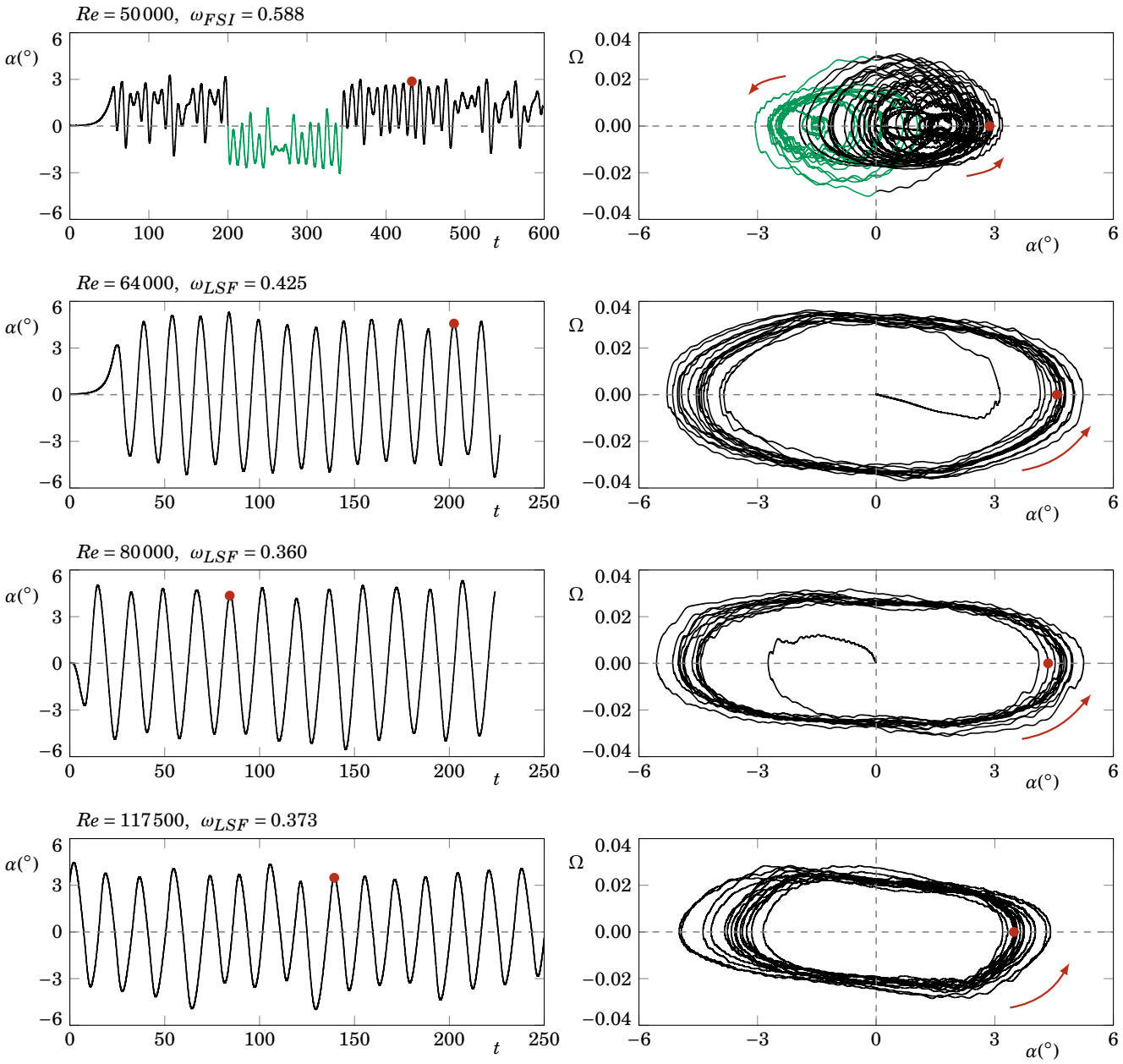

Figure 5.20 – *Transition between regimes R_4 and R_6: time history (left) and phase diagram of the angular displacement versus the angular velocity, α–Ω, (right), for $K_s^{dim} = 0.3$Nm and four different Reynolds numbers: $Re = 50\,000$, $Re = 64\,000$, $Re = 80,000$ and $Re = 117\,000$. The red dots represent the position of the snapshots sketched in figure 5.22, while the red arrows represent the direction of the time evolution in the phase diagrams. The green curve for $Re = 50\,000$ highlights the period of time where an oscillation around a negative angular position is found.*

number increase is caused by a homoclinic bifurcation. We consider that a rigorous investigation on this matter merits of being explored in future works.

Although Poirel *et al.* (2008) reported global oscillations starting at $Re = 45\,000$, the Re threshold discrepancy between

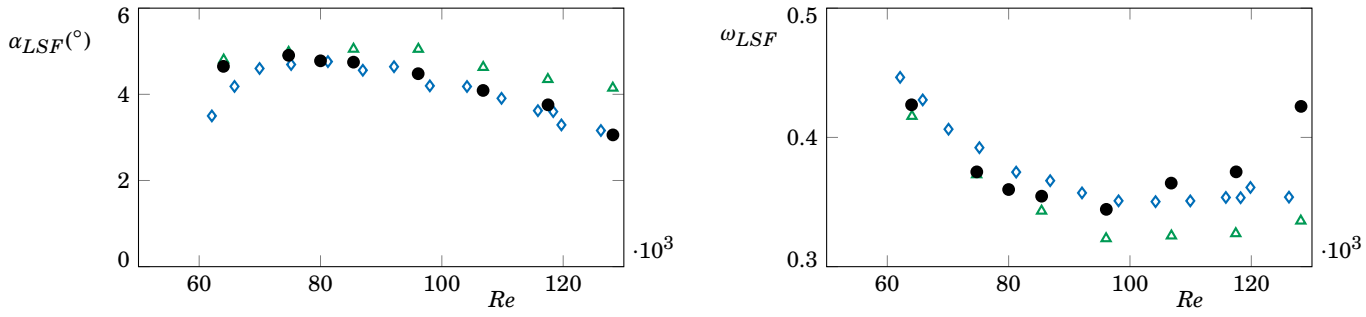

Figure 5.21 – *Evolution of the averaged maximum and minimum pitch amplitude (left) and the pitch angular frequency (right) with the Reynolds number for* $K_s^{dim} = 0.3\text{Nm}$*, associated to the laminar separation flutter phenomenon: the present results, with the black circles, the two-dimensional results from Lapointe et al. (2011), with the green triangles, and the experimental data from Poirel et al. (2008), with the blue diamonds.*

the experiments and the present results is likely linked, from one side, to the experimental sensitivity to flow perturbations and, from the other side, to the two-dimensional numerical model used for the present coupled simulations. Indeed, chapter 1 reported that, for the fixed airfoil case at $\alpha = 0^\circ$, the flow became unstable to three-dimensional perturbations around $Re \approx 30\,000$. Not only the airfoil in this case is moving, the Re number is considerable higher. However, this does not invalidate the present results, obtained with a two-dimensional model, as the flow is mainly two-dimensional for a considerable portion of the airfoil surface.

In the second Reynolds number considered, $Re = 64\,000$, the global oscillations of the airfoil incidence around $\alpha = 0^\circ$ are clear. These global oscillations, identified as the regime R_6, correspond to the phenomenon described in the literature as the laminar separation flutter (LSF). We denote the averaged amplitude of oscillation by α_{LSF}, with a value of $\alpha_{LSF} = 4.65^\circ$ for this Re. Associated to the global oscillations, we have the frequency of the laminar separation flutter, denoted ω_{LSF}, with a value of $\omega_{LSF} = 0.425$. Two additional cases are considered, at $Re = 80\,000$ and $Re = 117\,500$, where the laminar separation flutter is also observed.

The LSF phenomenon is further characterised in the range $64\,000 \leq Re \leq 128\,200$. Figure 5.21 presents the evolution of the mean maximum amplitude of the LSF α_{LSF} and the corresponding frequency ω_{LSF}, as function of the Reynolds

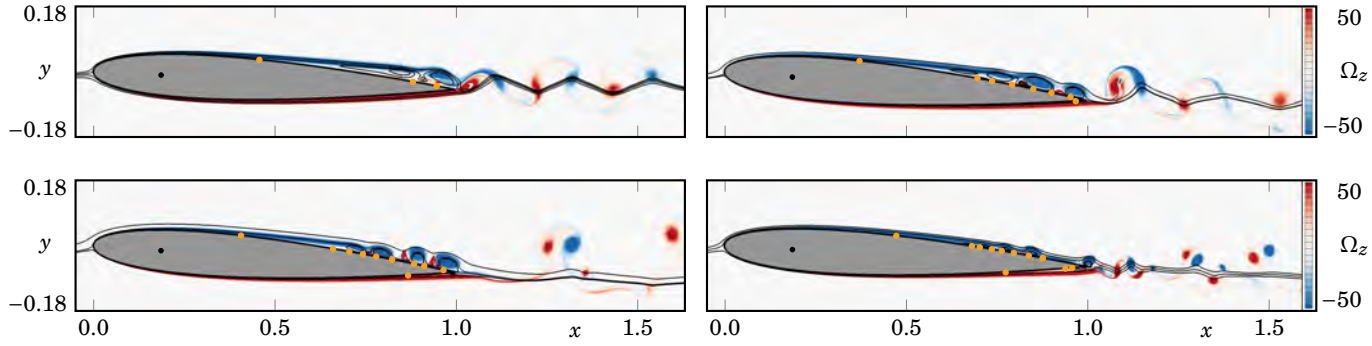

Figure 5.22 – *Spanwise vorticity field of four snapshots of two-dimensional coupled time-marching simulations for* $K_s^{dim} = 0.3\text{Nm}$ *at* $Re = 50\,000$ *(top left),* $Re = 64\,000$ *(top right),* $Re = 80\,000$ *(bottom left) and* $Re = 117\,500$ *(bottom right). The instants position in time is identified in figure 5.20. The yellow dots over the airfoil surface represent the separation and reattachment points.*

number. The results are compared with the experimental data from Poirel *et al.* (2008) (blue diamonds) and with the two-dimensional coupled time-marching simulations present in Lapointe *et al.* (2011) (green triangles). A reasonable agreement is found with both references. Concerning the amplitude curve, the low frequency oscillations are characterised by a first sub-regime, where α_{LSF} increases with the Reynolds number, corresponding to the first Reynolds numbers studied. From there, a second sub-regime is found, where the amplitude of the LSF oscillations decrease. These two sub-regimes are also identified on the frequency curve. In the first sub-regime, the LSF frequency presents a monotonic decrease, up to $Re \approx 95\,000$. Although the good agreement of α_{LSF} on this sub-regime, the present results show an increase of ω_{LSF} on the second sub-regime, while the reference data shows a plateau.

The spanwise vorticity field associated to instantaneous solutions at four Reynolds numbers is presented in figure 5.22. These instants are located on a maximum value of α during a low oscillation cycle, having a zero angular velocity. Their exact position on the time history is highlighted by the red dots in figure 5.20. Concerning the case at $Re = 50\,000$, we observe the formation of a recirculation zone on the upper surface of the airfoil for the range $0.46 < X < 0.88$. From this position, a second smaller bubble is formed above the trailing edge of the airfoil. For this particular time instant, the vortex shedding structures on the wake of the airfoil present a well organised arrangement, similar to a classic vortex shedding of a fixed incidence simulation. Concerning the case at $Re = 64\,000$, we observe the presence of several bubbles along the upper surface, starting at $X = 0.37$. Further, we report the separation of the boundary layer of the lower surface, at $X_d^{down} = 0.97$. The same topological behaviour is found on the upper and lower surfaces for $Re = 80\,000$ and $Re = 117\,500$. We note that, for the instants considered, the structure of the vortex shedding becomes more disorganised as the Reynolds number increases. Concomitantly, we observe that the boundary layer thickness decreases as the Reynolds number increases.

Conclusions

In this chapter, we analyse the nonlinear dynamics of a NACA0012 airfoil mounted on a torsional spring and immersed in a two-dimensional Navier–Stokes flow. The different regimes are investigated firstly by fixing the Reynolds number at $Re = 20\,000$ and varying the structural stiffness of the airfoil. Initially, five regimes are identified. In a first regime, we find that the structural stiffness is high enough to "hold" the structure at the position $\alpha = 0°$. This regime is characterised by pitch oscillations of negligible amplitude, at the frequency of the vortex shedding phenomenon, around the primary equilibrium position. In a second regime, at a lower K_s, we characterise the cases where the structure tends to a steady equilibrium position at a nonzero angle of attack. We also find negligible pitch oscillations at the frequency of the vortex shedding phenomenon. The third and fourth regimes, obtained for even lower values of K_s, are characterised by a chaotic fluid–structure dynamics, with high-amplitude low-frequency pitch oscillations around a nonzero mean angle of incidence. In the latter regime, the pitching dynamics switches between oscillations around positive and negative (time-averaged) angle of incidence. An additional nonlinear regime is found using a different initialisation strategy, where quasi-periodic oscillations are found. Therewith, a bifurcation diagram is sketched as function of the K_s parameter, identifying different branches for the same structural parameters. In particular, for a finite range of structural stiffness values, a bistable behaviour is identified characterised by the coexistence of chaotic and quasi-periodic solutions. For this Reynolds number, we do not observe a fluid–structure dynamics characterising the so-called laminar separation flutter, *i.e.*, a symmetric high-amplitude low-frequency pitching oscillations around the zero angle of incidence. This is coherent with the existing literature, that only reports this phenomenon for higher values of Re.

In a second part of chapter 5, we fix the structure parameters in accordance with the literature (in particular, the value of the structural stiffness is fixed to 0.3Nm), and we investigate the emergence of the laminar separation flutter

as the Reynolds number increases. For the Reynolds number $Re = 50\,000$, we observe an intermittent dynamics of the pitching oscillation around opposite mean values of the angle of incidence, as for the case in regime R_4, described for $Re = 20\,000$. By increasing the Reynolds number to $Re = 64\,000$, the laminar separation flutter appears. The evolution of the pitching amplitude and low frequency with the Reynolds number is finally described, showing a good agreement with both experimental and numerical results reported in the literature.

In the following chapter, we continue the linear analysis made in the previous chapter, applying it to the second equilibrium position. The aim will be to use the linear analysis to possibly explain the emergence of the quasi-periodic solutions reported in this chapter for a closed range of K_s values.

Chapter 6

Secondary aeroelastic instability

In the previous chapter, several nonlinear regimes were described for the self-sustained pitch oscillations of a NACA0012 airfoil on the low-to-moderate Reynolds number regime, using a two-dimensional Navier–Stokes model. The behaviour of these regimes depends on the values of the structural stiffness and on the Reynolds number.

In this chapter, we propose to investigate the linear stability of the second equilibrium position ($\overline{\alpha} \neq 0°$) which has been described in the previous chapter. For the first described regime, this second equilibrium may be stable since it was observed using temporal simulations of the governing equations. We wish here to confirm the stability of that case and determine whether the flutter mode can be found unstable in the remaining cases. This chapter is divided into two parts. In the first part, we investigate the stability of the second equilibrium position via both mean flow and Floquet FSI analyses for $Re = 20\,000$, using two-dimensional simulations for the computation of the mean and periodic flow solutions. In the second part, we perform a mean flow FSI analysis for the equilibrium points given by time- and spanwise-averaged solutions issued from three-dimensional simulations at $Re = 50\,000$.

6.1 Linear stability analyses around mean and periodic flow solutions at $Re = 20\,000$

In this section, we perform the linear stability of the second equilibrium solution ($\overline{\alpha} \neq 0°$) for the Reynolds number $Re = 20\,000$ and various structural stiffness coefficients. The linear stability of mean flows is first investigated using the classical formulation (equations 1.33, page 37) and the Reynolds stress formulation (equation 1.40, page 42) introduced in chapter 1. A Floquet analysis around the time-periodic solution is then performed.

The incidence of the equilibrium states where the linear stability analyses are carried out were presented in the previous chapter, in section 5.2. From the equilibrium relation (equation 1.24, page 30) between the aerodynamic moment m_z and the restoring elastic couple, we obtain that the incidence of the airfoil at an equilibrium position, denoted $\overline{\alpha}_b$, satisfies

$$\overline{\alpha}_b = -\frac{m_z(\overline{\boldsymbol{q}}_b)}{K_s}, \tag{6.1}$$

where K_s is the structural stiffness. As explained in previous chapter, for the angle $\overline{\alpha}_1 = 0°$, the mean flow solution $\overline{\boldsymbol{q}}_b$ is symmetric and the aerodynamic moment vanishes. This is the primary equilibrium state. On the other hand, $\overline{\alpha}_2$ represents the secondary equilibrium position around which we carry out the linear stability analyses of this chapter. Apart from the value of K_s, fixed by the above expression, the remaining parameters taken into account for the structural

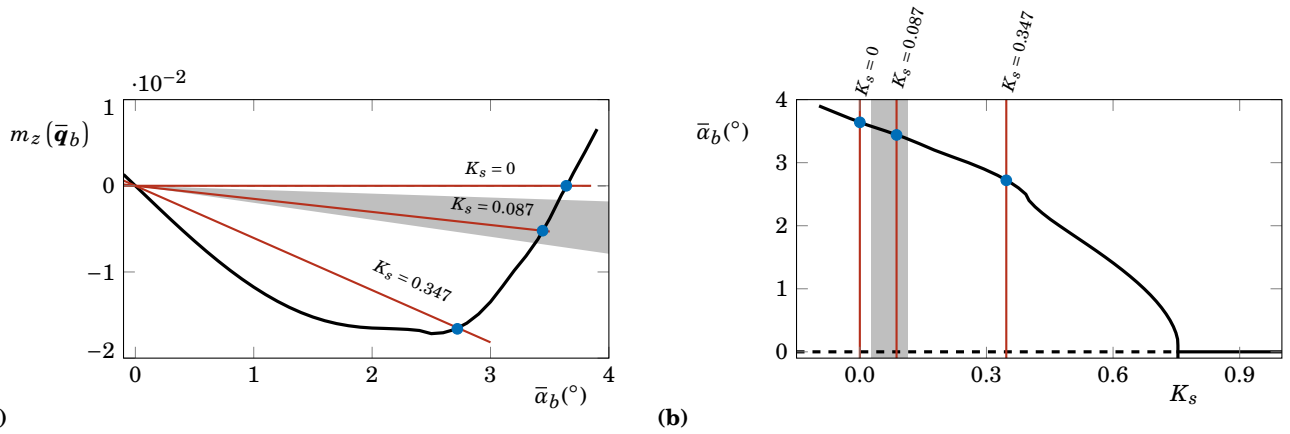

Figure 6.1 – *On the left, evolution of the two-dimensional mean aerodynamic moment coefficient, associated to fixed incidence simulations, with the angle of attack (black line), for Re = 20 000. On the right, evolution of the admissible equilibrium points with the structural stiffness (black line). The red lines and the blue dots represent the different values of structural stiffness considered and the corresponding quasi-steady equilibrium points, respectively. The grey zone indicates the closed range of K_s values where a quasi-periodic solution is found in the temporal FSI simulations. The highlighted admissible secondary equilibrium positions are $K_s = 0$ ($\bar{\alpha}_2 = 3.64°$), $K_s = 0.087$ ($\bar{\alpha}_2 = 3.44°$) and $K_s = 0.347$ ($\bar{\alpha}_2 = 2.72°$).*

system are reported in table 1.1 (page 23).

In figure 6.1a, we recall the m_z–$\bar{\alpha}_b$ curve, where we highlight with the red slope three of the K_s cases studied in the previous chapter, each one illustrating a different nonlinear regime. At the same time, we recall in figure 6.1b the admissible values of K_s for the second equilibrium states as function of the angle of attack. The blue dots represent the corresponding second equilibrium positions, fixing the incidence at which the linear stability analyses are carried out. The case $K_s = 0.347$ (in regime R_2) corresponds to the highest structural stiffness considered for which a second equilibrium position is possible. In this case, the coupled time-marching simulations show a convergence of the angular displacement to a weak amplitude high frequency limit cycle oscillation. The mean angular displacement matches the equilibrium position predicted by equation 6.1 ($\bar{\alpha}_2 = 2.72°$). For the case $K_s = 0.087$ (in regime R_3), the coupled time-marching simulations show the emergence of a low frequency oscillation of the angular displacement around a mean angle slightly inferior to the value $\bar{\alpha}_2 = 3.44°$, predicted by equation 6.1. The case $K_s = 0$ (in regime R_4) represents the limiting case where no structural stiffness is considered. For this case, the quasi-steady equilibrium position is found at the angle where the aerodynamic moment is again zero, *i.e.*, $\bar{\alpha}_2 = 3.64°$. As the previous K_s, the coupled time-marching simulations show a limit cycle oscillation, but with a higher amplitude when compared to the previous K_s case. A larger discrepancy is found between the equilibrium position and the mean angular displacement from the nonlinear simulations. Further, the amplitude of the angular oscillations is high enough to cause a jump in the mean angular oscillations, from the positive incidence side to the negative.

In addition to these three regimes, the grey zone in figure 6.1 highlights the closed range of K_s values where a quasi-periodic regime R_5 is found in the temporal FSI simulations. In the following paragraphs, we try to predict the emergence of this phenomenon with the linear stability analyses.

In the first part of this section, we conduct our analysis around the different mean flow solutions issued from two-dimensional simulations found for each equilibrium angle, using the classical formulation. For that, the Krylov–Schur method described in section 3.2.1 (page 117) is used, allowing the computation of any fluid–structure eigenpair $(\sigma, \bar{\boldsymbol{q}})$

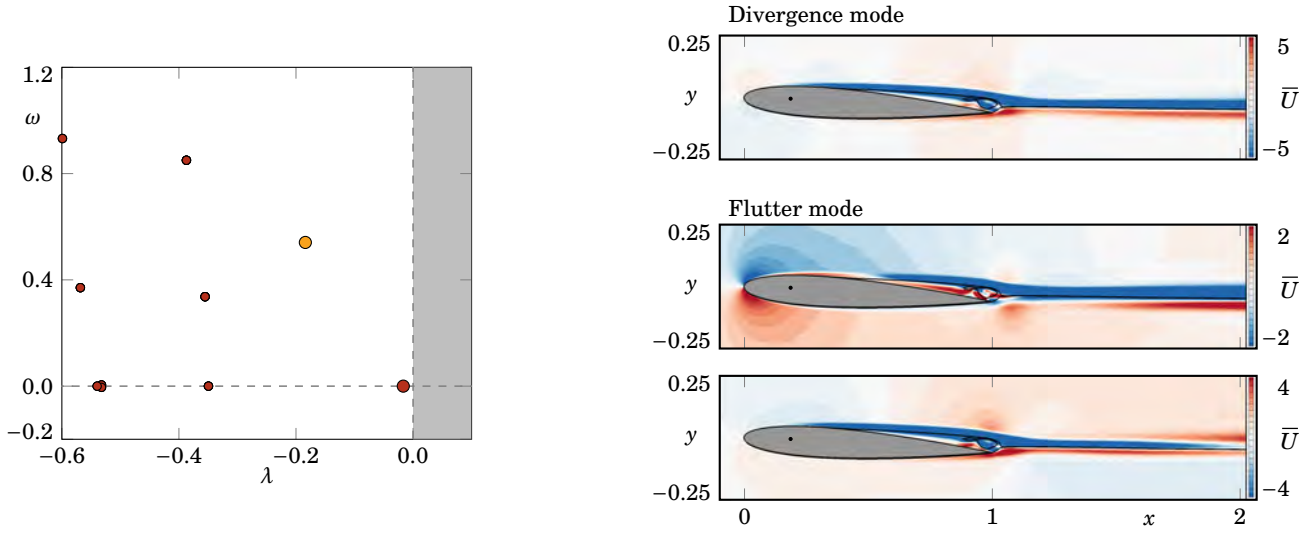

Figure 6.2 – *Classical formulation of the mean flow linear stability analysis at Re = 20 000 and $\bar{\alpha}_2 = 3.44°$, corresponding to a structural stiffness of $K_s = 0.087$. On the left, the eigenvalue spectrum representation close to the origin0 The bigger red and yellow circles represent the divergence and flutter eigenvalues, respectively. On the right, the streamwise velocity of the real part of the divergence eigenmode (top) and of the real and imaginary parts of the flutter eigenmode (centre and bottom, respectively). The black isocontour lines represent the streamlines enclosing the recirculation zone of the corresponding mean flow solution.*

in the spectrum, depending on the prescribed shift parameter. We recall that the eigenmode can be decomposed into its fluid and solid components as $\bar{\boldsymbol{q}} = \left[\bar{\boldsymbol{q}}_f, \bar{\theta}, \bar{\Omega}\right]^T$. In a second part, the same exercise is carried out for the Reynolds stress formulation, highlighting the differences between the two approaches. In the third part, a Floquet FSI linear stability analysis is conducted around the periodic flow field for each equilibrium angle. We rely on the method described in appendix B for the computation of the leading Floquet multipliers μ and associated eigenpairs $(\sigma, \boldsymbol{q})$. We recall that the Floquet eigenmode can be decomposed into its fluid and solid components as $\boldsymbol{q} = \left[\boldsymbol{q}_f, \theta, \Omega\right]^T$. As done in chapters 3 and 4, the hat notation $\hat{\bullet}$ is dropped from the eigenmodes in order to simplify the notations.

6.1.1 Classical formulation of the mean flow linear stability analyses

The classical formulation of the mean flow stability analysis is used to study the stability of different secondary equilibrium points. We start by analysing the three cases at $\bar{\alpha}_2 = 2.72°$, $3.44°$ and $3.64°$, followed by the equilibrium points on the K_s range where the quasi-periodic nonlinear solutions were observed in the previous chapter. We seek to identify the linear eigenmodes associated to the structure, namely the divergence and flutter modes, described in chapters 3 and 4 in the case of the primary equilibrium angle.

We start by presenting the results associated to the incidence $\bar{\alpha}_2 = 3.44°$, corresponding to the intermediate value of structural stiffness $K_s = 0.087$. At this angle of attack, the coupled time-marching simulations predicted either a chaotic solution or a quasi-periodic solution, vibrating at a low frequency. We expect to predict the linear onset of the latter solution.

On the left of figure 6.2, we present the eigenvalue spectrum. We first note that the divergence eigenvalue is found on the stable side of the spectrum, at $\sigma = -0.0167$, close to the marginal stability position at the origin of the spectrum.

The real part of the streamwise velocity component $\overline{U}$ of the corresponding eigenmode is presented on the top right of figure 6.2. The black isocontour lines represent the streamlines of the mean flow solution encompassing the time-averaged recirculation region that can be found for this angle of attack. We note the presence of the negative values of $\overline{U}$, represented by the blue colour, starting on the separated shear layer of the upper surface, towards the wake of the airfoil. The negative values of $\overline{U}$ are also significant inside the recirculation bubble, where the mean flow vortex structures are present. At the same time, the positive values of $\overline{U}$ (red colour) are mainly found on the lower half of the wake of the airfoil, starting at the rear of the trailing edge, and below the vortex structures of the recirculation zone.

Similarly to the divergence eigenvalue, the flutter eigenvalue is also present in the stable side of the spectrum, at $\sigma = -0.1840 + 0.5408\text{i}$. The real and imaginary parts of the streamwise velocity component $\overline{U}$ of the corresponding flutter eigenmode are presented on the centre and bottom right of figure 6.2. The real part of $\overline{U}$ is characterised by an initial positive region (in red) on the location of the mean flow attached boundary layer of the upper surface, from the leading edge up to the separation point. From there, we observe an inversion of the sign of $\overline{U}$, from the location of the mean flow separation point to the wake of the airfoil. The positive values of $\overline{U}$ can also be found on the "dead air" region of the mean flow and on the lower half of the airfoil wake, at the rear of the trailing edge. Additionally, a dipole-like spatial structure is found with a centre at the leading edge of the airfoil, with significant values of $\overline{U}$ on the inviscid zones of the mean flow field. The imaginary part of $\overline{U}$ presents a similar spatial structure as the divergence eigenmode, except for the sign inversion at the wake for $x \approx 2$, associated to the low frequency oscillation character of the flutter eigenvalue. Finally, we note that, even if the flutter eigenvalue is stable, its frequency ($\omega = 0.541$) compares reasonably well with the low frequencies found for both the quasi-periodic ($\omega_{FSI} = 0.435$) and chaotic ($\omega_{FSI} = 0.428$) solutions of the nonlinear simulations.

Two mean flow linear stability analyses are also carried out for the other K_s cases, $K_s = 0.347$ and $K_s = 0$. A summary of the obtained eigenvalues is present in table 6.1. For the case at $K_s = 0.347$, the flutter eigenvalue is stable. This is coherent with the fact that the nonlinear simulations do not present a low frequency oscillation (regime R_2). Further, in this case the divergence eigenvalue is found to coalesce with a stable static eigenvalue, leading to a pair of low frequency complex conjugate eigenmodes, located on the stable side of spectrum. Concomitantly, the case at $K_s = 0$ also presents a flutter eigenvalue that is stable. Even if a chaotic nonlinear solution was found in the previous chapter for regime R_4, a stable limit cycle oscillation (*i.e.*, a solution only vibrating at the vortex shedding frequency) has also found. This can be discerned at the end of the red branch in figure 5.16, page 176. Therefore, the presence of a stable flutter mode in the linear stability results is coherent with the nonlinear results.

In order to study the emergence of the quasi-periodic solutions observed in the nonlinear simulations of the previous chapter (appearing in the range $K_s \in [0.026 - 0.113]$), we conduct different mean flow analyses for the range of structure

K_s^{dim}(Nm)	0.020	0.005	0.000
K_s	0.347	0.087	0.000
$\bar{\alpha}_2$	2.72°	3.44°	3.64°
ω_{FSI} (quasi-periodic)	—	0.435	—
ω_{FSI} (chaotic)	—	0.428	0.324
Divergence eigenvalue	—	−0.0167	−0.0578
Flutter eigenvalue	−0.2541 + 0.5105i	−0.1840 + 0.5408i	−0.1773 + 0.5135i

Table 6.1 – *Classical formulation of the mean flow linear stability analysis at Re* = 20 000*: summary of the divergence and flutter eigenvalues for three different second equilibrium positions. Comparison with the frequency of the nonlinear simulations found for the quasi-periodic and chaotic branches.*

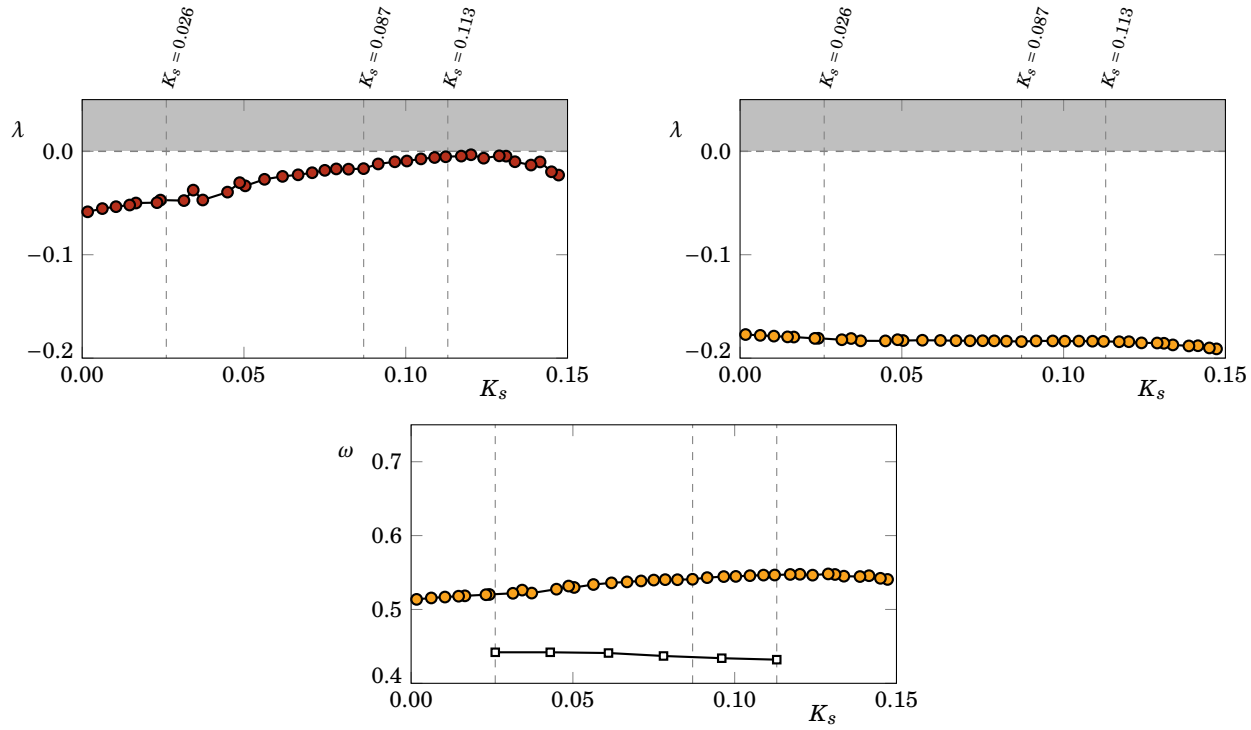

Figure 6.3 – *Classical formulation of the mean flow linear stability analysis at Re = 20 000: evolution of the growth rate of the divergence eigenvalue (upper left, in red) and flutter eigenvalue (upper right, in yellow) with the value of K_s. On the bottom, evolution of the frequency of the flutter eigenvalue with K_s, with the low frequency of the quasi-periodic solutions represented by the squares.*

stiffness of $K_s \in [0 - 0.15]$. The evolution of the growth rate and frequency of both divergence and flutter eigenvalues as function of K_s is present in figure 6.3. We can observe that the growth rate of the divergence eigenvalue remains negative for the K_s range considered, decreasing as K_s decreases, or equivalently, as the secondary equilibrium angle increases. At the same time, we observe that the growth rate of flutter eigenvalue is also negative for all the K_s values. Further, we observe that this growth rate remains constant as the K_s changes, with no visible effect of the emergence of the low frequency oscillation present on the nonlinear simulations. Concerning the frequency of the flutter mode, on the bottom the figure, we observe a decrease of its value as K_s decreases.

In view of the present results, we observe that the linear stability analysis does not predict the low frequency emergence, present in the nonlinear simulations, in particular, the emergence of the quasi-periodic oscillations. This fact can be associated to several reasons. First, this disagreement can be associated to the hypotheses made in chapter 1, on the derivation of the mean flow equations. In particular, we highlight the hypothesis made on the angular displacement and velocity components, whose fast time scale contributions were considered small for the computation of the mean flow solution. The effect of these contributions on the structural oscillation were estimated in the previous chapter with the help of the transfer functions H_θ and H_Ω. The transfer function associated to the angular displacement presented values with an order of magnitude of 10^{-4} for the range where the quasi-periodic solutions were observed (see for instance table 5.9). However, the H_Ω presented an order of magnitude of 10^{-2}. We will not test the validity of that assumption in the following sections.

Second, the disagreement between the linear predictions and the nonlinear simulations can be associated to the

hypotheses made on the derivation of the linearised equations of the mean flow. For the classical formulation, this derivation was made from the linearised equations of the Floquet eigenproblem. In particular, we highlight in red the three terms neglected in equation 1.32 (page 36), two of them containing a fast time scale contribution coming from the angular velocity component:

$$\sigma\overline{\hat{\boldsymbol{U}}}+\overline{\hat{\Omega}}\left[\boldsymbol{e}_z\times\overline{\boldsymbol{U}}_b\right]+\left(\left[\overline{\hat{\boldsymbol{U}}}-\overline{\hat{\boldsymbol{U}}}_w\right]\cdot\nabla\right)\overline{\boldsymbol{U}}_b+\left(\left[\overline{\boldsymbol{U}}_b-\overline{\boldsymbol{U}}_w\right]\cdot\nabla\right)\overline{\hat{\boldsymbol{U}}}-\nabla\cdot\boldsymbol{\sigma}\left(\overline{\hat{\boldsymbol{U}}},\overline{\hat{p}}\right)$$
$$+\overline{\hat{\Omega}_{ft}\left[\boldsymbol{e}_z\times\boldsymbol{U}_{b,ft}\right]}+\overline{\left(\left[\hat{\boldsymbol{U}}_{ft}-\hat{\boldsymbol{U}}_{w,ft}\right]\cdot\nabla\right)\boldsymbol{U}_{b,ft}}+\overline{\left(\boldsymbol{U}_{b,ft}\cdot\nabla\right)\hat{\boldsymbol{U}}_{ft}}=\boldsymbol{0}.$$

The fast time scale contribution of the angular velocity component is directly found on the first term, and indirectly found on the second one, as part of the fast time scale contribution of rigid-body velocity field, $\hat{\boldsymbol{U}}_{w,ft}$. The strength of these hypotheses can be tested by comparing the present results with the results from a Floquet analysis, in which these terms are present. This is done in a subsequent section on this chapter.

Third, the disagreement between the linear predictions and the nonlinear simulations can be associated to the fact that in the classical formulation of the mean flow eigenproblem, we do not take into account the variation of the divergence of the Reynolds stress tensor with respect to the state variables. This is taken into account in the Reynolds stress formulation, introduced in section 1.5.2, page 40. The influence of this term is tested in the following section.

6.1.2 Reynolds stress formulation of the mean flow linear stability analyses

We continue our investigation by comparing the two proposed formulations for the mean flow linear stability analysis, introduced in sections 1.4.4 and 1.5.2. We recall from the system 1.40 (page 42) that the difference between the two formulations is the inclusion of the linearisation of divergence of the Reynolds stress tensor with respect to the state variables on the momentum equation, denoted $\boldsymbol{f}$. We consider that this term only depends on the angular displacement

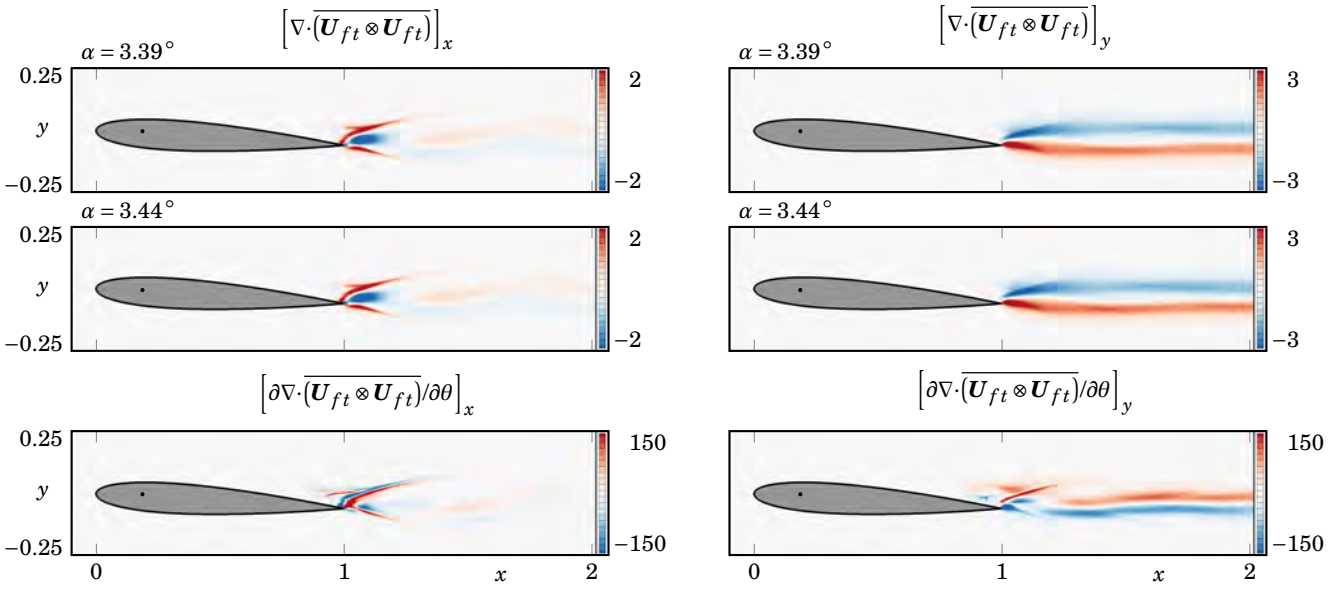

Figure 6.4 – *Spatial distribution of the streamwise and cross-stream components of the divergence of the Reynolds stress for $\alpha = 3.39°$ (top plots) and $\alpha = 3.44°$ (centre plots) and corresponding difference (bottom plots).*

component $\bar{\theta}$ and we approximate the quantity $\boldsymbol{f}$ via a finite difference scheme for two fixed angular displacements, such that

$$\boldsymbol{f}\left(\overline{\boldsymbol{U}}, \bar{p}, \bar{\theta}, \bar{\Omega}\right) \approx \boldsymbol{f}\left(\bar{\theta}\right) = \bar{\theta}\, \frac{\partial \boldsymbol{g}}{\partial \theta}\bigg|_{\theta=\bar{\theta}_b} \approx \bar{\theta}\, \frac{\boldsymbol{g}(\bar{\theta}_b + \delta\bar{\theta}_b) - \boldsymbol{g}(\bar{\theta}_b)}{\delta\bar{\theta}_b},$$

where $\boldsymbol{g} = \nabla\cdot\overline{[\boldsymbol{U}_{ft} \otimes \boldsymbol{U}_{ft}]}$ is the divergence of the Reynolds stress tensor. The inclusion of this term modifies the fluid–structure Jacobian matrix, L, in particular the term that represents a unitary angular displacement of the airfoil structure, $\boldsymbol{v}_\theta$, highlighted in red:

$$\mathsf{L} = \begin{bmatrix} \mathsf{L}_f\left(\overline{\boldsymbol{U}}_b\right) & (\boldsymbol{v}_\theta -) & \boldsymbol{v}_\Omega \\ \boldsymbol{0} & 0 & 1 \\ \boldsymbol{m}^T & -K_s & -D_s \end{bmatrix}.$$

The streamwise and cross-stream fields of $\boldsymbol{g}$ for two different angles of attack are represented in figure 6.4, in the top and centre figures. The two considered incidences are distanced of 0.05°. Their finite difference is also represented on the bottom figures, for $\alpha = 3.44°$, corresponding to a backward finite difference scheme. We can first note that the streamwise component of $\boldsymbol{g}$ is mainly concentrated near the trailing edge, for both incidences. On the other hand, the cross-stream component presents important values along the upper and lower sides of the wake. This behaviour is also observed on the finite difference between the two fields presented on the bottom figures.

We now compare results of the two mean flow formulations for the intermediate case at $\bar{\alpha}_2 = 3.44°$ ($K_s = 0.087$, where both regimes R_3 and R_5 are found). On the left of figure 6.5, we present the eigenvalue spectra for the classical (circles) and Reynolds stress (triangles) formulations. First, we note that the inclusion of the Reynolds stress term has a stabilising effect on the divergence eigenvalue (red marks). A coalescence of the divergence mode with a stable static eigenvalue occurs and they become a pair of low frequency eigenvalues, located on the stable side of the spectrum.

Concerning the flutter eigenvalue (yellow marks), we observe a more unstable eigenmode for the Reynolds stress

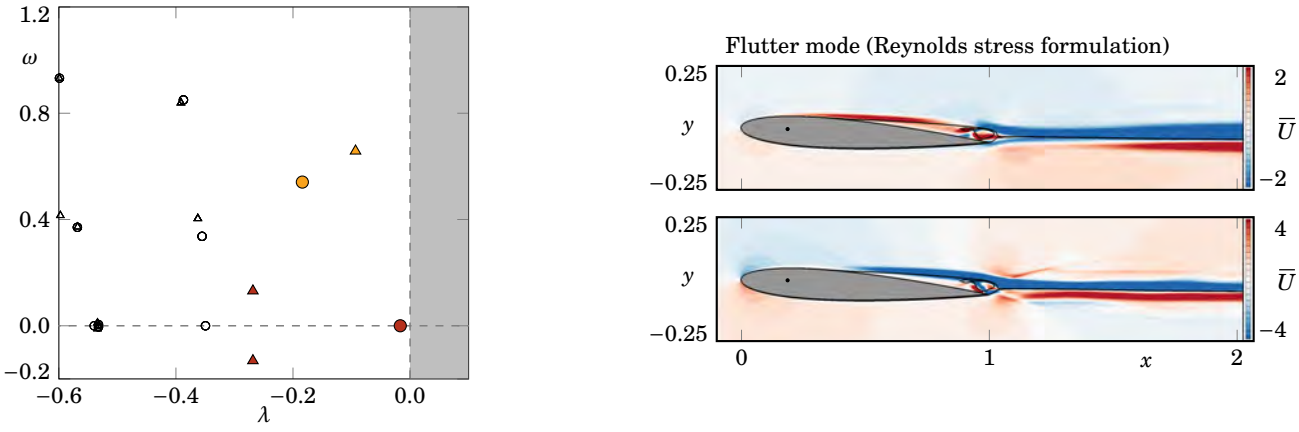

Figure 6.5 – *Comparison between the classical formulation (circles) and the Reynolds stress formulation (triangles) of the mean flow linear stability analysis at Re = 20 000 and $\bar{\alpha}_2 = 3.44°$, corresponding to a structural stiffness of $K_s = 0.087$. On the left, the eigenvalue spectrum representation close to the origin. The red and yellow circles represent the divergence and flutter eigenvalues, respectively. On the right, the streamwise velocity of the real and imaginary parts of the flutter eigenmode. The black isocontour lines represent the streamlines enclosing the recirculation zone of the corresponding mean flow solution.*

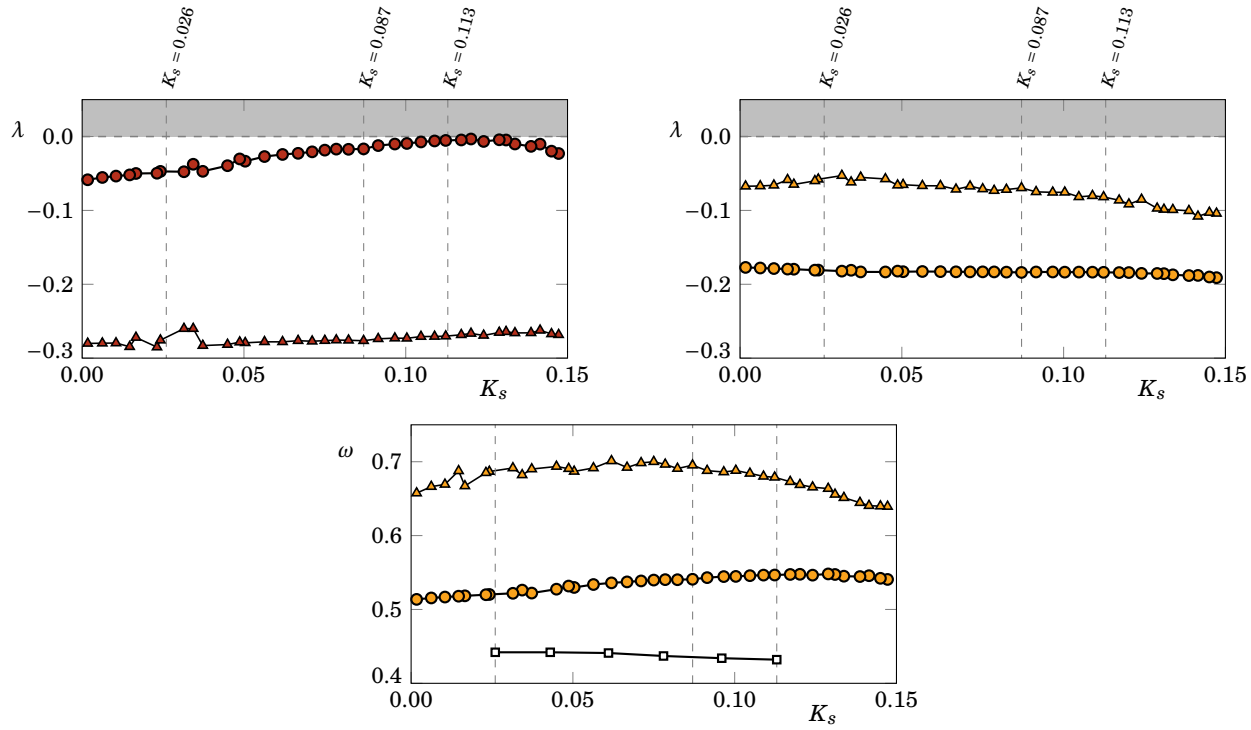

Figure 6.6 – *Comparison between the classical formulation (circles) and the Reynolds stress formulation (triangles) of the mean flow linear stability analysis at Re = 20 000: evolution of the growth rate of the divergence eigenvalues (left) and flutter eigenvalues (right) with the value of K_s. On the bottom, evolution of the frequency of the flutter eigenvalue with K_s, with the low frequency of the quasi-periodic solutions represented by the squares.*

formulation, even if it remains on the stable side of the spectrum. Further, we note that the frequency is slightly higher for this new formulation. The real part of the streamwise velocity component $\overline{U}$ of the flutter eigenmode is presented on the top right of figure 6.5. As in the previous formulation, we note the presence of the negative values of $\overline{U}$, represented by the blue colour, on the wake of the airfoil. However, the positive valued region (red colour) is extended from the abscissa of the separation boundary layer point up to the recirculation vortex zone, in contrast with the previous formulation where the positive valued region is mainly located on the first half of the airfoil. Concerning the imaginary part, the topology of the streamwise velocity for both formulations is similar. However, the Reynolds stress formulation presents the signature of the additional term, present on the wake of the airfoil, below and above the wake streamwise axis. This form resembles the spatial distribution of the terms that are included in this formulation, represented in the lower plots of figure 6.4.

To better understand the influence of this term for different equilibrium positions, we continue our investigation by performing different mean flow analyses across the K_s range previously studied ($K_s \in [0 - 0.15]$). The evolution of the growth rate of both the degenerated divergence and flutter eigenvalues as function of K_s is present on the upper side of figure 6.6. As previously noted, the growth rate of the degenerated divergence mode has lower values for the Reynolds stress formulation. The values remain roughly constant across the K_s range considered. At the same time, we observe that the growth rate of the flutter eigenvalue has higher values for all the K_s values, when compared to flutter eigenvalues of the classical formulation. Further, we note that, as K_s decreases from the higher value considered ($K_s = 0.15$) to the lower limit of the observed quasi-periodic solutions ($K_s = 0.026$), the growth rate of the flutter eigenvalue increases. For the remaining range, $K_s \in [0 - 0.026]$, we observe a slight decrease of the growth rate of the flutter eigenvalue as K_s

decreases. Concerning the evolution of the frequency of the flutter mode, on the bottom the figure, we observe larger values for the Reynolds stress formulation compared to the classical formulation. We also observe larger discrepancies when compared to the low frequency of the quasi-periodic solutions, even if both frequencies remain on the same order of magnitude.

Although the flutter eigenvalues are located on the stable side of the spectrum, the account for the Reynolds stress term appears to have a destabilising effect, with a sensitivity to the value of K_s, and hence to the equilibrium position. The fact that the maximum value of the growth rate of the flutter eigenvalue is located on the lower K_s limit of the nonlinear quasi-periodic oscillations may be due to two reasons. First, the stability analyses are made around an equilibrium position given by the aerodynamic moment curve associated to the mean flow field at static positions. As observed in figure 5.16, a slight difference can be noted between the incidence of the mean flow fields at static incidences and the mean incidence of the quasi-periodic solutions. We propose in a future work to carry out the mean flow stability analyses around a mean flow issued from the time-averaged solutions of the quasi-periodic simulations. A second cause for the shift on the location of the maximum value of the growth rate of the flutter eigenvalue may be the finite difference scheme considered in this section for the computation of the additional Reynolds stress term. A backward finite difference scheme was used. For a future work, we propose to explore a central finite difference scheme to avoid this shift on the growth rate evolution.

Since the mean flow analyses do not provide conclusive results on the appearance of a flutter instability that might explain the quasi-periodic oscillations observed in the temporal simulations, we now perform a Floquet analysis of the periodic solutions at the quasi-steady secondary equilibrium positions.

6.1.3 Floquet linear stability analyses

We extend the linear stability analysis to periodic flow solutions via a Floquet FSI linear stability analysis. The periodicity of the flow is associated to the high frequency vortex shedding phenomenon. As described in section 1.3.2 (page 28), the high frequency fluctuations of the flow field are reflected in the aerodynamic moment exerted on the airfoil. However, no resonant interaction between the fluctuation of the periodic aerodynamic moment and the airfoil oscillation

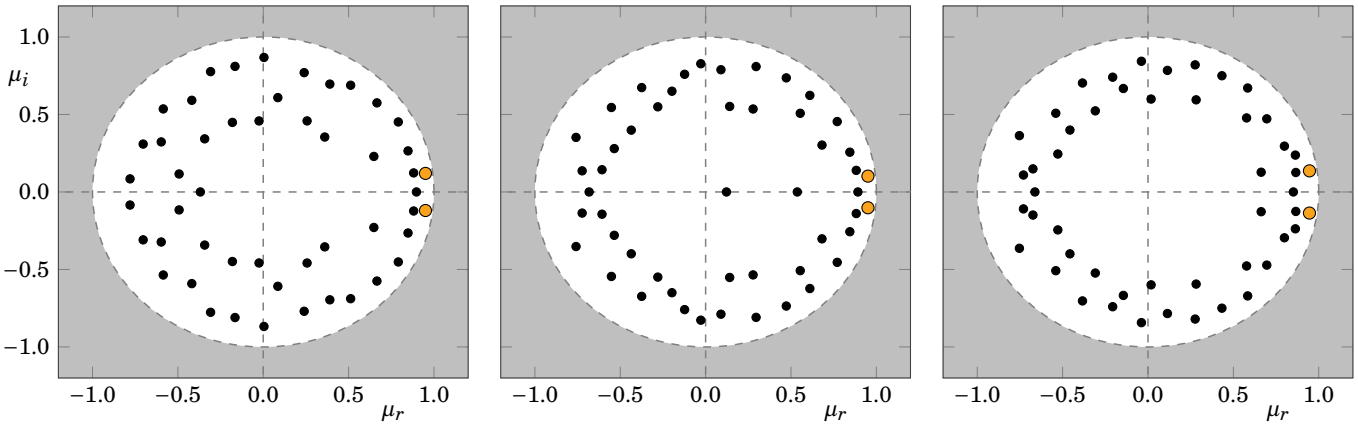

Figure 6.7 – *Floquet multipliers on the complex plane* (μ_r, μ_i) *for the Floquet FSI analysis at* $Re = 20\,000$ *on the secondary equilibrium point: on the left,* $K_s = 0.347$ *(*$\overline{\alpha}_2 = 2.72°$*), on the centre,* $K_s = 0.087$ *(*$\overline{\alpha}_2 = 3.44°$*), on the right,* $K_s = 0$ *(*$\overline{\alpha}_2 = 3.64°$*). The yellow circles represent the flutter Floquet multipliers The unstable region outside the unit circle* $|\mu| > 1$ *is represented by the grey zone.*

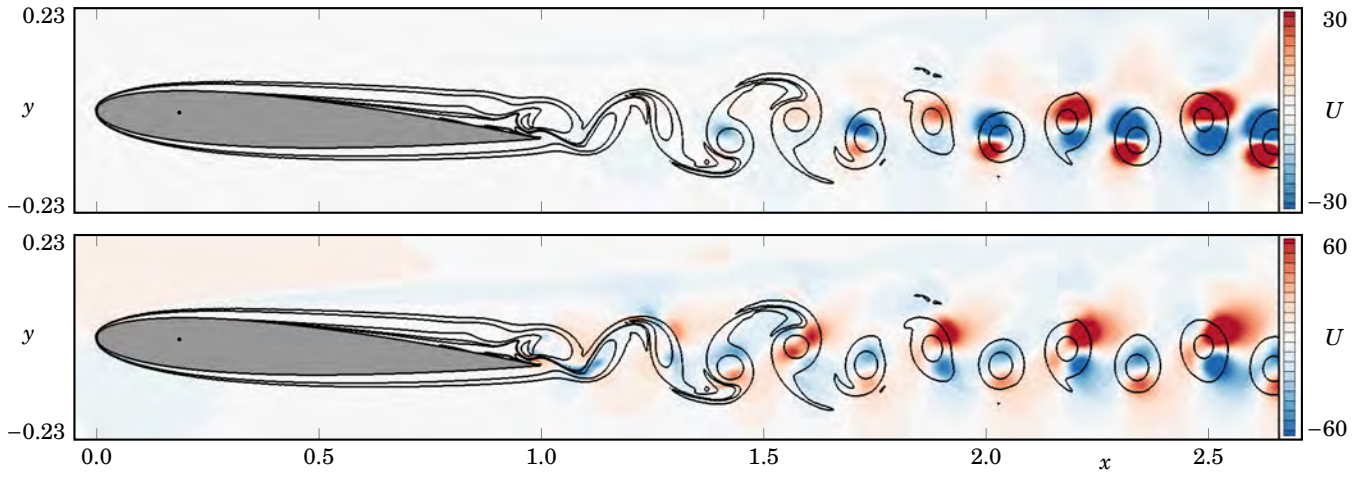

Figure 6.8 – *Instantaneous streamwise velocity of the flutter Floquet eigenmode for Re = 20 000, $\bar{\alpha}_2 = 3.44°$ and $K_s = 0.087$: real and imaginary parts on the top and bottom plots, respectively. The black isocontours represent the spanwise vorticity of the corresponding instant of the periodic flow ($\Omega_z = \pm 20$ and $\Omega_z = \pm 2$).*

exists, the fast time scale amplitude of the latter being consequently very small. Still, the high frequency (nonlinear) aerodynamic fluctuations may play a role in the destabilisation process of the flutter mode. As shown in chapter 1, the classical formulation of the mean flow stability analysis can be derived from the Floquet analysis of the periodic flow and neglecting some terms (equation 1.32, page 36, already recalled in this chapter). These terms correspond to the mean value of the quadratic interactions between high frequency components of the Floquet eigenmodes and the periodic flow. To assess their role in the destabilisation process, the Floquet FSI linear stability analysis is carried out around the periodic flow fields found at the static incidences 2.72°, 3.44° and 3.64°.

As a reminder, we note that it is usual to describe the Floquet growth/decay over a period T via the Floquet multipliers $\mu = \mathrm{e}^{\sigma T}$. This quantity represents the complex amplitude gain of the periodic Floquet eigenmode over one period, *i.e.*, $\boldsymbol{q}(\boldsymbol{X}, t+T) = \mu \boldsymbol{q}(\boldsymbol{X}, t)$, where $\boldsymbol{q}$ represents the fluid–structure Floquet eigenmode.

Figure 6.7 presents the Floquet multipliers on the complex plane for the three equilibrium points considered. The Floquet multipliers associated to the flutter eigenvalues are highlighted with the bigger yellow circles. The unstable region is represented by the grey zone, where $|\mu| > 1$. All represented Floquet multipliers, including the ones associated to the flutter mode are found on the stable region $|\mu| < 1$. Although several static eigenmodes are located on the μ_r axis, the Floquet multiplier associated to the divergence eigenmode is not clearly discerned from the remaining stable static Floquet multipliers. This is due to the fact that the numerical method implemented here has a poor convergence rate for stable Floquet multipliers far from the marginal line $|\mu| = 1$. We also note that no Floquet multiplier is found at $(\mu_r, \mu_i) = (1, 0)$, in contrast to the results at the primary equilibrium position (see figure 4.10, page 151). This is due to the fact that the time derivative of the periodic flow solution, $\left[\partial \boldsymbol{q}_{f,b}/\partial t, 0, 0\right]^T$, no longer corresponds to an eigenvector of the Floquet FSI eigenproblem, associated to the eigenvalue $\sigma = 0$.

Concerning the flutter mode, its instantaneous streamwise velocity component (real and imaginary parts) associated to the initial periodic flow instant is depicted in figure 6.8, for the intermediate case at $\bar{\alpha}_2 = 3.44°$ ($K_s = 0.087$). The black isocontour lines correspond to the spanwise vorticity associated to the instantaneous solution of the periodic flow. The flutter eigenmode is normalised with respect to its angular displacement component θ, such that $|\theta| = 1$. Both real and imaginary components are characterised by significant values on the core of the instantaneous vortex shedding structures

K_s	$\bar{\alpha}_2$	Floquet multiplier μ	Eigenvalue σ	θ	Ω	$m_z(\boldsymbol{q}_f)$
0.347	2.72	$0.9502 + 0.1198\mathrm{i}$	$-0.1321 + 0.3835\mathrm{i}$	$-0.7241 + 0.6897\mathrm{i}$	$-0.1678 - 0.3675\mathrm{i}$	$-0.2972 - 0.0305\mathrm{i}$
0.087	3.44	$0.9507 + 0.1020\mathrm{i}$	$-0.1357 + 0.3240\mathrm{i}$	$-0.6907 + 0.7231\mathrm{i}$	$-0.1405 - 0.3220\mathrm{i}$	$-0.2709 + 0.0206\mathrm{i}$
0.000	3.64	$0.9458 + 0.1362\mathrm{i}$	$-0.1365 + 0.4294\mathrm{i}$	$-0.1877 + 0.9822\mathrm{i}$	$-0.3986 - 0.2089\mathrm{i}$	$-0.2658 - 0.0053\mathrm{i}$

Table 6.2 – *Summary of the Floquet multipliers, eigenvalues, solid components of the eigenmodes and aerodynamic moment coefficients for the flutter mode at Re = 20 000 for the three equilibrium positions considered.*

of the periodic flow. These values increase in magnitude, as the instability is convected downstream. Interestingly, no significant values are found on the vortex shedding formation region, immediately after the trailing edge of the airfoil, as opposed to the flutter Floquet eigenmode found for the primary equilibrium angle (see figure 4.12, page 153). The physical interpretation of this Floquet eigenmode and its link with the flutter mode identified in the mean flow analysis would deserve a better investigation, for instance by following the work by Benetti Ramos *et al.* (2021).

Table 6.2 summarises the main scalar results associated to the flutter mode for the three incidences. The first two columns identify the three cases considered. The third column presents the Floquet multipliers located on the side $\mu_i > 0$ of the spectra. The corresponding eigenvalues σ are reported in the forth column. Their real part remain approximatively constant for the three values of stiffness, while significant changes are observed in their frequency. The fifth and sixth columns present the solid components of the flutter eigenmode. The last column presents the aerodynamic moment associated to the fluid component of the flutter Floquet eigenmodes. We note that the values present in the last three columns depend on the instantaneous Floquet eigenmode considered along the period of the flow field around which the stability is studied, as well as on its normalisation.

We observe that the flutter eigenmodes of the Floquet FSI analysis present a higher growth rate and a lower frequency that the ones associated to the mean flow FSI analysis. However, all the computed eigenvalues are located on the stable side of the spectrum. For the case $K_s = 0.087$, we conclude that the onset of the quasi-periodic solution, associated to the low angular oscillation frequency, is not explained by the above linear stability analysis, as in the case of both formulations of the mean flow analyses.

6.2 Mean flow linear stability analyses at $Re = 50\,000$

In this section, we reconsider the case at $Re = 50\,000$, where the DNS simulations at different angles of attack were carried out. The Reynolds number corresponds to one of the main values present on the literature at which the laminar separation flutter phenomenon was firstly observed (Poirel *et al.*, 2008). In that way, in this section we perform different mean flow FSI linear stability analyses around the mean flow solutions issued from the three-dimensional simulations. The mean flow is obtained by averaging the three-dimensional solutions in time and in the spanwise direction. The mean flow characteristics were detailed in section 2.2 (page 88), in particular for the angles $\bar{\alpha}_b > 0\,^\circ$ where the second equilibrium positions are found. Only the classical formulation associated to the mean flow analysis is presented in this section, as the DNS simulations are not sufficiently close in incidence to compute the additional Reynolds stress term with a finite difference method.

In the first part of this section, we describe the values of the second equilibrium positions for the present case, that can be found on the aerodynamic moment curve associated to the mean flow solutions issued from 3D simulations. In a second part, we present the results of the mean flow analyses using the classical formulation.

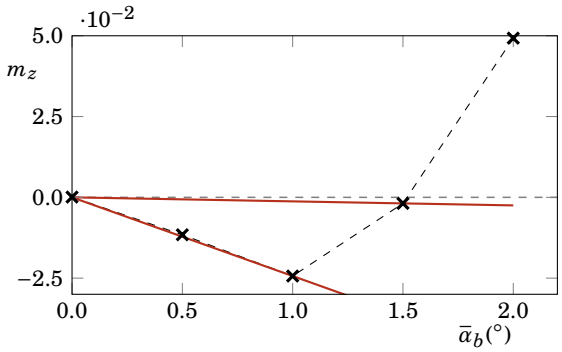

Figure 6.9 – *Evolution of the mean flow aerodynamic moment coefficient, associated to fixed incidence three-dimensional simulations, with the angle of attack (black line), for* $Re = 50\,000$*. The red slopes represent the two values of structural stiffness used:* $K_s = 1.395$*, for* $\bar{\alpha}_2 = 1^\circ$ *and* $K_s = 0.071$*, for* $\bar{\alpha}_2 = 1.5^\circ$*.*

6.3 Quasi-steady equilibrium positions for mean flow solutions from 3D simulations

The second equilibrium points can be found in a similar way as described previously, *i.e.*, as a solution of the equality $\bar{\alpha}_b = -m_z(\bar{\boldsymbol{q}}_b)/K_s$. For the three-dimensional case, the number of simulations performed was limited. Therefore, the equilibrium points are defined at fixed angular positions, where the aerodynamic moment is known and the structural stiffness is derived. The simulations were carried out for angles up to $\bar{\alpha}_b = 2^\circ$, with a step of 0.5°.

Figure 6.9 presents the evolution of the aerodynamic moment associated to the time- and spanwise-averaged solution as function of the angle of attack. From the available simulations, three angles of attack are selected: the cases at $\bar{\alpha}_2 = 0.5^\circ$, 1° and 1.5°. The corresponding values of the structural stiffness are then computed from the fixed angle $\bar{\alpha}_2$ and associated aerodynamic moment and are represented by the red slopes in the figure. Since the cases $\bar{\alpha}_2 = 0.5^\circ$ and $\bar{\alpha}_2 = 1^\circ$ present the same slope, their structure rigidity at the equilibrium point is the same. These cases present the highest value of K_s for which the second equilibrium point can be found, with a value of $K_s = 1.395$ ($K_s^{dim} = 0.502$Nm). On the other hand, the case at $\bar{\alpha}_2 = 1.5^\circ$ almost corresponds to the limiting case of a zero structural stiffness, with a value of $K_s = 0.071$ ($K_s^{dim} = 0.026$Nm). The case at $\bar{\alpha}_2 = 2^\circ$ is not considered, since a negative structural stiffness would be required for the structural equilibrium equation to be satisfied.

6.3.1 Classical formulation of the mean flow linear stability analyses

In this section, we present the results associated to a mean flow FSI stability analysis for $\bar{\alpha}_2 = 0.5^\circ$, 1° and 1.5°, using a classical formulation. These results are present in figure 6.10, with the spectrum representation of the FSI eigenvalues near the origin on the left and the real and imaginary parts of the streamwise velocity field associated to the flutter mode on the right. We recall that the corresponding mean flow solutions are described in section 2.2.3 and can be observed in figure 2.32 (page 99). For the first equilibrium incidence ($\bar{\alpha}_2 = 0.5^\circ$, $K_s = 1.395$), the mean flow is characterised by a separation of the boundary layer on both lower and upper surfaces of the airfoil. The linear stability results are present on the top of figure 6.10. The spectrum is characterised by several stable eigenvalues. In particular, we identify the divergence eigenmode, along the real axis, located at $\sigma = -0.0268$. At the same time, one finds the flutter mode (yellow circle) also on the stable side of the spectrum at $\sigma = -0.1102 + 0.6709$. We represent the eigenvalue of the structure equation in vacuum with the black cross ($\sigma_s = -0.0231 + 0.6028$i). As already noted previously, the fluid has the effect

of stabilising the flutter mode and increasing its frequency. Concerning the spatial structure of the real and imaginary parts of the streamwise velocity associated to the flutter mode (on the top right), both parts are similar to the flutter mode discussed in figure 6.2. In particular, we highlight the change in sign of the real part of streamwise velocity near the trailing edge, as well as the dipole-like spatial structure found with a centre at the leading edge of the airfoil, with significant values of $\overline{U}$ on the inviscid zones of the mean flow field. Concerning the imaginary part, we observe significant values only from the second half of the airfoil up to the airfoil wake.

For the equilibrium incidence at $\bar{\alpha}_2 = 1^\circ$ ($K_s = 1.395$), the results are present on the centre of figure 6.10. The mean flow solution is characterised by a laminar separation bubble, present on the upper surface of the airfoil for the range $0.56 < X < 1$, while the boundary layer on the lower surface remains attached for the entire chord length (see figure 2.32). The spectrum is also characterised by several stable eigenvalues. However, the divergence mode has coalesced with a stable static eigenvalue, leading to a pair of low frequency complex conjugate eigenvalues, located on the stable side of spectrum. The flutter eigenvalue (yellow circle) is located at $\sigma = -0.1139 + 0.6628$, near the eigenvalue of the structure equation at $\sigma_s = -0.0231 + 0.6028\mathrm{i}$ (black cross). The corresponding spatial structure of the real and imaginary parts of the streamwise velocity are present on the right of the figure. We highlight the change in sign of the streamwise velocity around the location of the separation point of the boundary layer on the upper surface of the associated mean flow solution.

Next, we present the results associated to a mean flow FSI stability analysis for the case $\bar{\alpha}_2 = 1.5^\circ$ ($K_s = 0.071$), with the results present on the bottom of figure 6.10. Similar to the previous angle of attack considered, the mean flow solution is characterised by a laminar separation bubble, present on the upper surface of the airfoil for the range $0.51 < X < 1$, while the boundary layer on the lower surface remains attached for the entire chord length. Additionally, we reported in chapter 2 the emergence of a secondary separation and reattachment, present inside the laminar separation bubble. Observing the fluid–structure spectrum, all eigenvalues are again found on the stable side of the spectrum. Concerning the divergence eigenvalues, a coalesced complex pair of eigenvalues is found, as in the case at $\bar{\alpha}_2 = 1^\circ$, but at a significantly lower growth rate. The flutter eigenvalue, located at $\sigma = -0.0518 + 0.2889\mathrm{i}$, is characterised by a lower frequency, when compared to the flutter eigenvalue of the previous analyses. At the same time, the decrease of K_s leads to an increase of its growth rate, although the eigenmode is still stable. We note the proximity of the flutter eigenvalue to the structure eigenvalue ($\sigma_s = -0.0232 + 0.1345\mathrm{i}$). The real and imaginary parts of the streamwise velocity of the flutter mode are represented on the bottom right of figure 2.32. The spatial structure of both parts resembles to the flutter mode at $\bar{\alpha}_2 = 1^\circ$.

With all the eigenvalues present on the stable side of the spectrum, we conclude that a linear stability analysis performed under the present hypotheses could not predict the quasi-periodic dynamics that precedes the laminar separation flutter.

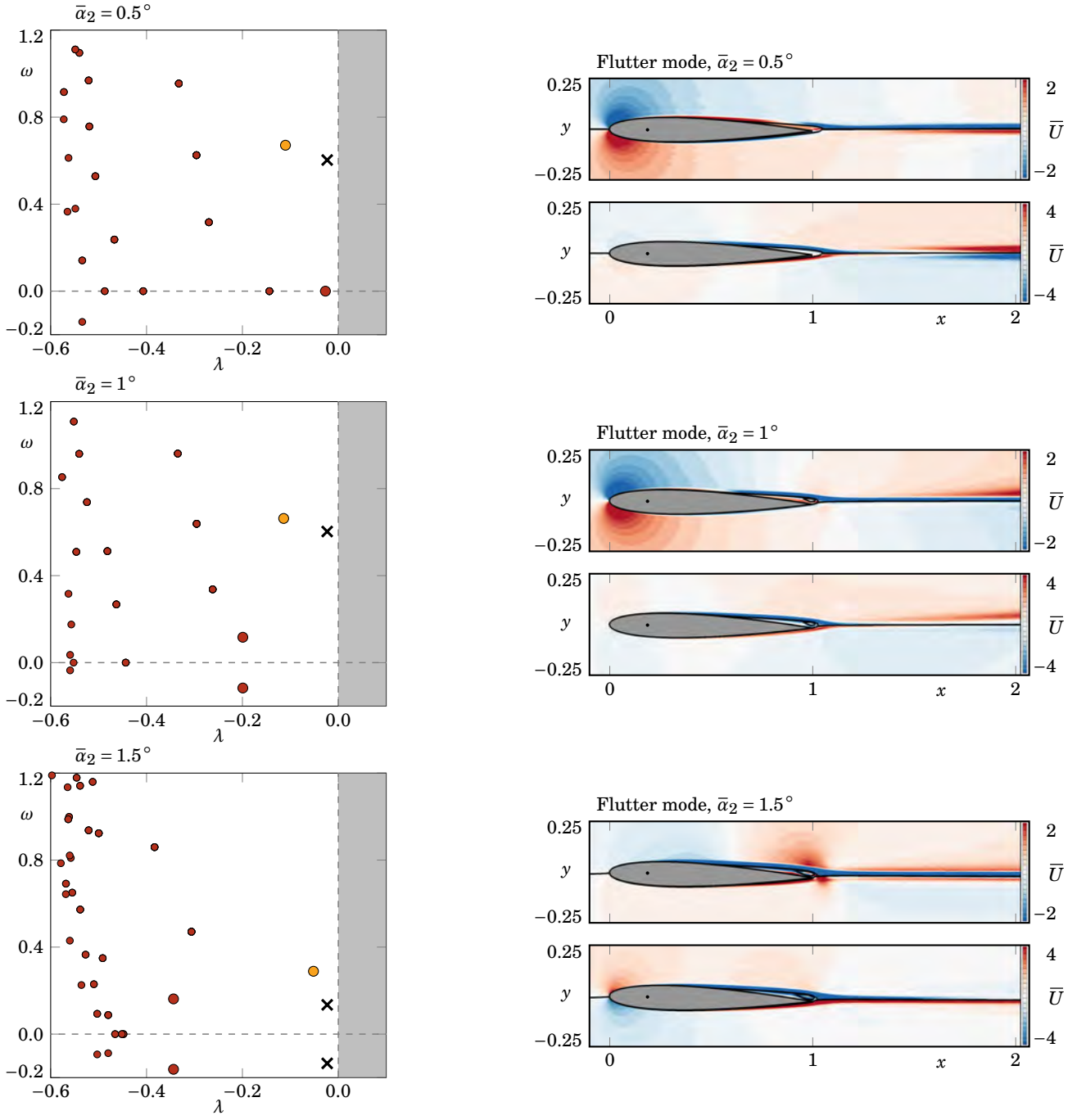

Figure 6.10 – *Classical formulation of the mean flow linear stability analysis at* $Re = 50\,000$ *and different secondary equilibrium positions: the equilibrium at* $\bar{\alpha}_2 = 0.5°$ *(top plots), at* $\bar{\alpha}_2 = 1°$ *(centre plots) and* $\bar{\alpha}_2 = 1.5°$ *(bottom plots). On the left, we represent the eigenvalue spectrum close to the origin. The bigger red and yellow circles represent the divergence and flutter eigenvalues, respectively. The black crosses represent the eigenvalues of the structure in vacuum. On the right, we represent the real and imaginary parts of the streamwise velocity of the flutter eigenmode. The black isocontour lines represent the streamlines enclosing the recirculation zone of the corresponding mean flow solution.*

Conclusions and perspectives

This thesis represents an effort towards a better understanding of the laminar separation flutter phenomenon, characterised by self-sustained pitch oscillations of a NACA0012 airfoil in a low-to-moderate Reynolds number regime. This is accomplished with the help of several specifically designed linear and nonlinear methods, such as global linear stability analysis, Floquet stability analysis and coupled time-marching simulations.

Theoretical and numerical methods for fluid–structure linear stability analyses

In this thesis, the study of the fluid–structure instabilities is grounded on several theoretical and numerical developments, introduced in chapters 1 and 3. Chapter 1 starts with the presentation of the governing equations of the flow dynamics, the Navier–Stokes equations, in a non-inertial frame of reference, which provides a foundation for the linear stability analyses framework. In turn, the airfoil structure is modelled as a rigid body mounted on a linear torsional spring-damped system. The core of this chapter is presented afterwards, where we derive the equations associated to the linear stability analyses. There, we introduce a decomposition of the fluid and solid variables into a slow and fast time scale components and we proceed to make several hypotheses on the latter components of the solid variables, based on the response of the structure to fast time scale forcing oscillations, coming from the aerodynamic moment coefficient. With that, we first arrive to a system of linear stability equations describing the infinitesimal fluid–structure perturbations around a periodic flow state (Floquet stability analysis). We then continue with several hypotheses in order to arrive to the equations of the mean flow linear stability analyses. In this case, two different formulations are introduced, one of them taking into account the variation of the divergence of the Reynolds stress tensor with the angular displacement.

Following the theoretical developments of the mean flow stability analyses, introduced in chapter 1, we present in chapter 3 several methods to arrive to the eigenpairs of a mean flow eigenvalue problem. These methods are applied to the case at $Re = 50\,000$ and $\alpha = 0°$, also explored in Negi *et al.* (2021). We start with a classical Krylov–Schur method relying on a shift-and-invert transformation, allowing the computation of all eigenvalues present on a particular region of the fluid–structure spectrum. This method is based on the exact formulation of the mean flow eigenvalue problem, where the inversion of the fluid–structure Jacobian is obtained by solely inverting the fluid Jacobian and by some additional matrix-vector product operations. This allows the identification of an unstable static mode, which we label *divergence mode*, responsible for the divergent departure of the structure from its primary equilibrium point at $\alpha = 0°$. This is confirmed by a quasi-steady approximation, where a negative aerodynamic stiffness is found. A second eigenvalue is identified, on the stable side of the spectrum, which we label *flutter mode*, due to the proximity of its frequency with the frequency of the laminar separation flutter phenomenon, reported in the literature. The association of the latter mode to the structure is better understood with the introduction of the fluid transfer function, defined as the ratio between the aerodynamic moment of a linearised fluid response to the solid motion and the angular displacement. The computation of the fluid transfer function near the obtained fluid–structure eigenvalues enables to understand the effect of the flow on

the coupled instability, in particular the importance of some stable hydrodynamic eigenmodes. Based on this information, a second method for computing the fluid–structure eigenvalues is then introduced, relying on the transformation of the original eigenproblem into a reduced-size nonlinear eigenproblem, solved via a Newton iterative procedure, where at each nonlinear iteration, the exact value of the fluid transfer function has to be calculated. We end the chapter with the implementation of an approximative model for computing the fluid–structure eigenmodes, based on the approximation of the fluid transfer function by a sum of rational functions. The denominator of the rational functions is based on two stable hydrodynamic eigenmodes, found to have a paramount influence on the behaviour of the fluid transfer function.

Flow behaviour in a low-to-moderate Reynolds number regime

The linear stability analyses on this thesis were carried out around a base equilibrium solution that corresponds to either a mean flow or a periodic flow with a fixed incidence. These solutions are characterised in chapter 2, where no interaction between the fluid and the wing was taken into account. In that way, chapter 2 is devoted to the description of the flow field around a NACA0012 profile wing and the corresponding aerodynamic forces acting on it from a Reynolds number of $Re = 1\,000$ to $Re = 65\,000$, at different angles of attack. We start by describing the onset of a vortex shedding oscillation at $\alpha = 0^\circ$ on the wake of a NACA0012 airfoil via two-dimensional Navier–Stokes computations. This is followed by the description of the mean flow and the periodic flow solutions appearing at different incidences, corresponding to the base equilibrium solutions of the linear stability analyses present in subsequent chapters. The flow being purely two-dimensional, we then investigate the emergence of three-dimensional instabilities in the airfoil spanwise direction, by the means of a hydrodynamic Floquet stability analysis. For the considered incidence, $\alpha = 0^\circ$, the first instabilities arise around $Re = 30\,000$ for a wavenumber of $\beta = 50$ via a mode B instability. In a second part of this chapter, we conducted Direct Numerical Simulations at $Re = 50\,000$ for five angles of attack, between 0° and 2°, in order to characterise both instantaneous and spectral properties of the flow field. In particular, these simulations enable to compute a time- and spanwise-averaged solution, later used in the mean flow stability analyses, accounting for the three-dimensional effects present on the flow field at this Reynolds number. We end the chapter with an investigation of the behaviour of the aerodynamic moment coefficient associated to the time- and spanwise-averaged flow fields as function of the angle of attack. The initial negative slope of this coefficient, at $\alpha = 0^\circ$, indicates that a divergent instability could be present on the fluid–structure system, depending on the value of the structural stiffness of the torsional spring. The aerodynamic moment coefficient for each angular displacement is decomposed into its frictional and pressure components. The latter is evaluated using an alternative approach, based on the spatial distribution of the different terms of the Navier–Stokes equations, rather than the classic approach based on a stress integration over the fluid–solid interface.

In these purely fluid explorations, no particular restrictions are imposed to the static angle of attack, which was fixed for each simulation. However, when the torsional degree of freedom of the structure is introduced in the subsequent chapters, the admissible equilibrium incidences are fixed by the relation between the mean aerodynamic moment at fixed incidences and the structural stiffness, as $\bar{\alpha} = m_z\left(\bar{\boldsymbol{q}}_b\right)/K_s$. In particular, as a consequence of the behaviour of the aerodynamic moment for small incidences, two equilibrium positions are identified: a primary equilibrium position, at $\bar{\alpha}_1 = 0^\circ$, and a second equilibrium position, $\bar{\alpha}_2$, found for the lower values of the structural stiffness. These equilibrium positions are then studied in the subsequent chapters using both linear and nonlinear analyses.

Linear analysis: onset of a divergent behaviour of the structure

After the identification of an unstable static eigenvalue at $\bar{\alpha}_1 = 0^\circ$ during the discussion of the different methods used to solve a mean flow analysis (chapter 3), this primary instability of the fluid–structure system is described in

detail in chapter 4. We start the chapter with a description of both divergence and flutter eigenmodes using a classical formulation of mean flow linear stability analysis (introduced in chapter 1). The presence of an unstable zero-frequency mode confirms the results obtained in the mean flow linear stability analysis of Negi *et al.* (2021). We then investigate the effect of different parameters on the behaviour of these modes. This includes a variation of the structural parameters, the aeroelastic centre, the Reynolds number and the thickness of the airfoil. Concerning the variation of the structural stiffness, K_s, we observe a stabilisation of the divergence mode as K_s is increased. A similar behaviour is found when the structural damping is increased, however with the static eigenmode remaining on the unstable side of the spectrum. The variation of the Reynolds number enables to conclude that the destabilisation of the divergence mode appears at $Re = 32\,000$, for the nominal values of the structural parameters. This threshold appears at a higher Reynolds number as the thickness of the airfoil is decreased. At the end of the chapter, the linear analysis is extended to a periodic flow field, using a Floquet analysis. Although no significant changes are noted on the eigenvalues, a clear difference is noted between the divergence eigenmode of the mean flow analysis and the mean component of the Floquet divergence eigenmode, highlighting the importance of taking into account a periodic flow solution for a FSI linear stability analysis.

Nonlinear analysis: coupled time behaviour beyond the linear divergence onset

After the onset of a divergent behaviour of the structure incidence, nonlinear simulations are required to describe the subsequent evolution of the fluid–structure dynamics. In that sense, the nonlinear behaviour of the fluid–structure system beyond a linear hypothesis is explored in chapter 5, using two-dimensional coupled time-marching simulations. The aim is to reproduce some of the results of the investigations present in the literature on the laminar separation flutter phenomenon for $Re \geq 50\,000$ (Poirel *et al.*, 2008, 2011; Barnes *et al.*, 2016, 2018), as well as to explore the nonlinear regimes at lower Reynolds numbers, that ultimately lead to the global limit cycle oscillations observed in the literature. To our knowledge, no investigation in the literature has addressed this latter objective.

In a first part of chapter 5, we describe different regimes of the fluid–structure system at a Reynolds number of 20 000, by varying the structural stiffness parameter. The first regime, observed for the highest values of K_s, is characterised by pitch oscillations of negligible amplitude around the primary equilibrium position at $\bar{\alpha} = 0°$. The second regime, obtained for lower values of K_s, is also characterised by negligible pitch oscillations occurring this time around the secondary equilibrium position at a nonzero angle of incidence ($\bar{\alpha} \neq 0°$). The third and fourth regimes, obtained for even lower values of K_s, are characterised by a chaotic fluid–structure dynamics, with high-amplitude low-frequency pitch oscillations around a nonzero mean angle of incidence. In the latter regime, the pitching dynamics switches between oscillations around positive and negative (time-averaged) angles of incidence. In between these four regimes, an additional nonlinear regime was found using a different initialisation strategy, characterised by a quasi-periodic behaviour, *i.e.*, characterised by a high frequency associated to the vortex shedding phenomenon and a low frequency associated to the pitch oscillations. Therewith, a bifurcation diagram is sketched as function of the K_s parameter, identifying the coexistence of different branches. In particular, for a finite range of structural stiffness values, a bistable behaviour is identified characterised by the coexistence of chaotic and quasi-periodic solutions. The emergence of these quasi-periodic solutions is then investigated in the last chapter using a linear stability framework. For this Reynolds number, we do not observe a fluid–structure dynamics characterising the so-called laminar separation flutter, *i.e.*, a symmetric high-amplitude low-frequency pitching oscillations around the zero angle of incidence.

In a second part of chapter 5, we fix the structure parameters in accordance with the literature (in particular, the value of the structural stiffness is fixed to 0.3Nm), and we investigate the emergence of the laminar separation flutter as the Reynolds number increases. For the Reynolds number $Re = 50\,000$, we observe an intermittent dynamics of the pitching oscillation around opposite mean values of the angle of incidence, as for the third regime described for

$Re = 20\,000$. By increasing the Reynolds number to $Re = 64\,000$, the laminar separation flutter appears. The evolution of the pitching amplitude and low-frequency with the Reynolds number is finally described, showing a good agreement with both experimental and numerical results reported in the literature.

Linear analysis: stability of the second equilibrium position

The thesis ends with an investigation of the linear stability analysis of the second equilibrium position, in chapter 6. We investigate the linear stability of the second equilibrium position ($\bar{\alpha} \neq 0\,°$), around which several nonlinear regimes were identified in chapter 5. For the regime at $Re = 20\,000$ which converges to a static incidence, this second equilibrium is confirmed to be stable, with both the flutter and divergence modes located on the stable side of the fluid–structure spectrum. This is confirmed by both mean flow and Floquet linear analyses. Subsequently, we carry out a mean flow analysis using a classical formulation for a range of equilibrium incidences where both chaotic and quasi-periodic solutions were found. However, the low frequency flutter mode is found to remain on the stable side of the spectrum. To understand these contradictory results obtained with nonlinear temporal simulations and linear mean flow analyses, we discussed and reconsidered some of the assumptions underlying the linear mean flow analysis. The first one concerns the high frequency aerodynamic flow unsteadiness that is (obviously) neglected when considering a mean flow analysis. The derivation of the governing equations performed in chapter 1 suggested that these high frequency oscillations of the periodic (purely-hydrodynamic) flow may play a role in the linearised low-frequency fluid–structure dynamics, even if no resonance was found between the two frequencies. To assess their influence for the present case, we performed a Floquet analysis of the periodic flow (instead of a mean flow analysis) for the equilibrium solutions at $\bar{\alpha} \neq 0\,°$ and parameters for which quasi-periodic and chaotic dynamics were previously observed. The results indicate that the high frequency oscillations neglected in the mean flow analysis tend to destabilise the flutter eigenmode. However, this sole effect cannot explain its destabilisation. A second hypothesis is investigated, concerning the inclusion of the Reynolds stress term in the equations of the mean flow eigenproblem. In particular, we restrict our analysis to the variation of this term with the angular perturbation. The results show a destabilisation effect in the flutter eigenvalue, even if the flutter eigenvalue remains on the stable side of the spectrum. A maximum on the flutter growth rate evolution with the equilibrium incidence is found in the range where the quasi-periodic solutions were observed. We conclude that the inclusion of the Reynolds stress term in the perturbation dynamics has an important effect, which would be pertinent to be addressed in future investigations. In particular, the inclusion of the remaining terms of the Reynolds stress variation on the mean flow eigenproblem equations, namely the effect of the fluid variable perturbations, can be achieved using a RANS turbulence model. This investigation is started in appendix E and discussed briefly in the perspectives. Finally, in the second part of this last chapter, we investigate the linear stability of three equilibrium positions at $Re = 50\,000$, using the time- and spanwise-averaged flow solutions issued from the Direct Numerical Simulations at $\bar{\alpha} \neq 0\,°$. With all the eigenvalues present on the stable side of the spectrum, we conclude that a linear stability analysis performed under the present hypotheses could not predict the quasi-periodic dynamics that precedes the laminar separation flutter.

Perspectives

Several points on this manuscript deserve to be further investigated in future works.

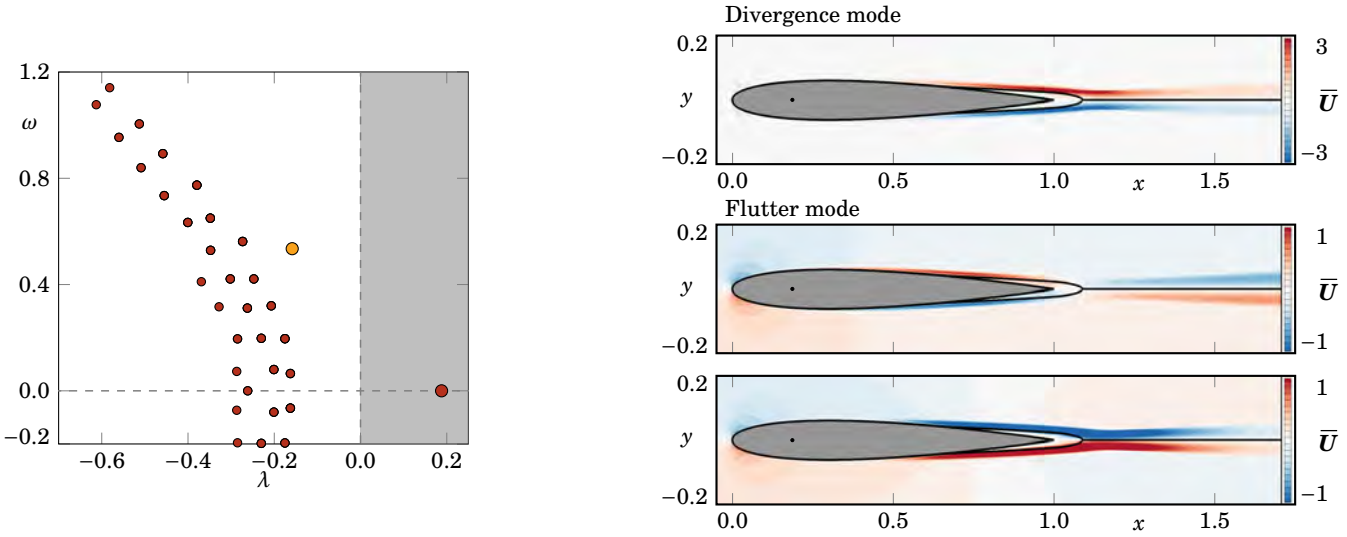

Figure 10 – *Mean flow FSI linear stability analysis of the RANS mean flow using the Spalart–Allmaras turbulence model and the Baş–Çakmakçıoğlu turbulence transition model at* $Re = 50\,000$*,* $\alpha = 0°$ *and* $K_s^{dim} = 0.15\text{Nm}$*: on the left, the eigenvalue spectrum representation close to the origin. The bigger red and yellow circles represent the divergence and flutter eigenvalues, respectively. On the right, the streamwise velocity* $\overline{U}$ *of the real part of the divergence eigenmode (top) and of the real and imaginary parts of the flutter eigenmode (centre and bottom, respectively). The black isocontour lines represent the streamlines enclosing the recirculation zone of the corresponding mean flow solution.*

Flow description in low-to-moderate Reynolds number regimes

From a purely fluid point of view, the work presented in chapter 2 could be enriched in several directions. First, it would be interesting to characterise the onset of the vortex shedding via a purely-hydrodynamic linear stability analysis at low incidences, as classically done for the case of the circular cylinder. Several difficulties in this path were already highlighted in section 2.1.1, related to the strongly convective character of the instability, with the first attempts to predicting this threshold reported in appendix C. Second, it would be interesting to further characterise the onset of the three-dimensional perturbations using a Floquet analysis for non-zero incidence angles, as started in appendix C. While the present work reports the first instabilities appearing at $Re = 30\,000$ for $\alpha = 0°$ via a mode B instability, this transition to a three-dimensional state was reported in the literature to take place via a mode C instability for $(\alpha, Re) = (12.5°, 1\,082)$ and $(\alpha, Re) = (15°, 730)$, on a NACA0015 airfoil (Deng *et al.*, 2017). One can note the gap between these two investigations, both in terms of Reynolds number and in terms of incidence. In future investigations, it would be interesting to continue the investigations of appendix C and describe the transition from the mode B to the mode C, as the incidence increases, as well as characterise the threshold Reynolds number, that is expected to vary significantly as the incidence increases.

Fluid–structure investigations

Concerning the fluid–structure temporal simulations, these were conducted in this thesis using a two-dimensional Navier–Stokes model. Firstly, it would be interesting to investigate if all the regimes observed at $Re = 20\,000$ would still exist using a URANS or a three-dimensional modelling. From a numerical point of view, we suggest to use a more efficient strategy for the temporal scheme, based for example on an incremental projection algorithm, as done for the

Direct Numerical Simulations of the present thesis. Secondly, it would be interesting to explore the unstable branches of the bifurcation diagram present in chapter 5. This can be achieved by using methods adapted to capture these unstable solutions, in particular periodic and quasi-periodic solutions, as the Time Spectral Method (Mavriplis *et al.*, 2011) or a Chebyshev-based time-spectral method (Ekici *et al.*, 2020). Third, it would be interesting to explore even lower Reynolds number regimes. As reported in chapter 2, the stability derivative associated to the aerodynamic moment coefficient becomes negative even before the onset of a vortex shedding. This indicates that a divergent instability could be present on the fluid–structure system before the onset of the unsteadiness on the flow field, depending on the value of the torsional spring stiffness. In preliminary investigations at $\alpha = 6.4\,^\circ$, not reported in this thesis, we found the transition from a homoclinic orbit around the secondary equilibrium position to a steady solution at the primary equilibrium as the Reynolds number decreases, at a threshold of $Re = 1\,430$. We consider that this case represents an interesting dynamic system, presenting different unexplored regimes that can be further investigated in future works.

Reynolds-averaged Navier–Stokes modelling

Concerning the fluid–structure linear stability analysis, the difficulties found on the last chapter of this thesis enable us to identify possible paths for improving the linear predictions in future works. In particular, we suggest the exploration of the mean flow linear stability analysis using a RANS modelling, where the effect of the neglected terms associated to the Reynolds stress linearisation is taken into account. In particular, a RANS formulation presents a methodological advantage, since it takes into account the variation of the divergence of the Reynolds stress tensor with respect to all state variables. Further, this is independent of the choice for the model closure. The first steps on this investigation are reported in appendix E, using a Spalart–Allmaras closure model. Further, the laminar-turbulent transition of the flow field is obtained via an algebraic transition model, namely the Baş–Çakmakçıoğlu (BC) model. The results of a mean flow fluid stability analysis around the primary equilibrium point at $Re = 50\,000$ are displayed in figure 10. As noted, we are able to capture the unstable divergence eigenmode, as in the analysis presented in chapters 3 and 4. However, we show in appendix E that more work needs to be done in order to capture the laminar-turbulent transition for the cases at $\alpha \neq 0\,^\circ$ and, in particular, to capture the evolution of the aerodynamic moment with the angle of attack where the secondary equilibrium positions would be found.

Resolvent-based analysis

Finally, a different idea, not tested in this thesis, would be to investigate the effect of an external forcing noise on the flutter mode. Indeed, the stable flutter mode is close to the zero growth rate axis, so that a large amplification of the pitching oscillations close to its frequency can be expected under the action of external noise. The resolvent analysis, classically applied in aerodynamics (Sipp *et al.*, 2010), can be extended to describe some instabilities arising in fluid–structure interaction problems, either in the framework of parallel flows (Luhar *et al.*, 2015) or in the framework of non-parallel flows (Pfister *et al.*, 2022).

Appendix A

Notes on the fluid model derivation and the airfoil geometry generation

A.1 Additional notes on the fluid model derivation

The present section serves as auxiliary guide to the derivations used in chapter 1, during the change of reference frame of the Navier–Stokes equations. A similar demonstration is presented in Jallas (2018), Moulin (2020) and Benetti Ramos (2020). For a compressible framework, see also Kračmar *et al.* (2014); Galdi *et al.* (2019, 2020).

We start by noting from the rule chain that, for a generic scalar function β, the following equalities hold:

$$\begin{cases} \dfrac{\partial \beta}{\partial x} = \dfrac{\partial \beta}{\partial X}\dfrac{\partial X}{\partial x} + \dfrac{\partial \beta}{\partial Y}\dfrac{\partial Y}{\partial x} \Leftrightarrow \dfrac{\partial \beta}{\partial x} = \cos(\theta)\dfrac{\partial \beta}{\partial X} - \sin(\theta)\dfrac{\partial \beta}{\partial Y}\,, & \text{(A.1a)} \\ \dfrac{\partial \beta}{\partial y} = \dfrac{\partial \beta}{\partial X}\dfrac{\partial X}{\partial y} + \dfrac{\partial \beta}{\partial Y}\dfrac{\partial Y}{\partial y} \Leftrightarrow \dfrac{\partial \beta}{\partial y} = \sin(\theta)\dfrac{\partial \beta}{\partial X} + \cos(\theta)\dfrac{\partial \beta}{\partial Y}\,. & \text{(A.1b)} \end{cases}$$

Recalling the rotation matrix definition in equation 1.1, page 18, the above equations directly give us the relation of the pressure gradient between the two frames of reference, as stated in the following Identity.

Identity 1. *(pressure term)* $\overset{\boldsymbol{x}}{\nabla}{}^T p(\boldsymbol{x},t) = \mathbb{R}\,\overset{\boldsymbol{X}}{\nabla}{}^T p(\boldsymbol{X},t)$

The $\boldsymbol{x}$ and $\boldsymbol{X}$ notations over the nabla operator indicate the variables with which the space derivatives are made.

Identity 2. *(continuity term)* $\overset{\boldsymbol{x}}{\nabla}\cdot\boldsymbol{u}(\boldsymbol{x},t) = \overset{\boldsymbol{X}}{\nabla}\cdot\boldsymbol{U}(\boldsymbol{X},t)$

The equality can be demonstrated by recalling that $\boldsymbol{U}(\boldsymbol{x},t) = \mathbb{R}^T\boldsymbol{u}(\boldsymbol{X},t)$:

$$\begin{aligned} &\overset{\boldsymbol{x}}{\nabla}\cdot\boldsymbol{u}(\boldsymbol{x},t) = \partial_x[u(\boldsymbol{x},t)] + \partial_y[v(\boldsymbol{x},t)] + \partial_z[w(\boldsymbol{x},t)] \\ &= \cos(\theta)\partial_X[u(\boldsymbol{X},t)] - \sin(\theta)\partial_Y[u(\boldsymbol{X},t)] + \sin(\theta)\partial_X[v(\boldsymbol{X},t)] + \cos(\theta)\partial_Y[v(\boldsymbol{X},t)] + \partial_Z[w(\boldsymbol{X},t)] \\ &= \partial_X[\cos(\theta)u(\boldsymbol{X},t) + \sin(\theta)v(\boldsymbol{X},t)] + \partial_Y[-\sin(\theta)u(\boldsymbol{X},t) + \cos(\theta)v(\boldsymbol{X},t)] + \partial_Z[w(\boldsymbol{X},t)] \\ &= \partial_X[U(\boldsymbol{X},t)] + \partial_Y[V(\boldsymbol{X},t)] + \partial_Z[W(\boldsymbol{X},t)] = \overset{\boldsymbol{X}}{\nabla}\cdot\boldsymbol{U}(\boldsymbol{X},t)\blacksquare \end{aligned} \tag{A.2}$$

Identity 3. *(convective term[1])* $\overset{\boldsymbol{x}}{\nabla}\cdot\left[\rho\boldsymbol{u}\otimes\boldsymbol{u}\right]=\mathbb{R}\overset{\boldsymbol{X}}{\nabla}\cdot\left[\rho\boldsymbol{U}\otimes\boldsymbol{U}\right]$

This identity is valid for the compressible convection term, which can be simplified at the end to an incompressible hypothesis. One can start by decomposing the above operation into a sum of outer products:

$$\overset{\boldsymbol{x}}{\nabla}\cdot\left[\rho\boldsymbol{u}\otimes\boldsymbol{u}\right]=\underbrace{\rho\boldsymbol{u}\left(\overset{\boldsymbol{x}}{\nabla}\cdot\boldsymbol{u}\right)}_{1^{\text{st}}\text{ term}}+\underbrace{\left(\boldsymbol{u}\cdot\overset{\boldsymbol{x}}{\nabla}\right)\rho\boldsymbol{u}}_{2^{\text{nd}}\text{ term}}. \tag{A.3}$$

Concerning the first term (null for incompressible flows), one will find:

$$\rho\boldsymbol{u}\left(\overset{\boldsymbol{x}}{\nabla}\cdot\boldsymbol{u}\right)=\rho\boldsymbol{u}\left(\overset{\boldsymbol{X}}{\nabla}\cdot\boldsymbol{U}\right)=\mathbb{R}\rho\boldsymbol{U}\left(\overset{\boldsymbol{X}}{\nabla}\cdot\boldsymbol{U}\right). \tag{A.4}$$

For the second term, one will find:

$$\begin{aligned}
&\begin{bmatrix} u\partial_x(\rho u) & + & v\partial_y(\rho u) & + & w\partial_z(\rho u)\\ u\partial_x(\rho v) & + & v\partial_y(\rho v) & + & w\partial_z(\rho v)\\ u\partial_x(\rho w) & + & v\partial_y(\rho w) & + & w\partial_z(\rho w)\end{bmatrix}\\
&=\begin{bmatrix} u\left[\cos(\theta)\partial_X(\rho u)-\sin(\theta)\partial_Y(\rho u)\right] & + & v\left[\sin(\theta)\partial_X(\rho u)+\cos(\theta)\partial_Y(\rho u)\right] & + & w\partial_Z(\rho u)\\ u\left[\cos(\theta)\partial_X(\rho v)-\sin(\theta)\partial_Y(\rho v)\right] & + & v\left[\sin(\theta)\partial_X(\rho v)+\cos(\theta)\partial_Y(\rho v)\right] & + & w\partial_Z(\rho v)\\ u\left[\cos(\theta)\partial_X(\rho w)-\sin(\theta)\partial_Y(\rho w)\right] & + & v\left[\sin(\theta)\partial_X(\rho w)+\cos(\theta)\partial_Y(\rho w)\right] & + & w\partial_Z(\rho w)\end{bmatrix}\\
&=\begin{bmatrix} \partial_X(\rho u)[\cos(\theta)u+\sin(\theta)v] & + & \partial_Y(\rho u)[-\sin(\theta)u+\cos(\theta)v] & + & w\partial_Z(\rho u)\\ \partial_X(\rho v)[\cos(\theta)u+\sin(\theta)v] & + & \partial_Y(\rho v)[-\sin(\theta)u+\cos(\theta)v] & + & w\partial_Z(\rho v)\\ \partial_X(\rho w)[\cos(\theta)u+\sin(\theta)v] & + & \partial_Y(\rho w)[-\sin(\theta)u+\cos(\theta)v] & + & w\partial_Z(\rho w)\end{bmatrix}\\
&=\begin{bmatrix} \partial_X(\rho u)U & + & \partial_Y(\rho u)V & + & \partial_Z(\rho u)W\\ \partial_X(\rho v)U & + & \partial_Y(\rho v)V & + & \partial_Z(\rho v)W\\ \partial_X(\rho w)U & + & \partial_Y(\rho w)V & + & \partial_Z(\rho w)W\end{bmatrix}=\left(\boldsymbol{U}\cdot\overset{\boldsymbol{X}}{\nabla}\right)\rho\boldsymbol{u}=\mathbb{R}\left(\boldsymbol{U}\cdot\overset{\boldsymbol{X}}{\nabla}\right)\rho\boldsymbol{U}.
\end{aligned} \tag{A.5}$$

Substituting these two terms on equation A.3, one find the required property:

$$\mathbb{R}\rho\boldsymbol{U}\left(\overset{\boldsymbol{X}}{\nabla}\cdot\boldsymbol{U}\right)+\mathbb{R}\left(\boldsymbol{U}\cdot\overset{\boldsymbol{X}}{\nabla}\right)\rho\boldsymbol{U}=\mathbb{R}\overset{\boldsymbol{X}}{\nabla}\cdot\left[\rho\boldsymbol{U}\otimes\boldsymbol{U}\right]\blacksquare \tag{A.6}$$

Identity 4. *(strain rate tensor term[2])* $\overset{\boldsymbol{x}}{\nabla}\cdot[\overset{\boldsymbol{x}}{\nabla}\boldsymbol{u}+(\overset{\boldsymbol{x}}{\nabla}\boldsymbol{u})^T]=\mathbb{R}\overset{\boldsymbol{X}}{\nabla}\cdot[\overset{\boldsymbol{X}}{\nabla}\boldsymbol{U}+(\overset{\boldsymbol{X}}{\nabla}\boldsymbol{U})^T]$

Lets start by proving that $\overset{\boldsymbol{x}}{\nabla}\boldsymbol{u}+(\overset{\boldsymbol{x}}{\nabla}\boldsymbol{u})^T=\overset{\boldsymbol{X}}{\nabla}\boldsymbol{U}+(\overset{\boldsymbol{X}}{\nabla}\boldsymbol{U})^T$. From Identity 1, the nabla operator can be rearranged as

$$\overset{\boldsymbol{x}}{\nabla}=\left(\overset{\boldsymbol{x}}{\nabla^T}\right)^T=\left(\mathbb{R}\overset{\boldsymbol{X}}{\nabla^T}\right)^T=\overset{\boldsymbol{X}}{\nabla}\mathbb{R}^T. \tag{A.7}$$

[1]The following convention is used for the outer product: $a_i\otimes b_j=C_{ij}$, with a_i and b_j the components of two vector fields and C_{ij} the entry corresponding to the i^{th} line and j^{th} column of a matrix.

[2]The following convention is used for the gradient of a vector field: $\nabla\boldsymbol{a}=a_{i,j}\boldsymbol{e}_i\otimes\boldsymbol{e}_j$, with $\boldsymbol{a}$ a vector field defined on an orthonormal coordinate basis $[\boldsymbol{e}_1,\boldsymbol{e}_2,\boldsymbol{e}_3]^T$. Concomitantly, the divergence of a 2^{nd} order tensor (matrix), $\boldsymbol{C}$, is defined as $\nabla\cdot\boldsymbol{C}=C_{ij,j}\boldsymbol{e}_i$. The notation comma followed by a subscript denotes the partial differentiation with respect to the corresponding coordinate of that subscript.

Since $\boldsymbol{u} = \mathbb{R}\boldsymbol{U}$, one readily obtains that $\overset{\boldsymbol{x}}{\nabla}\boldsymbol{u} + (\overset{\boldsymbol{x}}{\nabla}\boldsymbol{u})^T = \overset{\boldsymbol{X}}{\nabla}\boldsymbol{U} + (\overset{\boldsymbol{X}}{\nabla}\boldsymbol{U})^T$. From here, since that for the divergence of a matrix $\boldsymbol{C}$ one has $\nabla\cdot\boldsymbol{C} = \mathbb{R}\nabla\cdot\boldsymbol{C}$ (Identity 3), the identity is retrieved by writing:

$$\overset{\boldsymbol{x}}{\nabla}\cdot[\overset{\boldsymbol{X}}{\nabla}\boldsymbol{U} + (\overset{\boldsymbol{X}}{\nabla}\boldsymbol{U})^T] = \mathbb{R}\overset{\boldsymbol{X}}{\nabla}\cdot[\overset{\boldsymbol{X}}{\nabla}\boldsymbol{U} + (\overset{\boldsymbol{X}}{\nabla}\boldsymbol{U})^T]\blacksquare \tag{A.8}$$

Identity 5. *(frame velocity development)* $\frac{\mathrm{d}(\boldsymbol{X}-\boldsymbol{X}_{EC})}{\mathrm{d}t} = -\boldsymbol{\Omega}\times(\boldsymbol{X}-\boldsymbol{X}_{EC}) - \dot{\boldsymbol{X}}_{EC}$

This identity is used in equation 1.4, on page 20. We start by noting that the coordinates in the relative frame (attached to the airfoil) are transformed into the absolute one with the equality $(\boldsymbol{X}-\boldsymbol{X}_{EC}) = \mathbb{R}^T(\boldsymbol{x}-\boldsymbol{x}_{EC})$. Then, one has

$$\frac{\mathrm{d}\left(\mathbb{R}[\theta(t)]^T(\boldsymbol{x}-\boldsymbol{x}_{EC})\right)}{\mathrm{d}t} = \frac{\mathrm{d}\mathbb{R}^T}{\mathrm{d}\theta}\frac{\mathrm{d}\theta}{\mathrm{d}t}(\boldsymbol{x}-\boldsymbol{x}_{EC}) + \mathbb{R}^T\frac{\mathrm{d}(-\boldsymbol{x}_{EC})}{\mathrm{d}t}. \tag{A.9}$$

Noting that $\mathrm{d}\theta/\mathrm{d}t \equiv \Omega$ and $\boldsymbol{\Omega} = [0,0,\Omega]^T$ (angular velocity), the first term is developed as

$$\begin{aligned}
\frac{\mathrm{d}\mathbb{R}^T}{\mathrm{d}\theta}\frac{\mathrm{d}\theta}{\mathrm{d}t}(\boldsymbol{x}-\boldsymbol{x}_{EC}) &= \begin{bmatrix} -\sin(\theta) & \cos(\theta) & 0 \\ -\cos(\theta) & -\sin(\theta) & 0 \\ 0 & 0 & 0 \end{bmatrix}\Omega\mathbb{R}(\boldsymbol{X}-\boldsymbol{X}_{EC}) \\
&= \begin{bmatrix} 0 & 1 & 0 \\ -1 & 0 & 0 \\ 0 & 0 & 0 \end{bmatrix}\Omega(\boldsymbol{X}-\boldsymbol{X}_{EC}) \\
&= \Omega\begin{bmatrix} (Y-Y_{EC}) \\ -(X-X_{EC}) \\ 0 \end{bmatrix} = -\boldsymbol{\Omega}\times(\boldsymbol{X}-\boldsymbol{X}_{EC}).
\end{aligned} \tag{A.10}$$

On the other hand, the second term of equation A.9 corresponds to the pure translation velocity of the elastic centre of the rigid airfoil and can be explicitly posed as:

$$-\mathbb{R}^T\frac{\mathrm{d}(\boldsymbol{x}_{EC})}{\mathrm{d}t} = -\mathbb{R}^T\begin{bmatrix} -U^\infty \\ 0 \\ 0 \end{bmatrix} = -U^\infty\begin{bmatrix} -\cos(\theta) \\ \sin(\theta) \\ 0 \end{bmatrix} = -\dot{\boldsymbol{X}}_{EC}. \tag{A.11}$$

Assembling both terms, one arrives to

$$\frac{\mathrm{d}(\boldsymbol{X}-\boldsymbol{X}_{EC})}{\mathrm{d}t} = -\boldsymbol{\Omega}\times(\boldsymbol{X}-\boldsymbol{X}_{EC}) - \dot{\boldsymbol{X}}_{EC}\blacksquare \tag{A.12}$$

A.2 Airfoil geometry generation

NACA 4-digit airfoil

The shape of the NACA airfoils was developed by the National Advisory Committee for Aeronautics (NACA)—ancestor of the National Aeronautics and Space Administration (NASA) agency—during the late 1920s and into the 1930s[3]. In a four-digit series, the first digit represents the maximum camber as percentage of the chord, the second digit represents

[3] See https://history.nasa.gov/SP-4305/guide.htm.

the position of the maximum camber in tenths of the chord from the leading edge, and the last two integers represent the maximum thickness of the airfoil, in percent of the chord. From the first two digits of the designation "NACA0012", one infers that the profile has no camber, being symmetric with respect to the chord line. The last two digits indicate that the airfoil has a ratio of 12% between its thickness and chord length.

The coordinates of a symmetrical airfoil shape are given by

$$(x, y) = \left(x, \pm 5t\left[0.2969\sqrt{x} - 0.126x - 0.3516x^2 + 0.2843x^3 - 0.1036x^4\right]\right), \tag{A.13}$$

with t the maximum thickness as a fraction of the chord (given by the last two digits of the NACA four-digit) divided by 100. Note that at $x = 1$ (the trailing edge of the airfoil), the thickness is zero, corresponding to a sharp trailing edge. On a future work, one may test a minor modification of the trailing edge, by rounding the trailing edge and avoiding the sharp edge. This modification can, for example, improve the convergence rate of the numerical simulations, namely on RANS computations, where the distance to the airfoil must be accurately calculated.

Eppler E387 airfoil

This airfoil geometry is used on the validations of the RANS models, in section E.2.4, page 230. The Eppler E387 airfoil belong to a family of airfoil generated using an inverse design approach. In particular, the airfoil shape is obtained by specifying a target pressure distribution about airfoil at different angles of attack (Eppler, 1990). The coordinates of the Eppler E387 were exported from the UIUC airfoil coordinates database website[4], with which a spline interpolating these points was generated, using a python language code (van Rossum *et al.*, 2009). The sharp trailing edge was rounded to avoid numerical issues associated to the mesh tolerance procedure. The generation of the mesh followed the steps described in section 1.7.3, page 48 for the NACA airfoil.

A.3 Relation between the convection term of the mean flow Navier–Stokes momentum equation and the quantity Q

The following demonstration explains the equivalence stated in equation 2.13, page 106, which states:

$$\int_\Omega [(\boldsymbol{U}\cdot\nabla)\boldsymbol{U}]\cdot\nabla\phi_M \,\mathrm{d}\Omega = \cancelto{0}{\int_\Gamma \phi_M [(\boldsymbol{U}\cdot\nabla)\boldsymbol{U}]\,\mathrm{d}\Gamma,} - \int_\Omega \phi_M \nabla\cdot[(\boldsymbol{U}\cdot\nabla)\boldsymbol{U}]\,\mathrm{d}\Omega \tag{A.14a}$$

$$= \int_\Omega 2\phi_M Q \,\mathrm{d}\Omega\,. \tag{A.14b}$$

The overbar notation, identifying $\overline{\boldsymbol{U}}$ as a mean flow velocity field, is dropped to simplify the notation. In this expression, the border integrals on Γ are zero, since the potential function is null at infinity and the convection term is null on the airfoil border. Developing the term present on the right side volume integral of equation A.14a gives:

$$\nabla\cdot[(\boldsymbol{U}\cdot\nabla)\boldsymbol{U}] \equiv \nabla\boldsymbol{U} : (\nabla\boldsymbol{U})^T = (\partial_x U)^2 + (\partial_y V)^2 + (\partial_z W)^2 + 2\partial_x V\partial_y U + 2\partial_x W\partial_z U + 2\partial_y W\partial_z V\,. \tag{A.15}$$

[4] See https://m-selig.ae.illinois.edu/ads/coord_database.html.

On the other hand, the quantity Q is defined as

$$Q = \tfrac{1}{2}\left(\left\|\boldsymbol{\Omega}^r\right\|^2 - \left\|\boldsymbol{S}\right\|^2\right) \quad \text{with} \begin{cases} \boldsymbol{\Omega}^r = \dfrac{1}{2}\left(\nabla\boldsymbol{U} - (\nabla\boldsymbol{U})^T\right), & \text{(A.16a)} \\ \boldsymbol{S} = \dfrac{1}{2}\left(\nabla\boldsymbol{U} + (\nabla\boldsymbol{U})^T\right), & \text{(A.16b)} \end{cases}$$

where $\boldsymbol{\Omega}^r$ and $\boldsymbol{S}$ correspond to the antisymmetric/skew-symmetric (rotation tensor) and symmetric (shear strain tensor) parts of $\nabla\boldsymbol{U}$, respectively[5]. Their development is given by:

$$\left\|\boldsymbol{\Omega}^r\right\|^2 = \frac{1}{2}\boldsymbol{\Omega}\cdot\boldsymbol{\Omega} = \frac{1}{2}\left((\partial_y U)^2 + (\partial_x V)^2 + (\partial_z U)^2 + (\partial_x W)^2 + (\partial_z V)^2 + (\partial_y W)^2\right) - \partial_y U\partial_x V - \partial_z U\partial_x W - \partial_z V\partial_y W\,,$$

$$\left\|\boldsymbol{S}\right\|^2 = \frac{1}{2}\left((\partial_x U)^2 + (\partial_y V)^2 + (\partial_z W)^2 + (\partial_y U)^2 + (\partial_x V)^2 + (\partial_z U)^2 + (\partial_x W)^2 + (\partial_z V)^2 + (\partial_y W)^2\right) + \partial_y U\partial_x V + \partial_z U\partial_x W + \partial_z V\partial_y W\,, \quad \text{(A.17a)}$$

(A.17b)

where $\boldsymbol{\Omega}$ is the vorticity vector. After subtracting the latter quantities, one obtains the development present in equation A.15, which enables to conclude that

$$\nabla\cdot[(\boldsymbol{U}\cdot\nabla)\boldsymbol{U}] = -2Q\,. \tag{A.18}$$

In that way, the equality A.14 is demonstrated, having

$$\int_\Omega [(\boldsymbol{U}\cdot\nabla)\boldsymbol{U}]\cdot\nabla\phi_M \,\mathrm{d}\Omega = \int_\Omega 2\phi_M Q \,\mathrm{d}\Omega \blacksquare$$

A.4 Linearisation of the SUPG and grad-div stabilisations

In this section, we define the linearisation of the SUPG and grad-div terms. Due to time constrains during the writing process of this manuscript, only the main lines of the linearisation are presented. We recall from equation 1.57 that, for each element, the SUPG stabilisation reads

$$\tau_{SUPG}\mathsf{R}\cdot\left[\left(\boldsymbol{U}^h - \boldsymbol{u}_w^h\cdot\nabla\right)\boldsymbol{v}^h\right],$$

where R represents the strong residual of the Navier–Stokes moment equation. The linearisation of this term with respect to the fluid velocity state variable reads

$$\frac{\partial\left\{\tau_{SUPG}\mathsf{R}\cdot\left[\left(\boldsymbol{U}^h - \boldsymbol{u}_w^h\cdot\nabla\right)\boldsymbol{v}^h\right]\right\}}{\partial\boldsymbol{U}} = \frac{\partial\tau_{SUPG}}{\partial\boldsymbol{U}}\left[\mathsf{R}\cdot\left[\left(\boldsymbol{U}^h - \boldsymbol{u}_w^h\cdot\nabla\right)\boldsymbol{v}^h\right]\right] + \tau_{SUPG}\frac{\partial\mathsf{R}}{\partial\boldsymbol{U}}\cdot\left[\left(\boldsymbol{U}^h - \boldsymbol{u}_w^h\cdot\nabla\right)\boldsymbol{v}^h\right] + \tau_{SUPG}\mathsf{R}\cdot\left(\nabla\boldsymbol{v}^h\right). \tag{A.19}$$

Concomitantly, the linearisation of the SUPG stabilisation with respect to the fluid pressure state variable reads

$$\frac{\partial\left\{\tau_{SUPG}\mathsf{R}\cdot\left[\left(\boldsymbol{U}^h - \boldsymbol{u}_w^h\cdot\nabla\right)\boldsymbol{v}^h\right]\right\}}{\partial p} = \tau_{SUPG}\frac{\partial\mathsf{R}}{\partial p}\cdot\left[\left(\boldsymbol{U}^h - \boldsymbol{u}_w^h\cdot\nabla\right)\boldsymbol{v}^h\right]. \tag{A.20}$$

[5]For a tensor of order 2 (*i.e.*, a matrix), a skew-symmetric matrix has the property $\mathsf{A}^T = -\mathsf{A}$, while a symmetry matrix has the property $\mathsf{A} = \mathsf{A}^T$.

The same reasoning can be made for the grad-div term. Further, one must also perform this linearisation for the Spalart–Allmaras equation, in the case of using a RANS model.

Appendix B

Notes on several numerical aspects

The appendix is centred on some of the numerical aspects that were solved in this thesis. In particular, the first section is devoted to the numerical inversion of a matrix, while the second section is devoted to the numerical approach for solving the Floquet eigenproblem.

B.1 Numerical inversion of a matrix

One of the numerical challenges concerns the inversion of the matrices obtained in the different methods in this thesis. For that, we present in the following paragraphs, two approaches used in this thesis for the inversion of a system, posed as $\mathsf{A}\boldsymbol{x} = \boldsymbol{b}$: a direct approach and an iterative approach.

B.1.1 Direct approach for matrix inversion

In a first approach, one performs a direct inversion of A, providing the exact solution $\boldsymbol{x} = \mathsf{A}^{-1}\boldsymbol{b}$ after a finite amount of elementary operations. The accuracy of direct methods can be limited by the condition number of A, $\kappa(\mathsf{A}) = \|\mathsf{A}\| \cdot \left\|\mathsf{A}^{-1}\right\|$. Therefore, the exact solution is obtained for well-conditioned matrices (low κ), within a tolerance margin caused by the rounding errors. However, ill-conditioned matrices can produce erroneous solutions (see Rump (2013) for further details).

The most common method for a direct inversion is the LU factorisation, where the matrix to be inverted is decomposed as a product of a lower triangular matrix, L, and an upper triangular matrix, U (Duff *et al.*, 2007). The linear system is then solved by forward and back substitutions of the systems $\mathsf{L}\boldsymbol{y} = \boldsymbol{b}$ and $\mathsf{U}\boldsymbol{x} = \boldsymbol{y}$, respectively. The use of this approach usually passes through an already implemented library, such as UMFPACK (Davis, 2002), SuperLU (Li, 2005) or MUMPS (Amestoy *et al.*, 2001), which takes advantage of both matrix sparsity and parallel layout and covers complex-valued systems.

However, this approach becomes infeasible as the size of the system increases. This increase is usually associated to an increase on the number of elements of the space discretisation and/or to an increase on the order of the polynomial degree of the finite element functions used. The main limitation associated to this size increase is the storage requirements for L and U, making the use of a direct procedure prohibitive for the bigger matrix systems to be solved in this thesis (*e.g.*, in the DNS simulations). To bypass these obstacles, a different approach, based on an iterative resolution, is presented in the next paragraphs.

B.1.2 Iterative approach for matrix inversion

In this second approach, the inversion of A is obtained by iteratively improve the approximate solution until a given tolerance is satisfied. The term *iterative method* refers to a wide range of techniques, most of them classified either as *stationary* or *nonstationary* methods. In short, the former methods are older and simpler to understand and to implement, but usually not as effective as the latter, nonstationary methods.

In an iterative method, one starts with a guess solution $\boldsymbol{x}_0$ (often just the zero vector) and successively refines this guess in order to obtain a more accurate approximation to the linear system at each step (Simoncini *et al.*, 2007). The power of most iterative methods lies in the cheapness of each iteration, since it only involves matrix-vector product operations (with A and/or A^H). Moreover, the A matrix does not need to be explicitly available—and therefore assembled and stored—, as one only has to be able to apply the matrix-vector operation through a given function. In practice, the iterative method may be much more complicated than the multiplication of a vector by a sparse matrix. For example, this operation may include the application of a preconditioning strategy, which may also require the solution of a large linear systems, as detailed below.

Most of the current iterative methods are based on the Krylov subspace, introduced in the 1950s (Hestenes *et al.*, 1952), in which the approximate solution is searched, based on an optimality condition (Saad, 2003). This subspace can be defined as

$$\mathscr{K}^k(\mathsf{A}, \boldsymbol{r}_0) = \operatorname{span}\left\{\boldsymbol{r}_0, \mathsf{A}\boldsymbol{r}_0, \mathsf{A}^2\boldsymbol{r}_0, \ldots, \mathsf{A}^{k-1}\boldsymbol{r}_0\right\}, \tag{B.1}$$

where $\boldsymbol{r}_0 = \boldsymbol{b} - \mathsf{A}\boldsymbol{x}_0$. The approximate solution at stage k will be such that

$$\boldsymbol{x}_k \in \boldsymbol{x}_0 + \mathscr{K}^k(\mathsf{A}, \boldsymbol{r}_0). \tag{B.2}$$

The use of this iterative approach is often performed inside a Newton iteration[1], for example for time spectral methods, or at each time step, for time-marching schemes.

One of the most popular schemes present in the literature is the Generalised Minimum Residual Method (GMRES) (Saad *et al.*, 1986), an Arnoldi-based method[2] applicable to general unsymmetrical systems. This technique minimises the residual norm over all vectors in $\boldsymbol{x}_0 + \mathscr{K}^k(\mathsf{A}, \boldsymbol{r}_0)$.

Since the dimension of the subspace increases at each linear iteration, there is an increase amount of storage needed as the number of linear GMRES iterations increases. This obstacle is often bypassed in the literature by either restarting the Krylov sequence (Baker *et al.*, 2005) or truncating the Arnoldi orthogonalization.

Finally, the rate at which an iterative method converges depends greatly on the spectrum of the matrix to be inverted. Hence, iterative methods usually involve a second matrix—a preconditioner—that transforms the matrix A into one with a more favourable spectrum, *i.e.*, a matrix with a lower condition number (Barrett *et al.*, 1994). This transformation will increase the cost of each linear iteration. However, the use of a good preconditioner will improve the linear convergence, overcoming the extra cost associated to the construction of the preconditioner at each Newton iteration or time step and its application at each linear iteration. Further, in the present thesis, the construction of the preconditioner for the time-marching of the DNS simulations is based on the deterioration of its relative performance, as explained in section 1.8.4 (page 67). Therefore, its construction is not required at each time step. Different preconditioning strategies are introduced in the following paragraphs.

[1] The synergistic combination of Newton-type methods for solving nonlinear equations and Krylov subspace methods to tackle each Newton correction is often labelled as Jacobian-free Newton–Krylov methods (Knoll *et al.*, 2004), used for example in Time Spectral Methods.

[2] The Arnoldi method is a procedure for constructing an orthogonal basis of the Krylov subspace $\mathscr{K}^k(\mathsf{A}, \boldsymbol{r}_0)$.

B.1.3 Preconditioning strategies

The original problem $\mathsf{A}\boldsymbol{x} = \boldsymbol{b}$ can be transformed into an equivalent problem, based on a right preconditioning, as:

$$\mathsf{A}\mathsf{P}^{-1}\mathsf{P}\boldsymbol{x} = \boldsymbol{b} \Leftrightarrow \begin{cases} \mathsf{A}\mathsf{P}^{-1}\boldsymbol{y} &= \boldsymbol{b} \\ \mathsf{P}\boldsymbol{x} &= \boldsymbol{y} \end{cases}, \tag{B.3}$$

or based on a left preconditioning as

$$\mathsf{P}^{-1}\mathsf{A}\boldsymbol{x} = \mathsf{P}^{-1}\boldsymbol{b}\,. \tag{B.4}$$

The preconditioner strategy may also be applied to both left and right sides of A, leading to the so-called *symmetric preconditioners*. One well-known example is the symmetric successive over-relaxation (SSOR) preconditioner (Habetler *et al.*, 1961).

Theoretically, both systems give the same solution as the original system as long as the preconditioner matrix P is nonsingular. However, in practice, one has to be cautious with the termination criterion of the linear iterations, since that, for the left preconditioner, the preconditioned residual norm is evaluated as $\left\|\boldsymbol{r}_k^P\right\| = \left\|\mathsf{P}^{-1}\boldsymbol{r}_k\right\|$, whereas for the right preconditioner, it corresponds to the true residual $\left\|\boldsymbol{r}_k^P\right\| = \|\boldsymbol{r}_k\|$ (Ghai *et al.*, 2018). In general, if P is well-conditioned, both spectra of $\mathsf{A}\mathsf{P}^{-1}$ and $\mathsf{P}^{-1}\mathsf{A}$ are identical and the two approaches converge to the same solution. The details of the preconditioner implementation for the time-marching of the DNS simulations are present in section 1.8.4 (page 67)

B.2 Numerical method for solving the Floquet eigenproblem

In this section, we present the numerical approach to obtain the Floquet multipliers associated to a Floquet eigenproblem. This general approach is here applied to a fluid–structure problem.

The equations governing a periodic flow and the corresponding linearised Floquet FSI eigenproblem are presented in sections 1.4.1 and 1.4.3 (pages 31 and 34). One of the most used methods to compute the Floquet multipliers is to compute the eigenvalues of the monodromy matrix $\boldsymbol{\Phi}$, also called propagator. This matrix is defined as the operator that propagates a perturbation at an arbitrary initial time $\boldsymbol{q}'(t)$ over a period T of the vortex shedding phenomenon, such that

$$\boldsymbol{q}'(t+T) = \boldsymbol{\Phi}\boldsymbol{q}'(t)\,. \tag{B.5}$$

The matrix $\boldsymbol{\Phi}$ can be obtained by time-marching the linearised equations 1.27 (page 33) over one period for N_{dof} linearly independent initial perturbations (Peletan *et al.*, 2013), where N_{dof} represents the number of degrees of freedom of the space discretised equations. However, this approach is infeasible due to the size of the present problem (cf. table 1.5, page 49). Alternatively, $\boldsymbol{\Phi}$ can be approximated by a low-dimensional matrix, based on an Arnoldi algorithm (Arnoldi, 1951), present in algorithm 1. The method is based on the idea of creating a vector basis that is used to construct the low-dimensional approximation of $\boldsymbol{\Phi}$. The resulting basis, formed by the vectors $\boldsymbol{v}_j$, is a basis of the Krylov subspace, as proved in Saad (2011), page 131, with a basis size of N_{basis}. In order to obtain the N_{basis} vectors of the Krylov subspace basis, the linearised equations 1.27 are solved N_{basis} times, over one period. This is illustrated by the first step, in line 2, that consists in time-marching the linearised equations over one vortex shedding period, represented by the operator $\tilde{\boldsymbol{\Phi}}$. This is accomplished using the numerical scheme presented in section 1.7.10. As initial condition at $j = 1$, we impose a unitary angular displacement, *i.e.*, $\boldsymbol{v}_1 = \left[\boldsymbol{q}'_{f,1}, \theta'_1, \Omega'_1\right]^T = [\boldsymbol{0}, 1, 0]^T$. The resulting vector $\boldsymbol{w}$ is then normalised using a Gram–Schmidt process. The coefficients $h_{i,j}$ correspond to the nonzero entries of an upper Hessenberg matrix, $\boldsymbol{H}$,

representing the low-dimensional approximation of $\boldsymbol{\Phi}$ [3].

The normalisation in line 9 corresponds to the discrete norm of the FSI vector, which can be written as

$$\|\boldsymbol{w}\| = \boldsymbol{q}_f^H \mathsf{M}_f \boldsymbol{q}_f + \theta^H \theta + \Omega^H \Omega \,. \tag{B.6}$$

The low-dimensional approximation of $\boldsymbol{\Phi}$ is given in equation 6.9 of Saad (2011) by

$$\boldsymbol{V}^H \boldsymbol{\Phi} \boldsymbol{V} = \boldsymbol{H} \,, \tag{B.7}$$

where $\boldsymbol{V}$ is the $N_{dof} \times N_{basis}$ matrix whose column vectors are the Krylov basis vectors. The Hessenberg matrix has a size of $N_{basis} \times N_{basis}$. The complete spectrum of the latter matrix is computed using LAPACK (Anderson *et al.*, 1999). The leading eigenvalues of $\boldsymbol{\Phi}$, are therefore approximated by the eigenvalues of the low-dimensional matrix $\boldsymbol{H}$, noted $\sigma_H^{N_{basis}}$. At the same time, the original eigenvectors are approximated by the so-called Ritz approximate eigenvectors $\hat{\boldsymbol{q}}_H^{N_{basis}}$, calculated from the eigenvectors of the Hessenberg matrix, denoted $\boldsymbol{y}_H$:

$$\sigma \approx \sigma_H^{N_{basis}} \,, \tag{B.8a}$$

$$\hat{\boldsymbol{q}} \approx \hat{\boldsymbol{q}}_H^{N_{basis}} = \boldsymbol{V} \boldsymbol{y}_H \,. \tag{B.8b}$$

The number of Ritz eigenpairs $(\sigma_H^{N_{basis}}, \hat{\boldsymbol{q}}_H^{N_{basis}})$ usually represents a small fraction of size of the original problem, N_{dof}. However, it constitutes a good approximation of the corresponding eigenpairs of $\boldsymbol{\Phi}$, with the quality of the approximation increasing with the increase of N_{basis}. The reconstructed eigenmodes are associated to the arbitrary initial time used in the time integration over one period. For the simulations present in this thesis, the number of Arnoldi vectors is fixed at $N_{basis} = 50$ for the computations at $\alpha = 0^\circ$ and at $N_{basis} = 80$ for the computations at $\alpha \neq 0^\circ$, such that the eigenvalues of interest converge to five significant digits.

Algorithm 1 Arnoldi method with modified Gram–Schmidt orthogonalisation

1: **for** $j = 1, 2, \ldots, N_{basis}$ **do**
2: Time-marching linearised equations: $\boldsymbol{w} \leftarrow \tilde{\boldsymbol{\Phi}} \boldsymbol{v}_j$
3: Modified Gram–Schmidt orthogonalisation:
4: **for** $i = 1, 2, \ldots, j$ **do**
5: $h_{i,j} = (\boldsymbol{w}, \boldsymbol{v}_i)$
6: $\boldsymbol{w} \leftarrow \boldsymbol{w} - h_{i,j} \boldsymbol{v}_i$
7: **end for**
8: $j+1, j$ entry of the Hessenberg matrix:
9: $h_{j+1,j} = \|\boldsymbol{w}\|$
10: Normalisation of the next initial condition:
11: $\boldsymbol{v}_{j+1} \leftarrow \boldsymbol{w} / h_{j+1,j}$
12: **end for**

[3] A Hessenberg matrix is a square matrix, which is *almost* triangular. Mathematically, we define an upper Hessenberg matrix to have $h_{ij} = 0$ for all i, j with $i > j + 1$.

Appendix C

Stability analysis of a NACA0012 airfoil at low incidences

This appendix reports some additional results on both linear stability analysis around a base flow solution and a hydrodynamic Floquet stability analysis around a period flow solution.

C.1 Base flow linear stability analysis: onset of the vortex shedding

This section appears associated to the discussion of chapter 2, page 71, when the emergence of the vortex shedding phenomenon was described. In this section, some preliminary results are reported, where we use a base flow linear stability analysis to predict the onset of the vortex shedding phenomenon on the wake of a NACA0012 airfoil at low incidences. The results are only briefly discussed, due to the time constraints associated to the writing of the present thesis.

The formulation of the base flow linear stability analysis is similar to the classical formulation of the mean flow analysis, derived in section 1.4.4, page 35. However, instead of using a mean flow solution, we use a base flow solution computed using a Newton method, following the traditional approach in stability analysis of fluid flows (see for instance Fabre *et al.* (2019a)).

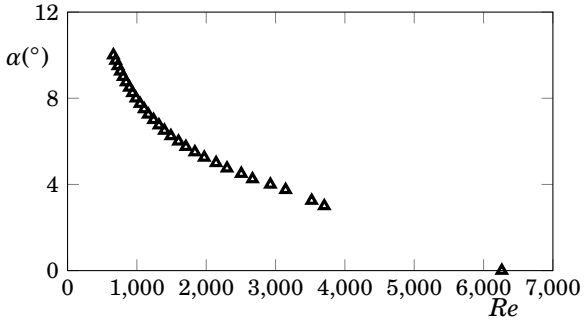

Figure C.1 – *Evolution of angle of attack of the critical Reynolds number, for which an unstable mode in a base flow linear stability analysis emergences.*

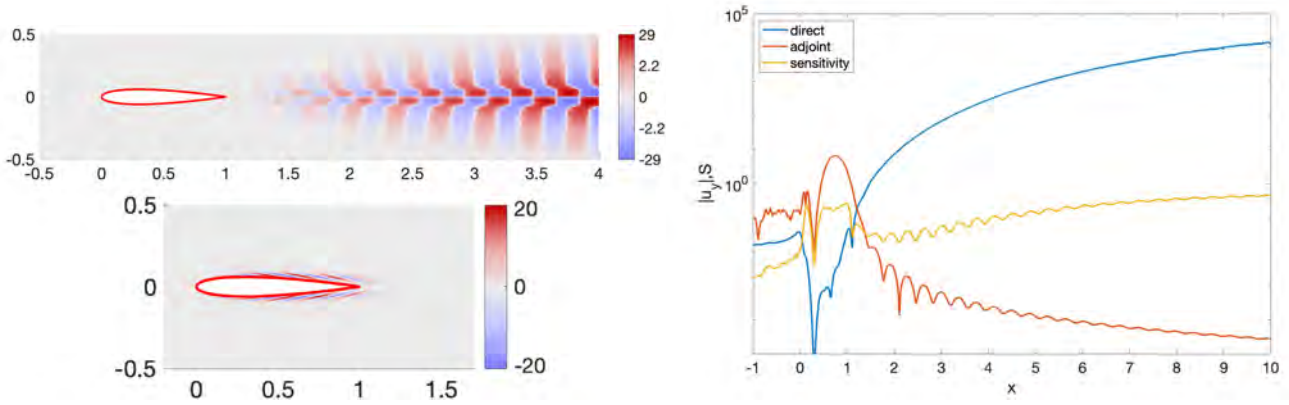

Figure C.2 – *On the left, spatial distribution of the unstable eigenmode associated to the direct LSA (top) and adjoint LSA (bottom) for* $Re = 6000$ *and* $\alpha = 0°$. *On the right, the values of these fields and the corresponding sensitivity, along the wake axis* ($y = 0$).

Figure C.1 maps the critical Reynolds number as function of the incidence. For high incidences, as the case of $\alpha = 10°$, the critical Reynolds number is as low as $Re = 660$. This value is in agreement with the literature data (see for instance figure 3.8 of Rolandi (2021)). As the incidence decreases, the critical Reynolds number increases. For the case $\alpha = 0°$, the critical Reynolds number is estimated to be around $Re = 6200$. However, this value varies with the outlet distance, as the instability is highly convected downstream. The present computations use a domain outlet at $L_x = 20$. However, no convergence of the eigenvalues was found with the increase of the outlet distance. To study this phenomenon, we sketch on the left side of figure C.2 the marginal eigenmode found from a direct linear stability analysis and the associated adjoint mode. The structural sensitivity, calculated as in Giannetti *et al.* (2007), is depicted in figure C.3 for an outlet domain at $L_x = 4$. On the right side of figure C.2, we sketch the values of these fields along the wake axis ($y = 0$). We can see that the sensitivity has an order of magnitude of 1 along the entire wake axis. Therefore, we can see that a base flow linear stability analysis will not be appropriate for computing the emergence of the vortex shedding phenomenon, even if the domain was largely extended. Two zone with important values of the sensitivity are found: a first zone near the trailing edge of the airfoil, similar to the wavemaker zone found at the rear of a circular cylinder, and a second zone on the wake of the airfoil, whose position varies with L_x.

Some preliminary results, not present here, show that the onset of the vortex shedding for cases where the instability

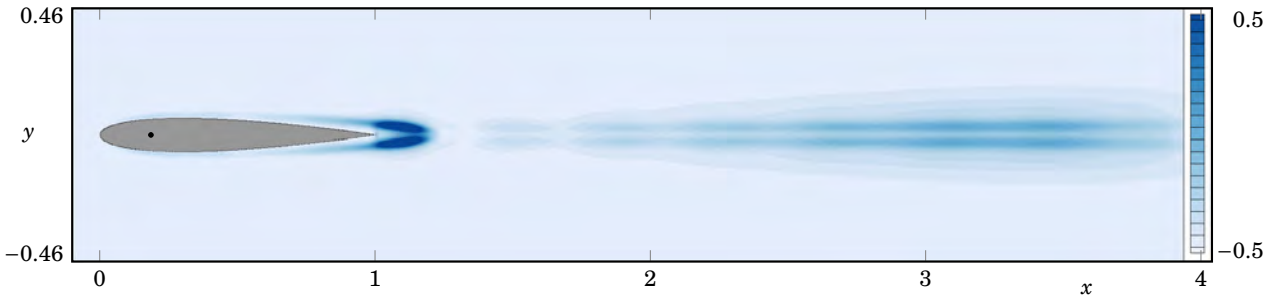

Figure C.3 – *Sensitivity field associated to the leading eigenmode of a stability analysis conducted at* $Re = 6000$ *and* $\alpha = 0°$.

is highly convected downstream could be predicted using a complex mapping strategy (Sierra *et al.*, 2020).

C.2 Hydrodynamic Floquet stability analysis: onset of three-dimensional instabilities

This section reports some additional results on the Floquet stability analysis around a periodic flow field, in particular for the angles of $\alpha = 5°$ and $\alpha = 6°$. The results for the case at $\alpha = 0°$ are reported in section 2.1.5 (page 84) for different Reynolds numbers, with the first instability appearing around $Re = 30\,000$.

For the case at $\alpha = 5°$, the three-dimensional instabilities appear around $Re = 7\,000$. The results are present in figure C.4. In particular, we observe the evolution of the absolute value of the leading Floquet multipliers as function of the spanwise wavenumber β, for three Reynolds numbers. The Floquet multipliers correspond to synchronous Floquet eigenmodes. The corresponding spanwise velocity of the Floquet eigenmode for $Re = 7\,000$ and $\beta = 50$ is also represented in the figure. We note that its spatial structure has an even RT-symmetry, as the case of the mode B of the cylinder and the NACA0012 case at $\alpha = 0°$, analysed in section 2.1.5. Further, we report the emergence of a branch of modes of type C (period-doubling) for $Re = 7\,500$. All the modes on this branch are stable.

In order to study the transition between an instability due to a mode B towards an instability due to a mode C, we do the same exercise for $\alpha = 6°$. The results are present in figure C.5. By observing the evolution of the absolute value of the leading Floquet multipliers as function of the spanwise wavenumber β, for three Reynolds numbers, we see that a marginal Floquet multiplier is found around $Re = 5\,500$ and $\beta = 70$. This time, the represented branches are associated to synchronous Floquet eigenmodes of type C, where a period doubling can be observed on the eigenmode spatial structure. The emergence of this mode C is coherent with the literature results that reported three-dimensional instabilities of type C for higher angles of attack. For example, Samuthira Pandi *et al.* (2019) reports the three-dimensional instability of type

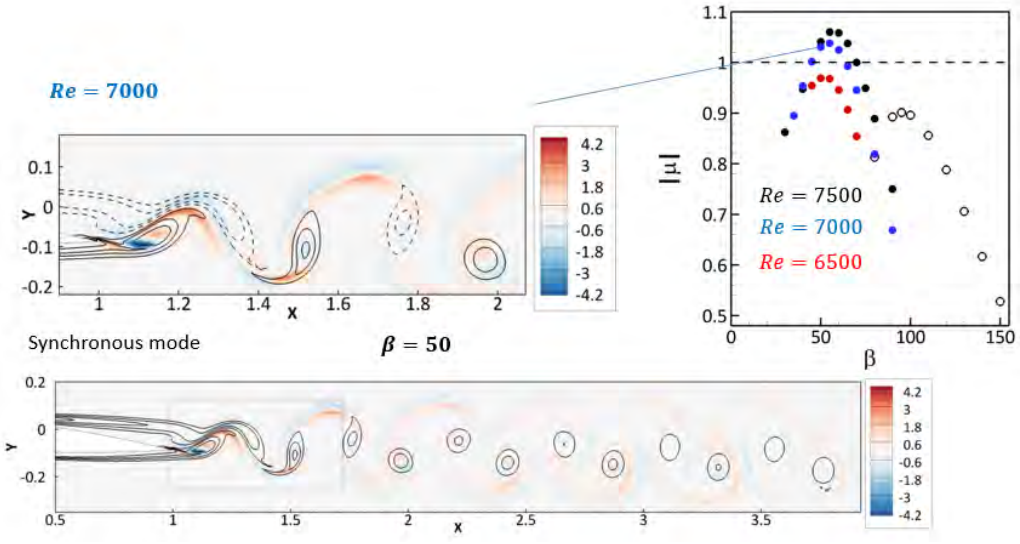

Figure C.4 – *Hydrodynamic Floquet stability analysis at $\alpha = 5°$ for three different Reynolds numbers: evolution of the magnitude of the Floquet multipliers with the forcing spanwise wavenumber (top right) and spanwise velocity of the most unstable Floquet eigenmode at $Re = 7\,000$ and $\beta = 50$.*

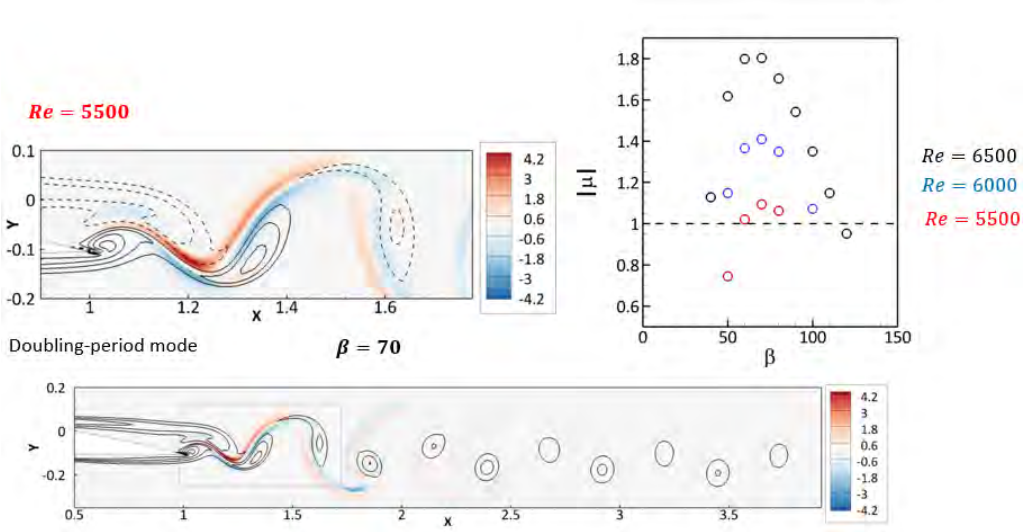

Figure C.5 – *Hydrodynamic Floquet stability analysis at $\alpha = 6°$ for three different Reynolds numbers: evolution of the magnitude of the Floquet multipliers with the forcing spanwise wavenumber (top right) and spanwise velocity of the most unstable Floquet eigenmode at $Re = 5\,500$ and $\beta = 50$.*

C for $(\alpha, Re) = (10°, 1\,280.9)$ on an Eppler 61 airfoil, while Deng *et al.* (2017) reports them for $(\alpha, Re) = (12.5°, 1\,082)$ and $(\alpha, Re) = (15°, 730)$ on a NACA0015 airfoil.

Appendix D

Notes on the approximation of the fluid transfer function via a Taylor expansion

In this appendix, we expose the different attempts that we conducted during this thesis, where we aim at approximating the fluid transfer function, present in chapters 3 and 4. The objective is to inform the future readers of the techniques that did not work on the present thesis. We only report the formulation used, due to the time constraints associated to the writing of the present thesis.

D.0.1 Taylor expansion of the fluid transfer function around origin

In this section, we present an approximation of the fluid transfer function around origin, which corresponds to the quasi-steady approximation at higher orders. For that, we recall the development previously presented in equation 1.45c, approximating the resolvent operator by a Taylor expansion around $\sigma = 0$, by assuming a small perturbation $\delta\sigma$:

$$
\begin{aligned}
&\boldsymbol{m}^T\left(\delta\sigma \mathsf{M}_f - \mathsf{L}_f\right)^{-1}(\boldsymbol{v}_\theta + \delta\sigma \boldsymbol{v}_\Omega)\bar{\theta} \\
\approx &\boldsymbol{m}^T\left[-\mathsf{L}_f^{-1} - \delta\sigma \mathsf{L}_f^{-1}\mathsf{M}_f\mathsf{L}_f^{-1} - \delta\sigma^2\left(\mathsf{L}_f^{-1}\mathsf{M}_f\right)^2\mathsf{L}_f^{-1} - \delta\sigma^3\left(\mathsf{L}_f^{-1}\mathsf{M}_f\right)^3\mathsf{L}_f^{-1} + \dots\right](\boldsymbol{v}_\theta + \delta\sigma \boldsymbol{v}_\Omega)\bar{\theta} \\
\approx &\boldsymbol{m}^T\left[-\mathsf{L}_f^{-1}\boldsymbol{v}_\theta - \left(\mathsf{L}_f^{-1}\boldsymbol{v}_\Omega + \mathsf{L}_f^{-1}\mathsf{M}_f\mathsf{L}_f^{-1}\boldsymbol{v}_\theta\right)\delta\sigma - \left(\left(\mathsf{L}_f^{-1}\mathsf{M}_f\right)^2\mathsf{L}_f^{-1}\boldsymbol{v}_\theta + \mathsf{L}_f^{-1}\mathsf{M}_f\mathsf{L}_f^{-1}\boldsymbol{v}_\Omega\right)\delta\sigma^2\right]\bar{\theta} \\
&-\boldsymbol{m}^T\left[\left(\left(\mathsf{L}_f^{-1}\mathsf{M}_f\right)^3\mathsf{L}_f^{-1}\boldsymbol{v}_\theta + \left(\mathsf{L}_f^{-1}\mathsf{M}_f\right)^2\mathsf{L}_f^{-1}\boldsymbol{v}_\Omega\right)\delta\sigma^3 + \dots\right]\bar{\theta}\,.
\end{aligned}
$$

We note that, in the first line, we used the identity $\delta\sigma\bar{\theta} = \overline{\Omega}$. In this development, in addition to the added inertia, added damping and added stiffness coefficients defined in equations 3.22c, we obtain the added coefficients for the higher orders, defined as

$$
a_i = \boldsymbol{m}^T\left(\mathsf{L}_f^{-1}\mathsf{M}_f\right)^i\mathsf{L}_f^{-1}\boldsymbol{v}_\theta + \boldsymbol{m}^T\left(\mathsf{L}_f^{-1}\mathsf{M}_f\right)^{i-1}\mathsf{L}_f^{-1}\boldsymbol{v}_\Omega\,, \tag{D.1}
$$

where the subscript $\bullet_i$ denotes the new order considered. The problem 3.1 can be approximated at order n as

$$
\sum_{i=3}^{n}\left(a_i\sigma^i\right) + (I_s + I_a)\sigma^2 + (D_s + D_a)\sigma + (K_s + K_a) = 0\,. \tag{D.2}
$$

D.0.2 Taylor expansion of the fluid transfer function around complex value

Instead of doing the Taylor development of the resolvent operator around zero, we could also consider the development around a nonzero complex value σ_0, such that $\sigma = \sigma_0 + \delta\sigma$. We start by noting that the term $\sigma \mathsf{M}_f - \mathsf{L}_f$ can be developed as

$$\sigma \mathsf{M}_f - \mathsf{L}_f = \left[\delta\sigma \mathsf{M}_f + (\sigma_0 \mathsf{M}_f - \mathsf{L}_f)\right] = (\sigma_0 \mathsf{M}_f - \mathsf{L}_f)\left[(\sigma_0 \mathsf{M}_f - \mathsf{L}_f)^{-1} \delta\sigma \mathsf{M}_f + \mathbb{1}\right].$$

In this way, the Taylor expansion around $\sigma = \sigma_0 + \delta\sigma$ reads:

$$\begin{aligned}
&\boldsymbol{m}^T \left[(\sigma_0 \mathsf{M}_f - \mathsf{L}_f)^{-1} \delta\sigma \mathsf{M}_f + \mathbb{1}\right]^{-1} (\sigma_0 \mathsf{M}_f - \mathsf{L}_f)^{-1} (\boldsymbol{v}_\theta + \sigma_0 \boldsymbol{v}_\Omega + \delta\sigma \boldsymbol{v}_\Omega)\bar{\theta} \\
\approx &\boldsymbol{m}^T \left[\mathbb{1} - \delta\sigma (\sigma_0 \mathsf{M}_f - \mathsf{L}_f)^{-1} \mathsf{M}_f + \delta\sigma^2 (\sigma_0 \mathsf{M}_f - \mathsf{L}_f)^{-2} \mathsf{M}_f^2 + \dots\right] (\sigma_0 \mathsf{M}_f - \mathsf{L}_f)^{-1} (\boldsymbol{v}_\theta + \sigma_0 \boldsymbol{v}_\Omega + \delta\sigma \boldsymbol{v}_\Omega)\bar{\theta} \\
\approx &\boldsymbol{m}^T \left[\mathsf{R}_f(\sigma_0) - \delta\sigma \mathsf{R}_f(\sigma_0)\mathsf{M}_f \mathsf{R}_f(\sigma_0) + \delta\sigma^2 (\mathsf{R}_f(\sigma_0)\mathsf{M}_f)^2 \mathsf{R}_f(\sigma_0) + \dots\right] (\boldsymbol{v}_\theta + \sigma_0 \boldsymbol{v}_\Omega + \delta\sigma \boldsymbol{v}_\Omega)\bar{\theta}.
\end{aligned}$$

We can identify the added coefficients as

$$K_a = -\boldsymbol{m}^T \left[\mathsf{R}_f(\sigma_0)(\boldsymbol{v}_\theta + \sigma_0 \boldsymbol{v}_\Omega)\right], \tag{D.3a}$$

$$D_a = -\boldsymbol{m}^T \left[-\mathsf{R}_f(\sigma_0)\mathsf{M}_f \mathsf{R}_f(\sigma_0)(\boldsymbol{v}_\theta + \sigma_0 \boldsymbol{v}_\Omega) + \mathsf{R}_f(\sigma_0)\boldsymbol{v}_\Omega\right], \tag{D.3b}$$

$$I_a = -\boldsymbol{m}^T \left[(\mathsf{R}_f(\sigma_0)\mathsf{M}_f)^2 \mathsf{R}_f(\sigma_0)(\boldsymbol{v}_\theta + \sigma_0 \boldsymbol{v}_\Omega) - \mathsf{R}_f(\sigma_0)\mathsf{M}_f \mathsf{R}_f(\sigma_0)\boldsymbol{v}_\Omega\right], \tag{D.3c}$$

$$a_i = -\boldsymbol{m}^T \left[((-i)\mathsf{R}_f(\sigma_0)\mathsf{M}_f)^i \mathsf{R}_f(\sigma_0)(\boldsymbol{v}_\theta + \sigma_0 \boldsymbol{v}_\Omega) + ((-i)\mathsf{R}_f(\sigma_0)\mathsf{M}_f)^{i-1} \mathsf{R}_f(\sigma_0)\boldsymbol{v}_\Omega\right]. \tag{D.3d}$$

The problem 3.1 can be approximated at order n as

$$\sum_{i=3}^{n} \left(a_i \sigma^i\right) + (I_s + I_a)\sigma^2 + (D_s + D_a)\sigma + (K_s + K_a) = 0. \tag{D.4}$$

Appendix E

Mean flow fluid–structure analysis based on RANS aerodynamic model

In this appendix, we summarise some of the work done on a different aerodynamic model for the present thesis. We decided to include this investigation as an appendix for two reasons: (i) in order to not overload the main chapters of this thesis and (ii) due to a lack of time to describe the last part of this investigation, where the reader will find some figures that are not commented.

In the main chapters of this thesis, we studied the fluid–structure instability arising on an airfoil with a pitch degree of freedom at transitional Reynolds numbers. In particular, a mean flow FSI linear stability analysis for both a primary equilibrium position, at $\alpha = 0^\circ$, and secondary equilibrium position, at $\alpha \neq 0^\circ$, was performed. The mean flow was obtained from either two or three-dimensional time-marching simulations.

Alternatively, we consider in this chapter a different aerodynamic model, with which we describe the mean flow field at the transitional Reynolds number of $Re = 50\,000$: the Reynolds-Averaged Navier–Stokes (RANS) equations. The laminar-turbulent transition of the flow field is either obtained via a numerical transition behaviour of the Spalart–Allmaras (SA) model, upon correct choice of the boundary free-stream condition, or via an algebraic transition model, namely the Baş–Çakmakçıoğlu (BC) model.

In that way, the objectives of this chapter are threefold: first, we present the formulation associated to the computation of a RANS mean flow solution, and we validate some numerical aspects, for the mean flow computations and for the mean flow LSA analyses. Second, we provide a physical description of the mean flow solution at $\alpha = 0^\circ$, following the two approaches for modelling the laminar-turbulent transition. Third, we carry out a mean flow linear stability analysis at $\alpha = 0^\circ$, first for a purely-hydrodynamic formulation, followed by the FSI formulation, with the obtained RANS mean flow solution. Forth, we describe the mean flow fields for $\alpha > 0^\circ$, namely the evolution of the mean flow aerodynamic moment with the incidence.

E.1 Problem description

E.1.1 Reynolds-averaged Navier–Stokes equations

The Reynolds-Averaged Navier–Stokes (RANS) approach has become a very common tool used in industry, as practical flows in aerospace applications have a partial or fully turbulent character. Instead of solving all the turbulent scales with a

DNS, a RANS simulation is based on the decomposition of the instantaneous flow quantities into their time-averaged and instantaneous fluctuating quantities, where the latter correspond to the small turbulent scales, which are not resolved, but modelled. The scale of the turbulent motions being far larger than the supra-molecular scale, the Navier–Stokes model remains valid in the turbulent regime. Although the concept of turbulence has evolved during the last decade, Hinze (1975) has delineated it in the following way:

> *Turbulent fluid motion is an irregular condition of flow in which the various quantities show a random variation with time and space coordinates, so that statistically distinct average values can be discerned.*

The study of turbulent flows is complex due to their inherent properties of unsteadiness, three-dimensionality and sensitivity to perturbations. To tackle these difficulties, a statistical approach, introduced by Reynolds (1895), has become the most suited form to treat this problem. The decomposition of the flow field as the sum of a mean value and a fluctuation can be posed as

$$\boldsymbol{q}_f(\boldsymbol{X},t) = \overline{\boldsymbol{q}}_f(\boldsymbol{X}) + \boldsymbol{q}'_f(\boldsymbol{X},t), \tag{E.1}$$

where the mean flow $\overline{\boldsymbol{q}}_f(\boldsymbol{X})$ can be defined, under the hypothesis of ergodicity[1], as

$$\overline{\boldsymbol{q}}_f(\boldsymbol{X}) = \lim_{T\to\infty} \frac{1}{T} \int_0^T \boldsymbol{q}_f(X,Y,Z,t)\,\mathrm{d}t\,. \tag{E.2}$$

The fluctuation $\boldsymbol{q}'_f$ has, by definition, a zero time average, *i.e.*, $\overline{\boldsymbol{q}'}_f = 0$. Under the scope of the present thesis, we also make the hypothesis that the mean flow is statistically homogeneous in the $\boldsymbol{e}_z$-direction, which reads

$$\overline{\boldsymbol{q}}_f(X,Y) = \lim_{T,Z\to\infty} \frac{1}{Z} \int_0^Z \frac{1}{T} \int_0^T \boldsymbol{q}_f(X,Y,Z,t)\,\mathrm{d}t\mathrm{d}Z\,. \tag{E.3}$$

Since the RANS computations are conducted in a two-dimensional domain, the $\boldsymbol{e}_z$-component of the different vectorial quantities is omitted from the notation. After introducing the Reynolds decomposition on equations 1.5 and averaging the result, ones arrives to the RANS equations:

$$\left(\left[\overline{\boldsymbol{U}} - \overline{\boldsymbol{U}}_w\right]\cdot\nabla\right)\overline{\boldsymbol{U}} - \nabla\cdot\boldsymbol{\sigma}\left(\overline{\boldsymbol{U}},\overline{p}\right) + \nabla\cdot\left[\overline{\boldsymbol{U}'\otimes\boldsymbol{U}'}\right] = \boldsymbol{0}\,, \tag{E.4a}$$

$$\nabla\cdot\overline{\boldsymbol{U}} = 0\,, \tag{E.4b}$$

with $\overline{\boldsymbol{U}}(\boldsymbol{X},t) = \left[\overline{U},\overline{V}\right]^T$ the mean flow velocity, with a null component on the spanwise direction, $\overline{\boldsymbol{U}}_w = U^\infty\left[-\cos\left(\bar{\theta}\right),\sin\left(\bar{\theta}\right)\right]^T$ the mean rigid-body velocity field and $\overline{\boldsymbol{U}'\otimes\boldsymbol{U}'}$ the *Reynolds stress* tensor. These equations form a system which is not closed, contrary to the Navier–Stokes equations. Additional modelling is therefore necessary in order to close the problem. The Reynolds stresses represent extra terms—six in three dimensions, three in two dimensions, since the tensor is symmetric—composed of one-point correlations of velocity fluctuations. These additional terms appear as a consequence of the nonlinearity of the convective term, but can be viewed as a diffusive flux, justifying their designation as *stresses*. The trace of this tensor is twice the turbulent kinetic energy, $k = \frac{1}{2}\left(\overline{U'U'} + \overline{V'V'}\right)$.

Based on the RANS equations, one can extend the reasoning to the *Unsteady Reynolds-Averaged Navier–Stokes*

[1] Ergodicity implies that time average (obtained from a *sufficiently* long realisation) and ensemble average (obtained from a set of realisations) are equivalent. See (Frisch, 1995, p. 49) for further insight.

equations (URANS). Indeed, while equation E.1 is mathematically well defined, one could never respect the limit requirement on T, present in equations E.2 and E.3. In practice, it is sufficient to consider T much longer relative to the maximum period of the fluid fluctuation. Further, there are some flows for which the mean flow may contain a slow variation with time that are not turbulent in nature, as a mean vortex shedding phenomenon. In that sense, equation E.1 can be modified to accommodate such application:

$$\boldsymbol{q}_f(\boldsymbol{X},t) = \overline{\boldsymbol{q}}_f(\boldsymbol{X},t) + \boldsymbol{q}'_f(\boldsymbol{X},t). \tag{E.5}$$

Following this decomposition, ones arrives to the URANS equations:

$$\frac{\partial \overline{\boldsymbol{U}}}{\partial t} + \overline{\boldsymbol{\Omega}} \times \overline{\boldsymbol{U}} + \left(\left[\overline{\boldsymbol{U}} - \overline{\boldsymbol{U}}_w\right]\cdot\nabla\right)\overline{\boldsymbol{U}} - \nabla\cdot\boldsymbol{\sigma}\left(\overline{\boldsymbol{U}},\overline{p}\right) + \nabla\cdot\left[\overline{\boldsymbol{U}'\otimes\boldsymbol{U}'}\right] = \boldsymbol{0}, \tag{E.6a}$$

$$\nabla\cdot\overline{\boldsymbol{U}} = 0, \tag{E.6b}$$

where, this time, $\overline{\boldsymbol{U}}_w = \overline{\boldsymbol{\Omega}} \times (\boldsymbol{X} - \boldsymbol{X}_{EC}) + \dot{\overline{\boldsymbol{X}}}_{EC}$. Due to time constrains during the writing process of this manuscript, all the results present in this appendix are for RANS computations.

In order to compute all the mean flow properties of the turbulent flow under consideration, one has to make further assumptions on the Reynolds stress unknowns. We proceed by posing an extra hypothesis over the Reynolds stress, introduced by Boussinesq, sought to mimic the molecular gradient-diffusion process. The Boussinesq hypothesis (Boussinesq, 1877; Schmitt, 2007), often called the "Boussinesq approximation"—which leads to confusion with a completely different concept associated with natural convection—states that small-scale turbulent stress should be linearly proportional to the mean (large-scale) strain rates. In this regard, it can be hypothesised that, for incompressible fluids, the nondimensional Reynolds stress tensor can be approximated as[2]

$$\overline{\boldsymbol{U}'\otimes\boldsymbol{U}'} \approx -2\nu_t\boldsymbol{S}\left(\overline{\boldsymbol{U}}\right) + \frac{2}{3}k\mathbb{1}, \tag{E.7}$$

where ν_t is the turbulent eddy viscosity. The RANS equations can therefore be posed as

$$\left(\left[\overline{\boldsymbol{U}} - \overline{\boldsymbol{U}}_w\right]\cdot\nabla\right)\overline{\boldsymbol{U}} + \nabla\overline{p} - 2\nabla\cdot\left[(\nu+\nu_t)\boldsymbol{S}\left(\overline{\boldsymbol{U}}\right)\right] = \boldsymbol{0}, \tag{E.8a}$$

$$\nabla\cdot\overline{\boldsymbol{U}} = 0. \tag{E.8b}$$

The closure of the model is presented next. Henceforward, the notation $\bar{\bullet}$ is dropped to simplify the notation.

E.1.2 Spalart–Allmaras closure model

The resulting RANS equations represent a system that ultimately need to be supplemented with a turbulence model closure, as the Baldwin–Lomax model (Baldwin *et al.*, 1978), the k–ω model (Wilcox, 1994), the k–ϵ model (Jones *et al.*, 1972), the SST k–ω model (Menter, 1993, 1994) or the Spalart–Allmaras (SA) model (Spalart *et al.*, 1992, 1994), among others. A summary of the main turbulence models from the literature can be found on the online Turbulence Modelling Resource provided by NASA (Rumsey, 2021). These closures were often built to model a fully turbulent flow. In the present case, where the flow field remains laminar over a large portion of the airfoil surface (including in the separation zone),

[2] Consider $c = 1$ and $U^\infty = 1$ for the nondimensionalisation of the present variables.

the traditional RANS approaches fail to capture the location and extent of the transition region and consequently, fail to capture the laminar separation phenomenon. In order to overcome this problem, aerodynamicists have tried to either complement the RANS turbulence models with further equations, dedicated to the prediction of the laminar-turbulent transition onset, or to adjust the turbulence models and their initial conditions, without further additional equations. We first introduce in this section a modified version of the SA model, with which the laminar-turbulent transition can be predicted upon careful choice of the inlet conditions. An alternative option is proposed in the next section, where an additional transitional model is considered.

The SA model is referred to as a one-equation model since it involves only one additional transport equation for the calculation of the turbulence eddy viscosity, the turbulent kinetic energy being taken into account on the pressure term. This form of transport equation is attractive due to its simplicity of implementation and less demanding computational requirements, when compared to other models as the k–ω or the k–ϵ. The model has been shown to be accurate for most attached and mildly separated aerodynamic flows (Celić *et al.*, 2006; Freeman *et al.*, 2014).

The original model was proposed by Spalart *et al.* (1992, 1994) with originally four versions, the first one applicable only to free shear flows and a last one applicable to viscous flows configurations past solid bodies and with laminar regions and a specified turbulent transition location. In subsequent investigations, the SA model was improved in order to increase numerical stability and to describe natural laminar-turbulent transition. The modified model used in the present thesis is based on the modifications introduced by Olivier (2008), Allmaras *et al.* (2012) and Crivellini *et al.* (2013, 2014) and is detailed on the appendix A of Franceschini (2019). The main modifications of the SA model aim to increase the numerical convergence and stability of the discrete system of equations, by ensuring the positivity of certain terms of the model, as the Spalart–Allmaras turbulent variable $\tilde{\nu}$. The additional Spalart–Allmaras equation reads:

$$\frac{\partial \tilde{\nu}}{\partial t} + ([\boldsymbol{U} - \boldsymbol{U}_w]\cdot\nabla)\,\tilde{\nu} = s + \nabla\cdot\left(\eta\nabla\tilde{\nu}\right), \tag{E.9}$$

where s represents a nonlinear source term and η a diffusion coefficient. The relation between the turbulent variable and the turbulent eddy viscosity is given by

$$\nu_t = f_{v1}\max(0, \tilde{\nu}), \tag{E.10}$$

whereas the diffusion coefficient and production terms are defined with the help of $\chi = \tilde{\nu}/\nu$ as

$$\eta = \begin{cases} \nu(1+\chi)/\sigma, & \chi \geq 0 \\ \nu(1+\chi+\chi^2)/\sigma, & \chi < 0 \end{cases}. \tag{E.11}$$

The nonlinear source term s is composed by the sum of three terms, the production, the cross-diffusion and the destruction terms, given by

$$s = \begin{cases} c_{b1}\tilde{\Omega}\tilde{\nu} & + \frac{c_{b2}}{\sigma}\|\nabla\tilde{\nu}\|^2 - f_w c_{w1}\frac{\tilde{\nu}^2}{d^2}, & \chi \geq 0 \\ c_{b1}\Omega\tilde{\nu}g_n & + \frac{c_{b2}}{\sigma}\|\nabla\tilde{\nu}\|^2 + c_{w1}\frac{\tilde{\nu}^2}{d^2}, & \chi < 0 \end{cases}. \tag{E.12}$$

The remaining functions are defined as

$$\tilde{\Omega} = \Omega + \frac{\tilde{\nu}}{\kappa^2 d^2} f_{v2} \quad \text{with} \quad \Omega = \sqrt{\|\nabla\times\boldsymbol{U}\|^2}, \tag{E.13}$$

$$f_{v2} = 1 - \frac{\chi}{1+\chi f_{v1}}, \tag{E.14}$$

$$f_{v1} = \frac{\chi^3}{\chi^3 + c_{v1}^3}, \tag{E.15}$$

$$f_w = g\left[\frac{1+c_{w3}^6}{g^6+c_{w3}^6}\right]^{1/6}, \tag{E.16}$$

$$g = r + c_{w2}(r^6 - r), \tag{E.17}$$

$$g_n = 1 - \frac{1000\chi^2}{1+\chi^2}, \tag{E.18}$$

and

$$r^* = \frac{\tilde{\nu}}{\tilde{S}\kappa^2 d^2},\ r = \begin{cases} r_{max}, & r^* < 0 \\ r^*, & 0 \le r^* < r_{max} \\ r_{max}, & r^* \ge r_{max} \end{cases}, \tag{E.19}$$

with the constants defined as

$$\sigma = 2/3,\ c_{b1} = 0.1355,\ c_{b2} = 0.622,\ \kappa = 0.41,\ c_{w1} = c_{b1}/\kappa^2 + (1+c_{b2})/\sigma,\ c_{w2} = 0.3,\ c_{w3} = 2,\ c_{wv1} = 7.1,\ \text{and}\ r_{max} = 10. \tag{E.20}$$

The variable d represents the distance to the wall[3]. The variable Ω is modified with a user defined parameter M, to numerically avoid performing the square root of numbers with an order of magnitude of the machine precision, such that:

$$\Omega = \sqrt{\|\nabla \times \boldsymbol{U}\|^2 + M^2} - M.$$

This parameters is fixed at 10^{-4}. We note that the function Ω is differentiable and retains the properties $\Omega > 0$ and $\Omega = 0$ for $\nabla \times \boldsymbol{U} = 0$.

An additional modification, proposed by Spalart *et al.* (2020) is taken into account, where the constant c_{w2}, responsible for controlling the skin friction, becomes a variable depending on the fluid space as

$$c_{w2} = c_{w4} + \frac{c_{w5}}{\left(\chi/40+1\right)^2}, \tag{E.21}$$

with $c_{w4} = 0.21$ and $c_{w5} = 1.5$.

The additional initial and boundary conditions associated to the SA transport equation can be posed as

$$\tilde{\nu}(\boldsymbol{X}, 0) = \tilde{\nu}_0(\boldsymbol{X}) \quad \boldsymbol{X} \in \Omega_f, \tag{E.22a}$$

$$\tilde{\nu}(\boldsymbol{X}, t) = \tilde{\nu}^\infty \quad \boldsymbol{X} \in \Gamma_{in}, \tag{E.22b}$$

$$\tilde{\nu}(\boldsymbol{X}, t) = 0 \quad \boldsymbol{X} \in \Gamma_w, \tag{E.22c}$$

$$\nabla\tilde{\nu}\cdot\boldsymbol{n}_\infty = 0 \quad \boldsymbol{X} \in \Gamma_{out}, \tag{E.22d}$$

where $\tilde{\nu}_0$ is an initial condition field and $\tilde{\nu}^\infty$ is the inlet value condition. The latter was originally fixed around 3ν to 5ν, as the target applications were fully turbulent, with a flow that was essentially turbulent everywhere vorticity exits. Subsequent works have noticed that the SA model, due to a purely numerical artefact, was able to capture a laminar-turbulent transition when $\tilde{\nu}^\infty$ is sufficiently small (Rumsey, 2007). Other models, as the k–ϵ model, has shown a similar transition behaviour (Rumsey *et al.*, 2006). The presence of a laminar separation bubble on over an airfoil was studied by Crivellini *et al.* (2013, 2014) by decreasing the $\tilde{\nu}^\infty$ up to zero. This approach is illustrated in the preliminary results, in section E.2.3, page 228.

[3]The numerical computation of the distance is based on the Poisson equation method. See for instance (Tucker, 2003).

E.1.3 Turbulence transition model

Instead of taking advantage of a purely numerical feature of the SA model for capturing the laminar separation, one can introduce a turbulence transition model with the aim of controlling the turbulence production on the field. In a general sense, the RANS transition models can be divided into two main class of models. In a first class, one finds models built from first principles and physical arguments, as the k_T–k_L–ω model of Walters *et al.* (2008), based on the concept of laminar kinetic energy. In a second class, one finds models based on the combination of experimental correlations with locally formulated transport equations. These models include the γ–$Re_{\theta t}$ model for the SST k–ω turbulence closure (Menter *et al.*, 2006; Langtry *et al.*, 2006, 2009; Menter *et al.*, 2015) or for the Spalart–Allmaras closure (Medida *et al.*, 2011; D'Alessandro *et al.*, 2017b,a), among others. The comparison between different RANS based transition models can be found in Abdollahzadeh *et al.* (2017); Kim *et al.* (2019); Lopes *et al.* (2020).

The aforementioned models need the resolution of additional transport equations, usually associated to an additional computational expense. An alternative option is the use of algebraic models, known as zero-equation models, where the transition is controlled by a scalar equation depending on several flow field characteristics. In the present thesis, we implemented the Baş–Çakmakçıoğlu (BC) model, originally proposed in Baş *et al.* (2013); Çakmakçıoğlu *et al.* (2018) and modified in Çakmakçıoğlu *et al.* (2020); Mura *et al.* (2020). The idea is to multiply the production term s in the Spalart–Allmaras equation E.9, by an intermittency function, γ_{BC}, responsible for damping the turbulence production until some transition onset criterion is achieved. The intermittency function, valued between 0, enforcing no production in SA equation, and 1, unchanged the SA production, is defined as

$$\gamma_{BC} = 1 - \mathrm{e}^{\left(-\sqrt{\tau_1}-\sqrt{\tau_2}\right)}, \tag{E.23}$$

where the τ_1 and τ_2 are defined as

$$\tau_1 = \frac{\max(Re_\theta - Re_{\theta c}, 0)}{\chi_1 Re_{\theta c}}, \tag{E.24a}$$

$$\tau_2 = \max\left(\chi_2 \frac{\nu_t}{\nu}, 0\right), \tag{E.24b}$$

and the momentum thickness Reynolds numbers defined as

$$Re_\theta = \frac{d^2 S}{2.193\nu}, \tag{E.25a}$$

$$Re_{\theta c} = 803.73(Tu_\infty + 0.6067)^{-1.027}, \tag{E.25b}$$

with $\chi_1 = 0.002$, $\chi_2 = 50$ and $Tu_\infty = 0.1\%$ calibration constants. The critical momentum thickness Reynolds number, $Re_{\theta c}$, is based on an empirical correlation based on zero pressure gradient flat plate from Menter *et al.* (2006). The value of $\tilde{\nu}^\infty$ can be set between 0.015ν and 0.025ν. We fix it to its lower value. The Tu_∞ represents the freestream turbulent intensity, in percent. Originally, in other RANS models, as the SST k–ω, this value is calculated locally using the turbulent kinetic energy, k, to then be injected in the transition models. However, the SA model does not have the ability to calculate the local turbulent kinetic energy and thus the local Tu_∞. Inspired by Medida (2014), which coupled the SA model with a γ–$Re_{\theta t}$ transition model, the authors of the BC model considered a constant Tu_∞ over the entire field.

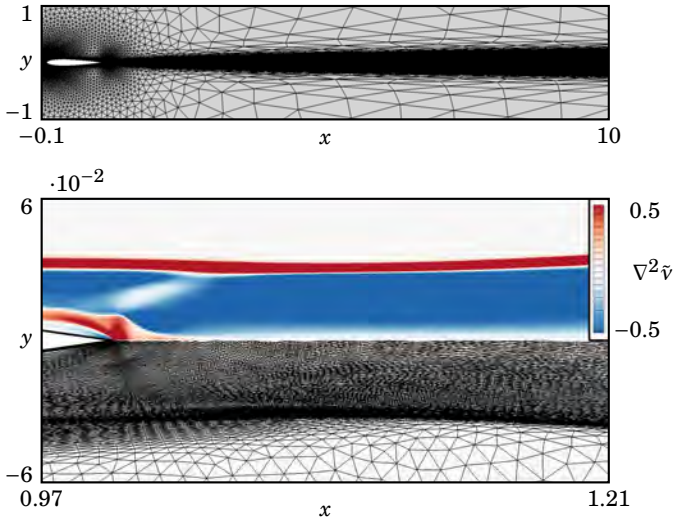

Triangle number	200 258
P_2 space size	401 980
P_1 space size	100 861
$[P_2]^2/P_1/P_2$ space size	1 306 801

Figure E.1 & Table E.1 – *On the left, visualisation of the RANS mesh on the wake of the airfoil (top) and near the trailing edge (bottom), where the trace of the Hessian of Spalart–Allmaras variable, which corresponds to its Laplacian, $\nabla^2\tilde{\nu}$, is depicted. On the right, the number triangles of a typical RANS mesh for $Re = 50\,000$ and $\alpha = 0°$, along with the size of the P_2, P_1, and RANS FEM spaces.*

E.2 Numerical aspects and preliminary results

E.2.1 Meshes for two-dimensional RANS computations

We present here the numerical strategy for constructing the two-dimensional mesh for RANS computations. The generation of the RANS meshes follows the same principles detailed in chapter 1, excepting the fact that the mesh is now adapted in the complete domain, namely on the wake of the airfoil up to the outlet boundary, as present in figure E.1. This decision is mainly due to the stiffness of the Spalart–Allmaras model, when considering $\tilde{\nu}^\infty = 0$. More precisely, the sharp variations of $\tilde{\nu}$ need to be accurately approximated for the computations to converge. Since the mesh procedure is based on the Hessian of the considered fields, we decided to represent one of its components: the trace of the Hessian associated to $\tilde{\nu}$, which corresponds to the Laplacian of $\tilde{\nu}$. Along with the adapted mesh, this field near the trailing edge region is depicted on the bottom left of figure E.1, for $Re = 50\,000$ and $\alpha = 0°$. One can see that the adaptation procedure has refined in the zones where $\nabla^2\tilde{\nu}$ has a high absolute value.

The general dimensions of the domain are identical to the two-dimensional computations, except the height of the first cell, fixed to 10^{-5}, with an expansion ratio of 1.075, so that $y^+ \sim O(1)$ for the flow regimes in the present manuscript. The anisotropic factor is fixed at 20. A summary of the main figures for the $Re = 50\,000$ and $\alpha = 0°$ case is present in table E.1. The computations for different incidences were carried out by changing the boundary condition associated to the airfoil velocity. The adaptation to the corresponding fields is made such that the number of triangles is kept roughly constant ($\pm 10\,000$ triangles).

E.2.2 Mesh convergence

The convergence of the RANS meshes is exemplified here for a numerical simulation using the SA-BC model for $Re = 50\,000$ and $\alpha = 0°$. Table E.2 summarises the details of the three meshes compared and their associated results.

Mesh	# triangles	Anisotropic factor	C_D	L_{recirc}	X_d^{up}	Divergence mode	Flutter mode
M_0^{RANS}	132380	10^6	0.020093	0.067609	0.672192	0.195026	$-0.157012+0.536747$i
$\boldsymbol{M_1^{RANS}}$	192780	20	0.020097	0.067704	0.664279	0.194638	$-0.157101+0.536985$i
M_2^{RANS}	290174	10	0.020097	0.067716	0.666270	0.194451	$-0.157208+0.536636$i

Table E.2 – *Convergence of the mean flow RANS properties and corresponding FSI eigenvalues for the SA-BC model at* $Re = 50000$ *and* $\alpha = 0°$.

Three different values of anisotropic factor were used in the mesh adaptation process: a first one fixed at 10^6, leading to a fully anisotropic mesh, and two lower values (20 and 10), leading to less "squeezed" cells and therefore meshes with a higher number of elements. For reference, an isotropic mesh corresponds to the value of 1. In regards to the present results, all three meshes present and adequate spatial resolution in order to capture the flow behaviour. However, it was observed that the Newton method (presented next) used to obtain the RANS solutions has numerically harder to converge when an excessive anisotropy on the mesh was considered. For that reason, mesh M_1^{RANS} has chosen, as represented the best equilibrium between the number of elements and the anisotropic factor.

E.2.3 Newton method

The steady RANS system can be put as

$$\boldsymbol{R}_{RANS}\left(\boldsymbol{q}_f\right) = \boldsymbol{0}. \tag{E.26}$$

This system represents a nonlinear time-independent problem, that can be solved with the help of a Newton method, similar to the systems solved in section 1.7.8 (page 58). However, as the initial solution is generally not sufficiently near the searched solution, a relaxation coefficient, $0 < \gamma_{Newton} \leq 1$, is added to the method. As γ_{Newton} tends to 1, the Newton tends to an exact the Newton method. At the nonlinear iteration i, the state vector correction of the next iteration, $\delta\boldsymbol{q}_f^{i+1}$,

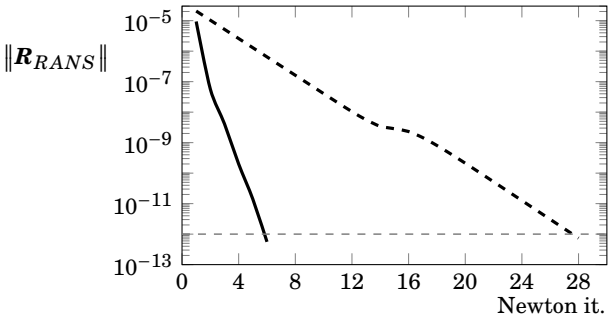

Figure E.2 – *Evolution of the RANS equations residual with the nonlinear Newton iterations at* $Re = 50000$ *for two cases: case 1 (solid line), for a computation from* $\alpha = 0°$ *to* $\alpha = 0.05°$*, with a relaxation parameter of* $\gamma_{Newton} = 1$*; case 2 (dashed line), for a computation from* $\alpha = 0°$ *to* $\alpha = 0.11°$*, with a relaxation parameter of* $\gamma_{Newton} = 0.5$*. The absolute tolerance, represented by the dashed grey line is fixed at* 10^{-12}.

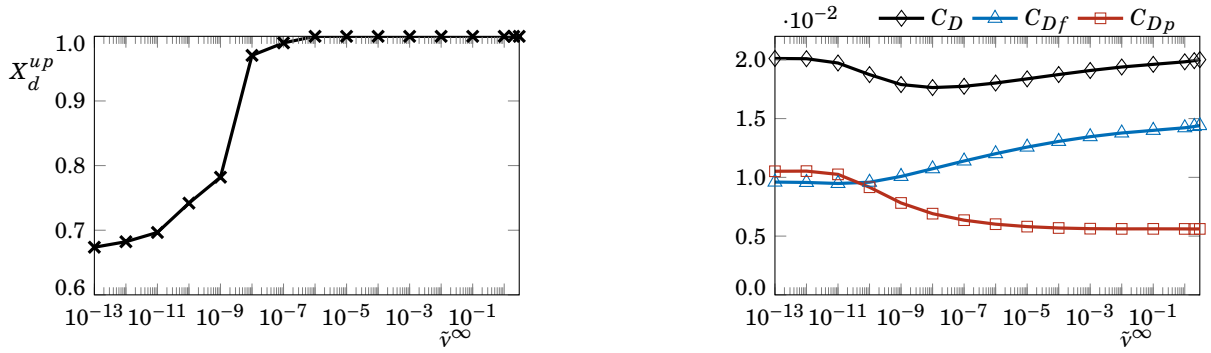

(a) **(b)**

Figure E.3 – *Variation of the abscissa of the upper boundary layer separation point, on the left, and variation of C_D, C_{Df} and C_{Dp} coefficients, on the right, with $\tilde{\nu}^{\infty}$, for the SA model at $Re = 50\,000$ and $\alpha = 0°$.*

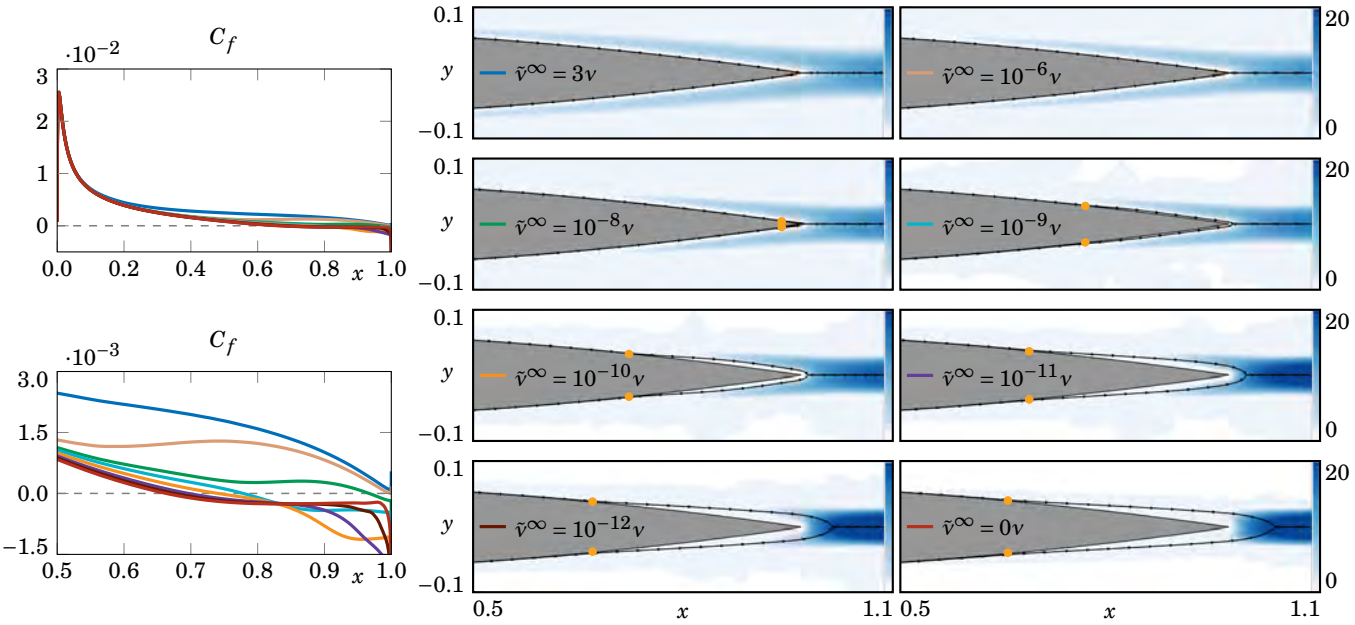

Figure E.4 – *On the left, variation of the C_f distribution over the airfoil upper surface with $\tilde{\nu}^{\infty}$. On the right, the corresponding fields of ν_t/ν, with the yellow dots representing the separation positions.*

is computed by solving a linear system posed as

$$\left.\frac{\partial \boldsymbol{R}_{RANS}}{\partial \boldsymbol{q}_f}\right|_{\boldsymbol{q}_f=\boldsymbol{q}_f^i} \delta \boldsymbol{q}_f^{i+1} = -\boldsymbol{R}_{RANS}\left(\boldsymbol{q}_f^i\right). \tag{E.27}$$

The solution of the next nonlinear iteration is then computed as $\boldsymbol{q}_f^{i+1} = \boldsymbol{q}_f^i + \gamma_{Newton}\delta\boldsymbol{q}_f^{i+1}$. The conclusion of the algorithm is based on the absolute discrete norm of the nonlinear residual, which is required to be inferior to 10^{-12}.

An example of the nonlinear convergence with the iteration number is depicted in figure E.2 at $Re = 50\,000$ for two cases: case 1 (solid line), for a computation from $\alpha = 0°$ to $\alpha = 0.05°$, with a value of $\gamma_{Newton} = 1$ for the relaxation

parameter; case 2 (dashed line), for a computation from $\alpha = 0°$ to $\alpha = 0.11°$, with a value of $\gamma_{Newton} = 0.5$. The relaxation parameter is essential, as the case two did not converge for $\gamma_{Newton} = 1$.

The solution of the SA-BC model is obtained from an initial solution using the SA model with $\tilde{\nu}^{\infty} = 0$. In turn, the SA model solution for $\tilde{\nu}^{\infty} = 0$ is obtained by slowly decreasing the $\tilde{\nu}^{\infty}$ from a fully turbulent case at $\tilde{\nu}^{\infty} = 3\nu$, towards the null value. This descent is illustrated in figure E.3, where, on the left figure, the abscissa of the separation point of the upper boundary layer, X_d^{up}, is sketched as function of $\tilde{\nu}^{\infty}$. This separation point does not exist for the cases $\tilde{\nu}^{\infty} > 10^{-8}\nu$ and tends to $X_d^{up} = 0.67$ as $\tilde{\nu}^{\infty}$ tends to zero. The associated drag coefficient, C_D, is depicted in figure E.3b, where the corresponding friction and pressure components, C_{Df} and C_{Dp}, respectively, are also presented. One can see that, for high turbulent cases, the drag coefficient is dominated by the frictional component, as the boundary layer is mostly turbulent. As $\tilde{\nu}^{\infty}$ tends to zero, the emergence of the separation is accompanied with an increase of the pressure component and a decrease of the frictional component, up to the case $\tilde{\nu}^{\infty} = 0$, where both contributions are of equal importance.

Figure E.4 shows the ν_t/ν fields for eight different values of $\tilde{\nu}^{\infty}$ and their corresponding skin friction distribution C_f over the upper surface. A zoom of the C_f, on the second half of the airfoil enables to identify the curve associated to $\tilde{\nu}^{\infty} > 10^{-8}\nu$ as the first one with a negative C_f, near the trailing edge, coherent with the emergence of the separation points on the airfoil surface.

E.2.4 Spalart–Allmaras model validation

The validation of the Spalart–Allmaras model is made with respect to one of the validation cases present in Crivellini *et al.* (2014): the Eppler E387 airfoil, at $Re = 100\,000$ and $\alpha = 6°$. The mesh was generated in a similar way as for the NACA0012 airfoil, detailed previously, using the data set points for the airfoil present in McGhee *et al.* (1988). The trailing edge was rounded up at $X = 0.98$, due to numerical reasons. For the case $\tilde{\nu}^{\infty} = 0$, the pressure coefficient distribution, C_p, on the airfoil surface is depicted on the left of figure E.5. The present results, in the blue line, are in good agreement with the ones from Crivellini *et al.* (2014), represented by the red lines. Additionally, experimental data from McGhee *et al.* (1988) is also depicted by the black circles. The major difference is present on the upper surface around $X = 0.6$, where

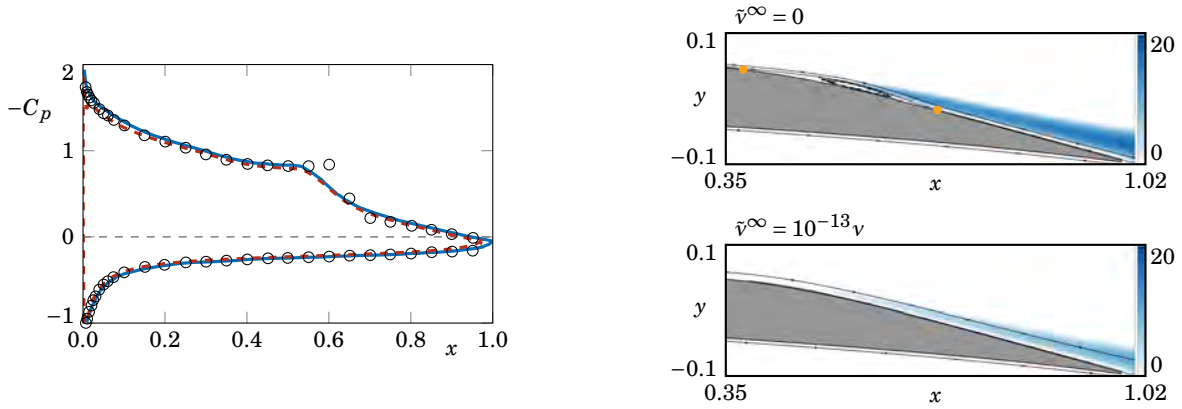

Figure E.5 – *Validation of the Spalart–Allmaras model on the Eppler E387 airfoil at $Re = 100\,000$ and $\alpha = 6°$: on the left, the C_p distribution over the airfoil for the present results (solid blue line), for Crivellini* et al. *(2014) (dashed red lines) and for experimental data from McGhee* et al. *(1988) (black circles). On the right, the ν_t/ν field for the cases $\tilde{\nu}^{\infty} = 0$ and $\tilde{\nu}^{\infty} = 10^{-13}\nu$, with the yellow dots representing the separation and reattachment positions of the former case.*

a plateau of the C_p is found. The constant value is associated to the presence of a recirculation bubble, which length is underestimated by the numerical simulations. The ν_t/ν field of the present simulation is depicted on the top right of figure E.5, where a zoom on this separated zone was made. The recirculation bubble is illustrated by the isolines of velocity. The separation, present at $X_d^{up} = 0.37$ is followed by a transition to a turbulence regime, where the values of ν_t/ν start to increase, followed by a turbulent reattachment at $X_r^{up} = 0.68$.

To illustrate the sensitivity of the SA model to $\tilde{\nu}^\infty$, the same representation is present on the bottom right of figure E.5, for $\tilde{\nu}^\infty = 10^{-13}\nu$. In this case, a recirculation zone is not present since the boundary layer does not separate and the transition of the boundary layer occurs while the flow is attached to the airfoil surface.

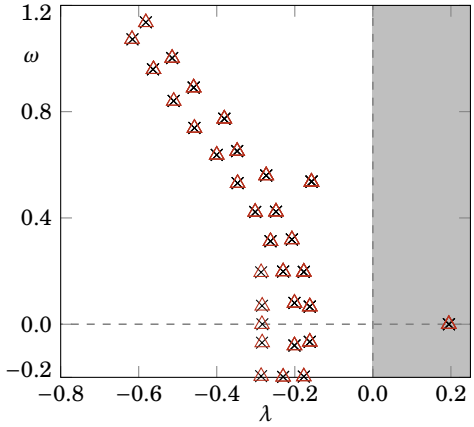

	Divergence mode	Flutter mode
$\tau_{SUPG,1}$	0.194902	$-0.157120 + 0.536800\mathrm{i}$
$\tau_{SUPG,2}$	0.194639	$-0.157411 + 0.535535\mathrm{i}$
Error	$2.63{\cdot}10^{-4}$	$2.91{\cdot}10^{-4} + 1.26{\cdot}10^{-3}\mathrm{i}$

Figure E.6 & Table E.3 – *Effect of the τ_{SUPG} definition on the RANS FSI spectrum at $Re = 50\,000$ and $\alpha = 0°$: the black crosses represent the $\tau_{SUPG,1}$ definition from Tezduyar et al. (1992) and the red triangles the $\tau_{SUPG,2}$ definition from Codina (2000). The table presents the divergence and flutter eigenvalues, along with the respective absolute error of their real and imaginary parts.*

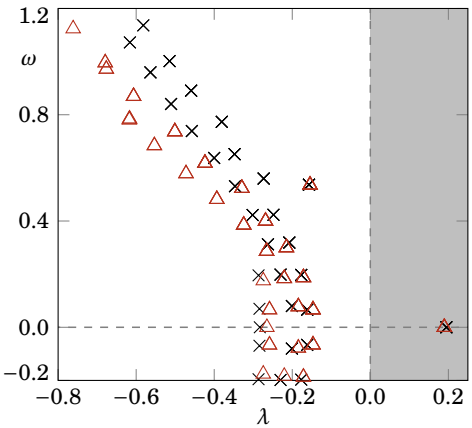

	Divergence mode	Flutter mode
$h_{K,1}$	0.194902	$-0.157120 + 0.536800\mathrm{i}$
$h_{K,2}$	0.189539	$-0.154481 + 0.535282\mathrm{i}$
Error	$5.36{\cdot}10^{-3}$	$2.63{\cdot}10^{-3} + 1.52{\cdot}10^{-3}\mathrm{i}$

Figure E.7 & Table E.4 – *Effect of the h_K definition on the RANS FSI spectrum at $Re = 50\,000$ and $\alpha = 0°$: the black crosses represent the $h_{K,1}$ definition from Franceschini (2019) and the red triangles the $h_{K,2}$ definition corresponding to the local minimum edge length. The table presents the divergence and flutter eigenvalues, along with the respective absolute error of their real and imaginary parts.*

E.2.5 Influence of the SUPG stabilisation and h_K definition

In this section, we discuss the influence of the SUPG stabilisation and corresponding h_K definition on the mean flow FSI linear stability analysis around the NACA0012 airfoil for the SA model with $\tilde{\nu}^\infty = 0$, $Re = 50\,000$ and $\alpha = 0°$. The two definitions of τ_{SUPG} tested are given by equations 1.58 and 1.59 (page 54). Their influence in only tested on the linear stability results, with fixed mean flow for all tests. A spectrum representation of the results is present in figure E.6, with a comparison of the divergence and flutter eigenvalues in table E.3. The spectrum shows no difference between the presented eigenvalues for the two stabilisations, where the absolute error has a magnitude of 10^{-3} for the both eigenvalues. The definition of $\tau_{SUPG,1}$ is employed in the rest of this appendix.

The same analysis is made for the two definitions of h_K, given by equations 1.60 and 1.61 (page 54), where the spectrum is present in figure E.7 and the divergence and flutter eigenvalues present in table E.4. This time, the choice of h_K has a clear influence on the eigenvalues other than the divergence and flutter ones. The $h_{K,1}$ definition tends to stabilise the eigenvalues with a higher frequency and to slightly destabilise the eigenvalues near the $\omega = 0$ axis. Concerning the two FSI eigenvalues, a small influence is noted, with the absolute error of order 10^{-3}. The definition of $h_{K,2}$ is employed in the rest of this appendix.

E.3 RANS mean flow description for $Re = 50\,000$ and $\alpha = 0°$

In this section, the flow over a NACA0012 airfoil at $Re = 50\,000$ and $\alpha = 0°$ is considered. In particular, the searched flow field is a steady solution of the RANS equations. The main difficulty in the computation of the mean flow solution passes trough the correct description of the laminar separation over the airfoil surface, as observed in the time- and spanwise-averaged solutions of the DNS simulations present in chapter 2. In order to achieve this flow laminarity over most part of the airfoil surface, two techniques are used and analysed throughout this chapter.

First, the Spalart–Allmaras closure model is used, without additional equations for transition modelling. The proper description of the laminar separation and subsequent transition of the separated boundary layer over the airfoil is obtained by considering a null boundary free-stream condition on the Spalart–Allmaras equation. As recognized by Rumsey (2007), the SA model, is able to describe a turbulent transition of a separated flow, if the boundary free-stream condition for $\tilde{\nu}$ (the Spalart–Allmaras equation variable) is sufficiently small.

In a second part, the flow laminarity is obtained via the introduction of the Baş–Çakmakçıoğlu (BC) transition model. The BC model tries to take into account the laminar to turbulent transition characteristics of the flow with the inclusion of an intermittency function. The role of this intermittency function is to trigger the transition of the flow by controlling the production term in the Spalart–Allmaras equation.

E.3.1 Mean flow for SA model with $\tilde{\nu}^\infty = 0$

This section is dedicated to the mean flow description using the SA closure model and setting the free-stream Spalart–Allmaras variable to zero, *i.e.*, $\tilde{\nu}^\infty = 0$. The final solution is obtained from a fully turbulent initial solution at the same Reynolds number. Then, the $\tilde{\nu}^\infty$ is carefully decreased from its original value $\tilde{\nu}^\infty = 3\nu$ to $\tilde{\nu}^\infty = 0$. This numerical process is described in section E.2.

The spanwise vorticity of the mean flow field is presented in figure E.8. The black lines represent the streamlines enclosing the recirculation zone at the rear of the airfoil. The flow remains attached from the leading edge to the point $X_d = 0.668$, where a laminar separation occurs. This separation occurs at the same abscissa on the upper and lower sides of the symmetric airfoil as the incidence is zero. This separation is represented by the yellow dots on the figure. From this

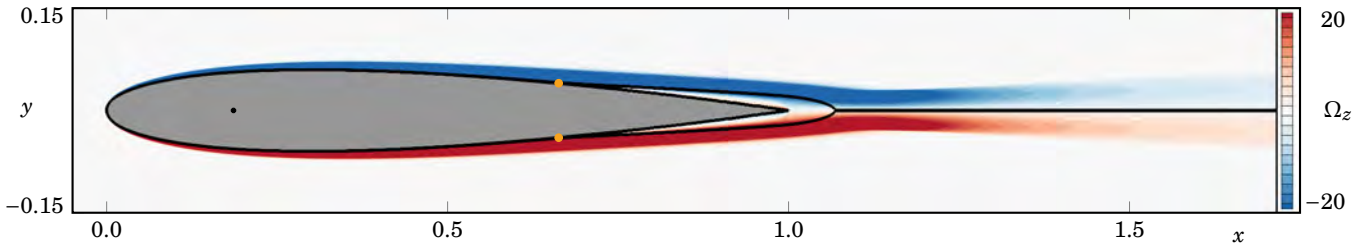

Figure E.8 – *Spanwise vorticity field of the RANS mean flow for Re = 50 000 and α = 0°, using the SA model with $\tilde{\nu}^{\infty} = 0$. The yellow dots over the airfoil surface represent the separation points.*

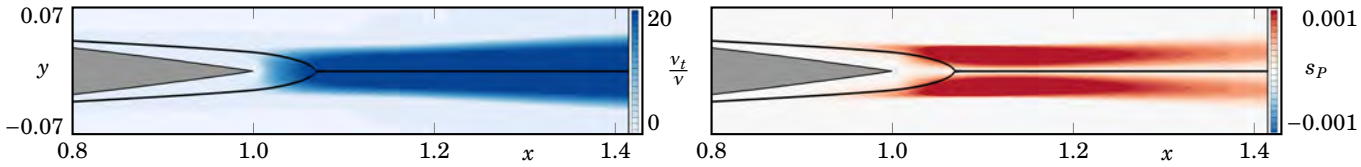

Figure E.9 – *Quantity ν_t/ν, on the left, and the production term of the SA model, on the right, for the RANS mean flow at Re = 50 000 and α = 0°, using the SA model with $\tilde{\nu}^{\infty} = 0$.*

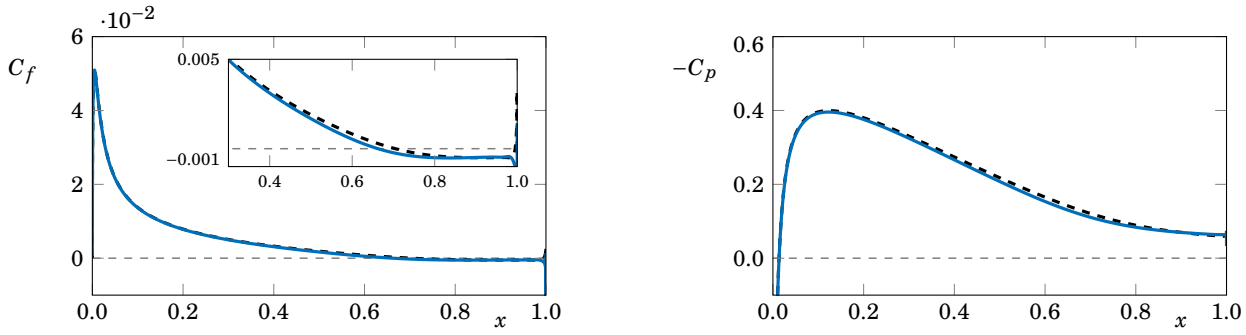

Figure E.10 – *Comparison of the C_f distribution, on the left, and $-C_p$ distribution, on the right, between the RANS mean flow using the SA model with $\tilde{\nu}^{\infty} = 0$ (solid blue lines) and the mean flow issued from 3D simulations (dashed black lines) for Re = 50 000 and α = 0°.*

point, a separated boundary layer emerges on both sides of the airfoil. These layers encounter each other at the rear of the airfoil, for $X = 1.068$. As a consequence, a recirculation zone. If one compares the present mean flow with the mean flow from the two-dimensional time-marching simulations, where no turbulence model is taken into account (figure 4.1, page 143), we can clearly see the difference in the wake zone, due to the fact that the RANS simulations do not that into account the vortex-shedding phenomenon. The use of URANS for computing a mean flow solution is not present here due to time constrains on the writing process of this manuscript.

In order to better understand the laminar-turbulent transition appearing on the separated boundary layer, the ratio ν_t/ν and the production term in the SA model are sketched in figure E.9. The former characterises the relative importance of the turbulent eddy-viscosity modelled, with respect to the fluid kinematic viscosity. We first confirm that these terms tend to zero as we approach the airfoil surface. This is a natural behaviour, as the turbulent ceases to exist at the wall. Additionally, the eddy viscosity also tends to zero on the cross-stream direction, where the perturbation of the flow field

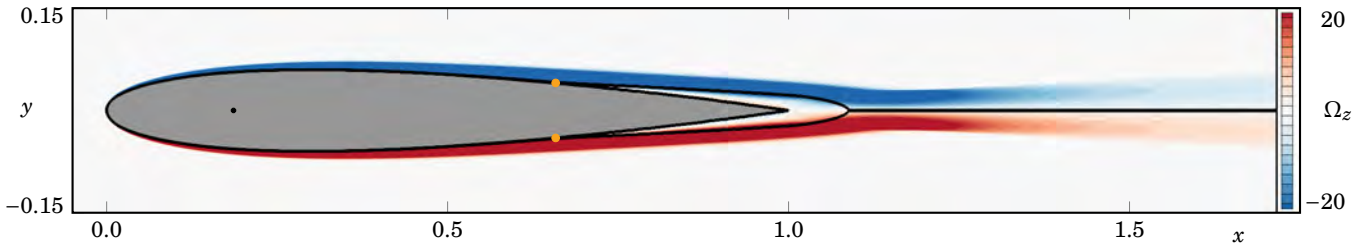

Figure E.11 – *Spanwise vorticity field of the RANS mean flow for Re = 50 000 and α = 0°, using the SA-BC model. The yellow dots over the airfoil surface represent the separation points.*

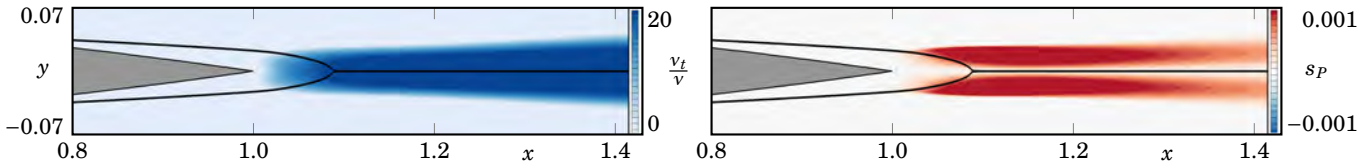

Figure E.12 – *Quantity ν_t/ν, on the left, and the production term of the SA model, on the right, for the RANS mean flow at Re = 50 000 and α = 0°, using the SA-BC model.*

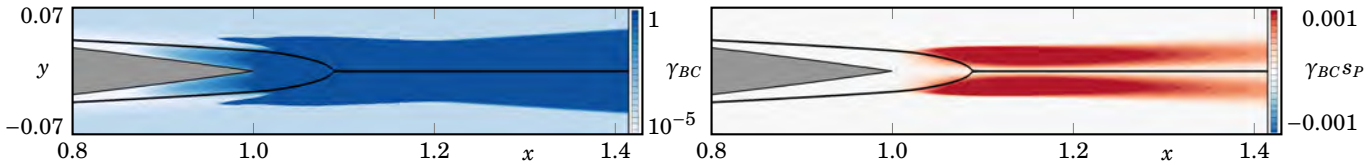

Figure E.13 – *Intermittency function, on the left, and the product of the intermittency function with the production term of the SA model, on the right, of the RANS mean flow for Re = 50 000 and α = 0°, using the SA-BC model.*

due to the presence of the airfoil tends to zero. In contrast, the ratio ν_t/ν is high on the wake of the airfoil, where the flow is turbulent. The presence of this turbulence is a direct consequence of the production term s_P, depicted on the right of figure E.9. We suggest in a future work to compare the s_P term with the production of turbulent kinetic energy from the DNS simulations (see equation 22 of Mettot *et al.* (2014)).

In figure E.10, we compare the C_f and C_p distributions of the RANS SA model with the DNS data. We find a very good agreement for this angle of attack.

E.3.2 Mean flow for SA-BC model

The same procedure done in the previous paragraph is made here for the RANS SA-BC model, with the results present in figures E.11 to E.14. The results are qualitatively the same. In particular, we sketch the intermittency function in figure E.13 and we see that the intermittency only has values on the wake of the airfoil. Along the boundary layers, the flow remains completely laminar.

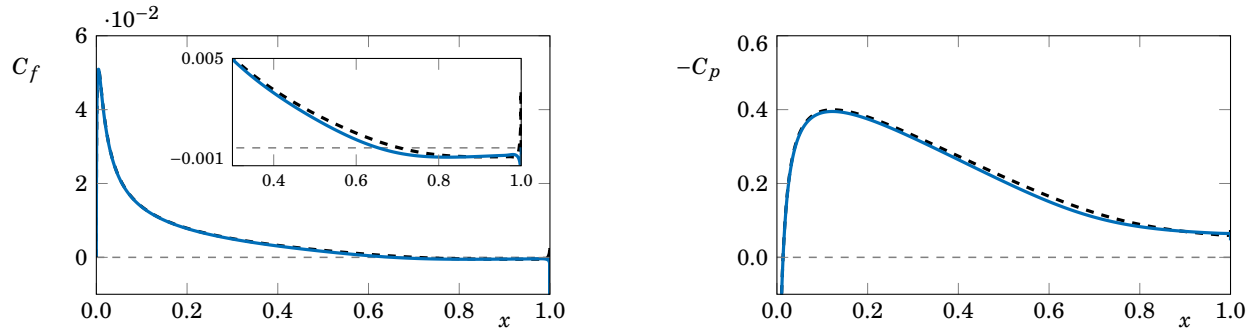

Figure E.14 – *Comparison of the C_f distribution, on the left, and $-C_p$ distribution, on the right, between the RANS mean flow using the SA-BC model (solid blue lines) and the mean flow issued from 3D simulations (dashed black lines) for Re = 50 000 and α = 0°.*

E.4 RANS mean flow FSI linear stability analysis for $Re = 50\,000$ and $\alpha = 0°$

We compare in figure E.15 the purely-hydrodynamic spectrum of a mean flow linear stability analysis, using the two different mean flow solutions analysed previously. Even if qualitatively the two mean flow solutions were the same, we observe a significant difference in the linear stability analysis results, in particular on the region of the high frequencies of the spectrum. We note that an unstable mode is present on the right spectrum, corresponding to a hydrodynamic linear

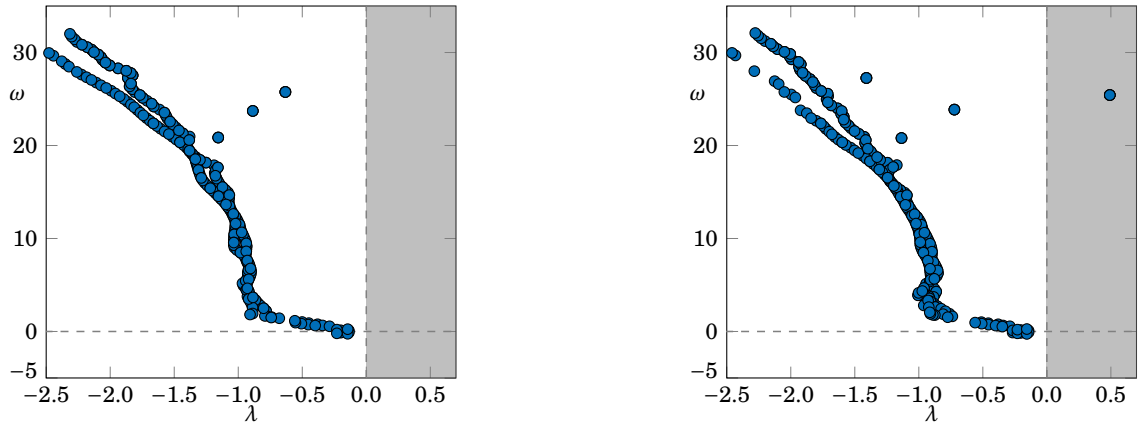

Figure E.15 – *Hydrodynamic linear stability analysis of the RANS mean flow: spectrum for Re = 50 000 and α = 0° using the SA model with $\tilde{\nu}^{\infty} = 0$, on the left, and using the SA-BC model, on the right.*

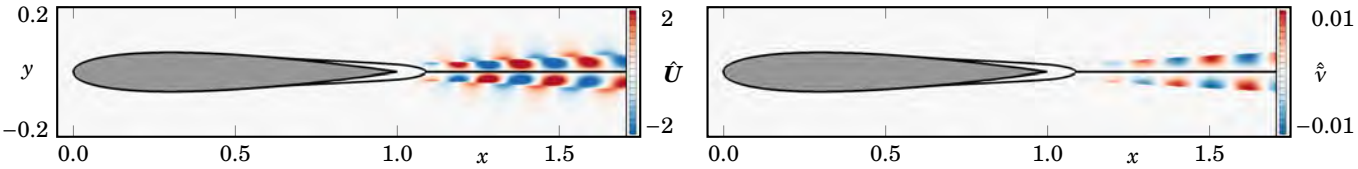

Figure E.16 – *Real part of the streamwise velocity and $\hat{\nu}$ SA model variable of the vortex shedding eigenmode from a hydrodynamic mean flow linear stability analysis around the RANS SA-BC mean flow at Re = 50 000 and α = 0°.*

stability analysis around the mean flow of a RANS SA-BC formulation. The unstable mode is associated to the vortex shedding instability. In view of these results, a mean flow from URANS computations can be computed with the SA-BC, whose associated results are not present here due to time constrains associated to the writing process of this manuscript.

We continue our analysis with the SA-BC model. Figure E.17 presents a fluid–structure spectrum, already present in the conclusion of this thesis (page 203), for the nominal values of the structure parameters. We can observe the presence of an unsteady divergence mode, while the flutter mode is stable. These results are in accordance with the analyses made in chapters 3 and 4. The spatial distribution of the divergence and flutter modes is present in the following figures. Due to the lack of time in the writing process of this thesis, these results are not commented.

The fluid–structure modes can also be computed using a quasi-laminar approximation (Mettot *et al.*, 2014). In this analysis, the perturbation on the Spalart–Allmaras variable is not considered. However, we take into account the value of ν_t on the linearised momentum equations. This approximation results in a problem of the same size as the mean flow problems solved in the main chapters of this thesis. The quasi-laminar fluid–structure spectrum is present in figure E.20. We note that both divergence and flutter eigenvalues are still well predicted with this simplification. Their numerical values are compared in table E.5.

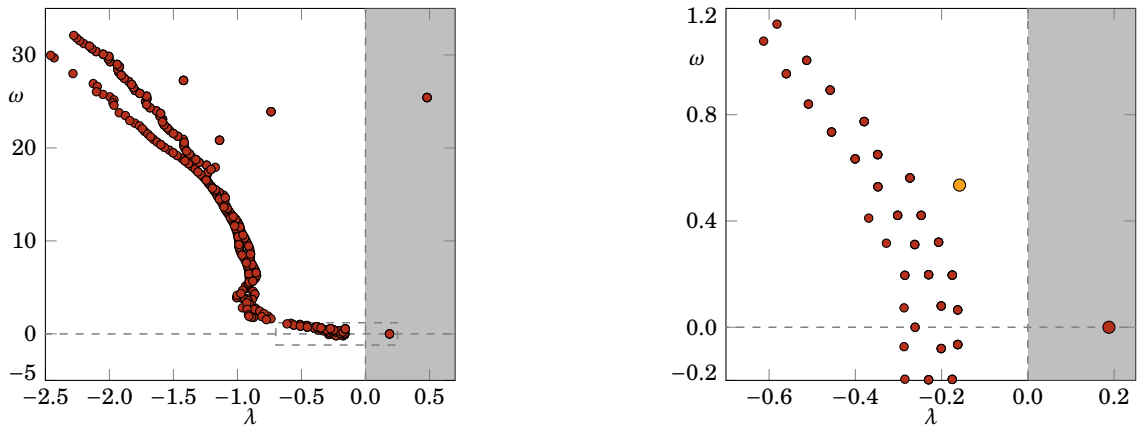

Figure E.17 – *Mean flow FSI linear stability analysis of the RANS mean flow using the SA-BC model: spectrum for* $Re = 50\,000$ *and* $\alpha = 0°$.

Mean flow model	SA-BC	SA-BC quasi-laminar	From 3D simulations
Divergence eigenvalue	0.1879	0.1948	0.2238
Flutter eigenvalue	$-0.1584 + 0.5350\mathrm{i}$	$-0.1590 + 0.5363\mathrm{i}$	$-0.1435 + 0.5245\mathrm{i}$

Table E.5 – *Summary of the divergence and flutter eigenvalues obtained for: a RANS FSI mean flow analysis around a mean flow computed with a SA-BC model, a RANS FSI quasi-laminar mean flow analysis around the same mean flow and the results from the FSI analysis around a mean flow issued from 3D simulations, taken from table 4.2 (page 150).*

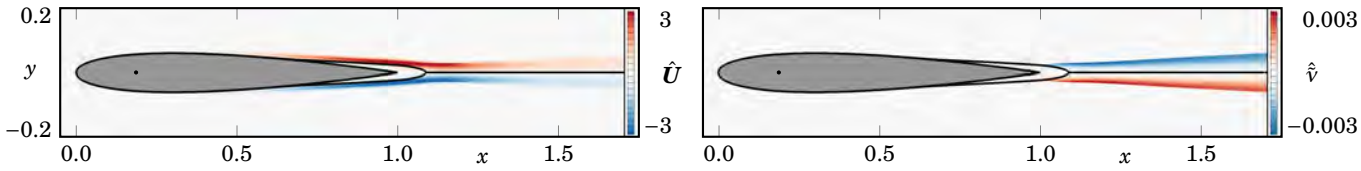

Figure E.18 – *Real part of the streamwise velocity and* $\hat{\tilde{\nu}}$ *SA model variable of the divergence eigenmode from a mean flow FSI linear stability analysis around the RANS SA-BC mean flow at Re* = 50 000 *and* $\alpha = 0°$.

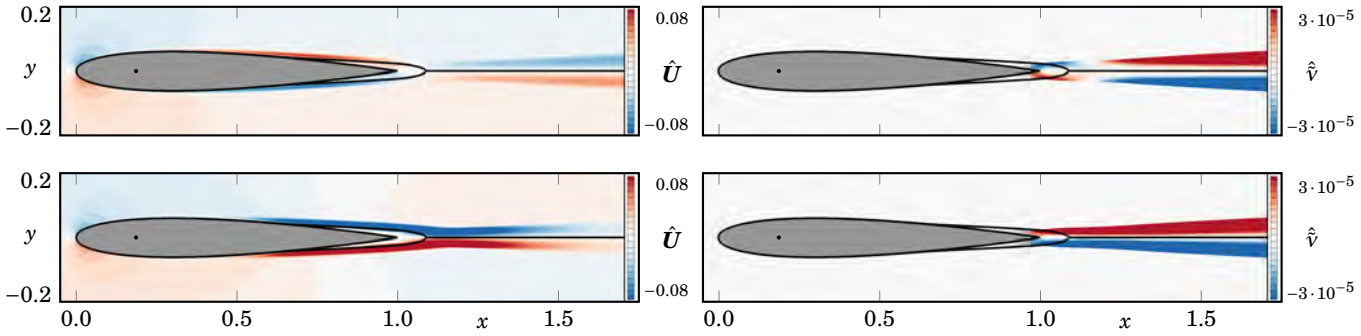

Figure E.19 – *Real (top figures) and imaginary (bottom figures) parts of the streamwise velocity and* $\hat{\tilde{\nu}}$ *SA model variable of the flutter eigenmode from a mean flow FSI linear stability analysis around the RANS SA-BC mean flow at Re* = 50 000 *and* $\alpha = 0°$.

E.5 RANS mean flow description for $Re = 50\,000$ and $\alpha > 0°$

In a first part, we describe the evolution of the mean flow aerodynamic moment with the angle of attack for the SA model, using $\tilde{\nu}^{\infty} = 0$. The main results are present in figure E.21. One can see that the predicted curve tends to deviate from the three-dimensional data (blue crosses) as the angle of attack increases, with a smaller zone where the aerodynamic moment is negative. In contrast, the evolution of the aerodynamic curve for the SA-BC model predicts a

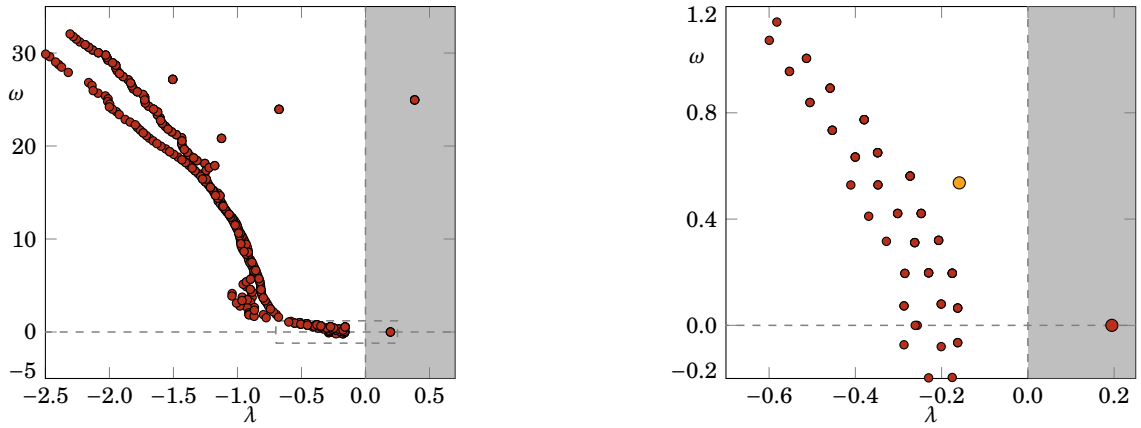

Figure E.20 – *Quasi-laminar mean flow FSI linear stability analysis of the RANS mean flow using the SA-BC model: spectrum for Re* = 50 000 *and* $\alpha = 0°$.

larger negative zone, as present in figure E.22.

As a first step for a future work, we fix the incidence at $\alpha = 1.5°$ on the SA-BC model and we modify the value of $\tilde{\nu}^\infty$ up until the point where the aerodynamic moment of this "improved" SA-BC model matches the value of mean flow issued from the DNS simulations. The value of $\tilde{\nu}^\infty$ has increased from its baseline value of $\tilde{\nu}^\infty = 0.015\nu$ up to $\tilde{\nu}^\infty = 0.672\nu$. This process is made manually, but it can be made with a variational data-assimilation procedure, as done in the investigation of one of our colleges in an ONERA internship (Al Jamous, 2021).

The values of the pressure component of the aerodynamic moment local contribution along the airfoil surface for the SA-BC and the "improved" SA-BC are sketched in figure E.23. Additionally, we also sketch the pressure distribution. We note that by only optimising the global value of the aerodynamic moment, we manage to obtain a very good agreement between the "improved" model and the DNS mean flow for the local quantities sketched.

With this value of $\tilde{\nu}^\infty$, we sketch in figure E.24 the aerodynamic moment as function of the incidence, that presents a better agreement with the DNS data than the previous unmodified models.

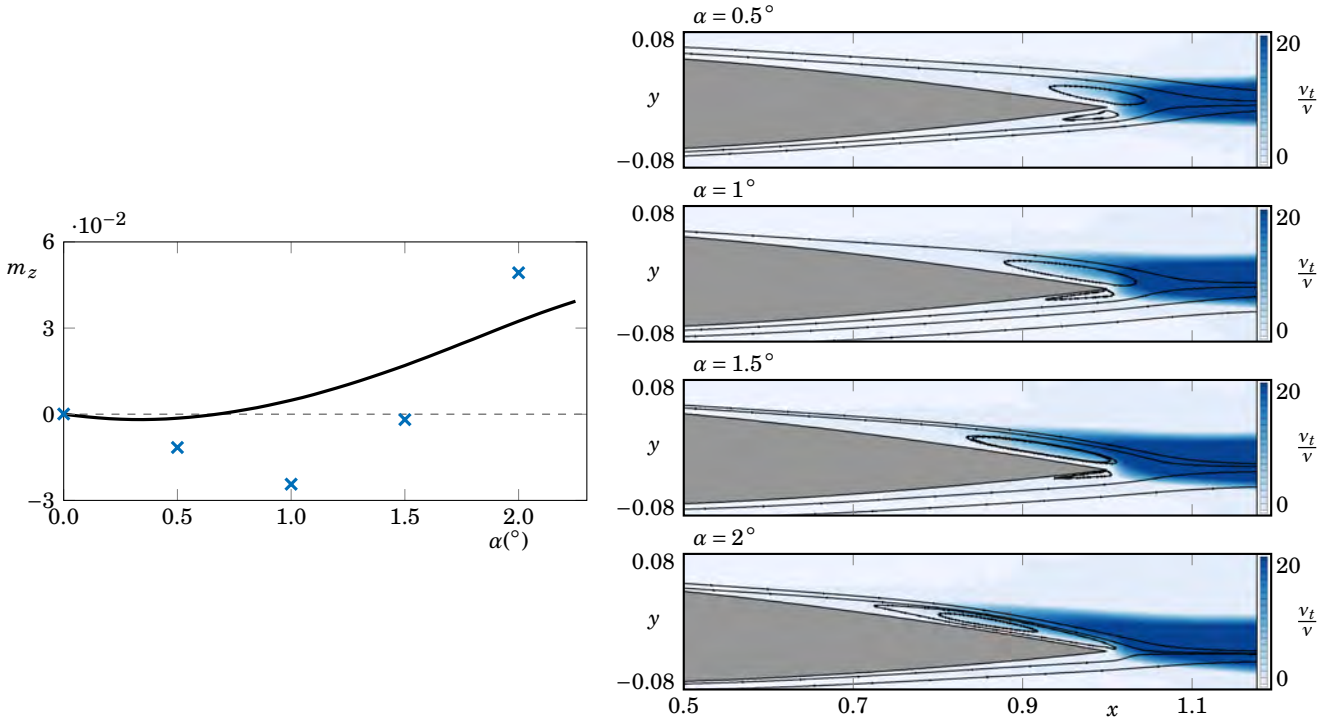

Figure E.21 – m_z *evolution with the incidence of the RANS mean flow for Re* = 50 000*, using the SA model with* $\tilde{\nu}^\infty = 0$.

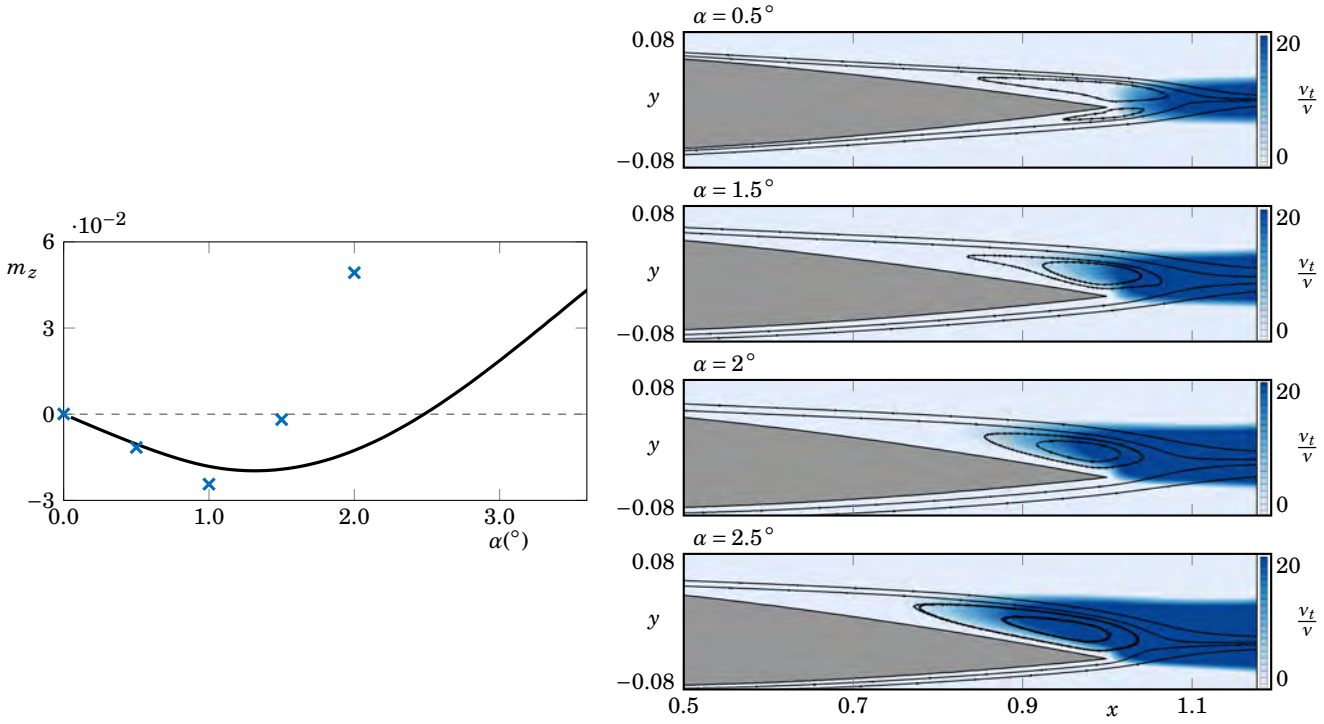

Figure E.22 – *m_z evolution with the incidence of the RANS mean flow for Re = 50 000, using the SA-BC model.*

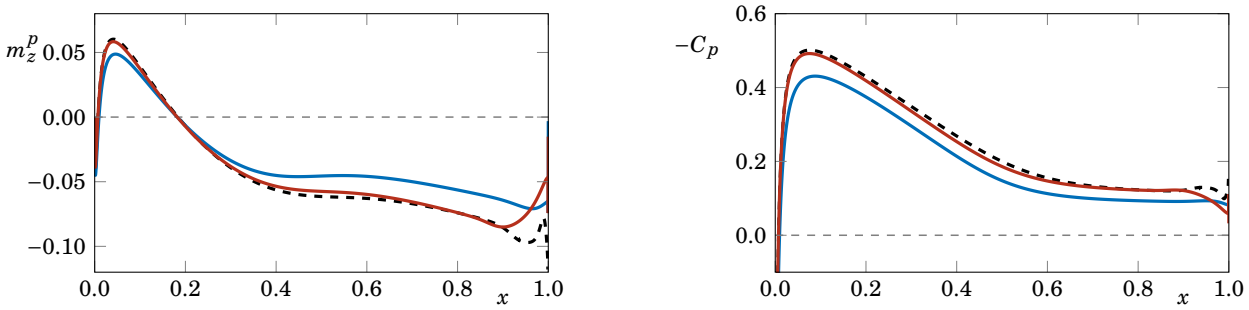

Figure E.23 – *Comparison of the m_z^p and C_p distributions over the upper surface of the airfoil between the mean flow using a SA-BC model (solid blue line), using the "improved" SA-BC, where $\tilde{\nu}^\infty = 0.672\nu$ (solid red line) and the 3D results (black dashed line).*

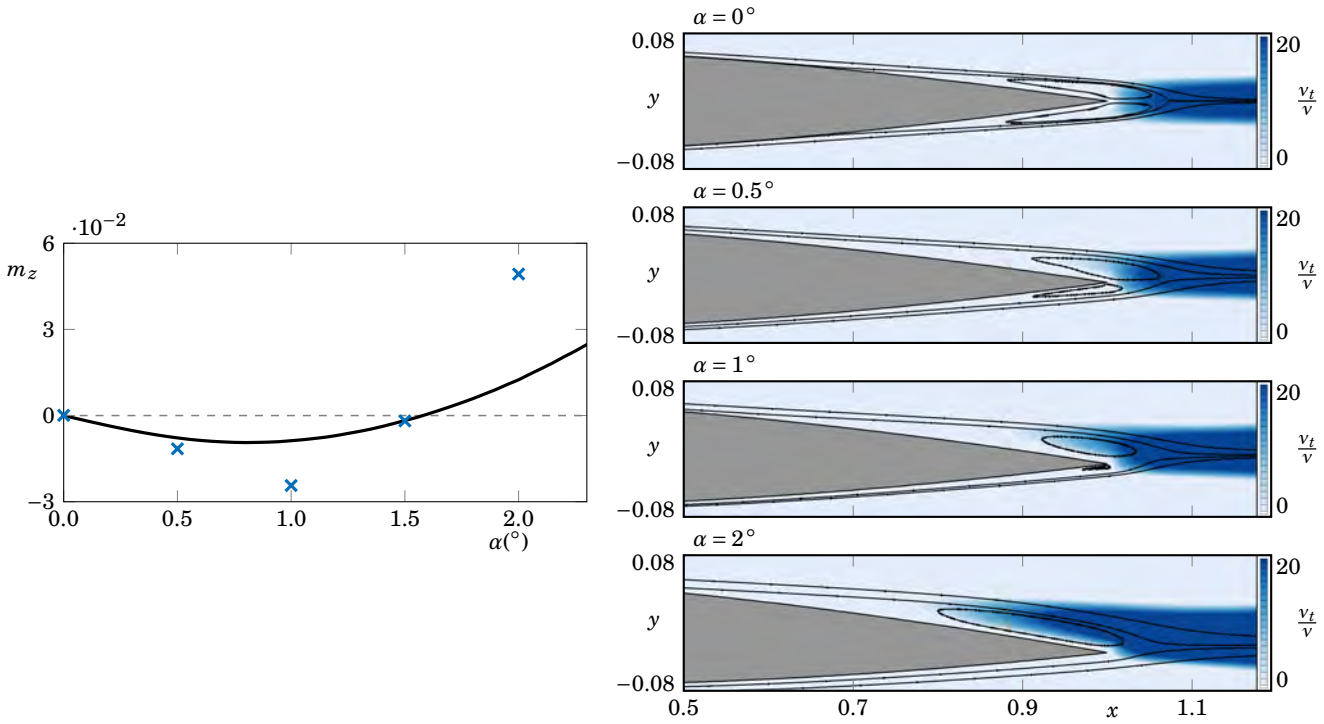

Figure E.24 – m_z *evolution with the incidence of the RANS mean flow for Re* = 50 000*, using a modified SA-BC model, where* $\tilde{\nu}^{\infty} = 0.672\nu$.

Bibliography

Abdollahzadeh, M., Esmaeilpour, M., Vizinho, R., Younesi, A. and Pàscoa, J. C. (2017). *Assessment of RANS turbulence models for numerical study of laminar-turbulent transition in convection heat transfer*. International Journal of Heat and Mass Transfer **115**, 1288–1308.
doi: 10.1016/j.ijheatmasstransfer.2017.08.114 — Cited on page 226.

Achour, N. (2022). *Interactions fluide-structure proche de la surface libre : application à la récupération d'énergie et aux instabilités*. Ph.D. thesis, École Doctorale Mécanique, Énergétique, Génie Civil et Procédés (Toulouse, France) — Cited on page 2.

Al Jamous, M. (2021). *Hybrid prediction of flows around airfoils with laminar separation through data assimilation*. Rapport de stage de recherche, Ecole Polytechnique, Paris — Cited on page 238.

Allmaras, S. R., Johnson, F. T. and Spalart, P. R. (2012). *Modifications and Clarifications for the Implementation of the Spalart–Allmaras Turbulence Model*. 7th International Conference on Computational Fluid Dynamics (ICCFD7) **ICCFD7-1902**, 1–11.
URL: https://www.iccfd.org/iccfd7/assets/pdf/papers/ICCFD7-1902_paper.pdf — Cited on page 224.

Amandolese, X., Michelin, S. and Choquel, M. (2013). *Low speed flutter and limit cycle oscillations of a two-degree-of-freedom flat plate in a wind tunnel*. Journal of Fluids and Structures **43**, 244–255.
doi: https://doi.org/10.1016/j.jfluidstructs.2013.09.002 — Cited on page 4.

Amestoy, P. R., Duff, I. S., L'Excellent, J.-Y. and Koster, J. (2001). *A Fully Asynchronous Multifrontal Solver Using Distributed Dynamic Scheduling*. SIAM Journal on Matrix Analysis and Applications **23** (1), 15–41.
doi: 10.1137/S0895479899358194 — Cited on pages 116, 119, and 211.

Anderson, E., Bai, Z., Bischof, C., Blackford, S., Demmel, J., Dongarra, J., Du Croz, J., Greenbaum, A., Hammarling, S., McKenney, A. and Sorensen, D. (1999). *LAPACK Users' Guide*. Society for Industrial and Applied Mathematics, Philadelphia, PA, 3rd edition.
ISBN: 0-89871-447-8 — Cited on pages 117 and 214.

Anyoji, M., Nonomura, T., Aono, H., Oyama, A., Fujii, K., Nagai, H. and Asai, K. (2014). *Computational and Experimental Analysis of a High-Performance Airfoil Under Low-Reynolds-Number Flow Condition*. Journal of Aircraft **51** (6), 1864–1872.
doi: 10.2514/1.C032553 — Cited on page 7.

Arnold, D. N., Brezzi, F. and Fortin, M. (1984). *A stable finite element for the stokes equations*. Calcolo **21**, 337–344.
doi: 10.1007/BF02576171 — Cited on page 51.

Arnoldi, W. E. (1951). *The principle of minimized iterations in the solution of the matrix eigenvalue problem*. Quarterly of Applied Mathematics **9** (1), 17–29.
doi: 10.1090/qam/42792 — Cited on pages 117 and 213.

Assemat, P., Fabre, D. and Magnaudet, J. (2012). *The onset of unsteadiness of two-dimensional bodies falling or rising freely in a viscous fluid: a linear study*. Journal of Fluid Mechanics **690**, 173–202.
doi: 10.1017/jfm.2011.419 — Cited on pages 13, 133, and 142.

Auriti, L. and DeLaurier, J. (2004). *Analysis of the Flight Attempt by Samuel Langley's "Great Aerodrome"*. Journal of Aircraft **41** (6), 1430–1439.
doi: 10.2514/1.5139 — Cited on page 1.

Babuška, I. (1973). *The finite element method with Lagrangian multipliers*. Numerische Mathematik **20** (3), 179–192.
doi: 10.1007/BF01436561 — Cited on page 50.

Baş, O., Çakmakçıoğlu, S. Ç. and Kaynak, Ü. (2013). *A Novel Intermittency Distribution Based Transition Model For Low-Re Number Airfoils*. In *31st*

AIAA Applied Aerodynamics Conference. 1–13.
doi: 10.2514/6.2013-2531 — Cited on page 226.

Bai, P., Li, F., Liu, Q. and Zhan, H. (2016). *Evolution of the Non-linear and Unsteady Low Reynolds Number Laminar Separation Bubble around the Airfoil with Small angle of attack*. 46th AIAA Fluid Dynamics Conference
doi: 10.2514/6.2016-4337 — Cited on page 8.

Baker, A. H., Jessup, E. R. and Manteuffel, T. (2005). *A Technique for Accelerating the Convergence of Restarted GMRES*. SIAM Journal on Matrix Analysis and Applications **26** (4), 962–984.
doi: 10.1137/S0895479803422014 — Cited on page 212.

Balay, S., Abhyankar, S., Adams, M. F., Brown, J., Brune, P., Buschelman, K., Constantinescu, E. M., Dalcin, L., Dener, A., Eijkhout, V., Gropp, W. D., Hapla, V., Isaac, T., Jolivet, P., Karpeyev, D., Kaushik, D., Knepley, M. G., Kong, F., Kruger, S., May, D. A., Curfman McInnes, L., Tran Mills, R., Mitchell, L., Munson, T., Roman, J. E., Rupp, K., Sanan, P., Sarich, J., Smith, B. F., Zampini, S., Zhang, H., Zhang, H. and Zhang, J. (2022). *PETSc/TAO Users Manual*. Technical Report ANL-21/39 - Revision 3.17, Argonne National Laboratory.
URL: https://petsc.org/release/docs/manual/manual.pdf — Cited on page 67.

Baldwin, B. and Lomax, H. (1978). *Thin-layer approximation and algebraic model for separated turbulent flows*. In *AIAA 16th Aerospace Sciences Meeting, paper 78-257*. 1–8.
doi: 10.2514/6.1978-257 — Cited on pages 4 and 223.

Barkley, D. (2006). *Linear analysis of the cylinder wake mean flow*. Europhysics Letters (EPL) **75** (5), 750–756.
doi: 10.1209/epl/i2006-10168-7 — Cited on page 12.

Barkley, D. and Henderson, R. D. (1996). *Three-dimensional Floquet stability analysis of the wake of a circular cylinder*. Journal of Fluid Mechanics **322**, 215–241.
doi: 10.1017/S0022112096002777 — Cited on pages 12 and 84.

Barmby, J. G., Cunningham, H. J. and Garrick, I. E. (1951). *Study of Effects of Sweep on the Flutter of Cantilever Wings*. NACA Technical Report 1014
URL: https://ntrs.nasa.gov/citations/19930092069 — Cited on page 3.

Barnes, C. J. and Visbal, M. R. (2016). *High-Fidelity LES Simulations of Self-Sustained Pitching Oscillations on a NACA0012 Airfoil at Transitional Reynolds Numbers*. In *54th AIAA Aerospace Sciences Meeting*. 1–22.
doi: 10.2514/6.2016-1353 — Cited on pages 10, 11, 158, and 201.

Barnes, C. J. and Visbal, M. R. (2018). *On the role of flow transition in laminar separation flutter*. Journal of Fluids and Structures **77**, 213–230.
doi: 10.1016/j.jfluidstructs.2017.12.009 — Cited on pages 10, 11, 158, and 201.

Barnes, C. J. and Visbal, M. R. (2019). *Stiffness effects on laminar separation flutter*. Journal of Fluids and Structures **91**, 102767.
doi: 10.1016/j.jfluidstructs.2019.102767 — Cited on pages 11 and 158.

Barrett, R., Berry, M., Chan, T. F., Demmel, J., Donato, J., Dongarra, J., Eijkhout, V., Pozo, R., Romine, C. and van der Vorst, H. (1994). *Templates for the Solution of Linear Systems: Building Blocks for Iterative Methods*. Society for Industrial and Applied Mathematics, Philadelphia, PA, 1st edition.
ISBN: 978-0-898-71328-2 — Cited on page 212.

Bauer, F. L. (1957). *Das Verfahren der Treppeniteration und verwandte Verfahren zur Lösung algebraischer Eigenwertprobleme*. Zeitschrift für Angewandte Mathematik und Physik **8**, 214–235.
doi: 10.1007/BF01600502 — Cited on page 117.

Beedy, J., Barakos, G., Badcock, K. J. and Richards, B. E. (2003). *Non-linear analysis of stall flutter based on the ONERA aerodynamic model*. The Aeronautical Journal **107** (1074), 495–510.
doi: 10.1017/S0001924000134001 — Cited on page 4.

Bendiksen, O. O. (2011). *Review of unsteady transonic aerodynamics: Theory and applications*. Progress in Aerospace Sciences **47** (2), 135–167.
doi: 10.1016/j.paerosci.2010.07.001 — Cited on pages 4 and 5.

Benetti Ramos, L. H. (2020). *Self-propulsion and fluid-mediated interaction of flapping wings in viscous flows*. Ph.D. thesis, École Doctorale Mathématiques et Informatique (Bordeaux, France) — Cited on pages 45, 142, and 205.

Benetti Ramos, L. H., Marquet, O., Bergmann, M. and Iollo, A. (2021). *Fluid–solid Floquet stability analysis of self-propelled heaving foils*. Journal of Fluid Mechanics **910**, A28.
doi: 10.1017/jfm.2020.1021 — Cited on pages 13, 142, and 195.

Bergen, A. and Vittal, V. (2000). *Power system analysis*. Prentice Hall, New Jersey, NJ, 2nd edition.
ISBN: 978-0-136-91990-2 — Cited on page 60.

Bisplinghoff, R. L., Ashley, H. and Halfman, R. L. (1955). *Aeroelasticity*. Addison-Wesley Publishing Company, Cambridge, 1st edition.
ISBN: 978-0-486-69189-3 — Cited on pages 2, 4, 12, and 141.

Blackburn, H. M., Marques, F. and Lopez, J. M. (2005). *Symmetry breaking of two-dimensional time-periodic wakes*. Journal of Fluid Mechanics **522**, 395–411.
doi: 10.1017/S0022112004002095 — Cited on page 84.

Bodnár, T., Gald, G. P. and Necasova, S. (2020). *Fluids Under Pressure*. Birkhäuser Basel, Basel, 1st edition.
ISBN: 978-3-030-39638-1 — Cited on page 53.

Boldo, S., Clément, F., Faissole, F., Martin, V. and Mayero, M. (2017). *A Coq Formal Proof of the Lax-Milgram Theorem*. In *Proceedings of the 6th ACM SIGPLAN Conference on Certified Programs and Proofs*. 79–89.
doi: 10.1145/3018610.3018625 — Cited on page 48.

Boussinesq, J. (1877). *Essai sur la théorie des eaux courantes*. Mémoires présentés par divers savants à l'Académie des Sciences de l'Institut de France **XXIII** (1), 1–680.
URL: https://gallica.bnf.fr/ark:/12148/bpt6k56673076.texteImage — Cited on page 223.

Braack, M., Burman, E., John, V. and Lube, G. (2007). *Stabilized finite element methods for the generalized Oseen problem*. Computer Methods in Applied Mechanics and Engineering **196** (4), 853–866.
doi: 10.1016/j.cma.2006.07.011 — Cited on page 53.

Bratt, J. B. and Chinneck, A. (1954). *Measurements of mid-chord pitching moment derivatives at high speeds*. In *Aeronautical Research Council Reports & Memoranda, No. 2680*. 1–36.
URL: https://reports.aerade.cranfield.ac.uk/handle/1826.2/3224 — Cited on page 5.

Bratt, J. B., Raymer, W. G. and Townsend, J. E. G. (1962). *Measurements of the Direct Pitching-Moment Derivatives for Two-Dimensional Flow at Subsonic and Supersonic Speeds and for a Wing of Aspect Ratio 4 at Subsonic Speeds*. In *Aeronautical Research Council Reports & Memoranda, No. 3257*. 1–56.
URL: https://citeseerx.ist.psu.edu/viewdoc/download?doi=10.1.1.227.1956&rep=rep1&type=pdf — Cited on page 5.

Brezzi, F. and Fortin, M. (1991). *Mixed and Hybrid Finite Element Methods*. Springer-Verlag, New York, 1st edition.
ISBN: 978-1-461-27824-5 — Cited on page 51.

Brooks, A. N. and Hughes, T. J. R. (1982). *Streamline upwind/Petrov-Galerkin formulations for convection dominated flows with particular emphasis on the incompressible Navier–Stokes equations*. Computer Methods in Applied Mechanics and Engineering **32** (1), 199–259.
doi: 10.1016/0045-7825(82)90071-8 — Cited on page 53.

Buckingham, E. (1914). *On Physically Similar Systems; Illustrations of the Use of Dimensional Equations*. Physical Review **4**, 347–376.
doi: 10.1103/PhysRev.4.345 — Cited on page 19.

Busquet, D. (2020). *Study of a high Reynolds number flow around a two dimensional airfoil at stall : an approach coupling a RANS framework and bifurcation theory*. Ph.D. thesis, Institut Polytechnique de Paris (Paris, France) — Cited on page 6.

Canton, J., Auteri, F. and Carini, M. (2017). *Linear global stability of two incompressible coaxial jets*. Journal of Fluid Mechanics **824**, 886–911.
doi: 10.1017/jfm.2017.290 — Cited on page 73.

Canuto, C., Hussaini, M., Quateroni, A. and Zang, T. (2006). *Spectral Methods: Fundamentals in Single Domains*. Springer Berlin, Heidelberg, Berlin, 1st edition.
ISBN: 978-3-540-30725-9 — Cited on page 45.

Çakmakçıoğlu, S. Ç., Baş, O., Mura, R. and Kaynak, Ü. (2018). *A correlation-based algebraic transition model*. Proceedings of the Institution of Mechanical Engineers, Part C: Journal of Mechanical Engineering Science **232** (21), 3915–3929.
doi: 10.1177/0954406217743537 — Cited on page 226.

Çakmakçıoğlu, S. Ç., Baş, O., Mura, R. and Kaynak, Ü. (2020). *A Revised One-Equation Transitional Model for External Aerodynamics*. AIAA Aviation 2020 Forum
doi: 10.2514/6.2020-2706 — Cited on page 226.

Celić, A. and Hirschel, E. H. (2006). *Comparison of Eddy-Viscosity Turbulence Models in Flows with Adverse Pressure Gradient*. AIAA Journal **44** (10),

2156–2169.
doi: 10.2514/1.14902 — Cited on page 224.

Chan, T. F. and Shao, J. P. (1995). *Parallel complexity of domain decomposition methods and optimal coarse grid size*. Parallel Computing **21** (7), 1033–1049.
doi: 10.1016/0167-8191(95)00009-D — Cited on page 50.

Chen, Z., Xiao, T., Wang, Y. and Qin, N. (2021). *Laminar separation bubble dynamics and its effects on thin airfoil performance during pitching-up motion*. Proceedings of the Institution of Mechanical Engineers, Part G: Journal of Aerospace Engineering **235** (16), 2479–2492.
doi: 10.1177/0954410021999529 — Cited on page 7.

Chevalier, C. and Pellegrini, F. (2008). *PT-Scotch: A tool for efficient parallel graph ordering*. Parallel Computing **34** (6), 318–331.
doi: 10.1016/j.parco.2007.12.001 — Cited on page 50.

Chomaz, J.-M. (2005). *Global Instabilities in spatially developing flows: non-normality and nonlinearity*. Annual Review of Fluid Mechanics **37** (1), 357–392.
doi: 10.1146/annurev.fluid.37.061903.175810 — Cited on page 115.

Chorin, A. J. (1968). *Numerical solution of the Navier-Stokes equations*. Mathematics of Computation **22**, 745–762.
doi: 10.1090/S0025-5718-1968-0242392-2 — Cited on page 56.

Christodoulou, K. N. and Scriven, L. E. (1988). *Finding leading modes of a viscous free surface flow: An asymmetric generalized eigenproblem*. Journal of Scientific Computing **3**, 355–406.
doi: 10.1007/BF01065178 — Cited on page 117.

Clark, R., Cox, D., Curtiss, H. C. J., Edwards, J. W., Hall, K. C., Peters, D. A., Scanlan, R., Simiu, E., Sisto, F. and Strganac, Th. W. (2004). *A Modern Course in Aeroelasticity*. Springer, Netherlands, 1st edition.
ISBN: 978-1-402-02711-6 — Cited on pages 12 and 141.

Cliffe, K. A., Garratt, T. J. and Spence, A. (1993). *Eigenvalues of the discretized Navier-Stokes equation with application to the detection of Hopf bifurcations*. Advances in Computational Mathematics **1**, 337–356.
doi: 10.1007/BF02072015 — Cited on page 117.

Codina, R. (2000). *Stabilization of incompressibility and convection through orthogonal sub-scales in finite element methods*. Computer Methods in Applied Mechanics and Engineering **190** (13), 1579–1599.
doi: 10.1016/S0045-7825(00)00254-1 — Cited on pages 54, 55, and 231.

Collar, A. R. (1946). *The Expanding Domain of Aeroelasticity*. The Journal of the Royal Aeronautical Society **50** (428), 613–636.
doi: 10.1017/S0368393100120358 — Cited on page 1.

Corke, T. C. and Thomas, F. O. (2015). *Dynamic Stall in Pitching Airfoils: Aerodynamic Damping and Compressibility Effects*. Annual Review of Fluid Mechanics **47** (1), 479–505.
doi: 10.1146/annurev-fluid-010814-013632 — Cited on page 4.

Cossu, C. and Morino, L. (2000). *On the instability of a spring-mounted circular cylinder in a viscous flow at low Reynolds numbers*. Journal of Fluids and Structures **14** (2), 183–196.
doi: 10.1006/jfls.1999.0261 — Cited on pages 12 and 142.

Cottet, G.-H. and Koumoutsakos, P. D. (2000). *Vortex Methods: Theory and Practice*. Cambridge University Press, Cambridge, 1st edition.
ISBN: 978-0-511-52644-2 — Cited on page 45.

Courant, R. (1943). *Variational methods for the solution of problems of equilibrium and vibrations*. Bulletin of the American Mathematical Society **49**, 1–23.
doi: 10.1090/s0002-9904-1943-07818-4 — Cited on page 50.

Crivellini, A. and D'Alessandro, V. (2014). *Spalart–Allmaras model apperent transition and RANS simulations of laminar separation bubbles on airfoils*. International Journal of Heat and Fluid Flow **47**, 70–83.
doi: 10.1016/j.ijheatfluidflow.2014.03.002 — Cited on pages 224, 225, and 230.

Crivellini, A., D'Alessandro, V. and Bassi, F. (2013). *A Spalart–Allmaras turbulence model implementation in a discontinuous Galerkin solver for incompressible flows*. Journal of Computational Physics **241**, 388–415.
doi: 10.1016/j.jcp.2012.12.038 — Cited on pages 224 and 225.

Crouch, J. D. and Herbert, Th. (1993). *A note on the calculation of Landau constants*. Physics of Fluids A: Fluid Dynamics **5** (1), 283–285.
doi: 10.1063/1.858785 — Cited on page 124.

Curtiss, C. F. and Hirschfelder, J. O. (1952). *Integration of Stiff Equations*. Proceedings of the National Academy of Sciences **38** (3), 235–243.
doi: 10.1073/pnas.38.3.235 — Cited on pages 55, 58, and 61.

D'Alessandro, V., Garbuglia, F., Montelpare, S. and Zoppi, A. (2017a). *A Spalart–Allmaras local correlation–based transition model for Thermo–fuid dynamics*. Journal of Physics: Conference Series **923**, 012029.
doi: 10.1088/1742-6596/923/1/012029 — Cited on page 226.

D'Alessandro, V., Montelpare, S., Ricci, R. and Zoppi, A. (2017b). *Numerical modeling of the flow over wind turbine airfoils by means of Spalart–Allmaras local correlation based transition model*. Energy **130**, 402–419.
doi: 10.1016/j.energy.2017.04.134. See Corrigendum on doi: 10.1016/j.energy.2018.07.073. — Cited on page 226.

Datta, S. (2017). *Bifurcations of a Van der Pol oscillator in a double well*. arXiv: Chaotic Dynamics
URL: https://arxiv.org/pdf/1709.10126.pdf — Cited on page 180.

Davis, T. A. (2002). *A Column Pre-Ordering Strategy for the Unsymmetric-Pattern Multifrontal Method*. ACM Transactions on Mathematical Software **30** (2), 165–195.
doi: 10.1145/992200.992205 — Cited on pages 116 and 211.

Deng, J., Sun, L. and Shao, X. (2017). *Floquet stability analysis in the wake of a NACA0015 airfoil at post-stall angles of attack*. Physics of Fluids **29** (9), 094104.
doi: 10.1063/1.5003578 — Cited on pages 84, 85, 88, 203, and 218.

Deuflhard, P. (2011). *Newton Methods for Nonlinear Problems: Affine Invariance and Adaptive Algorithms*. Springer-Verlag Berlin Heidelberg, Berlin, 1st edition.
ISBN: 978-3-642-23898-7 — Cited on page 58.

Dimitriadis, G. and Li, J. (2009). *Bifurcation Behavior of Airfoil Undergoing Stall Flutter Oscillations in Low-Speed Wind Tunnel*. AIAA Journal **47** (11), 2577–2596.
doi: 10.2514/1.39571 — Cited on page 4.

Donea, J., Huerta, A., Ponthot, J.-P. and Rodríguez-Ferran, A. (2004). *Arbitrary Lagrangian–Eulerian Methods* **in** Stein, E., Borst, R. and Hughes, T. J. R. (eds) Encyclopedia of Computational Mechanics , John Wiley & Sons, chapter 14. 413–437.
doi: 10.1002/0470091355.ecm009 — Cited on page 17.

Dowell, E. H. (2004). *A Modern Course in Aeroelasticity*, volume 217. Springer, Cham, 5th edition.
ISBN: 978-3-319-09452-6 — Cited on page 43.

Duff, I. S., Erisman, A. M. and Reid, J. K. (2007). *Direct Methods for Sparse Matrices*. Oxford University Press, United Kingdom, 2nd edition.
ISBN: 978-0-198-50838-0 — Cited on page 211.

Duff, I. S. and Scott, J. A. (1993). *Computing Selected Eigenvalues of Sparse Unsymmetric Matrices Using Subspace Iteration*. ACM Transactions on Mathematical Software **19** (2), 137–159.
doi: 10.1145/152613.152614 — Cited on page 117.

Dušek, J., Le Gal, P. and Fraunié, P. (1994). *A numerical and theoretical study of the first Hopf bifurcation in a cylinder wake*. Journal of Fluid Mechanics **264**, 59–80.
doi: 10.1017/S0022112094000583 — Cited on page 71.

Edwards, J. (1979). *Applications of Laplace transform methods to airfoil motion and stability calculations*. In *20th Structures, Structural Dynamics, and Materials Conference*. 465–482.
doi: 10.2514/6.1979-772 — Cited on page 123.

Ekici, K., Djeddi, R., Li, H. and Frankel, J. I. (2020). *Modeling periodic and non-periodic response of dynamical systems using an efficient Chebyshev-based time-spectral approach*. Journal of Computational Physics **417**, 109560.
doi: 10.1016/j.jcp.2020.109560 — Cited on page 204.

ElAwad, Y. A. and ElJack, E. M. (2019). *Numerical investigation of the low-frequency flow oscillation over a NACA-0012 aerofoil at the inception of stall*. International Journal of Micro Air Vehicles **11**, 1–17.
doi: 10.1177/1756829319833687 — Cited on page 8.

Elimelech, Y., Arieli, R. and Iosilevskii, G. (2005). *On the Onset of Transition at Low Reynolds Number Flow Over Airfoils*. 4th AIAA Theoretical Fluid Mechanics Meeting.
doi: 10.2514/6.2005-5311 — Cited on page 71.

Elimelech, Y., Arieli, R. and Iosilevskii, G. (2007). *Flow over NACA-0009 and Eppler-61 Airfoils at Reynolds Numbers 5000 and 60,000*. AIAA Journal **45** (10), 2414–2421.
doi: 10.2514/1.22376 — Cited on page 71.

Elston, J. R., Sheridan, J. and Blackburn, H. M. (2004). *Two-dimensional Floquet stability analysis of the flow produced by an oscillating circular cylinder in quiescent fluid*. European Journal of Mechanics - B/Fluids **23** (1), 99–106.
doi: 10.1016/j.euromechflu.2003.05.002 — Cited on page 13.

Eppler, R. (1990). *Airfoil Design and Data*. Springer, Berlin, Heidelberg, 1st edition.
ISBN: 978-3-540-52505-9 — Cited on page 208.

Eymard, R., Gallouët, T. and Herbin, R. (2000). *Finite volume methods*. In *Solution of Equation in $\mathbb{R}^n$ (Part 3), Techniques of Scientific Computing (Part 3)*, Elsevier, volume 7 of *Handbook of Numerical Analysis*. 713–1018 — Cited on page 45.

Fabre, D., Citro, V., Ferreira Sabino, D., Bonnefis, P., Sierra, J., Giannetti, F. and Pigou, M. (2019a). *A Practical Review on Linear and Nonlinear Global Approaches to Flow Instabilities*. Journal of Fluid Mechanics **70** (6), 060802.
doi: 10.1115/1.4042737 — Cited on pages 72, 74, and 215.

Fabre, D., Longobardi, R., Bonnefis, P. and Luchini, P. (2019b). *The acoustic impedance of a laminar viscous jet through a thin circular aperture*. Journal of Fluid Mechanics **864**, 5–44.
doi: 10.1017/jfm.2018.1008 — Cited on page 120.

Fabre, D., Longobardi, R., Citro, V. and Luchini, P. (2020). *Acoustic impedance and hydrodynamic instability of the flow through a circular aperture in a thick plate*. Journal of Fluid Mechanics **885**, A11.
doi: 10.1017/jfm.2019.953 — Cited on page 120.

Fiordilino, J. A., Layton, W. and Rong, Y. (2018). *An efficient and modular grad–div stabilization*. Computer Methods in Applied Mechanics and Engineering **335**, 327–346.
doi: 10.1016/j.cma.2018.02.023 — Cited on page 55.

Floquet, G. (1883). *Sur les équations différentielles linéaires à coefficients périodiques*. Annales scientifiques de l'École Normale Supérieure **2**, 47–88.
doi: 10.24033/asens.220 — Cited on pages 34 and 84.

Förster, Ch., Wall, W. A. and Ramm, E. (2009). *Stabilized finite element formulation for incompressible flow on distorted meshes*. International Journal for Numerical Methods in Fluids **60** (10), 1103–1126.
doi: 10.1002/fld.1923 — Cited on page 54.

Franca, L. P. and Frey, S. L. (1992). *Stabilized finite element methods: II. The incompressible Navier–Stokes equations*. Computer Methods in Applied Mechanics and Engineering **99** (2), 209–233.
doi: 10.1016/0045-7825(92)90041-H — Cited on pages 53 and 55.

Franca, L. P. and Hughes, T. J. R. (1988). *Two classes of mixed finite element methods*. Computer Methods in Applied Mechanics and Engineering **69** (1), 89–129.
doi: 10.1016/0045-7825(88)90168-5 — Cited on page 55.

Franceschini, L. (2019). *Steady-State Harmonic Analysis of Nonlinear Networks*. Ph.D. thesis, Université Paris-Saclay (Paris, France) — Cited on pages 54, 224, and 231.

Freeman, J. A. and Roy, C. J. (2014). *Verification and validation of Reynolds-averaged Navier–Stokes turbulence models for external flow*. Aerospace Science and Technology **32** (1), 84–93.
doi: 10.1016/j.ast.2013.11.004 — Cited on page 224.

Frisch, U. (1995). *Turbulence, the Legacy of A. N. Kolmogorov*. Cambridge University Press, Cambridge, 1st edition.
ISBN: 978-0-521-45713-2 — Cited on page 222.

Fung, Y. C. (2008). *An introduction to the theory of aeroelasticity*. Courier Dover Publications, New York, 1st edition.
ISBN: 978-0-486-46936-2 — Cited on page 2.

Furquan, M. and Mittal, S. (2021). *Multiple lock-ins in vortex-induced vibration of a filament*. Journal of Fluid Mechanics **916**, R1.
doi: 10.1017/jfm.2021.209 — Cited on pages 13 and 142.

Galdi, G. P., Mácha, V. and Nečasová, Š. (2019). *On the Motion of a Body with a Cavity Filled with Compressible Fluid*. Arch Rational Mech Anal **232**, 232.
doi: 10.1007/s00205-018-01351-8 — Cited on page 205.

Galdi, G. P., Mácha, V. and Nečasová, Š. (2020). *On weak solutions to the problem of a rigid body with a cavity filled with a compressible fluid, and their asymptotic behavior*. International Journal of Non-Linear Mechanics **121**, 103431.
doi: 10.1016/j.ijnonlinmec.2020.103431 — Cited on page 205.

Gao, C., Zhang, W. and Ye, Z. (2016). *A new viewpoint on the mechanism of transonic single-degree-of-freedom flutter*. Aerospace Science and Technology **52**, 144–156.
doi: 10.1016/j.ast.2016.02.029 — Cited on page 5.

Garrick, I. E. and Reed III, W. H. (1981). *Historical Development of Aircraft Flutter*. Journal of Aircraft **18** (11), 897–912.
doi: 10.2514/3.57579 — Cited on page 1.

Garrick, I. E. and Rubinow, S. I. (1946). *Flutter and oscillating air-force calculations for an airfoil in a two-dimensional supersonic flow*. NACA Technical Note 1158
URL: https://ntrs.nasa.gov/citations/19930081835 — Cited on page 4.

Ghai, A., Lu, C. and Jiao, X. (2018). *A comparison of preconditioned Krylov subspace methods for large-scale nonsymmetric linear systems*. Numerical Linear Algebra with Applications **26** (1), e2215.
doi: 10.1002/nla.2215 — Cited on page 213.

Giannetti, F. and Luchini, P. (2007). *Structural sensitivity of the first instability of the cylinder wake*. Journal of Fluid Mechanics **581**, 167–197.
doi: 10.1017/S0022112007005654 — Cited on page 216.

Girault, V. and Raviart, P.-A. (1979). *Finite Element Approximation of the Navier–Stokes Equations*. Springer-Verlag Heidelberg, Berlin, 1st edition.
ISBN: 978-3-540-09557-6 — Cited on page 45.

Glauert, H. (1930). *The force and moment on an oscillating aerofoil* **in** Vorträge aus dem Gebiete der Aerodynamik und verwandter Gebiete: Aachen 1929. Springer Berlin Heidelberg, 88–95
doi: 10.1007/978-3-662-33791-2_16 — Cited on pages 1 and 4.

Govardhan, R. and Williamson, C. H. K. (2000). *Modes of vortex formation and frequency response of a freely vibrating cylinder*. Journal of Fluid Mechanics **420**, 85–130.
doi: 10.1017/S0022112000001233 — Cited on page 171.

Guermond, J. L., Minev, P. and Shen, J. (2006). *An overview of projection methods for incompressible flows*. Computer Methods in Applied Mechanics and Engineering **195** (44), 6011–6045.
doi: 10.1016/j.cma.2005.10.010 — Cited on pages 47 and 56.

Habetler, G. J. and Wachspress, E. L. (1961). *Symmetric successive overrelaxation in solving diffusion difference equations*. Mathematics of Computation **15**, 356–362.
doi: 10.1090/S0025-5718-1961-0129139-9 — Cited on page 213.

Halfman, R. L., Johnson, H. C. and Haley, S. M. (1951). *Evaluation of high-angle attack aerodynamic-derivative data and stall-flutter prediction techniques*. NACA Technical Note 2533
URL: https://apps.dtic.mil/sti/citations/ADA380217 — Cited on page 4.

Hancock, G. J., Wright, J. R. and Simpson, A. (1985). *On the teaching of the principles of wing flexure-torsion flutter*. The Aeronautical Journal **89** (888), 285–305.
doi: 10.1017/S0001924000015050 — Cited on page 3.

Hansbo, P. and Szepessy, A. (1990). *A velocity-pressure streamline diffusion finite element method for the incompressible Navier–Stokes equations*. Computer Methods in Applied Mechanics and Engineering **84** (2), 175–192.
doi: 10.1016/0045-7825(90)90116-4 — Cited on pages 53 and 55.

Hansen, M. O. L., Sørensen, J. N., Voutsinas, S., Sørensen, N. and Madsen, H. Aa. (2006). *State of the art in wind turbine aerodynamics and aeroelasticity*. Progress in Aerospace Sciences **42** (4), 285–330.
doi: 10.1016/j.paerosci.2006.10.002 — Cited on page 4.

He, W., Gioria, R. S., Pérez, J. M. and Theofilis, V. (2017). *Linear instability of low Reynolds number massively separated flow around three NACA airfoils*.

Journal of Fluid Mechanics **811**, 701–741.
doi: 10.1017/jfm.2016.778 — Cited on page 84.

Hecht, F. (1998). *The Mesh Adapting Software: BAMG*. INRIA Report
URL: https://scirp.org/reference/referencespapers.aspx?referenceid=3042507 — Cited on page 49.

Hecht, F. (2012). *New development in FreeFem++*. Journal of Numerical Mathematics **20** (3-4), 251–265.
doi: 10.1515/jnum-2012-0013 — Cited on pages 49 and 119.

Hendrickson, B. and Leland, R. (1994). *The Chaco user's guide, version 2.0*. Technical report, Tech. Report SAND94–2692 Sandia National Laboratories, Albuquerque, NM.
URL: https://www.researchgate.net/publication/264824986_The_Chaco_User's_Guide_Version_20 — Cited on page 50.

Hernandez, V., Roman, J. E. and Vidal, V. (2005). *SLEPc: A scalable and flexible toolkit for the solution of eigenvalue problems*. ACM Trans. Math. Software **31** (3), 351–362.
doi: 10.1145/1089014.1089019 — Cited on pages 117 and 119.

Hestenes, M. R. and Stiefel, E. (1952). *Methods of conjugate gradients for solving linear systems*. Journal of research of the National Bureau of Standards **49** (5), 409–436.
doi: 10.6028/jres.049.044 — Cited on page 212.

Hinze, J. O. (1975). *Turbulence*. McGraw-Hill, New York, 2nd edition.
ISBN: 978-0-070-29037-2 — Cited on page 222.

Hoarau, Y., Braza, M., Ventikos, Y., Faghani, D. and Tzabiras, G. (2003). *Organized modes and the three-dimensional transition to turbulence in the incompressible flow around a NACA0012 wing*. Journal of Fluid Mechanics **496**, 63–72.
doi: 10.1017/S0022112003006530 — Cited on page 85.

Hood, P. and Taylor, C. (1974). *Navier–Stokes equations using mixed interpolation* **in** Oden, J. T., Zienkiewicz, O. C., Gallagher, R. H. and Taylor. C. (eds) Finite Element Methods in Flow Problems , Huntsville Press, University of Alabama. 121–132 — Cited on page 51.

Horton, H. (1968). *Laminar separation in two and three dimensional incompressible flow*. Ph.D. thesis, University of London (London, England) — Cited on page 6.

Hosseini, S. M., Vinuesa, R., Schlatter, P., Hanifi, A. and Henningson, D. S. (2016). *Direct numerical simulation of the flow around a wing section at moderate Reynolds number*. International Journal of Heat and Fluid Flow **61**, 117–128.
doi: 10.1016/j.ijheatfluidflow.2016.02.001 — Cited on page 89.

Hughes, T. J. R. and Franca, L. P. (1987). *A new finite element formulation for computational fluid dynamics: VII. The stokes problem with various well-posed boundary conditions: Symmetric formulations that converge for all velocity/pressure spaces*. Computer Methods in Applied Mechanics and Engineering **65** (1), 85–96.
doi: 10.1016/0045-7825(87)90184-8 — Cited on page 52.

Hughes, T. J. R., Franca, L. P. and Balestra, M. (1986). *A new finite element formulation for computational fluid dynamics: V. Circumventing the babuška-brezzi condition: a stable Petrov-Galerkin formulation of the stokes problem accommodating equal-order interpolations*. Computer Methods in Applied Mechanics and Engineering **59** (1), 85–99.
doi: 10.1016/0045-7825(86)90025-3 — Cited on page 52.

Hunt, J. C. R., Wray, A. A. and Moin, P. (1988). *Eddies, stream, and convergence zones in turbulent flows*. Technical report, Center for Turbulence Research Report CTR-S88, pp. 193–208.
URL: https://ntrs.nasa.gov/citations/19890015184 — Cited on page 89.

Hussain, A. K. M. F. and Reynolds, W. C. (1970). *The mechanics of an organized wave in turbulent shear flow*. Journal of Fluid Mechanics **41** (2), 241–258.
doi: 10.1017/S0022112070000605 — Cited on page 26.

Iorio, M. C., González, L. M. and Ferrer, E. (2014). *Direct and adjoint global stability analysis of turbulent transonic flows over a NACA0012 profile*. International Journal for Numerical Methods in Fluids **76** (3), 147–168.
doi: https://doi.org/10.1002/fld.3929 — Cited on page 116.

Jaffe, A. M. (2006). *The Millennium Grand Challenge in Mathematics*. Notices of the American Mathematical Society **53** (6), 652–660.
URL: https://www.ams.org/notices/200606/fea-jaffe.pdf — Cited on page 45.

Jallas, D. (2018). *Stabilité d'écoulements de sillages périodiques générés par des ailes battantes*. Ph.D. thesis, École Doctorale Mécanique, Énergétique, Génie Civil et Procédés (Toulouse, France) — Cited on pages 79 and 205.

Jallas, D., Marquet, O. and Fabre, D. (2017). *Linear and nonlinear perturbation analysis of the symmetry breaking in time-periodic propulsive wakes*. Physical Review E **95**, 063111.
doi: 10.1103/PhysRevE.95.063111 — Cited on pages 13 and 142.

Jeong, J. and Hussain, F. (1995). *On the identification of a vortex*. Journal of Fluid Mechanics **285**, 69–94.
doi: 10.1017/S0022112095000462 — Cited on pages 89 and 106.

Jones, B. M. (1934). *Stalling*. The Journal of the Royal Aeronautical Society **38** (285), 753–770.
doi: 10.1017/S0368393100109782 — Cited on page 7.

Jones, K. D. and Platzer, M. F. (1997). *Airfoil geometry and flow compressibility effects on wings and blade flutter*. 36th AIAA Aerospace Sciences Meeting and Exhibit
doi: 10.2514/6.1998-517 — Cited on page 4.

Jones, L. E., Sandberg, R. D. and Sandham, N. D. (2006). *Direct numerical simulation of the flow around an airfoil with unsteady wake*. Proceedings of European Conference on Computational Fluid Dynamics (ECCOMAS CFD) , 1–18
URL: https://citeseerx.ist.psu.edu/viewdoc/download?doi=10.1.1.551.7890&rep=rep1&type=pdf — Cited on page 89.

Jones, L. E., Sandberg, R. D. and Sandham, N. D. (2008). *Direct numerical simulations of forced and unforced separation bubbles on an airfoil at incidence*. Journal of Fluid Mechanics **602**, 175–207.
doi: 10.1017/S0022112008000864 — Cited on pages 7, 85, and 89.

Jones, R. T. (1940). *The unsteady lift of a wing of finite aspect ratio*. NACA Technical Report 681
URL: https://ntrs.nasa.gov/citations/19930091758 — Cited on page 123.

Jones, W. P. and Launder, B. E. (1972). *The prediction of laminarization with a two-equation model of turbulence*. International Journal of Heat and Mass Transfer **15** (2), 301–314.
doi: 10.1016/0017-9310(72)90076-2 — Cited on page 223.

Kakkavas, C. (1998). *Computational Investigation of Subsonic Torsional Airfoil Flutter*. Ph.D. thesis, Naval Postgraduate School (California, USA) — Cited on page 4.

Karniadakis, G. and Sherwin, S. (2013). *Spectral/hp Element Methods for Computational Fluid Dynamics*. Oxford University Press, Oxford, 2nd edition.
ISBN: 978-0-198-52869-2 — Cited on page 51.

Karpel, M. (1981). *Design for active and passive flutter suppression and gust alleviation*. NACA CR-3482
URL: https://ntrs.nasa.gov/citations/19820005274 — Cited on page 123.

Karpel, M. (1982). *Design for Active Flutter Suppression and Gust Alleviation Using State-Space Aeroelastic Modeling*. Journal of Aircraft **19** (3), 221–227.
doi: 10.2514/3.57379 — Cited on page 123.

Karypis, G. and Kumar, V. (1998). *A Fast and High Quality Multilevel Scheme for Partitioning Irregular Graphs*. SIAM Journal on Scientific Computing **20** (1), 359–392.
doi: 10.1137/S1064827595287997 — Cited on page 50.

Kean, K., Neilan, M. and Schneier, M. (2021). *The Scott-Vogelius Method for Stokes Problem on Anisotropic Meshes*.
arXiv: https://arxiv.org/abs/2109.14780 — Cited on page 55.

Keane, A. J., Sóbester, A. and Scanlan, J. P. (2017). *Small Unmanned Fixed-wing Aircraft Design*. John Wiley & Sons, Ltd, United Kingdom, 1st edition.
ISBN: 978-1-119-40630-3 — Cited on page 149.

Kelvin, L. W. T. (1887). *XXI. Stability of fluid motion – Rectilineal motion of viscous fluid between two parallel planes*. The London, Edinburgh, and Dublin Philosophical Magazine and Journal of Science **24** (147), 188–196.
doi: 10.1080/14786448708628078 — Cited on pages 12 and 115.

Kiergan, N. B. and Tomamichel, J. J. (1942). *A study of flutter in one degree of freedom*. Ph.D. thesis, California Institute of Technology (California, USA).
doi: 10.7907/NX9K-JT57 — Cited on page 4.

Kim, D., Kim, Y., Li, J., Wilson, R. V., Martin, J. E. and Carrica, P. M. (2019). *Boundary Layer Transition Models for Naval Applications: Capabilities and Limitations*. Journal of Ship Research **63** (04), 294–307.
doi: 10.5957/JOSR.09180066 — Cited on page 226.

Knoll, D. A. and Keyes, D. E. (2004). *Jacobian-free Newton–Krylov methods: a survey of approaches and applications*. Journal of Computational Physics **193** (2), 357–397.
doi: 10.1016/j.jcp.2003.08.010 — Cited on page 212.

Kobel'kov, G. M. (1995). *On solving the Navier–Stokes equations at large Reynolds numbers*. Russian Journal of Numerical Analysis and Mathematical Modelling **10** (1), 33–40.
doi: doi:10.1515/rnam.1995.10.1.33 — Cited on page 55.

Kojima, R., Nonomura, T., Oyama, A. and Fujii, K. (2013). *Large-Eddy Simulation of Low-Reynolds-Number Flow Over Thick and Thin NACA Airfoils*. Journal of Aircraft **50** (1), 187–196.
doi: 10.2514/1.C031849 — Cited on page 8.

Kolář, V. (2007). *Vortex identification: New requirements and limitations*. International Journal of Heat and Fluid Flow **28** (4), 638–652.
doi: 10.1016/j.ijheatfluidflow.2007.03.004 — Cited on page 89.

Kou, J., Zhang, W., Liu, Y. and Li, X. (2017). *The lowest Reynolds number of vortex-induced vibrations*. Physics of Fluids **29** (4), 041701.
doi: 10.1063/1.4979966 — Cited on pages 13 and 142.

Kračmar, S., Nečasová, Š. and Novotný, A. (2014). *The motion of a compressible viscous fluid around rotating body*. Ann Univ Ferrara **60**, 189–208.
doi: 10.1007/s11565-014-0212-5 — Cited on page 205.

Kuznetsov, Y. A. (2006). *Elements of Applied Bifurcation Theory*. Springer New York, NY, 1st edition.
ISBN: 978-0-387-21906-6 — Cited on page 175.

Lambourne, N. C. (1968). *Flutter in one degree of freedom* **in** Pike, E. C. (eds) Manual on Aeroelasticity , AGARD Report No. 578; Part V, chapter 5. 1–61 — Cited on page 5.

Lanczos, C. (1950). *An iteration method for the solution of the eigenvalue problem of linear differential and integral operators*. Journal of research of the National Bureau of Standards **45** (4), 255–282.
doi: 10.6028/jres.045.026 — Cited on page 117.

Landau, L. D. and Lifshitz, E. M. (1987). *Fluid Mechanics, Second Edition: Volume 6 (Course of Theoretical Physics)*. Pergamon Press, United Kingdom, 2nd edition.
ISBN: 978-0-750-62767-2 — Cited on pages 18 and 22.

Langtry, R. B. and Menter, F. R. (2009). *Correlation-Based Transition Modeling for Unstructured Parallelized Computational Fluid Dynamics Codes*. AIAA Journal **47** (12), 2894–2906.
doi: 10.2514/1.42362 — Cited on page 226.

Langtry, R. B., Menter, F. R., Likki, S. R., Suzen, Y. B., Huang, P. G. and Völker, S. (2006). *A Correlation-Based Transition Model Using Local Variables–Part II: Test Cases and Industrial Applications*. Journal of Turbomachinery **128** (3), 423–432.
doi: 10.1115/1.2184353 — Cited on page 226.

Lapointe, S. and Dumas, G. (2011). *Improved Numerical Simulations of Self-Sustained Oscillations of a NACA0012 with Transition Modeling*. In *41st AIAA Fluid Dynamics Conference and Exhibit*. 1–15.
doi: 10.2514/6.2011-3258 — Cited on pages 182 and 183.

Lee, B. H. K., Jiang, L. Y. and Wong, Y. S. (1999). *Flutter of an airfoil with a cubic restoring force*. Journal of Fluids and Structures **13** (1), 75–101.
doi: 10.1006/jfls.1998.0190 — Cited on page 3.

Lee, S.-J. and Jang, Y.-G. (2005). *Control of flow around a NACA 0012 airfoil with a micro-riblet film*. Journal of Fluids and Structures **20** (5), 659–672.
doi: 10.1016/j.jfluidstructs.2005.03.003 — Cited on page 96.

Lehmkuhl, O., Rodríguez, I., Borrell, R. and Oliva, A. (2013). *Low-frequency unsteadiness in the vortex formation region of a circular cylinder*. Physics of Fluids **25** (8), 085109.
doi: 10.1063/1.4818641 — Cited on page 92.

Lehoucq, R. B. and Sorensen, D. C. (1996). *Deflation Techniques for an Implicitly Restarted Arnoldi Iteration*. SIAM Journal on Matrix Analysis and Applications **17** (4), 789–821.
doi: 10.1137/S0895479895281484 — Cited on page 117.

Lei, J., Zhang, J. and Niu, J. (2020). *Effect of active oscillation of local surface on the performance of low Reynolds number airfoil*. Aerospace Science and Technology **99**, 105774.
doi: 10.1016/j.ast.2020.105774 — Cited on page 7.

Lesshafft, L. (2017). *Artificial eigenmodes in truncated flow domains*. Theoretical and Computational Fluid Dynamics **32**, 245–262.
doi: 10.1007/s00162-017-0449-6 — Cited on page 73.

Li, S. and Liu, W. K. (2002). *Meshfree and particle methods and their applications*. Applied Mechanics Reviews **55** (1), 1–34.
doi: 10.1115/1.1431547 — Cited on page 45.

Li, X. S. (2005). *An Overview of SuperLU: Algorithms, Implementation, and User Interface*. ACM Transactions on Mathematical Software **31** (3), 302–325.
doi: 10.1145/1089014.1089017 — Cited on pages 116 and 211.

Loiseau, J.-Ch., Bucci, M. A., Cherubini, S. and Robinet, J.-Ch. (2018). *Time-Stepping and Krylov Methods for Large-Scale Instability Problems* **in** Gelfgat A. (eds) Computational Modelling of Bifurcations and Instabilities in Fluid Dynamics. Computational Methods in Applied Sciences , Springer, Cham, volume 50, chapter 2. 33–73.
doi: 10.1007/978-3-319-91494-7_2 — Cited on page 116.

Lopes, R., Eça, L. and Vaz, G. (2020). *On the Numerical Behavior of RANS-Based Transition Models*. Journal od Fluids Engineering **142** (5), 051503.
doi: 10.1115/1.4045576 — Cited on page 226.

Lorenz, E. N. (1963). *Deterministic Nonperiodic Flow*. Journal of Atmospheric Sciences **20** (2), 130–141.
doi: 10.1175/1520-0469(1963)020<0130:DNF>2.0.CO;2 — Cited on page 168.

Lube, G. and Tobiska, L. (1990). *A Nonconforming Finite Element Method of Streamline Diffusion Type for the Incompressible Navier–Stokes Equations*. Journal of Computational Mathematics **8** (2), 147–158.
URL: http://www.jstor.org/stable/43692474 — Cited on page 53.

Luhar, M., Sharma, A. S. and McKeon, B. J. (2015). *A framework for studying the effect of compliant surfaces on wall turbulence*. Journal of Fluid Mechanics **768**, 415–441.
doi: 10.1017/jfm.2015.85 — Cited on page 204.

Marquet, O., Leontini, J. S., Zhao, J. and Thompson, M. C. (2022). *Hysteresis of two-dimensional flows around a NACA0012 airfoil at Re=5000 and linear analyses of their mean flow.* International Journal of Heat and Fluid Flow **94**, 108920.
doi: 10.1016/j.ijheatfluidflow.2021.108920 — Cited on pages 80 and 171.

Mavriplis, D. J. and Yang, Z. (2011). *Time Spectral Method for Periodic and Quasi-Periodic Unsteady Computations on Unstructured Meshes*. Mathematical Modelling of Natural Phenomena **6** (3), 213–236.
doi: 10.1051/mmnp/20116309 — Cited on page 204.

McCloughan, J. and Suslov, S. A. (2020). *Linear stability and saddle-node bifurcation of electromagnetically driven electrolyte flow in an annular layer*. Journal of Fluid Mechanics **887**, A23.
doi: 10.1017/jfm.2020.29 — Cited on page 124.

McCullough, G. B. and Gault, D. E. (1951). *Examples of Three Representative Types of Airfoil-section Stall at Low Speed*. NACA Technical Note 2502
URL: https://ntrs.nasa.gov/citations/19930083422 — Cited on page 7.

McGhee, R. J., Walker, B. S. and Millard, B. F. (1988). *Experimental Results for Eppler 387 Airfoil at low Re numbers in Langley Low Turbulence Pressure Tunnel*. NASA Technical Report No. 4062
URL: https://ntrs.nasa.gov/citations/19890001471 — Cited on page 230.

Medida, S. (2014). *Correlation-based Transition Modeling for External Aerodynamic Flows*. Ph.D. thesis, University of Maryland (Maryland, USA) — Cited on page 226.

Medida, S. and Baeder, J. D. (2011). *Application of the Correlation-based γ–$Re_{\theta t}$ Transition Model to the Spalart–Allmaras Turbulence Model*. In *20th AIAA Computational Fluid Dynamics Conference*. 1–21.
doi: 10.2514/6.2011-3979 — Cited on page 226.

Meirovitch, L. (2001). *Fundamentals of Vibrations*. McGraw-Hill, Boston, USA, 1st edition.
ISBN: 978-0-071-18174-7 — Cited on page 29.

Meliga, P. and Chomaz, J.-M. (2011). *An asymptotic expansion for the vortex-induced vibrations of a circular cylinder*. Journal of Fluid Mechanics **671**,

137–167.
doi: 10.1017/S0022112010005550 — Cited on pages 13 and 142.

Menon, K. and Mittal, R. (2021a). *On the initiation and sustenance of flow-induced vibration of cylinders: insights from force partitioning*. Journal of Fluid Mechanics **907**, A37.
doi: 10.1017/jfm.2020.854 — Cited on page 104.

Menon, K. and Mittal, R. (2021b). *Significance of the strain-dominated region around a vortex on induced aerodynamic loads*. Journal of Fluid Mechanics **918**, R3.
doi: 10.1017/jfm.2021.359 — Cited on page 106.

Menter, F. R. (1993). *Zonal Two Equation k-w Turbulence Models For Aerodynamic Flows*. In *23rd Fluid Dynamics, Plasmadynamics, and Lasers Conference*. 1–16.
doi: 10.2514/6.1993-2906 — Cited on page 223.

Menter, F. R. (1994). *Two-equation eddy-viscosity turbulence models for engineering applications*. AIAA Journal **32** (8), 1598–1605.
doi: 10.2514/3.12149 — Cited on page 223.

Menter, F. R., Langtry, R. B., Likki, S. R., Suzen, Y. B., Huang, P. G. and Völker, S. (2006). *A Correlation-Based Transition Model Using Local Variables–Part I: Model Formulation*. Journal of Turbomachinery **128** (3), 413–422.
doi: 10.1115/1.2184352 — Cited on page 226.

Menter, F. R., Smirnov, P. E., Liu, T. and Avancha, R. (2015). *A One-Equation Local Correlation-Based Transition Model*. Flow, Turbulence and Combustion **95**, 583–619.
doi: 10.1007/s10494-015-9622-4 — Cited on page 226.

Mettot, C., Sipp, D. and Bézard, H. (2014). *Quasi-laminar stability and sensitivity analyses for turbulent flows: Prediction of low-frequency unsteadiness and passive control*. Physics of Fluids **26** (4), 045112.
doi: 10.1063/1.4872225 — Cited on pages 234 and 236.

Micheletti, S., Perotto, S. and Picasso, M. (2003). *Stabilized Finite Elements on Anisotropic Meshes: A Priori Error Estimates for the Advection-Diffusion and the Stokes Problems*. SIAM Journal on Numerical Analysis **41** (3), 1131–1162.
doi: 10.1137/S0036142902403759 — Cited on page 54.

Mittal, R. and Iaccarino, G. (2005). *Immersed Boundary Methods*. Annual Review of Fluid Mechanics **37** (1), 239–261.
doi: 10.1146/annurev.fluid.37.061903.175743 — Cited on page 17.

Mittal, S. (2000). *On the performance of high aspect ratio elements for incompressible flows*. Computer Methods in Applied Mechanics and Engineering **188** (1), 269–287.
doi: 10.1016/S0045-7825(99)00152-8 — Cited on page 54.

Mougin, G. and Magnaudet, J. (2002). *The generalized Kirchhoff equations and their application to the interaction between a rigid body and an arbitrary time-dependent viscous flow*. International Journal of Multiphase Flow **28** (11), 1837–1851.
doi: 10.1016/S0301-9322(02)00078-2 — Cited on pages 17 and 22.

Moulin, J. (2020). *On the flutter bifurcation in laminar flows: linear and nonlinear modal methods*. Ph.D. thesis, École Doctorale de l'Institut Polytechnique de Paris (Paris, France) — Cited on pages 45 and 205.

Moulin, J. and Marquet, O. (2021). *Flow-induced instabilities of springs-mounted plates in viscous flows: A global stability approach*. Physics of Fluids **33** (3), 034133.
doi: 10.1063/5.0038368 — Cited on pages 13 and 142.

Moulin, J. and Marquet, O. (2022). *Hard and soft flutter of thin plates in laminar incompressible flows: weakly and strongly nonlinear analyses*. To be published
URL: https://w3.onera.fr/erc-aeroflex/sites/w3.onera.fr.erc-aeroflex/files/docs/paper/moulinmarquet-jfm2020-nonlinearflutter.pdf — Cited on page 3.

Mueller, T. J. (1951). *Low Reynolds Number Vehicles*. AGARDograph No. 288
URL: https://apps.dtic.mil/sti/citations/ADA153233 — Cited on pages 6 and 141.

Mueller, T. J. and Batill, S. M. (1982). *Experimental Studies of Separation on a Two-Dimensional Airfoil at Low Reynolds Numbers*. AIAA Journal **20** (4), 457–463.
doi: 10.2514/3.51095 — Cited on pages 8, 9, and 79.

Mura, R. and Çakmakçıoğlu, S. Ç. (2020). *A Revised One-Equation Transitional Model for External Aerodynamics - Part I: Theory, Validation and Base Cases*. In *AIAA Aviation 2020 Forum*. 1–28.
doi: 10.2514/6.2020-2714 — Cited on page 226.

Málek, J. and Strakoš, Z. (2015). *Preconditioning and the Conjugate Gradient Method in the Context of Solving PDEs*. SIAM, Philadelphia, Pennsylvania, 1st edition.
ISBN: 978-1-611-97383-9 — Cited on page 57.

Navier, C. L. M. H. (1827). *Mémoire sur les lois d'écoulement des fluides*. Mémoires de l'Académie des Sciences de l'Institut de France **6**, 389–440 — Cited on page 19.

Navrose and Mittal, S. (2016). *Lock-in in vortex-induced vibration*. Journal of Fluid Mechanics **794**, 565–594.
doi: 10.1017/jfm.2016.157 — Cited on pages 13 and 142.

Negi, P. S. (2019). *Stability and Transition in Pitching Wings*. Ph.D. thesis, KTH Royal Institute of Technology (Stockholm, Sweden) — Cited on page 142.

Negi, P. S., Hanifi, A. and Henningson, D. S. (2021). *On the onset of aeroelastic pitch-oscillations of a NACA0012 wing at transitional Reynolds numbers*. Journal of Fluids and Structures **105**, 103344.
doi: 10.1016/j.jfluidstructs.2021.103344 — Cited on pages 13, 14, 142, 143, 144, 199, and 201.

Ohtake, T., Nakae, Y. and Motohashi, T. (2007). *Nonlinearity of the Aerodynamic Characteristics of NACA0012 Aerofoil at Low Reynolds Numbers*. Journal of the Japan Society for Aeronautical and Space Sciences **55** (644), 439–445.
doi: 10.2322/jjsass.55.439 — Cited on pages 8, 9, 79, and 101.

Olivier, T. A. (2008). *A High-Order and Adaptive and Discontinuous Galerkin Finite Element Method for the Reynolds-Averaged Navier–Stokes Equations*. Ph.D. thesis, Massachusetts Institute of Technology (Massachusetts, USA) — Cited on page 224.

Olshanskii, M., Lube, G., Heister, T. and Löwe, J. (2009). *Grad–div stabilization and subgrid pressure models for the incompressible Navier–Stokes equations*. Computer Methods in Applied Mechanics and Engineering **198** (49), 3975–3988.
doi: 10.1016/j.cma.2009.09.005 — Cited on page 55.

Olshanskii, M. A. (2002). *A low order Galerkin finite element method for the Navier–Stokes equations of steady incompressible flow: a stabilization issue and iterative methods*. Computer Methods in Applied Mechanics and Engineering **191** (47), 5515–5536.
doi: 10.1016/S0045-7825(02)00513-3 — Cited on page 55.

Olver, P. J. (2014). *Introduction to Partial Differential Equations*. Springer International Publishing, Switzerland, 1st edition.
ISBN: 978-3-319-02098-3 — Cited on page 124.

Owen, P. R. and Klanfer, L. (1955). *On the Laminar Boundary Layer Separation from the Leading edge of a Thin Aerofoil*. Aeronautical Research Council Current Papers Technical Report No. 220
URL: https://reports.aerade.cranfield.ac.uk/bitstream/handle/1826.2/233/arc-cp-0220.pdf?sequence=1&isAllowed=y — Cited on page 7.

Padua, D. (2011). *Encyclopedia of Parallel Computing*. Springer Publishing Company, Incorporated, Boston, MA, 1st edition.
ISBN: 978-0-387-09844-9 — Cited on page 50.

Patil, M. J. and Hodges, D. H. (2004). *On the importance of aerodynamic and structural geometrical nonlinearities in aeroelastic behavior of high-aspect-ratio wings*. Journal of Fluids and Structures **19** (7), 905–915.
doi: 10.1016/j.jfluidstructs.2004.04.012 — Cited on page 4.

Peletan, L., Baguet, S., Torkhani, M. and Jacquet-Richardet, G. (2013). *A comparison of stability computational methods for periodic solution of nonlinear problems with application to rotordynamics*. Nonlinear Dynamics **72**, 3.
doi: 10.1007/s11071-012-0744-0 — Cited on page 213.

Pfister, J.-L., Fabbiane, N. and Marquet, O. (2022). *Global stability and resolvent analyses of laminar boundary-layer flow interacting with viscoelastic patches*. Journal of Fluid Mechanics **937**, A1.
doi: 10.1017/jfm.2022.72 — Cited on page 204.

Pfister, J.-L. and Marquet, O. (2020). *Fluid–structure stability analyses and nonlinear dynamics of flexible splitter plates interacting with a circular cylinder flow*. Journal of Fluid Mechanics **896**, A24.
doi: 10.1017/jfm.2020.284 — Cited on pages 13, 43, and 142.

Pham, K. G. and Suslov, S. A. (2018). *On the definition of Landau constants in amplitude equations away from a critical point*. Royal Society Open

Science **5** (11), 180746.
doi: 10.1098/rsos.180746 — Cited on page 124.

Pironneau, O. (1989). *The Finite Element Methods for Fluids*. Wiley, Paris, 1st edition.
ISBN: 978-0-471-92255-1 — Cited on page 50.

Poirel, D., Harris, Y. and Benaissa, A. (2008). *Self-sustained aeroelastic oscillations of a NACA0012 airfoil at low-to-moderate Reynolds numbers*. Journal of Fluids and Structures **24** (5), 700–719.
doi: 10.1016/j.jfluidstructs.2007.11.005 — Cited on pages 10, 23, 141, 143, 144, 157, 158, 179, 180, 181, 182, 183, 195, and 201.

Poirel, D. and Mendes, F. (2012). *Experimental Investigation of Small Amplitude Self-Sustained Pitch-Heave Oscillations of a NACA0012 Airfoil at Transitional Reynolds Numbers*. 50th AIAA Aerospace Sciences Meeting including the New Horizons Forum and Aerospace Exposition
doi: 10.2514/6.2012-40 — Cited on pages 11 and 158.

Poirel, D. and Mendes, F. (2014). *Experimental small-amplitude self-sustained pitch–heave oscillations at transitional Reynolds numbers*. AIAA Journal **52** (8), 1581–1590.
doi: 10.2514/1.J052541 — Cited on pages 11 and 158.

Poirel, D., Métivier, V. and Dumas, G. (2011). *Computational aeroelastic simulations of self-sustained pitch oscillations of a NACA0012 at transitional Reynolds numbers*. Journal of Fluids and Structures **27** (8), 1262–1277.
doi: 10.1016/j.jfluidstructs.2011.05.009 — Cited on pages 10, 158, and 201.

Pranesh, C., Sivapragasam, M., Deshpande, M. D. and Narahari, H. K. (2019). *Negative lift characteristics of NACA 0012 aerofoil at low Reynolds numbers*. Sādhanā **44** (21), 1–6.
doi: 10.1007/s12046-018-1008-6 — Cited on pages 9 and 79.

Provansal, M., Mathis, C. and Boyer, L. (1987). *Bénard-von Kármán instability: transient and forced regimes*. Journal of Fluid Mechanics **182**, 1–22.
doi: 10.1017/S0022112087002222 — Cited on pages 12, 71, and 72.

Quartapelle, L. and Napolitano, M. (1983). *Force and moment in incompressible flows*. AIAA Journal **21** (6), 911–913.
doi: 10.2514/3.8171 — Cited on page 104.

Quarteroni, A., Sacco, R. and Saleri, F. (1991). *Numerical Mathematics*. Springer, Berlin, 2nd edition.
ISBN: 978-3-540-34658-6 — Cited on pages 56, 58, and 61.

Rannacher, R. (2000). *Finite Element Methods for the Incompressible Navier-Stokes Equations*, Birkhäuser Basel, Basel. 191–293 — Cited on page 45.

Rayleigh, L. (1879). *On the Stability, or Instability, of certain Fluid Motions*. Proceedings of the London Mathematical Society **s1-11** (1), 57–72.
doi: 10.1112/plms/s1-11.1.57 — Cited on pages 12 and 115.

Razak, N. A., Andrianne, T. and Dimitriadis, G. (2011). *Flutter and Stall Flutter of a Rectangular Wing in a Wind Tunnel*. AIAA Journal **49** (10), 2258–2271.
doi: 10.2514/1.J051041 — Cited on page 4.

Reynolds, O. (1883). *XXIX. An experimental investigation of the circumstances which determine whether the motion of water shall be direct or sinuous and of the law of resistance in parallel channels*. Philosophical Transactions of the Royal Society of London **174**, 935–982.
doi: 10.1098/rstl.1883.0029 — Cited on pages 12 and 115.

Reynolds, O. (1895). *IV. On the dynamical theory of incompressible viscous fluids and the determination of the criterion*. Philosophical Transactions of the Royal Society of London. (A.) **186**, 123–164.
doi: 10.1098/rsta.1895.0004 — Cited on page 222.

Reynolds, W. C. and Hussain, A. K. M. F. (1972). *The mechanics of an organized wave in turbulent shear flow. Part 3. Theoretical models and comparisons with experiments*. Journal of Fluid Mechanics **54** (2), 263–288.
doi: 10.1017/S0022112072000679 — Cited on page 26.

Rocard, Y. (1943). *Dynamique générale des vibrations*. Masson & Cie, Paris, France, 1st edition.
ISBN: 978-2-225-30613-6 — Cited on page 3.

Rodríguez, I., Lehmkuhl, O., Borrell, R. and Oliva, A. (2013). *Direct numerical simulation of a NACA0012 in full stall*. International Journal of Heat and Fluid Flow **43**, 194–203.
doi: 10.1016/j.ijheatfluidflow.2013.05.002 — Cited on page 89.

Roger, K. L. (1977). *Airplane Math Modeling Methods for Active Control Design*. AGARD-CP-228 — Cited on page 123.

Roger, K. L., Hodges, G. E. and Felt, L. (1975). *Active Flutter Suppression—A Flight Test Demonstration*. Journal of Aircraft **12** (6), 551–556.
doi: 10.2514/3.59833 — Cited on page 123.

Rolandi, L. V. (2021). *Stabilité des écoulements compressibles à bas nombres de Reynolds*. Ph.D. thesis, École Doctorale Mécanique, Énergétique, Génie Civil et Procédés (Toulouse, France) — Cited on page 216.

Rump, S. M. (2013). *Accurate solution of dense linear systems, part I: Algorithms in rounding to nearest*. Journal of Computational and Applied Mathematics **242**, 157–184.
doi: 10.1016/j.cam.2012.10.010 — Cited on page 211.

Rumsey, C. L. (2007). *Apparent transition behavior of widely-used turbulence models*. International Journal of Heat and Fluid Flow **28** (6), 1460–1471.
doi: 10.1016/j.ijheatfluidflow.2007.04.003 — Cited on pages 225 and 232.

Rumsey, C. L. (2021). *Langley Research Center: Turbulence Modeling Resource*. Accessed: 2021-09-21 — Cited on page 223.

Rumsey, C. L., Pettersson Reif, B. A. and Gatski, T. B. (2006). *Arbitrary Steady-State Solutions with the K-Epsilon Model*. AIAA Journal **44** (7), 1586–1592.
doi: 10.2514/1.18015 — Cited on page 225.

Runyan, H. L. (1951). *Single-degree-of-freedom-flutter calculations for a wing in subsonic potential flow and comparison with an experiment*. NACA Technical Note 2396
URL: https://ntrs.nasa.gov/citations/19930090966 — Cited on pages 4 and 5.

Runyan, H. L., Cunningham, H. J. and Watkins, C. E. (1952). *Theoretical Investigation of Several Types of Single Degree of Freedom Flutter*. Journal of the Aeronautical Sciences **19** (2), 101–110.
doi: 10.2514/8.2171 — Cited on page 4.

Saad, Y. (2003). *Iterative Methods for Sparse Linear Systems*. Society for Industrial and Applied Mathematics, 2nd edition.
ISBN: 978-0-898-71534-7 — Cited on page 212.

Saad, Y. (2011). *Numerical Methods for Large Eigenvalue Problems*. Society for Industrial and Applied Mathematics, 2nd edition.
ISBN: 978-1-611-97072-2 — Cited on pages 117, 213, and 214.

Saad, Y. and Schultz, M. H. (1986). *GMRES: A Generalized Minimal Residual Algorithm for Solving Nonsymmetric Linear Systems*. SIAM Journal on Scientific and Statistical Computing **7** (3), 856–869.
doi: 10.1137/0907058 — Cited on pages 56 and 212.

Sabino, D., Fabre, D., Leontini, J. S. and Lo Jacono, D. (2020). *Vortex-induced vibration prediction via an impedance criterion*. Journal of Fluid Mechanics **890**, A4.
doi: 10.1017/jfm.2020.104 — Cited on pages 13, 120, and 142.

Samuthira Pandi, J. S. and Mittal, S. (2019). *Wake transitions and laminar separation bubble in the flow past an Eppler 61 airfoil*. Physics of Fluids **31** (11), 114102.
doi: 10.1063/1.5113823 — Cited on pages 85, 88, and 217.

Sari, J., Cremonesi, F., Khalloufi, M., Cauneau, F., Meliga, P., Mesri, Y. and Hachem, E. (2018). *Anisotropic adaptive stabilized finite element solver for RANS models*. International Journal for Numerical Methods in Fluids **86** (11), 717–736.
doi: 10.1002/fld.4475 — Cited on pages 54 and 55.

Schmid, P. J. and Henningson, D. S. (2012). *Stability and Transition in Shear Flows*. Springer, New York, NY, 1st edition.
ISBN: 978-1-461-30185-1 — Cited on page 12.

Schmitt, F. G. (2007). *About Boussinesq's turbulent viscosity hypothesis: historical remarks and a direct evaluation of its validity*. Comptes Rendus Mécanique **335** (9), 617–627.
doi: 10.1016/j.crme.2007.08.004 — Cited on page 223.

Scott, L. R. and Vogelius, M. (1985). *Norm estimates for a maximal right inverse of the divergence operator in spaces of piecewise polynomials*. Mathematical Modelling and Numerical Analysis **19**, 111–143.
doi: 10.1051/m2an/1985190101111 — Cited on page 55.

Sears, W. R. (1941). *Some Aspects of Non-Stationary Airfoil Theory and Its Practical Application*. Journal of the Aeronautical Sciences **8** (3), 104–108.
doi: 10.2514/8.10655 — Cited on page 3.

Shan, H., Jiang, L. and Liu, C. (2005). *Direct numerical simulation of flow separation around a NACA 0012 airfoil*. Computers & Fluids **34** (9), 1096–1114.
doi: 10.1016/j.compfluid.2004.09.003 — Cited on page 89.

Shimoyama, K. and Kamisori, K. (2017). *Study of Aerodynamic and Heat-Exhaust Characteristics for a High-Altitude Long-Endurance Unmanned-Aerial-Vehicle Airfoil*. Journal of Aircraft **54** (4), 1317–1327.
doi: 10.2514/1.C033978 — Cited on page 7.

Sierra, J., Fabre, D. and Citro, V. (2020). *Efficient stability analysis of fluid flows using complex mapping techniques*. Computer Physics Communications **251**, 107100.
doi: 10.1016/j.cpc.2019.107100 — Cited on page 217.

Simoncini, V. and Szyld, D. B. (2007). *Recent computational developments in Krylov subspace methods for linear systems*. Numerical Linear Algebra with Applications **14** (1), 1–59.
doi: 10.1002/nla.499 — Cited on page 212.

Sipp, D. and Lebedev, A. (2007). *Global stability of base and mean flows: a general approach and its applications to cylinder and open cavity flows*. Journal of Fluid Mechanics **593**, 333–358.
doi: 10.1017/S0022112007008907 — Cited on page 12.

Sipp, D., Marquet, O., Meliga, P. and Barbagallo, A. (2010). *Dynamics and Control of Global Instabilities in Open-Flows: A Linearized Approach*. Applied Mechanics Reviews **63** (3).
doi: 10.1115/1.4001478 — Cited on pages 115, 116, and 204.

Smilg, B. (1949). *The Instability of Pitching Oscillations of an Airfoil in Subsonic Incompressible Potential Flow*. Journal of the Aeronautical Sciences **16** (11), 691–696.
doi: 10.2514/8.11885 — Cited on page 4.

Sorensen, D. C. (1992). *Implicit Application of Polynomial Filters in a k-Step Arnoldi Method*. SIAM Journal on Matrix Analysis and Applications **13** (1), 357–385.
doi: 10.1137/0613025 — Cited on page 117.

Spalart, P. R. and Allmaras, S. R. (1992). *A one-equation turbulence model for aerodynamic flows*. In 30th Aerospace Sciences Meeting and Exhibit – AIAA Paper
doi: 10.2514/6.1992-439 — Cited on pages 223 and 224.

Spalart, P. R. and Allmaras, S. R. (1994). *A one-equation turbulence model for aerodynamic flows*. Recherche Aerospatiale **1**, 5–21 — Cited on pages 223 and 224.

Spalart, P. R. and Garbaruk, A. V. (2020). *Correction to the Spalart–Allmaras Turbulence Model, Providing More Accurate Skin Friction*. AIAA Journal **58** (5), 1903–1905.
doi: 10.2514/1.J059489 — Cited on page 225.

Sreenivasan, K. R., Strykowski, P. J. and Olinger, D. J. (1987). *Hopf bifurcation, Landau equation, and vortex shedding behind circular cylinders*. In *Forum on Unsteady Flow Separation*. 1–13, provided by the SAO/NASA Astrophysics Data System.
URL: https://ui.adsabs.harvard.edu/abs/1987fufs.proc....1S — Cited on pages 12 and 72.

Stewart, G. W. (2001). *A Krylov–Schur Algorithm for Large Eigenproblems*. SIAM Journal on Matrix Analysis and Applications **23** (3), 601–614.
doi: 10.1137/S0895479800371529 — Cited on page 117.

Stewart, G. W. (2002). *Addendum to "A Krylov–Schur Algorithm for Large Eigenproblems"*. SIAM Journal on Matrix Analysis and Applications **24** (2), 599–601.
doi: 10.1137/S0895479802403150 — Cited on page 117.

Stokes, G. G. (1845). *On the theories of the internal friction of fluids in motion, and of the equilibrium and motion of elastic solids*. Transactions of the Cambridge Philosophical Society **8**, 287–319 — Cited on page 19.

Strikwerda, J. C. (1984). *Finite Difference Methods for the Stokes and Navier–Stokes Equations*. SIAM Journal on Scientific and Statistical Computing **5** (1), 56–68.
doi: 10.1137/0905004 — Cited on page 45.

Stüben, K. (2001). *A review of algebraic multigrid*. Journal of Computational and Applied Mathematics **128** (1), 281–309.
doi: 10.1016/S0377-0427(00)00516-1 — Cited on page 57.

Tammisola, O. (2012). *Oscillatory sensitivity patterns for global modes in wakes*. Journal of Fluid Mechanics **701**, 251–277.
doi: 10.1017/jfm.2012.156 — Cited on page 73.

Tang, D. M. and Dowell, E. H. (1992). *Flutter and stall response of a helicopter blade with structural nonlinearity*. Journal of Aircraft **29** (5), 953–960.
doi: 10.2514/3.46268 — Cited on page 4.

Tani, I. (1964). *Low-speed flows involving bubble separations*. Progress in Aerospace Sciences **5**, 70–103.
doi: 10.1016/0376-0421(64)90004-1 — Cited on page 8.

Tank, J., Smith, L. and Spedding, G. R. (2017a). *On the possibility (or lack thereof) of agreement between experiment and computation of flows over wings at moderate Reynolds number*. Interface Focus **7** (1), 20160076.
doi: 10.1098/rsfs.2016.0076 — Cited on pages 9, 79, and 101.

Tank, J., Smith, L. and Spedding, G. R. (2017b). *Correction to 'On the possibility (or lack thereof) of agreement between experiment and computation of flows over wings at moderate Reynolds number'*. Interface Focus **7** (3), 20170024.
doi: 10.1098/rsfs.2017.0024 — Cited on pages 9, 79, and 101.

Tchoufag, J., Fabre, D. and Magnaudet, J. (2014a). *Global linear stability analysis of the wake and path of buoyancy-driven disks and thin cylinders*. Journal of Fluid Mechanics **740**, 278–311.
doi: 10.1017/jfm.2013.642 — Cited on pages 13 and 142.

Tchoufag, J., Magnaudet, J. and Fabre, D. (2014b). *Linear instability of the path of a freely rising spheroidal bubble*. Journal of Fluid Mechanics **751**, R4.
doi: 10.1017/jfm.2014.340 — Cited on pages 13 and 142.

Tezduyar, T. E., Mittal, S., Ray, S. E. and Shih, R. (1992). *Incompressible flow computations with stabilized bilinear and linear equal-order-interpolation velocity-pressure elements*. Computer Methods in Applied Mechanics and Engineering **95** (2), 221–242.
doi: 10.1016/0045-7825(92)90141-6 — Cited on pages 54 and 231.

Theodorsen, T. (1935). *General Theory of Aerodynamic Instability and the Mechanism of Flutter*. NACA Technical Report No. 496
URL: https://ntrs.nasa.gov/api/citations/19800006788/downloads/19800006788.pdf — Cited on pages 1, 3, 123, and 141.

Theofilis, V. (2003). *Advances in global linear instability analysis of nonparallel and three-dimensional flows*. Progress in Aerospace Sciences **39** (4), 249–315.
doi: 10.1016/S0376-0421(02)00030-1 — Cited on page 115.

Thomas, J. P., Dowell, E. H. and Hall, K. C. (2002). *Nonlinear Inviscid Aerodynamic Effects on Transonic Divergence, Flutter, and Limit-Cycle Oscillations*. AIAA Journal **40** (4), 638–646.
doi: 10.2514/2.1720 — Cited on page 3.

Tran, C. T. and Petot, D. (1980). *Semi-empirical model for the dynamic stall of airfoils in view of the application to the calculation of responses of a helicopter blade in forward flight*. In *Sixth European Rotorcraft and Powered Lift Aircraft Forum*. 1–23, Paper No. 48.
URL: http://hdl.handle.net/20.500.11881/1835 — Cited on page 4.

Tsiloufas, S. P., Gioria, R. S., Meneghini, J. R. and Carmo, B. S. (2009). *Floquet stability analysis of the flow around an airfoil*. 20th International Congress of Mechanical Engineering , 4337
URL: https://www.abcm.org.br/anais/cobem/2009/pdf/COB09-1133.pdf — Cited on page 84.

Tucker, P. G. (2003). *Differential equation-based wall distance computation for DES and RANS*. Journal of Computational Physics **190** (1), 229–248.
doi: 10.1016/S0021-9991(03)00272-9 — Cited on page 225.

Tuckerman, L. S. and Barkley, D. (2000). *Bifurcation Analysis for Timesteppers*. In E. Doedel and L. Tuckerman (editors), *Numerical Methods for Bifurcation Problems and Large-Scale Dynamical Systems*. Springer New York, New York, NY, 453–466 — Cited on page 116.

Témam, R. (1969). *Sur l'approximation de la solution des équations de Navier–Stokes par la méthode des pas fractionnaires (II)*. Archive for Rational Mechanics and Analysis **33**, 377–385.
doi: 10.1007/BF00247696 — Cited on page 56.

Ueda, T. and Dowell, E. H. (1984). *Flutter analysis using nonlinear aerodynamic forces*. Journal of Aircraft **21** (2), 101–109.
doi: 10.2514/3.48232 — Cited on page 3.

van Kan, J. (1986). *A Second-Order Accurate Pressure-Correction Scheme for Viscous Incompressible Flow*. SIAM Journal on Scientific and Statistical Computing **7** (3), 870–891.
doi: 10.1137/0907059 — Cited on page 57.

van Rossum, G. and Drake, F. L. (2009). *Python 3 Reference Manual*. CreateSpace, Scotts Valley, CA.
ISBN: 1-44141-269-7 — Cited on page 208.

Vepa, R. (1977). *Finite state modeling of aeroelastic systems*. NACA CR-2779
URL: https://ntrs.nasa.gov/citations/19770012545 — Cited on page 123.

Volker, J. (2016). *Finite Element Methods for Incompressible Flow Problems*. Springer International Publishing, Cham, 1st edition.
ISBN: 978-3-319-45749-9 — Cited on pages 47 and 51.

von Kármán, Th. and Sears, W. R. (1938). *Airfoil Theory for Non-Uniform Motion*. Journal of the Aeronautical Sciences **5** (10), 379–390.
doi: 10.2514/8.674 — Cited on page 1.

Walters, D. K. and Cokljat, D. (2008). *A Three-Equation Eddy-Viscosity Model for Reynolds-Averaged Navier–Stokes Simulations of Transitional Flow*. Journal od Fluids Engineering **130** (12), 121401.
doi: 10.1115/1.2979230 — Cited on page 226.

Welch, P. (1967). *The use of fast Fourier transform for the estimation of power spectra: A method based on time averaging over short, modified periodograms*. IEEE Transactions on Audio and Electroacoustics **15** (2), 70–73.
doi: 10.1109/TAU.1967.1161901 — Cited on page 94.

White, F. M. (1991). *Viscous Fluid Flow*. McGraw-Hill, 2nd edition.
ISBN: 978-0-070-69712-6 — Cited on page 19.

Wilcox, D. C. (1994). *Turbulence Modeling for CFD*. DCW Industries, Inc., La Canada, 1st edition.
ISBN: 978-0-963-60510-8 — Cited on page 223.

Williamson, C. H. K. (1996a). *Vortex Dynamics in the Cylinder Wake*. Annual Review of Fluid Mechanics **28** (1), 477–539.
doi: 10.1146/annurev.fl.28.010196.002401 — Cited on pages 12 and 84.

Williamson, C. H. K. (1996b). *Three-dimensional wake transition*. Journal of Fluid Mechanics **328**, 345–407.
doi: 10.1017/S0022112096008750 — Cited on page 84.

Williamson, C. H. K. and Govardhan, R. (2008). *A brief review of recent results in vortex-induced vibrations*. Journal of Wind Engineering and Industrial Aerodynamics **96** (6), 713–735.
doi: 10.1016/j.jweia.2007.06.019 — Cited on page 171.

Williamson, C. H. K. and Roshko, A. (1988). *Vortex formation in the wake of an oscillating cylinder*. Journal of Fluids and Structures **2** (4), 355–381.
doi: 10.1016/S0889-9746(88)90058-8 — Cited on page 171.

Winslow, J., Otsuka, H., Govindarajan, B. and Chopra, I. (2018). *Basic Understanding of Airfoil Characteristics at Low Reynolds Numbers (10^4–10^5)*. Journal of Aircraft **55** (3), 1050–1061.
doi: 10.2514/1.C034415 — Cited on page 9.

Xia, T., Dong, H., Yang, L., Liu, S. and Jin, Z. (2021). *Investigation on flow structure and aerodynamic characteristics over an airfoil at low Reynolds number—A review*. AIP Advances **11** (5), 050701.
doi: 10.1063/5.0044717 — Cited on page 8.

Yates Jr., E. C. (1966). *Modified-strip-analysis method for predicting wing flutter at subsonic to hypersonic speeds*. Journal of Aircraft **3** (1), 25–29.
doi: 10.2514/3.43702 — Cited on page 3.

Yildirim, I., Rindt, C. C. M. and van Steenhoven, A. A. (2013). *Mode C flow transition behind a circular cylinder with a near-wake wire disturbance*. Journal of Fluid Mechanics **727**, 30–55.
doi: 10.1017/jfm.2013.230 — Cited on page 84.

Yonemoto, K., Takato, K., Ochi, H. and Fujie, S. (2008). *Kutta Condition Violation in Two-Dimensional NACA0012 Airfoil at Low Reynolds Number*. 26th AIAA Applied Aerodynamics Conference , 1–11
doi: 10.2514/6.2008-6399 — Cited on pages 9 and 79.

Yuan, W., Poirel, D. and Wang, B. (2013). *Simulations of Pitch–Heave Limit-Cycle Oscillations at a Transitional Reynolds Number*. AIAA Journal **51** (7), 1716–1732.
doi: 10.2514/1.J052225 — Cited on pages 11 and 158.

Zhang, C., Hedrick, T. L. and Mittal, R. (2015a). *Centripetal Acceleration Reaction: An Effective and Robust Mechanism for Flapping Flight in Insects*.

PLoS ONE **10** (8), 1–16.
doi: 10.1371/journal.pone.0132093 — Cited on page 104.

Zhang, W., Li, X., Ye, Z. and Jiang, Y. (2015b). *Mechanism of frequency lock-in in vortex-induced vibrations at low Reynolds numbers*. Journal of Fluid Mechanics **783**, 72–102.
doi: 10.1017/jfm.2015.548 — Cited on pages 13 and 142.

Zhu, Y., Su, Y. and Breuer, K. (2020). *Nonlinear flow-induced instability of an elastically mounted pitching wing*. Journal of Fluid Mechanics **899**, A35.
doi: 10.1017/jfm.2020.481 — Cited on page 158.